

UNIVERZITA KARLOVA / CHARLES UNIVERSITY
LÉKAŘSKÁ FAKULTA V PLZNI / FACULTY OF
MEDICINE IN PILSEN



Histologické hodnocení experimentálních modelů
onemocnění jater

Využití metod kvantitativní histologie v hodnocení mikroskopické stavby
jater

Histological evaluation of experimental models of liver
diseases

Application of quantitative histology methods in liver microstructure
evaluation

Dizertační práce/Ph.D. Thesis

Školitel/Advisor: prof. MUDr. Mgr. Zbyněk Tonar, Ph.D.

Konzultantka/Co-advisor: Ing. Petra Kochová, Ph.D.



Plzeň/Pilsen 2022

MUDr. Anna Malečková

Bibliografické informace

Autorka: MUDr. Anna MALEČKOVÁ

Název práce: Histologické hodnocení experimentálních modelů onemocnění jater

Podtitul: Využití metod kvantitativní histologie v hodnocení mikroskopické stavby jater

Jazyk práce: český, anglický

Typ práce: Dizertační práce k získání akademického titulu Ph.D.

Univerzita: Univerzita Karlova

Fakulta: Lékařská fakulta v Plzni

Ústav: Ústav histologie a embryologie

Specializace: Anatomie, histologie, embryologie

Forma studia: prezenční

Školitel: prof. MUDr. et Mgr. Zbyněk Tonar, Ph.D.

Konzultantka: Ing. Petra Kochová, Ph.D.

Počet stran: 242

Klíčová slova: kvantitativní histologie; stereologie; játra; modely jaterních onemocnění

Title: Histological evaluation of experimental models of liver diseases

Subtitle: Application of quantitative histology methods in liver microstructure evaluation

Keywords: quantitative histology; stereology; liver; models of liver diseases

Prohlášení:

Prohlašuji, že jsem závěrečnou práci zpracovala samostatně a že jsem řádně uvedla a citovala všechny použité prameny a literaturu. Současně prohlašuji, že práce nebyla využita k získání jiného nebo stejného titulu.

Souhlasím s trvalým uložením elektronické verze mé práce v databázi systému meziuniverzitního projektu Theses.cz za účelem soustavné kontroly podobnosti kvalifikačních prací.

V Plzni 10. 5. 2022

Anna Malečková

Podpis

Abstrakt

Zvířecí modely jsou hojně využívány při studiu patogeneze a progresu jaterních onemocnění či při vývoji nových strategií jejich terapeutického ovlivnění. Zaměření této dizertační práce na velký zvířecí model, prase domácí, odráží současný trend na poli experimentální medicíny, tedy využití modelů co nejbližších člověku tak, aby byly výsledky experimentů co nejpřesněji přenositelné do humánní medicíny. V rutinní patologické praxi je histologické hodnocení nedílnou součástí procesu stanovení diagnózy a závažnosti jaterního poškození. Analogicky je tedy histopatologické vyšetření tkáně zařazeno do designu experimentálních studií na játrech prasete. Naším cílem bylo aplikovat metody kvalitativního a kvantitativního histologického hodnocení a ověřit jejich využitelnost na játrech prasete. Metody kvantifikace zahrnovaly jak automatickou obrazovou analýzu dat, tak stereologické metody zaručující vysokou reprodukovatelnost studií a porovnatelnost výsledků z různých experimentů. Dizertační práce je založena na celkem 10 pracích: třech přehledových pracích a sedmi výsledkových pracích. Výsledkové práce vycházejí ze šesti studií, jejichž šest závěrů můžeme shrnout následovně:

Závěr 1: Vyvinuli jsme open-source software QuantAn pro automatickou analýzu mikrocév nasnímaných pomocí 3D zobrazovacích metod, např. pomocí výpočetní tomografie s vysokým rozlišením (mikro-CT). Metody, na nichž je hodnocení v softwaru QuantAn založeno, jsou v souladu se standardy používanými ve stereologických metodách. Analýza dat získaných automatickou kvantifikací pomocí softwaru QuantAn identifikovala pravděpodobné zdroje chyb v měření, které je třeba při nastavování kvantitativních algoritmů zohlednit. QuantAn je volně dostupný pro výzkumníky zabývající se stochastickou geometrií mikrocév.

Závěr 2: Vyvinuli a otestovali jsme open-source software TelGen pro generování virtuálních modelů vláknitých a porézních struktur se známými morfometrickými parametry. Software TelGen je vhodným nástrojem pro kalibraci a testování nastavení kvantifikace obrazových dat získaných a hodnocených pomocí mikro-CT zařízení. Zároveň může sloužit k testování nastavení stereologických mřížek užívaných při kvantitativních analýzách trojrozměrných struktur.

Závěr 3: Objemový podíl vaziva v játrech zdravých zvířat byl větší u samců než u samic a byl větší na periférii jater než kolem žil v parakavální a paraportální oblasti.

Primární zdrojová data popisující objemový podíl vaziva v jednotlivých lalocích a v oblastech jater souvisejících s cévním zásobením jsou ve formě kontinuálních proměnných volně přístupná pro výzkumníky zabývající se studiem jaterní fibrózy na velkém zvířecím modelu. Data mohou být využita k výpočtu minimálního počtu vzorků nutného k prokázání nárůstu nebo poklesu množství vaziva v experimentech na játrech prasete.

Závěr 4: Délková hustota jaterních sinusoid a žlučových kapilár v játrech zdravých zvířat byla nižší u samců než u samic a byla nižší na periférii jater než kolem žil v parakavální a paraportální oblasti. Zároveň byla vyšší délková hustota jaterních sinusoid a žlučových kapilár spojena s lokálním nárůstem počtu menších hepatocytů a s menším výskytem vaziva. Nalezená intrahepatická a intersexuální variabilita v morfologii jater prasete by měla být zohledněna při plánování a vyhodnocování experimentů využívajících histologické hodnocení vzorků. Primární data popisující délkovou hustotu jaterních sinusoid a žlučových kapilár v šesti lalocích a ve třech oblastech vztažených k cévnímu zásobení jsou volně k dispozici ve formě kontinuálních proměnných. Data mohou být využita pro výpočet minimálního počtu vzorků nutného k odhalení změn v játrech prasete.

Závěr 5: Na základě biochemické, ultrasonografické a histologické analýzy se nám podařilo pomocí aplikace pyrrolizidinového alkaloidu monokrotalinu vytvořit velký zvířecí model sinusoidálního obstrukčního syndromu. Podání jedné intravenózní dávky mezenchymálních kmenových buněk zlepšilo celkové přežití zvířat se sinusoidálním obstrukčním syndromem po parciální jaterní resekci.

Závěr 6: Experiment simulující poranění jater prasete při nárazu poskytl komplexní pohled na mechanismus vzniku jaterního poranění na makroskopické i mikroskopické úrovni. Primární biomechanická data byla zveřejněna spolu s publikací a mohou sloužit k validaci výpočetních modelů mechanické odpovědi jater v okamžiku nárazu. Mikroskopická analýza prokázala, že se trhliny v játrech nešíří náhodně, ale jejich propagace je závislá na orientaci hlavních vláknitých složek stromatu jater a interlobulárních sept. Toto zjištění je významné zejména pro přenos dat z experimentů na játrech prasete se signifikantně větším množstvím vaziva na játra lidská.

Závěry vyplývající z rešerše literatury a z dat předložených výsledkových studií lze shrnout následovně. Postupy využívající automatické softwary pro obrazovou analýzu dat by měly být vždy kalibrovány, neboť výsledky jejich měření jsou ovlivněny kvalitou

vstupních dat a nastavením segmentačních algoritmů. Pro kalibraci postupů a validaci dat lze s výhodou využít robustní a reprodukovatelné metody, jako je např. stereologie. Rozsáhlé zmapování mikroskopických parametrů, jako je množství vaziva a délková hustota jaterních sinusoid a žlučových kapilár, v odlišných oblastech jater prasete umožňuje nyní na základě uveřejněných dat a popisných statistik plánování experimentů s eticky opodstatněným počtem jedinců a tkáňových vzorků. Na základě našich experimentálních studií bylo demonstrováno, že játra prasete jsou vhodným orgánem pro modelování různorodých fyziologických i patologických stavů vyskytujících se u lidí. V předložené práci jsme popsali experimenty na játrech prasete zahrnující regeneraci, rozvoj jaterního onemocnění, ale i mechanické chování jater prasete během simulace nárazu a tupého poranění orgánů. Všechny studie byly zveřejněny společně s primárními naměřenými daty.

Abstract

Animal models are widely used for research of liver diseases pathogenesis and progression and for development of new treatment strategies in hepatology. The dissertation thesis focuses on large animal model, specifically swine. The use of animals, which are anatomically and physiologically close to humans, allows us to bridge the gap between the experimental and human medicine. Histopathological analysis of the liver biopsies is still a fundamental part of liver disease diagnosis and therefore, it is also a part of the experimental design of the studies using the porcine liver. Our aim was to apply qualitative and quantitative histological methods of evaluation on porcine liver and to assess their usability in experimental medicine. The quantitative methods included automated image analysis as well as stereological methods, which guaranteed high reproducibility and comparability of the experimental results. The dissertation thesis is based on 10 manuscripts. Three of them are published reviews associated with the main topic of the thesis. Seven original manuscripts resulted from six experimental studies – their six conclusions are listed bellow:

Conclusion 1: We developed an open-source software QuantAn for quantification of microvessels visualized by 3D imaging methods, such as computed tomography with high resolution (micro-CT). The methods implemented in the QuantAn software are consistent with the main principles used in stereology. Analysis of the morphometric results acquired by the QuantAn software revealed the probable sources of errors in measurements, which needed to be addressed when adjusting the segmentation algorithms. QuantAn software is now freely available for researchers focusing on the microvessels stochastic geometry.

Conclusion 2: We developed and tested an open-source software TeIGen for generating standardized image data of fibrous and porous structures with known morphometric parameters. TeIGen software might be used for calibration of the automated quantitative analysis using software provided by micro-CT manufacturers and for validation of the data from such automated image analyses. TeIGen software might also serve as a practical tool for testing of stereological probes used in quantitative analysis of structures in 3D.

Conclusion 3: Volume fraction of connective tissue in the liver of healthy pigs was greater in male than in female animals and was greater in the periphery of the liver than in the paracaval and paraportal regions. The primary morphometric data describing the

distribution of the connective tissue in six hepatic lobes and three regions related to the hepatic vasculature are now available in a form of continuous variables. The data can be used for power analysis to justify the minimal number of samples required to detect the expected increase or decrease of connective tissue in further studies concerning the hepatic fibrosis.

Conclusion 4: The length density of hepatic sinusoids and bile canaliculi in the healthy porcine liver was smaller in male than in female animals and was smaller in the periphery of the liver than in the paracaval and paraportal regions. The local increase in length density was associated with increased number of smaller hepatocytes and with decreased volume fraction of connective tissue. The demonstrated intrahepatic and intersexual variability of porcine liver morphometry should be taken into account when planning experiments on porcine liver, that involve histological evaluation of the tissue samples. Primary morphometric data describing the length density of hepatic sinusoids and bile canaliculi among six hepatic lobes and among three regions related to the liver vasculature are now freely available in a form of continuous variables. Based on the data, power sample analysis should be performed prior to the experiments on porcine liver.

Conclusion 5: We established a large animal model of sinusoidal obstruction syndrome, which was induced by administration of pyrrolizidine alkaloid monocrotaline. The syndrome was confirmed by biochemical analysis of peripheral blood samples, by ultrasound examination and by histological evaluation of liver biopsies. Single dose of mesenchymal stem cells administered via portal vein improved the overall survival of the animals with sinusoidal obstruction syndrome after partial liver resection.

Conclusion 6: An experiment simulating blunt trauma of porcine liver during impact situation provided us with a complex description of the injury mechanism on the macroscopic and microscopic level. Freely available primary biomechanical data might be used for validation of computational models of liver mechanical behavior. The microscopic analysis demonstrated, that the ruptures did not propagate through the liver randomly, but rather along the reticular fibers and interlobular septa. The propagation of the ruptures along the main components of the liver stroma should be taken into consideration when adapting the results to the human liver, which contains significantly less connective tissue than porcine liver.

We can summarize the conclusions based on the current literature and on the results of the studies as follows. The quantitative methods based on the automated image analysis should be always calibrated, because the measured data depend on the settings of the

segmentation algorithms. Robust and highly reproducible stereological methods might be used as appropriate tools for calibration of image analysis methods and for validation of their results. Freely available data describing the distribution of the morphometric parameters within porcine liver, such as volume fraction of connective tissue and length density of hepatic sinusoids and bile canaliculi, allow to design experiments with justified minimal numbers of animals and tissue samples. The results of the experimental studies demonstrated, that the porcine liver is a suitable model organ for studying of various physiological and pathological conditions in humans. We described experiments on porcine liver, that involved regeneration, progression of liver disease and mechanical behavior of the liver in impact situation. The primary data were provided together with all the published manuscripts.

Předmluva

Do projektů týkajících se tématu této dizertační práce jsem se na školícím pracovišti Ústavu histologie a embryologie zapojovala již během svého pregraduálního studia na Lékařské fakultě v Plzni. Pod vedením svého školitele, prof. MUDr. Mgr. Zbyňka Tonara, Ph.D., jsem se podílela na histologickém kvantitativním hodnocení řady experimentů na měkkých i tvrdých tkáních a postupně jsem získávala první výsledky vedoucí k publikačním výstupům. První výsledkový článek v časopise s faktorem impaktu, který je součástí této dizertační práce, byl tedy publikován ještě před zahájením mého postgraduálního studia (Jiřík et al. 2016).

S nástupem do doktorského studijního programu Anatomie, histologie a embryologie bylo třeba zmapovat současný stav poznání relevantní k tématu dizertační práce. Rozsáhlá rešerše současné literatury vedla k publikaci tří přehledových článků, z nichž vycházejí tři úvodní kapitoly této dizertační práce. Jedná se o publikaci v českém recenzovaném časopise zabývající se zvířecími modely jaterních onemocnění (Malečková et al. 2019) a dvě publikace v časopisech s faktorem impaktu, jedna týkající se využití jater prasete v biomedicině (Eberlová et al. 2020) a druhá vycházející ze zkušeností se stereologickým hodnocením reálných experimentů z našeho pracoviště (Kolinko et al. 2022).

Další členění dizertační práce je založeno na výsledkových studiích, jejichž uspořádání je založeno na následujících cílech. Prvním cílem byl vývoj nových metod kvantitativní analýzy jater prasete, a to konkrétně metod obrazové analýzy dat validovaných pomocí robustních stereologických metod (Jiřík et al. 2016, Jiřík et al. 2018). V dalším kroku jsme se zaměřili na kvantitativní popis zdravých jater prasete, jakožto významného zvířecího modelového orgánu v hepatologii (Mik et al. 2018, Malečková et al. – manuskript zaslán do časopisu *Annals of Anatomy*). S využitím stereologických metod se nám podařilo získat kvantitativní data nezbytná pro plánování experimentů na játrech prasete, konkrétně pro výpočet minimálního počtu zvířat a vzorků nezbytných pro odhalení změn v mikrostruktuře jater. V neposlední řadě jsme pak zúročili poznatky týkající se mikrostruktury jater a úspěšně aplikovali stereologické metody při hodnocení reálných experimentů na játrech prasete (Pálek et al. 2018, Pálek et al. 2020, Malečková et al. 2021).

Při plánování designu studií a zpracování výsledků jsem intenzivně spolupracovala s konzultantkou dizertační práce, Ing. Petrou Kochovou, Ph.D., z Fakulty aplikovaných

věd Západočeské univerzity (ZČU). Dizertační práce byla zpracována na dvou školících pracovištích, proto jsou některé z předložených prací afiliovány LFP UK a další ZČU. Na předložených výstupech jsem se podílela následujícím způsobem:

1. **Malečková A** et al. (*Rozhl Chir.*, 2019); Příloha I: Prvoautorská přehledová publikace v českém recenzovaném časopise *Rozhledy v chirurgii*. Provedla jsem rešerši současné literatury, konzultovala jsem obsah s širokým týmem odborníků nejen z oboru histologie, ale také s experimentálními chirurgy a patology. Jako první a korespondující autor jsem se z největší části podílela na sepsání a revizi manuskriptu.
2. Eberlová L, **Malečková A** et al. (*J Surg Res.*, 2020); Příloha II: Rešerše literatury, zpracování části manuskriptu týkající se histologické stavby jater prasete a možností jejího hodnocení, obrazová dokumentace, revize manuskriptu.
3. Kolinko Y, **Malečková A** et al. (*Anat Histol Embryol.*, 2022); Příloha III: Rešerše literatury, zpracování části manuskriptu týkající se využití skenů histologických řezů pro vzorkování zorných polí, revize manuskriptu.
4. Jiřík M, Tonar Z, **Králíčková A** et al. (*Int J Comput Assist Radiol Surg.*, 2016); Příloha IV: Kvantitativní hodnocení mikro-CT skenů korozivních preparátů mikrocév v játrech prasete, příspěvek do manuskriptu v podobě metodiky a výsledků hodnocení.
5. Jiřík M, ..., **Malečková A** et al. (*Microsc Res Tech.*, 2018); Příloha V: Testování kalibrace softwaru proti výsledkům kvantitativního hodnocení získanými stereologickými metodami, revize manuskriptu.
6. Mik P, Tonar Z, **Malečková A** et al. (*J Comp Pathol.*, 2018); Příloha VI: Rešerše literatury na téma jaterní fibrózy, sběr a histologické zpracování vzorků, sepsání a revize manuskriptu.
7. **Malečková A** et al. (článek odeslán do časopisu *Ann Anat*); Příloha VII: Prvoautorská publikace, v níž jsem zároveň korespondujícím autorem. Provedla jsem sběr a histologické zpracování vzorků jater prasete, kvantitativní analýzu založenou na hodnocení dvou kvantitativních parametrů na celkem 4428 mikrofotografiích, statistické zpracování dat, sepsání manuskriptu.
8. Palek R, ..., **Králíčková A** et al. (*Rozhl Chir.*, 2019); Příloha VIII: rešerše literatury, histologická analýzy vzorků jater prasete, revize manuskriptu.
9. Palek R, Rosendorf J, **Malečková A** et al. (*Anticancer Res.*, 2020); Příloha IX: kvalitativní a kvantitativní analýza vzorků jater prasete, statistické zpracování dat,

sepsání částí manuskriptu týkajících se histologického hodnocení a jejích výsledků, revize manuskriptu.

10. **Malečková A** et al. (*Physiol Meas.*, 2021); Příloha X: Prvoautorská publikace, v níž jsem se podílela na designu studie a mechanické části experimentu. Publikace byla podpořena v rámci projektu GA UK 1098120. Byla jsem zodpovědná za sběr a histologické zpracování vzorků, kvantitativní analýzu šíření trhlin parenchymem jater prasete, statistické zpracování dat a sepsání manuskriptu.

V Plzni 10. 5. 2022

Poděkování

Od mého nástupu do Ph.D. studia se mnohé změnilo. Celosvětová pandemie ovlivnila nejen mé studium, ale vše kolem nás. To, co se nezměnilo, byli lidé, na které jsem se mohla vždy spolehnout a o které jsem se mohla vždy opřít. V souvislosti s mým studiem to byl především můj školitel, prof. MUDr. Mgr. Zbyněk Tonar, Ph.D., který mi byl nejen skvělým vedoucím, ale stále je mi velmi blízkým člověkem. Nikdy jsem od něj neslyšela odmítnutí, když jsem potřebovala jeho radu v profesním i osobním životě, a vždy jsem u něj našla ochotu pomoci a hlavně porozumění. Děkuji za hodiny strávené v kanceláři plné knih, u mikroskopu a nad výzkumnými daty.

Velkým vzorem pro mě byla a vždy bude paní rektorka, prof. MUDr. Milena Králíčková, Ph.D. Děkuji za to, že jsem byla na Ústav histologie a embryologie pod jejím vedením srdečně přijata a mohla jsem začít pracovat v inspirativním prostředí plném podpory a příležitostí. Paní rektorky si nesmírně vážím v profesní i osobní rovině a jsem hrdá na to, že i já se mohu počítat mezi její blízké spolupracovníky.

Vědecká práce je v první řadě založená na fungující spolupráci. Chtěla bych tedy poděkovat všem, se kterými jsem se mohla zapojit do zajímavých projektů, kteří se podíleli na přípravě publikací a kteří se mnou ochotně sdíleli své zkušenosti. Jedná se o tým na Ústavu histologie a embryologie LFP UK, o chirurgický tým Biomedicínského centra a v neposlední řadě další doktorandy v oborové radě, se kterými jsme se vzájemně během studií podporovali. Jmenovitě bych ráda zmínila svou konzultantku Ing. Petru Kochovou, Ph.D., kterou obdivuji za její profesionální přístup a za to, že umí věci dotáhnout do konce.

V neposlední řadě patří velké díky mému muži Ing. Jiřímu Malečkovi. Po jeho boku jsem bez úhony prošla celým studiem a vytvořil pro mě láskyplné zázemí, ve kterém jsem vždy našla útěchu a bezmeznou oporu. Děkuji za přečtení celé této práce a za jazykovou korekturu, která mi ukázala, že ne vždy si lidé rozumějí, i když mluví stejným jazykem. Se svým mužem si rozumím i beze slov, přesto bych mu chtěla na závěr ještě jednou poděkovat.

Obsah

Bibliografické informace	2
Abstrakt	4
Abstract	7
Předmluva	10
Poděkování	13
Obsah	14
Použité zkratky	18
1 Teoretický úvod	19
1.1 Zvířecí modely jaterních onemocnění	19
1.2 Anatomická a histologická stavba jater	20
1.2.1 Morfologie jater člověka	20
1.2.2 Morfologie jater zvířecích modelů jaterních onemocnění.....	24
1.3 Histologické hodnocení jater v patologii a v experimentech.....	27
1.3.1 Kvalitativní hodnocení mikroskopické stavby jater	27
1.3.2 Kvantitativní hodnocení mikroskopické stavby jater	32
2 Cíle a hypotézy dizertace	35
2.1 Kvantifikace jaterních mikrocév v korozivních preparátech jater zobrazených pomocí mikro-CT	36
2.1.1 Motivace a cíle práce.....	36
2.1.2 Hypotézy.....	36
2.2 Generování virtuálních obrazových dat pro kalibraci vyšetřování vláknitých a porézních struktur pomocí mikro-CT	37
2.2.1 Motivace a cíle práce.....	37
2.2.2 Hypotézy.....	37
2.3 Mapování rozložení vaziva v játrech prasete.....	38
2.3.1 Motivace a cíle práce.....	38

2.3.2	Hypotézy.....	38
2.4	Délková hustota jaterních sinusoid a žlučových kapilár v játrech prasete.....	39
2.4.1	Motivace a cíle práce.....	39
2.4.2	Hypotézy.....	39
2.5	Histologické hodnocení jater prasete s indukovaným sinusoidálním obstrukčním syndromem – studie vlivu aplikace mezenchymálních kmenových buněk na průběh onemocnění.....	40
2.5.1	Motivace a cíle práce.....	40
2.5.2	Hypotézy.....	41
2.6	Analýza šíření trhlin játry prasete.....	41
2.6.1	Motivace a cíle práce.....	41
2.6.2	Hypotézy.....	42
3	Materiál a metody.....	43
3.1	Kvantifikace jaterních mikrocév v korozivních preparátech jater zobrazených pomocí mikro-CT.....	43
3.2	Generování virtuálních obrazových dat pro kalibraci vyšetřování vláknitých a porézních struktur pomocí mikro-CT.....	44
3.3	Mapování rozložení vaziva v játrech prasete.....	45
3.4	Délková hustota jaterních sinusoid a žlučových kapilár v játrech prasete.....	46
3.5	Histologické hodnocení jater prasete s indukovaným sinusoidálním obstrukčním syndromem – studie vlivu aplikace mezenchymálních kmenových buněk na průběh onemocnění.....	47
3.6	Analýza šíření trhlin játry prasete.....	49
4	Výsledky a diskuze.....	51
4.1	Kvantifikace jaterních mikrocév v korozivních preparátech jater zobrazených pomocí mikro-CT.....	51
4.1.1	Hlavní zjištění.....	51
4.1.2	Publikace.....	51

4.2	Generování virtuálních obrazových dat pro kalibraci vyšetřování vláknitých a porézních struktur pomocí mikro-CT	52
4.2.1	Hlavní zjištění.....	52
4.2.2	Publikace	52
4.3	Mapování rozložení vaziva v játrech prasete.....	53
4.3.1	Hlavní zjištění.....	53
4.3.2	Publikace	53
4.4	Délková hustota jaterních sinusoid a žlučových kapilár v játrech prasete.....	54
4.4.1	Hlavní zjištění.....	54
4.4.2	Publikace	54
4.5	Histologické hodnocení jater prasete s indukovaným sinusoidálním obstrukčním syndromem – studie vlivu aplikace mezenchymálních kmenových buněk na průběh onemocnění.....	54
4.5.1	Hlavní zjištění.....	54
4.5.2	Publikace	55
4.6	Analýza šíření trhlin játry prasete	56
4.6.1	Hlavní zjištění.....	56
4.6.2	Publikace	56
5	Závěry práce	57
6	Literatura	60
7	Seznam obrázků.....	70
8	Seznam tabulek.....	71
9	Publikační činnost autorky	72
9.1	Publikace vztahující se k tématu dizertační práce	72
9.1.1	Časopisy s faktorem impaktu	72
9.1.2	Ostatní recenzované časopisy	73
9.2	Publikace mimo rámec dizertační práce	74
9.2.1	Časopisy s faktorem impaktu	74

9.2.2	Ostatní recenzované časopisy.....	75
9.3	Kapitoly v monografiích.....	75
10	Přílohy – plná znění předložených prací.....	76
10.1	Příloha I.....	76
10.2	Příloha II.....	87
10.3	Příloha III.....	98
10.4	Příloha IV.....	119
10.5	Příloha V.....	137
10.6	Příloha VI.....	156
10.7	Příloha VII.....	170
10.8	Příloha VIII.....	198
10.9	Příloha IX.....	207
10.10	Příloha X.....	225

Použité zkratky

AALD	-	Alkoholem podmíněné jaterní poškození (<i>alcohol-associated liver disease</i>)
AAST	-	Škála pro hodnocení závažnosti jaterního poškození (<i>American Association for the Surgery of Trauma</i>)
AIS	-	Škála pro hodnocení závažnosti jaterního poškození (<i>Abbreviated Injury Scale</i>)
ALD	-	Akutní jaterní onemocnění (<i>acute liver disease</i>)
ALP	-	Alkalická fofatáza
ALT	-	Alaninaminotransferáza
AST	-	Aspartátaminotransferáza
CLD	-	Chronické jaterní onemocnění (<i>chronic liver disease</i>)
CT	-	Vazivo (<i>connective tissue</i>).
GGT	-	Gamaglutamyltransferáza
ICT	-	Interlobulární vazivo (<i>interlobular connective tissue</i>)
L_v	-	Délková hustota (<i>length density, length per volume</i>)
METAVIR	-	Skórovací systém pro hodnocení rozsahu jaterní fibrózy (<i>Meta-analysis of Histological Data in Viral Hepatitis</i>)
mikro-CT	-	Výpočetní tomografie s vysokým rozlišením
MSC	-	Mezenchymální kmenové buňky (<i>mesenchymal stem cells</i>)
NAFLD	-	Nealkoholová steatóza (<i>non-alcoholic fatty liver disease</i>)
NASH	-	Nealkoholová steatohepatitida (<i>non-alcoholic steatohepatitis</i>)
N_v	-	Numerická hustota (<i>numerical density, number per volume</i>)
P'_L	-	Reálná hodnota denzity průsečíků s rovinou (<i>intersection intensity</i>)
PAS	-	Histologické barvení pro průkaz polysacharidů (<i>Periodic Acid Schiff</i>)
PBC	-	Primární biliární cirhóza
PCCT	-	Pericentrální vazivo (<i>pericentral connective tissue</i>)
P_L	-	Teoretická hodnota denzity průsečíků s rovinou (<i>theoretical intersection intensity</i>)
PSC	-	Primární sklerotizující cholangitida
PSCT	-	Peisinosoidální vazivo (<i>perisinusoidal connective tissue</i>)
SOS	-	Sinusoidální obstrukční syndrom (<i>sinusoidal obstruction syndrome</i>)
SURS	-	Systematické jednotné náhodné vzorkování (<i>systematic uniform random sampling</i>)
S_v	-	Povrchová hustota (<i>surface density, surface per volume</i>)
UZ	-	Ultrazvuk
V_v	-	Objemový podíl (<i>volume fraction, volume density, volume per volume</i>)

1 Teoretický úvod

1.1 Zvířecí modely jaterních onemocnění

V důsledku jaterních onemocnění zemřou každoročně přibližně dva miliony lidí (Asrani et al. 2019). Terminálním stádiem většiny chronických jaterních onemocnění je jaterní cirhóza, která je příčinou nejen vysoké mortality, ale také morbidity pacientů přispívající ke snížené kvalitě života. Jako nejčastější příčiny cirhózy jater se v západních vyspělých zemích udávají konzumace alkoholu vedoucí k alkoholem podmíněnému jaternímu poškození (*alcohol-associated liver disease, AALD*) a nealkoholová steatóza a steatohepatitida (*non-alcoholic fatty liver disease, NAFLD; non-alcoholic steatohepatitis, NASH*) spojená mimo jiné s životním stylem vedoucím k obezitě. V asijských zemích je nejčastější příčinou cirhózy virová hepatitida B, případně virová hepatitida C, která může vyústit v hepatocelulární karcinom (Asrani et al. 2019).

Studium patogeneze a progresu akutních jaterních onemocnění (*acute liver disease, ALD*) a chronických jaterních onemocnění (*chronic liver disease, CLD*) s využitím zvířecích modelů je jednou z možných cest k vývoji nových terapeutických strategií v hepatologii. Jako hlavní modelové organizmy se využívají zejména malí laboratorní hlodavci – myši a potkani, jejichž hlavními výhodami jsou možnosti genové manipulace či nižší finanční náklady na experiment. Hlodavci jsou také častěji využíváni jako modelové organizmy pro studium jaterní fibrózy, která se u lidí a větších zvířecích modelů vyvíjí po dobu měsíců či let; naopak u hlodavců k jejímu rozvoji dochází časněji. Hlavní nevýhodou experimentů na hlodavcích je ovšem jen omezená přenositelnost výsledků do humánní medicíny (Starkel a Leclercq 2011).

Anatomicky bližší člověku jsou velké zvířecí modely, a to zejména prase domácí, které je hojně využíváno pro studium ALD a akutního jaterního selhání (van de Kerkhove 2004). Oproti hlodavcům vykazuje prase vyšší anatomickou a fyziologickou podobnost s člověkem a může tedy sloužit jako spojovací článek mezi experimentální a humánní medicínou. Práce s velkými zvířecími modely je ovšem zatížena vyšší cenou experimentů vázanou zejména na zajištění základních potřeb zvířete (krmivo, ustájení apod.). Nižší počet zvířat v experimentu v porovnání s experimenty s hlodavci může navíc ovlivnit závěry studií v důsledku interindividuální variability – každý design studie by měl tedy vycházet nejen ze zásad koncepce 3R (*replacement, reduction, refinement*), ale měla by

být také předem provedena analýza počtu zvířat potřebných k prokázání předpokládaných biologických rozdílů.

Podrobný přehled zvířecích modelů jaterních onemocnění s jejich hlavními výhodami a nevýhodami, včetně příkladů konkrétních studií využívajících zvířecí modely, byl publikován v českém recenzovaném časopise *Rozhledy v chirurgii*. Publikace (Malečková et al. 2019) je součástí této dizertační práce jako příloha I na str. 76.

1.2 Anatomická a histologická stavba jater

Analýza experimentů využívajících zvířecí modely jaterních onemocnění zahrnuje často histologické hodnocení změn v mikroskopické stavbě jater. Znalost mikroarchitektoniky jater, včetně rozdílů v mikroskopické stavbě mezi játry člověka a játry modelových organismů, je základním předpokladem pro získání validních histologických dat.

1.2.1 Morfologie jater člověka

Játra jsou se svou hmotností pohybující se mezi 1500–1800 g u dospělého muže a 1200–1500 g u dospělé ženy (přibližně 3 % tělesné hmotnosti) největší žlázou těla (Čihák 2013, Hůlek et al. 2018). Nacházejí se intraperitoneálně v pravém a částečně v levém horním kvadrantu břišní dutiny pod brániční klenbou. Vazivový obal jater (*capsula fibrosa hepatis*) je kryt serózní vrstvou (*peritoneum viscerale*) všude mimo oblast jater, která pevně srůstá s bránicí (*area nuda*). Na játrech popisujeme *facies diaphragmatica* přiléhající k bránici a *facies visceralis*, na jejíž ploše můžeme najít štěrby (*fissurae*) ve tvaru písmene H ohraničující čtyři jaterní laloky – *lobus hepatis dexter*, *lobus hepatis sinister*, *lobus quadratus* a *lobus caudatus*.

Z klinického hlediska je důležitější členění jater na jaterní segmenty dle Couinauda (1954), které odráží uspořádání a větvení cévních a žlučových struktur v játrech. Játra mají duální cévní zásobení probíhající cestou *vena portae hepatis* (dále jen *vena portae*), jež představuje funkční oběh, a cestou *arteria hepatica propria*, jež tvoří nutritivní oběh. Po vstupu do jater skrz *porta hepatis* se cévy společně větví na lalokové a segmentové větve, jejichž dalším větvením vznikají interlobulární a cirkumlobulární cévy. Z nich krev vstupuje do jaterních sinusoid a dále do *venae centrales*. *Venae centrales* jaterních lalůček se spojují a vytvářejí žilní odtok z jater, jehož větve probíhají

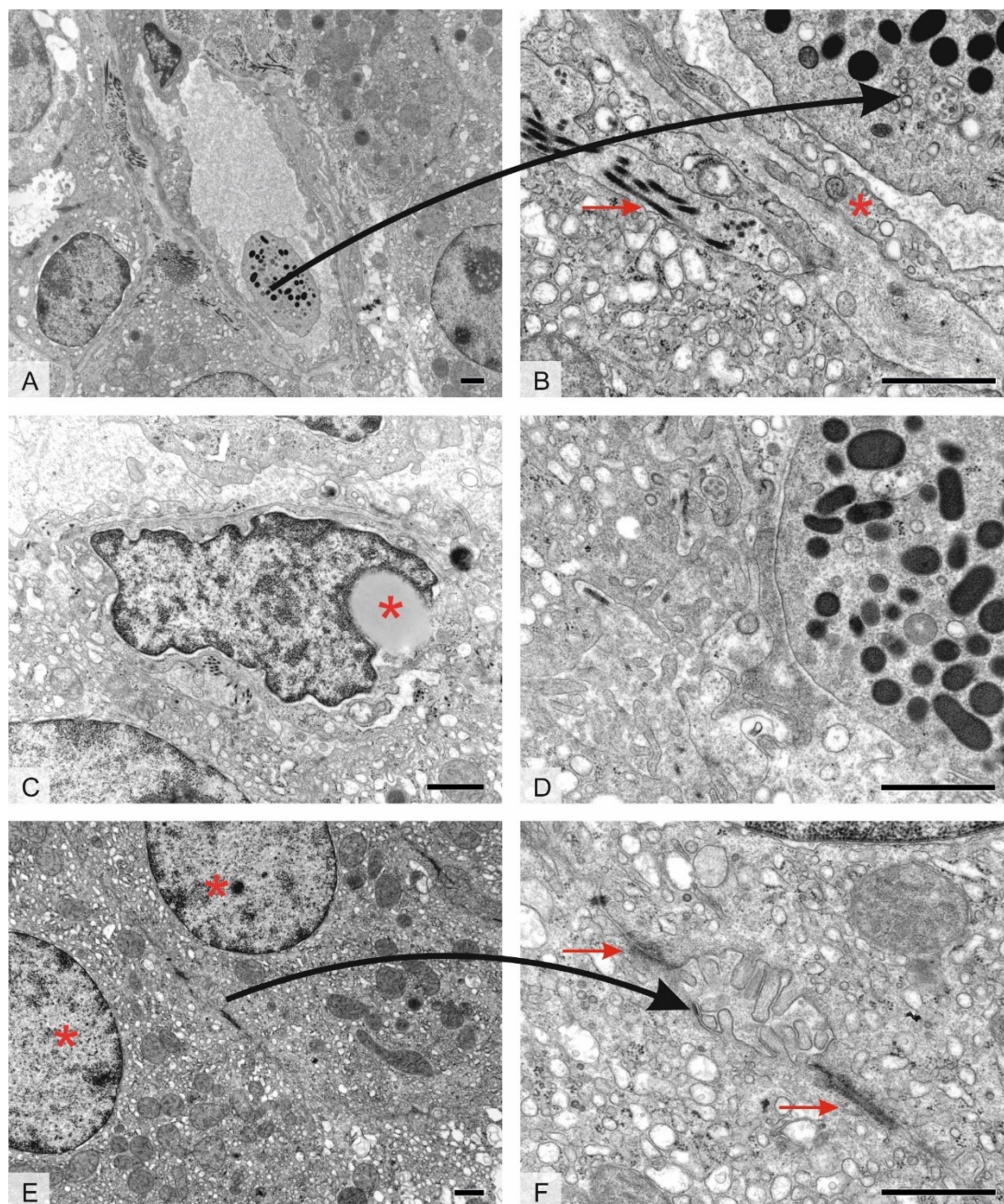
Teoretický úvod

játry nezávisle na větvích *vena portae* a *arteria hepatica propria*. Žíly opouštějí játra v podobě tří *venae hepaticae*, které ústí do *vena cava inferior*.

Detailní mikroskopickou stavbu jater poprvé popsal Kiernan v roce 1833 (Kiernan 1833). Jaterní parenchym je uspořádán do zhruba šestiúhelníkových jaterních lalůček (*lobuli hepatici classici*), které jsou tvořeny radiálně uspořádanými trámci hepatocytů (*hepatocytů*) směřujícími k *vena centralis* uprostřed jaterního lalůčku. Mezi trámci hepatocytů se nacházejí jaterní sinusoidy vystlané nesouvislým endotelem s nesouvislou bazální laminou (obrázek 1A a B), kterými protéká krev smíšená z funkčního a nutritivního oběhu směrem k *vena centralis*. Jaterní sinusoidy jsou oddělené od hepatocytů perisinusoidovým (Disseho) prostorem (*spatium perisinusoideum*) s četnými retikulárními vlákny (obrázek 1B), ve kterém se nacházejí mimo jiné jaterní hvězdčité buňky (Itoovy buňky, *cellulae perisinusoidales*, *cellulae accumulantes adipem*) (obrázek 1C). V játrech se dále nacházejí jaterní makrofágy (Kupfferovy buňky, *macrophagocytů stellati*) (obrázek 1D). Na styku jaterních lalůček se nacházejí vazivové portobiliární prostory (*spatium portale*) obsahující portální triády (*trias hepatica*; Glissonova trias): interlobulární větve *vena portae*, *arteria hepatica propria* a *ductus bilifer*. Kromě této trojice struktur probíhají v portobiliárních prostorech také mízní cévy a nemyelinizovaná nervová vlákna.

Funkční dělení jaterního parenchymu představují jaterní aciny (*acini hepatici*), které mají tvar kosočtverce, tedy dvou trojúhelníků přiléhajících k sobě základnami (hranice mezi dvěma sousedními jaterními lalůčky) s vrcholy v sousedních *venae centrales*. Hepatocyty jsou v jaterním acinu zásobeny jednou cirkumlobulární cévou (*vena circumlobularis*) a na základě obsahu kyslíku a živin v protékající krvi je můžeme rozdělit do tří zón: zóna I (*zona peripherica*), zóna II (*zona intermedia*) a zóna III (*zona centralis*). Členění jaterního parenchymu do tří zón bylo poprvé popsáno Rappaportem v roce 1958 (Rappaport a Wilson 1958) a částečně vysvětluje lokalizaci patologických lézí souvisejících s poruchami perfúze jaterního parenchymu. Zároveň do určité míry odpovídá členění parenchymu na základě exprese enzymů v hepatocytech do tzv. metabolických zón (*metabolic zonation*) (Lamers et al. 1989).

Dalším možným členěním jaterního parenchymu je vymezení portálních lalůček (*lobuli portales*), které mají tvar trojúhelníku s vrcholy ve třech sousedních *venae centrales* a s portální triádou uprostřed. Hepatocyty portálního lalůčku produkují žluč, která je odváděna jedním interlobulárním žlučovodem.



Obrázek 1 – Játra prasete (transmisní elektronový mikroskop). **A.** Jaterní sinusoida s fenestrovaným endotelem, v jejímž průsvitu se nachází neutrofilní granulocyt s azurofilními granuly; **B.** Detail jaterní sinusoidy a endotelových buněk (hvězdička) z obrázku A. V perisinusoidálním prostoru jsou zobrazena retikulární vlákna (červená šipka); **C.** Hvězdicovitá buňka s velkou tukovou vakuolou (hvězdička) nacházející se v perisinusoidálním prostoru; **D.** Perisinusoidální prostor mezi trámci hepatocytů a přilehlým nesouvislým endotelem jaterní sinusoidy. V detailu je zobrazena část makrofágu (Kupfferovy buňky) s lysozomy; **E.** Dva přilehlé hepatocyty s kulatými jádry (hvězdičky), jejichž cytoplazmatická membrána tvoří počáteční úsek žlučových cest – žlučovou kapiláru; **F.** Detail žlučové kapiláry z obrázku E. Spojení hepatocytů je zajištěno těsnými spoji (červené šipky), které zabraňují prosakování žluči. Měřítko = 1 μm . Za pořízení mikrofotografií děkuji MUDr. Jiřímu Uhlíkovi, Ph.D., Ústav histologie a embryologie, 2. lékařská fakulta, Univerzita Karlova.

Teoretický úvod

Exokrinní funkce jater, neboli produkce žluči, je na morfologické úrovni vyjádřena rozvětveným systémem intrahepatálních žlučových cest. Jejich počáteční segment, žlučový kanálek (žlučová vlasečnice; žlučová kapilára; *canaliculus bilifer*; *bile canaliculus*), je lokalizován intralobulárně a je charakterizován jako prostor s průměrem okolo 1 μm nacházející se mezi dvěma hepatocyty (obrázek 1E a F). Stěna žlučových kanálků je tvořena cytoplazmatickými membránami přiléhajících hepatocytů. Ve vnější třetině jaterního lalůčku na žlučové kapiláry navazují žlučové Heringovy kanálky (*canales biliferi*), jejichž stěna je již vystlána cholangiocyty. Heringovy kanálky opouštějí jaterní lalůček a formují interlobulární žlučovody (*ductus interlobulares*), které retrográdně provázejí větve *vena portae* a *arteria hepatica propria*. Systém žlučvodů se spojuje do podoby dvou vývodů *ductus hepaticus dexter et sinister*, které opouští játra a jsou základem extrahepatálních žlučových cest.

Mikroskopické uspořádání jaterního parenchymu vzniká na základě vysoce specializované polarity hepatocytů. Apikální povrch cytoplazmatické membrány hepatocytů se podílí na tvorbě žlučových kapilár, zatímco bazální doména sousedí s jaterními sinusoidami. Naše znalosti týkající se mechanismů vývoje a udržení polarity buněk vycházejí zejména ze studia tkáňových kultur. Při studiu polarity hepatocytů ovšem narážíme na omezenou schopnost hepatocytů vytvořit *in vitro* multipolární uspořádání (Treyer a Müsch 2013), které vzniká nejen na podkladě interakcí mezi samotnými hepatocyty, ale též je třeba zajistit působení dalších buněk a tkání, např. sinusoidálních endotelových buněk (Treyer a Müsch 2013).

Růst a interakce hepatocytů v tkáňových kulturách či při regeneraci jater do určité míry odpovídá embryonálnímu vývoji jater a diferenciaci původně nepolarizovaných hepatoblastů ve vysoce polarizované buňky (Lemaigre 2009, Ober a Lemaigre 2018, Treyer a Müsch 2013). Nedávný rozvoj metod pro trojrozměrnou analýzu tkání umožnil detailní studium morfogeneze jater v modelových organizmech (Ober a Lemaigre 2018). Základ jater entodermového původu se u člověka objevuje v polovině 3. týdne embryonálního vývoje, kdy se ve vyklenutí entodermu předního střeva diferencují bipotentní hepatoblasty, které se dále mohou diferencovat jak v hepatocyty, tak v cholangiocyty (Sadler 2011). V iničiálních fázích jsou hepatoblasty rozmístěny mezi hematopoetickými kmenovými buňkami. Postupně dochází k proliferaci buněk a k jejich propojování pomocí adhezních spojení. To vede ke vzniku prvních souvislých žlučových kapilár s rozšířeným průsvitem a hepatocyty uspořádanými do útvarů připomínajících

aciny. Rychlým růstem a propojováním kanálků vzniká výsledná síť intrahepatálních žlučovodů.

I přes pokrok ve studiu morfogeneze jater stále máme jen omezené množství informací o vzájemné interakci trámců hepatocytů, žlučovodů a cév (Ober a Lemaigre 2018). Detailní popis mechanismů vývoje jater, včetně popisu morfometrických parametrů struktur, na jejichž tvorbě se podílí multipolarita hepatocytů, může přispět k porozumění procesů spojených s jaterní regenerací či progresí jaterních onemocnění. Poznatky mohou být také využity při vývoji *in vitro* modelů jaterního parenchymu přibližujících se skutečnému uspořádání a polaritě hepatocytů (Ober a Lemaigre 2018).

1.2.2 Morfologie jater zvířecích modelů jaterních onemocnění

Nejčastěji využívanými zvířecími modely v hepatologii jsou myš a potkan (Malečková et al. 2019). V morfologii jater obou živočišných druhů jsou oproti člověku určité rozdíly, nicméně celková podobnost ve struktuře a funkci je dostatečná k tomu, aby umožnila efektivní využití jater myši a potkana ve výzkumu. Hlavní popisované rozdíly se týkají zejména anatomické stavby jater (tabulka 1), neboť rozčlenění jater na jednotlivé laloky je druhově specifické (Treuting et al. 2017).

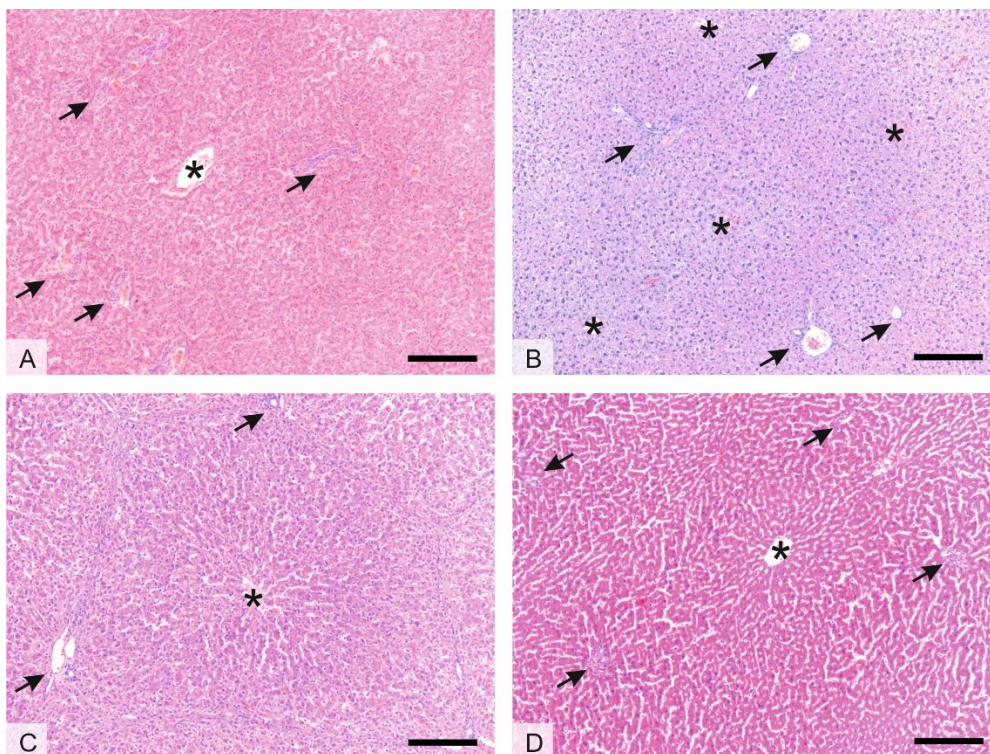
Oproti tomu mikroskopické členění na jaterní lalůčky můžeme považovat u člověka, myši a potkana za obdobné, přestože se i na mikroskopické úrovni nacházejí specifické rozdíly (obrázek 2). U myši tyto rozdíly zahrnují např. nezřetelně oddělené trámce hepatocytů zejména v zóně III, či menší portobiliární prostory s portálními triádami (obrázek 2B). Dalším rozdílem je hromadění glykogenu v cytoplazmě hepatocytů po jídle, které je viditelné jako projasnění cytoplazmy v zóně III. Z hlediska modelování CLD je významné zejména menší množství vaziva, k jehož výraznému zvýšení nedochází ani při závažném poškození jater (Treuting et al. 2017).

Stále větší význam získávají pro hepatologický výzkum játra prasete (více než 5000 nálezů v databázi Medline (<https://www.ncbi.nlm.nih.gov/pubmed/>) při zadání výrazů ((pig) AND liver) AND experim*), březen, 2022). Makroskopicky je nejvýraznějším rozdílem oproti lidským játrům členění na laloky, jejichž počet a velikost závisí na konkrétním plemeni (tabulka 1). Na mikroskopické úrovni se popisuje členění na jaterní lalůčky, které jsou oproti lidským játrům jasně ohraničeny vazivovými interlobulárními septy (obrázek 2C). Trojrozměrná struktura jaterního stromatu prasete je v současnosti využívána pro vývoj decelularizovaných jaterních skafoldů, které by po

Teoretický úvod

osídlení buňkami jater mohly sloužit jako náhrady orgánů pro pacienty s jaterním selháním (Massaro et al. 2021, Moulisová et al. 2020).

Podrobný popis morfologie jater prasete na makroskopické i mikroskopické úrovni, včetně přehledu využití tohoto modelového organismu v biomedicíně, byl publikován v časopise *The Journal of Surgical Research*. Publikace (Eberlová et al. 2020) je součástí této dizertační práce jako příloha II na str. 87.



Obrázek 2 – Srovnání histologické stavby jater člověka (A), myši (B), prasete (C) a potkana (D). Mikroskopická struktura jater je charakterizována přítomností jaterních lalůček složených z trámců hepatocytů s *vena centralis* ve středu (hvězdičky) a portobiliárními prostory s portálními triádami na hranicích lalůček (šípky). Jaterní lalůčky a portobiliární prostory u myši (B) jsou rozměrově menší. V játrech prasete (C) je významně vyšší množství vaziva, které vidíme v podobě interlobulárních sept jasně ohraničujících jaterní lalůček. Barvení hematoxylin a eosin *Měřítka* = 100 μ m.

Tabulka 1 – Srovnání anatomie jater člověka a nejčastěji využívaných zvířecích modelů – myši, potkana a prasete. Hodnoty převzaty z následujících publikací: Eberlová et al. (2020); Kogure et al. (1999); Swindle a Smith (2016); Treuting et al. (2017).

Rys	Člověk	Myš	Potkan	Prase
Velikost	1500 g 3 % hmotnosti těla	2 g 6 % hmotnosti těla	15 g 6 % hmotnosti těla	Dle plemene 1,5 % hmotnosti těla
Laloky	4: dexter (největší), sinister caudatus quadratus	4: medialis sinister (největší) dexter (rozdělený) caudatus	4: caudatus sinister middle dexter	4 – 6: dle plemene sinister lateralis sinister medialis dexter lateralis dexter medialis caudatus quadratus
Žlučník	Pod lobus dexter	Prorůstá skrze lobus medialis	Nepřítomen	Mezi lobus dexter lateralis a quadratus

1.3 Histologické hodnocení jater v patologii a v experimentech

1.3.1 Kvalitativní hodnocení mikroskopické stavby jater

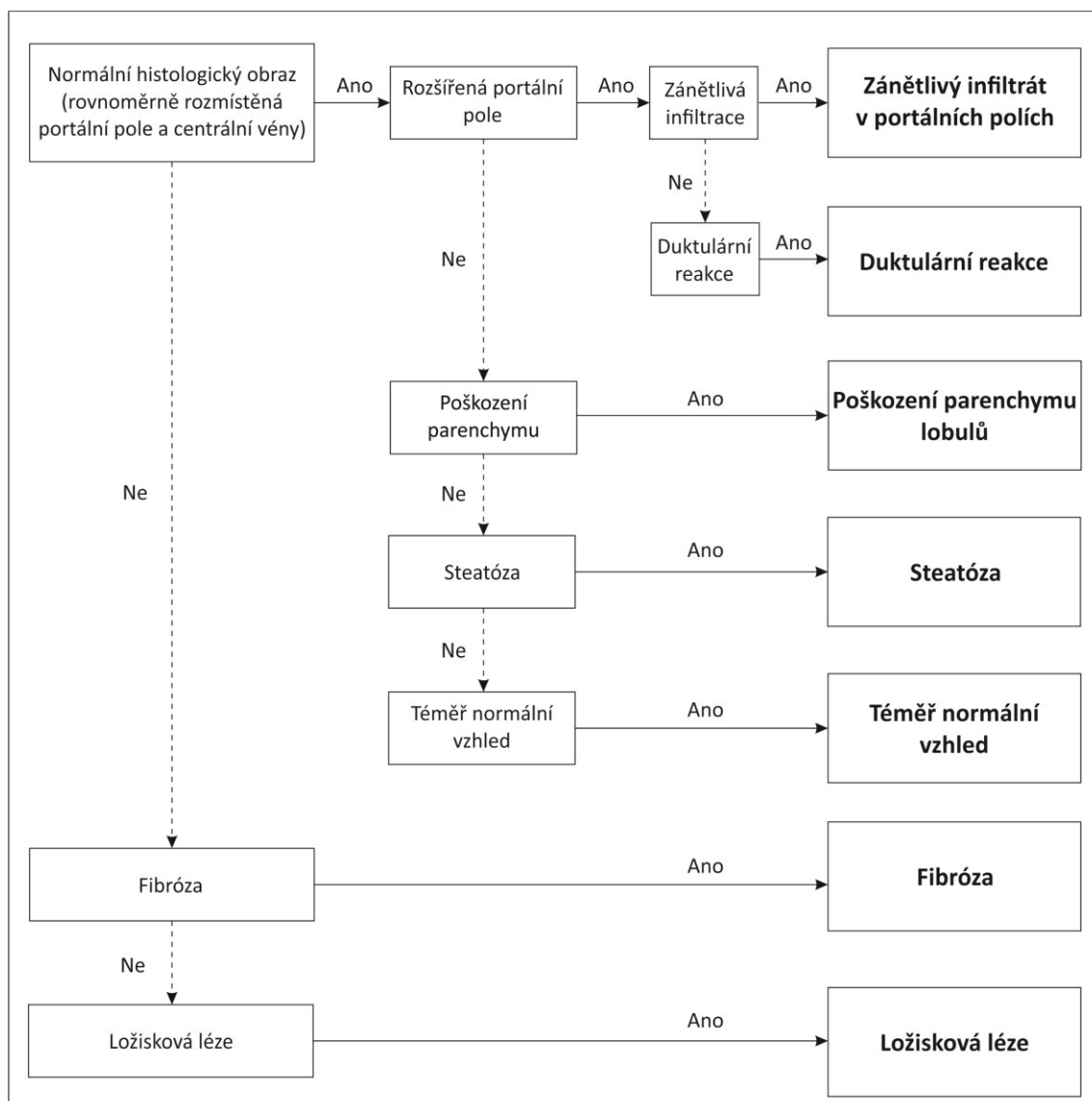
Jaterní biopsie patří mezi základní diagnostické techniky a vhodně doplňuje nové diagnostické a léčebné metody v hepatologii. Správný odběr a fixace vzorku jsou pro histopatologické vyšetření stejně důležité jako dostatečná velikost a kvalita odebrané tkáně. V rutinní praxi se využívá celá řada histochemických barvení, jejichž přehled je uveden v tabulce 2.

Tabulka 2 – Přehled nejčastěji využívaných metod histologického barvení v diagnostice jaterních onemocnění. HBsAg – povrchový antigen viru hepatitidy B (HBV).

Histologické barvení	Zobrazené struktury	Využití v diagnostice
Hematoxylin a eosin	Přehledné barvení	Základní mikroarchitektonika jater
Trichrom – Massonův trichrom	Kolagenní vlákna	Zhodnocení rozsahu fibrózy Posouzení mikroarchitektoniky jater – zvýraznění portálních polí, <i>vena centralis</i>
Barvení dle Gomoriho	Retikulární vlákna	Posouzení mikroarchitektoniky jater – kondenzace retikulárních vláken (nekróza); rozšíření trámců (regenerace)
Barvení dle Foucheta	Biliverdin	Cholestáza
Perlsova reakce s berlínskou modří	Fe pigment	Lokalizace a rozsah depozit Fe pigmentu Zvýraznění pigmentovaných makrofágů
Periodic acid-Schiff (PAS)	Glykogen, bazální membrány	Glykogenové inkluze v hepatocytech – Wilsonova choroba, deficit alfa-1-antitrypsinu, glykogenózy apod.
Orcein	HBsAg, Cu depozita, elastická vlákna	Hepatitida B, Wilsonova choroba, chronická onemocnění žlučových cest

Teoretický úvod

Vlastní vyšetření mikroskopické stavby vzorku by mělo být systematické a mělo by zahrnovat popis mikroarchitektoniky jater, portálních polí a lobulárního parenchymu. Normální histologický obraz je charakterizován přítomností portálních polí a centrálních žil umístěných v jaterním parenchymu v pravidelných rozestupech. Na základě přítomnosti nepravidelností a změn v těchto třech parametrech pak můžeme rozdělit základní morfologické vzorce či obrazce jaterního poškození do sedmi kategorií. Dle algoritmu na obrázku 3 lze ve vzorku jater identifikovat nejvýznamněji zastoupený vzorec, který následně slouží jako vodítko při diferenciální diagnóze příčiny jaterního poškození. Níže jsou přehledně uvedeny možné typy jaterního poškození včetně popisu jejich morfologie a příkladů onemocnění.



Obrázek 3 – Algoritmus hodnocení histopatologického obrazu v jaterní biopsii.
Převzato a upraveno dle Saxena (2018).

Zánětlivý infiltrát v portálních polích – „*The blue portal tract*“

Hlavním znakem u tohoto typu poškození je rozšíření portálních polí zánětlivým buněčným infiltrátem, který jim propůjčuje modrý vzhled na preparátech barvených hematoxylinem a eosinem (obrázek 4A). Zánět se může rozšiřovat do okolního jaterního parenchymu a může způsobovat poškození hepatocytů různého stupně. Diagnózu onemocnění způsobujícího toto postižení lze stanovit na základě identifikace buněčných typů podílejících se na zánětlivé infiltraci a na základě výskytu dalších histopatologických znaků jako např. přítomnost intracytoplazmatických inkluzí (*ground-glass cells* – hepatitida B), přemostujících nekrot (autoimunitní hepatitida) či postižení portálních žlučvodů (primární sklerotizující cholangitida – PSC; primární biliární cirhóza – PBC).

Dukturní reakce – „*The bilious portal tract*“

Rozšíření portálních polí je u tohoto vzorce způsobeno proliferací žlučvodů, otokem, fibrózou (např. koncentrická peridukální fibróza, tzv. *onion-skinning* u PSC (obrázek 4B)) a neutrofilní zánětlivou infiltrací či přítomností granulomů (sarkoidóza, PBC). Také mohou být přítomny známky cholestázy (sepsy).

Poškození parenchymu lobulů – „*The distressed lobule*“

Poškození vlastního jaterního parenchymu bývá kombinací zánětu, nekrózy, městnání, cholestázy a probíhající regenerace (obrázek 4C). Může být doprovázeno změnami v portálních polích, které ovšem nejsou dominantním nálezem. Jedná se o častý nález u řady onemocnění, nebývá proto patognomický.

Steatóza – „*The bubbly liver*“

Steatóza je charakterizována nahromaděním tukových vakuol, které jsou na preparátech zpracovaných základním histologickým barvením viditelné jako vodojasné kulovité útvary v cytoplazmě hepatocytů (obrázek 4E, F). Dle velikosti vakuol lze steatózu rozdělit na (i.) makrovezikulární – jedna velká tuková vakuola vytlačující jádro na periferii buňky (obrázek 4E); (ii.) mikrovezikulární – množství drobných tukových vakuol, sama o sobě má diagnostickou vypovídací hodnotu (Reyův syndrom, těhotenská steatohepatóza); (iii.) smíšenou – morfologicky kombinace makro- a mikrovezikulární steatózy (obrázek 4F). Zároveň můžeme nacházet akumulaci lipidů v Kupfferových buňkách a v portálních makrofázích. Steatóza je typickým obrazem alkoholového a nealkoholového postižení jater, malnutrice či dědičných metabolických onemocnění (Niemannova-Pickova choroba, galaktosémie apod.).

Téměř normální vzhled – „*Calm, but not quiet*“

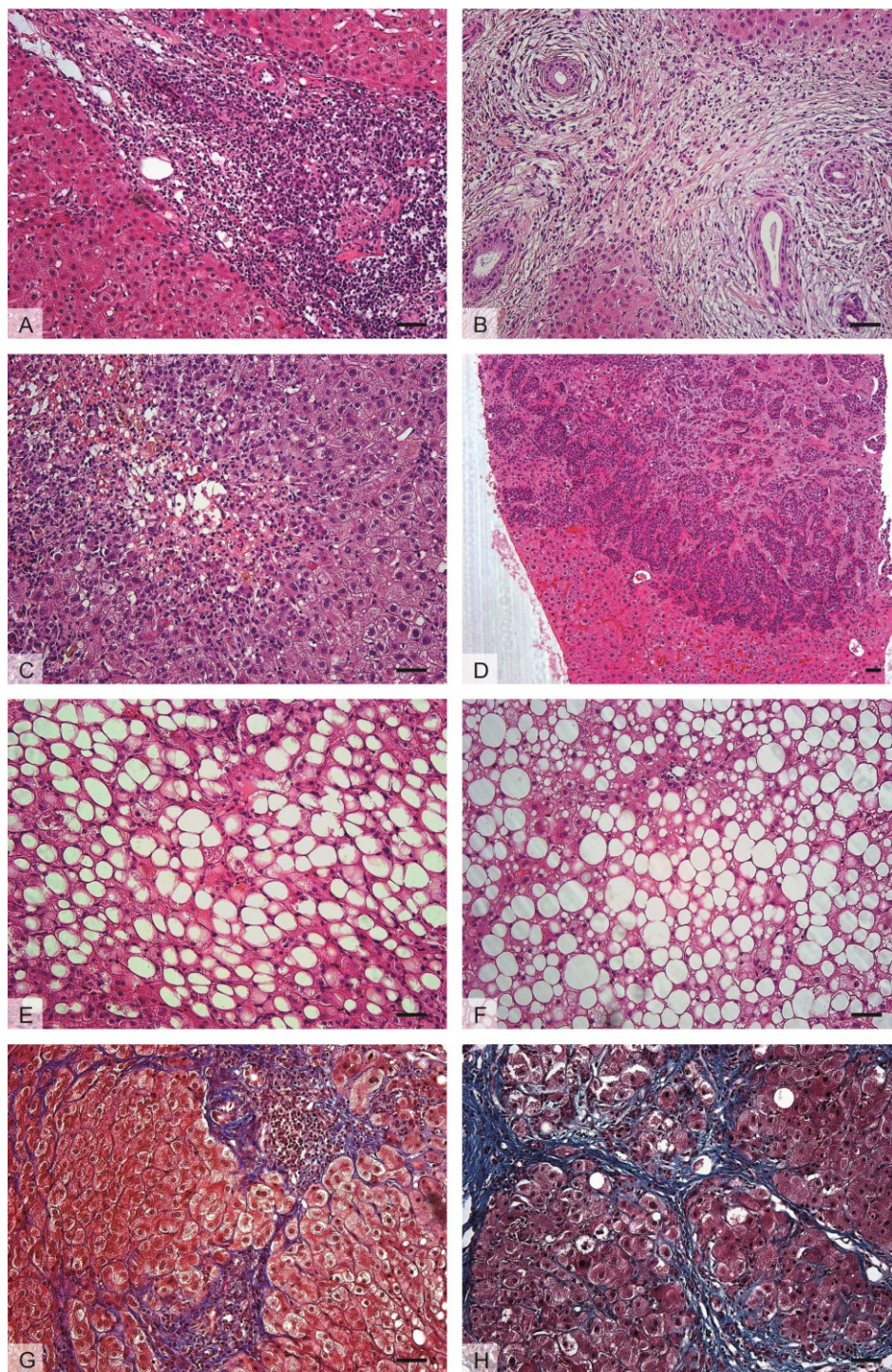
V histopatologickém obraze nenacházíme žádný z nejčastějších znaků jaterního onemocnění, jako je zánět, duktulární reakce, nekróza hepatocytů, steatóza či fibróza. Nevýrazné změny mohou být viditelné při větším zvětšení – lymfocyty v jaterních sinusoidách (hepatitida C), intracytoplazmatické inkluze (hepatitida B) či zvětšené bledé hepatocyty (diabetes mellitus). Nepravidelnosti v mikroarchitektonice jater mohou ukazovat na přítomnost nádorového bujení či regenerativních uzlů.

Fibróza, cirhóza – „*The scarred liver*“

Přítomnost vazivové tkáně, která významně narušuje mikroarchitektoniku jater, je nejvýraznějším znakem tohoto vzorce (obrázek 4G, H). Podezření na fibrotické změny můžeme mít již při makroskopické inspekci vzorku – kvůli křehkosti tkáně dochází často k jeho fragmentaci. Rozsah fibrózy může být od mírné fibrotizace (periportální fibrotizace) přes střední a těžkou fibrózu (porto-portální a porto-centrální septa) (obrázek 4G) až po cirhózu. Cirhóza je charakterizována přítomností sept a uzlů, ve kterých jsou jaterní trámce tvořeny dvěma a více řadami hepatocytů (obrázek 4H). Aktivitu cirhózy hodnotíme dle intenzity zánětu – u neaktivní cirhózy není přítomen uvnitř uzlů ani zánět ani nekróza a hranice mezi uzly a septy jsou jasně viditelné. Fibróza přecházející v cirhózu je konečným stádiem většiny chronických jaterních onemocnění.

Solidní léze – „*A pushy kind of guy*“

Normální jaterní parenchym je nahrazen nádorovou tkání (obrázek 4D). Ztráta uniformní distribuce portálních polí a centrálních vén je nejlepším vodítkem pro rozpoznání tohoto vzorce. Příčinami vzniku obrazu mohou být maligní i benigní nádory jater včetně metastáz či parazitárních infekcí.



Obrázek 4 – Příklady morfologických obrazů poškození mikrostruktury jater. A. Zánětlivý infiltrát v portálních polích, primární biliární cirhóza (PBC); **B.** Duktulární reakce – koncentrická periduktální fibróza (*onion-skinning*) kolem poškozených žlučovodů doprovázená otokem a zánětlivou infiltrací, primární sklerotizující cholangitida (PSC); **C.** Poškození parenchymu lobulů – centrilobulární nekróza, akutní hepatitida; **D.** Solidní léze – tumorózní tkáň nahrazující pravidelnou mikroarchitektoniku jaterního parenchymu, jaterní metastáza neuroendokrinního tumoru; **E.** Makrovezikulární steatóza – velká tuková vakuola vytlačující jádro na periferii buňky, nealkoholová steatohepatitida (non-alcoholic steatohepatitis, NASH); **F.** Smíšená steatóza – alkoholová steatohepatitida; **G. a H.** Fibróza a cirhóza, alkoholové poškození jater. Barvení hematoxylin a eosin (A – F), Massonův trichrom (G, H). *Měřítka* = 50 μ m.

1.3.2 Kvantitativní hodnocení mikroskopické stavby jater

Semikvantitativní skórovací systémy a jejich limitace

Kvalitativní popis jaterní biopsie s určením nejvýznamnějších vzorců jaterního poškození je základním pilířem histopatologické diagnostiky. Stejně významným je při hodnocení závažnosti nálezu využití semikvantitativních skórovacích systémů využívaných zejména při hodnocení chronických jaterních onemocnění. Skórovací systémy neslouží k určení primární diagnózy, ale spíše k určení závažnosti postižení, případně předpovědi progresu nálezu či odpovědi na léčbu.

V případě steatotického poškození jater lze např. využít specifické skórovací systémy vycházející ze stanovení přibližného procentuálního zastoupení hepatocytů s tukovými vakuolami, ze stanovení přítomnosti zánětu a ze stanovení přítomnosti tzv. balonové degenerace hepatocytů (*ballooning degeneration*) (Brunt et al. 1999, Kleiner et al. 2004). *Ballooned hepatocytes* se vyznačují světlou cytoplasmou a nahromaděním tekutin, což vede ke zvětšení buněk a ztrátě jejich typického tvaru (Saxena 2018). Skórovací systémy hodnotící závažnost chronického jaterního postižení využívají stanovení tzv. „*grade*“ určujícího aktivitu zánětu a „*stage*“ popisujícího stupeň fibrózy, která se vyvíjí a progreduje při chronickém poškození jater. V současnosti jsou nejvíce využívány tři systémy klasifikace: Battsova-Ludwigova klasifikace (Batts a Ludwig 1995), klasifikace dle Ishaka (Knodell et al. 1981) a klasifikace METAVIR (*Meta-analysis of Histological Data in Viral Hepatitis*) (Bedossa a Poynard 1996).

Grading (určení „*grade*“) vychází ze stanovení přítomnosti zánětu a nekrózy v periportální, intralobulární a portální oblasti. Každá z lézí je ohodnocena body, kdy vyšší číslo koresponduje s vyšší závažností nálezu. Body ze všech oblastí se sčítají a dohromady vytvářejí „*grade*“ zánětu v biopsii. *Staging* (určení „*stage*“) hodnotí rozsah a lokalizaci jaterní fibrózy. Ve všech skórovacích systémech dosahují hodnoty od 0 (žádná fibróza) po nejvyšší hodnotu (cirhóza) – hlavním cílem je tedy určení, zda jaterní postižení dosáhlo úrovně cirhózy. Další hodnoty neodrážejí přímo rozsah fibrózy, ale spíše její lokalizaci (Saxena 2018, Hůlek et al. 2018).

Zavedení semikvantitativních skórovacích systémů umožnilo v některých případech optimalizovat léčbu pacientů na základě předpovědi progresu jaterního poškození či hodnocení účinku léčby. Nicméně je třeba mít na paměti limitace související s metodikou kvantifikace v jaterních biopsiích. Jedním z významných faktorů ovlivňujících *grading* a *staging* je reprezentativnost vzorku, tzv. „*sampling error*“.

Teoretický úvod

V současnosti jsou vzorky jater nejčastěji odebírány metodou perkutánní biopsie naslepo nebo pod ultrazvukovou (UZ) kontrolou (Hůlek et al. 2018). K odběru se využívají bioptické jehly s průměrem 1,4 mm – vzhledem k celkovému objemu jater se tedy jedná jen o velmi malé vzorky tkáně. V zásadě lze i z těchto vzorků stanovit základní diagnózu, nicméně kvantifikace aktivity onemocnění a rozsahu fibrózy může být zatížena nedostatečnou reprezentativností odebraného vzorku.

Další limitací semikvantitativních skórovacích systémů je závislost výsledků hodnocení na osobě hodnotitele. Číselná hodnocení nejsou absolutními naměřenými hodnotami, ale vycházejí z pozorování hodnotitele. Rozsah jaterního poškození je definován např. termíny „mírný, střední, těžký“ („*mild, moderate, severe*“). Popis je závislý na subjektivním hodnocení pozorovatele. Rozdíly mezi hodnotiteli (*interobserver variability*) jsou často závislé na zkušenostech patologa a doporučuje se tedy, aby byly biopsie hodnoceny simultánně alespoň dvěma patology (The French METAVIR Cooperative Study Group 1994, Rousselet et al. 2005).

Možnosti kvantifikace v jaterní biopsii a jejich limitace

Přesné stanovení množství vaziva v jaterních biopsiích může být jednou z cest, jak se vyhnout významné variabilitě v hodnocení rozsahu fibrózy mezi hodnotiteli. Kvantifikovat množství vaziva je možné za využití metod obrazové analýzy dat (*computer-assisted morphometric image analysis*) (Saxena 2018). Měření jsou nicméně závislá na kvalitě zpracovaných vzorků, zejména na robustním barvení poskytujícím dostatečný kontrast hledané tkáně k pozadí, na parametrech nastavení softwaru pro analýzu obrazu a v neposlední řadě na strategii vzorkování tkáně – tedy na určení velikosti a místa odběru vzorků (Wang a Hou 2015). Množství vaziva navíc nekoresponduje se závažností jaterního postižení, kdy je vyšší „*stage*“ dán spíše lokalizací a charakterem fibrózy než celkovým nárůstem množství vaziva. K určení závažnosti onemocnění a předpovědi progresu by tedy měla být kvantitativní informace doplněna o informaci ohledně rozložení vaziva či dalšího jaterního poškození v kontextu k mikroarchitektonice jaterního parenchymu (Saxena 2018).

Validaci metod obrazové analýzy lze provést porovnáním výsledků měření s výsledky získanými robustními metodami kvantifikace, jako např. stereologickými metodami. Studie zpracovaná autory Homeyer et al. (2017) hodnotila rozsah steatotického poškození jater pomocí automatické obrazové analýzy a validovala výsledky s využitím bodové testovací mřížky. Motivací pro vývoj algoritmů obrazové

Teoretický úvod

analýzy je zejména menší pracnost a menší časová náročnost v porovnání se stereologickými metodami, které nicméně představují „zlatý standard“ kvantitativní histologie.

Tzv. *design-based stereology* vychází z principů stochastické geometrie a není založena na obtížně ověřitelných předpokladech týkajících se tvaru, velikosti, orientace či distribuce hodnocených struktur (Howard a Reed 1998, Mouton 2002). V současné chvíli existuje celá řada studií shrnujících praktická doporučení, jak lze postupovat při plánování a designu kvantitativního histologického hodnocení orgánů včetně jater (Kolinko et al. 2021, Marcos et al. 2012, Tschanz et al. 2014). Zásadním krokem zaručujícím nevychýlené odhady (*unbiased estimates*) sledovaných parametrů je využití systematického jednotného náhodného vzorkování tkáně (*systematic uniform random sampling*, SURS), které je nedílnou součástí plánování stereologického hodnocení. Jedinou účinnou cestou, jak se vyhnout vychýlení a zajistit přesnost měření, je standardizace postupu vzorkování (Hsia et al. 2010). Příklady histologického kvantitativního hodnocení v játrech prasete včetně použitých metod barvení jsou přehledně uvedeny v tabulce 3.

Problematika vzorkování od úrovně orgánů (počet odebraných tkáňových bločků) po úroveň jednotlivých histologických řezů (počet a velikost zorných polí, tzv. *fields of view*, určení oblastí zájmu, tzv. *regions of interest*) s využitím metod virtuální mikroskopie byla podrobně diskutována ve článku Kolinko et al. (2021) publikovaném v impaktovaném časopise *Anatomia, Histologia, Embryologia*. Publikace je součástí této dizertační práce v podobě přílohy III na str. 98.

Tabulka 3 – Příklady histologického kvantitativního hodnocení v játrech prasete.

Histologické barvení	Zobrazené struktury	Kvantitativní hodnocení	Studie
Hematoxylin a eosin	Přehledné barvení	Rozsah hemoragické nekrózy	Pálek et al. 2020
Anilinová modř	Kolagenní vlákna	Množství vaziva	Mik et al. 2018
Reticulin kit	Retikulární vlákna	Šíření trhlín játry	Malečková et al. 2021
Periodic acid-Schiff (PAS)	Glykokalyx membrán hepatocytů	Počet a velikost hepatocytů	Junatas et al. 2017
Lektinová histochemie	Jaterní sinusoidy a žlučové kapiláry	Délková hustota jaterních sinusoid a žlučových kapilár	Malečková et al. příloha IX

2 Cíle a hypotézy dizertace

Zvířecí modely jsou hojně využívány při studiu patogeneze a progresu jaterních onemocnění či při vývoji nových strategií jejich terapeutického ovlivnění. Zaměření této dizertační práce na velký zvířecí model, prase domácí, odráží současný trend na poli experimentální medicíny, tedy využití modelů co nejbližších člověku tak, aby byly výsledky experimentů co nejpřesněji přenositelné do humánní medicíny. V rutinní patologické praxi je histologické hodnocení nedílnou součástí procesu stanovení diagnózy a závažnosti jaterního poškození. Analogicky je tedy histopatologické vyšetření tkáně zařazeno do designu experimentálních studií na játrech prasete. Naším cílem bylo aplikovat metody kvalitativního a kvantitativního histologického hodnocení a ověřit jejich využitelnost na játrech prasete. Metody kvantifikace zahrnovaly jak automatickou obrazovou analýzu dat, tak stereologické metody zaručující vysokou reprodukovatelnost studií a porovnatelnost výsledků z různých experimentů. Následující zformulované výzkumné otázky shrnují základní problémy řešené v předložených pracích:

1. Jakými nástroji lze automatizovat a zefektivnit kvantitativní analýzu mikrocév jater zobrazených pomocí výpočetní tomografie s vysokým rozlišením (mikro-CT)?
2. Jak lze validovat data získaná automatickou analýzou mikro-CT skenů mikrocév a jak automatická mikro-CT vyšetření kalibrovat?
3. Jak je v jednotlivých oblastech jater prasete rozloženo vazivo a jak souvisí množství vaziva s pohlavím jedince?
4. Jak jsou v jednotlivých oblastech jater prasete rozloženy jaterní sinusoidy a žlučové kapiláry a jak souvisí jejich rozložení s pohlavím jedince?
5. Jaký je dopad aplikace mezenchymálních kmenových buněk na histologické změny v játrech a jaký bude mít vliv na celkový průběh onemocnění a přežití prasat se sinusoidálním obstrukčním syndromem po parciální hepatektomii?
6. Jak souvisí mikroskopická stavba jater prasete se šířením trhlin játry v experimentu simulujícím tupé poranění?

Postupné zodpovězení těchto šesti výzkumných otázek a formulování závěrů bylo hlavním cílem níže předložených prací. Stručný popis motivace, formulovaných hypotéz, metodiky i výsledků a následná diskuze jsou uvedeny v následujících kapitolách.

2.1 Kvantifikace jaterních mikrocév v korozivních preparátech jater zobrazených pomocí mikro-CT

2.1.1 Motivace a cíle práce

Mikrovaskulární síť jater hraje klíčovou roli ve fyziologických i patologických procesech probíhajících ve tkáních jater. Navzdory důležitosti mikrovaskulární sítě jater máme jen omezené množství dat popisující její trojrozměrné uspořádání. Jednou z možností vizualizace trojrozměrné sítě mikrocév je využití korozivních preparátů (Lametschwandtner et al. 2005) a jejich zobrazení pomocí mikro-CT (Schladitz 2011). S využitím stereologických metod (Howard a Reed 1998, Mouton 2002, Mühlfeld 2014), které jsou zlatým standardem kvantitativní histologie, je pak možné mikrocévní síť zrekonstruovat na základě statistického popisu její geometrie. Získání dostatečného objemu dat stereologickými metodami, tedy manuální kvantifikací, je nicméně velmi časově náročné a zatěžující pro osobu hodnotitele. Cílem této studie bylo vyvinout open-source software pro kvantifikaci mikro-CT skenů korozivních preparátů mikrocév jater prasete. Validace dat získaných automatickou kvantifikací byla provedena na základě porovnání s daty získanými stereologickou kvantifikací.

2.1.2 Hypotézy

$H_0(A)$: Výsledky kvantifikace popisující objemy, povrchy, délky a počty jaterních mikrocév získané automatickou kvantifikací se neliší od výsledků získaných manuální kvantifikací.

Podrobná metodika, výsledky, diskuze a závěry jsou v plném rozsahu součástí publikace v časopise *International Journal of Computer Assisted Radiology and Surgery* (Jiřík et al. 2016). Publikace je k dispozici v příloze IV na str. 119 této dizertační práce.

2.2 Generování virtuálních obrazových dat pro kalibraci vyšetřování vláknitých a porézních struktur pomocí mikro-CT

2.2.1 Motivace a cíle práce

Mikro-CT je v současnosti preferovanou metodou používanou v analýzách trojrozměrných struktur, jakými jsou např. rentgen-kontrastní biomateriály, tvrdé tkáně či korozivní preparáty mikrocév (Jiřík et al. 2016). Hlavní výhodou mikro-CT oproti klasické mikroskopii, které se svým rozlišením v rozsahu desítek až jednotek mikrometrů blíží, je možnost zobrazení trojrozměrných struktur a jejich charakterizace pomocí kvantitativní analýzy vybraných prostorových parametrů. Automatická kvantitativní analýza těchto parametrů, jakými jsou např. objem, povrch, délka nebo počet objektů, vyžaduje segmentaci obrazových dat v důsledku nedostatečného kontrastu mikro-CT skenů. Kvantitativní data získaná pomocí mikro-CT jsou často prezentována jako přesná, ovšem míra vychýlení v závislosti na segmentačních algoritmech je neznámá. Cílem studie bylo vyvinout software pro generování trojrozměrných virtuálních modelů vláknitých a porézních struktur se známými morfometrickými parametry – objemem, povrchem, délkou a počtem objektů – a poskytnout tak data a softwarový nástroj pro kalibraci automatických analýz mikro-CT skenů. Dalším cílem bylo najít potenciální zdroje chyb v měření a poskytnout praktické rady, jak se nepřesnostem v měření vyhnout.

2.2.2 Hypotézy

Cílem této studie bylo vytvořit softwarový nástroj vhodný pro testování kvantitativních postupů v analýze trojrozměrných dat. Byla provedena rozsáhlá citlivostní analýza dat, konkrétní hypotézy testovány nebyly.

Podrobná metodika, výsledky, diskuze a závěry jsou v plném rozsahu součástí publikace v časopise *Microscopy Research and Technique* (Jiřík et al. 2018). Publikace je k dispozici v příloze V na str. 137 této dizertační práce.

2.3 Mapování rozložení vaziva v játrech prasete

2.3.1 Motivace a cíle práce

Jaterní fibróza je postižením jater, které významně ovlivňuje morbiditu a mortalitu pacientů (Asrani et al. 2019). Rozsah fibrózy je u člověka stanoven na základě jaterní biopsie s využitím semikvantitativních skórovacích systémů. Skórovací systémy jsou nicméně značně subjektivní a vykazují variabilitu výsledků jak mezi hodnotiteli, tak i mezi hodnoceními stanovenými jedním hodnotitelem (Saxena 2018). V současnosti se k modelování jaterní fibrózy využívají malé zvířecí modely (Starkel a Leclercq 2011), ale i velké zvířecí modely vykazující anatomickou a fyziologickou podobnost s člověkem, a to zejména modely prasete (Yasmin et al. 2021). Studium zvířecích modelů jaterní fibrózy přispívá k objasnění patogeneze a progresu fibrózy a může být také využito ke stanovení účinnosti různých terapeutických přístupů (Berumen et al. 2021). Žádná z dosud publikovaných studií na játrech prasete se nezabývala kvantitativní analýzou množství vaziva s využitím vysoce reprodukovatelných stereologických metod a neposkytla informaci o distribuci vaziva v jednotlivých anatomických oblastech jater.

Cílem studie bylo odhadnout množství vaziva v játrech prasete pomocí standardizovaných stereologických metod a získat data o distribuci vaziva ve zdravých samčích a samičích játrech prasete, a to v šesti jaterních lalocích a ve třech oblastech vztažených k cévnímu zásobení jater (periferní, parakaválná a paraportální oblast). Dalším cílem bylo poskytnutí popisných statistik pro odhad minimálního počtu vzorků tak, abychom byli schopni odhalit relativní změny v množství vaziva v experimentálních studiích využívajících játra prasete.

2.3.2 Hypotézy

$H_0(A)$: Objemový podíl vaziva v játrech prasete se neliší mezi samčími a samičími játry.

$H_0(B)$: Objemový podíl vaziva v játrech prasete se neliší mezi šesti jaterními laloky.

$H_0(C)$: Objemový podíl vaziva v játrech prasete se neliší mezi třemi oblastmi jater vztaženými k cévnímu zásobení jater.

Podrobná metodika, výsledky, diskuze a závěry jsou v plném rozsahu součástí publikace v časopise *Journal of Comparative Pathology* (Mik et al. 2018). Publikace je k dispozici v příloze VI na str. 156 této dizertační práce.

2.4 Délková hustota jaterních sinusoid a žlučových kapilár v játrech prasete

2.4.1 Motivace a cíle práce

Vzájemné prostorové uspořádání trámců hepatocytů, jaterních sinusoid a žlučových kapilár je odrazem jedinečné polarity hepatocytů – cytoplazmatická membrána jejich apikální (luminální) domény se podílí na tvorbě počátečních úseků intrahepatických žlučových cest, bazální doména je přivrácena k jaterním sinusoidám, přesněji k perisinusoidálnímu Disseho prostoru. Přestože žlučové kapiláry a jaterní sinusoidy vystlané specializovaným fenestrovaným nesouvislým endotelem přispívají k řadě fyziologických i patologických pochodů v játrech, např. k regeneraci jater (Gracia-Sancho et al. 2021, Meyer et al. 2020, Sørensen et al. 2015), není často těmto strukturám přisuzována větší pozornost při hodnocení jaterních biopsií na rutinních tenkých řezech. Žádná z dosud publikovaných studií také neposkytla informace týkající se kvantitativních morfometrických parametrů popisujících jaterní sinusoidy a žlučové kapiláry v játrech prasete.

Cílem naší studie bylo kvantifikovat délkovou hustotu jaterních sinusoid a žlučových kapilár ve zdravých játrech prasete. Dalším cílem bylo poskytnutí primárních kvantitativních dat a popisných statistik, které budou vhodné pro výpočet minimálního počtu vzorků pro odhalení relativních změn v délkové hustotě jaterních sinusoid a žlučových kapilár v šesti jaterních lalocích a ve třech oblastech vztažených k cévnímu zásobení jater.

2.4.2 Hypotézy

H₀(A): Délková hustota jaterních sinusoid a žlučových kapilár v játrech prasete se neliší mezi samčími a samičími játry.

H₀(B): Délková hustota jaterních sinusoid a žlučových kapilár v játrech prasete se neliší mezi šesti jaterními laloky.

H₀(C): Délková hustota jaterních sinusoid a žlučových kapilár v játrech prasete se neliší mezi třemi oblastmi jater vztaženými k cévnímu zásobení jater.

H₀(D): Délková hustota jaterních sinusoid a žlučových kapilár nekoreluje s dříve publikovanými daty popisujícími počet a velikost hepatocytů (Junatas et al. 2017) a objemový podíl vaziva v játrech prasete (Mik et al. 2018).

Podrobná metodika, výsledky, diskuze a závěry jsou v plném rozsahu součástí publikace zaslané do časopisu *Annals of Anatomy*. Současné znění publikace je k dispozici v příloze VII na str. 170 této dizertační práce.

2.5 Histologické hodnocení jater prasete s indukovaným sinusoidálním obstrukčním syndromem – studie vlivu aplikace mezenchymálních kmenových buněk na průběh onemocnění

2.5.1 Motivace a cíle práce

Sinusoidální obstrukční syndrom (*sinusoidal obstruction syndrome, SOS*), dříve označovaný jako veno-okluzivní choroba (*veno-occlusive disease*), je onemocnění charakterizované postižením jaterních cév, které vzniká v důsledku toxického poškození endotelu jaterních sinusoid (Bayraktar et al. 2007, DeLeve et al. 1999). SOS způsobuje závažné komplikace po transplantaci hematopoetických kmenových buněk a je spojen s požitím pyrrolizidinových alkaloidů (např. monokrotalinu) či s léčbou oxaliplatinou u pacientů s jaterními metastázami kolorektálního karcinomu (Floyd et al. 2006, Valla a Cazals-Hatem 2016). Klinicky se projevuje bolestivou hepatomegalií, ikterem a přírůstkem váhy v závislosti na retenci tekutin (Saxena 2018). U pacientů s jaterními metastázami kolorektálního karcinomu může rozvoj SOS indukovaný podáváním oxaliplatinu ohrozit možnost resekce jaterních metastáz, a tím snížit šanci pacienta na přežití.

Histologicky nacházíme v časných stádiích poškození stěny sinusoid následované vznikem centrilobulárních hemoragických nekróz. Reaktivní fibrotické změny center jaterních lalůček se objevují po obnovení kontinuity sinusoidálních endotelových buněk a regresi nekrotických změn (DeLeve et al. 1999).

Cílem práce bylo vytvořit velký zvířecí model SOS pomocí aplikace pyrrolizidinového alkaloidu monokrotalinu. Po vytvoření velkého zvířecího modelu SOS bylo dalším cílem zjistit vliv aplikace mezenchymálních kmenových buněk (*mesenchymal stem cells, MSC*) na průběh SOS a na celkové přežití zvířat po resekci části jaterního parenchymu. Cílem histologické analýzy bylo vyhodnotit vliv aplikace mezenchymálních kmenových buněk na histologický obraz jater se syndromem SOS, a to na základě: (i) kvantifikace objemového podílu hemoragické nekrózy 14. a 28. den po aplikaci monokrotalinu; (ii) kvantifikace morfoloicky viabilního jaterního parenchymu

14. a 28. den po aplikaci monokrotalinu; (iii) popisu kvalitativních histologických změn jako je přítomnost zánětlivé infiltrace, reaktivních fibrotických změn či steatózy.

2.5.2 Hypotézy

H₀(A): Objemový podíl nekrózy, viabilního jaterního parenchymu a fibrotických lézí v játrech prasete po indukci SOS se neliší mezi kontrolní skupinou a experimentální skupinou, které byly aplikovány mezenchymální kmenové buňky.

H₀(B): Parametry měřené pomocí ultrazvukového vyšetření – objem jater, průměr *vena portae*, maximální rychlost průtoku v extrahepatální části *v. portae* a šířka stěny žlučníku – se neliší mezi kontrolní skupinou a experimentální skupinou, které byly aplikovány mezenchymální kmenové buňky.

H₀(C): Parametry stanovené biochemickou analýzou periferní krve – bilirubin, alkalická fosfatáza (ALP), gamaglutamyltransferáza (GGT), aspartátaminotransferáza (AST), alaninaminotransferáza (ALT), amoniak, urea a kreatinin – se neliší mezi kontrolní skupinou a experimentální skupinou, které byly aplikovány mezenchymální kmenové buňky.

Podrobná metodika, výsledky, diskuze a závěry jsou v plném rozsahu součástí publikace v časopise *Rozhledy v chirurgii* (Pálek et al. 2018) a publikace v časopise *Anticancer Research* (Pálek et al. 2020). Publikace jsou k dispozici v příloze VIII na str. 198 a v příloze IX na str. 207 této dizertační práce.

2.6 Analýza šíření trhlin játry prasete

2.6.1 Motivace a cíle práce

Dopravní nehody jsou nejčastější příčinou tupého poranění břicha, které je často doprovázeno poraněním parenchymatózních orgánů, zejména jater a sleziny. Prevence vzniku poranění a včasná předpověď jeho závažnosti může vést k významnému snížení morbidity a mortality pacientů (Xu et al. 2018). Současný trend v oblasti předpovědi závažnosti poranění tkání a orgánů při nárazu spočívá ve vývoji výpočetních modelů lidského těla, které slouží k simulaci různých mechanismů poranění (Golman et al. 2014). Modely jsou založené na morfometrických datech získaných zejména z měření v různých typech zobrazovacích metod, jako je např. výpočetní tomografie nebo magnetická rezonance (Gayzik et al. 2011). Druhým typem dat nezbytným pro výpočetní modely jsou

Cíle a hypotézy dizertace

data popisující biomechanické chování orgánů a tkání – data lze získat z biomechanických experimentů.

Biomechanické experimenty týkající se jater byly v minulosti prováděny jak na lidských orgánech (Conte et al. 2012), tak na orgánech prasete (Chen et al. 2018). Při využití zvířecích orgánů je nicméně vždy nutné mít na paměti rozdílnou mikroskopickou stavbu, která může ovlivnit celkové mechanické chování orgánu. Navzdory významnému prokrvení jater a dříve popsanému vztahu mezi závažností poranění a náhlým vzestupem intravaskulárního tlaku (Sparks et al. 2007) byla dosud jen malá pozornost věnována experimentům na celých játrech prasete s důrazem na měření změn intravaskulárního tlaku v okamžiku nárazu.

Cílem naší studie bylo popsat biomechanické chování celých jater prasete v okamžiku nárazu během experimentu simulujícího tupé poranění břišních orgánů. Zvláštní důraz byl kladen na popis vztahu změn intravaskulárního tlaku v závislosti na energii dopadu. Biomechanické měření bylo doplněno o analýzu závažnosti poranění (Kozar et al. 2018) a histologickou kvantitativní analýzu šíření trhliny játry prasete ve vztahu k hlavním vláknitým složkám jaterního stromatu. Dalším cílem bylo poskytnutí primárních mechanických dat, která by byla veřejně k dispozici pro vývoj modelů poranění jater.

2.6.2 Hypotézy

$H_0(A)$: Závažnost poranění a hodnota nárůstu intravaskulárního tlaku v okamžiku nárazu se neliší v závislosti na energii dopadu.

$H_0(B)$: Trhlina se játry prasete šíří náhodně, nezávisle na hlavních vláknitých složkách jaterního stromatu.

Podrobná metodika, výsledky, diskuze a závěry jsou v plném rozsahu součástí publikace v časopise *Physiological Measurement* (Malečková et al. 2021). Publikace je k dispozici v příloze X na str. 225 této dizertační práce.

3 Materiál a metody

3.1 Kvantifikace jaterních mikrocév v korozivních preparátech jater zobrazených pomocí mikro-CT

Analyzované vzorky jater pocházely ze dvou selat, plemeno přeštické černostrakaté (sele 1: věk₁ = 6 týdnů, m₁ = 12 kg; sele 2: věk₂ = 10 týdnů, m₂ = 25 kg). Zvířata byla před hepatektomií heparinizována, abychom zabránili vzniku krevních sraženin. Veškerá manipulace s orgány probíhala pod vodní hladinou z důvodu prevence vzniku vzduchových bublin. Vlastní korozivní preparát byl vytvořen intraportální aplikací pryskyřice Biodur E20 Plus (Biodur products, Heidelberg, Německo), která kompletně vyplnila cévní řečiště (náplň dosáhla *v. cava caudalis* a *a. hepatica propria*). Po 24 hodinách polymerizace pryskyřice byly okolní tkáně jater odstraněny pomocí 15% roztoku KOH. Detailní popis přípravy korozivního preparátu je popsán v publikaci (Eberlová et al. 2016).

Dva náhodně vybrané vzorky korozivních preparátů byly naskenovány pomocí stacionárního mikro-CT zařízení (Xradia XCT 400, Xradia, Pleasanton, CA, USA). Výsledkem byly 2 sestavy obrázků čítající 1000 za sebou jdoucích řezů s velikostí pixelu v rozmezí 1,88–4,68 μm. Pro kvantitativní analýzu byly vybrány dva soubory obrazových dat: (i) náhodně vybrané oblasti (n = 10) o velikosti 350 × 350 pixelů, každá oblast byla tvořena 50 za sebou jdoucími řezy; (ii) ručně ohraničené oblasti (n = 4) reprezentující klasický jaterní lalůček.

Ve vybraných obrazových datech byly za pomoci stereologických metod implementovaných v softwaru Ellipse (ViDiTo, Košice, Slovensko) kvantifikovány parametry shrnuté v tabulce 4.

Identické sady obrázků byly použity pro kvantifikaci mikrocév pomocí nově vyvinutého open-source softwaru QuantAn (Jířík 2015). Při analýze mikrocévní sítě pomocí softwaru QuantAn byly cévy převedeny na jednoduché lineární segmenty a na jejich spojení, tzv. procesem skeletonizace. Výstupy analýzy zahrnují grafickou reprezentaci dat (histogramy) a vyčíslení kvantitativních parametrů (V_V, S_V, L_V, N_V, tortuosita – poměr mezi délkou cévy a vzdáleností mezi dvěma uzlovými body). Data získaná automatickou analýzou pomocí softwaru QuantAn byla porovnána s daty z manuálního hodnocení – Wilcoxonův párový test.

Další podrobnosti nutné pro reprodukovatelnost studie jsou uvedeny v příloze IV na str. 119.

Tabulka 4 – Přehled parametrů použitých pro kvantifikaci mikrocév v játrech prasete.

Parametr	Zkratka	Jednotka	Definice	Možná biologická interpretace	Metoda kvantifikace
Objemový podíl	V_v	(–)	Objem mikrocév v referenčním objemu	Relativní objem tkáně okupovaný krevními cévami	Bodová testovací mřížka
Povrchová hustota	S_v	mm^{-1}	Povrch mikrocév v referenčním objemu	Relativní povrch mikrocév vhodný pro výměnu metabolitů	Sonda Fakir
Délková hustota	L_v	mm^{-2}	Délka mikrocév v referenčním objemu	Délka mikrocév odrážející okamžitou perfúzi tkáně	Manuální trasování cév
Numerická hustota	N_v	mm^{-3}	Počet mikrocév v referenčním objemu	Míra větvení a propojení mikrocévní sítě odrážející angiogenezi ve tkáni	Manuální počítání uzlových bodů

3.2 Generování virtuálních obrazových dat pro kalibraci vyšetřování vláknitých a porézních struktur pomocí mikro-CT

V nově vyvinutém softwaru TeIGen (Jiřík 2017) naprogramovaném v jazyce Python byly vygenerovány virtuální sady obrázků napodobující obrazová data z micro-CT skenů vláknitých a porézních struktur. Jako předloha pro generované struktury, včetně realistického šumu na pozadí obrázků, sloužily reálné skeny biomateriálů využívaných pro výrobu umělých cévních náhrad (Horáková et al. 2018) a jako výplně pro urychlení kostního hojení (Suchý et al. 2015). Generované sady obrázků měly známou velikost voxelu a známé hodnoty morfometrických parametrů. Parametry byly stanoveny na základě analýzy reálných mikro-CT skenů (Jiřík et al. 2016) – objem, povrch, délka a počet objektů v referenčním objemu. Celkem 40 vygenerovaných sad obrázků bylo následně kvantifikováno pomocí softwaru CTAn (Skyscan CT analyzer), který byl

navržen k analýze mikro-CT skenů. Výsledky kvantifikace pomocí softwaru CTAn byly porovnány se skutečnými hodnotami morfometrických parametrů vygenerovaných pomocí softwaru TeIGen, a to včetně odchylek ve výstupech způsobených nastavením segmentačních algoritmů.

Další podrobnosti nutné pro reprodukovatelnost studie jsou uvedeny v příloze V na str. 137.

3.3 Mapování rozložení vaziva v játrech prasete

Studie byla založena na analýze jater z celkem 12 zdravých selat plemene přeštické černostrakaté – šest samic a šest kastrovaných sameců. Věk zvířat byl 9–15 týdnů, hmotnost 25–45 kg ($34,3 \pm 5,3$ kg; průměr \pm směrodatná odchylka). Zvířata byla usmrcena v celkové anestezii aplikací kardioplegického roztoku KCl. Objem čerstvých jater dosahoval 0,64–1,2 l ($0,87 \pm 0,15$ l; průměr \pm směrodatná odchylka).

Z každých jater bylo odebráno celkem 36 tkáňových bločků o rozměrech $25 \times 25 \times 15$ mm. Tkáňové bločky reprezentovaly šest jaterních laloků a tři oblasti jater vztahované k cévnímu zásobení (periferní, parakavální a paraportální). Z každého laloku bylo odebráno šest tkáňových bločků, vždy dva z každé cévně zásobené oblasti. Celkem bylo analyzováno 415 vzorků.

Z každého bločku byly připraveny 3 μ m silné řezy se znáhodněnou rovinou řezu (Mühlfeld 2014), které byly obarveny anilinovou modří za účelem vizualizace kolagenních vláken (Merck KGaA, Darmstadt, Německo). Metodou systematického uniformního náhodného vzorkování byla nasnímána z každého řezu zorná pole, na která byla v softwaru Ellipse (ViDiTo, Košice, Slovenská republika) promítnuta bodová testovací mřížka. Kvantifikované parametry jsou shrnuty v tabulce 5. Kvantifikace byla založena na analýze 2905 mikrofotografií.

Statistická analýza dat byla provedena v softwaru Statistica Base 11 (StatSoft, Inc. Tulsa, Oklahoma, USA). Některá data vykazovala nenormální rozložení (Shapiro-Wilkův test), pro další analýzy jsme tedy využili neparametrické testy – Kruskalova-Wallisova ANOVA a Mannův-Whitneyův U-test. Minimální počet vzorků nutných pro odhalení relativních změn v množství vaziva byl vypočítán dle Chow et al. (2008).

Další podrobnosti nutné pro reprodukovatelnost studie jsou uvedeny v příloze VI na str. 156.

Tabulka 5 – Přehled kvantitativních parametrů hodnocených ve studii rozložení vaziva v játrech prasete. ICT – interlobulární vazivo (*interlobular connective tissue*), PSCT – peisinusoidální vazivo (*perisinusoidal connective tissue*), PCCT – pericentrální vazivo (*pericentral connective tissue*), CT – vazivo (*connective tissue*).

Parametr	Zkratka	Definice	Zorná pole	Zvětšení
Objemový podíl interlobulárního vaziva	V _V (ICT)	Podíl vaziva v oblasti obklopující jaterní lalůček	3	10×
Objemový podíl perisinusoidálního vaziva	V _V (PSCT)	Podíl vaziva v oblasti kolem jaterních sinusoid uvnitř jaterního lalůčku	4	20×
Objemový podíl pericentrálního vaziva	V _V (PCCT)	Podíl vaziva v oblasti kolem <i>vena centralis</i> uvnitř jaterního lalůčku	4	20×
Celkový objemový podíl vaziva	V _V (CT)	V _V (ICT) + V _V (PSCT) + V _V (PCCT)	–	–

3.4 Délková hustota jaterních sinusoid a žlučových kapilár v játrech prasete

V této studii byly analyzovány stejné tkáňové vzorky jako v předchozích studiích zabývajících se počtem a velikostí hepatocytů (Junatas et al. 2017) a distribucí vaziva v játrech prasete (Mik et al. 2018). Z každého ze 12 jater zdravých přeštických černostrakatých prasat (šest samic a šest samců) bylo získáno 36 tkáňových bločků, které reprezentovaly šest jaterních laloků a tři rozdílné oblasti jater s ohledem na jejich cévní zásobení (periferní, parakavální a paraportální). Z každého bločku byly získány tři řezy se znáhodněnou rovinou řezu (Mühlfeld 2014), které byly obarveny metodou lektinové histochemie za využití lektinu *Ricinus communis* agglutinin I. Metoda umožnila vizualizaci endotelu jaterních sinusoid a výstelky žlučových kapilár. Z každého řezu byla metodou systematického uniformního náhodného vzorkování nasnímána čtyři zorná pole objektivem se zvětšením 40×, celkem 12 zorných polí na bloček. Délková hustota jaterních sinusoid a žlučových kapilár byla vypočítána v závislosti na počtu průsečíků cév (cévních profilů) s rovinou řezu. Celkem byly výsledky založeny na kvantifikaci 4428 mikrofotografií ze 369 tkáňových bločků.

Porovnání hodnot délkové hustoty jaterních sinusoid a žlučových kapilár mezi jaterními laloky a oblastmi jater s ohledem na cévní zásobení bylo provedeno obdobným způsobem jako ve studii rozložení vaziva (Mik et al. 2018) pomocí neparametrických testů – Kruskalova-Wallisova ANOVA a Mannův-Whitneyův U-test. Navíc byla provedena korelace nově získaných dat s výsledky studie počtu a velikosti hepatocytů (Junatas et al. 2017) a rozložení vaziva (Mik et al. 2018). Minimální počet vzorků nutných pro odhalení relativních změn v délkové hustotě jaterních sinusoid a žlučových kapilár byl vypočítán dle Chow et al. (2008).

Další podrobnosti nutné pro reprodukovatelnost studie jsou uvedeny v příloze VII na str. 170.

3.5 Histologické hodnocení jater prasete s indukovaným sinusoidálním obstrukčním syndromem – studie vlivu aplikace mezenchymálních kmenových buněk na průběh onemocnění

Do pilotní studie, jejímž cílem bylo etablování velkého zvířecího modelu SOS, bylo zařazeno 27 zvířat plemene přeštické černostrakaté – 12 samic a 15 samců. Zvířatům byla v celkové anestezii intraportálně aplikovaná dávka monokrotalinu v množství 180 mg/kg (n = 5) nebo 36 mg/kg (n = 22). Sedmý den po aplikaci byla provedena resekce levého laterálního laloku jater a 21. den byla zvířata usmrcena. V průběhu experimentu byly prováděny odběry periferní krve za účelem stanovení biochemických markerů a ultrazvuková vyšetření jater. Vzorky jater z 0., 7. a 21. dne byly podrobeny histologickému vyšetření.

Do navazující studie po úspěšném etablování velkého zvířecího modelu SOS bylo zařazeno celkem 21 prasat, plemeno přeštické černostrakaté – 16 samic a 5 kastrovaných samců. Věk zvířat byl 3–4 měsíce, hmotnost 23–44 kg. Zvířata byla rozdělena do dvou skupin: i) kontrolní skupina (n = 12) a ii) experimentální skupina (n = 8), ve které byly zvířatům intravenózně aplikovány MSC izolované z kostní dřeně zdravých prasat. Jedno ze zvířat bylo v důsledku předčasného úhynu před 7. dnem experimentu ze studie vyřazeno. U všech zvířat byl v 0. den indukován SOS intraportální aplikací monokrotalinu v dávce 36 mg/kg, která byla stanovena na základě výsledků pilotní studie. 7. den experimentu byly kontrolní skupině podány MSC. 14. den experimentu byla všem jedincům provedena resekce levého laterálního laloku jater v celkové anestezii. 28. den experimentu byla zvířata usmrcena. V průběhu experimentu byla zvířata pravidelně

Materiál a metody

monitorována a bylo prováděno ultrazvukové vyšetření (objem jater, průměr *vena portae*, maximální rychlost průtoku v extrahepatální části *vena portae* a šířka stěny žlučníku) a biochemické vyšetření (bilirubin, ALP, GGT, AST, ALT, amoniak, urea a kreatinin).

Histologická analýza zahrnovala hodnocení 59 tkáňových bločků. Od všech zvířat byl na začátku experimentu (0. den) odebrán vzorek levého laterálního laloku, vzorek z resekátu levého laterálního laloku jater po resekci (14. den) a náhodný vzorek jater na konci experimentu (28. den, případně den předčasného uhynutí zvířete). Z každého bločku byly připraveny 4 μm silné řezy, které byly obarveny hematoxylinem a eosinem a také anilinovou modří (Merck KGaA, Darmstadt, Německo). Metodou SURS byla nasnímána z každého řezu zorná pole, na která byla v softwaru Ellipse (ViDiTo, Košice, Slovenská republika) promítnuta bodová testovací mřížka. Kvantifikované parametry jsou shrnuty v tabulce 6. K porovnání kvantitativních histologických dat byl využit neparametrický test ANOVA. Kvantitativní výsledky byly doplněny o kvalitativní pozorování, tedy o přítomnost hemoragické nekrózy, zánětlivé infiltrace, steatózy a reaktivních fibrotických změn.

Další podrobnosti nutné pro reprodukovatelnost studie jsou uvedeny v příloze VIII na str. 198 a v příloze IX na str. 207.

Tabulka 6 – Přehled parametrů kvantifikovaných v játrech prasete pro určení rozsahu jaterního poškození v důsledku sinusoidálního obstrukčního syndromu.

Parametr	Zkratka	Definice	Zorná pole	Zvětšení
Objemový podíl nekrózy	V_V (necrosis, liver)	Rozsah centrilobulární hemoragické nekrózy.	6	10 \times
Objemový podíl parenchymu	V_V (parenchyma, liver)	Viabilní jaterní parenchym reprezentovaný hepatocyty uspořádanými do trámců s neporušenou jadernou membránou a jasnou eosinofilní cytoplazmou.	8	40 \times

3.6 Analýza šíření trhlin játry prasete

Játra prasete plemene přeštické černostrakaté ($n = 24$) byla odebrána heparinizovaným zvířatům v celkové anestezii. Játra byla rozdělena do čtyř skupin ($n = 6$) v závislosti na výšce pádu dřevěné desky z výšky 200, 300, 400 a 500 mm. Před vlastním odběrem byly cestou *vena portae* a *vena cava caudalis* zavedeny katetry pro následné měření změn v intravaskulárním tlaku. Po odběru byla játra uchována v chladu a cestou zavedených katetrů byl změřen turgor, který byl v případě potřeby pomocí fyziologického roztoku (0,9% roztok NaCl) upraven na 7 cm vodního sloupce (5,15 mm Hg), což odpovídá fyziologickému tlaku ve *vena portae in vivo*. Mechanický test byl proveden uniformní kompresí jater s využitím pádu dřevěné desky o hmotnosti 6,22 kg a rozměrech 29,5 × 29,5 cm. Rychlost dopadu desky byla měřena pomocí dvojice laserů umístěných po stranách měřícího zařízení. Energie dopadu byla vypočtena v závislosti na rychlosti dopadu, výšce pádu a ploše jater, na kterou deska dopadla. Intravaskulární tlak byl měřen čidly zavedenými v katetrech ve *vena portae* a *vena cava caudalis* (tabulka 7).

Ihned po dokončení mechanického experimentu byla popsána pozice veškerých poranění ve vztahu k jaterním lalokům. Délka trhlin a hloubka poškození jaterního parenchymu, změřená po rozkrájení jater na 1 cm silné plátky, byly základem hodnocení závažnosti poranění v souladu s doporučeními vydanými organizací *American Association for the Surgery and Trauma (AAST) – AAST injury grade* a *AIS severity* (Kozar et al. 2018). Šíření trhliny játry bylo na mikroskopické úrovni změřeno pomocí stereologických metod na řezech barvených pomocí Reticulin kitu (BioGnost, Zagreb, Croatia), který umožnil vizualizaci retikulárních vláken. Analýza byla založena na statistickém porovnání teoretické hodnoty denzity průsečíků retikulárních vláken P_L stanovené pomocí izotropní stereologické mřížky o známých parametrech s reálnou hodnotou denzity průsečíků vláken P'_L v délce trhliny (tabulka 7). Obdobná analýza byla provedena za účelem stanovení šíření trhliny ve vztahu k interlobulárním septům. Trhlina by se šířila tkání náhodně, pokud by se hodnoty teoretické a reálné denzity průsečíků statisticky nelišily ($P_L = P'_L$). V případě, že by byl mezi hodnotami statisticky významný rozdíl, trhlina by se šířila nenáhodně podél vazivové složky jater ($P'_L < P_L$) nebo napříč vazivovou složkou ($P'_L > P_L$) (Kubíková et al. 2017, Tonar et al. 2008). K porovnání hodnot teoretické a reálné denzity průsečíků byl využit Wilcoxonův párový test. Porovnání biomechanických výsledků mezi experimentálními skupinami bylo z důvodu

Materiál a metody

nenormálního rozložení dat (Shapirův-Wilkův test) provedeno s využitím statistického neparametrického testu – Kruskalova-Wallisova ANOVA.

Další podrobnosti nutné pro reprodukovatelnost studie jsou uvedeny v příloze X na str. 225.

Tabulka 7 – Přehled biomechanických a stereologických parametrů využitých ve studii experimentálního poranění jater prasete.

Mechanické parametry			
Parametr	Označení	Jednotka	Definice
Rychlost dopadu	v	ms ⁻¹	Rychlost dřevěné desky změřená laserem
Relativní plocha dopadu	S	%	Plocha orgánu přímo zasažená dřevěnou deskou vztažená k celkové ploše jater
Maximální intravaskulární tlak	p	mm Hg	Tlak v okamžiku dopadu měřený ve <i>vena portae</i> a <i>vena cava caudalis</i>
Energie dopadu – laser	E _K	Jm ⁻²	Energie v okamžiku dopadu odvozená od rychlosti pádu desky změřené pomocí laserů
Energie dopadu – výška	E _P	Jm ⁻²	Energie v okamžiku dopadu odvozená od výšky pádu desky
Závažnost poranění	AAST/AIS	–	Rozsah poranění – délka a hloubka trhlin po dopadovém testu

Stereologické parametry			
Parametr	Označení	Jednotka	Definice
Teoretická hodnota denzity průsečíků retikulárních vláken	P _L (ret.)	mm ⁻¹	Hodnota vypočítaná na základě počtu průsečíků retikulárních vláken s náhodně orientovanou izotropní sondou
Reálná hodnota denzity průsečíků retikulárních vláken	P' _L (ret.)	mm ⁻¹	Skutečný počet průsečíků retikulárních vláken v délce trhliny
Teoretická hodnota denzity průsečíků interlobulárních sept	P _L (septum)	mm ⁻¹	Hodnota vypočítaná na základě počtu průsečíků interlobulárních sept s náhodně orientovanou izotropní sondou
Reálná hodnota denzity průsečíků interlobulárních sept	P' _L (septum)	mm ⁻¹	Skutečný počet průsečíků interlobulárních sept v délce trhliny

4 Výsledky a diskuze

4.1 Kvantifikace jaterních mikrocév v korozivních preparátech jater zobrazených pomocí mikro-CT

4.1.1 Hlavní zjištění

Podařilo se nám vyvinout a otestovat open-source software QuantAn pro kvantifikaci korozivních preparátů mikrocév zobrazených pomocí mikro-CT skenů, který je volně dostupný pro výzkumníky zabývající se stochastickou geometrií jaterních mikrocév ve 3D. Parametry naměřené manuální kvantifikací pomocí robustních stereologických metod odpovídaly hodnotám naměřeným testovaným softwarem QuantAn, který lze proto dále doporučit pro kvantifikaci zmíněných parametrů v dalších studiích. Analýza dat získaných automatickou kvantifikací pomocí softwaru QuantAn identifikovala pravděpodobné zdroje chyb v měření. Pro minimalizaci takových chyb je v softwaru implementována možnost zobrazení dopadu změn v nastavení softwaru na měřené parametry, které by vždy mělo reflektovat míru kontrastu, rozlišení a rozměry kvantifikovaných cév.

Výsledky kvantitativní analýzy mikrocévního řečiště navíc poskytly předběžná data o morfometrii jaterního lalůčku prasete. Získaná data popisující objemový podíl a povrchovou, délkovou a numerickou hustotu mikrocév by mohla přispět k interpretaci rutinních CT vyšetření či by mohla být využita k vytvoření počítačových modelů jaterní perfúze či angiogeneze.

4.1.2 Publikace

JIŘÍK, Miroslav, TONAR, Zbyněk, **KRÁLÍČKOVÁ, Anna**, EBERLOVÁ, Lada, MÍRKA, Hynek, KOCHOVÁ, Petra, GREGOR, Tomáš, HOŠEK, Petr, SVOBODOVÁ, Miroslava, ROHAN, Eduard, KRÁLÍČKOVÁ, Milena, LIŠKA, Václav, 2016. Stereological quantification of microvessels using semiautomated evaluation of X-ray microtomography of hepatic vascular corrosion casts. *International journal of computer assisted radiology and surgery*. 11(10), 1803–1819. ISSN 1861-6410. Dostupné z: <https://doi.org/10.1007/s11548-016-1378-3>.
IF_(JCR2015) = 1,827 Q2 (Engineering, biomedical)

Publikace je součástí dizertační práce jako příloha IV na str. 119.

4.2 Generování virtuálních obrazových dat pro kalibraci vyšetřování vláknitých a porézních struktur pomocí mikro-CT

4.2.1 Hlavní zjištění

Vyvinuli a otestovali jsme open-source software TeIGen, který umožňuje generování 3D virtuálních modelů vláknitých a porézních struktur se známými morfometrickými parametry – objemem, povrchem, délkou a počtem objektů. Program je schopen generovat struktury s velikostí voxelu odpovídající rozlišení v reálných mikro-CT skenech biomateriálů, a to včetně intenzity šumu pozadí. Analýza citlivosti výsledků mikro-CT měření s různým nastavením prahování systému ukázala vliv rozlišení obrázků a šumu pozadí na přesnost mikro-CT kvantifikace. Velikost chyby byla větší s vyšší intenzitou pozadí a s menším rozlišením, zejména pokud velikost voxelu překročila 1/10 velikosti typického měřeného objektu. Pro uživatele mikro-CT zařízení byly zároveň popsány situace, které vedou k nejčastějším a nejzávažnějším odchýlkám v měření tak, aby bylo možné vhodným nastavením chybám předcházet.

Software TeIGen může zároveň sloužit k testování nastavení hustoty stereologických mřížek používaných ke kvantifikaci. Mřížky s příliš vysokou hustotou zvyšují pracnost hodnocení, aniž by významně zpřesňovaly měření. Naopak mřížky s nízkou hustotou mohou vést k chybě neznámé velikosti. Program TeIGen umožňuje vygenerovat obrazové scény s přesně známými hodnotami morfometrických parametrů, a tím umožňuje uživateli kvantifikovat chybu měření při určitém konkrétním nastavení hustoty mřížky.

4.2.2 Publikace

JIŘÍK, Miroslav, BARTOŠ, Martin, TOMÁŠEK, Petr, **MALEČKOVÁ, Anna**, KURAL, Tomáš, HORÁKOVÁ, Jana, LUKÁŠ, David, SUCHÝ, Tomáš, KOCHOVÁ, Petra, HUBÁLEK KALBÁČOVÁ, Marie, KRÁLÍČKOVÁ, Milena, TONAR, Zbyněk, 2018. Generating standardized image data for testing and calibrating quantification of volumes, surfaces, lengths, and object counts in fibrous and porous materials using X-ray microtomography. *Microscopy research and technique*. 81(6), 551–568. ISSN 1059-910X. Dostupné z: <https://doi.org/10.1002/jemt.23011>. **IF(JCR2017) = 1,087. Q3 (Microscopy)**

Publikace je součástí dizertační práce jako příloha V na str. 137.

4.3 Mapování rozložení vaziva v játrech prasete

4.3.1 Hlavní zjištění

Množství vaziva v játrech prasete vykazovalo značnou interindividuální variabilitu – mezi jednotlivými zvířaty i mezi pohlavími – a intraindividuální variabilitu – mezi jednotlivými jaterními laloky i mezi oblastmi vztaženými k cévnímu zásobení jater. Objemový podíl vaziva byl větší u samců než u samic. Největší množství vaziva se nacházelo v lobus quadratus u samců a v lobus caudatus u samic. Oblastí vztaženou k cévnímu zásobení s největším množstvím vaziva byla u obou pohlaví periferie jaterních laloků. Objemový podíl interlobulárního vaziva tvořil více než 99 % celkového množství vaziva, objemový podíl intralobulárního vaziva (perisinusoidální a pericentrální vazivo) byl zanedbatelný.

Primární zdrojová data byla publikována společně s manuskriptem ve formě kontinuálních proměnných a jsou volně přístupná pro výzkumníky zabývající se studiem jaterní fibrózy na velkém zvířecím modelu. Popisné statistiky vycházející z publikovaných dat lze využít pro výpočet minimálního počtu zvířat při plánování experimentů zahrnujících kvantitativní histologickou analýzu množství vaziva v játrech prasete.

4.3.2 Publikace

MIK, Patrik, TONAR, Zbyněk, **MALEČKOVÁ, Anna**, EBERLOVÁ, Lada, LIŠKA, Václav, PÁLEK, Richard, ROSENDORF, Jáchym, JIŘÍK, Miroslav, MÍRKA, Hynek, KRÁLÍČKOVÁ, Milena, WITTER, Kirsti, 2018. Distribution of Connective Tissue in the Male and Female Porcine Liver: Histological Mapping and Recommendations for Sampling. *Journal of comparative pathology*. 162, 1–13. ISSN 0021-9975. Dostupné z: <https://doi.org/10.1016/j.jcpa.2018.05.004>. **IF_(JCR2017) = 1,364. Q2 (Veterinary sciences)**

Publikace je součástí dizertační práce jako příloha VI na str. 156.

4.4 Délková hustota jaterních sinusoid a žlučových kapilár v játrech prasete

4.4.1 Hlavní zjištění

Délková hustota jaterních sinusoid a žlučových kapilár byla nižší na periférii v porovnání s dalšími oblastmi jater – tedy s parakavální a paraportální oblastí. Zároveň byla délková hustota nižší u kastrováných samců než u samic. Jaterní laloky měly srovnatelné hodnoty délkové hustoty jaterních sinusoid i žlučových kapilár. Korelace výsledků analýzy délkové hustoty s daty popisujícími počet a velikost hepatocytů a distribuci vaziva v játrech prasete ukázala, že délková hustota jaterních sinusoid a žlučových kapilár je spojena s lokálním nárůstem počtu menších hepatocytů a s lokálním poklesem množstvím vaziva. Primární data popisující distribuci délkové hustoty jaterních sinusoid a žlučových kapilár jsou ve formě spojených proměnných součástí publikace a mohou sloužit k výpočtu minimálního počtu zvířat, včetně jejich pohlaví, nutných pro odhalení očekávaných morfologických změn v játrech prasete.

4.4.2 Publikace

MALEČKOVÁ, Anna, MIK, Patrik, LIŠKA, Václav, PÁLEK, Richard, ROSENDORF, Jáchym, WITTER, Kirsti, TONAR, Zbyněk. Periphery of porcine hepatic lobes has the smallest length density of hepatic sinuoids and bile canaliculi: a stereological histological study. Publikace byla zaslána do časopisu *Annals of Anatomy*.

Publikace je součástí dizertační práce jako příloha VII na str. 170.

4.5 Histologické hodnocení jater prasete s indukovaným sinusoidálním obstrukčním syndromem – studie vlivu aplikace mezenchymálních kmenových buněk na průběh onemocnění

4.5.1 Hlavní zjištění

Podařilo se nám vytvořit velký zvířecí model SOS vyvolaný aplikací alkaloidu monokrotalinu v dávce 36 mg/kg. SOS byl potvrzen na základě biochemických vyšetření, na základě makroskopického vyšetření viditelných změn na játrech a na základě histologického vyšetření, při němž tkáň 7. den po aplikaci monokrotalinu vykazovala

přítomnost rozsáhlých centrilobulárních nekróz. Všechna zvířata ve skupině s dávkou monokrotalinu 180 mg/kg uhynula předčasně v prvním týdnu od zahájení experimentu.

Výsledky navazující studie, která zkoumala vliv aplikace MSC na průběh SOS, byly následující. V kontrolní skupině předčasně uhynulo celkem šest zvířat ze 12. Všechna zvířata z experimentální skupiny, kterým byly podány MSC, přežila celý experiment. Výsledky UZ ani biochemických vyšetření neukázaly statisticky významné rozdíly mezi oběma skupinami. Histologická analýza vzorků jater odebraných v době resekce levého laterálního laloku potvrdila u všech zvířat přítomnost SOS. Nejvýznamnějším histopatologickým nálezem byla u těchto vzorků přítomnost rozsáhlých centrilobulárních hemoragických nekróz. Rozsah nekróz byl srovnatelný u obou experimentálních skupin. Pro posouzení funkční zdatnosti poškozených jater jsme zvolili kvantifikaci objemu viabilního jaterního parenchymu, jehož objemový podíl byl srovnatelný u obou skupin. Objem morfologicky nepoškozeného parenchymu vhodně doplňuje data o rozsahu hemoragických nekróz. Objem parenchymu byl totiž ovlivněn nejen rozsahem nekróz, ale také reaktivními fibrotickými změnami, dilatací jaterních sinusoid a zánětlivou infiltrací. Tyto nálezy byly hodnoceny pouze kvalitativně.

4.5.2 Publikace

PÁLEK, Richard, LIŠKA, Václav, TŘEŠKA, Vladislav, ROSENDORF, Jáchym, EMINGR, Michal, TÉGL, Václav, **KRÁLÍČKOVÁ, Anna**, BAJCUROVÁ, Kristýna, JIŘÍK, Miroslav, TONAR, Zbyněk, 2018. Sinusoidální obstrukční syndrom indukovaný monokrotalinem v experimentu na velkém zvířeti – pilotní studie. *Rozhledy v chirurgii*. 97(5), 214–221. ISSN 0035-9351

Publikace je součástí dizertační práce jako příloha VIII na str. 198.

PÁLEK, Richard, ROSENDORF, Jáchym, **MALEČKOVÁ, Anna**, VIŠTEJNOVÁ, Lucie, BAJCUROVÁ, Kristýna, MÍRKA, Hynek, TÉGL, Václav, BRZOŇ, Ondřej, KUMAR, Arvind, BEDNÁŘ, Lukáš, TONAR, Zbyněk, HOŠEK, Petr, MOULISOVÁ, Vladimíra, EBERLOVÁ, Lada, TŘEŠKA, Vladislav, LIŠKA, Václav, 2020. Influence of Mesenchymal Stem Cell Administration on The Outcome of Partial Liver Resection in a Porcine Model of Sinusoidal Obstruction Syndrome. *Anticancer research*. 40(12), 6817–6833. ISSN 0250-7005. Dostupné z: <https://doi.org/10.21873/anticancer.14704>. IF_(JCR2019) = 1,994. Q4 (Oncology)

Publikace je součástí dizertační práce jako příloha IX na str. 207.

4.6 Analýza šíření trhlin játry prasete

4.6.1 Hlavní zjištění

Výsledky mechanického měření ukázaly, že vyšší rychlost v okamžiku nárazu, a tedy vyšší energie nárazu, vedla k závažnějšímu poranění jater. Analýza vztahu mezi rychlostí a hodnotou maximálního intravaskulárního tlaku ukázala vzrůstající trend (vyšší rychlost vedla k vyšším hodnotám maximálního tlaku), který nicméně nebyl statisticky signifikantní. Na makroskopické úrovni se trhliny šířily především podél rozhraní jaterního parenchymu a vaziva obklopujícího velké jaterní cévy v oblasti hilu. Na mikroskopické úrovni se trhliny šířily nenáhodně – preferenčně se šířily podél retikulárních vláken a podél interlobulárních sept.

4.6.2 Publikace

MALEČKOVÁ, Anna, KOCHOVÁ, Petra, PÁLEK, Richard, LIŠKA, Václav, MIK, Patrik, BOŃKOWSKI, Tomasz, HORÁK, Miroslav, TONAR, Zbyněk, 2021. Blunt injury of liver: mechanical response of porcine liver in experimental impact test. *Physiological measurement*. 42(2), 025008. ISSN 0967-3334. Dostupné z: <https://doi.org/10.1088/1361-6579/abdf3c>. **IF_(JCR2020) = 2,833 Q3 (Engineering, biomedical)**

Publikace je součástí dizertační práce jako příloha X na str. 225.

5 Závěry práce

Prezentované publikace odpověděly na výzkumné otázky formulované v kapitole 2 Cíle a hypotézy dizertace následujícím způsobem:

1. Jakými nástroji lze automatizovat a zefektivnit kvantitativní analýzu mikrocév jater zobrazených pomocí mikro-CT?

Závěr 1: Vyvinuli jsme open-source software QuantAn pro automatickou analýzu mikrocév nasnímaných pomocí 3D zobrazovacích metod, např. pomocí mikro-CT. Metody, na nichž je hodnocení v softwaru QuantAn založeno, jsou v souladu se standardy používanými ve stereologických metodách. Analýza dat získaných automatickou kvantifikací pomocí softwaru QuantAn identifikovala pravděpodobné zdroje chyb v měření, které je třeba při nastavování kvantitativních algoritmů zohlednit. QuantAn je volně dostupný pro výzkumníky zabývající se stochastickou geometrií mikrocév.

2. Jak lze validovat data získaná automatickou analýzou mikro-CT skenů mikrocév a jak automatická mikro-CT vyšetření kalibrovat?

Závěr 2: Vyvinuli a otestovali jsme open-source software TeIGen pro generování virtuálních modelů vláknitých a porézních struktur se známými morfometrickými parametry. Software TeIGen je vhodným nástrojem pro kalibraci a testování nastavení kvantifikace obrazových dat získaných a hodnocených pomocí mikro-CT zařízení. Zároveň může sloužit k testování nastavení stereologických mřížek užívaných při kvantitativních analýzách trojrozměrných struktur.

3. Jak je v jednotlivých oblastech jater prasete rozloženo vazivo a jak souvisí množství vaziva s pohlavím jedince

Závěr 3: Objemový podíl vaziva byl větší u samců než u samic a byl větší na periférii jater než kolem žil v parakavální a paraportální oblasti. Primární zdrojová data popisující objemový podíl vaziva v jednotlivých lalocích a v oblastech jater souvisejících s cévním zásobením jsou ve formě kontinuálních proměnných volně přístupná pro výzkumníky zabývající se studiem jaterní fibrózy na velkém zvířecím modelu. Data mohou být využita k výpočtu minimálního počtu vzorků nutného k prokázání nárůstu nebo poklesu množství vaziva v experimentech na játrech prasete.

4. Jak jsou v jednotlivých oblastech jater prasete rozloženy jaterní sinusoidy a žlučové kapiláry a jak souvisí jejich rozložení s pohlavím jedince?

Závěr 4: Délková hustota jaterních sinusoid a žlučových kapilár byla nižší u samců než u samic a byla nižší na periférii jater než kolem žil v parakavální a paraportální oblasti. Zároveň byla vyšší délková hustota jaterních sinusoid a žlučových kapilár spojena s lokálním nárůstem počtu menších hepatocytů a s menším výskytem vaziva. Nalezená intrahepatická a intersexuální variabilita v morfologii jater prasete by měla být zohledněna při plánování a vyhodnocování experimentů využívajících histologické hodnocení vzorků. Primární data popisující délkovou hustotu jaterních sinusoid a žlučových kapilár v šesti lalocích a ve třech oblastech vztažených k cévnímu zásobení jsou volně k dispozici ve formě kontinuálních proměnných. Data mohou být využita pro výpočet minimálního počtu vzorků nutného k odhalení změn v játrech prasete.

5. Jaký je dopad aplikace mezenchymálních kmenových buněk na histologické změny v játrech a jaký bude mít vliv na celkový průběh onemocnění a přežití prasat se sinusoidálním obstrukčním syndromem po parciální hepatektomii?

Závěr 5: Na základě biochemické, ultrasonografické a histologické analýzy se nám podařilo pomocí aplikace pyrrolizidinového alkaloidu monokrotalinu vytvořit velký zvířecí model sinusoidálního obstrukčního syndromu. Podání jedné intravenózní dávky mezenchymálních kmenových buněk zlepšilo celkové přežití zvířat se sinusoidálním obstrukčním syndromem po parciální jaterní resekcii.

6. Jak souvisí mikroskopická stavba jater prasete se šířením trhlin játry v experimentu simulujícím tupé poranění?

Závěr 6: Experiment simulující poranění jater prasete při nárazu poskytl komplexní pohled na mechanismus vzniku jaterního poranění na makroskopické i mikroskopické úrovni. Primární biomechanická data byla zveřejněna spolu s publikací a mohou sloužit k validaci výpočetních modelů mechanické odpovědi jater v okamžiku nárazu. Mikroskopická analýza prokázala, že se trhliny v játrech nešíří náhodně, ale jejich propagace je závislá na orientaci hlavních vláknitých složek stromatu jater a interlobulárních sept. Toto zjištění je významné zejména pro přenos dat z experimentů na játrech prasete se signifikantně větším množstvím vaziva na játra lidská.

Závěry práce

Výše uvedené závěry lze tedy shrnout následovně. Postupy využívající automatické softwary pro obrazovou analýzu dat by měly být vždy kalibrovány, neboť výsledky jejich měření jsou ovlivněny kvalitou vstupních dat a nastavením segmentačních algoritmů. Pro kalibraci postupů a validaci dat lze s výhodou využít robustní a reprodukovatelné metody, jako je např. stereologie. Rozsáhlé zmapování mikroskopických parametrů, jako je množství vaziva a délková hustota jaterních sinusoid a žlučových kapilár, v odlišných oblastech jater prasete umožňuje nyní na základě uveřejněných dat a popisných statistik plánování experimentů s eticky opodstatněným počtem jedinců a tkáňových vzorků. Na základě našich experimentálních studií bylo demonstrováno, že játra prasete jsou vhodným orgánem pro modelování různorodých fyziologických i patologických stavů vyskytujících se u lidí. V předložené práci jsme popsali experimenty na játrech prasete zahrnující regeneraci, rozvoj jaterního onemocnění, ale i mechanické chování jater prasete během simulace nárazu a tupého poranění orgánů. Všechny studie byly zveřejněny společně s primárními naměřenými daty.

6 Literatura

- ASRANI, Sumeet K, DEVARBHAVI, Harshad, EATON, John, KAMATH, Patrick S, 2019. Burden of liver diseases in the world. *Journal of hepatology*. 70(1), 151–171. ISSN 0168-8278. Dostupné z: <https://doi.org/10.1016/j.jhep.2018.09.014>
- BATTS, Kenneth P, LUDWIG, Jurgen, 1995. Chronic hepatitis. An update on terminology and reporting. *The American journal of surgical pathology*. 19(12), 1409–1417. ISSN 0147-5185. Dostupné z: <https://doi.org/10.1097/00000478-199512000-00007>
- BAYRAKTAR, Ulas-Darda, SEREN, Soley, BAYRAKTAR, Yusuf, 2007. Hepatic venous outflow obstruction: three similar syndromes. *World journal of gastroenterology*. 13(13), 1912–1927. ISSN 1007-9327. Dostupné z: <https://doi.org/10.3748/wjg.v13.i13.1912>
- BEDOSSA, Pierre, POYNARD, Thierry, 1996. An algorithm for the grading of activity in chronic hepatitis C. The METAVIR Cooperative Study Group. *Hepatology*. 24(2), 289–293. ISSN 1527-3350. Dostupné z: <https://doi.org/10.1002/hep.510240201>
- BERUMEN, Jennifer, BAGLIERI, Jacopo, KISSELEVA, Tatiana, MEKEEL, Kristin, 2021. Liver fibrosis: Pathophysiology and clinical implications. *WIREs mechanisms of disease*. 13(1), e1499. ISSN 2692-9368. Dostupné z: <https://doi.org/10.1002/wsbm.1499>
- BRUNT, Elizabeth M, JANNEY, Christine G, Di BISCEGLIE, Adrian M, NEUSCHWANDER-TETRI, Brent A, BACON, Bruce R, 1999. Nonalcoholic steatohepatitis: a proposal for grading and staging the histological lesions. *The American journal of gastroenterology*. 94(9), 2467–2474. ISSN 0002-9270. Dostupné z: <https://doi.org/10.1111/j.1572-0241.1999.01377.x>
- CHEN, Joseph, BRAZILE, Bryn, PRABHU, Raj, PATNAIK, Sourav S, BERTUCCI, Robbin, RHEE, Hongjoo, HORSTEMEYER, MF, HONG, Yi, WILLIAMS, Lakiesha N, LIAO Jun, 2018. Quantitative Analysis of Tissue Damage Evolution in Porcine Liver With Interrupted Mechanical Testing Under Tension, Compression, and Shear. *Journal of biomechanical engineering*. 140(7), 0710101–07101010. eISSN 1528-8951. Dostupné z: <https://doi.org/10.1115/1.4039825>

Literatura

- CHOW, Shein-Chung, WANG, Hansheng, SHAO, Jun, 2008. *Sample Size Calculations in Clinical Research, Second ed.* New York: Chapman and Hall/CRC. ISBN 978-0-429-14463-9.
- ČIHÁK, Radomír, 2013. *Anatomie 2, Třetí upravené a doplněné vydání.* Praha: Grada Publishing. ISBN: 978-80-247-4788-0.
- CONTE, Cécile, GARCIA, Stéphane, ARNOUX, Pierre-Jean, MASSON, Catherine, 2012. Experimental multiscale analysis of liver damage and failure process under compression. *The journal of trauma and acute care surgery.* 72(3), 727–732. ISSN 2163-0755. Dostupné z: <https://doi.org/10.1097/TA.0b013e3182395e68>
- COUINAUD, Claude, 1954. Lobes et segments hépatiques: notes sur l'architecture anatomiques et chirurgicale du foie. *La Presse Medicale.* 62(33), 709–712. ISSN 0032-7867.
- DeLEVE, Laurie D, McCUSKEY, Robert S, WANG, Xiangdong, HU, Liping, McCUSKEY, Margaret K, EPSTEIN, Robert B, KANEL, Gary C, 1999. Characterization of a reproducible rat model of hepatic veno-occlusive disease. *Hepatology.* 29(6), 1779–1791. ISSN 1527-3350. Dostupné z: <https://doi.org/10.1002/hep.510290615>
- EBERLOVÁ, Lada, LIŠKA, Václav, MÍRKA, Hynek, GREGOR, Tomáš, TONAR, Zbyněk, PÁLEK, Richard, SKÁLA, Martin, BRŮHA, Jan, VYČÍTAL, Ondřej, KALUSOVÁ, Kristýna, HAVIAR, Stanislav, KRÁLÍČKOVÁ, Milena, LAMETSCHWANDTNER, Alois, 2016. Porcine liver vascular bed in Biodur E20 corrosion casts. *Folia morphologica.* 75(2), 154–161. ISSN 0015-5659. Dostupné z: <https://doi.org/10.5603/FM.a2015.0094>
- EBERLOVÁ, Lada, MALEČKOVÁ, Anna, MIK, Patrik, TONAR, Zbyněk, JIŘÍK, Miroslav, MÍRKA, Hynek, PÁLEK, Richard, LEUPEN, Sarah, LIŠKA, Václav, 2020. Porcine Liver Anatomy Applied to Biomedicine. *The Journal of surgical research.* 250, 70–79. ISSN 0022-4804. Dostupné z: <https://doi.org/10.1016/j.jss.2019.12.038>
- FLOYD, Justin, MIRZA, Irfan, SACHS, Bradley, PERRY, Micheal C, 2006. Hepatotoxicity of chemotherapy. *Seminars in oncology.* 33(1), 50–67. ISSN 0093-7754. Dostupné z: <https://doi.org/10.1053/j.seminoncol.2005.11.002>
- GAYZIK, Scott F, MORENO, Daniel P, GEER, Carol P, WUERTZER, Scott D, MARTIN, Shayn R, STITZEL, Joel D, 2011. Development of a full body CAD dataset for computational modeling: a multi-modality approach. *Annals of*

Literatura

- biomedical engineering*. 39(10), 2568–2583. ISSN 0090-6964. Dostupné z: <https://doi.org/10.1007/s10439-011-0359-5>
- GOLMAN, Adam J, DANELSON, Kerry A, MILLER, Logan E, STITZEL, Joel D, 2014. Injury prediction in a side impact crash using human body model simulation. *Accident; analysis and prevention*. 64, 1–8. ISSN 0001-4575. Dostupné z: <https://doi.org/10.1016/j.aap.2013.10.026>
- GRACIA-SANCHO, Jordi, CAPARRÓS, Esther, FERNÁNDEZ-IGLESIAS, Anabel, FRANCÉS, Rubén, 2021. Role of liver sinusoidal endothelial cells in liver diseases. *Nature reviews. Gastroenterology & hepatology*. 18(6), 411–431. ISSN 1759-5045 Dostupné z: <https://doi.org/10.1038/s41575-020-00411-3>
- HOMEYER, André, NASR, Patric, ENGEL, Christiane, KECHAGIAS, Stergios, LUNDBERG, Peter, EKSTEDT, Mattias, KOST, Henning, WEISS, Nick, PALMER, Tim, HAHN, Horst K, TREANOR, Darren, LUNDSTRÖM, Claes, 2017. Automated quantification of steatosis: agreement with stereological point counting. *Diagnostic pathology*. 12(1), 80. ISSN 1746-1596. Dostupné z: <https://doi.org/10.1186/s13000-017-0671-y>
- HORAKOVA, Jana, MIKES, Petr, SAMAN, Ales, SVARCOVA, Tereza, JENCOVA, Vera, SUCHY, Tomas, HECZKOVA, Bohdana, JAKUBKOVA, Sarka, JIROUSOVA, Jaroslava, PROCHAZKOVA, Renata, 2018. Comprehensive assessment of electrospun scaffolds hemocompatibility. *Materials science & engineering. C, Materials for biological applications*. 82, 330–335. ISSN 0928-4931. Dostupné z: <https://doi.org/10.1016/j.msec.2017.05.011>
- HOWARD, Vyvyan, REED, Matthew G, 2005. *Unbiased stereology. Three-dimensional measurement in microscopy. 2nd edition*. London: Garland Science. ISBN 978-1859960899.
- HSIA, Conie C, HYDE, Dallas M, OCHS, Matthias, WEIBEL, Ewald R; ATS/ERS Joint Task Force on Quantitative Assessment of Lung Structure, 2010. An official research policy statement of the American Thoracic Society/European Respiratory Society: standards for quantitative assessment of lung structure. *American journal of respiratory and critical care medicine*. 181(4), 394–418. ISSN 1535-4970. Dostupné z: <https://doi.org/10.1164/rccm.200809-1522ST>
- HŮLEK, Petr, URBÁNEK, Petr a kolektiv. 2014. *Hepatologie. 3. vydání*. Praha: Grada Publishing. ISBN: 978-80-271-0394-2.

Literatura

- JIŘÍK, Miroslav, 2015. QuantAn—Quantitative Analyser software. Dostupné z: <http://mjirik.github.io/quantan/>.
- JIŘÍK, Miroslav, TONAR, Zbyněk, KRÁLÍČKOVÁ, Anna, EBERLOVÁ, Lada, MÍRKA, Hynek, KOCHOVÁ, Petra, GREGOR, Tomáš, HOŠEK, Petr, SVOBODOVÁ, Miroslava, ROHAN, Eduard, KRÁLÍČKOVÁ, Milena, LIŠKA, Václav, 2016. Stereological quantification of microvessels using semiautomated evaluation of X-ray microtomography of hepatic vascular corrosion casts. *International journal of computer assisted radiology and surgery*. 11(10), 1803–1819. ISSN 1861-6410. Dostupné z: <https://doi.org/10.1007/s11548-016-1378-3>
- JIŘÍK, Miroslav, 2017. Teigen – TEst Image GENerator software. Dostupné z: <https://mjirik.github.io/teigen/>.
- JIŘÍK, Miroslav, BARTOŠ, Martin, TOMÁŠEK, Petr, MALEČKOVÁ, Anna, KURAL, Tomáš, HORÁKOVÁ, Jana, LUKÁŠ, David, SUCHÝ, Tomáš, KOCHOVÁ, Petra, HUBÁLEK KALBÁČOVÁ, Marie, KRÁLÍČKOVÁ, Milena, TONAR, Zbyněk, 2018. Generating standardized image data for testing and calibrating quantification of volumes, surfaces, lengths, and object counts in fibrous and porous materials using X-ray microtomography. *Microscopy research and technique*. 81(6), 551–568. ISSN 1059-910X. Dostupné z: <https://doi.org/10.1002/jemt.23011>
- JUNATAS, Khan L, TONAR, Zbyněk, KUBÍKOVÁ, Tereza, LIŠKA, Václav, PÁLEK, Richard, MIK, Patrik, KRÁLÍČKOVÁ, Milena, WITTER, Kirsti, 2017. Stereological analysis of size and density of hepatocytes in the porcine liver. *Journal of anatomy*. 230(4), 575–588. ISSN 0021-8782. Dostupné z: <https://doi.org/10.1111/joa.12585>
- van de KERKHOVE Maarten-Paul, HOEKSTRA, Ruurdje, van GULIK, Thomas M, CHAMULEAU, Robert A, 2004. Large animal models of fulminant hepatic failure in artificial and bioartificial liver support research. *Biomaterials*. 25(9), 1613–1625. ISSN 0142-9612. Dostupné z: [https://doi.org/10.1016/s0142-9612\(03\)00509-x](https://doi.org/10.1016/s0142-9612(03)00509-x)
- KIERNAN, Francis, 1833. The anatomy and physiology of the liver. *Philosophical Transactions of the Royal Society of London*. 123, 711–770. ISSN 0261-0523 doi:10.1098/rstl.1833.0031
- KLEINER, David E, BRUNT, Elizabeth M, VAN NATTA, Mark, BEHLING, Cynthia, CONTOS, Melissa J, CUMMINGS, Oscar W, FERRELL, Linda D, LIU, Yao-

Literatura

- Chang, TORBENSON, Michael S, UNALP-ARIDA, Aynur, YEH, Matthew, MCCULLOUGH, Arthur J, SANYAL, Arun J, & Nonalcoholic Steatohepatitis Clinical Research Network, 2005. Design and validation of a histological scoring system for nonalcoholic fatty liver disease. *Hepatology*. 41(6), 1313–1321. ISSN 1527-3350. Dostupné z: <https://doi.org/10.1002/hep.20701>
- KNODELL, Robert G, ISHAK, Kamal G, BLACK, William C, CHEN, Thomas S, CRAIG, Robert, KAPLOWITZ, Neil, KIERNAN, Thomas W, WOLLMAN, Jerome, 1981. Formulation and application of a numerical scoring system for assessing histological activity in asymptomatic chronic active hepatitis. *Hepatology*. 1(5), 431–435. ISSN 1527-3350. Dostupné z: <https://doi.org/10.1002/hep.1840010511>
- KOGURE, Kimitaka, ISHIZAKI, Masatoshi, NEMOTO, Masaaki, KUWANO, Hiroyuki, MAKUUCHI, Masatoshi, 1999. A comparative study of the anatomy of rat and human livers. *Journal of hepato-biliary-pancreatic surgery*. 6(2), 171–175. ISSN 1868-6982. Dostupné z: <https://doi.org/10.1007/s005340050101>
- KOLINKO, Yaroslav, MALEČKOVÁ, Anna, KOCHOVÁ, Petra, GRAJCIAROVÁ, Martina, BLASSOVÁ, Tereza, KURAL, Tomáš, TRAILIN, Andriy, ČERVENKOVÁ, Lenka, HAVRÁNKOVÁ, Jiřina, VIŠTEJNOVÁ, Lucie, TONAROVÁ, Pavla, MOULISOVÁ, Vladimíra, JIŘÍK, Miroslav, ZAVAĐÁKOVÁ, Anna, TICHÁNEK, Filip, LIŠKA, Václav, KRÁLÍČKOVÁ, Milena, WITTER, Kirsti, TONAR, Zbyněk, 2022. Using virtual microscopy for the development of sampling strategies in quantitative histology and design-based stereology. *Anatomia, histologia, embryologia*. 51(1), 3–22. ISSN 0340-2096. Dostupné z: <https://doi.org/10.1111/ahe.12765>
- KOZAR, Rosemary A, CRANDALL, Marie, SHANMUGANATHAN, Kathrikamanthan, ZARZAUR, Ben L, COBURN, Mike, CRIBARI, Chris, KAUPS, Krista, SCHUSTER, Kevin, TOMINAGA, Gail T; AAST Patient Assessment Committee, 2018. Organ injury scaling 2018 update: Spleen, liver, and kidney. *The journal of trauma and acute care surgery*. 85(6), 1119–1122. ISSN 0022-5282. Dostupné z: <https://doi.org/10.1097/TA.0000000000002058>
- KUBÍKOVÁ, Tereza, KOCHOVÁ, Petra, BRÁZDIL, Jan, ŠPATENKA, Jaroslav, BURKERT, Jan, KRÁLÍČKOVÁ, Milena, TONAR, Zbyněk, 2017. The composition and biomechanical properties of human cryopreserved aortas, pulmonary trunks, and aortic and pulmonary cusps. *Annals of Anatomy -*

Literatura

- Anatomischer Anzeiger*. 212, 17–26. ISSN 0940-9602. Dostupné z: <https://doi.org/10.1016/j.aanat.2017.03.004>
- LAMERS, Wouter H, HILBERTS, Aage, FURT, Erwin, SMITH, Jerry, JONGES, Geertruida N, van NOORDEN, Cornelis J, JANZEN, Jan W, CHARLES, Robert, MOORMAN, Antoon F, 1989. Hepatic enzymic zonation: a reevaluation of the concept of the liver acinus. *Hepatology*. 10(1), 72–76. ISSN 1527-3350 Dostupné z: <https://doi.org/10.1002/hep.1840100115>
- LAMETSCHWANDTNER, Alois, MINNICH, Bernd, STÖTTINGER, Bernhard, KRAUTGARTNER, Wolf D, 2005. Analysis of microvascular trees by means of scanning electron microscopy of vascular casts and 3D-morphometry. *Italian journal of anatomy and embryology = Archivio italiano di anatomia ed embriologia*. 110(2 Suppl 1), 87–95. ISSN 1122-6714.
- LEMAIGRE, Frédéric P, 2009. Mechanisms of liver development: concepts for understanding liver disorders and design of novel therapies. *Gastroenterology*. 137(1), 62–79. ISSN 0016-5085. Dostupné z: <https://doi.org/10.1053/j.gastro.2009.03.035>
- MALEČKOVÁ, Anna, TONAR, Zbyněk, MIK, Patrik, MICHALOVÁ, Květoslava, LIŠKA, Václav, PÁLEK, Richard, ROSENDORF, Jáchym, KRÁLÍČKOVÁ, Milena, TŘEŠKA, Vladislav, 2019. Zvířecí modely jaterních onemocnění a jejich využití v experimentální chirurgii. *Rozhledy v chirurgii*. 98(3), 100–109. ISSN 0035-9351.
- MALEČKOVÁ, Anna, KOCHOVÁ, Petra, PÁLEK, Richard, LIŠKA, Václav, MIK, Patrik, BOŃKOWSKI, Tomasz, HORÁK, Miroslav, TONAR, Zbyněk, 2021. Blunt injury of liver: mechanical response of porcine liver in experimental impact test. *Physiological measurement*. 42(2), 025008. ISSN 0967-3334. Dostupné z: <https://doi.org/10.1088/1361-6579/abdf3c>. Corrigendum: Blunt injury of liver: mechanical response of porcine liver in experimental impact test. *Physiological measurement*. 42(5). Dostupné z: <https://doi.org/10.1088/1361-6579/abf887>
- MARCOS, Ricardo, MONTEIRO, Rogério A, ROCHA, Eduardo, 2012. The use of design-based stereology to evaluate volumes and numbers in the liver: a review with practical guidelines. *Journal of anatomy*. 220(4), 303–317. ISSN 0021-8782. Dostupné z: <https://doi.org/10.1111/j.1469-7580.2012.01475.x>
- MASSARO, Maria S, PÁLEK, Richard, ROSENDORF, Jáchym, ČERVENKOVÁ, Lenka, LIŠKA, Václav, MOULISOVÁ, Vladimíra, 2021. Decellularized

- xenogeneic scaffolds in transplantation and tissue engineering: Immunogenicity versus positive cell stimulation. *Materials science & engineering. C, Materials for biological applications*. 127, 112203. ISSN 0928-4931. Dostupné z: <https://doi.org/10.1016/j.msec.2021.112203>
- MEYER, Kirstin, MORALES-NAVARRETE, Hernan, SEIFERT, Sarah, WILSCH-BRAEUNINGER, Michaela, DAHMEN, Uta, TANAKA, Elly M, BRUSCH, Lutz, KALAZIDZIS, Yannis, ZERIAL, Marino, 2020. Bile canaliculi remodeling activates YAP via the actin cytoskeleton during liver regeneration. *Molecular systems biology*. 16(2), e8985. eISSN 1744-4292. Dostupné z: <https://doi.org/10.15252/msb.20198985>
- MIK, Patrik, TONAR, Zbyněk, MALEČKOVÁ, Anna, EBERLOVÁ, Lada, LIŠKA, Václav, PÁLEK, Richard, ROSENDORF, Jáchym, JIŘÍK, Miroslav, MÍRKA, Hynek, KRÁLÍČKOVÁ, Milena, WITTER, Kirsti, 2018. Distribution of Connective Tissue in the Male and Female Porcine Liver: Histological Mapping and Recommendations for Sampling. *Journal of comparative pathology*. 162, 1–13. ISSN 0021-9975. Dostupné z: <https://doi.org/10.1016/j.jcpa.2018.05.004>
- MOULISOVÁ, Vladimíra, JIŘÍK, Miroslav, SCHINDLER, Claudia, ČERVENKOVÁ, Lenka, PÁLEK, Richard, ROSENDORF, Jáchym, ARLT, Janine, BOLEK, Lukáš, ŠŮSOVÁ, Simona, NIETZSCHE, Sandor, LIŠKA, Václav, DAHMEN, Uta, 2020. Novel morphological multi-scale evaluation system for quality assessment of decellularized liver scaffolds. *Journal of tissue engineering*. 11, 2041731420921121. ISSN 2041-7314. Dostupné z: <https://doi.org/10.1177/2041731420921121>
- MOUTON, Peter R, 2002. *Principles and Practices of Unbiased Stereology. An Introduction for Bioscientists*. Baltimore: The Johns Hopkins University Press. ISBN 978-0801867972.
- MÜHLFELD, Christian, 2014. Quantitative morphology of the vascularisation of organs: A stereological approach illustrated using the cardiac circulation. *Annals of Anatomy - Anatomischer Anzeiger*. 196(1), 12–19. ISSN 0940-9602. Dostupné z: <https://doi.org/10.1016/j.aanat.2012.10.010>
- OBER, Elke A, LEMAIGRE, Frédéric P, 2018. Development of the liver: Insights into organ and tissue morphogenesis. *Journal of hepatology*. 68(5), 1049–1062. ISSN 0168-8278. Dostupné z: <https://doi.org/10.1016/j.jhep.2018.01.005>

Literatura

- PÁLEK, Richard, LIŠKA, Václav, TŘEŠKA, Vladislav, ROSENDORF, Jáchym, EMINGR, Michal, TÉGL, Václav, KRÁLÍČKOVÁ, Anna, BAJCUROVÁ, Kristýna, JIŘÍK, Miroslav, TONAR, Zbyněk, 2018. Sinusoidální obstrukční syndrom indukovaný monokrotalinem v experimentu na velkém zvířeti - pilotní studie. *Rozhledy v chirurgii*. 97(5), 214–221. ISSN 0035-9351.
- PÁLEK, Richard, ROSENDORF, Jáchym, MALEČKOVÁ, Anna, VIŠTEJNOVÁ, Lucie, BAJCUROVÁ, Kristýna, MÍRKA, Hynek, TÉGL, Václav, BRZOŇ, Ondřej, KUMAR, Arvind, BEDNÁŘ, Lukáš, TONAR, Zbyněk, HOŠEK, Petr, MOULISOVÁ, Vladimíra, EBERLOVÁ, Lada, TŘEŠKA, Vladislav, LIŠKA, Václav, 2020. Influence of Mesenchymal Stem Cell Administration on The Outcome of Partial Liver Resection in a Porcine Model of Sinusoidal Obstruction Syndrome. *Anticancer research*. 40(12), 6817–6833. ISSN 0250-7005. Dostupné z: <https://doi.org/10.21873/anticancer.14704>
- RAPPAPORT, AM., WILSON, WD, 1958. The structural and functional unit in the human liver (liver acinus). *The Anatomical Record*. 130(4), 673–689. ISSN 1097-0185. Dostupné z: <https://doi.org/10.1002/ar.1091300405>
- ROUSSELET, Marie-Christine, MICHALAK, Sophie, DUPRÉ, Florence, CROUÉ, Anne, BEDOSSA, Pierre, SAINT-ANDRÉ, Jean-Paul, CALÈS, Paul, Hepatitis Network 49, 2005. Sources of variability in histological scoring of chronic viral hepatitis. *Hepatology*. 41(2), 257–264. ISSN 1527-3350. Dostupné z: <https://doi.org/10.1002/hep.20535>
- SADLER, Thomas W, 2011. *Langmanova lékařská embryologie. Překlad 10. vydání*. Praha: Grada publishing. ISBN 978-80-247-2640-3.
- SAXENA, Romil, 2018. *Practical Hepatic Pathology: A Diagnostic Approach. 2nd edition*. Philadelphia: Elsevier. ISBN: 978-0-443-06803-4.
- SCHLADITZ, Katja, 2011. Quantitative micro-CT. *Journal of microscopy*. 243(2), 111–117. ISSN 0022-2720. Dostupné z: <https://doi.org/10.1111/j.1365-2818.2011.03513.x>
- SØRENSEN, Karen K, SIMON-SANTAMARIA, Jaione, McCUSKEY, Robert S, SMEDSRØD, Bård, 2015. Liver Sinusoidal Endothelial Cells. *Comprehensive Physiology*. 5(4), 1751–1774. ISSN 2040-4603. Dostupné z: <https://doi.org/10.1002/cphy.c140078>
- SPARKS, Jessica L, BOLTE, John H 4th, DUPAIX, Rebecca B, JONES, Kenneth H, STEINBERG, Steven M, HERRIOTT, Rodney G, STAMMEN, Jason A,

Literatura

- DONNELLY, Bruce R, 2007. Using pressure to predict liver injury risk from blunt impact. *Stapp car crash journal*. 51, 401–432. ISSN 1532-8546.
- STARKEL, Peter, LECLERCQ, Isabelle A, 2011. Animal models for the study of hepatic fibrosis. *Best practice & research. Clinical gastroenterology*. 25(2), 319–333. ISSN 1521-6918. Dostupné z: <https://doi.org/10.1016/j.bpg.2011.02.004>
- SUCHÝ, Tomáš, ŠUPOVÁ, Monika, SAUEROVÁ, Pavla, VERDÁNOVÁ, Martina, SUCHARDA, Zbyněk, RÝGLOVÁ, Šárka, ŽALOUDKOVÁ, Margit, SEDLÁČEK, Radek, HUBÁLEK-KALBÁČOVÁ, Marie, 2015. The effects of different cross-linking conditions on collagen-based nanocomposite scaffolds-an in vitro evaluation using mesenchymal stem cells. *Biomedical materials (Bristol, England)*. 10(6), 065008. ISSN 1748-6041. Dostupné z: <https://doi.org/10.1088/1748-6041/10/6/065008>
- SWINDLE, Michael M, SMITH, Alison C, 2016. *Swine in the laboratory: surgery, anesthesia, imaging, and experimental techniques, third edition*. Boca Raton: Taylor & Francis Group. ISBN 978-1-4665-5347-7.
- The French METAVIR Cooperative Study Group, 1994. Intraobserver and interobserver variations in liver biopsy interpretation in patients with chronic hepatitis C. *Hepatology*. 20(1), 15-20. ISSN 1527-3350
- TONAR, Zbyněk, JANÁČEK, Jiří, NEDOROST, Lukáš, GRILL, Robert, BÁČA, Václav, ZÁTURA, František, 2009. Analysis of microcracks caused by drop shatter testing of porcine kidneys. *Annals of Anatomy - Anatomischer Anzeiger*. 191(3), 294–308. ISSN 0940-9602. Dostupné z: <https://doi.org/10.1016/j.aanat.2009.02.005>
- TREUTING, Piper, DINTZIS, Suzanne, MONTINE, Kathleen S, 2017. *Comparative anatomy and histology: a mouse, rat, and human atlas, 2nd edition*. Cambridge: Academic Press. ISBN: 978-0-12-802900-8.
- TREYER, Aleksandr, MÜSCH, Anne, 2013. Hepatocyte polarity. *Comprehensive Physiology*. 3(1), 243–287. ISSN 2040-4603. Dostupné z: <https://doi.org/10.1002/cphy.c120009>
- TSCHANZ, Stefan, SCHNEIDER, Jan P, KNUDSEN, Lars, 2014. Design-based stereology: Planning, volumetry and sampling are crucial steps for a successful study. *Annals of Anatomy - Anatomischer Anzeiger*. 196(1), 3–11. ISSN 0940-9602. Dostupné z: <https://doi.org/10.1016/j.aanat.2013.04.011>

Literatura

- VALLA, Dominique-Charles, CAZALS-HATEM, Dominique, 2016. Sinusoidal obstruction syndrome. *Clinics and research in hepatology and gastroenterology*. 40(4), 378–385. ISSN 2210-7401. Dostupné z: <https://doi.org/10.1016/j.clinre.2016.01.006>
- WANG, Yan, HOU, Jin-Lin, 2015. Current strategies for quantitating fibrosis in liver biopsy. *Chinese medical journal*. 128(2), 252–258. ISSN 0366-6999. Dostupné z: <https://doi.org/10.4103/0366-6999.149223>
- XU ,Tao, SHENG, Xiaoming, ZHANG, Tianyi, LIU, Huan, LIANG, Xiao, DING, Ao, 2018. Development and Validation of Dummies and Human Models Used in Crash Test. *Applied bionics and biomechanics*. 3832850. ISSN 1176-2322. Dostupné z: <https://doi.org/10.1155/2018/3832850>
- YASMIN, Alvi, REGAN, Daniel P, SCHOOK, Lawrence B, GABA, Ron C, SCHACHTSCHNEIDER, Kyle M, 2021. Transcriptional regulation of alcohol induced liver fibrosis in a translational porcine hepatocellular carcinoma model. *Biochimie*. 182, 73–84. ISSN 0300-9084. Dostupné z: <https://doi.org/10.1016/j.biochi.2020.12.022>

7 Seznam obrázků

Obrázek 1 – Játra prasete (transmisní elektronový mikroskop).	22
Obrázek 2 – Srovnání histologické stavby jater člověka (A), myši (B), prasete (C) a potkana (D).....	25
Obrázek 3 – Algoritmus hodnocení histopatologického obrazu v jaterní biopsii....	28
Obrázek 4 – Příklady morfologických obrazů poškození mikrostruktury jater.....	31

8 Seznam tabulek

Tabulka 1 – Srovnání anatomie jater člověka a nejčastěji využívaných zvířecích modelů – myši, potkana a prasete	26
Tabulka 2 – Přehled nejčastěji využívaných metod histologického barvení v diagnostice jaterních onemocnění	27
Tabulka 3 – Příklady histologického kvantitativního hodnocení v játrech prasete.	34
Tabulka 4 – Přehled parametrů použitých pro kvantifikaci mikrocév v játrech prasete.....	44
Tabulka 5 – Přehled kvantitativních parametrů hodnocených ve studii rozložení vaziva v játrech prasete.....	46
Tabulka 6 – Přehled parametrů kvantifikovaných v játrech prasete pro určení rozsahu jaterního poškození v důsledku sinusoidálního obstrukčního syndromu..	48
Tabulka 7 – Přehled biomechanických a stereologických parametrů využitých ve studii experimentálního poranění jater prasete.....	50

9 Publikační činnost autorky

9.1 Publikace vztahující se k tématu dizertační práce

9.1.1 Časopisy s faktorem impaktu

EBERLOVÁ, Lada, **MALEČKOVÁ, Anna**, MIK, Patrik, TONAR, Zbyněk, JIŘÍK, Miroslav, MÍRKA, Hynek, PÁLEK, Richard, LEUPEN, Sarah, LIŠKA, Václav, 2020. Porcine Liver Anatomy Applied to Biomedicine. *The Journal of surgical research*. 250, 70–79. ISSN 0022-4804. Dostupné z: <https://doi.org/10.1016/j.jss.2019.12.038>

IF_(JCR2019) = 1,841 Q3 (Surgery)

JIŘÍK, Miroslav, TONAR, Zbyněk, **KRÁLÍČKOVÁ, Anna**, EBERLOVÁ, Lada, MÍRKA, Hynek, KOCHOVÁ, Petra, GREGOR, Tomáš, HOŠEK, Petr, SVOBODOVÁ, Miroslava, ROHAN, Eduard, KRÁLÍČKOVÁ, Milena, LIŠKA, Václav, 2016. Stereological quantification of microvessels using semiautomated evaluation of X-ray microtomography of hepatic vascular corrosion casts. *International journal of computer assisted radiology and surgery*. 11(10), 1803–1819. ISSN 1861-6410. Dostupné z: <https://doi.org/10.1007/s11548-016-1378-3>

IF_(JCR2015) = 1,827 Q2 (Engineering, biomedical)

JIŘÍK, Miroslav, BARTOŠ, Martin, TOMÁŠEK, Petr, **MALEČKOVÁ, Anna**, KURAL, Tomáš, HORÁKOVÁ, Jana, LUKÁŠ, David, SUCHÝ, Tomáš, KOCHOVÁ, Petra, HUBÁLEK KALBÁČOVÁ, Marie, KRÁLÍČKOVÁ, Milena, TONAR, Zbyněk, 2018. Generating standardized image data for testing and calibrating quantification of volumes, surfaces, lengths, and object counts in fibrous and porous materials using X-ray microtomography. *Microscopy research and technique*. 81(6), 551–568. ISSN 1059-910X. Dostupné z: <https://doi.org/10.1002/jemt.23011>

IF_(JCR2017) = 1,087. Q3 (Microscopy)

KOLINKO, Yaroslav, **MALEČKOVÁ, Anna**, KOCHOVÁ, Petra, GRAJCIAROVÁ, Martina, BLASSOVÁ, Tereza, KURAL, Tomáš, TRAILIN, Andriy, ČERVENKOVÁ, Lenka, HAVRÁNKOVÁ, Jiřina, VIŠTEJNOVÁ, Lucie, TONAROVÁ, Pavla, MOULISOVÁ, Vladimíra, JIŘÍK, Miroslav, ZAVADÁKOVÁ, Anna, TICHÁNEK, Filip, LIŠKA, Václav, KRÁLÍČKOVÁ,

Milena, WITTER, Kirsti, TONAR, Zbyněk, 2022. Using virtual microscopy for the development of sampling strategies in quantitative histology and design-based stereology. *Anatomia, histologia, embryologia*. 51(1), 3–22. ISSN 0340-2096. Dostupné z: <https://doi.org/10.1111/ahe.12765>

IF_(JCR2020) = 1,114 Q3 (Veterinary sciences)

MALEČKOVÁ, Anna, KOCHOVÁ, Petra, PÁLEK, Richard, LIŠKA, Václav, MIK, Patrik, BOŇKOWSKI, Tomasz, HORÁK, Miroslav, TONAR, Zbyněk, 2021. Blunt injury of liver: mechanical response of porcine liver in experimental impact test. *Physiological measurement*. 42(2), 025008. ISSN 0967-3334. Dostupné z: <https://doi.org/10.1088/1361-6579/abdf3c>

IF_(JCR2020) = 2,833 Q3 (Engineering, biomedical)

MIK, Patrik, TONAR, Zbyněk, **MALEČKOVÁ, Anna**, EBERLOVÁ, Lada, LIŠKA, Václav, PÁLEK, Richard, ROSENDORF, Jáchym, JIŘÍK, Miroslav, MÍRKA, Hynek, KRÁLÍČKOVÁ, Milena, WITTER, Kirsti, 2018. Distribution of Connective Tissue in the Male and Female Porcine Liver: Histological Mapping and Recommendations for Sampling. *Journal of comparative pathology*. 162, 1–13. ISSN 0021-9975. Dostupné z: <https://doi.org/10.1016/j.jcpa.2018.05.004>

IF_(JCR2017) = 1,364. Q2 (Veterinary sciences)

PÁLEK, Richard, ROSENDORF, Jáchym, **MALEČKOVÁ, Anna**, VIŠTEJNOVÁ, Lucie, BAJCUROVÁ, Kristýna, MÍRKA, Hynek, TÉGL, Václav, BRZOŇ, Ondřej, KUMAR, Arvind, BEDNÁŘ, Lukáš, TONAR, Zbyněk, HOŠEK, Petr, MOULISOVÁ, Vladimíra, EBERLOVÁ, Lada, TŘEŠKA, Vladislav, LIŠKA, Václav, 2020. Influence of Mesenchymal Stem Cell Administration on The Outcome of Partial Liver Resection in a Porcine Model of Sinusoidal Obstruction Syndrome. *Anticancer research*. 40(12), 6817–6833. ISSN 0250-7005. Dostupné z: <https://doi.org/10.21873/anticanres.14704>

IF_(JCR2019) = 1,994. Q4 (Oncology)

9.1.2 Ostatní recenzované časopisy

MALEČKOVÁ, Anna, TONAR, Zbyněk, MIK, Patrik, MICHALOVÁ, Květoslava, LIŠKA, Václav, PÁLEK, Richard, ROSENDORF, Jáchym, KRÁLÍČKOVÁ, Milena, TŘEŠKA, Vladislav, 2019. Zvířecí modely jaterních onemocnění a jejich využití v experimentální chirurgii. *Rozhledy v chirurgii*. 98(3), 100–109. ISSN

0035-9351. Dostupné z: <https://www.prolekare.cz/en/journals/perspectives-in-surgery/2019-3/animal-models-of-liver-diseases-and-their-application-in-experimental-surgery-109398>

PÁLEK, Richard, LIŠKA, Václav, TŘEŠKA, Vladislav, ROSENDORF, Jáchym, EMINGR, Michal, TÉGL, Václav, **KRÁLÍČKOVÁ, Anna**, BAJCUROVÁ, Kristýna, JIŘÍK, Miroslav, TONAR, Zbyněk, 2018. Sinusoidální obstrukční syndrom indukovaný monokrotalinem v experimentu na velkém zvířeti – pilotní studie. *Rozhledy v chirurgii*. 97(5), 214–221. ISSN 0035-9351. Dostupné z: <https://www.prolekare.cz/en/journals/perspectives-in-surgery/2018-5-2/sinusoidal-obstruction-syndrome-induced-by-monocrotaline-in-a-large-animal-experiment-a-pilot-study-63663>

9.2 Publikace mimo rámec dizertační práce

9.2.1 Časopisy s faktorem impaktu

EBERLOVÁ, Lada, PÍŠOVÁ, Soňa, PAPEŽOVÁ, Lucie, MÍRKA, Hynek, HOŠEK, Petr, ŠTEFLOVÁ, Michaela, **MALEČKOVÁ, Anna**, KACHLÍK, David, ŠTĚPÁNEK, David, 2020. Bony canal and grooves of the middle meningeal artery: mythic structures in anatomy and neurosurgery? *Folia Morphologica*. 79(3), 450–461. ISSN 0015-5659. Dostupné z: <https://doi.org/10.5603/FM.a2019.0098>

IF_(JCR2019) = 0,941 Q3 (Anatomy & morphology)

FILOVÁ, Eva, TONAR, Zbyněk, LUKÁŠOVÁ, Věra, BUZGO, Matěj, LITVINEC, Andrej, RAMPICHOVÁ, Michala, BEZNOSKA, Jiří, PLENCNER, Martin, STAFFA, Andrea, DAŇKOVÁ, Jana, SOURAL, Miroslav, CHVOJKA, Jiří, **MALEČKOVÁ, Anna**, KRÁLÍČKOVÁ, Milena, AMLER, Evžen, 2020. Hydrogel Containing Anti-CD44-Labeled Microparticles, Guide Bone Tissue Formation in Osteochondral Defects in Rabbits. *Nanomaterials (Basel, Switzerland)*. 10(8), 1504. ISSN 2079-4991. Dostupné z: <https://doi.org/10.3390/nano10081504>

IF_(JCR2019) = 4,324 Q2 (Materials science, multidisciplinary)

GRAJCIAROVÁ, Martina, TUREK, Daniel, **MALEČKOVÁ, Anna**, PÁLEK, Richard, LIŠKA, Václav, TOMÁŠEK, Petr, KRÁLÍČKOVÁ, Milena, TONAR, Zbyněk, 2022. Are ovine and porcine carotid arteries equivalent animal models for

experimental cardiac surgery: A quantitative histological comparison. *Annals of Anatomy - Anatomischer Anzeiger*. 242, 151910. ISSN 0940-9602. Dostupné z: <https://doi.org/10.1016/j.aanat.2022.151910>

IF_(JCR2021) = 2,698 Q1 (Anatomy & Morphology)

9.2.2 Ostatní recenzované časopisy.

DVOŘÁKOVÁ, Jana, ČEDÍKOVÁ, Miroslava, **MALEČKOVÁ, Anna**, KULDA, Vlastimil, TONAR, Zbyněk, MÜLLEROVÁ, Dana, 2018. Vznik a vývoj tukové kapénky a její role ve zdraví a nemoci. *Časopis lékařů českých*. 157(5), 254–262. ISSN 0008-7335. Dostupné z: <https://www.prolekare.cz/casopisy/casopis-lekaru-ceskych/2018-5-3/vznik-a-vyvoj-tukove-kapenky-a-jeji-role-ve-zdravi-a-nemoci-105838>

JEDLIČKOVÁ, Hana, VOKURKA, Samuel, VOJTÍŠEK, Radovan, **MALEČKOVÁ, Anna**, 2019. Alopecie a poškození vlasů indukované onkologickou terapií. *Klinická onkologie*. 32(5), 353–359. ISSN 0862-495X. Dostupné z: <https://doi.org/10.14735/amko2019353>

9.3 Kapitoly v monografiích

GREGOR, Tomáš, KOCHOVÁ, Petra, EBERLOVÁ, Lada, NEDOROST, Lukáš, PROSECKÁ, Eva, LIŠKA, Václav, MÍRKA, Hynek, KACHLÍK, David, PIRNER, Ivan, ZIMMERMANN, Petr, **KRÁLÍČKOVÁ, Anna**, KRÁLÍČKOVÁ, Milena, TONAR, Zbyněk, 2012. Correlating Micro-CT Imaging with Quantitative Histology. In: GOSWAMI, Tarun, ed. *Injury and Skeletal Biomechanics*. Rijeka: InTech, 173–196. ISBN: 978-953-51-0690-6

TONAR, Zbyněk, EBERLOVÁ, Lada, POLÍVKA, Jiří, DAUM, Ondřej, WITTER, Kirsti, **KRÁLÍČKOVÁ, Anna**, GREGOR, Tomáš, NEDOROST, Lukáš, KOCHOVÁ, Petra, ROHAN, Eduard, KALUSOVÁ, Kristýna, PÁLEK, Richard, SKÁLA, Martin, GLANC, David, KRÁLÍČKOVÁ, Milena, LIŠKA, Václav, 2012. Stereological methods for quantitative assessment of hepatic microcirculation. In: Méndez-Villas, Antonio, ed. *Current Microscopy Contributions to Advances in Science and Technology. Vol. 1*. Badajoz: Formatex Research Center, 737–748. ISBN: 978-84-939843-5-9

10 Přílohy – plná znění předložených prací

10.1 Příloha I

MALEČKOVÁ, Anna, TONAR, Zbyněk, MIK, Patrik, MICHALOVÁ, Květoslava, LIŠKA, Václav, PÁLEK, Richard, ROSENDORF, Jáchym, KRÁLÍČKOVÁ, Milena, TŘEŠKA, Vladislav, 2019. Zvířecí modely jaterních onemocnění a jejich využití v experimentální chirurgii. *Rozhledy v chirurgii*. 98(3), 100–109. ISSN 0035-9351. Dostupné z: <https://www.prolekare.cz/en/journals/perspectives-in-surgery/2019-3/animal-models-of-liver-diseases-and-their-application-in-experimental-surgery-109398>

Zvířecí modely jaterních onemocnění a jejich využití v experimentální chirurgii

A. Malečková^{1,2}, Z. Tonar^{1,2}, P. Mik³, K. Michalová⁴, V. Liška^{2,5}, R. Pálek^{2,5}, J. Rosendorf^{2,5}, M. Králíčková^{1,2}, V. Třeška⁵

¹Ústav histologie a embryologie, Lékařská fakulta v Plzni, Univerzita Karlova

²Biomedicínské centrum, Lékařská fakulta v Plzni, Univerzita Karlova

³Evropské centrum excelence NTIS, Fakulta aplikovaných věd, Západočeská univerzita v Plzni

⁴Šiklův ústav patologie, Lékařská fakulta v Plzni, Univerzita Karlova

⁵Chirurgická klinika, Fakultní nemocnice Plzeň, Lékařská fakulta v Plzni, Univerzita Karlova

Souhrn

Akutní a chronická jaterní onemocnění představují širokou skupinu chorob, které často ohrožují pacienty na životě. Pochopení mechanismů stojících za patogenezi a progresí jaterního poškození je klíčové pro vývoj nových terapeutických strategií a léků. Nejvýznamnějším faktorem limitujícím studium patogeneze a progresu jaterních onemocnění je nedostatek vhodných zvířecích modelů. Do současné doby bylo etablováno množství zvířecích modelů napodobujících jaterní onemocnění u lidí. Hlodavci, konkrétně potkani a myši, představují největší skupinu modelů jaterních onemocnění. Tyto modely ovšem dokážou manifestovat všechny klinické aspekty jaterního onemocnění u lidí jen do omezené míry, především pro jejich omezenou anatomickou a fyziologickou podobnost s lidmi. Velké zvířecí modely reprezentované prasetem, významné zejména v oblasti modelování akutního jaterního selhání, jsou stále častěji využívány v modelování dalších akutních i chronických jaterních onemocnění. Přenos výsledků testování nových léčebných metod do humánní medicíny je závislý na vývoji dokonalejších zvířecích modelů reflektujících průběh jaterních onemocnění u lidí. Toto přehledné sdělení shrnuje dosud publikované zvířecí modely chronických i akutních jaterních onemocnění se zvláštním důrazem na velké zvířecí modely a jejich využití v experimentální chirurgii.

Klíčová slova: onemocnění jater – zvířecí modely – experimentální chirurgie, prase

Summary

Animal models of liver diseases and their application in experimental surgery

A. Maleckova, Z. Tonar, P. Mik, K. Michalova, V. Liska, R. Palek, J. Rosendorf, M. Kralickova, V. Treska

Both acute and chronic liver diseases are frequent and potentially lethal conditions. Development of new therapeutic strategies and drugs depends on understanding of liver injury pathogenesis and progression, which can be studied on suitable animal models. Due to the complexity of liver injury, the understanding of underlying mechanisms of liver diseases and their treatment has been limited by the lack of satisfactory animal models. So far, a wide variety of animals has been used to mimic human liver disease, however, none of the models include all its clinical aspects seen in humans. Rodents, namely rats and mice, represent the largest group of liver disease models despite their limited resemblance to human. On the other hand, large animal models like pigs, previously used mostly in acute liver failure modeling, are now playing an important role in studying various acute and chronic liver diseases. Although significant progress has been made, the research in hepatology should continue to establish animal models anatomically and physiologically as close to human as possible to allow for translation of the experimental results to human medicine. This review presents various approaches to the study of acute and chronic liver diseases in animal models, with special emphasis on large animal models and their role in experimental surgery.

Key words: liver disease – animal models – experimental surgery – pig

Rozhl Chir 2019;98:100–109

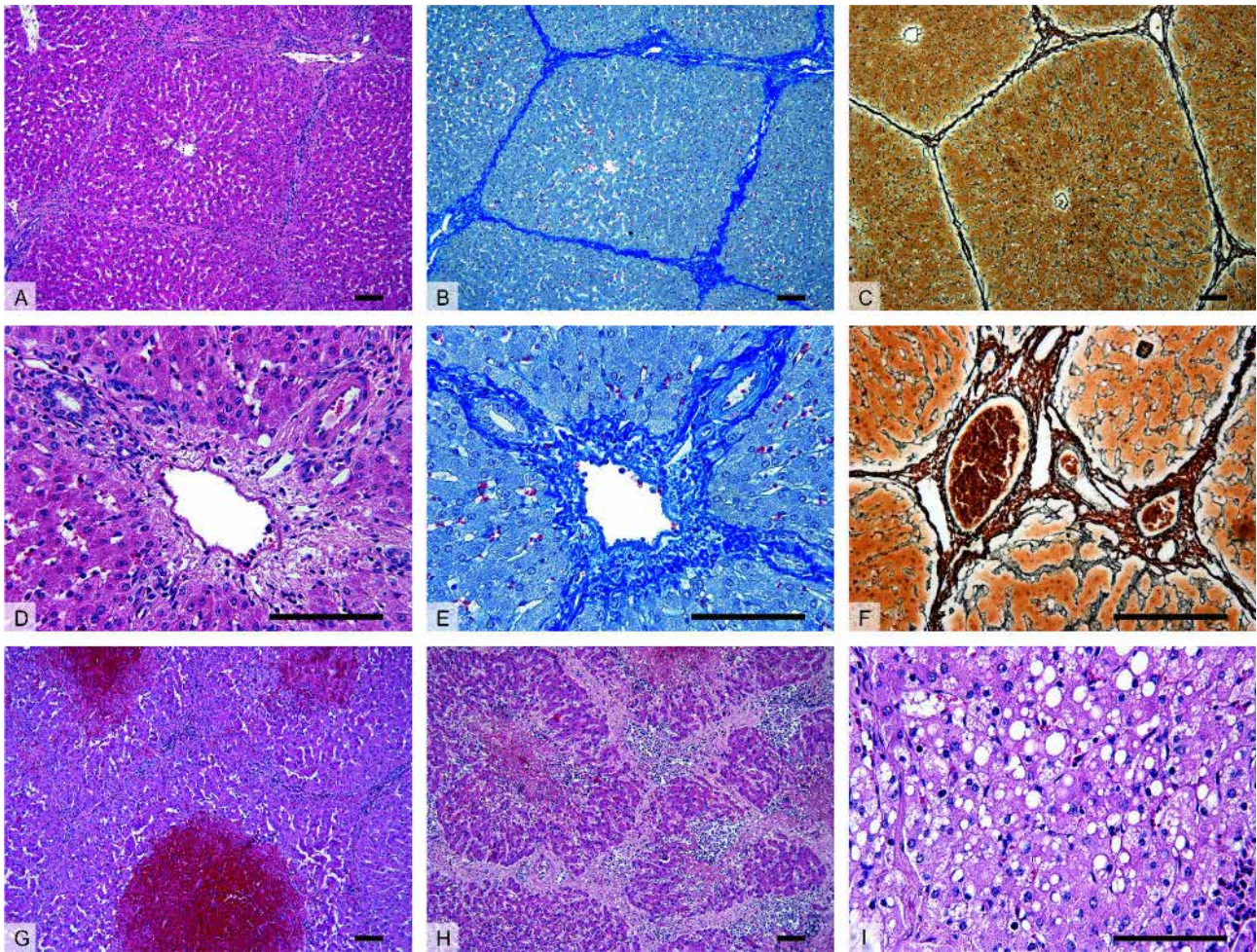
ÚVOD

Akutní jaterní onemocnění (acute hepatic injury, acute liver disease ALD) a chronická jaterní onemocnění (chronic liver disease CLD) představují širokou skupinu chorob jater s různou etiologií a mechanismem vzniku jaterního poškození. ALD mohou vyústit v akutní selhání jater (acute liver failure ALF) nebo přejít do chronicity. CLD typicky vedou k progresivní destrukci jaterního parenchymu a ve svém důsledku vyúsťují v jaterní fibrózu a cirhózu.

Navzdory pokroku v diagnostických a léčebných metodách v hepatologii stále zůstává řada nezodpovězených otázek týkajících se patogeneze, progresu

a případného terapeutického ovlivnění jaterních onemocnění. Jednou z vhodných cest ke zkoumání těchto mezer v poznání je experimentální využití zvířecích modelů jaterních onemocnění.

Do současné doby byly formou přehledných sdělení zmapovány oblasti zvířecích modelů akutních i chronických jaterních onemocnění [1–5]. ALD i CLD jsou nejčastěji modelovány na malých laboratorních savcích, kteří se uplatňují zejména díky své snadné genetické manipulovatelnosti, krátkému životnímu cyklu (dospějí v případě CLD do stadia fibrózy či cirhózy [5]) a cenové dostupnosti. Ovšem jejich malá anatomická a fyziologická podobnost s člověkem omezuje aplikovatelnost výsledků studií do humánní medicíny. Proto



Obr. 1: Histologický obraz zdravých (A–F) a patologicky změněných jater prasete (G–I)

A–C – Přehledné zvětšení zobrazující jaterní parenchym členěný v jednotlivé jaterní lalůčky, které jsou u prasete ohraničené oproti člověku významně větším množstvím vaziva.

D–F – Detail portobiliárních prostor obsahujících hepatickou trias – interlobulární větev a. hepatica propria, v. portae a žlučovodu.

G – Centrilobulární hemoragická nekróza u zvířete se sinusoidálním obstrukčním syndromem vyvolaným experimentální aplikací pyrrolizidinového alkaloidu monocrotalinu.

H – Nodulární transformace jaterní tkáně s porušenou mikrostrukturou jater a typicky zmoženým interlobulárním vazivem u jaterní cirhózy.

I – Steatóza jater charakterizována nahromaděním tukových vakuol v cytoplasmě hepatocytů v důsledku toxického poškození jater. Barvení: hematoxylin a eosin – přehledné barvení (A, D, G–I), anilinová modř a jádrová červen – detekce kolagenního vaziva (B, E), stříbření (impregnační metoda) (C, F) – detekce retikulárních vláken. Měřítka: 100 µm.

Fig. 1: Histology of healthy (A–F) and diseased (G–I) porcine liver

A–C – The liver parenchyma divided into morphological hepatic lobules, in pigs the lobules are demarcated by a significantly higher amount of connective tissue when compared to human.

D–F – Detail of portal tracts containing bile ducts and branches of the hepatic artery and portal vein surrounded by connective tissue.

G – Centrilobular hemorrhagic necrosis seen in animal with Sinusoidal Obstruction Syndrome, experiment included the application of alkaloid monocrotaline.

H – Cirrhotic liver histologically represented by nodular transformation of liver parenchyma with disruptions of liver microarchitecture and excessive amount of interlobular connective tissue.

I – Steatosis characterized by lipid droplets accumulation within hepatocytes caused by toxic liver injury.

Staining: hematoxylin and eosin staining (A, D, G–I), aniline blue staining, counterstained with nuclear fast red – detection of collagen connective tissue (B, E), silver impregnation technique – detection of reticular fibers.

Scale bars: 100 µm.

jsou zde tendence provádět experimenty původně s malými savci na modelech relevantnějších pro humánní medicínu, jako např. na praseti [6], jehož játra jsou do velké míry anatomicky a histologicky podobná játrům lidským (Obr. 1).

Naproti tomu v oblasti modelování ALF převažují velké zvířecí modely, které umožňují napojení na mimotělní oběh, opakované odběry krve a jsou vhodné pro nácvik chirurgických technik, které jsou na rozdíl od mikrochirurgických technik používaných na hlodavcích

Tab. 1: Srovnání zvířecích modelů jaterních onemocnění**Tab. 1: Comparison of animal models of liver diseases**

	Zvíře	Onemocnění	Výhody	Nevýhody
Velké zvířecí modely	prase pes	akutní selhání jater	anatomicky a fyziologicky podobné lidem možnost opakovaných odběrů krve napojení na mimotělní oběh návlek chirurgických technik	vysoká cena nutnost aplikace opakovaných dávek hepatotoxických látek dlouhá doba potřebná k rozvoji CLD
Malé zvířecí modely	myš potkan králík	akutní jaterní onemocnění chronická jaterní onemocnění	krátká doba potřebná k rozvoji CLD levné možnost genetické modifikace	anatomicky a fyziologicky málo podobné lidem velikost neumožňující opakované odběry krve a napojení na mimotělní oběh

Vysvětlivky: CLD – chronické jaterní onemocnění (chronic liver disease).

jednak méně náročné na dovednosti operátora, ale především bližší chirurgické praxi (Tab. 1).

V literatuře nacházíme množství způsobů dělení zvířecích modelů jaterních onemocnění, které se do jisté míry překrývají a duplikují. Liu et al. [4] navrhl rozdělení modelů CLD dle mechanismu vzniku jaterní fibrózy a cirhózy na (i.) klasické modely: neberou v potaz etiologii jaterního poškození, aplikací hepatotoxických látek dosahují u zvířat jaterní fibrózy, (ii.) modely napodobující specifická jaterní onemocnění: kladou důraz na etiologii CLD, která významným způsobem ovlivňuje patogenezi, progresi a prognózu CLD. Poněkud přehlednějším je zde navržené dělení, které zahrnuje většinu možností modelování jak akutního, tak chronického jaterního poškození (Tab. 2).

Cílem tohoto sdělení je představit zvířecí modely jaterních onemocnění a jejich současné využití v experimentu. Pro zachování kompatibility se zahraničními zdroji ponecháváme vedle některých pojmů v češtině i jejich ustálené protějšky v anglickém jazyce.

Tab. 2: Přehled zvířecích modelů jaterních onemocnění**Tab. 2: List of animal models of liver diseases**

Akutní selhání jater (ALF)
Chirurgické modely
Farmakologické modely
Infekční modely
Toxické poškození jater
Chemicky indukované modely
Lékové poškození jater
Alkoholové poškození jater
Modely imitující specifická jaterní onemocnění
Modely autoimunitní hepatitidy (AIH)
Modely primární biliární cirhózy (PBC)
Modely primární sklerozující cholangitidy (PSC)
Modely nealkoholické steatózy jater (NAFLD) a steatohepatitidy (NASH)
Modely virové hepatitidy
Invazivní model jaterní fibrózy
Geneticky modifikované myši

1. Zvířecí modely akutních a chronických jaterních onemocnění

Následující text shrnuje vybrané modely zvířecích modelů akutních a chronických jaterních onemocnění na základě literární rešerše. Rešerše byla provedena v databázi PubMed k datu 30. 8. 2018 s využitím klíčových slov: acute liver failure, chronic liver disease, animal models. Přehledná sdělení (review) byla následně doplněna o konkrétní studie s využitím klíčových slov nalezených v literatuře, např.: acetaminophen, acute liver failure, animal model, pig. V předkládaném článku jsou uvedena jak přehledná sdělení (review) na dané téma, tak příklady studií, které využily zvířecí model ke konkrétním experimentům, např. k testování podpůrných jaterních systémů (Tab. 4). Zahrnuty byly zejména studie s prasečími modely jaterních onemocnění.

1.1 Modely akutního jaterního selhání

Navzdory vysoké regenerační kapacitě hepatocytů a možnosti spontánního návratu jaterních funkcí zůstává pro pacienty s ALF bez uspokojivé regenerace jedinou terapeutickou možností ortotopická transplantace jater (orthotopic liver transplantation OLT). Ve většině případů OLT zlepšuje celkové přežití, ovšem počet pacientů na čekací listině pro transplantaci neustále přibývá [1]. Zlepšení regenerační kapacity jater lze dosáhnout arterializací portální vény (portal vein arterialization PVA), jak bylo testováno v experimentu na potkanech [7] a prasatech [8]. Současné léčebné možnosti používané k překlenutí čekací doby na OLT (tzv. „bridging“) jsou omezené a zahrnují transplantaci hepatocytů [9] a využití podpůrných jaterních systémů, tzv. „umělých jater“ (liver support systems) [10,11].

Pokusy o vysvětlení patofyziologických procesů a propojení metabolických změn s klinickými projevy ALF vyústily ve formulování dvou teorií: „toxin hypothesis“ a „critical mass theory“. „Toxin hypothesis“ předpokládala, že za klinické projevy ALF jsou zodpovědné nahromaděné látky jako např. amoniak, fenoly či volné žlučové kyseliny, které jsou ve zdravých játrech odbourávány. „Critical mass theory“ pak za příčinu jaterního selhání považovala ztrátu hepatocytů pod určitou kritickou mez, kdy již játra nejsou schopna udržovat svou

Tab. 3: Kritéria pro ideální zvířecí model akutního selhání jater (ALF) – převzato a upraveno dle Terblanche a Hickman [13]
Tab. 3: Criteria for an ideal animal model of acute liver failure (ALF) postulated by Terblanche and Hickman [13]

Kritérium	Charakteristika
Vratnost – reversibility	Při zavedení vhodné léčby by mělo být ALF potencionálně reverzibilní a model by měl při adekvátní léčbě přežít.
Opakovatelnost – reproducibility	Model musí být jednoduše reprodukovatelný.
Smrt z příčin jaterního selhání – death from liver failure	Měly by být přítomny biochemické, histologické a klinické změny odrážející průběh jaterního selhání u lidí a jaterní poškození by mělo vést přímo ke smrti modelu.
Terapeutické okno – therapeutic window	Mezi inzultem a úmrtím zvířete musí být dostatečný čas k nasazení a posouzení efektu léčby.
Velký zvířecí model – large animal model	Velikost zvířete musí umožnit pravidelné odběry krve a aplikaci mimotělního oběhu a model by měl být anatomicky a fyziologicky co nejbližší lidem.
Bezpečnost – minimal risk for personnel	Použité techniky a toxiny musí představovat minimální riziko pro personál.

metabolickou aktivitu na takové úrovni, aby dokázala zajistit podporu funkce dalších periferních orgánů. Hlubší studium problematiky ALF ovšem ukázalo, že mechanismus nahromadění toxických látek a ztráty syntetické kapacity jater nejsou jedinými mechanismy a že vlastní poškozené hepatocyty se podílejí na prohloubení a progresi ALF uvolňováním zánětlivých cytokinů či vazoaktivních látek [12]. Přesto dodnes zůstávají některé mechanismy ALF nepopsány. Pro studium patogeneze ALF a testování nových terapeutických přístupů z hlediska jejich bezpečnosti a efektivity je proto nezbytné etablovat zvířecí model, který bude co nejvíce reflektovat průběh ALF u člověka.

Terblanche a Hickman [13] počátkem 90. let navrhli systém šesti kritérií, která by měl ideální zvířecí model ALF splňovat (Tab. 3). V současnosti žádný zvířecí model ALF nesplňuje všechna popsaná kritéria. Pro vytvoření modelu ALF se využívají tři hlavní přístupy: chirurgický, farmakologický (toxický) a infekční model [1–3].

1.1.1 Chirurgické modely ALF

Chirurgické modely s výhodou využívají velká zvířata. Rozdělují se do 3 základních skupin: velká resekce (partial hepatectomy), hepatektomie (anhepatic model) a ischemický model (ischemic model, devaskularizace) (Tab. 4).

Modely velké jaterní resekce jsou pro svoji náročnost provedení, jež závisí na technickém vybavení a zkušenostech operátorů, těžko reprodukovatelné. Alternativou k prosté resekcí může být kombinace resekce s ischemií zbytku jaterního parenchymu [14].

Anhepatický model zahrnuje odstranění celého orgánu [15], je oproti předchozímu snadněji reprodukovatelný. Pro jeho využití v experimentu je mimo jiné důležitá i pooperační intenzivní péče: monitorování hemodynamických parametrů, zajištění ventilace, monitorování a případná úprava mikce, monitorování množství hemoglobinu, hematokritu a laktátu, elektrolytů v séru, acidobazické rovnováhy, krevních plynů a hladiny glukózy, které ovlivňují délku přežití zvířete, a tedy i délku terapeutického okna pro použití a testování nových léčebných strategií [16].

Ischemický model představuje dvoustupňový chirurgický výkon, při kterém se vytváří portokavální shunt s následným uzávěrem hepatické arterie [17]. Okluze může být dočasná, pak je model potenciálně reverzibilní, ovšem průběh ALF je značně nestálý a těžko reprodukovatelný. Jiným přístupem k vytvoření ischemického modelu je přerušovaná okluze v. portae a a. hepatica s následnou arteriální ligací [18]. Tento model splňuje všechna kritéria dle Terblanche a Hickmana s výjimkou reverzibility [13].

Tab. 4: Přehled chirurgických modelů akutního selhání jater a jejich současné využití v experimentu na praseti
Tab. 4: Surgical models of acute liver failure and their current application in experimental research on pigs

Typ modelu	Klinická relevance	Výhody	Omezení	Využití prasečího modelu v experimentu
Velká jaterní resekce Partial hepatectomy	resekční výkon pro nádorové onemocnění	reverzibilita	technicky náročné nereprodukovatelné	studium regenerace [48]
Hepatektomie Anhepatic model	hepatektomie pro rozsáhlé trauma či akutní rejekci orgánu po transplantaci	reprodukovatelnost	ireverzibilní vyločení vlivu poškozených hepatocytů na progresi ALF	BAL [49]
Ischemický model Ischemic model	dočasná ischemie při OLT	reverzibilita	nereprodukovatelný krátké přežití	BAL [50]

Vysvětlivky: OLT – ortotopická transplantace jater (orthotopic liver transplantation), BAL – bioartificial liver.

Tab. 5: Farmakologické modely akutního jaterního selhání a jejich využití v experimentu na praseti
Tab. 5: Pharmacological models of acute liver failure and their application in experimental research on pigs

Název sloučeniny	Mechanismus účinku poškození jater	Výhody	Omezení	Využití prasečího modelu v experimentu
Galaktosamin	narušení metabolismu RNA hepatocytů	zanedbatelné extrahepatální účinky	klinicky nerelevantní nereprodukovatelný riziko pro personál cena	BAL [51] aplikace MSC a jejich efekt na ALF [52]
Acetaminofen APAP	metabolizace pomocí cytochromu P450 a vznik toxického NAPQI	klinicky relevantní bezpečný	variabilita v odpovědi na dávku a v přežití extrahepatální toxicita: nefortoxicita, kardiotoxicita methemoglobinémie	BAL [53]
Tetrachlormetan CCl₄	metabolizace pomocí cytochromu P450 2E1 se vznikem toxických radikálů	vysoká mortalita	krátké terapeutické okno extrahepatální toxicita	PVA [8]

Vysvětlivky: ALF – akutní selhání jater (*acute liver failure*), NAPQI – *N*-acetyl-*p*-benzoquinone imine, BAL – bioartificial liver, PVA – portal vein arterialization, NO – oxid dusnatý, MSC – mezenchymální kmenové buňky (*mesenchymal stem cells*).

Tab. 6: Zvířecí modely toxického poškození jater
Tab. 6: Animal models of hepatic injury induced by hepatotoxins

Použitá látka	Mechanismus poškození [54]	Poškození jater	Zvíře	Využití modelu v experimentu
Skutečné hepatotoxiny				
• Tetrachlormethan CCl₄	metabolizace pomocí cytochromu P450 2E1 se vznikem toxických radikálů	akutní selhání jater fibróza/cirhóza	potkan myš	studium hepatoprotektivních látek [55] role miRNA ve fibrogenезi [56] terapie otrav CCl ₄ [57] studium hepatoprotektivních látek [58]
• Thioacetamid TAA	vznik intermediární metabolitu thioacetamid-S-oxidu a zvýšení oxidativního stresu	fibróza/cirhóza HCC, Cholangiokarcinom	potkan myš	studium hepatoprotektivních látek [59] role mikrobiomu ve fibrogenезi [60]
• Dimethylnitrosamin Diethylnitrosamin DMN/DEN	Alkylace DNA	fibróza/cirhóza HCC	potkan myš	role miRNA ve fibrogenезi [61] ovlivnění progresu fibrózy do HCC [62] role miRNA ve fibrogenезi [63]
Potenciální hepatotoxiny				
• Chemoterapeutika	specifický v závislosti na použitém chemoterapeutiku [64]	Sinusoidální obstrukční syndrom (SOS) CASH	potkan myš	terapeutické ovlivnění SOS [65] studium patogeneze SOS [66]
Ethanol	indukce cytochromu P450IIIЕ1 zvýšená hladina acetaldehydu oxidativní stres	ASH fibróza/cirhóza	prase potkan myš	regenerace jater s CASH [67] studium hepatoprotektivních látek [68] studium hepatoprotektivních látek [69]

Vysvětlivky: HCC – hepatocelulární karcinom, CASH – steatohepatitida spojená s chemoterapií (*chemotherapy-associated steatohepatitis*), ASH – alkoholová steatohepatitida (*alcoholic steatohepatitis*), ALD – alkoholové poškození jater (*alcoholic liver disease*).

1.1.2 Farmakologické modely

Většinu farmakologických zvířecích modelů ALF představují malí laboratorní savci [19–21]. Velké zvířecí modely jsou zatíženy nutností opakované aplikace poměrně vysokých dávek toxinu s nestálým klinickým průběhem ALF. Přesto velkých zvířecích modelů v současnosti přibývá, a to zejména pro testování jaterních podpůrných systémů. Nejvýznamnějšími toxiny, jejichž účinky byly studovány na řadě zvířecích druhů a které jsou v současnosti používány k vývoji modelu ALF, patří: galaktosamin [22], acetaminofen [23] a tetrachlormethan [8,24] (Tab. 5).

1.1.3 Infekční modely

Navzdory tomu, že virové hepatitidy jsou celosvětově jednou z nejčastějších příčin jaterního selhání, byly snahy o vytvoření zvířecího modelu na podkladě infekce dlouhou dobu neúspěšné. Myší modely hepatitidy B přispěly ke studiu patogeneze ALF, ovšem tento malý zvířecí model neumožňoval opakované krevní rozborů a připojení na mimotělní eliminační metody. Z tohoto důvodu se infekční modely prozatím ve studiu ALF neuplatnily.

1.2 Modely toxického poškození jater

Játra hrají zásadní roli v biotransformaci a eliminaci

Tab. 7: Zvířecí modely specifických jaterních onemocnění
Tab. 7: Animal models mimicking specific chronic liver diseases

Onemocnění	Kritéria („wish list“) pro ideální model	Zvíře	Princip modelu
Autoimunitní hepatitida AIH [26]	přítomnost autoprotilátek (ANA, ASMA) chronický zánět s přechodem do fibrózy přítomnost antigeně-specifických T-lymfocytů přítomnost nekrotizace na histologickém vyšetření	myš králík	indukované modely geneticky modifikované spontánní modely geneticky modifikované indukované modely přenos antigenů pomocí virů
Primární biliární cirhóza PBC [29]	převaha rozvoje PBC u samic přítomnost autoprotilátek (AMA) chronický zánět malých a střední intrahepatálních žlučovodů floridní duktulární reakce na histologickém vyšetření	myš	geneticky modifikované spontánní modely modely vyvolané enviromentálními faktory geneticky modifikované autoimunitní modely
Primární sklerozující cholangitida PSC [35]	převaha rozvoje PSC u samců progresivní zánět intra- a extrahepatických žlučovodů koncentrická periduktální fibróza (onion skinning) na histologickém vyšetření přítomnost nespecifického zánětu střev (UC) přechod do cholangiokarcinomu	potkan myš	chemicky indukované modely modely využívající infekční agens geneticky modifikované modely model GVHD
Nealkoholická steatóza a steatohepatitida NAFLD, NASH [37]	obezita Dyslipidémie inzulinová rezistence steatóza, zánět a balonová degenerace hepatocytů progredující ve fibrózu na histologickém vyšetření přechod do HCC	myš potkan	„dietary models“ MCD diet CDAA diet atherogenní dieta high-fat diet a její variace geneticky modifikované modely
Virová hepatitida B a C HBV [46] a HCV [45]	vnímavost k infekci replikace viru v organismu imunitní odpověď srovnatelná s lidmi Progrese do cirhózy přechod do HCC	šimpanz myš potkan kachna svišť	šimpanzí modely myši exprimující virové proteiny myši exprimující receptory pro HCV chimerické myši modely imunodeficientní chimerické modely imunokompetentní

Vysvětlivky: ANA – antinukleární autoprotilátky, ASMA – autoprotilátky proti hladkým svalovým buňkám, AMA – antimitochondriální protilátky, UC – ulcerózní kolitida, HCC – hepatocelulární karcinom, GVHD – reakce štěpu proti hostiteli, MCD diet – methionine and choline deficiency diet, CDAA diet – choline-deficient L-amino acid-defined diet.

exogenních látek, jejichž nadměrnou expozicí často dochází k jaternímu poškození. Opakované aplikace hepatotoxických látek představují klasický způsob indukce jaterní fibrózy u experimentálních zvířat. V závislosti na způsobu podávání ale mohou hepatotoxické látky místo jaterní fibrózy způsobit akutní jaterní poškození, až selhání (viz kapitola 1.1.2 Farmakologické modely ALF) (Tab. 5).

Z preventivního hlediska lze hepatotoxické látky, a tedy i zvířecí modely toxického poškození jater, dělit do dvou kategorií: (i.) skutečné hepatotoxiny – jejich podání vyvolá poškození jater u všech jedinců, jde především o produkty chemického průmyslu jako tetrachlormethan CCl_4 , thioacetamid (TAA), dimethylnitrosamin (DMN) a diethylnitrosamin (DEN) – a (ii.) potenciální hepatotoxiny – vyvolají poškození jater jen u části jedinců, jedná se především o léky, např. chemoterapeutika (Tab. 6). Zvláštní kapitolu tvoří alkoholové poškození jater.

1.2.1 Alkoholové poškození jater

Nadměrná konzumace alkoholu, ať už akutní, či chronická, je závažným sociálním, ekonomickým i zdravotním problémem. Alkoholové postižení jater zahrnuje stavy od poměrně nezávažné steatózy až po cirhózu jater s možností vzniku hepatocelulárního karcinomu.

Alkoholové poškození jater se nejčastěji modeluje na myších a potkanech. Nejrozšířenějším modelem je chronické podávání alkoholu (Lieber–DeCarli liquid diet; LD diet), chronická intragastrická aplikace alkoholu nebo kombinace podávání alkoholu se specifickou dietou (high-fat diet), s hepatotoxickými látkami nebo u geneticky modifikovaných myší [25].

1.3 Modely imitující specifická jaterní onemocnění

Společným znakem většiny chronických jaterních onemocnění je jejich vliv na histologickou stavbu jaterního parenchymu se vznikem jaterní fibrózy až cirhózy. Etiologické a patogenetické mechanismy zodpovědné za tyto změny se ovšem u jednotlivých specifických jaterních onemocnění liší a často je ani neznáme. Vytvoření zvířecích modelů je tak komplikováno nejen neznalostí etiopatogeneze onemocnění, ale také tím, že některé choroby se vyskytují pouze u lidí (virové hepatitidy). Prozatím se nedaří modely, které by měly všechny atributy lidského onemocnění, vytvořit (Tab. 7). Navzdory tomu jsou zvířecí modely specifických jaterních onemocnění ideálním nástrojem k pochopení vzniku a progresu CLD a k nalezení jejich účinné léčby.

1.3.1 Modely autoimunitní hepatitidy (autoimmune hepatitis AIH)

AIH je chronické zánětlivé onemocnění jater neznámé etiologie charakterizované přítomností autoantiláttek, histopatologickými změnami v játrech a klinickými příznaky vyplývajícími z jaterního poškození – únava, letargie, méně často ikterus. Charakteristickým diagnostickým klinickým znakem AIH je rychlá odpověď na imunosupresivní léčbu, která se vyskytuje asi u 90 % pacientů. Léčba AIH je založena na imunosupresivní terapii.

Zvířecí modely AIH lze vytvořit několika způsoby. V období před možností genetické manipulace modelových organismů se AIH indukovala aplikací jaterních antigenů nebo rostlinného lektinu concavalinu A, který nespecificky aktivuje T-lymfocyty a vede k poškození jater. Velkou skupinu modelů AIH ovšem představují geneticky modifikované myši modely [26] (Tab. 7).

1.3.2 Primární biliární cirhóza (primary biliary cirrhosis PBC)

PBC je chronické cholestatické onemocnění postihující malé a střední intrahepatální žlučovody a objevující se nejčastěji u žen středního věku (v páté a šesté dekádě života). Klasická forma PBC je spojena s přítomností antimitochondriálních protilátek v séru [27]. Aspekty ovlivňující etiologii ovšem zatím zůstávají neznámé a studie se zaměřují nejen na vnitřní, ale i environmentální faktory v rozvoji onemocnění [28]. Do současné doby bylo ke studiu etiopatogeneze a interakce možných genetických a environmentálních faktorů vytvořeno množství zvířecích modelů PBC (myši) [29]. PBC u těchto modelů vzniká buď spontánně u geneticky modifikovaných myši [30–32], nebo je indukována působením environmentálních faktorů na zvíře, jako je expozice xenobiotikům (např. 2-octynoic acid (2-OA) [32]) nebo působení infekční agens [33].

1.3.3 Primární sklerozující cholangitida (primary sclerosing cholangitis PSC)

Primární sklerozující cholangitida (primary sclerosing cholangitis PSC) patří mezi další chronické zánětlivé onemocnění jater postihující intra- a extrahepatické žlučové cesty a pomalu může progredovat k biliární cirhóze a jaternímu selhání. PSC se často vyskytuje u pacientů s nespecifickým střevním zánětem, zejména s ulcerózní kolitidou [34]. Klinické a laboratorní nálezy jako T-lymfocytární infiltrace v okolí cílových žlučovodů, přítomnost autoantilátek pANCA (perinukleární autoantilátky proti cytoplasmě neutrofilů, perinuclear antineutrophil cytoplasmatic antibodies) a spojitost s určitými HLA haplotypy a dalšími autoimunitními chorobami (UC) svědčí o autoimunitně zprostředkovaném mechanismu vzniku a progresu onemocnění. Ovšem v porovnání s jinými autoimunitními chorobami PSC špatně reaguje na imunosupresivní léčbu, vyskytuje se častěji u mužů (2–3:1) a je zde jen slabá korelace mezi hladinou sérových autoantilátek s klinickými a laboratorními nálezy.

Pollheimer a Fickert [35] rozdělují zvířecí modely PSC do několika skupin dle mechanismu indukce onemocně-

ní. Žádný z modelů ovšem ještě nezodpověděl všechny otázky týkající se patogeneze a progresu onemocnění.

1.3.4 Nealkoholická steatóza jater (non-alcoholic fatty liver disease NAFLD) a nealkoholická steatohepatitida (non-alcoholic steatohepatitis NASH)

NAFLD je v současné době nejčastějším chronickým progresivním jaterním onemocněním v rozvinutém světě, jehož prevalence se odhaduje až na 30 % populace. Ve většině případů je NAFLD úzce spojena s nadváhou a obezitou a s nimi spojenými metabolickými projevy, a to především inzulinovou rezistencí. Pokud jsou v játrech současně přítomny steatóza, zánět a poškození hepatocytů (balonová degenerace, ballooning), hovoříme o NASH, která může být doprovázena progresivní fibrózou a je spojena s vyšším rizikem vzniku hepatocelulárního karcinomu.

Nejlépe popsány a nejčastěji používanými modely NAFLD jsou tzv. „dietary models“, kde je navozeno jaterní poškození změnami ve stravě modelového organismu. Různé typy diet jsou pro zvířecí modely NASH klíčové. Představují buď vlastní příčinu NASH, nebo slouží jako spouštěče jaterního poškození u geneticky modifikovaných modelů. Diety jsou založeny buď na kaloricky bohaté stravě – fruktózová dieta, high-fat diet (HFD) – nebo na deficitu určitých živin podílejících se na správném metabolismu tuků – methionine and choline deficient diet (MCD diet), choline-deficient L-amino acid-defined diet (CDAA diet). Z geneticky modifikovaných modelů se nejčastěji uplatňují modely myši s diabetem [36,37].

1.3.5 Modely virové hepatitidy

Studium virové hepatitidy B a C bylo dlouho omezeno na *in vitro* podmínky nebo na studie probíhající na jediném zvířeti, které je k infekci těmito hepatotropními viry vnímavé – na šimpanzovi [38,39]. Šimpanzí model hrál klíčovou roli při studiu interakce hostitel-vir a bylo na něm možno testovat první antivirové strategie v léčbě infekce. Přelomovým objevem bylo objevení buněčných receptorů pro HBV a HCV, díky nimž bylo možné vytvořit buněčné linie pro studium životního cyklu a jednotlivých virových komponent *in vitro*. Základních strategií tvorby *in vivo* myších modelů virové infekce je několik. Jednou z nich je exprese virových proteinů nebo receptorů pro lidské viry samotnými hepatocyty u transgenních myši [40]. Další možností je vytvoření chimerických myši, a to transplantací lidských hepatocytů imunodeficientním myším [41,42]. Imunodeficientní organismy ovšem nedovolují studium imunitních mechanismů. Z tohoto důvodu byly vyvinuty imunokompetentní modely (potkan), kterých bylo dosaženo současnou transplantací lidských krvetvorných kmenových buněk [43,44].

V současnosti máme tedy k dispozici množství modelů jak pro preklinické testování antivirové terapie (imunodeficientní), tak pro studium imunitní odpovědi na léčbu (imunokompetentní). Žádný z modelů ovšem nespĺňuje všechna kritéria pro ideální model, a to zejména přechod do chronicity se vznikem jaterní cirhózy a eventuálně HCC [45,46].

1.4 Invazivní model jaterní fibrózy

Podvaz *ductus hepaticus communis* (bile duct ligation BDL) je invazivní metodou vyvolání sekundární biliární cirhózy. Obstrukce toku žluči způsobuje intrahepatální cholestázu, proliferaci žlučovýchodů, zánět v portobiliárních prostorech a fibrózu a vede ke vzniku sekundární biliární cirhózy a jaternímu selhání. BDL se provádí u potkanů, kteří nemají žlučník [47]

1.5 Geneticky modifikované myši jako zvířecí modely jaterních onemocnění

Geneticky modifikované myši se používají k modelování jaterní fibrózy, kdy vyřazení specifických genů nebo naopak jejich over-exprese umožňuje studium jejich fibrogenního nebo antifibrogenního vlivu exprimovaných faktorů [5]. Transgenní myši se uplatňují i při modelování specifických jaterních onemocnění, jak je uvedeno v předchozích kapitolách.

ZÁVĚR

Snahy o vytvoření zvířecích modelů jaterních onemocnění probíhají již několik desetiletí s většími či menšími úspěchy o přiblížení se průběhu jaterních chorob u lidí. Největší skupinu tvoří malé zvířecí modely reprezentované myšmi a potkany, které se využívají nejčastěji ke studiu etiopatogeneze a progresu onemocnění. Testování nových terapeutických přístupů, a to jak léků, tak invazivních metod, je ovšem z těchto modelů jen omezeně přenositelné do humánní medicíny.

Na druhou stranu velké zvířecí modely, ze kterých je často používaným modelem prase, představují spojující článek mezi experimentální medicínou a klinickou praxí. Uplatňují se zejména při studiu akutního selhání jater (Tab. 1), kde je velké zvíře jedním ze zásadních kritérií ideálního modelu, a stále častěji při vývoji nových chirurgických přístupů a invazivních terapeutických metod, jako jsou podpůrné jaterní systémy.

Využití anatomické a fyziologické podobnosti jater prasete s játry člověka může být s výhodou využito při přenosu výsledků experimentálních výzkumů do humánní klinické medicíny. Vývoj nových velkých zvířecích modelů jaterních onemocnění, např. v oblasti autoimunitních jaterních onemocnění, je ovšem zatížen řadou nevýhod spojených s prací s velkými zvířaty. Menší počet jedinců v porovnávaných skupinách ztěžuje statistické vyhodnocení experimentů s možným ovlivněním výsledků značnou interindividuální variabilitou. Oproti laboratorním hlodavcům by ale prasečí modely chronických jaterních onemocnění mohly přinést nové poznatky o mechanismech způsobujících jaterní poškození a umožnit tak přesnější diagnózu či účinnější léčbu našich pacientů.

Seznam zkratk

- AIH – autoimunitní hepatitida, autoimmune hepatitis
- ALD – akutní jaterní onemocnění, acute liver disease
- ALF – akutní selhání jater, acute liver failure
- AMA – antimitochondriální protilátky, anti-mitochondrial antibodies
- ANA – antinukleární protilátky, antinuclear antibodies

- APAP – acetaminophen
- ASH – alkoholová steatohepatitida (alcoholic steatohepatitis)
- ASMA – autoprotilátky proti hladkým svalovým buňkám, anti-smooth muscle antibodies
- BAL – bioartificial liver
- BDL – podvaz *ductus hepaticus communis*, bile duct ligation
- CASH – steatohepatitida spojená s chemoterapií, chemotherapy-associated steatohepatitis
- CDA diet – choline-deficient L-amino acid-defined diet
- CCI₄ – tetrachlormethan
- CLD – chronická jaterní onemocnění, chronic liver disease
- DEN – diethylnitrosamin
- DNM – dimethylnitrosamin
- GVHD – reakce štěpu proti hostiteli, graft versus host disease
- HBV – virus hepatitidy B, hepatitis B virus
- HCC – hepatocelulární karcinom, hepatocellular carcinoma
- HCV – virus hepatitidy C, hepatitis C virus
- HFD – dieta bohatá na tuky, high-fat diet
- MCD diet – methionine and cholin deficiency diet
- MSC – mezenchymální kmenové buňky, mesenchymal stem cells
- NAFLD – nealkoholická steatóza jater, non-alcoholic fatty liver disease
- NAPQI – N-acetyl parabenzoquinoneimine
- NASH – nealkoholická steatohepatitida, non-alcoholic steatohepatitis
- NO – oxid dusnatý, nitric oxide
- OLT – ortotopická transplantace jater, orthotopic liver transplantation
- pANCA – perinukleární autoprotilátky proti cytoplasmě neutrofilů, perinuclear antineutrophil cytoplasmic antibodies
- PBC – primární biliární cirhóza, primary biliary cirrhosis
- PSC – primární sklerozující cholangitida, primary sclerosing cholangitis
- PVA – arterIALIZACE portální vény, portal vein arterialization
- TAA – thioacetamid
- UC – ulcerózní kolitida, ulcerative colitis

Podpora:

Program rozvoje vědních oborů Univerzity Karlovy (Progres Q39); Národní program udržitelnosti I (NPU I) č. LO1503 poskytnutý Ministerstvem školství, mládeže a tělovýchovy; SVV 260390 Univerzity Karlovy; Univerzitní výzkumná centra UK UNCE/MED/006 „Univerzitní centrum klinické a experimentální jaterní chirurgie“; Projekt Aplikace moderních technologií v medicíně a průmyslu reg. č.: CZ.02.1.01/0.0/0.0/17_048/0007280 financovaného z EFRR.

Konflikt zájmů

Autoři článku prohlašují, že nejsou v souvislosti se vznikem tohoto článku ve střetu zájmů a že tento článek nebyl publikován v žádném jiném časopise.

1. Van De Kerkhove MP, Hoekstra R, Van Gulik TM, et al. Large animal models of fulminant hepatic failure in artificial and bioartificial liver support research. *Biomaterials* 2004;25:1613–25.
2. Rahman TM, Hodgson HJ. Animal models of acute hepatic failure. *Int J Exp Pathol* 2000;81:145–57.
3. Newsome PN, Plevris JN, Nelson LJ, et al. Animal models of fulminant hepatic failure: a critical evaluation. *Liver Transpl* 2000;6:21–31.
4. Liu Y, Meyer C, Xu C, et al. Animal models of chronic liver diseases. *AJP Gastrointest. Liver Physiol* 2013;304:G449–68.
5. Starkel P, Leclercq IA. Animal models for the study of hepatic fibrosis. *Best Pract Res Clin Gastroenterol* 2011;25:319–33.
6. Pálek R, Liška V, Třeška V, et al. Sinusoidal obstruction syndrome induced by monocrotaline in a large animal experiment – a pilot study. *Rozhl Chir* 2018;97:214–21.
7. Fan YD, Praet M, Van Huysse J, et al. Effects of portal vein arterialization on liver regeneration after partial hepatectomy in the rat. *Liver Transplant* 2002;8:146–52.
8. Zullo A, Cannistrà M, Cavallari G, et al. Liver regeneration induced by extracorporeal portal vein arterialization in a swine model of carbon tetrachloride intoxication. *Transplant Proc* 2015;47:2173–5.
9. Hughes RD, Mitry RR, Dhawan A. Current status of hepatocyte transplantation. *Transplantation* 2012;93:342–7.
10. Laleman W, Wilmer A, Evenepoel P, et al. Review article: Non-biological liver support in liver failure. *Aliment Pharmacol Ther* 2006;23:351–63.
11. Ryska O, Pantoflíček T, Lásziková E, et al. Současný význam biologických a nebiologických eliminačních metod v léčbě akutního selhání jater. *Rozhl Chir* 2008;87:291–6.
12. Losser M-R, Payen D. Mechanisms of liver damage. *Semin Liver Dis* 1996;16:357–67.
13. Terblanche J, Hickman R. Animal models of fulminant hepatic failure. *Dig Dis Sci* 1991;36:770–4.
14. Ladurner R, Hochleitner B, Schneeberger S, et al. Extended liver resection and hepatic ischemia in pigs: A new, potentially reversible model to induce acute liver failure and study artificial liver support systems. *Eur Surg Res* 2005;37:365–9.
15. Sosef MN, Van Gulik TM. Total hepatectomy model in pigs: Revised method for vascular reconstruction using a rigid vascular prosthesis. *Eur Surg Res* 2004;36:8–12.
16. Thiel C, Thiel K, Etspueler A, et al. Standardized intensive care unit management in an anhepatic pig model: new standards for analyzing liver support systems. *Crit Care* 2010;14:R138.
17. Nieuwoudt M, Kunniker R, Smuts M, et al. Standardization criteria for an ischemic surgical model of acute hepatic failure in pigs. *Biomaterials* 2006;27:3836–45.
18. Lee KU, Zheng L, Cho YB, et al. An experimental animal model of fulminant hepatic failure in pigs. *J Korean Med Sci* 2005;20:427–32.
19. Saracyn M. Hepatoprotective effect of nitric oxide in experimental model of acute hepatic failure. *World J Gastroenterol* 2014;20:17407.
20. Carvalho NR, Tassi CC, Dobraschinski F, et al. Reversal of bioenergetics dysfunction by diphenyl diselenide is critical to protection against the acetaminophen-induced acute liver failure. *Life Sci* 2017;180:42–50.
21. Zhang S, Zhu Z, Wang Y, et al. Therapeutic potential of Bama miniature pig adipose stem cells induced hepatocytes in a mouse model with acute liver failure. *Cytotechnology* 2018;70:1131–41.
22. Kalpana K, Ong HS, Soo KC, et al. An improved model of galactosamine-induced fulminant hepatic failure in the pig. *J Surg Res* 1999;82:121–30.
23. Thiel C, Thiel K, Etspueler A, et al. A reproducible porcine model of acute liver failure induced by intrajejunal acetaminophen administration. *Eur Surg Res* 2011;46:118–26.
24. Nayak NC, Chopra P, Dhar A, et al. Diverse mechanisms of hepatocellular injuries due to chemicals: evidence in rats administered carbon tetrachloride or dimethylnitrosamine. *Br J Exp Pathol* 1975;56:103–12.
25. Ghosh Dastidar S, Warner J, Warner D, et al. Rodent models of alcoholic liver disease: Role of binge ethanol administration. *Biomolecules* 2018;8:3.
26. Christen U, Holdener M, Hintermann E. Animal models of autoimmune hepatitis. *Autoimmun Rev* 2007;6:306–11.
27. Oertelt S, Rieger R, Selmi C, et al. A sensitive bead assay for antimitochondrial antibodies: Chipping away at AMA-negative primary biliary cirrhosis. *Hepatology* 2007;45:659–65.
28. Tanaka A, Leung PSC, Young HA, et al. Toward solving the etiological mystery of primary biliary cholangitis. *Hepatol Commun* 2017;1:275–87.
29. Katsumi T, Tomita K, Leung PSC, et al. Animal models of primary biliary cirrhosis. *Clin Rev Allergy Immunol* 2015;48:142–53.
30. Koarada S, Wu Y, Fertig N, et al. Genetic control of autoimmunity: Protection from diabetes, but spontaneous autoimmune biliary disease in a nonobese diabetic congenic strain. *J Immunol* 2004;173:2315–23.
31. Oertelt S, Lian Z-X, Cheng C-M et al. Anti-mitochondrial antibodies and primary biliary cirrhosis in TGF- receptor II dominant-negative mice. *J Immunol* 2006;177:1655–60.
32. Wakabayashi K, Lian Z-X, Moritoki Y, et al. IL-2 receptor $\alpha^{-/-}$ mice and the development of primary biliary cirrhosis. *Hepatology* 2006;44:1240–9.
33. Wang JJ, Yang GX, Zhang WC, et al. *Escherichia coli* infection induces autoimmune cholangitis and anti-mitochondrial antibodies in non-obese diabetic (NOD).B6 (Idd10/Idd18) mice. *Clin Exp Immunol* 2014;175:192–201.
34. Fausa O, Schrumpf E, Elgjo K. Relationship of inflammatory bowel disease and primary sclerosing cholangitis. *Semin Liver Dis* 1991;11:31–9.
35. Pollheimer MJ, Fickert P. Animal models in primary biliary cirrhosis and primary sclerosing cholangitis. *Clin Rev Allergy Immunol* 2015;48:207–17.
36. Santhekadur PK, Kumar DP, Sanyal AJ. Preclinical models of non-alcoholic fatty liver disease. *J Hepatol* 2018;68:230–7.
37. Van Herck MA, Vonghia L, Francque SM. Animal models of nonalcoholic fatty liver disease—a starter's guide. *Nutrients* 2017;9:1–13.
38. Bukh J. A critical role for the chimpanzee model in the study of hepatitis C. *Hepatology* 2004;39:1469–75.
39. Wieland SF. The chimpanzee model for hepatitis B virus infection. *Cold Spring Harb. Perspect Med* 2015;5:1–19.
40. Moriya K, Fujie H, Shintani Y, et al. The core protein of hepatitis C virus induces hepatocellular carcinoma in transgenic mice. *Nat Med* 1998;4:1065–7.
41. Dandri M, Burda MR, Török E, et al. Repopulation of mouse liver with human hepatocytes and in vivo infection with hepatitis B virus. *Hepatology* 2001;33:981–8.
42. Bissig K-D, Wieland SF, Tran P, et al. Human liver chimeric mice provide a model for hepatitis B and C virus infection and treatment. *J Clin Invest* 2010;120:924–30.
43. Washburn ML, Bility MT, Zhang L, et al. A humanized mouse model to study hepatitis C virus infection, immune response, and liver disease. *Gastroenterology* 2011;140:1334–44.
44. Billerbeck E, Mommersteeg MC, Shlomai A, et al. Humanized mice efficiently engrafted with fetal hepatoblasts and syngeneic immune cells develop human monocytes and NK cells. *J Hepatol* 2016;65:334–43.
45. Vercauteren K, De Jong YP, Meuleman P. HCV animal models and liver disease. *J Hepatol* 2014;61:S26–33.
46. Dandri M, Petersen J. Animal models of HBV infection. *Best Pract Res Clin Gastroenterol* 2017;31:273–9.
47. Abd El Mottebel DM, Ibrahim IAAEH, Elshazly SM. Sildenafil protects against bile duct ligation induced hepatic fibrosis in rats: Potential role for silent information regulator 1 (SIRT1). *Toxicol Appl Pharmacol* 2017;335:64–71.
48. Michalopoulos GK. Liver regeneration after partial hepatectomy. *Am J Pathol* 2010;176:2–13.
49. Abrahamse SL, Van De Kerkhove MP, Sosef MN, et al. Treatment of acute liver failure in pigs reduces hepatocyte function in a bioartificial liver support system. *Int J Artif Organs* 2002;25:966–74.
50. Lee J-H, Lee D-H, Lee S, et al. Functional evaluation of a bioartificial liver support system using immobilized hepatocyte spheroids in a porcine model of acute liver failure. *Sci Rep* 2017;7:3804. doi: 10.1038/s41598-017-03424-2.
51. Lv G, Zhao L, Zhang A et al. Bioartificial liver system based on choanoid fluidized bed bioreactor improve the survival time of fulminant hepatic failure pigs. *Biotechnol Bioeng* 2011;108:2229–36.
52. Sang J-F, Shi X-L, Han B, et al. Intraportal mesenchymal stem cell transplantation prevents acute liver failure through promoting cell proliferation and inhibiting apoptosis. *Hepatobiliary Pancreat Dis Int* 2016;15:602–11.
53. He G-L, Feng L, Cai L, et al. Artificial liver support in pigs with acetaminophen-induced acute liver failure. *World J Gastroenterol* 2017;23:3262.
54. Saxena R. Practical hepatic pathology:

- A diagnostic approach. Elsevier/Saunders, Philadelphia 2011.
55. Hamid M, Abdulrahim Y, Liu D, et al. The hepatoprotective effect of selenium-enriched yeast and gum Arabic combination on carbon tetrachloride-induced chronic liver injury in rats. *J. Food Sci* 2018;83:525–34.
 56. Ma L, Yang X, Wei R, et al. MicroRNA-214 promotes hepatic stellate cell activation and liver fibrosis by suppressing Sufu expression. *Cell Death Dis* 2018;9:1–13.
 57. Alam MF, Safhi MM, Anwer T, et al. Therapeutic potential of Vanillylacetone against CCl₄ induced hepatotoxicity by suppressing the serum marker, oxidative stress, inflammatory cytokines and apoptosis in Swiss albino mice. *Exp Mol Pathol* 2018;105:81–8.
 58. Sung YC, Liu YC, Chao PH, et al. Combined delivery of sorafenib and a MEK inhibitor using CXCR4-targeted nanoparticles reduces hepatic fibrosis and prevents tumor development. *Theranostics* 2018;8:894–905.
 59. Czechowska G, Celinski K, Korolczuk A, et al. Protective effects of melatonin against thioacetamide-induced liver fibrosis in rats. *J Physiol Pharmacol* 2015;66:567–79.
 60. Mazagova M, Wang L, Anfora AT, et al. Commensal microbiota is hepatoprotective and prevents liver fibrosis in mice. *FASEB J* 2015;29:1043–55.
 61. Chandel R, Saxena R, Das A, et al. Association of rno-miR-183-96-182 cluster with diethylnitrosamine induced liver fibrosis in Wistar rats. *J Cell Biochem* 2018;119:4072–84.
 62. Jilkova ZM, Kuyucu AZ, Kurma K, et al. Combination of AKT inhibitor ARQ 092 and sorafenib potentiates inhibition of tumor progression in cirrhotic rat model of hepatocellular carcinoma. *Oncotarget* 2018;9:11145–58.
 63. Marrone AK, Shpyleva S, Chappell G, et al. Differentially expressed microRNAs provide mechanistic insight into fibrosis-associated liver carcinogenesis in mice. *Mol Carcinog* 2016;55:808–17.
 64. King PD, Perry MC. Hepatotoxicity of chemotherapy. *Oncologist* 2001;6:162–76.
 65. Nakamura K, Hatano E, Narita M, et al. Sorafenib attenuates monocrotaline-induced sinusoidal obstruction syndrome in rats through suppression of JNK and MMP-9. *J. Hepatol* 2012;57:1037–43.
 66. Robinson SM, Mann DA, Manas DM, et al. The potential contribution of tumour-related factors to the development of FOLFOX-induced sinusoidal obstruction syndrome. *Br J Cancer* 2013;109:2396–403.
 67. Bruha J, Vycital O, Tonar Z, et al. Monoclonal antibody against transforming growth factor beta 1 does not influence liver regeneration after resection. *Large Animal Experiments* 2015;340:327–40.
 68. Chen X, Ying X, Sun W, et al. The therapeutic effect of fraxetin on ethanol-induced hepatic fibrosis by enhancing ethanol metabolism, inhibiting oxidative stress and modulating inflammatory mediators in rats. *Int Immunopharmacol* 2018;56:98–104.
 69. Choi Y, Abdelmegeed MA, Song BJ. Preventive effects of indole-3-carbinol against alcohol-induced liver injury in mice via antioxidant, anti-inflammatory, and anti-apoptotic mechanisms: Role of gut-liver-adipose tissue axis. *J Nutr Biochem* 2018;55:12–25.

MUDr. Anna Malečková
Ústav histologie a embryologie LF UK v Plzni
Karlovarská 48
301 00 Plzeň
anna.maleckova@lfp.cuni.cz

10.2 Příloha II

EBERLOVÁ, Lada, MALEČKOVÁ, Anna, MIK, Patrik, TONAR, Zbyněk, JIŘÍK, Miroslav, MÍRKA, Hynek, PÁLEK, Richard, LEUPEN, Sarah, LIŠKA, Václav, 2020. Porcine Liver Anatomy Applied to Biomedicine. *The Journal of surgical research.* 250, 70–79. ISSN 0022-4804. Dostupné z: <https://doi.org/10.1016/j.jss.2019.12.038>
IF_(JCR2019) = 1,841 Q3 (Surgery)

Available online at www.sciencedirect.com

ScienceDirect

journal homepage: www.JournalofSurgicalResearch.com

Research review

Porcine Liver Anatomy Applied to Biomedicine



Eberlova Lada, MD, PhD,^{a,b,*} Maleckova Anna, MD,^{b,c} Mik Patrik, MA,^{a,c}
 Tonar Zbynek, MD, PhD,^{b,c} Jirik Miroslav, MA, PhD,^b Mirka Hynek,^{b,d}
 Palek Richard, MD,^{b,e} Leupen Sarah, BA, PhD,^f
 and Liska Vaclav, MD, PhD^{b,e}

^a Faculty of Medicine in Pilsen, Department of Anatomy, Charles University, Pilsen, Czech Republic

^b Faculty of Medicine in Pilsen, Biomedical Centre, Charles University, Pilsen, Czech Republic

^c Faculty of Medicine in Pilsen, Department of Histology and Embryology, Charles University, Pilsen, Czech Republic

^d Department of Imaging Methods, University Hospital in Pilsen, Pilsen, Czech Republic

^e Department of Surgery, University Hospital in Pilsen, Pilsen, Czech Republic

^f Department of Biological Sciences, University of Maryland Baltimore County, Baltimore, Maryland

a r t i c l e i n f o

Article history:

Received 4 May 2019

Received in revised form

16 December 2019

Accepted 28 December 2019

Available online xxx

Keywords:

Biomedical research

Domestic pig

Liver

Anatomy

Histology

a b s t r a c t

Currently, there are at least 70 pure domestic pig breeds, but only certain breeds are used in biomedical research. The domestic pig liver is suitable for preclinical research because its size, physiology, and anatomy are similar to that of the human liver; in addition, there is a high degree of genetic similarity between the two species. For planning experiments and identifying improvements in both invasive and noninvasive methods of liver disease management, the morphological similarities and dissimilarities of the pig liver to its human counterpart must be taken into consideration along with sexual dimorphism and interindividual and interspecific variability. Recent histological evaluations based on stereological methods enable precise quantitative morphological estimates and guarantee their unbiased accuracy. The results thereof are crucial for revealing and assessing histological changes and can contribute to the optimization of study designs. New trends in computed tomography data processing have also been introduced. This review article summarizes the newest trends and findings in the field of porcine liver anatomy and histology as applicable to preclinical research.

© 2020 Elsevier Inc. All rights reserved.

Declaration of conflict of interest: none.

Photographs used in the text are original, and the pigs from which the liver was obtained were treated in accordance with EU directive for animal experiments. The surgical and anesthesiological procedures were certified by the Commission for Work with Experimental Animals at the Pilsen Medical Faculty of Charles University, Prague, and were under the control of the Ministry of Agriculture of the Czech Republic.

* Corresponding author. Faculty of Medicine in Pilsen, Department of Anatomy, Charles University, Karlovarska 48, 301 66 Pilsen, Czech Republic. Tel.: [p420377593302](tel:+420377593302); fax: [p420377593309](tel:+420377593309).

E-mail address: lada.eberlova@lfp.cuni.cz (E. Lada).

0022-4804/\$ - see front matter © 2020 Elsevier Inc. All rights reserved.

<https://doi.org/10.1016/j.jss.2019.12.038>

Introduction

The domestic pig (*Sus scrofa domesticus*) is an even-toed ungulate mammal. Genetic evidence indicates that this species developed from the wild boar in Southeast Asia approximately 5 million years ago, and domestication began in Eurasia approximately 10,000 years ago.¹ Hence, there is a general consensus that all variations of pigs (including mini/micro/minature) descend from the Eurasian wild boar. Swine were first used in biomedical research (BMR) in the 1940s, and their use has increased since the 1960s.² More recently, molecular biology and genetics have been applied to the breeding process to enhance selection for valuable traits. At present, the number of pig breeds is uncertain, but a review of more than 70 pure domestic pig breeds from all over the world is maintained on The Pig Site.³ Most of these breeds are primarily used for consumption, but certain small breeds are also used for BMR.⁴ Because the porcine genome, which consists of 18 autosomes and 2 sex chromosomes, has been sequenced and its extensive homology to humans has been demonstrated,⁵ genetically modified pigs have played an important role in translational studies focused on numerous diseases, including cancer, diabetes mellitus, Alzheimer's disease, cystic fibrosis, and Duchenne muscular dystrophy.⁶ In addition, because the structure and function of the porcine cardiovascular, renal, and gastrointestinal organs are similar to those of humans,⁷ these organs are extensively used in experimental surgery to test surgical techniques and experimental therapies^{4,8} before their use in humans (Table 1). In addition, the swine can live up to 10 years, thereby allowing the researchers long-term follow-up after experimental procedures.

The small pigs used in BMR, from an anatomical and physiological perspective, are similar to the domestic swine. The advantages of their small size are obvious: these pigs are easy to handle and house, and they require less food and test substances than larger pigs. Therefore, certain small breeds are predominantly used in pharmacology and toxicology studies for the testing of new drugs and medical devices⁴² (Table 1). Nevertheless, the availability of small breeds is limited.

Porcine liver gross anatomy

In terms of gross anatomy, from four to six liver lobes have been described in pigs (Table 2), and the right and left hemilivers are separated by a deep notch for the round ligament (Fig. 1A and B). The number and size of the lobes (segments) reported varies and thus may be breed-specific. Only the following five lobes are invariably present: the left lateral, left medial, right lateral, right medial, and the caudate lobe. From our experience with the Prestice Black-Pied pig breed,⁴⁸ which is in agreement with the veterinary anatomical textbooks,⁴⁹ the quadrate lobe is present occasionally (Fig. 1B and D). There also seems to be interbreed variability in the lobe proportions. Court *et al.*⁵⁰ found the left lateral lobe to be the largest, whereas Bekheit *et al.*,³⁵ based on computed tomography (CT) volumetry, assessed the right medial lobe to be the most voluminous.

Table 1 e Porcine liver applications in biomedical research.

Objects of research	References	Breed
Ablation, resection	9	Guangxi Bama minipig
	10	Wuzhishan pig
	11	Not mentioned
Biomechanics	12	Not mentioned
	13	Ecologically bred animals of various origins
Gene therapy	14,15	HSD11B1-transgenic pig
Imaging techniques, diagnostics	16	Duroc, Pietrain, Landrace, large white pig
	17	Bama miniature pig
Innovation of surgical techniques	18-21	Landrace pig
	19	Landrace pig
	21	Bama miniature pig
Liver transplantation	22	Micromini pigs (Fuji Micra Inc., Shizuoka, Japan)
	23	Landrace pig
	24	GalT-KO pig
	25	Yorkshire-Landrace pig
Liver traumatology	26	German domestic pig
	27,28	Not mentioned
	29	Chinese experimental hybrid pigs
Material testing	30	German Landrace pigs
	31	Not mentioned
Mathematical modeling, quantification	32	Prestice Black-Pied pig
	33	Prestice Black-Pied pig
	34	Prestice Black-Pied pig
Morphology, physiology	35	White pig
	36	Prestice Black-Pied pig
	37	Prestice Black-Pied pig
	38	Specific pathogen-free piglet
Pathogenesis, liver failure	39	Bama experimental miniature pig
	40	Bama experimental miniature pig
	41	Prestice Black-Pied pig
Pharmacology, toxicology	42	Minipig, review
	43	Landrace × large white pig
	44	Not mentioned
Regeneration	45	Polish white pig
	41,46,47	Prestice Black-Pied pig

In the pig, eight segments roughly similar to those in the human liver have been described⁵⁴⁻⁵⁶ (Tables 2 and 3; Fig. 1A and B). However, both the differences between pigs and

Table 2 e Liver segmental anatomy, literature review.

Breed	No of lobes	Name of the lobes	No of segments	Reference
Not mentioned	5	Right lateral, right medial, left lateral, left medial, caudate	8	35
Not mentioned	5	Right, left, right medial, left medial, caudate	8	50
Prestice Black-Pied pig	5 (6)	Right lateral, right medial, left lateral, left medial, caudate, quadrate occasionally	Not mentioned	34
Not mentioned	4	Right, left, right paramedian, left paramedian	8	51
Prestice Black-Pied pig	6	Right lateral, right medial, left lateral, left medial, caudate, quadrate	36	36
Not mentioned	3	Not named	8	52
Not mentioned	5	Right, left, right middle, left middle, caudate	8	53

humans and among breeds of pigs must be taken into account in extrapolating from porcine to human liver surgery. Unlike in the human liver, the so-called Rex-Cantlie line that divides the embryological and morphological right and left hemiliver is well marked in pigs by the deep notch for the round ligament, fissura ligament teretis (Fig. 1A and B). This line can be seen after ligation of the right or left lobar branch of the portal vein (PV).⁸ However, owing to the intraparenchymal thin-walled caudal vena cava (Fig. 1D), resection of the right lateral lobe in the pig liver is extremely difficult. The liver hilum is located dorsally on the visceral surface, and the PV ramifies a few centimeters outside the parenchyma out to the right lobe.^{50,53} The hepatic artery, the portal vein, and the common hepatic duct branch are accompanied by considerable connective tissue (Fig. 1B) that derives from the

perivascular fibrous capsule (of Glisson) and forms pedicles very similar to the ones found in the human liver.^{55,56} The gallbladder lies within the substance of the right medial lobe, if present, and it separates this lobe from the quadrate lobe⁴⁹ (Fig. 1BeD).

Although the PV supplies up to 90% of the blood volume and up to 2/3 of the oxygen supply to the liver, the hepatic artery proper is irreplaceable for its supply of the biliary tree (Fig. 1C). In experimental studies, embolization or ligation of a PV branch was used to stop the blood flow throughout a part of the liver. In this procedure, the part of the liver with restricted blood flow atrophies, whereas the rest of the tissue hypertrophies.⁸ This method is also used in human subjects, for example, in patients with colorectal carcinoma metastasis in the right liver lobe; after intestinal surgery and also most often

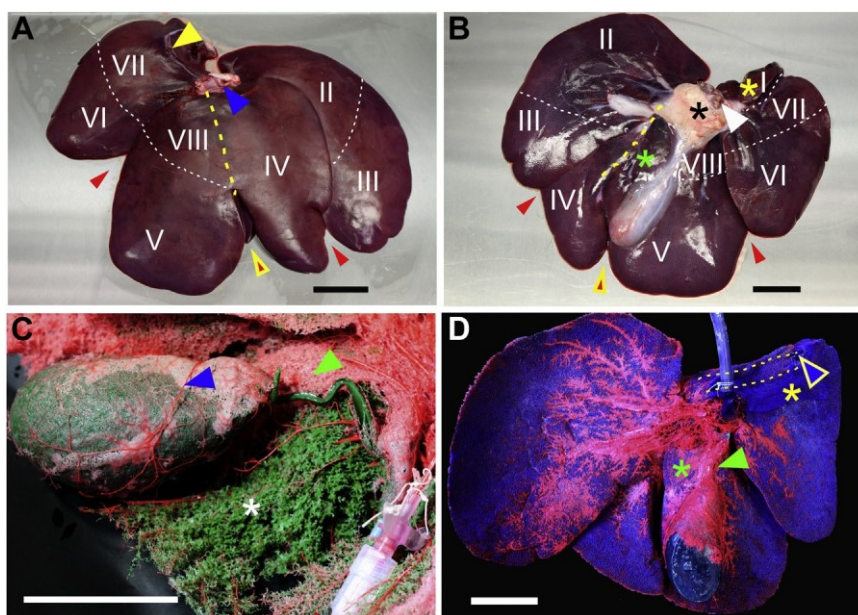


Fig. 1 e Porcine liver gross anatomy and corrosion casts, Prestice Black-Pied breed. (A, B) Segmental anatomy, diaphragmatic (A) and visceral surface (B). Interlobar notches (red arrowheads), notch for the ligamentum teres (yellow-red arrowheads), Rex-Cantlie line (yellow lines), coronary ligament (yellow arrowhead), caudal vena cava (blue arrowhead), portal vein (white arrowhead), hepatoduodenal ligament (black asterisk), caudate lobe (yellow asterisk), and quadrate lobe (green asterisk). (C, D) Vascular corrosion cast, filling with colored Biodur E20 Plus (Heidelberg, Germany) via the hepatic portal vein (blue), hepatic artery (red) and bile duct (green). Caudate lobe (yellow asterisk), quadrate lobe (green asterisk), cystic artery (blue arrowhead), capillary network of the cystic duct (green arrowheads), bile ductules (white asterisk), caudal vena cava course (yellow line), and orifice (yellow-blue arrowhead.) Scale bars 5 cm. (Color version of figure is available online.)

Table 3 e Porcine liver lobes and segments according to Court *et al.*⁵⁰ and Zanchet and Monteiro.⁵³

Corresponding parenchyma	Segment
Caudate lobe	S I
Left lateral lobe	S II, III
Left medial lobe	S IV
Right medial lobe	S V, VIII
Right lateral lobe	S VI, VII

after chemotherapy, embolization of the right PV is performed (the arterial supply is preserved to avoid necrosis.) The lobe with metastasis atrophies, whereas the contralateral lobe undergoes compensatory hypertrophy, which, after several weeks (provided that the parenchyma is functionally sufficient), allows for the resection of the part with the malignant deposit. Unfortunately, the growth of the nonoccluded liver is not always sufficient to avoid liver failure. Therefore, experimental studies using the porcine liver model for testing various occlusive methods and/or pharmacological treatments have been designed.^{8,46,57}

Porcine liver microanatomy

For studies of human liver diseases using the porcine liver model, detailed knowledge of liver microanatomy is necessary. The tissue structure of the porcine liver is similar to that

of the human liver.⁷ The parenchymal architecture is organized into well-defined, polygonal lobules centered around the central vein with portal triads at its corners (Figs. 2A and C, 3AeC). The portal lobules are demarcated by fibrous septa containing variable amounts of connective tissue (Fig. 3AeE). Three-dimensional (3-D) reconstruction of the porcine liver has revealed that the morphological lobule is pentagonal rather than hexagonal as it is described in humans.⁵⁸ However, the exact size and shape of portal lobules in the porcine liver and their spatial organization remain unknown.

The functional acinar concept, first described in the human liver by Rappaport,⁵⁹ divides the parenchyma into three concentric zones based on the perfusion of the liver: the classical lobule, portal lobule and acinus. As per this scheme, “metabolic zonation” refers to the differences in expression of the key metabolic genes in hepatocytes (HEPs) within different zones of the liver lobule; this zonation corresponds, to some degree, to the zones of the hepatic acinus.⁶⁰ However, this set of concepts is not sufficient to explain all the physiological and pathological processes in the liver.⁶¹

The morphometry and distribution of HEPs within the porcine liver was assessed by Junatas *et al.*³⁶ In healthy pigs of the Prestice Black-Pied breed,⁴⁸ each lobe contained HEPs of a comparable size, nuclearity, and density. However, the size and density were not uniformly distributed when comparing the different regions of the liver in relation to the hepatic vasculature (peripheral, paracaval, and periportal regions.) The reported fraction of binuclear HEPs, possibly linked to liver regeneration, was 4%. Interestingly, the number of nuclei

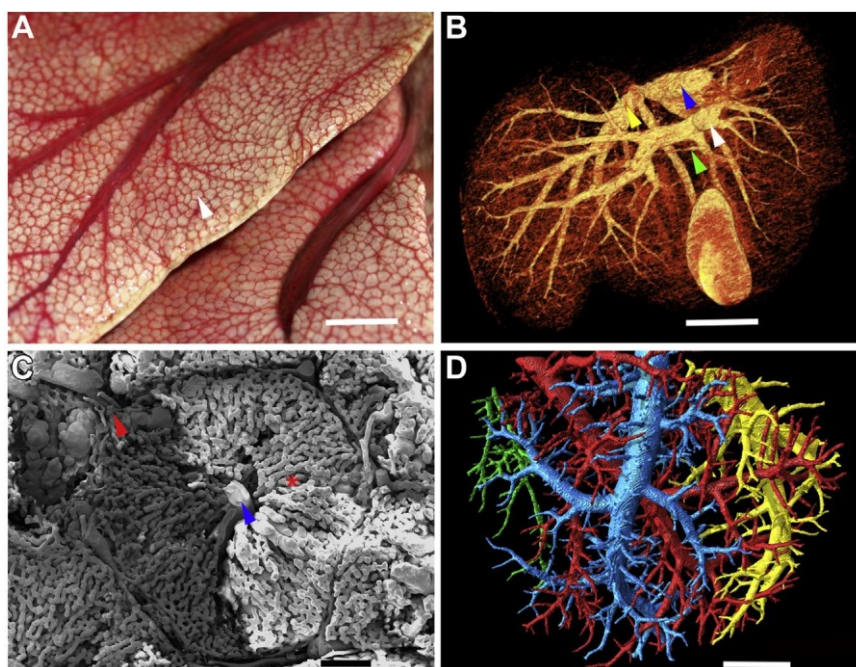


Fig. 2 e Vascular corrosion casts of pig liver, Prestice Black-Pied breed. Filling with colored Biodur E20 via the hepatic artery (A-C) and portal vein (B-D). (A) Classical hepatic lobule (white arrowhead) before corrosion. (B) Macro-CT, volume rendering technique. Syntopic view of portal and hepatic venous systems; hepatic vein (yellow arrowhead), portal vein (white arrowhead), hepatic duct (green arrowhead), and caudal vena cava (blue arrowhead). (C) Classical hepatic lobule in scanning electron microscopy. Portal triad in portal space (red arrowhead), sinusoids (red asterisk), and central vein (blue arrowhead). (D) Micro-CT, 3-D reconstruction, cast filled via the portal vein. Scale bars: 1 cm (A, D), 5 cm (B), 200 mm (C). (Color version of figure is available online.)

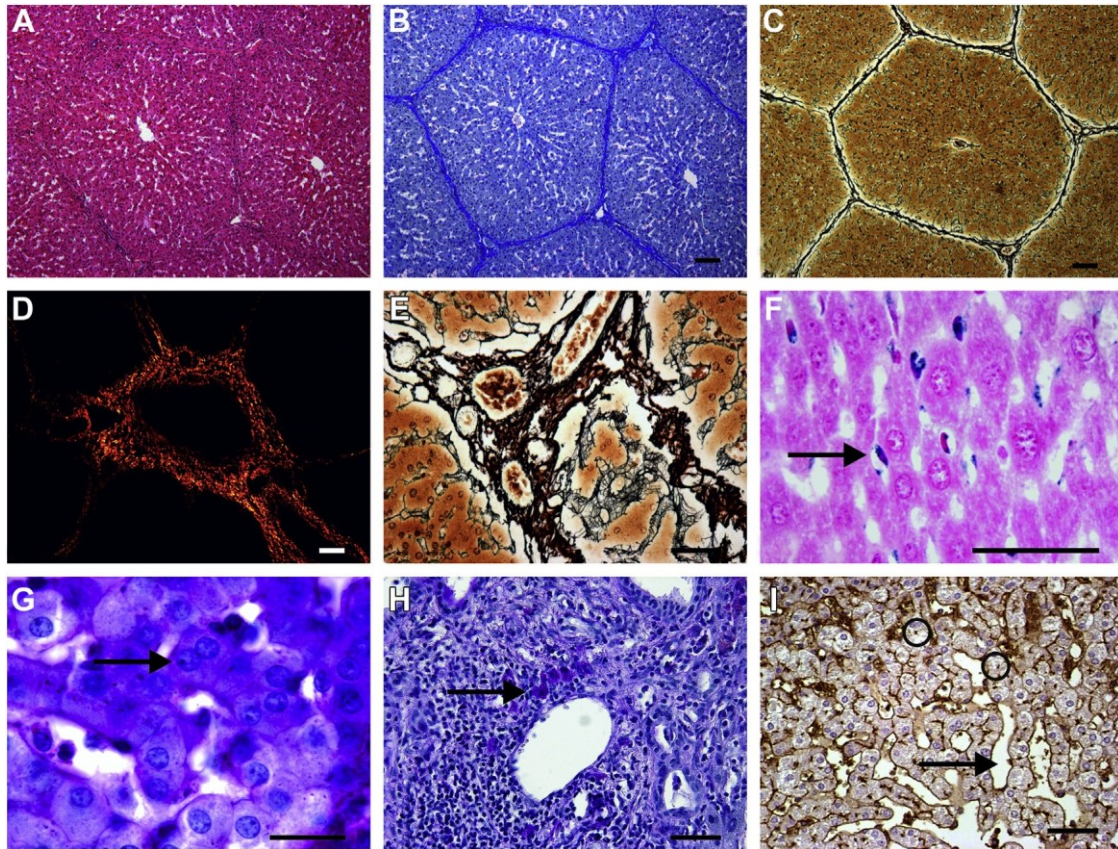


Fig. 3 e Porcine liver microanatomy in various histological staining methods. Hematoxylin and eosin staining (A), anilin blue staining counterstained with nuclear fast red:detection of collagen (B), Gomori reticulin staining:detection of reticular fibers (C, E), picosirius red staining in polarized light:detection of collagen I and III (D), Periodic acid-Shiff staining (G, H), lectin histochemistry staining using *Ricinus communis* Agglutinin lectin (I). (A-C) Demonstration of hepatic lobules clearly demarcated by connective tissue. (D, E) Detail of portal space containing bile ducts and branches of hepatic artery and portal vein surrounded by connective tissue. (F) Hepatic stellate cells (arrow). (G) Binuclear hepatocyte (arrow). (H) Cluster of Kupffer cells after phagocytosing cellular debris (arrow), a typical hallmark of hepatitis. (I) Discontinuous endothelium of hepatic sinusoids (arrow) and bile canaliculi formed by apical membranes of adjacent hepatocytes (circles). Scale bars: 100 μ m (A-C), 50 μ m (D-I). (Color version of figure is available online.)

does not always correspond with the ploidy of HEPs.⁶² However, the morphometry and distribution of HEPs was not mapped with respect to their position within the classical morphological hepatic lobules and liver acini.⁶³ Data on lobular and acinar distribution would provide valuable information concerning the role of HEPs in pathological processes, which predominantly involve the acinar zones. In addition, an estimation of the total number of HEPs within the different lobes⁶⁴ would serve as a powerful tool for comparing the functional capacity and regenerative potential of the hepatic lobes after a partial hepatectomy.^{47,65}

The exocrine function of the liver, bile production, is morphologically represented by a delicate intralobular network of channels, bile canaliculi (Fig. 3I), which drain the bile into the interlobular bile ducts. Hepatic sinusoids (Figs. 2C and 3I) are low-pressure vessels that lie between plates of HEPs and are lined by specialized endothelial cells and fixed macrophages called Kupffer cells (KCs) (Fig. 3H). The integrity of KCs has been linked to hepatocellular proliferation and

thus presumably plays a role in liver regeneration.⁶⁶ A recent study on the rat liver revealed that female rats have a greater number of HEPs and KCs and a larger fraction of binuclear cells than males.⁶³ These findings indicate a higher regenerative potential of the female liver. The stellate cells (Fig. 3F), which are also called Ito cells or fat-storing cells, are located in the perisinusoidal space (of Disse) between the HEPs and the sinusoids. They contain lipids that are involved in vitamin A metabolism and also play a leading role in fibrogenesis.⁶⁷

In the pig, design-based stereology^{64,68} (Fig. 4) has been demonstrated to be a powerful tool for assessing numerous morphological characteristics, namely, the number of HEPs and the amount of connective tissue within the porcine liver.^{36,37} Generating data on the morphometry and distribution of liver cells, together with the 3-D architecture of the vascular and biliary systems, could be the next step in understanding of liver function and pathophysiology and could increase the potential of successful xenotransplantation.⁶⁹ The evidence indicating that the liver is a sexually

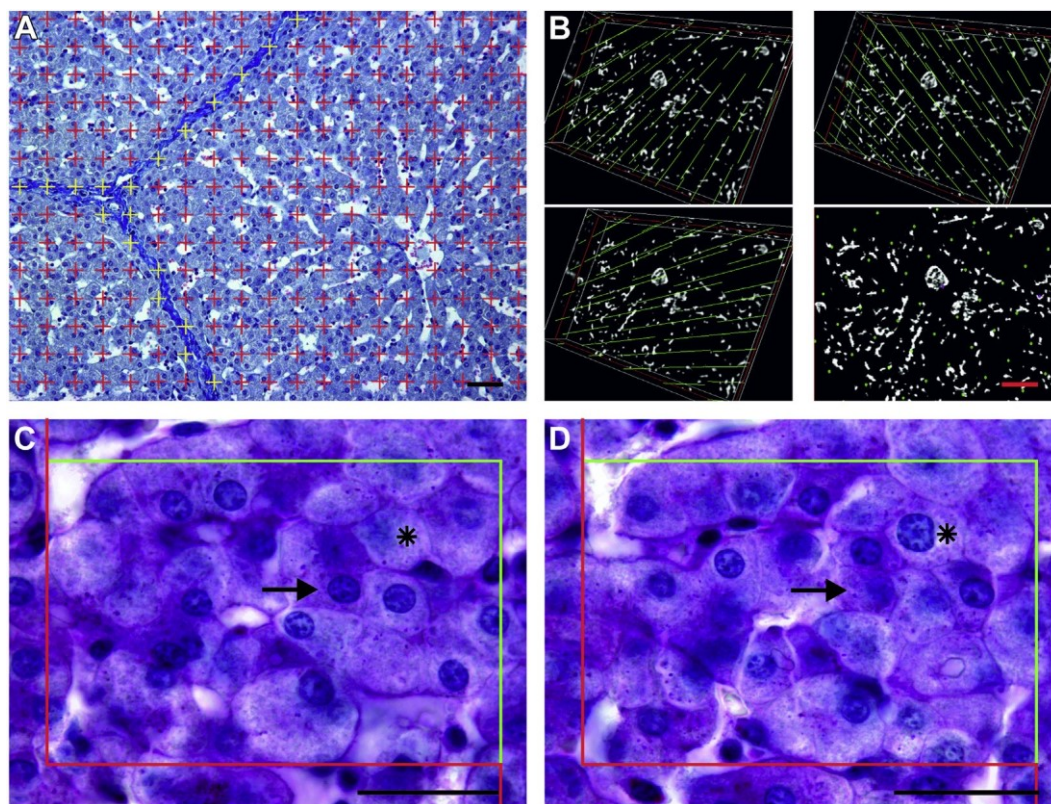


Fig. 4 e Demonstration of stereological methods for quantitative assessment in porcine liver. Point grid⁶⁸ used for the quantification of the connective tissue fraction, aniline blue with nuclear fast red staining. Points over the connective tissue within the predetermined area are highlighted in yellow (A). (B) Estimating the surface of microvessels in a series of m-CT scans of vascular corrosion cast using the fakir probe consisting of an isotropic grid with three differently oriented, perpendicular sets of probes with random initial orientation. Length of the probe intersections with the microvessel profiles is proportional to their surface (B). Demonstration of optical disector for estimating the numerical density of hepatocytes in two optical sections (C, D). The cell profiles with nuclei in focus in the bottom reference plane (C) and absent or out of focus in the look-up plane (D) that lie inside the counting frame or touch the green allowance borders but do not cross the red forbidden borders are counted (black arrow). The hepatocyte in focus in the look-up plane is not counted (marked with asterisk.) Scale bars: 50 mm (A), 100 mm (B); 20 mm (C, D). (Color version of figure is available online.)

dimorphic organ warrants consideration in the planning of experiments.^{37,63} Sufficient and systematic sampling is crucial for detecting the biological differences in liver tissue when studying liver regeneration, the pathophysiological mechanisms of liver diseases or the toxicity of drugs.⁶⁴

Liver connective tissue

Most types of chronic liver diseases lead to liver fibrosis and/or eventually to cirrhosis, that is, to the excessive accumulation of extracellular matrix, including fibrillar collagen. Staging and grading of liver fibrosis is a significant histopathological evaluation.^{61,70} In the human, six specific foci of liver fibrogenesis have been proposed for scoring. Namely, the portal, pericellular (perisinusoidal), pericentral (perivenular), centrilobular, ductal (periductal), and ductular fibrosis can be distinguished.⁶¹ The type and extent of fibrosis describes both the architecture of connective tissue and its amount and

measures how far the liver disease has progressed to its end stage—liver cirrhosis. In addition, the grade of the liver disease reflects the speed at which the disease will progress to its end stage. The amount and the architecture of connective tissue in the human liver is usually estimated during routine analysis of liver biopsies, usually as per one of the three most widely used scoring systems.⁷¹ However, the subjectivity and hence the lack of reproducible results of this routine biopsy scoring have been articulated.⁷²

For the study of the mechanisms of origin and spread of fibrosis, and also to assess the liver regenerative capacity, both small and large animals are widely used. However, small animal models have limitations due to their size and differential susceptibility to toxic agents or pathogens.⁷³⁻⁷⁵ A challenge in evaluating fibrosis using this model is that the normal porcine liver microscopically resembles fibrosis in the human; porcine liver lobules are clearly demarcated by the interlobular connective tissue septa that meet in the portal area (Fig. 3AeD). Moreover, according to the quantitative studies,

the distribution of intralobular and interlobular connective tissue in the healthy domestic pig varies with respect to sex and location within the liver.³⁷ In addition, the mean area fraction of the interlobular connective tissue is greater in male pigs; significant differences have also been found among individuals and liver lobes. Owing to the quantitative methods that provide us with objective and reproducible data, when both the sex of specimen and the position of the harvested tissue block are taken into account, more precise quantitative estimates can be achieved.^{37,64,76}

Corrosion casting

Perfusion is a key element to understand the physiology and regeneration of any organ. Because of having two blood inputs, liver perfusion is very complicated, and research is based on the analysis of the geometrical model of the vascular tree. To obtain the highest authenticity model of the 3-D vascular bed, vascular corrosion casts (VCCs) have been used for many decades.^{50,52,53,77} Current casting materials are able to fill the entire vascular bed, which needs to be preserved free from gas and blood clots. As it is almost impossible to obtain a human liver with these characteristics,⁷⁸ the porcine liver model is irreplaceable.⁷⁹ The gap between 2-D histological studies and 3-D microarchitecture can be bridged using X-ray microtomography and micro-CT.^{32,80} Micro-CT data of liver VCC represent another source to provide microvascular morphometry.³³ Using differently colored resins in the VCC (Figs. 1C and D, 2A) is also useful for teaching anatomy, as it enables the student to distinguish the vascular (biliary) beds and differentiates fine structures that cannot otherwise be demonstrated.^{34,81}

Computer vision algorithms in pig liver research

To model liver anatomy and the processes in the liver parenchyma, it is necessary to create macroscopic and microscopic models of the vascular bed. Obtaining imaging data with the required resolution from human patients are not possible for technical reasons, so the porcine liver model is often used. Many kinds of software have been designed to

analyze images from 3-D imaging devices; most of them were developed with regard to clinical practice. For the specific requirements of pig liver anatomy research, however, special software needed to be developed.^{37,82,83}

To extract the shape of the liver parenchyma and the macroscopic model of the vascular system, macro-CT with a resolution of ~1 mm was performed using pig liver corrosion casts (Fig. 2B). Segmentation of the liver parenchyma by the macro-CT was performed interactively by the modified graph-cut algorithm⁸³ available in the Lisa application.^{37,82} The preprocessing was carried out by resampling to a voxel size of 2 mm. Voxels representing the subject of interest (e.g., liver parenchyma) and background (other tissues) were selected. Of these, an intense Gaussian mixture model with three foreground and background components was created. Vascular bed segmentation was performed by a modified connected threshold algorithm. In postprocessing, binary morphological operations were applied. Extraction of the microvascular bed geometry was performed using the image data acquired from micro-CT with a resolution of ~2 mm (Fig. 2D). For the flow modeling and the vascular bed quantitative description, the software Quantan can be used³³ to estimate the radius, length, tortuosity, and branching angles. The application also enables the evaluation of the number of microvessel segments, the volume fraction, as well as the surface and length densities. Semiautomatic subtraction facilitates the evaluator's work and allows for more precise estimates.

Challenges and pitfalls of pig liver utilization in biomedical research

The domestic pig as an experimental animal was critical to many of the key shifts in research on serious human diseases. Although the detailed knowledge of (micro) anatomy is crucial both for designing and evaluation of most experiments, it is interesting that very few breed-related and/or gender-sensitive studies have been published on the anatomy of porcine organs yet. For this reason, we found useful to summarize the current knowledge of (micro) anatomy of the porcine liver to point out critical points in planning and assessment of studies conducted in this animal model (Table 4). Given the size of porcine organs and vast biological

Table 4 e Morphological differences between the normal porcine and human liver, based on Prestice Black-Pied pig breed.⁴⁸

Gross anatomy	Histology
<p>Pig: Deep fissures marking well-marked lobation, right and left hemiliver divided by the notch for ligamentum teres.^{8,79}</p> <p>Human: External lobation does not correspond to the functional (i.e. surgical) anatomy: three main fissures are not visible on the surface and contain three main hepatic veins; they divide the liver into four portal sectors; right and left hemiliver divided by Cantlie's line.⁵⁴</p>	<p>Pig: Irregular, rather pentagonal hepatic lobules (Fig. 2A) clearly demarcated by connective tissue septa (Fig. 3AeC). Caution, normal porcine liver microscopically resembles fibrosis in the human; more connective tissue in males.³⁷</p> <p>Human: Roughly hexagonal hepatic lobules,⁶¹ no interlobular septa, connective tissue found in interlobular space.⁸⁶</p>
<p>Pig: Superficial, extraparenchymal portal vein (PV) lobar branching visible from the visceral surface (Fig. 1D), the caudal caval vein runs through the left lateral lobe.^{50,53}</p> <p>Human: PV divides into the right and left branches at the hilum; only the left PV invariably gives extraparenchymal branches to segment I and sometimes IV.⁸⁶</p>	

variability, it is clear that morphological studies cannot be carried out without the use of stereological procedures.⁶⁸ Unbiased stereology also allows for setting up sampling optimization and the latest studies revealed different tissue structure depending on the sampling location.^{36,37,51,84} These procedures can be advantageously used also for evaluation in imaging methods such as (micro)CT or magnetic resonance imaging.⁸⁵

In experimental medicine, the pig liver is preferably used as a large animal model of acute liver disease and/or liver failure as it is suitable for extracorporeal circulation, repetitive blood sampling, and training of surgical techniques applicable to humans, for example, partial hepatectomies, orthotopic liver transplantation, or PV arterialization.⁸⁷ Unlike small animals, experiments on pigs and other large animal models are limited because of technically demanding treatment and higher financial costs that result in smaller cohorts, which due to considerable interindividual variability makes statistical evaluation and interpretation of results difficult.

Conclusions

A variety of modern pig breeds are available today, and they have been increasingly used in biomedical research. Despite recent efforts to obtain detailed knowledge of pig liver macroanatomy and microanatomy, very little is still known in accordance with biological variability, and certain issues need to be addressed for the appropriate translation of animal observations to clinical testing. Quantitative results based on stereology guarantee unbiased estimates that are able to reveal even subtle histological changes, and it is also possible to optimize the algorithm for study designs in accordance with sex, breed, or position of the harvested tissue block. Newly developed software is able to process data obtained from (micro)CT for 3-D reconstructions, quantitative estimations, and morphometrics, which is highly consistent with manual counting techniques. Volumetric data extracted from computer imaging methods can be used to model liver perfusion and optimal liver resection.

Acknowledgment

Funding sources: This work was supported from European Regional Development Fund, European Union-Project “Application of Modern Technologies in Medicine and Industry” [grant number CZ.02.1.01/0.0/0.0/17_048/0007280], by Charles University in Prague, Czechia [grants SVV number 260390 and 260392 and GAUK number 1206417]; Research Fund Progress [grant Q39] and by the “Center of Clinical and Experimental Liver Surgery” [grant UNCE/MED/006]. Micro-CT scanning was supported by the Ministry of Education, Youth and Sports under the National Sustainability Program I [projects CENTEM number CZ.1.05/2.1.March 00, 0088, CENTEM PLUS number LO1402 and LO1503 and Program I (NPU I) No. LO1503].

Author contribution: Eberlova Lada contributed the main conceptual idea and wrote most of the article; Maleckova Anna cowrote the article and provided histological figures;

Mik Patrik cowrote the article; and Tonar Zbynek provided critical revision and helped shape the manuscript. Palek Richard carried out literature research and analysis; Sarah Leupen performed language proofreading; Jirik Miroslav cowrote the article; Mirka Hynek provided CT scans and helped shape the manuscript; and Liska Vaclav provided critical revision and helped shape the manuscript.

Disclosure

The authors reported no proprietary or commercial interest in any product mentioned or concept discussed in this article.

references

- Larson G, Dobney K, Albarella U, et al. Worldwide phylogeography of wild boar reveals multiple centers of pig domestication. *Science*. 2005;307:1618e1621.
- Bustad LK, McClellan RO. Swine in biomedical research. *Science*. 1966;152:1526e1530.
- Breeds guide | The Pig Site. Available at: <https://thepigsite.com/>. Accessed March 21, 2019.
- Swindle MM. *Swine in the Laboratory: surgery, Anesthesia, imaging, and experimental techniques*. 3rd ed. Boca Raton, FL: CRC press; 2016.
- Groenen MAM, Archibald AL, Uenishi H, et al. Analyses of pig genomes provide insight into porcine demography and evolution. *Nature*. 2012;491:393e398.
- Perleberg C, Kind A, Schnieke A. Genetically engineered pigs as models for human disease. *Dis Model Mech*. 2018;11. <https://doi.org/10.1242/dmm.030783>.
- Lossi L, D’Angelo L, De Girolamo P, Merighi A. Anatomical features for an adequate choice of experimental animal model in biomedicine: II. Small laboratory rodents, rabbit, and pig. *Ann Anat*. 2016;204:11e28.
- Liska V, ed. *Experimental Surgery*. Plzen: Nava Publishing; 2016.
- Jiang K, Chen J, Liu Y, et al. Heat-irrigate effect of radiofrequency ablation on relevant regional hepatocyte in living swine liver-initial study on pathology. *Cell Biochem Biophys*. 2015;72:37e41.
- Dong J, Geng X, Yang Y, et al. Dynamic imaging and pathological changes in pig liver after MR-guided microwave ablation. *BMC Cancer*. 2018;18:397.
- Smolock AR, Cristescu MM, Vlasisavljevic E, et al. Robotically assisted sonic therapy as a noninvasive nonthermal ablation modality: proof of concept in a porcine liver model. *Radiology*. 2018;287:485e493.
- Wex C, Stoll A, Fröhlich M, Arndt S, Lippert H. How preservation time changes the linear viscoelastic properties of porcine liver. *Biorheology*. 2013;50:115e131.
- Wex C, Stoll A, Fröhlich M, Arndt S, Lippert H. Mechanics of fresh, frozen-thawed and heated porcine liver tissue. *Int J Hyperthermia*. 2014;30:271e283.
- Carreño O, Sendra L, Montalvá E, et al. A surgical model for isolating the pig liver in vivo for gene therapy. *Eur Surg Res*. 2013;51:47e57.
- Kang HY, Choi Y-K, Jeong YI, et al. Immortalization of porcine 11 beta-hydroxysteroid dehydrogenase type 1-transgenic liver cells using SV40 large T antigen. *Int J Mol Sci*. 2017;18:2625.
- Xiberta P, Boada I, Bardera A, Font-i-Furnols M. A semi-automatic and an automatic segmentation algorithm to remove the internal organs from live pig CT images. *Comput Electron Agric*. 2017;140:290e302.

17. Xie L-T, Xu D-X, Tian G, et al. Value of two-dimensional shear wave elastography for assessing acute liver congestion in a bama mini-pig model. *Dig Dis Sci*. 2018;63:1851e1859.
18. Court FG, Laws PE, Morrison CP, et al. Subtotal hepatectomy: a porcine model for the study of liver regeneration. *J Surg Res*. 2004;116:181e186.
19. Glowka TR, Standop J, Paschenda P, Czaplik M, Kalff JC, Tolba RH. Argon and helium plasma coagulation of porcine liver tissue. *J Int Med Res*. 2017;45:1505e1517.
20. Vrochides D, Kardassis D, Ntinias A, et al. A novel liver parenchyma transection technique using locking straight rigid ties. An experimental study in pigs. *J Invest Surg*. 2014;27:106e113.
21. Zhang Z-B, Gao W, Liu L, Shi Y, Ma N, Shen Z-Y. Development and assessment of normothermic machine perfusion preservation for extracorporeal splitting of pig liver. *Ann Transplant*. 2017;22:507e517.
22. Okada N, Mizuta K, Oshima M, et al. A novel split liver protocol using the subnormothermic oxygenated circuit system in a porcine model of a marginal donor procedure. *Transplant Proc*. 2015;47:419e426.
23. Vogel T, Brockmann JG, Pigott D, et al. Successful transplantation of porcine liver grafts following 48-hour normothermic preservation. *PLoS One*. 2017;12:e0188494.
24. Louras N, Patel M, Shah J, Sachs D, Vagefi P. Biochemistry profiles following pig-to-nonhuman primate liver xenotransplantation. *Am J Transplant*. 2018;18:763e764.
25. Determan C, Anderson R, Becker A, et al. Fed state prior to hemorrhagic shock and polytrauma in a porcine model results in altered liver transcriptomic response. *PLoS One*. 2014;9:e100088.
26. Fröhlich M, Hildebrand F, Weuster M, et al. Induced hypothermia reduces the hepatic inflammatory response in a swine multiple trauma model. *J Trauma Acute Care Surg*. 2014;76:1425e1432.
27. Eschbach D, Horst K, Sassen M, et al. Hypothermia does not influence liver damage and function in a porcine polytrauma model. *Technol Health Care*. 2018;26:209e221.
28. Mylonas AI, Orfanos NF, Karmanioliou II, et al. The effects of hemorrhagic shock secondary to hepatectomy in a swine model. *J Surg Res*. 2015;195:228e234.
29. Tao L, Li Q, Ren H, et al. Repair of extrahepatic bile duct defect using a collagen patch in a Swine model. *Artif Organs*. 2015;39:352e360.
30. Tanaka H, Fukushima K, Srinivasan PK, et al. Efficacy of the novel medical adhesive, MAR-VIVO-107, in an acute porcine liver resection model. *Surg Innov*. 2017;24:423e431.
31. Fu YB, Chui CK. Modelling and simulation of porcine liver tissue indentation using finite element method and uniaxial stress-strain data. *J Biomech*. 2014;47:2430e2435.
32. Králícková A, Eberlová L, Kalusová K, et al. Quantification of liver microcirculation using X-ray microtomography of vascular corrosion casts. *Key Eng Mater*. 2014;592:505e508.
33. Jirák M, Tonar Z, Králícková A, et al. Stereological quantification of microvessels using semiautomated evaluation of X-ray microtomography of hepatic vascular corrosion casts. *Int J Comput Assist Radiol Surg*. 2016;11:1803e1819.
34. Eberlova L, Liska V, Mirka H, et al. The use of porcine corrosion casts for teaching human anatomy. *Ann Anat*. 2017;213:69e77.
35. Bekheit M, Bucur PO, Wartenberg M, Vibert E. Computerized tomography-based anatomic description of the porcine liver. *J Surg Res*. 2017;210:223e230.
36. Junatas KL, Tonar Z, Kubíková T, et al. Stereological analysis of size and density of hepatocytes in the porcine liver. *J Anat*. 2017;230:575e588.
37. Mik P, Tonar Z, Malecková A, et al. Distribution of connective tissue in the male and female porcine liver: histological mapping and recommendations for sampling. *J Comp Pathol*. 2018;162:1e13.
38. Rogée S, Le Gall M, Chafey P, et al. Quantitative proteomics identifies host factors modulated during acute hepatitis E virus infection in the swine model. *J Virol*. 2015;89:129e143.
39. Wang J, Sun Z, Jiang J, et al. Proteomic signature of acute liver failure: from discovery and verification in a pig model to confirmation in humans. *Mol Cell Proteomics*. 2017;16:1188e1199.
40. Liska V, Treska V, Mirka H, et al. Inhibition of transforming growth factor beta-1 augments liver regeneration after partial portal vein ligation in a porcine experimental model. *Hepatogastroenterology*. 2012;59:235e240.
41. Yu R, Zhang Y, Lu Q, et al. Differentially expressed genes in response to cyadox in swine liver analyzed by DDRT-PCR. *Res Vet Sci*. 2018;118:72e78.
42. Swindle MM, Makin A, Herron AJ, Clubb FJ, Frazier KS. Swine as models in biomedical research and toxicology testing. *Vet Pathol*. 2012;49:344e356.
43. Lee KS, Santagostino SF, Li D, et al. Catheter-directed intraportal delivery of endothelial cell therapy for liver regeneration: a feasibility study in a large-animal model of cirrhosis. *Radiology*. 2017;285:114e123.
44. Bartas M, Cerven J, Oppelt J, et al. Liver regeneration during the associating liver partition and portal vein ligation for staged hepatectomy procedure in *Sus scrofa* is positively modulated by stem cells. *Oncol Lett*. 2018;15:6309e6321.
45. Filipponi F, Leoncini G, Campatelli A, et al. Segmental organization of the pig liver: anatomical basis of controlled partition for experimental grafting. *Eur Surg Res*. 1995;27:151e157.
46. Liska V, Treska V, Mirka H, et al. Interleukin-6 augments activation of liver regeneration in porcine model of partial portal vein ligation. *Anticancer Res*. 2009;29:2371e2377.
47. Bruha J, Vycital O, Tonar Z, Mirka H, Haidingerova L. Monoclonal antibody against transforming growth factor beta 1 does not influence liver regeneration after resection in large animal experiments. *In Vivo*. 2015;340:327e340.
48. Vrtková I. Genetic admixture analysis in prestige black-pied pigs. *Arch Anim Breed*. 2015;58:115e121.
49. König HE, Liebich HG, eds. *Anatomie domácich savců, 2. díl*. Bratislava: H & H; 2013:70e76.
50. Court FG, Wemyss-Holden SA, Morrison CP, et al. Segmental nature of the porcine liver and its potential as a model for experimental partial hepatectomy. *Br J Surg*. 2003;90:440e444.
51. Witter K, Tonar Z, Schöpfer H. How many layers has the adventitia? Structure of the arterial tunica externa revisited. *Anat Histol Embryol*. 2017;46:110e120.
52. Lehmann KS, Ritz J-P, Valdeig S, et al. Portal vein segmentation of a 3D-planning system for liver surgery— in vivo evaluation in a porcine model. *Ann Surg Oncol*. 2008;15:1899e1907.
53. Zanchet DJ, Montero EF. Pig liver sectorization and segmentation and virtual reality depiction. *Acta Cir Bras*. 2002;17:381e387.
54. Couinaud C. [Liver lobes and segments: notes on the anatomical architecture and surgery of the liver]. *Presse Med*. 1954;62:709e712.
55. Martins AC, Machado MA, Ferraz AA. Porcine liver: experimental model for the intra-hepatic glissonian approach. *Acta Cir Bras*. 2008;23:204e207.
56. Nykonenko A, Vavra P, Zonca P. Anatomic peculiarities of pig and human liver. *Exp Clin Transplant*. 2017;15:21e26.


57. Denys A, Prior J, Bize P, et al. Portal vein embolization: what do we know? *Cardiovasc Intervent Radiol*. 2012;35:999e1008.
58. Ekataksin W, Wake K. Liver units in three dimensions: I. Organization of argyrophilic connective tissue skeleton in porcine liver with particular reference to the “compound hepatic lobule”. *Am J Anat*. 1991;191:113e153.
59. Rappaport AM, Wilson WD. The structural and functional unit in the human liver (liver acinus). *Anat Rec*. 1958;130:673e689.
60. Lamers WH, Hilberts A, Furt E, et al. Hepatic enzymic zonation: a reevaluation of the concept of the liver acinus. *Hepatology*. 1989;10:72e76.
61. Saxena R. *Practical Hepatic Pathology: A Diagnostic Approach*. 2nd ed. Philadelphia, PA: Elsevier; 2018.
62. Tanami S, Ben-Moshe S, Elkayam A, Mayo A, Bahar Halpern K, Itzkovitz S. Dynamic zonation of liver polyploidy. *Cell Tissue Res*. 2017;368:405e410.
63. Marcos R, Lopes C, Malhães F, et al. Stereological assessment of sexual dimorphism in the rat liver reveals differences in hepatocytes and Kupffer cells but not hepatic stellate cells. *J Anat*. 2016;228:996e1005.
64. Marcos R, Monteiro RAF, Rocha E. The use of design-based stereology to evaluate volumes and numbers in the liver: a review with practical guidelines. *J Anat*. 2012;220:303e317.
65. Liska V, Treska V, Mirka H, et al. Preoperative use of biological therapy does not influence liver regeneration after large resection - porcine experimental model. *Tumor Biol*. 2012;33:102e103.
66. Yang K, Du C, Cheng Y, Li Y, Gong J, Liu Z. Augmenter of liver regeneration promotes hepatic regeneration depending on the integrity of Kupffer cell in rat small-for-size liver transplantation. *J Surg Res*. 2013;183:922e928.
67. Puche JE, Saiman Y, Friedman SL. Hepatic stellate cells and liver fibrosis. *Compr Physiol*. 2013;3:1473e1492.
68. Mouton PR. *Principles and Practices of Unbiased Stereology: An Introduction for Bioscientists*. Baltimore, MD: Johns Hopkins University Press; 2001.
69. Cooper DKC, Ayares D. The immense potential of xenotransplantation in surgery. *Int J Surg*. 2011;9:122e129.
70. Toosi AEK. Liver fibrosis: causes and methods of assessment, a review. *Rom J Intern Med*. 2015;53:304e314.
71. Batts KP, Ludwig J. Chronic hepatitis. An update on terminology and reporting. *Am J Surg Pathol*. 1995;19:1409e1417.
72. Bedossa P, Dargère D, Paradis V. Sampling variability of liver fibrosis in chronic hepatitis C. *Hepatology*. 2003;38:1449e1457.
- 73.
- D’Angelo L, Lossi L, Merighi A, de Girolamo P. Anatomical features for the adequate choice of experimental animal models in biomedicine: I. Fishes. *Ann Anat*. 2016;205:75e84.
74. Delire B, Stärkel P, Leclercq I. Animal models for fibrotic liver diseases: what we have, what we need, and what is under development. *J Clin Transl Hepatol*. 2015;3:53e66.
75. Starkel P, Leclercq IA. Animal models for the study of hepatic fibrosis. *Best Pract Res Clin Gastroenterol*. 2011;25:319e333.
76. Tschanz S, Schneider JP, Knudsen L. Design-based stereology: planning, volumetry and sampling are crucial steps for a successful study. *Ann Anat*. 2014;196:3e11.
77. Lametschwandtner A, Lametschwandtner U. Historical review and technical survey of vascular casting and scanning electron microscopy. In: *Scanning Electron Microscopy of Vascular Casts: Methods and Applications. Electron Microscopy in Biology and Medicine*. Boston, MA: Springer; 1992:1e11.
78. Debbaut C, Segers P, Cornillie P, et al. Analyzing the human liver vascular architecture by combining vascular corrosion casting and micro-CT scanning: a feasibility study. *J Anat*. 2014;224:509e517.
79. Eberlova L, Liska V, Mirka H, et al. Porcine liver vascular bed in Biodur E20 corrosion casts. *Folia Morphol*. 2016;75:154e161.
80. Schladitz K. Quantitative micro-CT. *J Microsc*. 2011;243:111e117.
81. Pálek R, Liska V, Eberlová L, et al. [Experimental processing of corrosion casts of large animal organs]. *Rozhl Chir*. 2018;97:222e228.
82. Lisa JM. Coputer-assisted liver surgery. 2018. Available at: <https://github.com/mjirik/lisa>. Accessed July 31, 2018.
83. Boykov YY, Jolly MP. Interactive graph cuts for optimal boundary amp; region segmentation of objects in N-D images. In: *Proceedings Eighth IEEE International Conference on Computer Vision. ICCV 2001*. Vol. 1. 2001:105e112. <https://doi.org/10.1109/ICCV.2001.937505>.
84. Tomášek P, Tonar Z, Grajciarová M, et al. Histological mapping of porcine carotid arteries - an animal model for the assessment of artificial conduits suitable for coronary bypass grafting in humans. *Ann Anat*. 2019;228:151434.
85. Bech J, Glud AN, Sangill R, et al. The porcine corticospinal decussation: a combined neuronal tracing and tractography study. *Brain Res Bull*. 2018;142:253e262.
86. Standring S. *Gray’s Anatomy: The Anatomical Basis of Clinical Practice*. 41st ed. China: Elsevier Limited; 2016:1166e1170.
87. Malecková A, Tonar Z, Mík P, et al. Animal models of liver diseases and their application in experimental surgery. *Rozhl Chir*. 2019;98:100e109.

10.3 Příloha III

KOLINKO, Yaroslav, MALEČKOVÁ, Anna, KOCHOVÁ, Petra, GRAJCIAROVÁ, Martina, BLASSOVÁ, Tereza, KURAL, Tomáš, TRAILIN, Andriy, ČERVENKOVÁ, Lenka, HAVRÁNKOVÁ, Jiřina, VIŠTEJNOVÁ, Lucie, TONAROVÁ, Pavla, MOULISOVÁ, Vladimíra, JIŘÍK, Miroslav, ZAVADÁKOVÁ, Anna, TICHÁNEK, Filip, LIŠKA, Václav, KRÁLÍČKOVÁ, Milena, WITTER, Kirsti, TONAR, Zbyněk, 2022. Using virtual microscopy for the development of sampling strategies in quantitative histology and design-based stereology. *Anatomia, histologia, embryologia*. 51(1), 3–22. ISSN 0340-2096. Dostupné z: <https://doi.org/10.1111/ahe.12765>
IF_(JCR2020) = 1,114 Q3 (Veterinary sciences)

REVIEW

Using virtual microscopy for the development of sampling strategies in quantitative histology and design-based stereology

Yaroslav Kolinko^{1,2} | Anna Malečková³ | Petra Kochová³ | Martina Grajciarová^{1,2} | Tereza Blassová^{1,2} | Tomáš Kural¹ | Andriy Trailin² | Lenka Červenková^{2,4} | Jiřina Havránková^{1,2} | Lucie Vištejnová^{1,2} | Pavla Tonarová² | Vladimíra Moulisová² | Miroslav Jiřík^{2,3} | Anna Zavadáková² | Filip Tichánek^{2,5} | Václav Liška^{2,6} | Milena Králíčková^{1,2} | Kirsti Witter⁷ | Zbyněk Tonar^{1,2} 

¹Department of Histology and Embryology, Faculty of Medicine in Pilsen, Charles University, Pilsen, Czech Republic

²Faculty of Medicine in Pilsen, Biomedical Center, Charles University, Pilsen, Czech Republic

³Faculty of Applied Sciences, European Centre of Excellence NTIS, University of West Bohemia, Pilsen, Czech Republic

⁴Department of Pathology, Third Faculty of Medicine, Charles University, Prague, Czech Republic

⁵Department of Pathological Physiology, Faculty of Medicine in Pilsen, Charles University, Pilsen, Czech Republic

⁶Department of Surgery and Biomedical Center, Faculty of Medicine in Pilsen, Charles University, Pilsen, Czech Republic

⁷Institute of Morphology, Department of Pathobiology, University of Veterinary Medicine Vienna, Vienna, Austria

Correspondence

Zbyněk Tonar, Department of Histology and Embryology, Faculty of Medicine in Pilsen, Charles University, Karlovarská 48, 301 66 Pilsen, Czech Republic.
Email: Zbynek.Tonar@lfp.cuni.cz

Funding information

Horizon 2020 Framework Programme, Grant/Award Number: 856620; Ministerstvo Zdravotnictví České Republiky, Grant/Award Number: 15-29241A and AZV NU20J-08-00009; Ministerstvo Školství, Mládeže a Tělovýchovy, Grant/Award Number: LO1503; Univerzita Karlova v Praze, Grant/Award Number: GACR No. 1313420, Progres Q39, SVV 260 536 and UNCE/MED/006; European Regional Development Fund, Grant/Award Number: AMTMI CZ.02.1.01/0.0/0.0/17_048/0007280 and FIND CZ.02.1.01/0.0/0.0/16_019/0000787

Abstract

Only a fraction of specimens under study are usually selected for quantification in histology. Multilevel sampling or tissue probes, slides and fields of view (FOVs) in the regions of interest (ROIs) are required. In general, all parts of the organs under study should be given the same probability to be taken into account; that is, the sampling should be unbiased on all levels. The objective of our study was to provide an overview of the use of virtual microscopy in the context of developing sampling strategies of FOVs for stereological quantification. We elaborated this idea on 18 examples from multiple fields of histology, including quantification of extracellular matrix and muscle tissue, quantification of organ and tumour microvessels and tumour-infiltrating lymphocytes, assessing osseointegration of bone implants, healing of intestine anastomoses and osteochondral defects, counting brain neurons, counting nuclei in vitro cell cultures and others. We provided practical implications for the most common situations, such as exhaustive sampling of ROIs, sampling ROIs of different sizes, sampling the same ROIs for multiple histological methods, sampling more ROIs with variable intensities or using various objectives, multistage sampling and virtual sampling. Recommendations were provided for pilot studies on systematic uniform random sampling of FOVs as a part of optimizing the efficiency of histological quantification to prevent over- or undersampling. We critically discussed the pros and cons of using virtual sections for sampling FOVs from whole scanned sections. Our review

demonstrated that whole slide scans of histological sections facilitate the design of sampling strategies for quantitative histology.

KEYWORDS

histological slides, quantitative microscopy, sampling, stereology, study design, veterinary histology

1 | INTRODUCTION

Virtual microscopy or digital microscopy is the digital conversion of light microscopic specimens at full resolution and their presentation over a computer network. The term 'virtual' refers to the examination of the specimens without direct contact with the object slide or the light microscope (Smart In Media AG, 2021). Virtual microscopy makes samples accessible to specialists without needing to be present and without needing to have extensive equipment (Saliba et al., 2012). It is discussed intensively in the frame of diagnosis and treatment of different diseases (telepathology, more than 1400 Scopus entries in September 2021) in human as well as in veterinary medicine (e.g. Bertram & Klopffleisch, 2017), resulting in the first guidelines by the respective expert groups (Jahn et al., 2020).

Another huge field of application for virtual microscopy is education and training, fuelled even more by the increased demand for remote learning during the COVID-19 pandemic (for reviews, see, e.g., Bertram & Klopffleisch, 2017; Kuo & Leo, 2019).

In addition, virtual microscopy is also a powerful tool for research. Our review demonstrates how whole slide scans of histological sections facilitate the design of sampling strategies for quantitative histology and how they can be compared to other technical options.

1.1 | Design-based stereology

Design-based stereology is a set of tools that allows quantification without making assumptions regarding the shape, size, distribution or orientation of the structures of interest (Howard & Reed, 2005; Mouton, 2002). Strict sampling rules have to be followed to achieve this independence; that is, stereology includes detailed prescriptions of the sampling procedure and guidelines on how to test its quality. Stereology has become the gold standard in morphometry due to its reproducibility and assumption-free design. A number of both general and organ-specific protocols, recommendations and algorithms have been published to facilitate planning and conducting quantitative histology studies (Table 1).

1.2 | Sampling in an integral part of design-based stereology

All the guidelines mentioned in Table 1 refer to sampling strategies on all levels of any reduction of material in histological studies.

Only a fraction of specimens under study are usually selected for quantification in histology. This multilevel sampling includes (i) taking tissue probes from large macroscopic organs that cannot be processed completely (i.e. porcine liver, human brain); (ii) selecting histological slides from tissue blocks that undergo exhaustive sectioning (not all slides are selected for further analysis); and (iii) selecting microscopic fields of view (FOVs) that are captured and analysed to represent various regions of interest (ROIs). In general, all parts of the organs under study should have the same probability of being taken into account; that is, the sampling should be unbiased on all levels (Howard & Reed, 2005; Tschanz et al., 2014). One of the advantages of stereological concepts in morphometry is that sampling is inherent to stereology. The attention given to the sampling is comparable to that paid to the analysis of micrographs, as sampling actually is part of any unbiased estimation. If design-based stereology, including sampling, is not used for quantitation in histology, the lack of standardized sampling threatens the repeatability of research. More than 70% of researchers encounter problems when trying to repeat another scientist's experiments (Baker 2016). More than 90 researchers from five continents have recently formulated a strategy to improve the reproducibility of research based on light microscopy (Nelson et al., 2021). We propose that proper sampling of microscopic specimens might be a significant contribution to this issue. Citing the paper by Hsia et al. (2010), "the only effective way to avoid bias and ensure accuracy is via standardization of sampling".

1.3 | Sampling strategies and their benefits with regard to magnification

Sampling is of cardinal importance and a practical necessity in morphometrics (Mayhew & Lucocq, 2015). Depending on the uniformity of the distribution of the item of interest, the sampling intensity would have to be greater (in the case of heterogeneous samples) or smaller (in the case of homogeneous samples). Unfortunately, the biological variability of the microscopic structures on the scale of large organs is mostly unknown in human organs as well as in large animal models. There is ongoing work to map the variability in histopathology to enable researchers to plan the sampling of tissue probes, slides and fields of view efficiently. The theoretical foundations for predicting the efficiency of systematic sampling are quite well known (Gundersen & Jensen, 1987; Gundersen et al., 1999; Gundersen & Osterby, 1981). In

TABLE 1 Examples of studies with recommendations and guidelines for quantitative studies in histology

Research field	Brief characteristics	Reference
General guidelines for microanatomy	Planning, volumetry and sampling as crucial steps for a successful study in quantitative anatomy	Tschanz et al., 2014 Vatsos et al., 2021
Cardiovascular microanatomy	Quantitative 3D morphology in cardiac research Quantification of vascular beds Vascularization of organs 3D characterization of capillary networks Numbers and lengths of brain capillaries	Mühlfeld et al., 2010 Dockery & Fraher, 2007 Mühlfeld, 2014 Eržen et al., 2011 Lokkegaard et al., 2001; Kubíková et al., 2018
Neuroanatomy and neurohistology	Total number of neurons in the subdivisions of the hippocampus Assessment of developmental neurotoxicity Morphometry of brain Morphometry of grey and white matter of spinal cord Morphometry of the pineal gland	West et al., 1991 Bolon et al., 2011 Selcuk & Tipirdamaz, 2020; Sadeghinezhad et al., 2020 Sadeghinezhad & Nyengaard, 2021; Cakmak & Karadag, 2019 Bolat et al., 2018
Gastrointestinal microanatomy	Practical stereology of the stomach and intestine. Morphometry of the oesophagus Volumes and numbers in the liver 3D counting of hepatocytes Quantification of hepatic connective tissue Morphometry of intestinal mucosa in nutritional studies	Nyengaard & Alwasel, 2014 Goodarzi et al., 2019 Marcos et al., 2012; Junatas et al., 2017; Mik et al., 2018 Van Ginneken et al., 2002; Casteleyn et al., 2010
Respiratory system	Policy Statement of the American Thoracic Society/ European Respiratory Society on quantitative assessment of lung structure Quantitative microscopy of the lung Study designs in diseases of the respiratory tract	Hsia et al., 2010 Ochs & Mühlfeld, 2013; Knudsen et al., 2021 Mühlfeld & Ochs, 2013
Urinary system	Application of stereology in kidney research	Nyengaard, 1999
Genital system	Stereology tools in testicular research	Noorafshan, 2014 Ferreira et al., 2021
Skeletal system	Stereology of femoral cartilage Standardized nomenclature for bone histomorphometry Quantification of bone microporosities	Noorafshan et al., 2016 Dempster et al., 2013, Parfitt et al., 1987 Tonar et al., 2011
Embryology	Stereology of the human placenta	Mayhew, 2014

Note: Papers compatible with design-based stereology are listed.

the past and in contrast, for example, to biochemistry, standards for sampling in histology seemed to have been neglected; not all authors customarily referred to sampling strategies, numbers of tissue probes, sections, FOVs or any repeatable rules for their selections. Currently, the sampling issue receives more attention as a part of quantitative morphomics that describes the 3D biological structures from gross anatomy to the micro- or even nanomorphome (Mayhew & Lucocq, 2015).

In microscopy, FOV sampling is closely related to the magnification used. When increasing the magnification, the area of the image field decreases quadratically, and the number of FOVs necessary to cover the same original area increases quadratically (Figure S1). Traditionally, it was recommended that the lowest magnification that enables the detection of the structures of interest be used (Howard & Reed, 2005; Mouton, 2002) to maximize the area of the FOVs. Introducing virtual slides into the research might seem to be a 'game changer'. However, whole slide sampling with automated quantitation still requires validation by humans to ensure that the readouts are correct. Combining the benefits of using slide scanners with a clever sampling strategy might be a very efficient tool in quantitative histology.

The aim of our paper was to provide an overview of the use of virtual microscopy in the context of developing sampling strategies for stereological quantification. We elaborated this idea on a number of examples from multiple fields of histology. We critically discussed the pros and cons of using virtual sections for sampling image fields (FOVs and ROIs) from whole scanned sections in quantitative histological studies.

2 | MATERIALS AND METHODS

2.1 | Origin of tissue blocks and histological staining

This paper uses examples of virtual slides from a number of studies representing various fields of quantitative histology. All the original illustrations were newly prepared from archive specimens for the purpose of this review. The origin of the specimen and their use for studying biological questions is summarized in Table 2. The staining methods used in the examples presented in this paper are summarized in Table 3.

TABLE 2 Origin of tissue samples and basic processing of the examples presented in this paper

Example	Origin	Biological question studied (Reference)
#1	Virtually generated standardized image datasets	Testing and calibrating quantification of volumes, surfaces, lengths and object counts (Jiřík et al., 2016, 2018).
#2	Human mesenchymal stem cells (hMSCs) isolated from bone marrow of healthy donors (A)	Metabolic activity assay comparing the ATP production rate and % of glycolysis and oxidative phosphorylation in hMSCs (Tonarova et al., 2021).
#S2	hMSCs isolated from bone marrow of healthy donors (B)	Cell growth assay and metabolic activity assay when studying the effects of different cross-linking conditions on collagen-based nanocomposite scaffolds; an in vitro evaluation using mesenchymal stem cells (Suchý et al., 2015).
#S3	Soft palate of an adult dog fixed in formalin, archive of (C)	Quantitation of connective tissue in the soft palate of the dog; pilot study to assess sampling intensity (unpublished results). This was motivated by assessment of operative outcome of veloplasty (e.g. Arai et al., 2016; Crosse et al., 2015; Dupré & Heidenreich, 2016; Pichetto et al., 2015; Tamburro et al., 2019).
#3	Porcine femurs with titan implants after 6 months of healing, (B)	Assessing osseointegration of titan implants with four different surface composition using quantification of bone-implant contact (BIC) according to Babuska et al. (2016).
#S4	Condylar cartilage and bone of rabbit femur (B)	Estimation of healing of osteochondral defects of condylar cartilage stimulated by three different tissue-engineered scaffolds (unpublished results).
#S5	Brains of female C57B1/6 mice (C)	Tracking the transduction of various viral vectors in neurons after being injected into mice brains (Hlavatý et al., 2017).
#4	Porcine liver (B)	Describe the propagation of the rupture caused by blunt trauma within liver parenchyma with respect to the liver microstructure, namely, the reticular fibres. Does the rupture propagate randomly or does the rupture follow some pattern through the tissue? (Malečková et al., 2021).
#S6	Porcine common carotid arteries (B)	Quantification of type I and type III collagen within tunica intima and media in porcine common carotid artery (Tomášek et al., 2020).
#S7	Archived canine lymph nodes and core biopsies from canine lymph nodes (C)	Quantification of microvessels in canine lymph nodes. Does the density of microvessels correlate with vascular endothelial growth factor expression? (Tonar et al., 2008; Wolfesberger et al., 2008).
	Patient-derived murine xenografts of mantle cell lymphoma (A)	Histological validation of quantitative in vivo monitoring of hypoxia and vascularization of patient-derived murine xenografts of mantle cell lymphoma using photoacoustic and ultrasound imaging (Keša et al., 2021).
#5	Small intestine of 12 to 14-week-old pigs used in research on healing of intestinal anastomoses (B)	Histological validation of healing of intestinal anastomosis, quantification of vascularization, inflammatory infiltration, and collagen formation (Rosendorf et al., 2020, 2021a, 2021b).
#S8	Human and ewe perineal body used for mechanical testing and microstructure quantification (D)	Quantification of volume fraction of smooth muscle, skeletal muscle, adipose cells, elastin, and type I collagen of the perineal body. Does the structure differ along the perineal body? (Kochová et al., 2019a, 2019b). Does the structure differ between the pregnant and post-menopausal ewe perineal bodies? (Kochová et al., 2019b)
#6	Resected human liver with hepatocellular carcinoma (E)	Quantification of CD8+ T cells in different regions of interest (tumour centre, inner and outer invasive margin, peritumoural area and non-tumour liver) can reflect the overall reaction of the immune system to tumour growth, penetration of immune cells through tumour border and expression of pro- and antiapoptotic factors by tumour cells and microenvironment (Andryi Trailin, unpublished results).
#S9	Mouse ovaries (B)	Discover the effects of exposure to bisphenol A analogs during breastfeeding on ovarian capacity of offspring. The quantification of primordial, primary, preantral, antral and atretic follicles (Nevoral et al., 2021).
#S10	The cerebellum of 3-month-old mouse model with degeneration of Purkinje cells (B)	Quantitative validation of potential abnormalities in total number of microvessels in the cerebellum layers of adult mice with degeneration of Purkinje cells (Kolinko et al., 2016).
#S11	Samples of human aortae collected during surgery for abdominal aortic aneurysm (AAA) repair (F)	Comparison of the expression of structural proteins, osteoprotegerin, and pentraxin 3 and the presence of immune factors (T and B lymphocytes, neutrophils and macrophages), microvessels and hypoxic cells in AAA and non-aneurysmatic aortic walls and exploration of their relationships (Blassova et al., 2019).

(Continues)

TABLE 2 (Continued)

Example	Origin	Biological question studied (Reference)
#7	Decellularized porcine liver tissue (B)	Quantitative analysis of morphological preservation of liver extracellular matrix (ECM) after decellularization with the purpose of generation a high-quality biological scaffold for liver tissue engineering (Moullisová et al., 2020)
#S12	3D collagen scaffolds containing dermal fibroblasts used as an in vitro model of dermis (B)	Development of a new method of total cell count determination in 3D collagen scaffolds in order to quantify cell proliferation (unpublished results).

Note: Most examples are based on studies already published, so references are provided for further details on the study design. All in vivo procedures were performed in compliance with the law of the Czech Republic, which is compatible with the legislation of the European Union and, wherever appropriate, were approved by the Ethics Committees in the following institutions where the samples originated: A – First Faculty of Medicine, Charles University; B – Faculty of Medicine in Pilsen, Charles University; C – Institute of Morphology, University of Veterinary Medicine Vienna, Austria; D – Centre for Surgical Technologies, KU Leuven, Leuven, Belgium; E – Department of Pathology, Faculty of Medicine in Pilsen, Czech Republic; and F – Department of Surgery, University Hospital in Pilsen. The examples are numbered according to their appearance in the Results section.

TABLE 3 Histological staining methods used in examples presented in the study

Example	Staining	Purpose and visualization of tissue components
#1	None (computer-generated virtual image).	Virtual sections through three-dimensional objects (spheres and cylinders) mimicking tissue components in X-ray microtomography.
#2	DAPI nuclear staining (Sigma-Aldrich).	Visualization of nuclei.
#S2	DAPI nuclear staining (Sigma-Aldrich, Burlington, MA) and Phalloidin-Alexa Fluor 488 (Life Technologies, Rockford, IL).	Visualization of nuclei and actin microfilaments.
#S3	Aniline blue and nuclear fast red.	Clear distinction of collagen fibres from other tissue components for automated quantitation.
#3	20% Giemsa's azur eosin methylene blue solution	New bone and connective tissue around titan implants within porcine femur.
#S4	Alcian blue staining and PAS reaction.	Detection of acidic and neutral glycosaminoglycans in newly formed cartilage.
#S5	Immunohistochemistry for enhanced green fluorescent protein (EGFP) (Chemicon International, Temecula, CA), counterstained with haematoxylin.	Identification of cells expressing the EGFP as a reporter gene detecting the cells transduced by a viral vector.
#4	Reticulin kit (BioGnost Ltd, Zagreb, Croatia).	Reticular fibres (collagen III) – component of extracellular matrix of connective tissue located in the interlobular septa and in the delicate network, that separates the hepatic sinusoids and hepatocytes
#S6	Picosirius red (Direct Red 80, Sigma-Aldrich, Munich, Germany).	Type I collagen (yellow-red colour) and type III collagen (green colour) visualized in polarized light (Rich & Whittaker, 2005).
#S7	Immunohistochemical detection of von Willebrand factor (polyclonal rabbit anti-human antibody, Dako, Glostrup, Denmark) combined with lectin histochemistry (WGA, Vector laboratories, Burlingame, CA). Avidin-biotin-peroxidase complex detection (Vector Laboratories). Counterstaining Mayer's haematoxylin.	Endothelium of blood microvessels within canine lymph nodes.
	Immunohistochemical detection of CD31 (rabbit anti-mouse CD31 monoclonal IgG, clone SP38, Thermo Fisher Scientific, Rockford, IL). Counterstained with haematoxylin.	Endothelium of blood microvessels within patient-derived murine xenografts of mantle cell lymphoma.
#5	Immunohistochemical detection of von Willebrand factor (ab6994Abcam, Cambridge, UK).	Endothelium of blood microvessels

(Continues)

TABLE 3 (Continued)

Example	Staining	Purpose and visualization of tissue components
	Immunohistochemical detection of Calprotectin (Monoclonal Antibody—MAC387Invitrogen MA1-81381, Thermo Fisher Scientific). Counterstaining Mayer's haematoxylin.	Granulocytes and tissue macrophages.
	Picrosirius Red.	Collagen observed in circularly polarized light.
#S8	Verhoeff's haematoxylin and green trichrome (Kocová, 1970).	Overall morphology; smooth and skeletal muscle of the perineal body.
	Orcein (Tanzer's orcein, Bowley Biochemical Inc., Danvers, MA, USA).	Adipose cells and elastin of the perineal body.
.	Picrosirius red (Direct Red 80, Sigma-Aldrich, Munich, Germany)	Type I collagen of perineal body was observed in polarized light.
#6	Immunohistochemical detection of CD8+ T cells (BOND™ Ready-to-Use monoclonal primary anti-CD8 Antibody 4B11, Leica Biosystems Newcastle Ltd, UK). Counterstaining Mayer's haematoxylin.	Tumour-infiltrating cytotoxic T cells as actors of antitumour immunity.
#S9	Haematoxylin and eosin	Primordial, primary, preantral, antral and atretic follicles within mice ovaries.
#S10	Immunohistochemical detection of laminin (polyclonal rabbit anti-laminin antibody, Dako, Glostrup, Denmark), counterstained with haematoxylin.	Detection of microvessels in individual layers of the cerebellar cortex in a mouse model of neurodegeneration.
#S11	Immunohistochemical detection of pentraxin 3 (polyclonal rabbit anti-human pentraxin3 antibody, Thermo Fischer Scientific) and MAC387 (monoclonal mouse anti-human macrophages/monocytes antibody, Thermo Fisher Scientific). Counterstaining Gill's haematoxylin.	Detection of Pentraxin 3, a protein produced in response to inflammatory signals in aortic wall. Detection of macrophages infiltrating the aortic wall in abdominal aortic aneurysms.
#7	Haematoxylin & eosin	Visualization of ECM proteins (stained reddish with eosin) and absence of cell nuclei in decellularized samples (lack of blue haematoxylin stain).
#S12	DAPI nuclear staining (Thermo Fisher Scientific, Rockford, IL)	Staining cell nuclei as countable structures for cell counting.

2.2 | Scanning virtual slides

As the paper focuses mainly on the sampling strategies in the context of various histological studies, the devices and techniques used for acquiring the images in the paper are briefly summarized in Table 4.

2.3 | Systematic uniform random sampling of microscopic FOVs

Multistage sampling in quantitative microscopy comprises several levels (Mayhew & Lucocq, 2015). During each step, a sample size divided by the whole specimen size represents the sampling fraction. In this paper, two levels will be considered: If, for example, every 10th histological section is selected from an exhaustively sectioned tissue block, and the position of the 1st section was selected randomly, the section sampling fraction (ssf) is 1/10. When considering a single slide, selecting 5 FOVs out of the 50 FOVs covering the whole section would represent an area sampling fraction (asf) of 1/10. The rules for the systematic uniform random sampling (SURS) are simple, regardless of the technical implementation (slide scanners, motorized microscope stages, manual sampling). The position

of the first FOV within the ROI is chosen randomly, for example, by multiplying the maximum ranges of XY coordinates of the ROI by randomly generated numbers (RND function in MS Excel). A previously selected pattern, named a sampling interval, determines the positions of the other FOVs (see, e.g., Mayhew & Lucocq, 2015 for review).

2.4 | Stereological techniques

The sampling strategies illustrated among the examples that follow were part of histological quantitative studies. All the quantitative morphometric parameters used in the examples presented in this study are explained in Table 5.

2.5 | Statistics of sampling density and evaluating the variability of the sampling

The sampling in histology introduces an error into the resulting data. Increasing the sampling frequency reduces the variability of the data but also increases the labour needed to complete the research.

TABLE 4 Devices and techniques used for acquisition of examples demonstrated in this study

Device and manufacturer	Properties, settings, software	Used in Example #:
Aperio ScanScope CS2 automatic slide scanner (Leica Biosystems, Vienna, Austria).	Bright field transmitted light microscope, 20× and 40× lens. Scanning time of 1 cm ² approx. 60 s (20× objective) or 90 s (40× objective) Automatic white balance Autofocus No immersion, no Z-stack tools SCANSCOPE 12.4.3 software. *SVS document format readable with freely downloadable IMAGESCOPE software, tiled images universally viewable in browsers. *.SVS can also be opened directly with IMAGEJ (Schneider et al., 2012) with the Bio-Formats Plugin or with FIJI (Schindelin et al., 2012).	#S3, #S5
Eclipse Ti-U microscope (Nikon, Tokyo, Japan), XYZ stepper motor focus drives Prior H117E1N4/F and PS3H122R_NB (Prior Scientific Instruments, Fulbourn, UK), Prior ProScan III stepper motor controller, digital camera Nikon DS-Fi2.	Bright field, polarized light and fluorescence microscopy 2×, 4×, 10×, 20×, 40×, 60× (oil immersion) objectives Scanning time of 1 cm ² approx. 25 min (10× objective) or 3.5 h (20× objective) Scanning and montage controlled by the NIS Elements AR software (v 5.11.03) *ND2 document format readable with freely downloadable NIS-Elements Viewer software Scanning in XY plane and in Z-axis. Export to universal format TIFF images.	#2, #S2, #S4, #5, #S6, #S9, #S10
Zeiss Axio Scan.Z1 Slide Scanner (Zeiss, Jena, Germany).	Bright field microscopy 20× and 40× objectives Scanning time of 1 cm ² approx. 5–10 min (20× objective) Scanning controlled by ZEISS ZEN BLUE software ZEISS ZEN MICROSCOPY free software offers both basic image analysis, as well as export functionality of the scanned images into TIFF or JPG file formats. Native pyramidal*.CZI files readable with FIJI.	#4, #S8, #S11, #7
Olympus CX41 microscope (Olympus, Tokyo, Japan) with Promicam 3-3CP camera (Promicra, Prague, Czech Republic).	Bright field and polarized light microscopy 2×, 4×, 10×, 20×, 40×, 60× (oil immersion) objectives Manual stage Scanning time of 1 cm ² takes approx. 30 min (10× objective) of manual work Stitching virtual slides manually using the ImageStitching module of the QUICKPHOTO INDUSTRIAL 3.2 software (Promicra, Prague, Czech Republic) Export to TIFF.	#3, #S6, #S7

Stereologists are used to calculate the variability on each level of the sampling to identify the major source of potential bias and to optimize the sampling procedures in terms of time and material costs, provided that enough precision remains to draw conclusions on a pre-determined level of confidence. Several measures of variability are illustrated for this purpose, such as standard deviations (SD), coefficient of error (CE; standard error of the mean of repeated estimates divided by the mean) and the estimates of CE for spatially correlated objects using the Matheron quadratic approximation method with various smoothness constants (Gundersen & Jensen, 1987; Slomianka & West, 2005). The relative percentage error used for comparing the data based on whole slide analysis vs. various levels of subsampling was calculated as $100 \times (\text{measured value} - \text{expected value}) / \text{expected value}$.

3 | EXAMPLES

A number of combinations of imaging approaches, uses of virtual slides, scanners, or individually sampled micrographs with various magnifications are presented in sequence corresponding to Tables 2, 3 and 5. The examples were tailored to facilitate the solving of

biological problems described in Table 2, and the strong and weak points are illustrated. Due to the number of possible combinations, the examples are ordered approximately in increasing complexity.

3.1 | Whole slide analysis vs. density of sampling multiple micrographs

Figure 1 (Example #1) demonstrates the effect of the intensity of sampling on the accuracy of the quantitative results. This can be done in virtually generated scenes. Considering the whole slide as the 'true expected value', the relative error increases with decreasing sampling intensity. In this case, intermediate sampling would provide results with an acceptable relative error. Similarly, Figure 2 (Example #2) compares automated counting of cell nuclei in a single well of a cell culture miniplate with counting based on 15 image fields. In cases of a more homogeneous distribution (Figure S2, Example #S2), the relative error of the sample is acceptably low. It is worth performing a pilot study of heterogeneous histological samples with multiple tissue components (Figure S3, Example #S3) that shows how the moving average depends on the sampling intensity.

TABLE 5 Quantitative morphometric parameters used in the examples presented in this study

Example	Quantitative parameter abbreviation (units)	Definition, reference area, interpretation	Objective used	Image fields sampled per slide	Typical area sampling fraction
#1	V_v (objects, section) (-)	The volume fraction of objects within a virtually generated section.	Not applicable	6	6/54 (0.11)
#2	Q_A (nuclei, well) (mm^{-2})	Two-dimensional density of cell nuclei per area of the well bottom in an 8-well XPF cell culture miniplate (Agilent, Santa Clara, CA).	4X 40X	Whole image processed 15	Whole image processed 15/160 (0.093)
#S2	Q_A (nuclei, well) (mm^{-2})	Two-dimensional density of cell nuclei per area of the well bottom in a 48-well cell culture plate (Thermo Scientific, Waltham, MA).	10X 40X	Whole image processed 9	Whole image was processed 9/22 (0.41)
#S3	A_A (connective tissue, palate) (-)	Mean area fraction of connective tissue in whole histological sections of the soft palate of a dog (pilot study).	20X (whole slide scan)	Analysis of whole slide scan	One whole slide scan analysis 0.003 to 0.005 in relation to one complete palatal half
#3	BIC	Bone-implant contact as the ratio of the profile length of direct contact between the implant profile and bone tissue and the total profile length of the implant surface.	10X	15	15/70 (0.214) related to the whole scan 15/15 (1.00) related to the bone-implant interface
#S4	V_v (cartilage, defect) (-)	The volume fraction of Alcian blue and PAS-positive cartilage within the healing bone defect.	10X	22	21/22 (0.95)
#S5	N (EGFP-positive neurons, brain) (-)	Absolute number of EGFP-positive neurons in the injected half of mouse brain.	40X (oil immers)	45-55	1/1 (exhaustive sampling)
#4	P'_L (interlobular septa, and P'_L (interlobular septa) (mm^{-1})	Real number of intersections of interlobular septa with rupture and predicted number of intersections based on the total length of the interlobular septa	Whole slide scan	Not applicable	Whole slide scan
#S6	P'_L (reticular fibres) and P'_L (reticular fibres) (mm^{-1})	Real number of intersections of reticular fibres with rupture and predicted number of intersections based on the total length of the reticular fibres	40X	10	Between 10/40 (0.25) and 10/50 (0.2)
#S6	A_A (type I collagen, int + med) (-)	The area fraction of type I collagen within the tunica intima and media ROI	40X	4	Between 4/23 (0.17) and 4/37 (0.11)
#S6	A_A (type III collagen, int + med) (-)	The area fraction of type III collagen within the tunica intima and media ROI	40X	4	Between 4/23 (0.17) and 4/37 (0.11)
#S7	Q_A (vWF and WGA-positive microvessels, lymph node) (mm^{-2})	The number of profiles of stained microvessels per sectional area of the lymph node.	40X	50-70	Between 50/1800 (0.028) and 70/2500 (0.03)
#S7	L_v (CD31+ microvessels, lymphoma) (mm^{-2})	The length density of stained microvessels per volume unit of lymphoma	40X	10	Between 10/40 (0.25) and 10/80 (0.125)
#5	V_v (objects, intestinal wall without mucosa located 3 mm proximally and distally from the anastomosis centre) (-)	The volume fraction of vWF positive cells within the ROI The volume fraction of MAC387-positive cells within the ROI The volume fraction of collagen within the ROI	20X 20X 20X	5-38 vWF 12-53 MAC387 8-24 PSR	Between 1/5 (0.20) and 1/3 (0.35) Approx. 1/2 (0.49) Between 1/3 (0.33) and 1/5 (0.22)

TABLE 5 (Continued)

Example	Quantitative parameter abbreviation (units)	Definition, reference area, interpretation	Objective used	Image fields sampled per slide	Typical area sampling fraction
#S8	V_V (smooth muscle; skeletal muscle, perineal body)	The volume fraction of smooth muscle and skeletal muscle within the ROI	10×	12	12/42 (0.3)
	V_V (adipose cells; elastin, perineal body)	The volume fraction of adipose cells and elastin within the ROI	10×	12	12/42 (0.3)
	V_V (type I collagen, perineal body)	The volume fraction of type I collagen within the ROI	10×	12	12/42 (0.3)
#6	Q_A (CD8-positive T cells, liver) (mm^{-2})	The number of profiles of stained CD8+ T cells per sectional area of the ROI of the liver.	20×	8 per ROI	8/133 0.064 in TC and NT ROIs:
				40 per slide	8/25 (0.32) in IL, OL and PT ROIs
#S9	N (different types of follicles)	The number of primordial, primary, preantral, antral and atretic follicles	20×	14	14/25 (0.56)
#S10	V_V (cerebellar layers, cerebellum) (-)	The volume fractions of histological layers of cerebellum.	20×	4-7	0.33
	N (microvessels, cerebellum) (-)	Number of microvessels calculated from the number of branching nodes according to Gundersen et al. (1993).	60×	20-40	0.33
#S11	A_A (pentraxin 3, wall) (-)	The area fraction of the pentraxin 3-positive cells within the whole wall reference area	40×	4	Between 4/112 (0.035) and 4/328 (0.012)
	A_A (MAC387, wall) (-)	The area fraction of the MAC387-positive macrophages within the whole wall reference area.	20×	4	Between 4/28 (0.143) and 4/82 (0.049)
#7	L (skeleton length, liver) (mm)	Length and 2D length density of the ECM within liver lobules.	40×	10	Typically 5/100 (0.05)
	L_A (ECM fibres, liver) (mm^{-2})	Number of EMC branching nodes per sectional area of liver lobules. Both parameters refer to the quality of network structure of sinusoidal vessel ECM in the decellularized scaffold.			
	Q_A (ECM branches, liver) (mm^{-2})				
#S12	N (nuclei, scaffold) (-)	Total cell number in the whole scaffold estimated from cell number in 1 column.	10×	9 columns from the 3D scaffold	$9 \times 1.4 \mu\text{l}/200 \mu\text{l} = 0.063$ (9 columns per scaffold)

Note: The magnification of the microscope objective, which was an approximate equivalent to the sampled image field area used for quantification of each parameter, is provided. The number of image fields that were sampled in each study is shown as well.

Abbreviations: A_A (component, space), Area fraction of the respective components within their reference spaces; BIC, bone-implant contact; L_V (component, space), Length density of objects per reference volume; N_V (component, space), Numerical density of objects per reference volume; Q_A (component, space), number of object profiles per section area; V_V (component, space), Volume fraction of the respective components within their reference spaces.

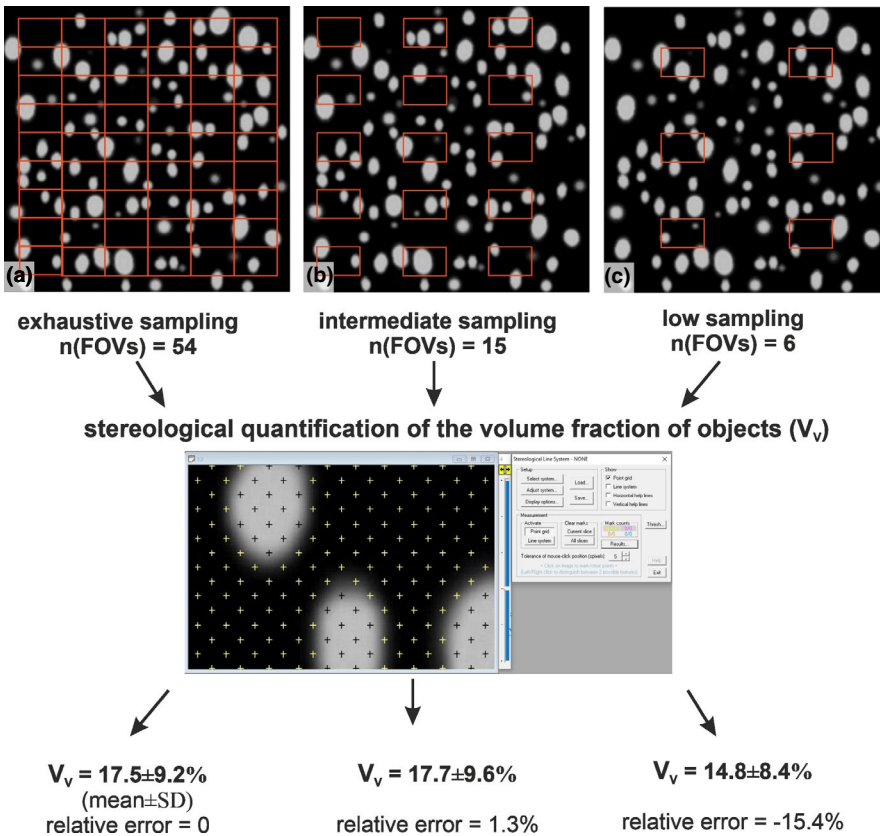


FIGURE 1 Example #1 demonstrates the effect of the intensity of sampling on the quantitative results in virtually generated slides with precisely known volume fractions of objects. A virtual slide was generated using TEIGEN software (Jiřík et al., 2018) with a precisely known volume fraction (V_V) of the white objects on the black background, mimicking the sectional profiles of cell bodies or matrix fibres. The scene was sampled with simulated fields of view (FOVs) exhaustively (a), with intermediate (b) and low (c) intensity. After stereological quantification using the point grid, the V_V was expressed as the mean \pm standard deviation (SD), and the relative percentage error of the estimate was calculated for each sampling intensity

3.2 | Slides requiring exhaustive sampling of the ROIs

In some studies, it is advisable to evaluate the complete ROI. This strategy prevails when the number of slides available is limited, such as in ground sections of bone implants (Figure 3, Example #3). Similar situations occur when the ROI has small dimensions, for example central regions of experimental bone defects in small animal models (Figure S4, Example #S4). Exhaustive sampling might also be needed in cases with significant biological variability among the study groups when counting every few cells matters, such as in counting virus-transduced neurons in mouse brains (Figure S5, Example #S5).

3.3 | Using the same sampling count but in ROIs of different absolute sizes

In some study designs without excessive biological variability, it is possible to maintain the same number of FOVs (Figure 4, Example #4). When the size of the specimens and ROI varies, this will result in a variable sampling density (the numerator is the same, the denominator varies), as in samples of proximal vs. distal segments of blood vessels (Figure S6, Example #S6) or large vs. small lymph nodes (Figure S7B, Example #S7). The case presented in Figure S7A (Example #S7) shows a very extensive sampling, the ex post analysis of which identified as an unnecessary and laborious oversampling when compared to Figure S7B.

3.4 | Sampling the same ROI for more histological staining methods

Quantifying the volume fractions of tissue components within the same ROI might require more histological staining. Figure 5 (Example #5) shows three stains within the same ROI and objective. It is of great advantage when the sampling is facilitated by a map that helps adjust the sampling density according to the variability of the structures under study, as provided by the estimates of CE in the STEREOLOGER software (v11.0; SRC Biosciences, Tampa, Florida, USA) (Figure 5H-I). When the CE becomes unacceptably high (Figure 5I), it is recommended to increase the *ssf*, *asf* or the density of the stereological grid. Figure S8 (Example #S8) shows a similar design.

3.5 | Sampling one or more ROIs with a variable intensity or using various objectives

Figure 6 (Example #6) illustrates a complex sampling problem that would be difficult to solve without planning on virtual slides. There were five ROIs in every slide, representing the tumoural area, three zones of the tumour invasive margin and healthy non-tumorous tissue. In all five ROIs, multiple structures of interest were identified immunohistochemically (CD8+ T lymphocytes shown, CD3+ T lymphocytes only discussed), and their occurrence within these ROIs was very variable and with different biological interpretations. To maintain the feasibility of such a complex task, two sampling densities were chosen, and part of the sampling variability was

FIGURE 2 Example #2 compares automated counting of cell nuclei in a composite image of a single well in a 8-well XFp cell culture miniplate (captured and stitched with a 4× objective) vs. automated counting in 15 image fields taken from the same well with a 40× objective after 24 h of cultivation (seeding cell density 70,000/cm²). (a) Raw image stitched from two fields of view of a 4× objective shows most of the well microplate. (b) All the nuclei were segmented, counted and highlighted using a watershed algorithm in CELLPROFILER 4.2.1 software (McQuin et al., 2018). The obvious benefit of this procedure was that the quantification was based on counting nearly 1900 nuclei. (c) As an alternative approach, 15 fields of view (FOVs) were sampled with a 40× objective (green rectangles) in a systematic uniform random manner from the well (outlined with a yellow polygon). The three rounded spaces for inserting sensor probes that were part of the well bottom profile were avoided. (d) Example of one of the 15 images that were processed in the same way as in b. The analysis provided a value of density of nuclei with a 4.4% error relative to the whole image analysis (b). The benefits of the sampling (c-d) were that the 40× objective provided a greater optical resolution. Fluorescence images, cell nuclei in blue stained with DAPI. Scale bars 500 μm (a-c), and 40 μm (d)

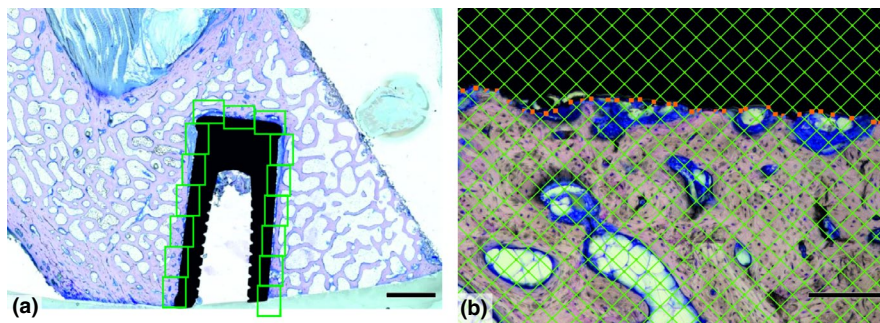
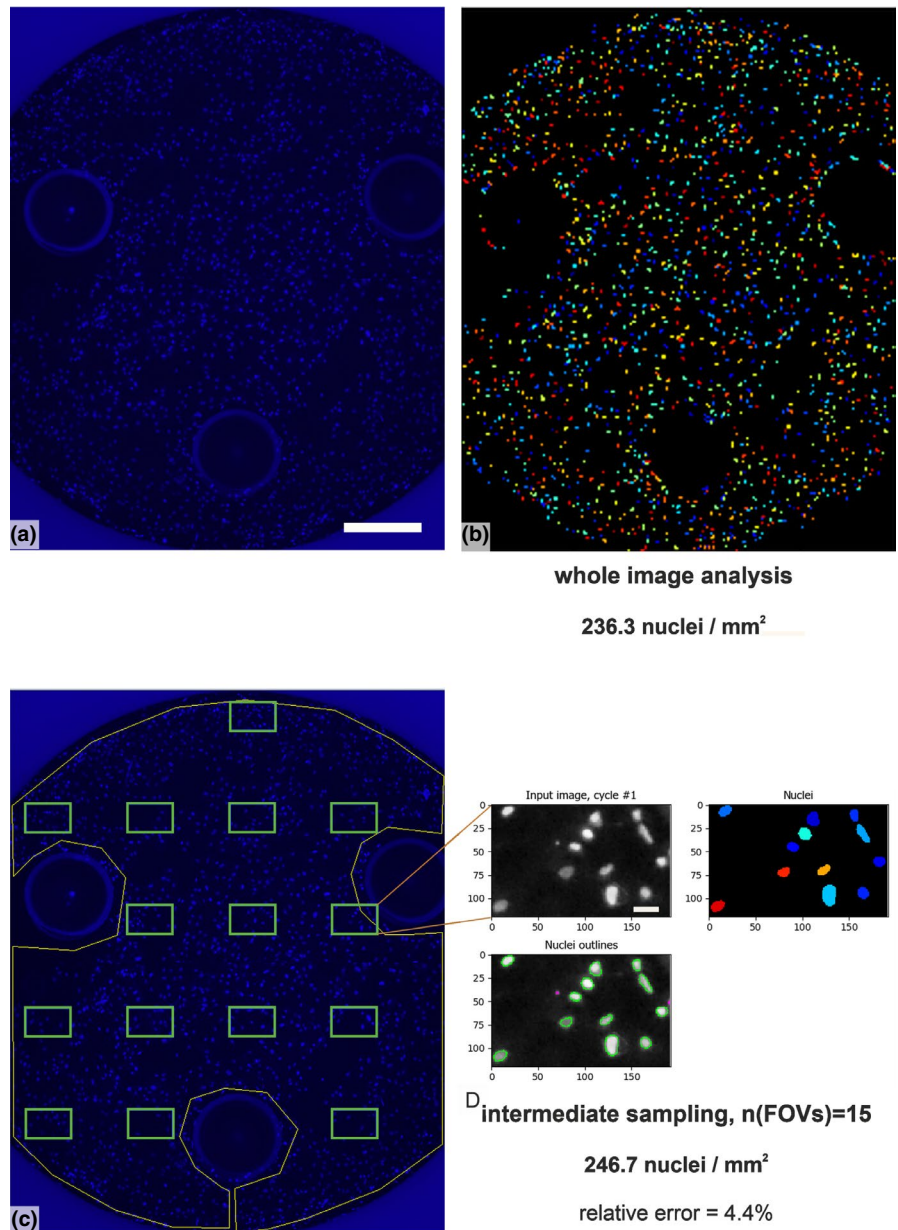


FIGURE 3 Example #3 shows the strategy of exhaustive sampling of an ROI in quantification of bone-implant contact (Babuska et al., 2016). (a) Fifteen ROIs from the bone-implant interface were taken from each slide. All adjacent fields showing the implant surface (black), bone (purple) and connective tissue (blue) were captured exhaustively. (b) Stereological grid randomly positioned over the micrograph; intersections between the test lines and the implant surface (orange points) and intersections between the implant-bone interface and test lines (light blue points). Giemsa's azur eosin methylene blue solution. Scale bar: 2 mm (a), 200 μm (b)

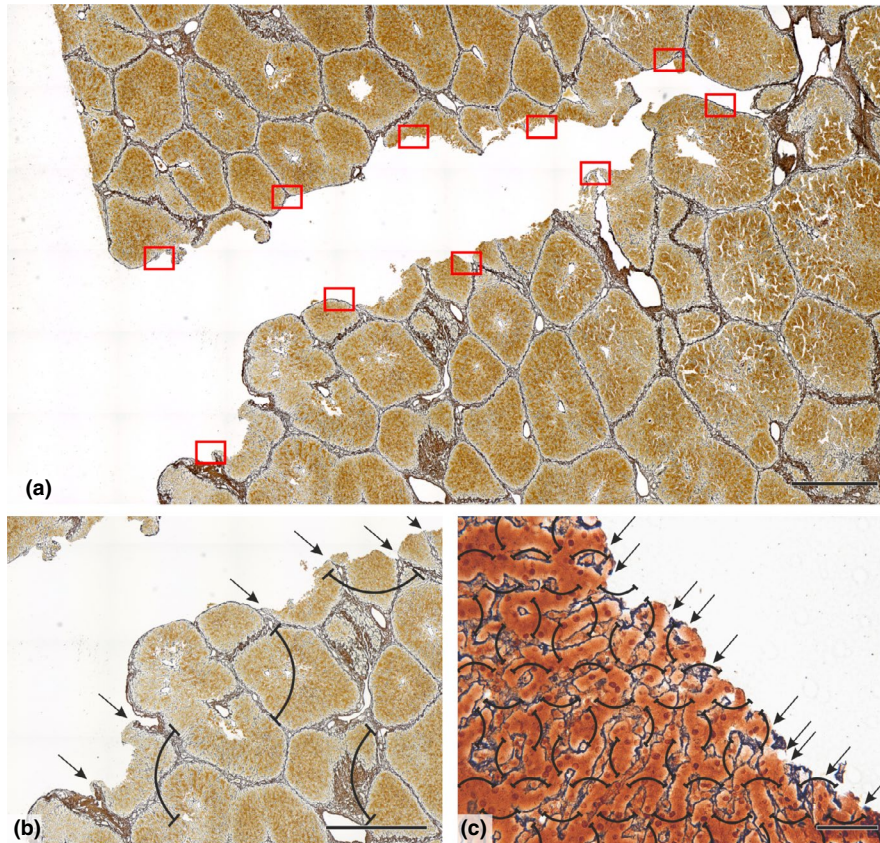
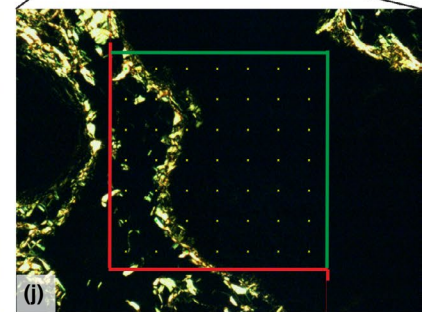
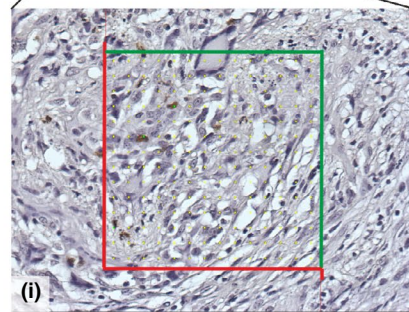
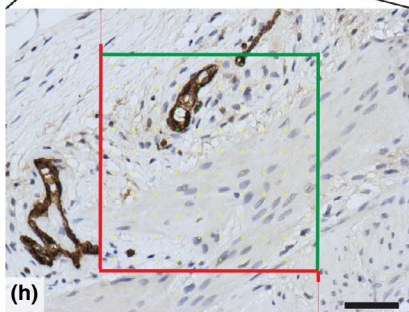
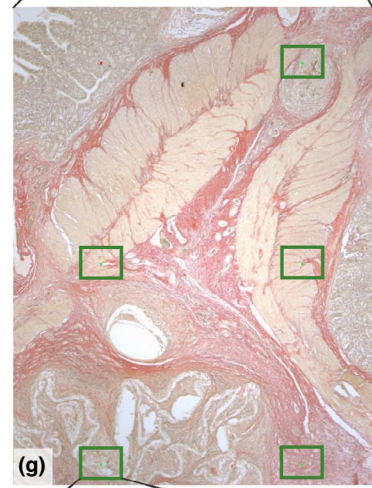
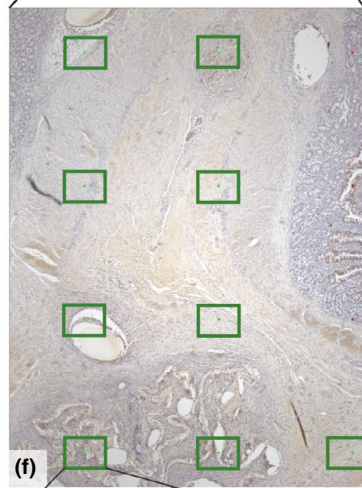
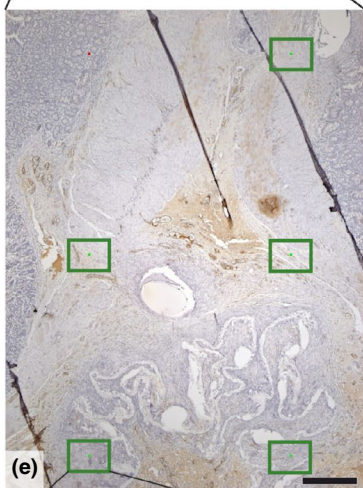
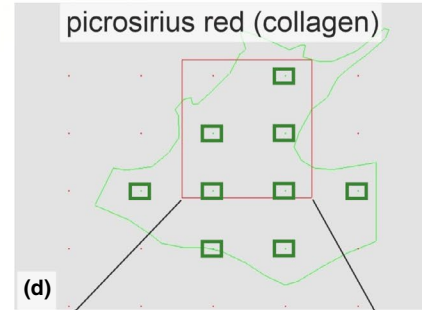
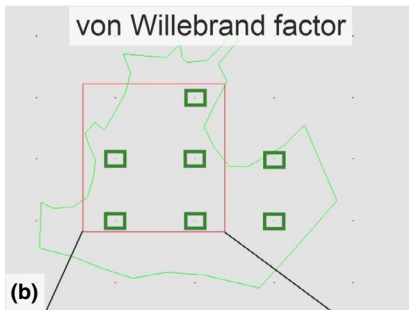
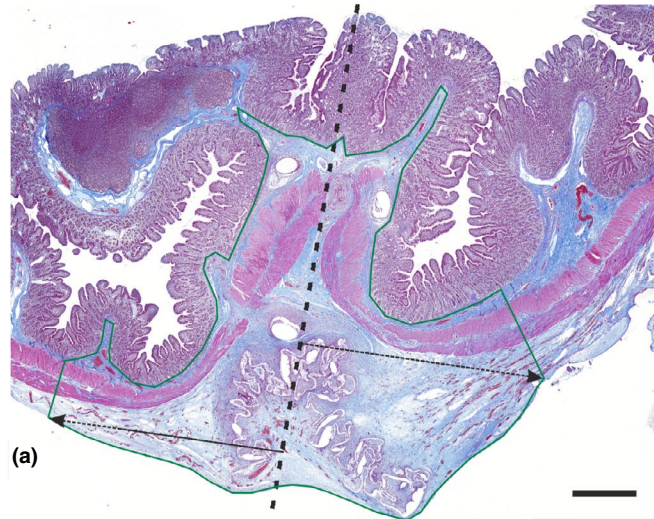


FIGURE 4 Example #4 shows the strategy of tissue sampling for the evaluation of rupture propagation through the porcine liver (Maleckova et al., 2021). (a) An overview of the scanned porcine liver sample showing a rupture in full length. The scanned samples were used to assess the spatial relationship of the rupture and the interlobular septa (analysis was performed along the entire length of the rupture [b]) and the spatial relationship of the rupture and the reticular fibres (analysis was performed in 10 fields of view taken in a systematic manner [red rectangles, C]). (b) Close-up of a part of the rupture-spatial relationship of the rupture and the interlobular septa that were assessed in 7 scanned histological slides (c) An actual field of view taken with a 40 \times objective shows spatial relationship of the rupture and the reticular fibres. This was determined by comparing the number of the intersections of the interlobular septa/reticular fibres with the rupture (arrows) and the theoretical intersection intensity based on the length density of the interlobular septa/reticular fibres. The length density was estimated using circular arc probes (black curves) as available in the ELLIPSE stereological software (ViDiTo). Reticulin kit staining was used for reticular fibre visualization. Scale bar: 1000 μ m (a, b), 50 μ m (c)

compensated with more or less dense counting grids (Figure 6B-D). Similarly, Figure S9 (Example #S9) demonstrates that the present settings were suitable for frequently occurring types of ovarian follicles but too low for the rare types. Figure S10 (Example #S10) shows a solution using lower magnification and less intense sampling

for the volume fractions of histological layers of cerebellum but a greater magnification and more intense sampling for counting cerebellar microvessels within the layers. Similarly, Figure S11 (Example #S11) shows two magnifications useful for two different components of the aortic wall.

FIGURE 5 Example #5 demonstrates three different sampling densities used for quantification of three parameters when evaluating the healing of intestinal anastomoses. The sampling was facilitated using STEREOLOGER software (Rosendorf et al., 2020, 2021a, 2021b). (a) Scanned slide shows the porcine small intestine. The centre of the healing anastomosis is highlighted with a dashed line. The green outline shows the ROI under study comprising the submucosa, muscularis, and serosa no more than 3 mm proximally and distally (dashed arrows) from the centreline. (b-d) Pan window maps of the scanned areas are screenshots captured from the STEREOLOGER software used for planning the sampling. The green polygon outlines the ROI, from which image fields of 20 \times objectives (green rectangles) were sampled in a systematic random uniform manner. The red rectangle shows the simulated image field of a 2 \times objective used for overview. The XY sampling step was 1500 μ m for quantification of vWF and collagen (b, d, e, g) or 1000 μ m for quantification of MAC387 (c, f). (e-g) Actual fields of view of 2 \times objectives for all three staining methods. The planned sampling for the 20 \times objectives is shown (green rectangles). (h-i) Actual fields of view of the 20 \times objectives for each staining method. Unbiased counting frames and the stereological point grid method were used for quantification of the volume fractions of individual components of the intestinal wall. On the bottom, recommendations on the total sampling variability (coefficient of error, CE, also considering the number of sections) are shown as provided in the Stereologer protocol. In vWF (h) and picrosirius red (i), the CE was sufficiently low. In MAC387, a greater point density is recommended due to the spatial variability of the distribution of inflammatory cells. Gomori trichrome kit (a), vWF immunohistochemistry (e, h), MAC387 immunohistochemistry (f, i), picrosirius red in bright field (g) and circularly polarized light (j). Scale bars 1 mm (a), 500 μ m (e-g) and 50 μ m (h-j)



Probe Volume Fraction (vWF)
CE 0.1294
Recommendations CE is acceptable.

Probe Volume Fraction (MAC387)
CE 0.2595
Recommendations Decrease the Area per Point.

Probe Volume Fraction (collagen)
CE 0.1188
Recommendations CE is acceptable.

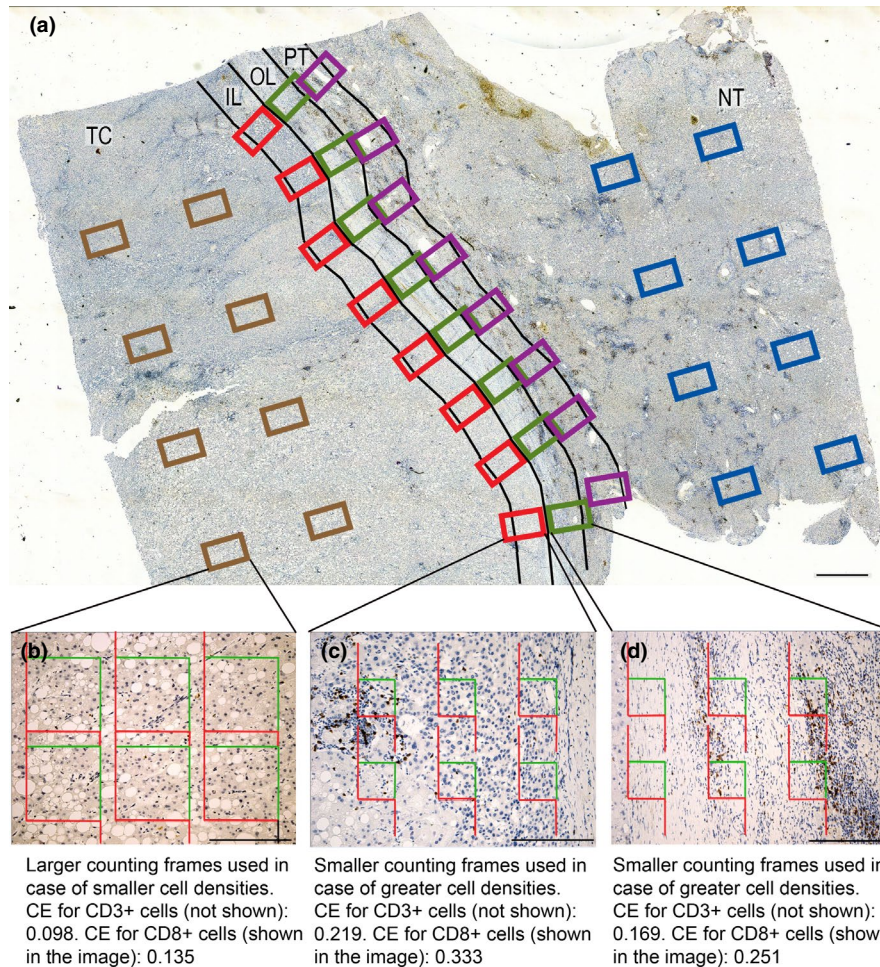


FIGURE 6 Example #6 demonstrates different sampling strategies in multiple ROIs for quantification of tumour-infiltrating CD8+ T cell infiltration in resected samples of human hepatocellular carcinoma. (a) Scanned slide with multiple ROIs: tumour centre (TC), inner layer (IL) of tumour invasive margin (TIM), outer layer (OL) of TIM, peritumoural area (PT) and non-tumour area (NT). The inner TIM and outer TIM were defined as 500 μm on each side of the border separating the malignant cell nests and adjacent non-tumour liver tissue or fibrous capsule (Hendry et al., 2017) towards TC or non-tumour liver, respectively. The TC represented the remaining tumour area. The PT region was defined as the 500 μm thick region immediately adjacent to the OL. Using a 20 \times objective, eight equidistant fields of view (FOVs) were taken from each ROI using systematic uniform random sampling (SURS). (b-d) CD8-immunopositive cell profiles were counted using unbiased counting frames. The choice of the number and size of unbiased counting frames (UCFs) varied depending on the cell density at a glance. For TC and NT, areas of UCF (from 8700 to 34,801 μm^2) and their number (6–9) per image varied according to the lymphocytic density, and therefore, sampling fraction per ROI varied as well. Six UCFs per image were used for the inner and outer TIM and for the PT region. The coefficients of error (CE) calculated for the whole population of CD3+ T lymphocytes (not shown in the micrographs) and for the CD8+ subpopulation separately (shown on the micrographs). CD8 immunohistochemistry (a-d). Scale bars 1000 μm (a), 200 μm (b-d)

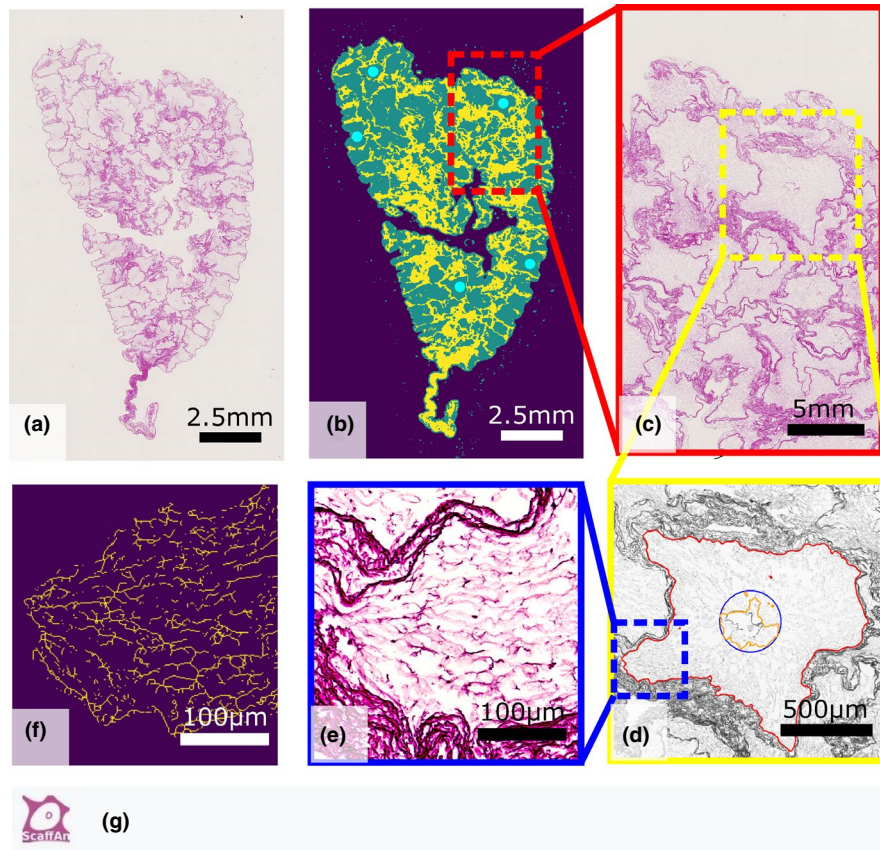
3.6 | Multistage sampling of FOVs and virtual sampling

Figure 7 (Example #7) shows a special case of multiscale sampling and analysis performed by a semiautomatic software tool when evaluating the quality and composition of decellularized liver. This demonstrates that tailoring a software tool to a specific problem might increase the efficiency of the whole work significantly, especially when the sampling of FOVs is an integral part of the quantification procedure. Figure S12 (Example #S12) demonstrates virtual sampling when counting fibroblasts within a 3D scaffold in vitro; such an approach requires programming skills, but the users are rewarded by a reasonable mapping of the variability of their results.

4 | DISCUSSION

4.1 | Sampling FOVs is only a part of a 3D multistage sampling

For any quantification, at least two criteria are to be met: (i) the staining should allow for a clear identification of all the structures under study, and (ii) borders of the reference space are clearly defined, either anatomically or by convention (Howard & Reed, 2005; Mouton, 2002). We would like to point out explicitly that the sampling of FOVs in virtual scanned sections illustrated above represents only a small part of the whole multistage sampling in quantitative histology. Therefore, the variability of results affected



PIG-003_J-18-0170_HE.ndpi

	Skeleton length	Branch number	Area [mm ²]	Scan Segmentation Empty Area [mm ²]	Scan Segmentation Septum Area [mm ²]	Scan Segmentation Sinusoidal Area [mm ²]
0	49.284	23278	0.953975	74.561654	25.290709	89.24516
1	39.998	19469	0.835566	74.561654	25.290709	89.24516
2	50.942	24941	0.939373	74.561654	25.290709	89.24516

FIGURE 7 Example #7 shows a quantitative assessment of the morphological quality of decellularized porcine liver to be used as a high-quality scaffold for liver tissue engineering. (a) Slide scans are evaluated by in-house developed open source software ScaffAn (<http://scaffan.kky.zcu.cz/>) as an integral part of a multiscale analysis (Moulisová et al., 2020). The resulting parameters describe the level of ECM structure preservation within individual lobules. It is a two-step procedure: (b) The first step is a whole scan analysis separating the lobules (segmentation to distinguish the sinusoidal ECM from more dense interlobular septa, triads and vessels) (Jirik et al., 2020, 2021). Typically, 5 lobules are then selected either manually by the end user or automatically (marked with cyan dots in b). The sampling is defined by a single lobule area and is not random, but it systematically reflects the morphological diversity of the sample (e.g. large vessels that are not the subject of analysis). (c) A close-up of a part of the analysed area. (d) The second step is lobular network analysis calculating parameters for individual lobules. Output parameters such as structure/skeleton lengths (mm) or branching points characterize the integrity of the sinusoidal vessel ECM network (detailed in e). These parameters are generated by using a set of algorithms, including image segmentation by the active contour model (Kass et al., 1988), texture analysis by the grey level cooccurrence matrix (Haralick, 1979) and skeletonization of the sinusoidal network (f). (g) An example of the online software output data

by the sampling of FOVs in a single slide represents only a small part of the total variability of data in the whole study. Other levels of sampling should also be emphasized, such as the number of subjects per study group, the sampling of tissue probes from organs, and the sampling of slides. We highly recommend classical papers on this topic (Gundersen & Osterby, 1981; Slomianka & West, 2005).

The importance of proper sampling of sections is elaborated in Figure S3. We found that the tissue composition of the canine soft palate was so heterogeneous that a whole half of the velum had to be sampled using a minimum of 10–15 sections distributed approximately uniformly throughout the complete tissue block to obtain reliable and robust results. Single sections cannot be used as 'representative' of this organ. Justifying the number of sections required

for a valid quantitative histological study is suggested in Figure S3D-E. However, even when a single slide is available (e.g. in archive material), the repeatability, reliability and correctness, even of simple quantification, might greatly benefit from correct FOV sampling.

4.2 | Choosing the FOV sampling intensity and practical implications

In all the examples presented, our effort was to spread the sampling items evenly and widely throughout the ROIs and specimens. This strategy is called systematic uniform random sampling, and it is superior and more efficient than simple (independent) random sampling, as it covers all parts under study uniformly (Mayhew & Lucocq, 2015). The examples illustrated above do not involve all possible situations in 2D sampling of FOVs in quantitative histology but might provide clues to the reader to most of these. We included mostly examples of sampling optimized in pilot studies but also problematic cases. Unnecessary intensive sampling (oversampling), for example in Figure 1A and Figure S7A, makes the work more laborious and expensive without providing new information. In contrast, insufficient sampling (undersampling), for example in Figure 1C and Figure S9C, Figure S10B,C, might compromise the study design and make it difficult to reach a pre-determined level of significance when testing statistical hypotheses, although biological differences might be present in the samples under study.

As the sampling error (introduced by all levels of the sampling procedure), represented by CE estimates, sums up with the biological variance (i.e. the differences between the samples themselves), according to Tschanz et al. (2014), it is always advisable to perform a pilot study on typical samples and groups under research. This allows for calculating a power sample analysis. Mapping both the total variability of our data and its components is an essential step when designing further studies on the same material, which involves calculating the minimum number of samples needed to compare the groups under study. Descriptive statistics of the pilot data (mean and standard deviation) are useful for the power sample analysis (Chow et al., 2008); for example, when planning an experiment and expecting one of the histological quantitative parameters to be increased by 20%, the minimum number of samples required per group would be calculated using the typical test power $\beta = 0.8$ (the type II error) and $\alpha = 0.05$ (type I error).

4.3 | Whole slide scanning vs. taking multiple micrographs

Currently, researchers have more technical options for acquiring virtual slides and planning the sampling of FOVs. The pros and cons of whole slide scanning vs. taking multiple individual micrographs are summarized in Table 6. An inexpensive alternative for acquiring virtual slides with large areas but high resolution might

TABLE 6 Pros and cons of two technical ways of sampling: Whole slide scanning vs. sampling multiple individual micrographs

Scanning whole slides	Sampling multiple individual micrographs
Histological scanner required.	Can be done even on routine microscopes with motorized or manual stage.
The data from the whole slide are always available, so more ROIs can be added when necessary.	Usually, is done once.
Can be fast and efficient when automated. However, issues occurring during the automated scanning do not appear until checked.	Usually, takes more time to be done. Any technical issues can be seen and solved immediately.
Problems with atypical size of archive slides might occur (Leica Biosystems, 2021). Either the holders are not adapted, or the slides might get stuck within the device.	Can be performed even if archive slides sometimes do not fit the feeding trays or holders of scanners (uniform slide dimensions and thickness required).
In some scanners, only bright field illumination technique and a limited choice of objectives are available. The use of immersion oil objectives is rare.	Can be done using any observation technique available of the microscope, for example fluorescence imaging, phase contrast, polarizing microscopy. No issues with using oil immersion easily.
Generates large datasets (typically 0.5–2 GB per typical histological slide). The pyramidal architecture of the files is usually optimized for viewing.	No special data infrastructure required.
Corresponds to state-of-the art of the whole-mount pathology (Look Hong et al., 2016; Rashid et al., 2019).	Does not permit whole-mount analysis (or this becomes extremely laborious).
In some scanners, multiplane (z-stack) scanning is possible to reflect the thickness of the slide. This might depend on the availability of high-aperture oil immersion objectives. Depth of focus problems might occur that cannot be solved automatically by the scanner software.	Optical sections could be captured in stacks using oil immersion objectives with high numerical aperture. Multiplane scanning might be crucial for studies involving confocal microscopy and requiring not only lateral resolution but also 3D information.
Using automated image-processing methods, the texture pattern of the whole sampling area can be analysed.	Analysing the whole slide would be very laborious or impossible. Texture patterns that exceed the size of individual micrographs are lost and cannot be analysed.

be image stitching, supported currently by stitching modules in most of the proprietary camera software solutions (extra costs in Nikon NIS ELEMENTS BR; ZEISS ZEN CORE, LEICA LAS). Moreover, free IMAGEJ (Schneider et al., 2012) and FIJI software can be used as well (Schindelin et al., 2012). However, stitched images do not support the pyramidal file architecture, and they may require more RAM than the optimized file formats of the slide scanners. Stitching algorithm also fail in case of optically empty regions.

5 | CONCLUSION

We conclude that combining scanning virtual slides in histology with efficient use of unbiased sampling is fully compatible with the plethora of data from quantitative microscopy, which can be expressed as the 'Do less well' rule (Gundersen & Osterby, 1981). Virtual microscopy proved to be extremely helpful to facilitate correct sampling at the level of individual slides. Uniform distribution of FOVs can also be reached using motorized microscope stages. Principles of SURS are beneficial not only for validity, efficiency and ethics of quantitative studies but also for improving accuracy and repeatability in qualitative studies. We suggest that modules supporting the SURS of FOVs with variable settings of ROIs and sampling intensity should be natively supported by all virtual slide scanners intended for scientific use.

ACKNOWLEDGEMENTS

This study was supported by the National Sustainability Program I (NPU I) Nr. LO1503 provided by the Ministry of Education, Youth and Sports of the Czech Republic and by the Charles University Research Fund (Progres Q39). LC, AT, VL, VM and MJ also received support from the Ministry of Education, Youth and Sports under the project FIND No. CZ.02.1.01/0.0/0.0/16_019/0000787 and from the European Regional Development Fund-Project 'Application of Modern Technologies in Medicine and Industry' (No. CZ.02.1.01/0.0/0.0/17_048/0007280). JH was supported by the Ministry of Health of the Czech Republic (Grant no: 15-29241A) and by the grant SVV-2020-2022 No. 260 536. MG was supported by the Charles University Grant Agency, project No. 1313420 and SVV 260 536. LC and VL received support from the Charles University grant UNCE/MED/006, and by the grant of Ministry of Health of the Czech Republic - AZV NU20J-08-00009. AT has received funding from the European Union's Horizon 2020 research and innovation programme under grant agreement N°856620. The analysis demonstrated in example O represented a pilot study for the dissertation project of Violeta García-Espín, supervised by Prof. Monika Egerbacher and Prof. Gilles Dupré (all University of Veterinary Medicine Vienna, Austria). The help of Dr. Stephan Handschuh (University of Veterinary Medicine Vienna) with the whole slide image analysis is gratefully acknowledged.

CONFLICT OF INTEREST

The authors declare no conflict of interest.

DATA AVAILABILITY STATEMENT

Primary data supporting the calculations in the examples can be requested from the authors or have been already published in the papers that were cited appropriately.

ORCID

Zbyněk Tonar  <https://orcid.org/0000-0002-7200-9894>

REFERENCES

- Arai, K., Kobayashi, M., Harada, Y., Hara, Y., Michishita, N., Ohkusu-Tsukada, K., & Takahashi, K. (2016). Histopathologic and immunohistochemical features of soft palate muscles and nerves in dogs with an elongated soft palate. *American Journal of Veterinary Research*, 77(1), 77-83. <https://doi.org/10.2460/ajvr.77.1.77>
- Babuska, V., Moztarzadeh, O., Kubikova, T., Moztarzadeh, A., Hrusak, D., & Tonar, Z. (2016). Evaluating the osseointegration of nanostructured titanium implants in animal models: Current experimental methods and perspectives (Review). *Biointerphases*, 11, 030801. <https://doi.org/10.1116/1.4958793>
- Baker, M. (2016). 1,500 scientists lift the lid on reproducibility. *Nature*, 533, 452-454. <https://doi.org/10.1038/533452a>
- Bertram, C. A., & Klopffleisch, R. (2017). The Pathologist 2.0: An update on digital pathology in veterinary medicine. *Veterinary Pathology*, 54, 756-766. <https://doi.org/10.1177/0300985817709888>
- Biosystems, L. (2021). *Tips for digital pathology slide scanning*. <https://www.leicabiosystems.com/resources/four-tips-for-digital-pathology-slide-scanning>
- Blasova, T., Tonar, Z., Tomasek, P., Hosek, P., Hollan, I., Treska, V., & Molacek, J. (2019). Inflammatory cell infiltrates, hypoxia, vascularization, pentraxin 3 and osteoprotegerin in abdominal aortic aneurysms - A quantitative histological study. *PLoS One*, 14, e0224818. <https://doi.org/10.1371/journal.pone.0224818>
- Bolat, D., Kürüm, A., & Canpolat, S. (2018). Morphology and quantification of sheep pineal glands at pre-pubertal, pubertal and post-pubertal periods. *Anatomia, Histologia, Embryologia*, 47(4), 338-345. <https://doi.org/10.1111/ahe.12359>
- Bolon, B., Garman, R. H., Gundersen, H. J. G., Allan Johnson, G., Kaufmann, W., Krinke, G., Little, P. B., Makris, S. L., Mellon, R. D., Sulik, K. K., & Jensen, K. (2011). Continuing education course #3: Current practices and future trends in neuropathology assessment for developmental neurotoxicity testing. *Toxicologic Pathology*, 39(1), 289-293. <https://doi.org/10.1177/0192623310386247>
- Cakmak, G., & Karadag, H. (2019). A stereological study on calculation of volume values regarding lumbosacral segments of quails. *Anatomia, Histologia, Embryologia*, 48, 164-174. <https://doi.org/10.1111/ahe.12437>
- Casteleyn, C., Rekecki, A., Van Der Aa, A., Simoens, P., & Van Den Broeck, W. (2010). Surface area assessment of the murine intestinal tract as a prerequisite for oral dose translation from mouse to man. *Laboratory Animals*, 44(3), 176-183. <https://doi.org/10.1258/la.2009.009112>
- Chow, S. C., Wang, H., & Shao, J. (2008). *Sample size calculations in clinical research*, 2nd ed. Chapman & Hall/CRC Biostatistics Series.
- Crosse, K. R., Bray, J. P., Orbell, G. M. B., & Preston, C. A. (2015). Histological evaluation of the soft palate in dogs affected by brachycephalic obstructive airway syndrome. *New Zealand Veterinary Journal*, 63(6), 319-325. <https://doi.org/10.1080/00480169.2015.1061464>
- Dempster, D. W., Compston, J. E., Drezner, M. K., Glorieux, F. H., Kanis, J. A., Malluche, H., Meunier, P. J., Ott, S. M., Recker, R. R., & Parfitt, A. M. (2013). Standardized nomenclature, symbols, and units for bone histomorphometry: A 2012 update of the report of the ASBMR

- Histomorphometry Nomenclature Committee. *Journal of Bone and Mineral Research*, 28(1), 2–17. <https://doi.org/10.1002/jbmr.1805>
- Dockery, P., & Fraher, J. (2007). The quantification of vascular beds: A stereological approach. *Experimental and Molecular Pathology*, 82, 110–120. <https://doi.org/10.1016/j.yexmp.2006.12.011>
- Dorph-Petersen, K. A., Nyengaard, J. R., & Gundersen, H. J. (2001). Tissue shrinkage and unbiased stereological estimation of particle number and size. *Journal of Microscopy*, 204, 232–246. <https://doi.org/10.1046/j.1365-2818.2001.00958.x>
- Dupré, G., & Heidenreich, D. (2016). Brachycephalic syndrome. *Veterinary Clinics of North America: Small Animal Practice*, 46(4), 691–707. <https://doi.org/10.1016/j.cvsm.2016.02.002>
- Eržen, I., Janáček, J., & Kubínová, L. (2011). Characterization of the capillary network in skeletal muscles from 3D data. *Physiological Research*, 60, 1–13. <https://doi.org/10.33549/physiolres.931988>
- Ferreira, V. F., Dias, F. C. R., Costa, K. L. C., da Matta, S. L. P., de Melo, F. R., & de Melo, F. C. S. A. (2021). Descriptive morphometry and stereology in accessing the testis structure and function of the marsupial *Philander frenatus* (Olfers, 1818) (Didelphimorphia: Didelphidae). *Anatomia, Histologia, Embryologia*, 50, 379–386. <https://doi.org/10.1111/ah.12642>
- Goodarzi, N., Akbari Bazm, M., Naseri, L., & Hosseini-pour, M. (2019). Histomorphometrical and stereological study of the oesophagus in the adult male Persian squirrel (*Sciurus anomalus*). *Anatomia, Histologia, Embryologia*, 48, 444–448. <https://doi.org/10.1111/ah.12465>
- Greiner, C., Grainger, S., Farrow, S., Davis, A., Su, J. L., Saybolt, M. D., Wilensky, R., Madden, S., & Sum, S. T. (2021). Robust quantitative assessment of collagen fibers with picosirius red stain and linearly polarized light as demonstrated on atherosclerotic plaque samples. *PLoS One*, 16, e0248068. <https://doi.org/10.1371/journal.pone.0248068>
- Gundersen, H. J., Boyce, R. W., Nyengaard, J. R., & Odgaard, A. (1993). The Conneulor: Unbiased estimation of connectivity using physical disectors under projection. *Bone*, 14, 217–222. [https://doi.org/10.1016/8756-3282\(93\)90144-y](https://doi.org/10.1016/8756-3282(93)90144-y)
- Gundersen, H. J., & Jensen, E. B. (1987). The efficiency of systematic sampling in stereology and its prediction. *Journal of Microscopy*, 147, 229–263. <https://doi.org/10.1111/j.1365-2818.1987.tb02837.x>
- Gundersen, H. J., & Osterby, R. (1981). Optimizing sampling efficiency of stereological studies in biology: Or 'do more less well!'. *Journal of Microscopy*, 121, 65–73. <https://doi.org/10.1111/j.1365-2818.1981.tb01199.x>
- Gundersen, H. J. G., Vedel Jensen, E. B., Kieu, K., & Nielsen, J. (1999). The efficiency of systematic sampling in stereology reconsidered. *Journal of Microscopy*, 193, 199–211. <https://doi.org/10.1046/j.1365-2818.1999.00457.x>
- Haralick, R. M. (1979). Statistical and structural approaches to texture. *Proceedings of the IEEE*, 67, 786–804. <https://doi.org/10.1109/PROC.1979.11328>
- Hendry, S., Salgado, R., Gevaert, T., Russell, P. A., John, T., Thapa, B., Christie, M., van de Vijver, K., Estrada, M. V., Gonzalez-Ericsson, P. I., Sanders, M., Solomon, B., Solinas, C., den Van Eynden, G. G. M., Allory, Y., Preusser, M., Hainfellner, J., Pruner, G., Vingiani, A., ... Fox, S. B. (2017). Assessing tumor-infiltrating lymphocytes in solid tumors: A Practical review for pathologists and proposal for a standardized method from the International Immunooncology Biomarkers Working Group: Part 1: Assessing the host immune response, TILs in invasive breast carcinoma and ductal carcinoma in situ, metastatic tumor deposits and areas for further research. *Advances in Anatomic Pathology*, 24, 235–251. <https://doi.org/10.1097/PAP.0000000000000162>
- Hlavatý, J., Tonar, Z., Renner, M., Panitz, S., Petznek, H., Schweizer, M., Schüle, S., Kloke, B. P., Moldzio, R., & Witter, K. (2017). Tropism, intracerebral distribution, and transduction efficiency of HIV- and SIV-based lentiviral vectors after injection into the mouse brain: A qualitative and quantitative in vivo study. *Histochemistry and Cell Biology*, 148, 313–329. <https://doi.org/10.1007/s00418-017-1569-1>
- Howard, C. V., & Reed, M. G. (2005). *Unbiased stereology: Three-dimensional measurement in microscopy*, 2nd ed. Garland Science.
- Hsia, C. C. W., Hyde, D. M., Ochs, M., & Weibel, E. R. (2010). An official research policy statement of the American Thoracic Society/European Respiratory Society: Standards for quantitative assessment of lung structure. *American Journal of Respiratory and Critical Care Medicine*, 181(4), 394–418. <https://doi.org/10.1164/rccm.200809-1522ST>
- Jahn, S. W., Plass, M., & Moinfar, F. (2020). Digital pathology: Advantages, limitations and emerging perspectives. *Journal of Clinical Medicine*, 9(11), 3697. <https://doi.org/10.3390/jcm9113697>
- Jiřík, M., Bartoš, M., Tomášek, P., Malečková, A., Kural, T., Horáková, J., Lukáš, D., Suchý, T., Kochová, P., Hubálek Kalbáčová, M., Králíčková, M., & Tonar, Z. (2018). Generating standardized image data for testing and calibrating quantification of volumes, surfaces, lengths, and object counts in fibrous and porous materials using X-ray microtomography. *Microscopy Research and Techniques*, 81, 551–568. <https://doi.org/10.1002/jemt.23011>
- Jirík, M., Gruber, I., Moulisova, V., Schindler, C., Cervenková, L., Palek, R., Rosendorf, J., Arlt, J., Bolek, L., Dejmejk, J., Dahmen, U., Zelezny, M., & Liska, V. (2021). Semantic segmentation of intralobular and extralobular tissue from liver scaffold H&E images. *Sensors*, 20, 7063. <https://doi.org/10.3390/s20247063>
- Jirík, M., Moulisova, V., Schindler, C., Cervenková, L., Palek, R., Rosendorf, J., Arlt, J., Bolek, L., Dejmejk, J., Dahmen, U., Jiríkova, K., Gruber, I., Liska, V., & Zelezny, M. (2020). MicrAnt: Towards regression task oriented annotation tool for microscopic images. *Lecture Notes in Computer Science*, 12148, 209–218. https://doi.org/10.1007/978-3-030-51002-2_15
- Jiřík, M., Tonar, Z., Králíčková, A., Eberlová, L., Mírka, H., Kochová, P., Gregor, T., Hošek, P., Svobodová, M., Rohan, E., Králíčková, M., & Liška, V. (2016). Stereological quantification of microvessels using semiautomated evaluation of X-ray microtomography of hepatic vascular corrosion casts. *International Journal of Computer Assisted Radiology and Surgery*, 11, 1803–1819. <https://doi.org/10.1007/s11548-016-1378-3>
- Junatas, K. L., Tonar, Z., Kubíková, T., Liška, V., Pálek, R., Mik, P., Králíčková, M., & Witter, K. (2017). Stereological analysis of size and density of hepatocytes in the porcine liver. *Journal of Anatomy*, 230, 575–588. <https://doi.org/10.1111/joa.12585>
- Kass, M., Witkin, A., & Terzopoulos, D. (1988). Snakes: Active contour models. *International Journal of Computer Vision*, 1, 321–331. <https://doi.org/10.1007/BF00133570>
- Keša, P., Pokorná, E., Grajciarová, M., Tonar, Z., Vočková, P., Trochet, P., Kopeček, M., Jakša, R., Šefc, L., & Klenar, P. (2021). Quantitative in vivo monitoring of hypoxia and vascularization of patient-derived murine xenografts of mantle cell lymphoma using photoacoustic and ultrasound imaging. *Ultrasound in Medicine & Biology*, 47, 1099–1107. <https://doi.org/10.1016/j.ultrasmedbio.2020.12.010>
- Knudsen, L., Brandenberger, C., & Ochs, M. (2021). Stereology as the 3D tool to quantitate lung architecture. *Histochemistry and Cell Biology*, 155, 163–181. <https://doi.org/10.1007/s00418-020-01927-0>
- Kochová, P., Cimrman, R., Jansová, M., Michalová, K., Kališ, K., Kubíková, T., & Tonar, Z. (2019). The histological microstructure and in vitro mechanical properties of the human female postmenopausal perineal body. *Menopause - The Journal of the North American Menopause Society*, 26, 66–77. <https://doi.org/10.1097/GME.00000000000001166>
- Kochová, P., Hympanová, L., Rynkevic, R., Cimrman, R., Tonar, Z., Deprest, J., & Kališ, V. (2019). The histological microstructure and in vitro mechanical properties of pregnant and postmenopausal ewe perineal body. *Menopause - The Journal of the North American*

- Menopause Society, 26, 1289–1301. <https://doi.org/10.1097/GME.0000000000001395>
- Kocová, J. (1970). Overall staining of connective tissue and the muscular layer of vessels. *Folia Morphologica*, 18, 293–295.
- Kolinko, Y., Cendelin, J., Kralickova, M., & Tonar, Z. (2016). Smaller absolute quantities but greater relative densities of microvessels are associated with cerebellar degeneration in Lurcher mice. *Frontiers in Neuroanatomy*, 10, 35. <https://doi.org/10.3389/fnana.2016.00035>
- Kubíková, T., Kochová, P., Tomášek, P., Witter, K., & Tonar, Z. (2018). Numerical and length densities of microvessels in the human brain: Correlation with preferential orientation of microvessels in the cerebral cortex, subcortical grey matter and white matter, pons and cerebellum. *Journal of Chemical Neuroanatomy*, 88, 22–32. <https://doi.org/10.1016/j.jchemneu.2017.11.005>
- Kuo, K.-H., & Leo, J. M. (2019). Optical versus virtual microscope for medical education: A systematic review. *Anatomical Sciences Education*, 12(6), 678–685. <https://doi.org/10.1002/ase.1844>
- Lokkegaard, A., Nyengaard, J. R., & West, M. J. (2001). Stereological estimates of number and length of capillaries in subdivisions of the human hippocampal region. *Hippocampus*, 11, 726–740. <https://doi.org/10.1002/hipo.1088>
- Look Hong, N. J., Clarke, G. M., Yaffe, M. J., & Holloway, C. M. B. (2016). Cost-effectiveness analysis of whole-mount pathology processing for patients with early breast cancer undergoing breast conservation. *Current Oncology*, 23, S23–S31. <https://doi.org/10.3747/co.23.2917>
- Malečková, A., Kochová, P., Pálek, R., Liška, V., Mik, P., Bońkowski, T., Horák, M., & Tonar, Z. (2021). Blunt injury of liver: Mechanical response of porcine liver in experimental impact test. *Physiological Measurement*, 42, 025008. <https://doi.org/10.1088/1361-6579/abdf3c>
- Marcos, R., Monteiro, R. A., & Rocha, E. (2012). The use of design-based stereology to evaluate volumes and numbers in the liver: A review with practical guidelines. *Journal of Anatomy*, 220, 303–317. <https://doi.org/10.1111/j.1469-7580.2012.01475.x>
- Mayhew, T. M. (2014). Estimating oxygen diffusive conductances of gas-exchange systems: A stereological approach illustrated with the human placenta. *Annals of Anatomy*, 196, 34–40. <https://doi.org/10.1016/j.aanat.2012.08.002>
- Mayhew, T. M., & Lucocq, J. M. (2015). From gross anatomy to the nanomorphome: Stereological tools provide a paradigm for advancing research in quantitative morphomics. *Journal of Anatomy*, 226, 309–321. <https://doi.org/10.1111/joa.12287>
- McQuin, C., Goodman, A., Chernyshev, V., Kamensky, L., Cimini, B. A., Karhohs, K. W., Doan, M., Ding, L., Rafelski, S. M., Thirstrup, D., Wiegarae, W., Singh, S., Becker, T., Caicedo, J. C., & Carpenter, A. E. (2018). Cell profiler 3.0: Next-generation image processing for biology. *PLoS Biology*, 16(7), e2005970. <https://doi.org/10.1371/journal.pbio.2005970>
- Mik, P., Tonar, Z., Malečková, A., Eberlová, L., Liška, V., Pálek, R., Rosendorf, J., Jiřík, M., Mírka, H., Králíčková, M., & Witter, K. (2018). Distribution of connective tissue in the male and female porcine liver: Histological mapping and recommendations for sampling. *Journal of Comparative Pathology*, 162, 1–13. <https://doi.org/10.1016/j.jcpa.2018.05.004>
- Moulišová, V., Jiřík, M., Schindler, C., Červenková, L., Pálek, R., Rosendorf, J., Arlt, J., Bolek, L., Šušová, S., Nietzsche, S., Liška, V., & Dahmen, U. (2020). Novel morphological multi-scale evaluation system for quality assessment of decellularized liver scaffolds. *Journal of Tissue Engineering*, 11, 2041731420921121. <https://doi.org/10.1177/2041731420921121>
- Mouton, P. R. (2002). *Principles and practices of unbiased stereology. An introduction for bioscientists*. The Johns Hopkins University Press.
- Mühlfeld, C. (2014). Quantitative morphology of the vascularisation of organs: A stereological approach illustrated using the cardiac circulation. *Annals of Anatomy*, 196, 12–19. <https://doi.org/10.1016/j.aanat.2012.10.010>
- Mühlfeld, C., Nyengaard, J. R., & Mayhew, T. M. (2010). A review of state-of-the-art stereology for better quantitative 3D morphology in cardiac research. *Cardiovascular Pathology*, 19, 65–82. <https://doi.org/10.1016/j.carpath.2008.10.015>
- Mühlfeld, C., & Ochs, M. (2013). Quantitative microscopy of the lung: A problem-based approach. Part 2: Stereological parameters and study designs in various diseases of the respiratory tract. *American Journal of Physiology, Lung Cellular and Molecular Physiology*, 305, L205–L221. <https://doi.org/10.1152/ajplung.00427.2012>
- Nelson, G., Boehm, U., Bagley, S., Bajcsy, P., Bischof, J., Brown, C. M., Dauphin, A., Dobbie, I. M., Eriksson, J. E., Faklaris, O., Fernandez-Rodriguez, J., Ferrand, A., Gelman, L., Gheisari, A., Hartmann, H., Kukat, C., Laude, A., Mitkovski, M., Munck, S., ... Nitschke, R. (2021). QUAREP-LiMi: A community-driven initiative to establish guidelines for quality assessment and reproducibility for instruments and images in light microscopy. *Journal of Microscopy*, 284, 56–73. <https://doi.org/10.1111/jmi.13041>
- Nevoral, J., Havráňková, J., Kolinko, Y., Prokešová, Š., Fenclová, T., Monsef, L., Žalmanová, T., Petr, J., & Králíčková, M. (2021). Exposure to alternative bisphenols BPS and BPF through breast milk: Noxious heritage effect during nursing associated with idiopathic infertility. *Toxicology and Applied Pharmacology*, 413, 115409. <https://doi.org/10.1016/j.taap.2021.115409>
- Noorafshan, A. (2014). Stereology as a valuable tool in the toolbox of testicular research. *Annals of Anatomy*, 196, 57–66. <https://doi.org/10.1016/j.aanat.2012.07.008>
- Noorafshan, A., Niazi, B., Mohamadpour, M., Hoseini, L., Hoseini, N., Owji, A. A., Rafati, A., Sadeghi, Y., & Karbalay-Doust, S. (2016). First and second order stereology of hyaline cartilage: Application on mice femoral cartilage. *Annals of Anatomy*, 208, 24–30. <https://doi.org/10.1016/j.aanat.2016.07.011>
- Nyengaard, J. R. (1999). Stereologic methods and their application in kidney research. *Journal of the American Society of Nephrology*, 10, 1100–1123. <https://doi.org/10.1681/ASN.V1051100>
- Nyengaard, J. R., & Alwasel, S. H. (2014). Practical stereology of the stomach and intestine. *Annals of Anatomy*, 196, 41–47. <https://doi.org/10.1016/j.aanat.2013.10.007>
- Ochs, M., & Mühlfeld, C. (2013). Quantitative microscopy of the lung: A problem-based approach. Part 1: Basic principles of lung stereology. *American Journal of Physiology, Lung Cellular and Molecular Physiology*, 305, L15–L22. <https://doi.org/10.1152/ajplung.00429.2012>
- Parfitt, A. M., Drezner, M. K., Glorieux, F. H., Kanis, J. A., Malluche, H., Meunier, P. J., Ott, S. M., & Recker, R. R. (1987). Bone histomorphometry: Standardization of nomenclature, symbols, and units: Report of the ASBMR Histomorphometry Nomenclature Committee. *Journal of Bone and Mineral Research*, 2(6), 595–610. <https://doi.org/10.1002/jbmr.5650020617>
- Pichetto, M., Arrighi, S., Gobetti, M., & Romussi, S. (2015). The anatomy of the dog soft palate. III. Histological evaluation of the caudal soft palate in brachycephalic neonates. *Anatomical Record*, 298(3), 618–623. <https://doi.org/10.1002/ar.23054>
- Rashid, S., Nir, G., Fazli, L., Boag, A. H., Siemens, D. R., Goldenberg, S. L., Abolmaesumi, P., & Salcudean, S. E. (2019). Automatic pathology of prostate cancer in whole mount slides incorporating individual gland classification. *Computer Methods in Biomechanics and Biomedical Engineering: Imaging & Visualization*, 3, 336–347. <https://doi.org/10.1080/21681163.2018.1514280>
- Rich, L., & Whittaker, P. (2005). Collagen and picrosirius red staining. A polarized light assessment of fibrillar hue and spatial distribution. *Journal of Morphological Sciences*, 22, 97–104.
- Rosendorf, J., Horakova, J., Klicova, M., Palek, R., Cervenkov, L., Kural, T., Hosek, P., Kriz, T., Tegl, V., Moulišová, V., Tonar, Z., Treska, V., Lukas, D., & Liska, V. (2020). Experimental fortification of intestinal

- anastomoses with nanofibrous materials in a large animal model. *Scientific Reports*, 10, 1134. <https://doi.org/10.1038/s41598-020-58113-4>
- Rosendorf, J., Klicova, M., Cervenkova, L., Horakova, J., Klapstova, A., Hosek, P., Palek, R., Sevcik, J., Polak, R., Treska, V., Chvojka, J., & Liska, V. (2021). Reinforcement of colonic anastomosis with improved ultrafine nanofibrous patch: Experiment on pig. *Biomedicines*, 9, 102. <https://doi.org/10.3390/biomedicines9020102>
- Rosendorf, J., Klicova, M., Cervenkova, L., Palek, R., Horakova, J., Klapstova, A., Hosek, P., Moulisova, V., Bednar, L., Tegl, V., Brzon, O., Tonar, Z., Treska, V., Lukas, D., & Liska, V. (2021). Double-layered nanofibrous patch for prevention of anastomotic leakage and peritoneal adhesions, experimental study. *In Vivo*, 35, 731–741. <https://doi.org/10.21873/invivo.12314>
- Sadeghinezhad, J., Aghabalazadeh Asl, M., Saeidi, A., & De Silva, M. (2020). Morphometrical study of the cat cerebellum using unbiased design-based stereology. *Anatomia, Histologia, Embryologia*, 49, 788–797. <https://doi.org/10.1111/ah.12583>
- Sadeghinezhad, J., & Nyengaard, J. R. (2021). Morphometry of cervical spinal cord in cat using design-based stereology. *Anatomia, Histologia, Embryologia*, 50, 746–755. <https://doi.org/10.1111/ah.12719>
- Saliba, V., Legido-Quigley, H., Hallik, R., Aaviksoo, A., Car, J., & McKee, M. (2012). Telemedicine across borders: A systematic review of factors that hinder or support implementation. *International Journal of Medical Informatics*, 81(12), 793–809. <https://doi.org/10.1016/j.ijmedinf.2012.08.003>
- Schindelin, J., Arganda-Carreras, I., Frise, E., Kaynig, V., Longair, M., Pietzsch, T., Preibisch, S., Rueden, C., Saalfeld, S., Schmid, B., Tinevez, J. Y., White, D. J., Hartenstein, V., Eliceiri, K., Tomancak, P., & Cardona, A. (2012). Fiji: An open-source platform for biological-image analysis. *Nature Methods*, 9, 676–682. <https://doi.org/10.1038/nmeth.2019>
- Schneider, C. A., Rasband, W. S., & Eliceiri, K. W. (2012). NIH Image to ImageJ: 25 years of image analysis. *Nature Methods*, 9, 671–675. <https://doi.org/10.1038/nmeth.2089>
- Selçuk, M. L., & Tipirdamaz, S. (2020). A morphological and stereological study on brain, cerebral hemispheres and cerebellum of New Zealand rabbits. *Anatomia, Histologia, Embryologia*, 49, 90–96. <https://doi.org/10.1111/ah.12489>
- Slomianka, L., & West, M. J. (2005). Estimators of the precision of stereological estimates: An example based on the CA1 pyramidal cell layer of rats. *Neuroscience*, 136, 757–767. <https://doi.org/10.1016/j.neuroscience.2005.06.086>
- Smart In Media AG. (2021, September 3). *Virtual microscopy—Overview and definition*. <https://www.virtual-microscopy.net>
- Suchý, T., Šupová, M., Sauerová, P., Verdánová, M., Sucharda, Z., Rýgllová, Š., Žaloudková, M., Sedláček, R., & Kalbáčková, M. H. (2015). The effects of different cross-linking conditions on collagen-based nanocomposite scaffolds—an in vitro evaluation using mesenchymal stem cells. *Biomedical Materials*, 10, 065008. <https://doi.org/10.1088/1748-6041/10/6/065008>
- Tamburro, R., Brunetti, B., Muscatello, L. V., Mantovani, C., & De Lorenzic, D. (2019). Short-term surgical outcomes and histomorphological evaluation of thermal injury following palatoplasty performed with diode laser or air plasma device in dogs with brachycephalic airway obstructive syndrome. *The Veterinary Journal*, 253, 105391. <https://doi.org/10.1016/j.tvjl.2019.105391>
- Tomášek, P., Tonar, Z., Grajciarová, M., Kural, T., Turek, D., Horáková, J., Pálek, R., Eberlová, L., Králíčková, M., & Liška, V. (2020). Histological mapping of porcine carotid arteries – An animal model for the assessment of artificial conduits suitable for coronary bypass grafting in humans. *Annals of Anatomy*, 228, 151434. <https://doi.org/10.1016/j.aanat.2019.151434>
- Tonar, Z., Egger, G. F., Witter, K., & Wolfesberger, B. (2008). Quantification of microvessels in canine lymph nodes. *Microscopy Research and Techniques*, 71, 760–772. <https://doi.org/10.1002/jemt.20619>
- Tonar, Z., Khadang, I., Fiala, P., Nedorost, L., & Kochová, P. (2011). Quantification of compact bone microporosities in the basal and alveolar portions of the human mandible using osteocyte lacunar density and area fraction of vascular canals. *Annals of Anatomy*, 193, 211–219. <https://doi.org/10.1016/j.aanat.2011.02.001.s>
- Tonarova, P., Lochovska, K., Pytlík, R., & Hubalek Kalbacova, M. (2021). The impact of various culture conditions on human mesenchymal stromal cells metabolism. *Stem Cells International*, 2021, 6659244. <https://doi.org/10.1155/2021/6659244>
- Tschanz, S., Schneider, J. P., & Knudsen, L. (2014). Design-based stereology: Planning, volumetry and sampling are crucial steps for a successful study. *Annals of Anatomy*, 196, 3–11. <https://doi.org/10.1016/j.aanat.2013.04.011>
- Van Ginneken, C., Meir, F. V., Sys, S., & Weyns, A. (2002). Stereologic characteristics of pig small intestine during normal development. *Digestive Diseases and Sciences*, 47(4), 868–878. <https://doi.org/10.1023/A:1014768806773>
- Vatsos, I. N. (2021). Planning and reporting of the histomorphometry used to assess the intestinal health in fish nutrition research—Suggestions to increase comparability of the studies. *Frontiers in Veterinary Science*, 8, 666044. <https://doi.org/10.3389/fvets.2021.666044>
- West, M. J., Slomianka, L., & Gundersen, H. J. (1991). Unbiased stereological estimation of the total number of neurons in the subdivisions of the rat hippocampus using the optical fractionator. *Anatomical Record*, 231, 482–497. <https://doi.org/10.1002/ar.1092310411>
- Wolfesberger, B., Tonar, Z., Witter, K., Guija de Arespacohaga, A., Skalicky, M., Walter, I., Thalhammer, J. G., & Egger, G. F. (2008). Microvessel density in normal lymph nodes and lymphomas of dogs and their correlation with vascular endothelial growth factor expression. *Research in Veterinary Science*, 85, 56–61. <https://doi.org/10.1016/j.rvsc.2007.07.008>

SUPPORTING INFORMATION


Additional supporting information may be found in the online version of the article at the publisher's website.

How to cite this article: Kolinko, Y., Malečková, A., Kochová, P., Grajciarová, M., Blassová, T., Kural, T., Trailin, A., Červenková, L., Havránková, J., Vištejnová, L., Tonarová, P., Moulisová, V., Jiřík, M., Zavaďáková, A., Tichánek, F., Liška, V., Králíčková, M., Witter, K., & Tonar, Z. (2021). Using virtual microscopy for the development of sampling strategies in quantitative histology and design-based stereology. *Anatomia, Histologia, Embryologia*, 00, 1–20. <https://doi.org/10.1111/ah.12765>

10.4 Příloha IV

JIŘÍK, Miroslav, TONAR, Zbyněk, **KRÁLÍČKOVÁ, Anna**, EBERLOVÁ, Lada, MÍRKA, Hýnek, KOCHOVÁ, Petra, GREGOR, Tomáš, HOŠEK, Petr, SVOBODOVÁ, Miroslava, ROHAN, Eduard, KRÁLÍČKOVÁ, Milena, LIŠKA, Václav, 2016. Stereological quantification of microvessels using semiautomated evaluation of X-ray microtomography of hepatic vascular corrosion casts. *International journal of computer assisted radiology and surgery*. 11(10), 1803–1819. ISSN 1861-6410. Dostupné z: <https://doi.org/10.1007/s11548-016-1378-3>
IF_(JCR2015) = 1,827 Q2 (Engineering, biomedical; Surgery)

Stereological quantification of microvessels using semiautomated evaluation of X-ray microtomography of hepatic vascular corrosion casts

Miroslav Jiřík^{1,6} · Zbyněk Tonar¹  · Anna Králíčková² · Lada Eberlová^{3,6} · Hynek Mírka^{4,6} · Petra Kochová¹ · Tomáš Gregor⁵ · Petr Hošek⁶ · Miroslava Svobodová⁶ · Eduard Rohan¹ · Milena Králíčková^{2,6} · Václav Liška^{6,7}

Received: 12 November 2015 / Accepted: 8 March 2016
© CARS 2016

Abstract

Purpose Quantitative description of hepatic microvascular bed could contribute to understanding perfusion CT imaging. Micro-CT is a useful method for the visualization and quan-

Electronic supplementary material The online version of this article (doi:10.1007/s11548-016-1378-3) contains supplementary material, which is available to authorized users.

B Zbyněk Tonar
zbynek.tonar@lfp.cuni.cz; tonar@ntis.zcu.cz

Miroslav Jiřík
mjirik@ntis.zcu.cz

Anna Králíčková
anna.kralicek@gmail.com

Lada Eberlová
lada.eberlova@lfp.cuni.cz

Hynek Mírka
mirka@fnplzen.cz

Petra Kochová
kochovap@ntc.zcu.cz

Tomáš Gregor
gregort@ntc.zcu.cz

Petr Hošek
petr.hosek@lfp.cuni.cz

Miroslava Svobodová
miroslavasvobodovams@gmail.com

Eduard Rohan
rohan@kme.zcu.cz

Milena Králíčková
milena.kralickova@lfp.cuni.cz

Václav Liška
liskav@fnplzen.cz

tification of capillary-passable vascular corrosion casts. Our aim was to develop and validate open-source software for the statistical description of the vascular networks in micro-CT scans.

Methods Porcine hepatic microvessels were injected with Biodur E20 resin, and the resulting corrosion casts were scanned with 1.9–4.7 μm resolution. The microvascular network was quantified using newly developed QuantAn software both in randomly selected volume probes ($n = 10$) and in arbitrarily outlined hepatic lobules ($n = 4$). The volumes, surfaces, lengths, and numbers of microvessel segments were estimated and validated in the same data sets with manual stereological counting. Calculations of tortuosity, radius histograms, length histograms, exports of the skeletonized vascular network into open formats, and an assessment of the degree of their anisotropy were performed.

¹ European Centre of Excellence NTIS, Faculty of Applied Sciences, University of West Bohemia, Univerzitní 22, 306 14 Pilsen, Czech Republic

² Department of Histology and Embryology, Faculty of Medicine in Pilsen, Charles University in Prague, Karlovarska 48, 301 66 Pilsen, Czech Republic

³ Department of Anatomy, Faculty of Medicine in Pilsen, Charles University in Prague, Karlovarska 48, 301 66 Pilsen, Czech Republic

⁴ Department of Imaging methods, Faculty of Medicine and University Hospital in Pilsen, Alej Svobody 80, 304 60 Pilsen, Czech Republic

⁵ New Technologies - Research Centre, University of West Bohemia, Univerzitní 8, 306 14 Pilsen, Czech Republic

⁶ Biomedical Center, Faculty of Medicine in Pilsen, Charles University in Prague, Alej Svobody 76, 323 00 Pilsen, Czech Republic

⁷ Department of Surgery, Faculty of Medicine in Pilsen, Charles University in Prague, Husova 3, 306 05 Pilsen, Czech Republic

Results Within hepatic lobules, the microvessels had a volume fraction of 0.13 ± 0.05 , surface density of $21.0 \pm 2.0 \text{ mm}^{-1}$, length density of $169.0 \pm 40.2 \text{ mm}^{-2}$, and numerical density of $588.5 \pm 283.1 \text{ mm}^{-3}$. Sensitivity analysis of the automatic analysis to binary opening, closing, threshold offset, and aggregation radius of branching nodes was performed.

Conclusion The software QuantAn and its source code are openly available to researchers working in the field of stochastic geometry of microvessels in micro-CT scans or other three-dimensional imaging methods. The implemented methods comply with reproducible stereological techniques, and they were highly consistent with manual counting. Preliminary morphometrics of the classical hepatic lobules in pig were provided.

Keywords Liver · Microvessels · Pig · Porcine · Python · Stereology · X-ray microtomography

Introduction

Clinical and experimental background of research on hepatic microcirculation

Recent research on experimental liver imaging aims to improve the precision of instrument guided liver surgery [1] and the automatic registration of intraoperative three-dimensional (3-D) ultrasound (US) and preoperative computed tomography (CT) [2]. Detection methods are being developed for the automatic segmentation of liver lesions [3]. Moreover, decision-making and planning the resection strategy in liver surgery are based on preoperative planning data acquired using CT, magnetic resonance imaging (MRI), or US [4], thus creating risk maps in liver surgery planning [5,6] or the planning of selective liver embolization [7]. However, liver microcirculation, which is of extreme importance for the transport of nutrients, biotransformation of metabolites, detoxification of harmful molecules, and synthesis of plasma proteins, still represents a background noise in routine CT, MRI, and US examinations. Current research approaches on hepatic microcirculation involve methods applicable in vivo, methods based on biopsies and histological analyses, and methods for non-survival experiments. Two-dimensional histological studies [8] provide great planar resolution, but only limited insight into the 3-D liver microcirculation. Even advanced histological studies [9] provide information gathered from 100- μm -thick tissue blocks at maximum. This can be improved using registration of multiple scanned histological slides guided by vessel structures [10,11]. The gap between the macroscopic imaging and histological evaluation can be bridged using micro-CT (X-ray microtomography

[12]) for the visualization and quantification of capillary-passable vascular corrosion casts.

Quantification of hepatic microcirculation

A recent quantitative study on three-dimensional capillary networks showed that an in-depth comparison is able to differentiate statistically between the microvessels in healthy and cancerous tissues [13]. A number of parameters were tested for this analysis, including the vessel diameters, branching densities, branching angles, vessel lengths, tortuosity, fractal dimension, and vessel volume fraction [13]. In quantitative studies, blood vessels may be represented using either conventional 3-D shape reconstructions based on particular observations or statistical models using continuous variables and generating. A comparison of the pros and cons of both approaches was recently given [14]. In microvessels, the shape variability exceeds the usual macroscopic interindividual and intraindividual morphological differences, which is a serious advantage of the stochastic geometry. This stereological approach does not aim to capture and reconstruct every single capillary, sinusoid, arteriole, or venule, but rather it relies on a statistical description of their geometry. One of the benefits of stochastic geometry is that it is possible to generate vascular trees with known statistical properties or with their various modifications, such as increased length density, branching density, and surface. Statistical models and the stereological approach are more robust to such technical problems because each source of bias may be identified, and its weight is inversely proportional to the number of stereological events counted (i.e. intersections with the stereological grids) [15,16].

The typical diameter of porcine hepatic microvessels (sinusoids) is approximately 15 μm [17]. If each of the microvessels is to be represented by at least 3–4 voxels, a reliable visualization of hepatic microvessels requires a resolution of approximately 5 μm . In experimental studies on liver microcirculation and regeneration after surgical resection [18], porcine liver is currently the best described and most suitable large animal model of human liver in terms of the organ size as well as gross and microscopic morphology and physiology. Due to the great local variability and anisotropy expected in hepatic microcirculation in pigs, an extensive sampling of periportal and peripheral regions of various hepatic lobes would be necessary to obtain representative data samples. However, even small samples of liver contain great numbers of microvascular structures. Preliminary results showed that a typical liver tissue block of $5 \times 5 \times 5 \text{ mm}$ (125 mm^3) may contain approximately 30,000–40,000 microvessel segments, with a total surface area of approximately 600 mm^2 and length of 10,000 mm [17]. To develop this technique in 3-D, an efficient and automated method for quantitative morphometry is necessary. Filling

this gap in the present knowledge would improve our understanding of normal hepatic circulation, the rearrangement of the hepatic vascular bed during portal hypertension, regenerating liver after surgical resection [18], experiments on liver cirrhosis or biliary obstruction, and in liver tumours and metastases. Therefore, the motivation of our study was to develop a reproducible method of assessment of hepatic microcirculation in a porcine model. We also aimed to validate the automatic method by comparing its results with manual quantification [19].

Aims of the study

For a statistically robust quantitative evaluation of the vascularization of organs, design-based stereological methods are available as the gold standard (for a review, see [20]). Unfortunately, even though the commercially available software packages supplied with most of the micro-CT facilities are quite efficient in thresholding the structures of interest and creating visual reconstructions, these software packages do not allow for the use of stereological variables for the statistical description of the vascular networks. Therefore, the aims of our study were as follows:

- To develop an open-source software for quantitative evaluation of microvessels in micro-CT scans.
- To validate the automatic quantification results against manually controlled stereological estimates of hepatic microvascular parameters. The following null hypothesis $H_0(A)$ should be tested: “Both the manual and automated methods give equivalent results describing the volumes, surfaces, lengths, and numbers of hepatic microvessels”.

Materials and methods

Animals and specimen preparation

Corrosion casts were prepared using livers of two piglets (aged 6 and 10 weeks, $m = 12$ and 25 kg, respectively) killed at the experimental facilities of the Biomedical Center of the Faculty of Medicine in Pilsen, Charles University in Prague. The animals were given appropriate care, and all the procedures were prepared and performed under the law of the Czech Republic, which is compatible with the legislation of the European Union. The detailed procedure of corrosion casting was recently described [21]. Briefly, before hepatectomy, the hepatic vascular bed was heparinized to prevent formation of thrombi. The liver and the blood vessels were kept under water to prevent air embolism. Biodur E20 Plus resin (Biodur Products, Heidelberg, Germany) was injected into the portal vein until it reached the caudal caval vein

and also the hepatic proper artery. After 24 h of polymerization, the liver tissue was removed using a corrosive 15 % potassium chloride solution (Fig. 1a). The left lateral hepatic lobe was removed, rinsed in 70 % alcohol, frozen in distilled water, and cut into $2 \times 1 \times 1$ cm ice blocks using a band saw (Fig. 1b).

The quality of the casts was controlled by scanning electron microscopy (Fig. 1c–d). This technique verified that interlobular veins, their circumlobular branches, liver sinusoids, and central veins were well filled. However, most interlobular arterioles and their periportal branches were not filled by the resin and therefore not included into the analysis. Most probably the capillary-passable polymer spread also through anastomoses between the portal and the arterial system at the level of greater vessels of these vascular trees. Blocks approximately $1 \times 1 \times 0.5$ cm were mounted on copper foils and fixed using wire stubs with conductive silver paste and sputtered with gold for 60 s [21,22]. Specimens were examined using a Stereoscan 250 SEM (Cambridge, U.K.) at an accelerating voltage of 10 kV. Preliminary imaging was performed with an SEM SU-70 (Hitachi, Japan) using an accelerating voltage of 1 kV. The scanning electron microscopy protocol did not require any pretreatment of specimens.

Micro-CT

Two randomly selected specimens were scanned using a stationary micro-CT device (Xradia XCT 400, Xradia, Pleasanton, CA, USA). To ensure high-resolution scanning and low spot size, an accelerating voltage of 20–60 kV was used with a power of 4 W. For each sample, 1000 images were obtained with a pixel size ranging between 1.88 and 4.68 μm . Two types of subsets of the scanned data sets were evaluated: (i) randomly cropped areas ($n = 10$) of 350×350 pixels, each consisting of 50 sections, and (ii) manually selected areas ($n = 4$) representing classical morphological hepatic lobules. The randomly sampled volume probes and manually selected hepatic lobules are illustrated in Fig. 1e,f.

Manual quantification: spatial statistics of hepatic microvessels

The stereological parameters used for the morphometry of the microvessels are listed in Table 1. Briefly, the reference volume and the volumes of microvessels were estimated using the point-counting technique (Fig. 2a, b) and the Cavalieri principle [23,24]. The surfaces of the microvessels were quantified using the fakir probe [25], which consists of an isotropic grid with three differently oriented sets of probes with random initial orientation (see Fig. 2c, d). The lengths of the microvessels were obtained using manually traced microvessel profiles with retained 3-D spatial orientation.

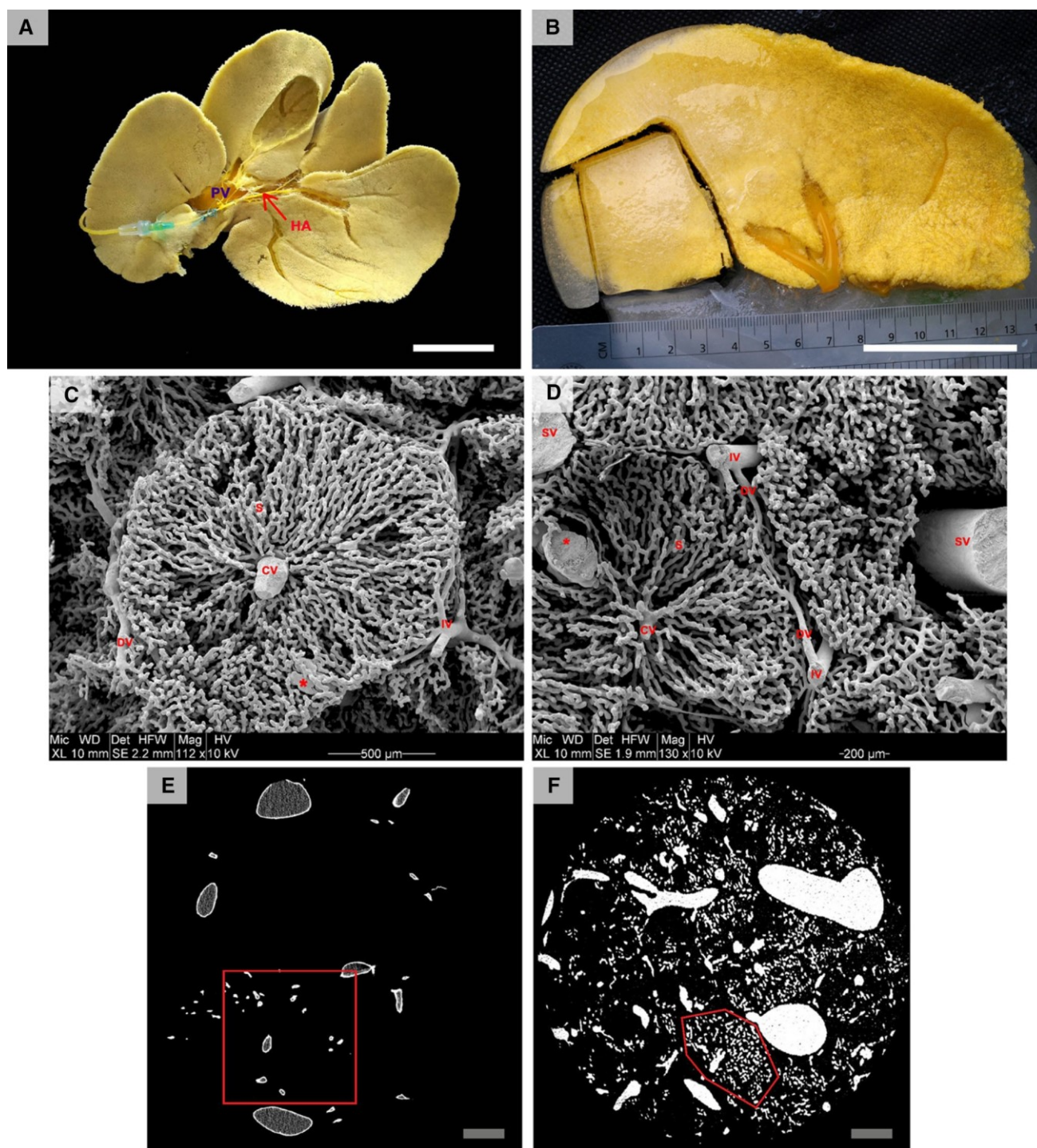


Fig. 1 Vascular corrosion casts of hepatic microcirculation and sampling of the micro-CT images. **a** Corrosion cast preparation of porcine hepatic blood vessels filled with Biodur E20 Plus (yellow). Visceral surface is shown with portal vein (PV) and hepatic artery proper (HA); *scale bar* 5 cm **b** left lateral lobe cut in ice blocks; *scale bar* 5 cm. **c, d** scanning electron micrographs showing the quality of the filling of the microvessels with the capillary-passable polymer: CV central vein, DV distributing (circumlobular) portal vein, IV interlobular (conducting)

portal vein, S sinusoids, SV sublobular vein; *asterisk* resin extravasation. Most interlobular and circumlobular arterioles and their peribiliary plexuses are not filled. **e, f** Samples of the micro-CT scanned stacks. **e** Randomly selected cropped area of 350×350 px (*red square*) from a data set scanned with pixel resolution $1.88 \mu\text{m}$. *Scale bar* $200 \mu\text{m}$. **f** Manually selected region representing microvessels of one hepatic lobule (*red polygonal area*) from a data set scanned with pixel resolution $4.67 \mu\text{m}$, *scale bar* $500 \mu\text{m}$

Table 1 Stereological parameters used for morphometry of the microvessels

Parameter	Abbreviation	Unit	Definition	Possible biological interpretation [11,15,49]
Volume fraction	V_V	(-)	Volume of microvessels/reference volume	Relative volume of the tissue occupied by the blood vessels
Surface density	S_V	(mm^{-1})	Surface of microvessels/reference volume	Relative surface area available for exchange of metabolites
Length density	L_V	(mm^{-2})	Length of microvessels/reference volume	Length related to the vascular resistance and tissue perfusion, depending also on the degree of branching
Numerical density	N_V	(mm^{-3})	Number of microvessels/reference volume	Showing the degree of branching and connectivity of the vascular network, reflecting the angiogenesis

The numerical density of the microvessels was quantified by counting branching nodes with a known valence in 3-D using the unbiased disector method [26], as follows:

$$\text{est } N_V(\text{nodes}) = \frac{\sum_{i=1}^n Q_i^-(\text{nodes}) \cdot p}{\sum_{i=1}^n P_i(\text{ref})} \cdot \frac{1}{a \cdot h} \quad (1)$$

where $\text{est } N_V(\text{nodes})$ is the estimated number of branching nodes per unit volume of the reference space, $Q_i^-(\text{nodes})$ is the number of nodes counted within the i th disector, $P_i(\text{ref})$ is the number of points of the auxiliary grid hitting the reference space, p is the total number of points of the auxiliary grid, a is the area of the counting frame, h denotes the height of the disector, and n is the number of disectors (sampling bricks). The counting is illustrated in Fig. 2e, f. Having counted the branching nodes, the connectivity of the microvascular system was described based on these nodal points, where the number of vessels that merged there was recorded for each of the observed nodes (valence of branching nodes), resulting in the parameter P_n defining the number of nodes of valence n . Based on this, it was possible to calculate the numerical density of microvessel segments, i.e. the number of microvessels per unit volume of tissue $N_V(\text{microvessels})$ using Eq. 2. This was based on the relation introduced by Lokkegaard et al. [27], but it was modified by adding the +1 member at the end of the equation to represent a continuous capillary network, as follows:

$$N_V(\text{microvessels}) = \frac{N(\text{microvessels})}{V(\text{ref})} = \frac{\sum_{i=1}^n \binom{n-2}{i} \cdot \frac{P_i}{2}}{\sum_{i=1}^n v(\text{dis})} + 1 \quad (2)$$

All the manual stereological quantification was performed using the Ellipse software (ViDiTo, Košice, Slovak Republic).

Automatic quantification: algorithm and software development

Identical image data sets ($n = 14$) that underwent manual quantification were analysed using our newly developed software QuantAn. The program was written in the Python

programming language. The software runs under Linux, Windows, or Mac OS operating systems. The QuantAn application is designed to quantitatively measure 3-D data from 3-D file formats (DICOM, MetaImage, Nrrd, TIFF) or from stacks of images (JPEG, BMP, TIFF, DICOM). The basic concept of the algorithm (Table 2) is a simplification of the target volume by the decomposition of the connected objects to simple linear segments and their joints (skeletonization). Most of the application functions can be performed non-interactively by using command line parameters.

Calibration (pixel spacing and slice spacing) is read from the source files, but it may be manually overridden by the user, if necessary (Fig. 3a). The user defines the region of interest (ROI) by using a crop tool to select an orthogonal data subset (Fig. 3b). For the x-, y-, and z-axes, the user marks voxels on the border of a requested area. If the orthogonal selection is insufficient, a more complex tool can be used, and a convex 3-D ROI is obtained from the various border pixels in the slices. This object can be added to or subtracted from the previously labelled ROI (Fig. 3c), and therefore, the final ROI can have a non-convex shape. A visual orientation within high dynamic range data is provided using a windowing function that maps a range of pixel values to a greyscale map, and it allows for controlling image contrast according to the user requirements.

The segmentation of data is performed by a combination of Gaussian filter preprocessing, thresholding, and binary opening and binary closing [28]. This procedure is controlled via threshold sliders in segmentation graphical user interface (GUI). Using threshold sliders, the automatic threshold sug-

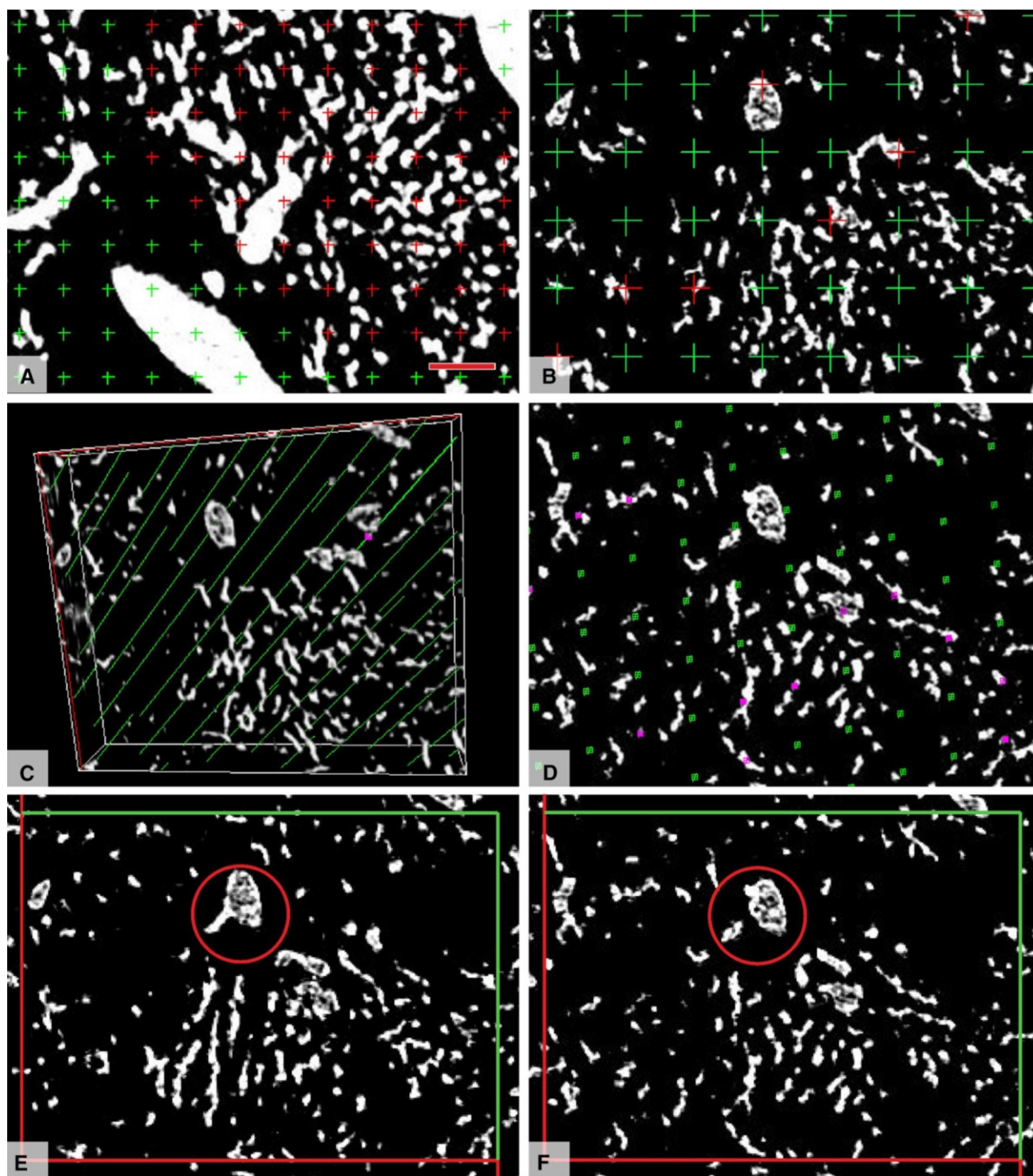


Fig. 2 Steps during the manual quantification of the micro-CT images of hepatic lobules. **a, b** The reference volume in the hepatic lobules and the volume of the microvessels was quantified using a randomly positioned stereological point grid and the Cavalieri principle. The points hitting the reference volume (**a**) or the microvessel profiles (**b**) were counted (*marked red*). The number of the intersections between the grid points and the reference volume (**a**) or microvessels was proportional to the volume of the reference region of interest (**a**), or to the volume of microvessels (**b**). Greater vessels with diameter $>60\ \mu\text{m}$ not belonging to the microvessels were omitted. **c, d** Surface of the microvessels

was quantified using isotropic fakir probes. The intersection lengths of the probes (*marked purple* on **d**) are proportional to the surface of the microvessels. **e, f** To calculate the number of microvessels, branching nodes were counted using the disector method. Once the branching nodes were found (**e**), they were tracked within the stack until they disappeared, and then they were counted, provided that they did not touch the forbidden borders (*red*) and were within the counting frame (or touching the *green allowance borders*). An example of a branching node with valence 3 is outlined in a circle (**e, f**). Scale bar $100\ \mu\text{m}$ shown in A, uniform calibration in all images (**a-f**)

Table 2 Outline of the steps of the algorithm

Input: Three-dimensional volumetric data with known size of voxel are read

1. Definition of the region of interest
 - 1.1. Orthogonal cropping
 - 1.2. Modifications of the region of interest (optional)
2. Segmentation
 - 2.1. Setting connected component seed (optional)
 - 2.2. Smoothing
 - 2.3. Thresholding
 - 2.4. Binary morphology postprocessing
3. Simplification
 - 3.1. Skeletonization
 - 3.2. Skeleton decomposition
 - 3.3. Aggregation of branching nodes (with user settings)
4. Quantitative analysis of the skeleton (Repeat step 4 for each vascular segment)
 - 4.1. Lengths of the vascular segments
 - 4.2. Radius of the vascular segments
 - 4.3. Volume of the vascular segments
 - 4.4. Numerical density of the vascular segments
5. Surface estimation

Output: Estimation of quantitative parameters (volume fraction of microvessels, surface density of microvessels, length density of microvessels, numerical density of microvessel segments, tortuosity, radius histogram, length histogram), and export of the results.

gested by the software for segmentation may be modified by the user. The user can set the segmentation seed in the beginning of this step (Fig. 3d). This seed is used to include a connected object only in the segmentation output (Fig. 3e). After the segmentation step, the data are processed with the 3-D skeletonization algorithm [29]. The branching nodes of the vascular segments are automatically detected, but the user may aggregate adjacent branching nodes (Fig. 3f) by setting the aggregation radius. If the detected branching points are closer than the aggregation radius, their spherical envelopes overlap and the points are not counted separately (Fig. 4). The preprocessing parameters used in our study were as follows: Gaussian filtering and binary opening were turned off; default number of iterations of binary closing was 2, the aggregation radius was 15 μm , and the threshold ranged between 1300 and 3800. A simple algorithm for estimating the recommended threshold value based on the widely used Otsu method [30] is provided. Examples of the skeletonized data are shown in Supplement 1.

A quantitative description of the vascular system is based on an analysis of each segment (Fig. 3g). The length is calculated using curve fitting. The radius is calculated via an averaging of the distance of a skeleton voxel to the nearest segment border [28]. The length, radius, and endpoints

of the segment are used for the calculation of other metrics. The surface density is calculated using the stereological isotropic fakir method [25]. There are two types of output: graphical (Fig. 3h) and numerical (quantitative). The numerical outputs are the values of the same parameters as estimated during the manual quantification (see Table 1), but they also include the following parameters: tortuosity (3-D length divided by the distance of both endpoints), histograms showing the distribution of vessel segment lengths with user-controlled number of histogram bins, and histograms showing a distribution of vessel segment diameters with user-controlled number of histogram bins. The quantitative data for all segments are exported as CSV files. These either are readable by spreadsheet applications, or could be processed by data scripts. Finally, the vessel skeleton is exported in the YAML open file format. For processing a stack consisting of 250×300 50 voxels using a computer with 8x Intel(R) Core(TM) i7-3770 @ 3.40GHz processor, 16 GB RAM, and NVIDIA GeForce GT 640 graphical adapter, the computational time is approximately 4 min. Routinely, the interactive settings take another 3 min.

Evaluation of isotropy of hepatic microvessels

Using the automatically traced skeletons of the microvessels, the degree of isotropy was evaluated separately for both randomly cropped regions and manually cropped lobules using three previously published methods: the $p(\chi^2)$ method, the *ellipsoidal anisotropy*, and *fractional anisotropy* [31–33]. The $p(\chi^2)$ method is based on the comparison between the observed length densities of lines and the discrete uniform distribution of the isotropic line system with the χ^2 test [33]. If the value of the length density is uniform in all directions, the system is isotropic. If there are some preferred directions with higher values of length density than in the other directions, the system is anisotropic. The p value of the test with the null hypothesis stating that the system of microvessels is isotropic is determined. This hypothesis should be rejected when $p(\chi^2) < 0.05$. The *ellipsoidal and fractional anisotropy* is based on counting eigenvalues of the length-weighted average tensor of the lines orientation [31]. The values of the *fractional anisotropy* range from 0 (isotropy) to 1 (absolute anisotropy), and the *ellipsoidal anisotropy* ranges from 1 (isotropy) to infinity (absolute anisotropy). The resulting line systems representing the number and orientation of microvessels in the liver were defined by the directions of the individual lines and their lengths. The space was divided into 100 regions given by angles of elevation and azimuth in such a way that all tetragons on the surface of the sphere bounded by subsistent azimuths and elevations had equal area. Azimuths are in the interval $[0, 2\pi]$. Elevations are from the interval $[0, \pi/2]$ and take the symmetry with respect to the origin into

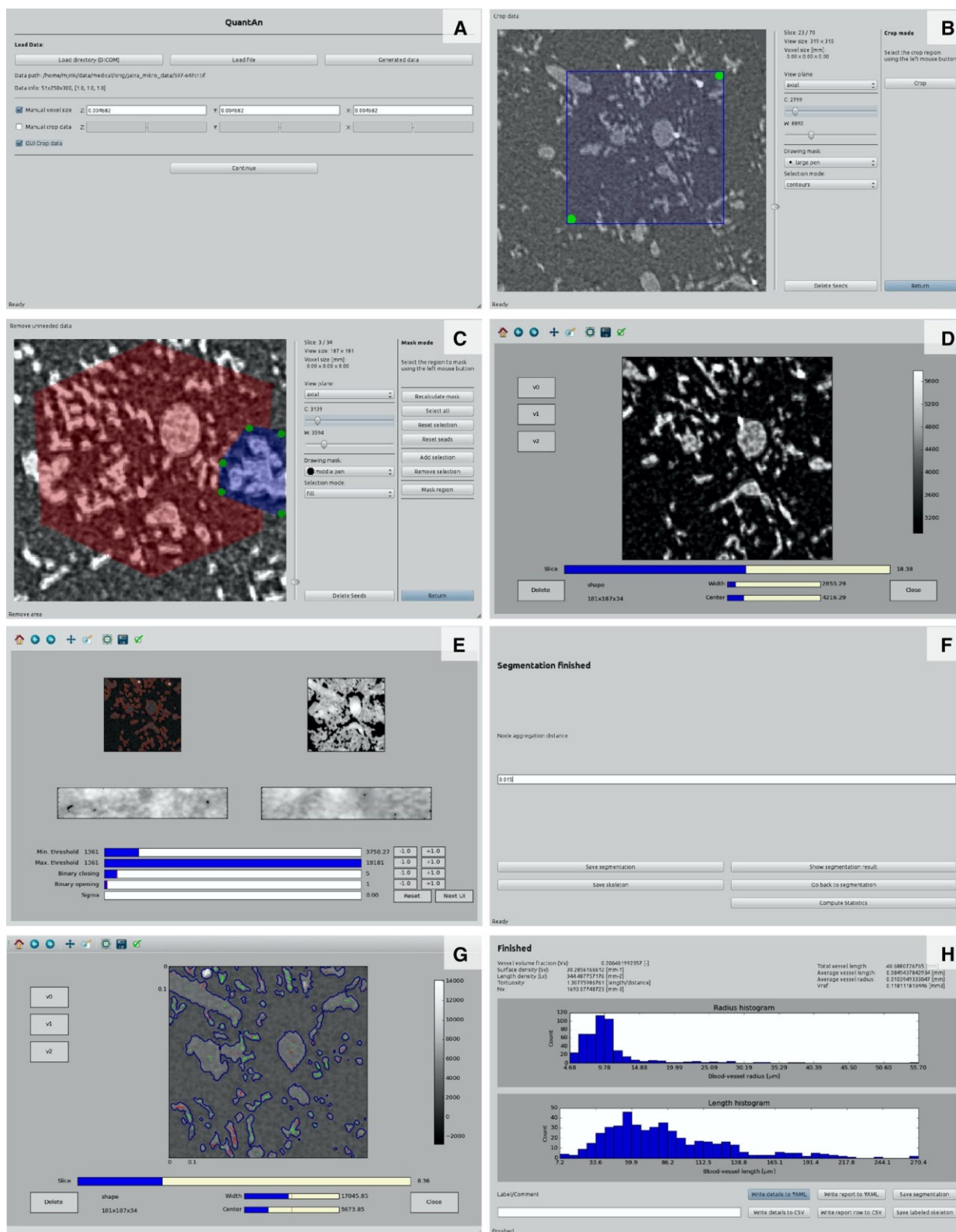


Fig. 3 Main steps during the automated quantification of the microvessels acquired with micro-CT and processed with the QuantAn software. **a** Input of the image data sets and calibration. **b** Cropping the region of interest using a drawing mask. **c** Additional modification of the region of interest by adding or subtracting areas in individual slides. **d** Setting

connected component seed samples at the beginning of skeletonization. **e** Thresholding. **f** Adjusting the distance below with adjacent branching nodes should be aggregated. **g** Reviewing the segmentation results. **h** The Results window with main quantitative characteristics and optional export of the results into statistical report files

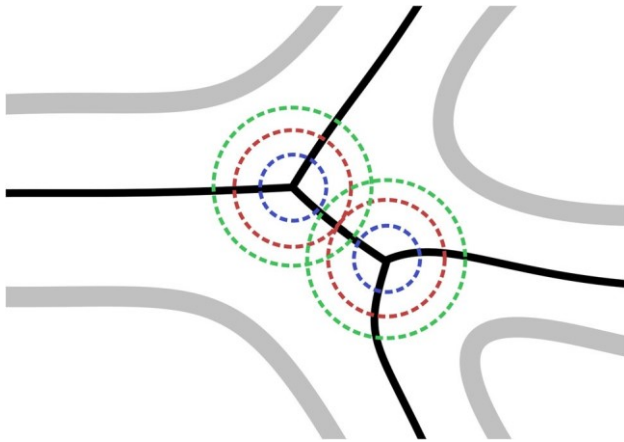


Fig. 4 Aggregation radius of the branching points. An important step during the analysis of the skeleton is to find the suitable size of aggregation radius to separate any adjacent branching nodes of the vascular skeleton. In our study, the optimum size was $15\ \mu\text{m}$, but the actual value may vary according to the vessels diameter and image data resolution. The picture shows the original microvessels (*grey borders*), their skeleton (*black lines*), and three pairs of circles representing the equators of 3-D spheres with various size: if the aggregation radius corresponds to the *blue spheres*, both branching nodes are counted separately; should the radius exceed the one of the *red spheres* and result into *green overlapping spheres*, the branching nodes are merged and counted as a single branching point

account. We used open software Esofsy [32] for isotropy quantification of hepatic microvessels.

Statistics

Shapiro–Wilk’s W test was used for the normality testing of the data. In some of the aortic segments, the distribution of the values differed from the normal distribution; therefore, we used nonparametric statistics for further analysis. The Wilcoxon matched pairs test was used to compare the automatic method with the manual estimates. The correlation between the automatic and manual quantification was evaluated using the Spearman correlation coefficient and Pearson linear correlation coefficient. These tests were used as available in the Statistica Base 11 package (StatSoft, Inc., Tulsa, OK, USA). Concordance correlation coefficients were calculated as first proposed and later corrected by Lin [34,35] using an online calculator [36].

Results

Open-source software for quantitative evaluation of microvessels

The source code of our software named QuantAn, which was written in the Python programming language, and all of the files necessary for its launching, the calculation of the results,

and the production of all graph types have been made openly available to the scientific community [37]. Analysis of sensitivity of the automatic processing of the micro-CT image data on binary opening, binary closing, threshold offset, and the aggregation radius of the branching nodes is shown in Fig. 5, with source data available in Supplement 2. Examples of effects of binary opening, binary closing, and Gaussian filter on preprocessing before the segmentation are shown in Supplement 3.

Comparing the manual and automated methods for evaluating the spatial statistics of hepatic microvessels

The complete data set with all the morphometric results obtained with the automatic method and with the manual counting for all of the samples is provided in Supplement 4. The data are shown in Fig. 6. Using the Wilcoxon matched pairs test, no significant differences between the automatic and the manual quantification were found in any of the following parameters: the volume fraction of microvessels (Fig. 6a), the surface density of microvessels (Fig. 6b), the length density of microvessels (Fig. 6c), and the numerical density of the microvessels (Fig. 6d). Both methods had a moderate to high concordance and were highly statistically correlated (Table 3).

Preliminary quantitative characteristics of morphological hepatic lobules

When calculating the four regions with arbitrarily selected morphological hepatic lobules, the following morphometric characteristics were found (mean \pm SD): In the lobules, the volume fraction of microvessels was 0.1 ± 0.05 , their surface density was $21.0\pm 2.0\ \text{mm}^{-1}$, their length density was $169.0\pm 40.2\ \text{mm}^{-2}$, and the numerical density of microvessels was $588.5\pm 283.1\ \text{mm}^{-3}$ (see Supplement 4 for the complete data set). Histograms showing the distribution of lengths and radiuses of microvessels within the hepatic lobules are demonstrated in Fig. 7b, d and compared to the distribution of microvessels within random hepatic volume probes (Fig. 7a, c). The original data for the histograms shown in Fig. 7 are provided in Supplement 5.

Evaluation of isotropy of hepatic microvessels

Based on the results of the $p(\chi^2)$ methods, the null hypothesis that the orientation (Fig. 8a) is isotropic can be retained in four selected samples of the hepatic lobules only, but it is rejected in ten volume probes sampled randomly from various parts of the liver (Fig. 8b and Supplement 4). This is in agreement with the *ellipsoidal and fractional anisotropies*, where the values are closer to zero than one in the ellipsoidal

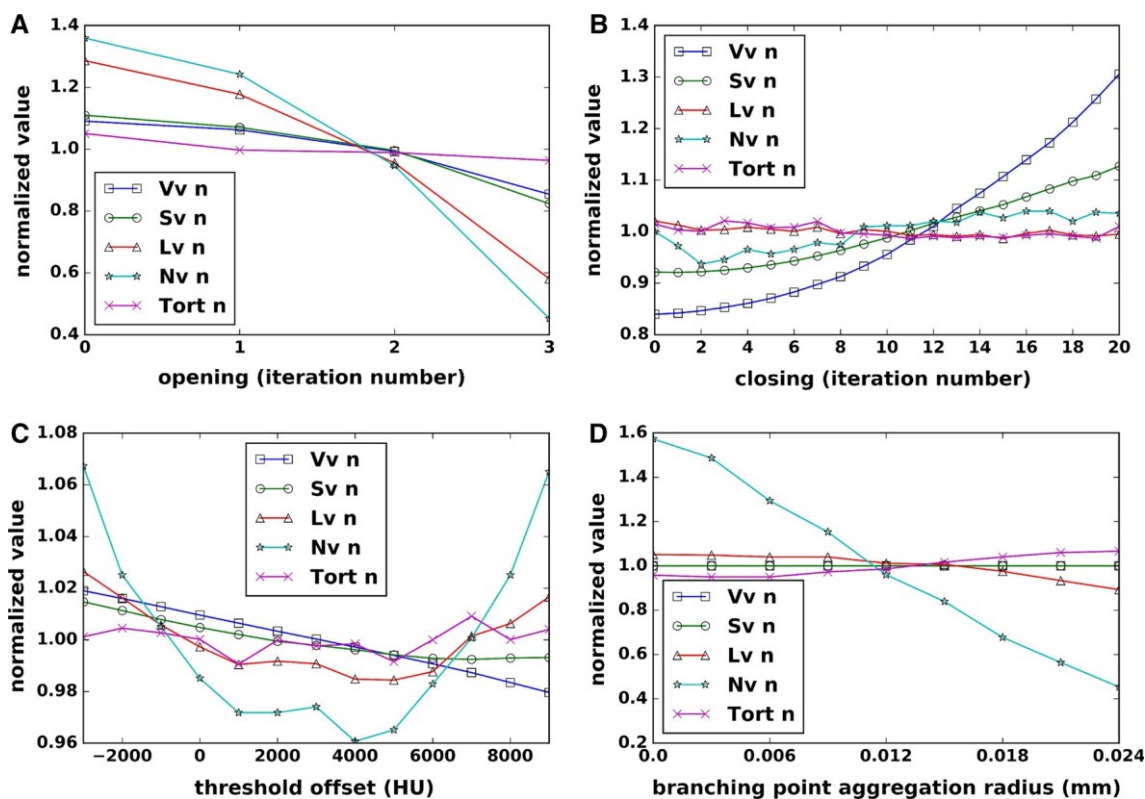


Fig. 5 Analysis of sensitivity of the automatic processing of the micro-CT image data. The effect of binary opening (a), binary closing (b), threshold offset (c) and the aggregation radius of the branching nodes (d) is shown. The normalized values (n) of the volume fraction (V_V), surface density (S_V), length density (L_V), numerical density (N_V), and

tortuosity ($Tort$) of microvessels were calculated as a ratio between the values for the present parameter plotted on the x-axis and the values averaged for all values within the tested range. HU Hounsfield density units. The source data to the graphs are available in Supplement 2

anisotropy case, and they are close to one in the fractional anisotropy case (Fig. 8b). However, pure isotropy was not detected, as in every case, a number of preferential directions were observed even though it was high. Isotropic samples from the hepatic lobules are demonstrated in Fig. 8c, e, and anisotropic samples from randomly selected volume probes are shown in Fig. 8d, f.

Discussion

Automatic quantification of volumes, surfaces, lengths, and numbers of microvessels was validated

The morphometric results obtained using the automatic method were not statistically distinguishable from the manually verified counting. Therefore, the $H_0(A)$ null hypothesis is retained, and the software is recommended for further quantification of all the four variables. Whereas the concordance between the manual and automatic measurement was satisfactorily high in surface and length densities (Table 3), it was only moderate in volume fraction and numerical density. The

scatterplots (Fig. 6) suggest that the source of bias came from the irregular borders of the hepatic lobules, but not from the randomly sampled excisions. Our results were achieved when working with the resolution of 1.9–4.9 μm , and this accuracy proved to be more than sufficient with respect to the typical dimensions of the smallest hepatic microvessels observed in our study (approximately 12–15 μm in diameter). The analysis of sensitivity showed that too many iterations of the binary opening (erosion followed by dilatation) result in loss of small objects and image details, including the branching points and whole vascular segments. Too many iterations of binary closing (dilatation followed by erosion) result in fusion of smaller objects and may increase the volume significantly. The automatic analysis of the skeleton branching nodes (and therefore also of the number of microvessels per volume unit calculated from the branching nodes) was mostly affected by the binary opening during the preprocessing and also by the aggregation radius of the branching points. The recommended value of the aggregation radius of the adjacent branching nodes is equal to the typical expected radius of the vessels in the data set. For our final results, the value of 15 μm was used. This parameter greatly affected the disec-

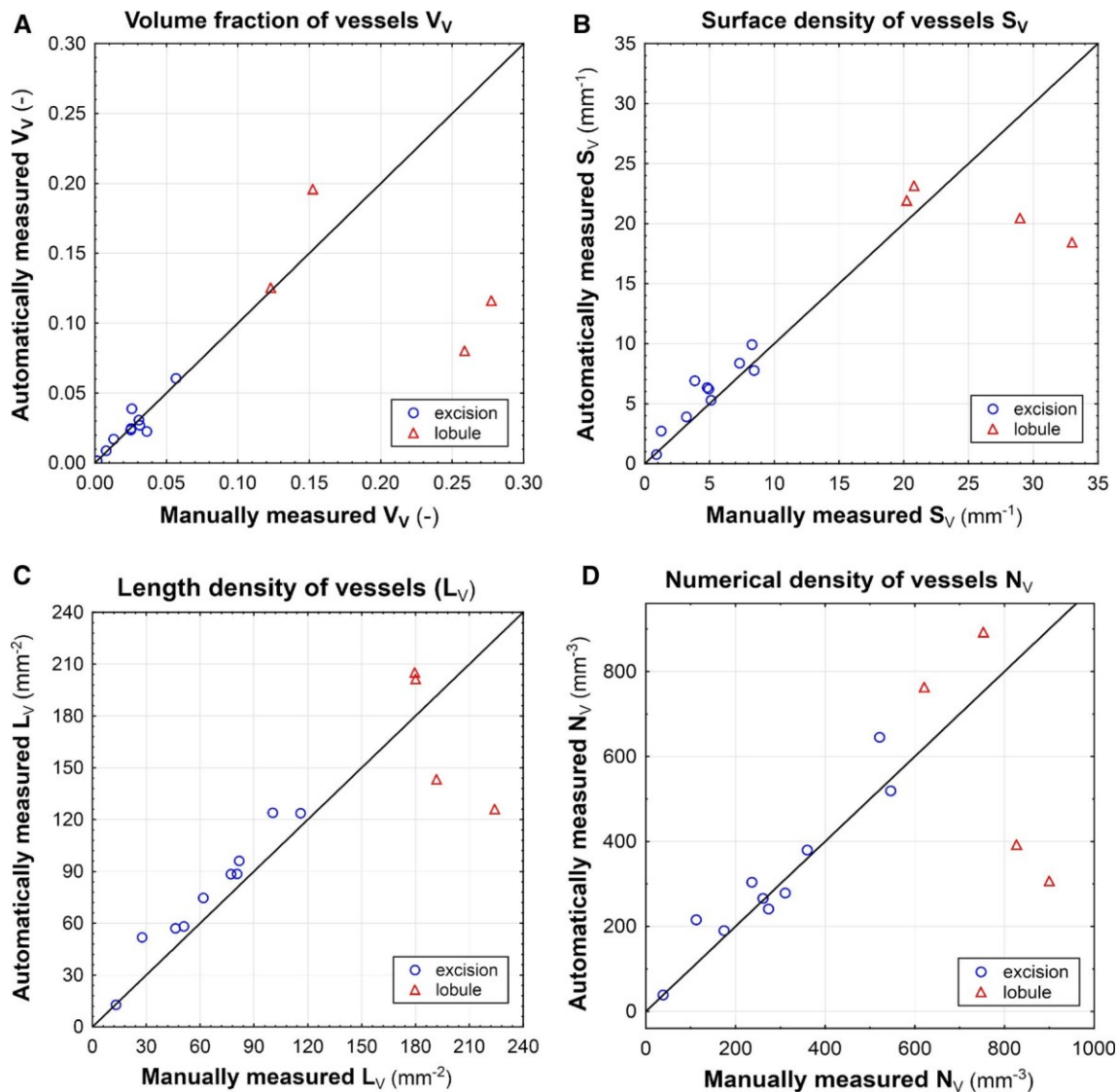


Fig. 6 Comparison of the automated and manual method. In all of the 14 data sets under study (ten excisions and four morphological lobules), four morphometric parameters were estimated using the automatic and the manual method, namely the volume fraction of microvessels (a), the surface density of microvessels (b), the length density of microvessels

(c), and the numerical density of the microvessels (d). No significant differences between the two methods were found in any of the parameters using the Wilcoxon matched pairs test. Data are displayed as scatterplots

tor counting rules and therefore the numerical density. Any users of the QuantAn software should not be satisfied with the default software settings, but they are encouraged to tailor their own settings corresponding to the contrast, resolution, and dimensions of microvessels within the image data. Inappropriate settings of the aggregation radius for the adjacent branching nodes may result in up to approximately 80–100% bias in the numerical density of vessel segments and 20% bias in the length density. To minimize the risk, the software allows for instant preview of the effects of settings of these parameters in the selected and zoomed region of interest.

Limitations of the study

Due to the low number of regions representing the hepatic morphological lobules ($n = 4$), the quantitative results provided in this feasibility study are preliminary only and need further verification in various parts of hepatic lobes. Although the corrosion casting technique provided great contrast to the micro-CT, the filling of all the capillary spaces depends on the injection pressure. Therefore, the repeatability of the corrosion casting needs to be tested. For a complete review on hepatic microvessels, the corrosion casting technique needs to be improved to fill also the interlobular arteries. We are

Table 3 Concordance correlation coefficients, Spearman's rank order correlations, and Pearson's linear correlations between the automatic and manual quantification

Parameter	Concordance	Spearman	Pearson
V_V	0.61	0.89*	0.72*
S_V	0.86	0.90*	0.91*
L_V	0.84	0.95*	0.86*
N_V	0.64	0.82*	0.65*

In four of the parameters (volume fraction V_V , surface density S_V , length density L_V , and numerical density N_V), the automatic method had a moderate to high concordance [34,35] with the manual measurements. All four parameters highly correlated with the manual measurements. Spearman and Pearson correlations significant at $p < 0.05$ are marked (*)

also aware of the fact that, unlike in vivo diagnostic methods [38], corrosion casting specimens do not entirely correspond to dynamic changes in real organ perfusion. Of course, corrosion casting does not provide information on the histological context of the microvessels, which is necessary for some tasks [9,39]. The spatial coordinate systems used for the evaluation of isotropy of the hepatic microvessels were not related to the anatomical directions. A more detailed analy-

sis of the isotropy of hepatic vessels remains to be performed in a separate study, but the present results proved the feasibility of the study. The algorithmic results were compared to the manual stereological measurements, because interactive stereological methods are widely accepted gold standard used for quantification of microvessels. So far, it was impossible to statistically discriminate between the automatic and manual method of quantification and the negative hypothesis of the study was retained. Moreover, it has to be noted that unlike the analysis of volumes, surfaces, lengths, and numbers of microvessels, the automatic analysis of lengths and radius of the microvessels (Fig. 7 and Supplement 5) has not been validated yet.

Relevance of the results to the medical research

Improving therapeutic possibilities in liver tumours induces increased demands on diagnostic imaging. The currently popular concept of multiparametric imaging utilizes, in addition to anatomically oriented methods, techniques of functional imaging, which, among others, include perfusion CT, perfusion MRI, or perfusion US. They are based on the evaluation of the kinetics of a tracer (e.g. contrast

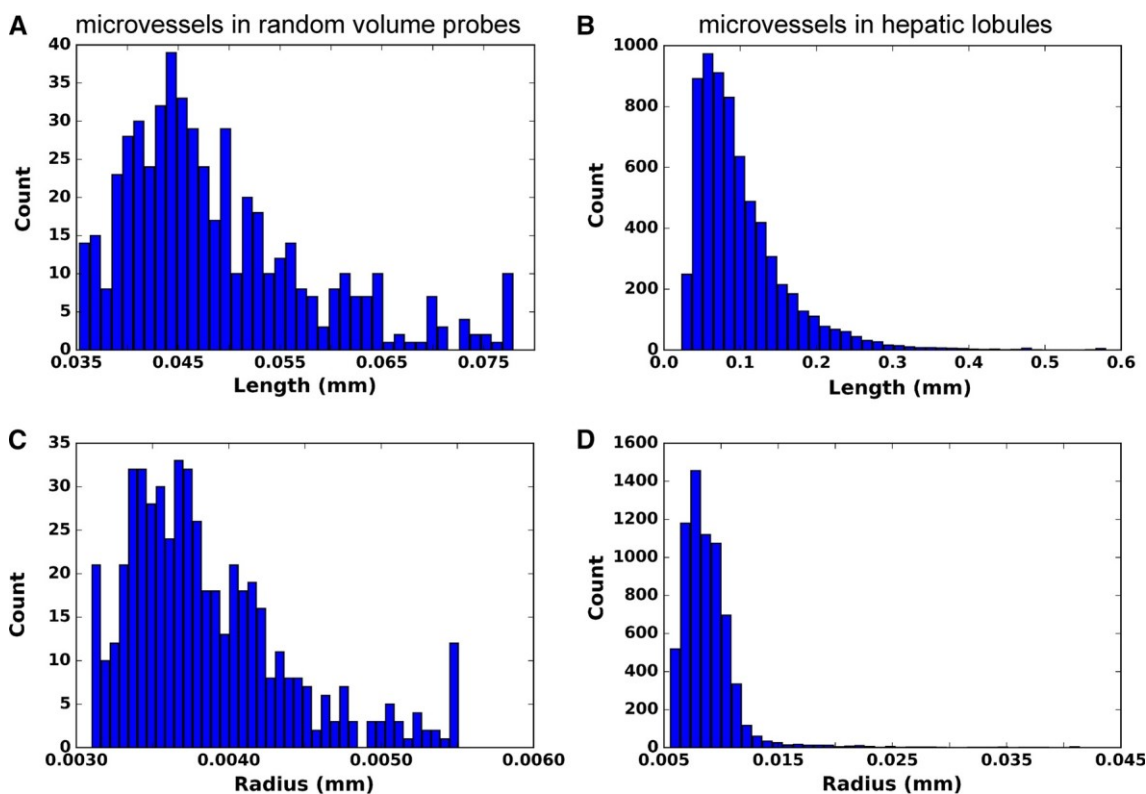


Fig. 7 Histograms of length and radius of microvessels in random volume probes (a, c) and in hepatic lobules (b, d). After automatic analysis of the vascular corrosion casts scanned with micro-CT, the data on lengths and radiuses of microvessels were summed up and the

histograms were calculated separately (i) for the ten volume probes randomly sampled from the liver (Fig. 7a, c) and (ii) for the four arbitrarily selected regions of morphological hepatic lobules (Fig. 7b, d)

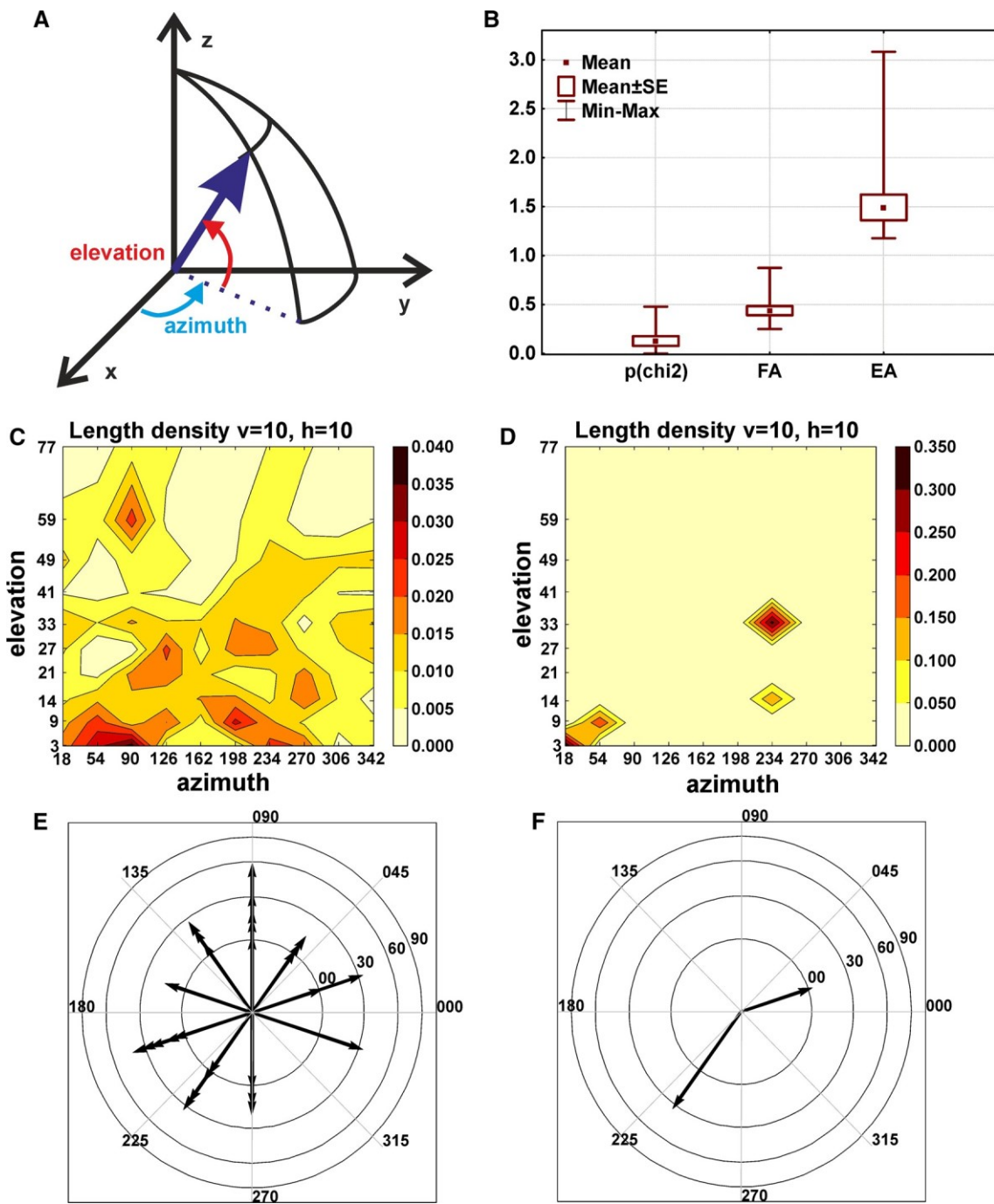


Fig. 8 Evaluating anisotropy of the liver microvessels using data obtained by the automatic method. **a** The angular description of points on a sphere: azimuth and elevation. **b** The values of $p(\chi^2)$, ellipsoidal (EA), and fractional anisotropy (FA). *Square dots* indicate the mean values, boxes span the standard deviation, and whiskers denote limit values. **c, d** Examples of the length densities of hepatic microvessels having many preferential directions (**c**) or few preferential directions (**d**). The colour scale corresponds to length densities, v is the number of parallels, and h is the number of meridians. The values of elevation and

azimuth are related to the mean value of angles in individual intervals of 100 regions. **e, f** Examples of the direction of hepatic microvessels covering 50 % of the length of all microvessels in the liver specimen: **e** corresponds to the plot **c** with many preferential directions, namely 26, that is close to being isotropic. **f** corresponds to the anisotropic system shown in **d** with a few preferential directions, namely 2. The Lambert azimuthal equal-area projection was used for the polar plots. *Radial lines* are azimuths, and concentric circles are elevations. The *arrows* indicate individual directions.

agent) injected into the vascular system using repeated scanning in short time intervals (1–2.5 s) [40]. The calculation of pharmacokinetic parameters is based on the analysis of the time enhancement curve of the liver parenchyma, vessels, and spleen during the first pass of contrast agent using a mathematical model that reflects the anatomical and functional characteristics of hepatic microcirculation (e.g. the maximum-slope, dual-slope, and deconvolution method in CT or the Tofts method in MRI) [41,42]. The refinement of these models based on detailed quantitative studies of orientation of normal and pathological hepatic microcirculation can lead to increased accuracy of perfusion studies. Moreover, spatial statistics of porcine hepatic microvessels are necessary for models of cell alignment along the microvessels in models of liver regeneration [39].

Pharmacokinetic parameters, which have a close relationship to the arrangement of the liver microcirculation, include blood flow, blood volume, permeability, transit time, arterial and portal perfusion fraction or hepatic perfusion index in perfusion CT and their analogues in perfusion MRI or US. They reflect not only the dynamics of the passage of the tracer through the hepatic capillary bed but also its anatomical structure. Several studies show that there is a relationship between blood volume and the density of capillary network or between permeability and leakage of tracer into the extravascular space, which may be involved in tumorous angiogenesis or liver fibrosis [40,43]. The density and tortuosity of capillary networks may influence liver blood flow and transit time. Close connections to the anatomical arrangement of the liver lobule also have parameters of arterial and portal perfusion fraction and hepatic perfusion index (ratio of portal perfusion fraction and total liver blood flow) [44]. Information about the state of hepatic microcirculation and neoangiogenesis in liver tumours is important in choosing the right therapeutic method (especially biological treatment) and in the follow-up on its effect. A higher rate of arterial perfusion, blood volume and permeability, which corresponds to high vascularity in the tumour, may predict a better response to biological treatment, and its decline after the first few therapeutic cycles indicates its good effect. Conversely, low values of these parameters prior to therapy indicate tumour hypoxia and less chance of a good therapeutic effect. Perfusion imaging can also be utilized to detect lesions that are occult in standard imaging or to evaluate the status of the surrounding liver parenchyma with regards to the stage of fibrosis, which, similarly to tumours, increases arterial perfusion [41,45,46]. Perfusion studies may also enhance the sensitivity of imaging methods in the evaluation of local treatments of tumours using ablation or chemoembolization methods, where the appearance of local arterial hyperperfusion indicates the recurrence of the tumour [47]. Detailed mapping of the hepatic microcirculation can also help in the computer-aided determination of the portal vein or hepatic

veins' vascular territories and in the prediction of the regenerative ability of the liver parenchyma, which may in the future lead to more accurate planning of major liver resections, especially in borderline operable patients. Moreover, automatic analysis of hepatic corrosive vascular casts in animal experiments with liver regeneration could demonstrate whether the newly regenerated microvascular network shows the same statistical morphometrics as the normal liver microvessels.

Further development of automatic evaluation of micro-CT data

Further development of the QuantAn software incorporates statistics of 3-D bifurcation angles [13]. The vascular network shall be alternatively characterized using the Euler number or Euler–Poincaré characteristic χ [20,48], which is related to the numerical density of capillaries ($N_V(\text{vessels}/\text{ref}) = -\chi(\text{vessels})/V(\text{dis})$). The software is publicly available not only for analysis of liver microvessels, but may be tested also in other branches microvascular research providing three-dimensional data, such as analysis of tumour microvessels [49], bone microvessels [50], or the vasa vasorum or major vessels [51]. The software uses the same stereological principles like other programs that are already available, e.g. the Stereology Analyzer [52], but unlike the Stereology Analyzer, QuantAn is completely free and open source, works not only with series of 2-D images, but natively with 3-D data, i.e. connecting the vascular segments in space, and it has more user-controlled automated procedures, such as thresholding, skeletonization, analysis of branching nodes, length, and diameter histograms. These automated functions allow for the use of stereological variables of complex vascular networks in studies involving many samples with high resolution.

Moreover, we will aim to generate and test phantom (artificial) vascular networks and trees statistically similar to the hepatic vascular bed in various conditions, such as normal liver perfusion, and rearrangement due to portal hypertension, liver regeneration, cirrhosis, or tumour infiltration, resulting in changes in fractal dimensions of microvessels [13]. Artificial vascular networks with known distributions of length and radius of microvascular segments should be used to validate the automatic analysis of these two parameters. The data are also suitable for determining anisotropy of the liver microcirculation used in computer models of liver perfusion based on homogenization techniques. The description of the portal venous, hepatic arterial, and hepatic venous tree anisotropy is crucial for the liver blood perfusion determination in patient-specific liver presurgery planning. This was already tested in the present data sets using the methods developed by Kochova et al. [33] (see Fig. 8 for illustration). Moreover, fabric tensor computed from CT and

micro-CT data of liver corrosion casts represents another way to describe the liver vessel tree anisotropy on a macro and micro scale. Furthermore, the fabric tensor expresses a step in the direction towards the permeability tensor determination, which is known from the Darcy law and the theory of fluid flow through a porous medium [53]. A number of ways for the construction of the fabric tensor are available [54]. Mechanics-based methods compute fabric tensor (or permeability tensor) directly from numerical simulations [55]. Morphology-based methods are less computationally expensive and are independent from boundary conditions applied during the numerical simulations. Therefore, our future research will focus on the morphology-based methods.

Another parameter that remains to be incorporated is the tortuosity of the microvessels. Interestingly, there are many definitions of tortuosity (for review, see [56]), and some of them are not mutually compatible. In general, tortuosity is understood as a geometric characteristic of the deviation of vessels from a straight line, which is potentially different in normal and pathological microvascular beds [13].

Conclusion

We developed the open-source software QuantAn for the quantitative evaluation of the volumes, surfaces, lengths, and numbers of microvessels in micro-CT scans of microvascular corrosion casts. The automatic analysis of the skeleton branching nodes (and therefore also of the number of microvessels per volume unit calculated from the branching nodes) was mostly affected by the binary opening during the preprocessing and also by the aggregation radius of the branching points. We provided preliminary morphometrics of the classical morphological hepatic lobules in porcine liver. All the methods comply with the highly reproducible stereological techniques, and they were highly consistent with manual counting results. This method is openly available to researchers who are interested in the stochastic geometry of microvessels in micro-CT scans.

Acknowledgments The authors thank to following research projects: The study was supported by the IGA MZ CR Project No. 13326. ZT and PK were also supported by the project LO1506 of the Czech Ministry of Education, Youth and Sports. MJ, AK, MK, PH, LE, HM, and VL were supported by the National Sustainability Program I (NPU I) Nr. LO1503 provided by the Ministry of Education, Youth and Sports of the Czech Republic and by the Prvok P36 project of the Charles University in Prague. LE was also supported by project SVV No. 260 170 of the Charles University in Prague and by the Austrian Agency for International Mobility and Cooperation in Education, Science and Research (OeAD). The results of TG (micro-CT) were developed within the CENTEM project, reg. no. CZ.1.05/2.1.00/03.0088, cofunded by the ERDF as part of the Ministry of Education, Youth and Sports OP RDI programme and, in the follow-up sustainability stage, supported through CENTEM PLUS (LO1402) by financial means from the Min-

istry of Education, Youth and Sports under the National Sustainability Programme I. Scanning electron microscopy SEM was partly supported by the European Regional Development Fund under Project “NTIS - New Technologies for Information Society”, European Centre of Excellence, CZ.1.05/1.1.00/02.0090.

Compliance with ethical standards

Conflict of interest The authors declare that they have no conflict of interest.

Statement on the welfare of animals All applicable international and national guidelines for the care and use of animals were followed. All procedures performed in animals were in accordance with the ethical standards of the institution at which the study was conducted. The experimental surgical and anaesthesiological procedures and the use of piglets in this study were certified by the Commission for Work with Experimental Animals at the Faculty of Medicine in Pilsen, Charles University, Prague, and they were under the control of the Ministry of Agriculture of the Czech Republic.

References

1. Markert M, Koschany A, Lueth T (2010) Tracking of the liver for navigation in open surgery. *Int J Comput Assist Radiol Surg* 5:229–235
2. Ribes D, Peterhans M, Anderegg S, Wallach D, Banz V, Kim-Fuchs C, Candinas D, Weber S (2012) Towards higher precision in instrument guided liver surgery: automatic registration of 3D ultrasound with pre-operative MeVis-CT. *Int J Comput Assist Radiol Surg* 7(Suppl 1):S141–S142
3. Schwier M, Moltz JH, Peitgen HO (2011) Object-based analysis of CT images for automatic detection and segmentation of hypodense liver lesions. *Int J Comput Assist Radiol Surg* 6:737–747
4. Wallach D, Peterhans M, Brun B, Banz V, Candinas D, Weber S (2012) Development of a surgical template system for application in image guided liver surgery. *Int J Comput Assist Radiol Surg* 7(Suppl 1):S142–S143
5. Hansen C, Zidowitz S, Preim B, Stavrou G, Oldhafer KJ, Hahn HK (2014) Impact of model-based risk analysis for liver surgery planning. *Int J Comput Assist Radiol Surg* 9:473–480
6. Hansen C, Zidowitz S, Ritter F, Lange C, Oldhafer K, Hahn HK (2012) Risk maps for liver surgery. *Int J Comput Assist Radiol Surg* 7(Suppl 1):S144–S145
7. Pichon E, Bekes G, Deschamps F, Solomon SB (2008) Development and preliminary evaluation of software for planning selective liver embolizations from three-dimensional rotational fluoroscopy imaging. *Int J Comput Assist Radiol Surg* 3:405–412
8. Tonar Z, Eberlová L, Polívka J, Daum O, Witter K, Králíčková A, Gregor T, Nedorost L, Kochová P, Rohan E, Kalusová K, Pálek R, Skála M, Glanc D, Králíčková M, Liška V (2012) Stereological methods for quantitative assessment of hepatic microcirculation. In: Méndez-Villas A (ed) *Current microscopy contributions to advances in science and technology*, Microscopy book series 2012 edition Formatex Research Center, Badajoz, pp 737–748
9. Hammad S, Hoehme S, Friebel A, von Recklinghausen I, Othman A, Begher-Tibbe B, Reif R, Godoy P, Johann T, Vartak A, Golka K, Bucur PO, Vibert E, Marchan R, Christ B, Dooley S, Meyer C, Ilkavets I, Dahmen U, Dirsch O, Böttger J, Gebhardt R, Drasdo D, Hengstler JG (2014) Protocols for staining of bile canalicular and sinusoidal networks of human, mouse and pig livers, three-dimensional reconstruction and quantification of tissue

- microarchitecture by image processing and analysis. *Arch Toxicol* 88:1161–1183
10. Schwier M, Böhler T, Hahn HK, Dahmen U, Dirsch O (2013) Registration of histological whole slide images guided by vessel structures. *J Pathol Inform* 4(Suppl):S10
 11. Wei W, Dirsch O, Mclean AL, Zafarnia S, Schwier M, Dahmen U (2015) Rodent models and imaging techniques to study liver regeneration. *Eur Surg Res* 54:97–113
 12. Schladitz K (2011) Quantitative micro-CT. *J Microsc* 243:111–117
 13. Lang S, Müller B, Dominietto MD, Cattin PC, Zanette I, Weitkamp T, Hieber SE (2012) Three-dimensional quantification of capillary networks in healthy and cancerous tissues of two mice. *Microvasc Res* 84:314–322
 14. Foruzan AH, Chen YW, Hori M, Sato Y, Tomiyama N (2014) Capturing large shape variations of liver using population-based statistical shape models. *Int J Comput Assist Radiol Surg* 9:967–977
 15. Stoyan D, Kendall WS, Mecke J (1995) *Stochastic geometry and its applications*. Wiley, New York
 16. Baddeley A, Jensen EB (2004) *Stereology for statisticians*. CRC, Boca Raton
 17. Králíčková A, Eberlová L, Kalusová K, Gregor T, Kochová P, Liška V, Králíčková M, Tonar Z (2014) Quantification of liver microcirculation using X-ray microtomography of vascular corrosion casts. *Key Eng Mat* 592–593:505–508
 18. Bruha J, Vycital O, Tonar Z, Mirka H, Haidingerova L, Benes J, Palek R, Skala M, Treska V, Liska V (2015) Monoclonal antibody against transforming growth factor Beta 1 does not influence liver regeneration after resection in large animal experiments. *In Vivo* 29:327–340
 19. Freiman M, Eliassaf O, Taieb Y, Joskowicz L, Azraq Y, Sosna J (2008) An iterative Bayesian approach for nearly automatic liver segmentation: algorithm and validation. *Int J Comput Assist Radiol Surg* 3:439–446
 20. Mühlfeld C (2014) Quantitative morphology of the vascularisation of organs: a stereological approach illustrated using the cardiac circulation. *Ann Anat* 196:12–19
 21. Eberlova L, Liska V, Mirka H, Gregor T, Tonar Z, Palek R, Skala M, Bruha J, Vycital O, Kalusova K, Haviar S, Kralickova M, Lametschwandtner A (2015) Porcine liver vascular bed in Biodur E20 corrosion casts. In Press. *Folia Morphol (Warsz)*. In press
 22. Lametschwandtner A, Miodonski A, Simonsberger P (1980) On the prevention of specimen charging in scanning electron microscopy of vascular corrosion casts by attaching conductive bridges. *Mikroskopie* 36:270–3
 23. Howard CV, Reed MG (1998) *Unbiased stereology: three-dimensional measurement in microscopy*. Springer, New York
 24. Mouton PR (2002) *Principles and practices of unbiased stereology: an introduction for bioscientists*. The Johns Hopkins University Press, Baltimore
 25. Kubínová L, Janáček J (1998) Estimating surface area by the isotropic fakir method from thick slices cut in an arbitrary direction. *J Microsc* 191:201–211
 26. Gundersen HJ, Bagger P, Bendtsen TF, Evans SM, Korbo L, Marcussen N, Moller A, Nielsen K, Nyengaard JR, Pakkenberg B (1988) The new stereological tools: disector, fractionator, nucleator and point sampled intercepts and their use in pathological research and diagnosis. *APMIS* 96:857–881
 27. Lokkegaard A, Nyengaard JR, West MJ (2001) Stereological estimates of number and length of capillaries in subdivisions of the hippocampal region. *Hippocampus* 11:726–740
 28. Jirik M, Kunes J, Zelezny M (2015) *Semiautomatic Quantitative Evaluation of Micro-CT Data*. *Lect Notes Comput Sc*. Accepted manuscript in Press
 29. Homann H (2007) Implementation of a 3D thinning algorithm. *Insight Journal*. <http://hdl.handle.net/1926/1292>. Accessed 30 Oct 2015
 30. Otsu N (1979) A threshold selection method from gray-level histograms. *IEEE Trans Sys Man Cyber* 9:62–66
 31. Dryden IL, Koloydenko A, Zhou D (2009) Non-Euclidean statistics for covariance matrices, with applications to diffusion tensor imaging. *Ann Appl Stat* 3:1102–1123
 32. Kochová P, Cimrman R (2010): Esofspy - evaluation of spatial orientation of fiber systems in Python. <http://docs.sfe.py.org/esofspy/>. Accessed 8 Oct 2015
 33. Kochová P, Cimrman R, Janáček J, Witter K, Tonar Z (2011) How to asses, visualize and compare the anisotropy of linear structures reconstructed from optical sections—A study based on histopathological quantification of human brain microvessels. *J Theor Biol* 286:67–78
 34. Lin LK (1989) A concordance correlation coefficient to evaluate reproducibility. *Biometrics* 45:255–268
 35. Lin LK (2000) A note on the concordance correlation coefficient. *Biometrics* 56:324–325
 36. NIWA (2012) Statistical calculators—Lin’s Concordance. <https://www.niwa.co.nz/node/104318/concordance>. Accessed 18 Dec 2015
 37. Jiřík M (2015) QuantAn—Quantitative Analyser software. <http://mjirik.github.io/quantan/>. Accessed 20 Jan 2016
 38. Yousefi S, Liu T, Wang RK (2015) Segmentation and quantification of blood vessels for OCT-based micro-angiograms using hybrid shape/intensity compounding. *Microvasc Res* 97:37–46
 39. Hoehme S, Brulport M, Bauer A, Bedawy E, Schormann W, Hermes M, Puppe V, Gebhardt R, Zellmer S, Schwarz M, Bockamp E, Timmel T, Hengstler JG, Drasdo D (2010) Prediction and validation of cell alignment along microvessels as order principle to restore tissue architecture in liver regeneration. *Proc Natl Acad Sci USA* 107:10371–10376
 40. Miles KA, Griffiths MR (2003) Perfusion CT: a worthwhile enhancement? *Brit J Radiol* 76:220–231
 41. Pandharipande PV, Krinsky GA, Rusinek H, Lee VS (2005) Perfusion imaging of the liver: current challenges and future goals. *Radiology* 234:661–673
 42. Tofts PS, Brix G, Buckley DL, Evelhoch JL, Henderson E, Knopp MV, Larsson HBW, Lee TY, Mayr NA, Parker GJM, Port Ruediger E, Taylor J, Weisskoff RM (1999) Estimating kinetic parameters from dynamic contrast-enhanced t1-weighted mri of a diffusable tracer: standardized quantities and symbols. *J Magn Reson Im* 10:223–232
 43. Zhong L, Wang WJ, Xu JR (2009) Clinical application of hepatic CT perfusion. *World J Gastroenterol* 15:907–911
 44. Van Beers BE, Leconte I, Materne R, Smith AM, Jamart J, Horsmans Y (2001) Hepatic perfusion parameters in chronic liver disease: dynamic CT measurements correlated with disease severity. *Am J Roentgenol* 176:667–673
 45. Cuenod C, Leconte I, Siauve N, Resten A, Dromain C, Poulet B, Frouin F, Clément O, Fria G (2001) Early changes in liver perfusion caused by occult metastases in rats: detection with quantitative CT 1. *Radiology* 218:556–561
 46. Goh V, Gourtsoyianni S, Koh DM (2013) Functional imaging of the liver. *Semin Ultrasound CT MR* 34:54–65
 47. Chen G, Ma DO, He W, Zhang BF, Zhao LQ (2008) Computed tomography perfusion in evaluating the therapeutic effect of transarterial chemoembolization for hepatocellular carcinoma. *World J Gastroenterol* 14:5738–5743
 48. Tang Y, Nyengaard JR, Andersen JB, Baandrup U, Gundersen HJ (2009) The application of stereological methods for estimating structural parameters in the human heart. *Anat Rec (Hoboken)* 292:1630–1647

49. Tonar Z, Egger GF, Witter K, Wolfesberger B (2008) Quantification of microvessels in canine lymph nodes. *Microsc Res Tech* 71:760–772
50. Tonar Z, Khadang I, Fiala P, Nedorost L, Kochová P (2011) Quantification of compact bone microporosities in the basal and alveolar portions of the human mandible using osteocyte lacunar density and area fraction of vascular canals. *Ann Anat* 193:211–219
51. Tonar Z, Kural T Jr, Kochová P, Nedorost L, Witter K (2012) Vasa vasorum quantification in human varicose great and small saphenous veins. *Ann Anat* 194:473–481
52. ADCIS (2015) Stereology Analyzer. <http://www.adcis.net/en/Products/Vertical/Stereology-Analyzer.html>. Accessed 20 Jan 2016
53. Coussy O (2004) *Poromechanics*. Wiley, Chichester
54. Moreno R, Borga M, Smedby O (2014) Techniques for computing fabric tensors: a review. In: Westin CF, Vilanova A, Burgeth B (eds) *Visualization and processing of tensors and higher order descriptors for multi-valued data*. Springer, Berlin, pp 271–292
55. Debbaut C, Vierendeels J, Casteleyn C, Cornillie P, Van Loo D, Simoens P, Van Hoorebeke L, Monbaliu D, Segers P (2012) Perfusion characteristics of the human hepatic microcirculation based on three-dimensional reconstructions and computational fluid dynamic analysis. *J Biomech Eng* 134:011003
56. Kalitzeos AA, Lip GY, Heitmar R (2013) Retinal vessel tortuosity measures and their applications. *Exp Eye Res* 106:40–46

10.5 Příloha V

JIŘÍK, Miroslav, BARTOŠ, Martin, TOMÁŠEK, Petr, MALEČKOVÁ, Anna, KURAL, Tomáš, HORÁKOVÁ, Jana, LUKÁŠ, David, SUCHÝ, Tomáš, KOCHOVÁ, Petra, HUBÁLEK KALBÁČOVÁ, Marie, KRÁLÍČKOVÁ, Milena, TONAR, Zbyněk, 2018. Generating standardized image data for testing and calibrating quantification of volumes, surfaces, lengths, and object counts in fibrous and porous materials using X-ray microtomography. *Microscopy research and technique*. 81(6), 551–568. ISSN 1059-910X. Dostupné z: <https://doi.org/10.1002/jemt.23011>
IF_(JCR2017) = 1,087. Q3 (Anatomy and morphology; Biology; Microscopy)

Generating standardized image data for testing and calibrating quantification of volumes, surfaces, lengths, and object counts in fibrous and porous materials using X-ray microtomography

Miroslav Jirík^{1*} | Martin Bartos^{2*} | Petr Tomásek³ | Anna Malečková^{1,3} |
Tomáš Kural³ | Jana Horáková⁴ | David Lukáš⁴ | Tomáš Suchý⁵ |
Petra Kochová⁶ | Marie Hubálek Kalbáčová^{1,7} |
Milena Králíčková^{1,3} | Zbynek Tonar^{1,3} 

¹Biomedical Center, Faculty of Medicine in Pilsen, Charles University, Pilsen, 323 00, Czech Republic

²Institute of Dental Medicine, First Faculty of Medicine, Charles University and General University Hospital in Prague, Prague 2, 128 01, Czech Republic

³Department of Histology and Embryology, Faculty of Medicine in Pilsen, Charles University in Prague, Pilsen, 301 66, Czech Republic

⁴Faculty of Textile Engineering, Technical University of Liberec, Liberec 1, 461 17, Czech Republic

⁵Department of Composites and Carbon Materials, Institute of Rock Structure and Mechanics, Academy of Sciences of the Czech Republic, Prague 8, Czech Republic

⁶European Centre of Excellence NTIS, Faculty of Applied Sciences, University of West Bohemia, Univerzitní 22, Pilsen, 306 14, Czech Republic

⁷Institute of Pathological Physiology, First Faculty of Medicine, Charles University, U nemocnice 5, 128 53 Prague, Czech Republic

Correspondence

Zbynek Tonar, Department of Histology and Embryology, Faculty of Medicine in Pilsen, Charles University, Karlovarska 48, 301 66 Pilsen, Czech Republic.
Email: zbynek.tonar@lfp.cuni.cz

Funding information

National Sustainability Program I (NPU I) Nr. LO1503 provided by the Ministry of Education, Youth and Sports of the Czech Republic, by the Progres Q39 and Progres Q29/LF1 (MB) projects of the Charles University, Grant/Award Numbers: SVV 260390/2017 and SVV 260392/2017 and UNCE/MED/006 projects of the Charles University. PK was supported by project LO1506 of the Czech Ministry of Education, Youth and Sports under program NPU I. ZT was also supported by the Ministry of Education, Youth and Sports under the project, Grant/Award Number: CZ.02.1.01/0.0/0.0/16_019/0000787. Technological development of post doc programs, Grant/Award Number: CZ.1.05/41.00/16.0346, Research and Development for Innovations Operational Programme (RDIOP)

Review Editor: Prof. George Perry

Abstract

Quantification of the structure and composition of biomaterials using micro-CT requires image segmentation due to the low contrast and overlapping radioopacity of biological materials. The amount of bias introduced by segmentation procedures is generally unknown. We aim to develop software that generates three-dimensional models of fibrous and porous structures with known volumes, surfaces, lengths, and object counts in fibrous materials and to provide a software tool that calibrates quantitative micro-CT assessments. Virtual image stacks were generated using the newly developed software TelGen, enabling the simulation of micro-CT scans of unconnected tubes, connected tubes, and porosities. A realistic noise generator was incorporated. Forty image stacks were evaluated using micro-CT, and the error between the true known and estimated data was quantified. Starting with geometric primitives, the error of the numerical estimation of surfaces and volumes was eliminated, thereby enabling the quantification of volumes and surfaces of colliding objects. Analysis of the sensitivity of the thresholding upon parameters of generated testing image sets revealed the effects of decreasing resolution and increasing noise on the accuracy of the micro-CT quantification. The size of the error increased with decreasing resolution when the voxel size exceeded 1/10 of the typical object size, which simulated the effect of the smallest details that could still be reliably quantified. Open-source software for calibrating quantitative micro-CT assessments by producing and saving virtually generated image data sets with known morphometric data was made freely available to researchers involved in morphometry of three-dimensional fibrillar and porous structures in micro-CT scans.

*The first two authors contributed equally to the manuscript.

KEYWORDS

fibers, Python, pores, scaffolds, spatial statistics, stereology, textile

1 | INTRODUCTION

1.1 | Assessment of the three-dimensional structure of fibrous and porous biomaterials using micro-CT: Present state and methodological problems

High-resolution quantitative X-ray microtomography (micro-CT) has become a method of choice for three-dimensional and quantitative (Schladitz, 2011) characterization of tissue-engineered scaffolds (Ho & Hutmacher, 2006) used, e.g., to support the healing of organs.

Newly manufactured biomaterials, such as electrospun nanofibrous scaffolds (Szentivanyi, Chakradeo, Zernetsch, & Glasmacher, 2011; Zhong, Zhang, & Lim, 2012) or fiber-polymer composite foams (Shen, Nutt, & Hull, 2004) undergo morphometric assessments before being used *in vitro* or *in vivo*. A good correlation between micro-CT and histology was found in bone research (Particelli et al., 2012). Software supplied by manufacturers of micro-CT facilities supports a plethora of morphometric parameters characterizing volume fractions, outer and inner surfaces (Pyka, Kerckhofs, Schrooten, & Wevers, 2014), porosities in bone and dental research (De Souza et al., 2013; Draenert et al., 2012; Karageorgiou & Kaplan, 2005; Tonar, Khadang, Fiala, Nedorost, & Kochová, 2011), pore size and distribution in bone scaffolds (Montufar, Vojtova, Celko, & Ginebra, 2017) and synthetic bone model foams (Gómez, Vlad, López, Navarro, & Fernández, 2013) and the topology of multiple phases of tissue scaffolds in user-defined regions of interest (ROIs). The three-dimensional and quantitative nature of the micro-CT makes it a tool of choice for estimating shrinkage of materials (Burey et al., 2018) and propagation of material fractures and cavitation (Neves, Coutinho, Alves, & de Assis, 2015). Some of the estimates are based on or fully compatible with stereological principles and spatial statistics (Baddeley & Jensen, 2004; Mouton, 2002; Stoyan, Kendall, & Mecke, 1995) and may be assessed automatically, provided the image data have a sufficient contrast (Jirík et al., 2016; Mouton et al., 2017). However, surfaces are especially potentially sensitive to the settings of the micro-CT scanning and further image postprocessing, such as resolution, noise, preferential spatial arrangement (anisotropy), filtration, and thresholding during binarization of grayscale images. The amount of potential bias introduced by these variables is generally unknown. The sensitivity of micro-CT to steps performed during thresholding might become an issue, especially in biomaterials combining multiple phases with similar or overlapping radiological opacity, such as partially mineralized collagen scaffolds combined with other substances, such as glycosaminoglycans. To the best of our knowledge, there are currently no published guidelines or fixed routines for thresholding biological samples, which is understandable due to the growing number of newly manufactured biomaterials and rapidly developing methodology of micro-CT. However, the entire measurement is as weak as its weakest link. Moreover, a precise knowledge of the morphometry of tissue-

engineered materials would be necessary to test the consistency of their production and biodegradation once implanted. The motivation of the work presented in this article is the absence of a freely accessible and reliable source of calibration tools for use as realistic phantoms that simulate the micro-CT image stacks. As far as we know, the manufacturers of micro-CT facilities do not provide users with such software, which could be used by micro-CT operators to (i) calculate the bias and error during the processing of micro-CT scanned stacks using phantom image series with known volumes, surfaces, lengths, and numbers of objects and (ii) demonstrate the impact of changes to the thresholding routines on the results of quantitative micro-CT.

1.2 | Preprocessing and segmentation of micro-CT images of biomaterials

Before quantification of the structure and composition of biomaterials, the micro-CT images undergo segmentation. This is not a straightforward and routinely standardized procedure due to the low contrast and overlapping radiopacity of biological materials. Although sophisticated approaches are now available for noise suppression or removal (Maia et al., 2015; Rau, Würfel, Lenarz, & Majdani, 2013), in micro-CT, the noise might overlap with the smallest nanofibers and microfibers of the tissue scaffolds. Currently used micro-CT devices (in our study, Bruker micro-CT, Belgium) are usually provided with a software package that is applicable for acquisition of projection images, their reconstruction into cross-section images, visualization of datasets (both in 2D and 3D), resizing, and production of a region or volume of interest (ROI, VOI), and finally, image meters are commonly available (e.g., Bruker). Currently, employment of operations for image processing is usually very convenient and user-friendly since the typical micro-CT user is neither an information-technology scientist nor a biomathematician. This has to be considered along with subjectivity in the assessment of many procedural parameters in image processing and binarization because exact evaluation of these processes and their calibration is not achievable to date. Manuals and detailed descriptions of both two-dimensional parameters (evaluation of each separate cross-section image in a dataset) and three-dimensional analysis (evaluation of the entire dataset) require image binarization (i.e., conversion of a grayscale image into a black and white image, where white pixels represent objects and black pixels represent the background), e.g., (Burghardt et al., 2007; Zhang, Yan, Chui, & Ong, 2010). This step is crucial, with substantial effect on image analysis results; its sensitivity is dependent on object properties (e.g., size, shape, density, and connections) that we would like to examine in our study. Two basic approaches can be differentiated: subjective threshold values assessment (especially in life sciences) and automatic threshold assessment leading to higher reproducibility (in material or technical sciences) (Stock, 2009).

Influences of threshold variations were assessed in several studies mostly focused on bone micro-CT 3D morphometry (Hara, Tanck, Homminga, & Huiskes, 2002; Jones et al., 2007; Parkinson, Badiei, & Fazzalari, 2008; Yan, Qi, Qiu, Teo, & Lei, 2012). We should consider progressive development of micro-CT devices (Landis & Keane, 2010), resulting in better spatial resolution and lower noise level, thus reducing (not eliminating) the dependency of result variations on threshold values. Possibilities of image binarization in CTAn software (Bruker Corporation, 2017) are as follows: global-threshold, adaptive threshold (mean, median, mean of minimal and maximal values), and Otsu threshold (automatic and automatic multi-level) (Otsu, 1979).

Usually, the signal to noise ratio has to be enhanced. This can be performed by, e.g., using filtering procedures—sharpening or smoothing in 2D or 3D (e.g., Gaussian blur, median, uniform, Kuwahara, unsharp mask). These are usually applied in grayscale images, but binary images can be filtered as well. After binarization, despeckle operations in 2D or 3D are used to remove white “noise” pixels (e.g., remove white/black speckles less than X pixels/voxels, remove pores, sweep—remove all object except the largest one). Many other procedures are offered by CTAn, e.g., morphological operations (dilatation, erosion, opening, and closing procedures), bitwise and arithmetical operations and geometrical transformations. Demonstration of image processing prior to micro-CT analysis is available in, e.g., (Buie, Campbell, Klinck, MacNeil, & Boyd, 2007). Eventually, we decided to perform image processing and binarization in the simplest manner (filtering, automatic thresholding, and despeckle) to minimize the number of variable processes influencing the results and enhance the time efficacy.

To summarize the main problem of quantitative imaging of biomaterials, the combination of various steps using mathematical morphology can affect the morphometric results in a significant but unpredictable manner. A good visual representation of the thresholded structures in micro CT scans does not always guarantee accuracy and precision in a quantitative sense. A solution to this problem would be generating virtual (phantom) data mimicking the real micro-CT examination and comparing the results of the thresholding routines to the a priori known results.

1.3 | Options in calibrating quantitative micro-CT

Micro-CT analysis results in 2D and 3D structural parameters values. However, verification of these values is generally not possible or hardly achievable in complex structures. Micro-CT results are very often presented as precise values even though they may be inaccurate or biased. Phantom models available for common micro-CT users with known parameters would allow calibration of micro-CT analysis procedure and assessment of its accuracy. To date such phantoms are lacking, since it is not possible to produce these phantoms (especially in case of complex interconnected structures and material porosity) at micrometer-scale with adequate level of confidence in its structural parameters. Calibration phantoms exist for material X-ray density assessment (Bone Mineral Density based on X-ray attenuation coefficient calibration) applicable e.g., in bone biology.

Using test images for calibration is a commonly used practice in imaging techniques. One of the most known test image is the Shepp-Logan phantom (Shepp & Logan, 1974). The discrete version of this image can also be generated using the SheppLogan plugin of the public domain ImageJ software (Schneider, Rasband, & Eliceiri, 2012). Several other ImageJ plugins are available for generating test images, such as Random Ovals, Fractal Generator, and RandomJ plugins. However, these algorithms generate two-dimensional images only and do not allow for modeling different object shapes. This prevents these plugins from being suitable for calibration of three-dimensional micro-CT. Spatial test objects can be generated using the freely available Gensei software (Cimrman, 2010; Tonar, Kochova, Cimrman, Witter, Janacek & Rohan, 2011). However, Gensei is limited to ellipsoids only.

1.4 | Aims of the study

The commercially available software packages supplied with most of the micro-CT facilities are notably efficient in thresholding the structures of interest, creating visual reconstructions, and quantitatively describing their geometry and composition. These software packages do provide the operator with sufficient feedback on how the final quantitative data might be affected by numerous combinations of procedures involving filtration, operations of mathematical morphology, and thresholding. Therefore, the aims of our study are as follows:

- To develop open-source software that generates three-dimensional models of fibrous and porous structures with known volumes, surfaces, lengths, and object counts in fibrous materials and to provide a software tool for calibrating quantitative micro-CT assessments.
- To identify combinations of object and image stack properties, which may easily lead to biased results using thresholding procedures of fibrous biomaterials in microCT.
- To provide practical recommendations on how to avoid potential pitfalls during segmentation in quantitative X-ray microtomography of fibrous and porous biomaterials.
- To help users of micro-CT understand where errors can occur, ensuring that micro-CT segmentation procedures can be proved to be valid and correct.

2 | MATERIALS AND METHODS

2.1 | Parameters used for spatial statistics of generated objects

The choice of the basic parameters to be quantified by our software generator was based on studies with real micro-CT (Jirík et al., 2016). This includes volume, surface, length, and number of objects, which are often expressed as relative densities calculated per ROI. The definitions, abbreviations, and possible biological interpretations in the context of biomaterials are summarized in Table 1. The simulation of biomaterials was inspired by real tissue scaffolds, namely: (i)

TABLE 1 Stereological parameters used for spatial statistics of artificially generated objects simulating biomaterials for in-vivo implantation

Parameter	Abbreviation	Unit	Definition	Possible biological interpretation in biomaterials
Volume density (fraction)	V_v	(2)	Volume of objects per Reference volume	measure of the in-vivo degradation of the total mass of a biomaterial
Surface density	S_v	(mm ²)	Surface of objects per Reference volume	relative surface area available for the release of substances; thrombogenicity
Length density	L_v	(mm ²)	Length of objects per Reference volume	fragmentation of fibers into shorter fragments as a measure of in-vivo material degradation
Numerical density	N_v	(mm ²)	Number of objects per Reference volume	showing the degree of branching and connectivity of the biomaterial or its remnants after some period of in-vivo degradation

electrospun polyesters (polycaprolactone) or polypropylene meshes used for manufacturing artificial vascular prostheses or reinforcement of scars (Horakova et al., 2018; Plencner et al., 2014) and consisting of fibers with diameters of 1–6 mm, occupying 25–70% of the volume fraction; and (ii) composite porous scaffolds (Gómez, Vlad, López, & Fernández, 2016; Prosecká et al., 2015; Suchý et al., 2015) manufactured for healing of bone defects and consisting of collagen, polyDL-lactide sub-micron fibers, and sodium hyaluronate, containing typically 70%–80% porosities.

2.2 | Generating virtual objects and image stacks: Algorithm and software development

The program was written in the Python programming language. The software runs under Linux, Windows or Mac OS operating systems. The TelGen application is designed to generate structures ranging in shape from very elongated fibers to spheres. The output is an image stack that mimics the data obtained using micro-CT and metadata describing the parameters of the generated 3D structure. The application can be used through a graphical user interface, noninteractively from the command line, or directly from the Python environment.

The graphical user interface is created using the pyqt module, the numpy, scipy and scikit modules are used for the calculations, 3D modeling is performed using the VTK package, and the pandas and seaborn packages are used for data processing. Loading and storing data is mediated by our io3d package, which uses SimpleITK and pydicom. 3D noise was generated by the ndnoise package created for this purpose.

The basic concept of the algorithm (Table 2) includes the definition of objects to generate, the generation of the framework of the fiber structure, the surface representation, the quantitative description, the volume representation, and finally the file storage.

The basic element used in this task is a tube. It is a cylindrical body that ends with hemispheres. The user can set parameters for object length, object radius, and parameters that affect the direction and isotropy of objects. The concept and implementation of quantitative measured isotropy was done according to Kočová, Cimrman, Janáček, Witter, and Tonar (2011). The fibrous structure is created by repeatedly inserting these objects into the sample area and can be affected

by allowing the overlay of the objects. The collision detection algorithm is based on minimum distance computation, and it is preprocessed by a bounding box collision detection algorithm (Jiménez, Thomas, & Torras, 2001; Moore & Wilhelms, 1988). This process ends when the object number, volume density, or maximum number of iterations defined by the user is reached.

To determine the geometrical properties of the generated objects, a triangulated model of the surface of each tube is created using the VTK package (Schroeder, Avila, & Hoffman, 2000; Schroeder, Martin, & Lorensen, 1998). The measurement_resolution parameter affects the number of triangulation points and hence the accuracy of the measurement and the computation time. By using the vtkBooleanOperation PolyDataFilter function, a connection of two objects is made in the case of a contact. The vtkMassProperties functions are used to determine the numeric volume and numeric body surface.

The intensities of the volume representation are controlled by the background_intensity parameters and the intensity_profile function, which defines the intensity depending on the relative distance from the center of the tube to its edge. The volume representation process begins by creating a 3D array with a homogeneous intensity corresponding to the selected background intensity. Tube-shaped objects are placed in this array in the first iteration. The radius and intensity of an object correspond to the intensity profile (Supporting Information S4A) with the highest relative radius. The second iteration places the same objects with different radius and intensity that correspond to the second largest relative radius of the intensity profile. The entire process is repeated until all the intensity profile values are used. Then, intensity filtering by a Gaussian filter with user-defined parameters is performed.

The next step is to add noise. For this purpose, the ndnoise module was created. The noise parameters are the minimum and maximum noise wavelengths in millimeters and the exponent that controls the ratio of the individual components to the wavelength.

Volumetric data are stored using the imtools package. Data can be stored in a single DICOM or RAW file or as a file series in JPG, PNG, TIFF, DICOM, etc. format. Together with volumetric data, the surface model in VTK and metadata are stored. Metadata contain information about the configuration and quantitative data for all object segments. They are exported in the open and human-readable YAML format or as

TABLE 2 Outline of the steps of the algorithm of the TelGen software

Input: Parameters defined by the user
1. Type of the generator: Objects or Porosities (Figure 2 and Supporting Information S4)
2. Definition of the objects to be generated <ul style="list-style-type: none"> 2.1. Properties of objects <ul style="list-style-type: none"> 2.1.1 Separate objects or Intersecting objects 2.1.2 Number of objects and volume fraction 2.1.3 Distribution of radii and lengths of cylinders and spheres 2.1.4 Isotropy of the objects 2.1.5 Intensity profiles of the objects on virtual micro-CT sections 2.2. Properties of generated virtual micro-CT stacks <ul style="list-style-type: none"> 2.2.1 Resolution and size in three dimensions (X 3 Y3Z) 2.2.2 Gaussian blur of the objects (optional) 2.2.3 Generating noise (parametric settings, optional) 2.2.4 Number of iterations for calculation of the numerical estimates of spatial statistics 2.2.5 Setting connected component seed (optional) 2.3 Saving all the parameters listed in steps 1.1-1.2 to a configuration file (YAML)
3. Generating the skeleton and envelopes of the objects (repeat step 2 until the desired values are reached) <ul style="list-style-type: none"> 3.1. Defining the empty sample area 3.2 Inserting a tube into the sample area according to the defined parameters 3.3. Quantitative analysis of the objects <ul style="list-style-type: none"> 3.3.1. Calculating analytical lengths, radii, volumes, surfaces 3.3.2. Numeric lengths, radii, volumes and surfaces calculation 3.3.3 Preview of the values for the user
4. Generating and saving virtual micro-CT stacks (volumetric data) (repeat step 2 until all intensity profile values are used) <ul style="list-style-type: none"> 4.1. Creating the initial volumetric array with the defined background intensity 4.2. Inserting tubes with intensity and radius according to the intensity profile from a high relative radius to a zero radius 4.3 Gaussian filtering 4.4. Inserting the noise 4.5. Image saving to a defined file format
Output: Three-dimensional volumetric data with a known voxel size and known values of quantitative parameters (volume fractions, surface densities, length densities, numerical densities). Export of the 3D model into VTK format. Export of the image stacks (DICOM, JPEG). Export of the morphometric results (CSV file).

CSV files. These are either readable by spreadsheet applications or processed by data scripts.

The computation time depends mainly on the dimensions of the requested volumetric representation and the measurement_resolution. To process a stack from our dataset consisting of 500 3 500 3 500 voxels with a measurement_resolution of 35 and element_number using a computer with an 8x Intel(R) Core(TM) i5-2520M CPU at 2.50 GHz, 8 GB RAM, and an NVIDIA GF119M NVS 4200M graphical adapter, the computation time is approximately 4 min. The minimum and maximum time on this dataset is 1 and 34 min, respectively.

2.3 | Evaluating numerical estimates of volume and surface vs. values calculated using analytic geometry

The parameters evaluated in the objects of our measurements are the surface, volume, length of cylindrical part l and radius of the spherical surfaces and cylindrical part r . From the specified length and radius, the analytical expression of surface S_{analytic} and volume V_{analytic} is given by the following equations.

$$S_{\text{analytic}} = 5\delta 2pr/p1 \ 4p \ r^2 \quad (1)$$

$$V_{\text{analytic}} = \frac{4}{3}pr^3 + 1pr^2l \quad (2)$$

One of our goals is also the modeling of connected objects. Analytical expressions of surfaces and volumes of such bodies are generally difficult and often do not have a definitive solution. For this reason, we use a numerical solution to this problem, which is based on the triangulation of the tube object. The base of the cylindrical part consists of a regular polygon. The number of its sides is given by the measurement_resolution parameter. The hemispheres are replaced by triangles with triangulation points located at the intersections of imaginary meridians and parallels. The triangulated tube is inscribed in the original object. Its surface and volume asymptotically approximate the analytically measured values with increasing measurement_resolution. This method of triangulation is further referred to as “inscribed.”

To increase the accuracy, we perform some compensation. The radius of the regular inscribed polygon that is the base of the cylindrical model is chosen so that the body on it has the same surface (volume, respectively) as the model cylinder. The compensated surface and volume radii are not the same. The hemisphere parts are unchanged. This method of triangulation with the compensation of the cylindrical part is referred to as “surface” and “volume.” The calculation is given by the following equation, where r is the radius of the model tube, n is the measurement_resolution, r_{eqsurf} is the radius of the surface compensated polygon, and r_{eqvol} is the radius of the polygon for volume compensation:

$$r_{eqSurf} = \frac{Dr}{n \sin^2 \theta} \quad (3)$$

$$r_{eqVol} = \frac{3V}{4\pi r_0^3} \quad (4)$$

Compensation of the spherical part is performed by experimental measurement using the equation for calculating the radius of the spherical part with knowledge of the surface or volume. r_c is the compensated factor, and r_0 is the model radius. These compensation methods are further referred to as “surface 1 sphere error” and “volume 1 sphere error.”

$$r_0 r_c = \frac{1}{2} \frac{S}{p} \quad (5)$$

$$r_0 r_c = \sqrt[3]{\frac{3V}{4\pi}} \quad (6)$$

Similarly, experimental measurements were made to estimate the compensation factor for the error compensation from the connection of the cylindrical and spherical parts. This is referred to as “volume 1 sphere error 1 joint error” and “volume 1 sphere error 1 joint error.” However, these corrections did not increase the precision of either volume or surface estimates and therefore were not included.

2.4 | Evaluating morphometric values using image processing on a micro-CT console

CTAn software (Skyscan CT analyzer (21)) was applied for image processing and subsequent 3D analysis using a “custom processing” mode. A universal procedure (a “standard” procedure) of image processing leading to acceptable and reproducible outcomes was found for datasets with the following variable parameters: *count*, *isotropy*, *noise*, and *resolution*. However, *noise* and *resolution* datasets required modification of the procedure based on the value of the variable parameter.

Standard procedure was based on filtering using Gaussian blur in 3D (with a radius of 2 voxels). Binarization was performed by an automatic Otsu threshold method to eliminate subjectivity in assessment of the threshold value. Noise reduction was achieved by a despeckle function (remove white speckles less than 12 voxels in 3D). *Resolution* variable datasets were filtered using Gaussian blur in 3D with reduction of the value of the radius (from 2 voxels to one voxel; for a pixel size of 80 μ m and higher, this operation was not performed). Binarization was achieved by an automatic Otsu threshold method in 3D. Despeckle was performed with decreasing value of the defined volume limit for object elimination (12 voxels and less; for a pixel size of 80 μ m and higher, this operation was not performed).

Image processing in datasets with a *noise* variable was based on Gaussian blur in 3D with a gradual increase in the radius value (from 2 to 5 voxels). The generated noise intensity was set to zero, but the standard deviation of the noise intensity gradually increased. Binarization was performed by a global threshold with an increase in the lower gray threshold value from 87 to 135 as noise was intensified. A despeckle operation was performed with an increase of the defined volume (remove white speckles less than: from 12 to 250 μ m. According

to preliminary results, noise reduction was preferred over object volume preservation, resulting in noise being binarized as an object.

Procedures in *noise* and *resolution* variables were modified regard-

ing object count and subjective assessment (more in 4.1). 3D analysis of the entire dataset and 3D analysis of all individual objects in the dataset were performed in each dataset after the described image processing. The following parameters were evaluated based on analysis: object count, mean and total object length, mean and total object volume, mean and total object surface, surface density (total object surface/dataset volume), and mean object diameter. Objects and volumes are calculated via the marching cubes method (Lorenson & Harvey, 1987). Object length was defined as the furthest distance between two points within the analyzed object volume. Mean diameter was calculated as structure thickness, which is based on object medial axis computation and a subsequent sphere-fitting algorithm. Because these spheres finally have known diameters, it can be used for structure thickness evaluation (Bruker Corporation, 2017; Hildebrand & Rueggsegger, 2003; Remy & Thiel, 2002). Typical time costs for performing the despeckle operation using a computer recommended for micro-CT SkyScan 1272 (Bruker) application (Intel(R) Xeon (R) CPU E5-2687W 3.1 GHz (2 processors), 128 GB RAM, NVIDIA Quadro 1 Tesla graphical adapter) were approximately 1–2 min (depending on number of selected parameters in analysis results).

3 | RESULTS

3.1 | Open-source software for generation of three-dimensional objects and virtual micro-CT image stacks

The source code of our software named TelGen, which was written in the Python programming language, all of the files necessary for its launch, the calculation of the results, and the production of all graph types have been made openly available to the scientific community (Jirík, 2017). The source data and configurations for generation of the following results and all the data sets described in this article can be downloaded as Supporting Information S1–S3. The documentation can be downloaded as well (Jirík & Tonar, 2018). The basic concept of the algorithm (Figure 1, Table 2) is to gather the required parameters of the phantom data from the user; generate, visualize and measure the data; receive approval from the user; and then save image stacks with all configuration files and quantitative results to disc. The software allows for the generation of noncolliding tubes, colliding tubes (for simulating of branching fibers and a greater volume fraction of the material), and isolated or connected (overlapping) porosities (Figure 2). Most of the application functions can be performed noninteractively using command line parameters.

3.2 | Comparing the numerical estimates of volume and surface with known true values calculated using analytic geometry

After implementing the corrections described above, there was very good agreement between the surfaces and volumes of tubes precisely

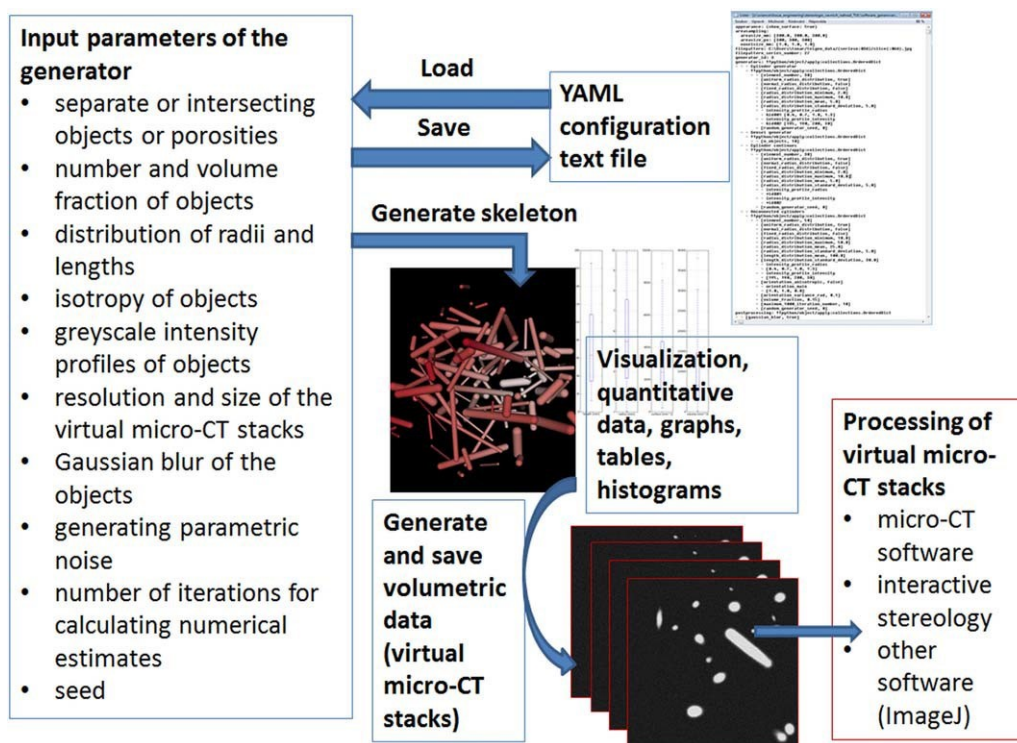


FIGURE 1 Main steps during the setting, generation, and processing of the fibrillar and porous three-dimensional objects and corresponding virtual micro-CT stacks. The user sets the required input parameters (see Table 2 for details) either manually or from a previously saved YAML configuration text file. The skeleton of the objects is generated together with a quantitative description of the objects (volumes, surfaces, and lengths), and the data can be visually checked by the user in the form of three-dimensional skeletons. Once the data meets the required settings, full volumetric data are generated and saved to disk as image sequences mimicking micro-CT stacks together with a three-dimensional model (VTK format) and tables containing all the morphometric results (CSV files). The resulting virtual micro-CT stacks can be loaded into any type of software supporting DICOM or JPEG image stacks [Color figure can be viewed at wileyonlinelibrary.com]

calculated using analytic geometry and the measurement done by the TelGen software (Figure 3 with source data provided as Supporting Information S1).

3.3 | Analysis of the sensitivity of surface error and volume error on the numbers of generated objects and measurement resolution

Based on these results and the computational time, the accuracy of surface and volume measurement was strongly dependent on the measurement resolution parameter and the radius compensation method. Compared to uncompensated methods (inscribed), methods using radius compensation provide improvement, especially for low values of *measure_resolution*. The lowest relative surface errors, expressed as $1003(\text{true value} - \text{numerical estimate})$, were achieved by implementing the cylinder surface 1 sphere error corrections. When combined with increasing resolution, the surface error was gradually reduced to values below 0.1 (Figure 4a–d). The volume error was successfully minimized by using the cylinder volume compensation or cylinder volume 1-sphere error compensation (Figure 4e–h), converging to an error below 0.1 even at lower resolutions than the surface (Figure 4h vs. Figure 4d). Based on these experiments and the time costs of the computations, we recommend using the “cylinder surface” method for surface

measurement. For volume measurement, we recommend the “cylinder volume 1 sphere error” method.

3.4 | Evaluating known morphometric values with analysis based on thresholding on the micro-CT console

For testing the sensitivity of the segmentation procedures using the SkyScan Bruker console micro-CT software, 40 image stacks were generated, representing low to high numbers of objects (Figure 5a), isotropy of objects (Figure 5b), resolution of stacks (Figure 5c), and noise (Figure 5d). After processing these phantom stacks (see Figure 6 for the main steps), situations leading to possible bias were identified (Figure 7). This included thresholding of the gradual transition of grayscale values between the objects and their background (Figure 7a), reduction of object count caused by peripheral sections of objects (Figure 7b), occasionally colliding objects (Figure 7c), and fragmentation due to binarization (Figure 7d).

There was an overall good agreement between the known surface and volume densities of generated objects and the results obtained on the micro-CT console within most of the range of values typical for bio-materials (Figure 8a,b). As shown in the Bland-Altman plots (Figure 8c,d), the disagreement between both measures gradually increased with increasing values of the densities.

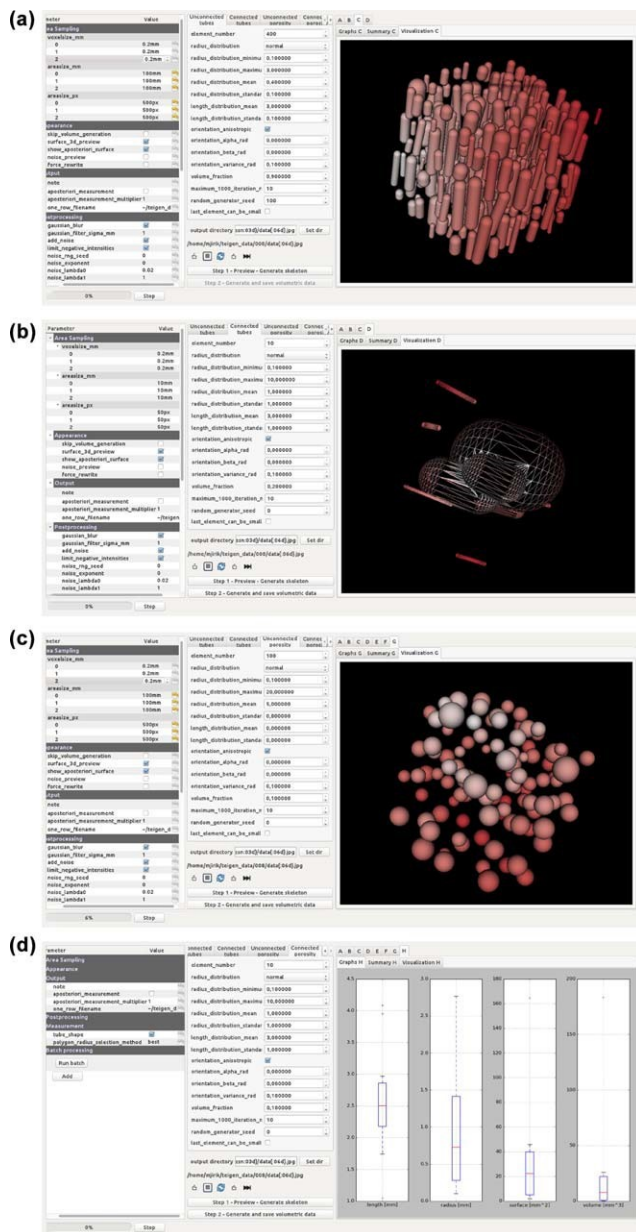


FIGURE 2 Graphical user interface of the four types of generators in the TelGen software. (a) Generating unconnected tubes, in this example with a highly anisotropic orientation. (b) Generating connected (colliding) tubes, in this example within a wide range of diameters. (c) Generating unconnected porosities, which may have shape of spheres or tubes. (d) Generating connected (overlapping) porosities, overview of morphometric data on length, radius, surface, and volume distribution in the preview window [Color figure can be viewed at wileyonlinelibrary.com]

A detailed analysis of sensitivity of the thresholding upon various values of parameters of generated testing image sets revealed that the changes in object count and the value of isotropy did not affect the accuracy of the micro-CT quantification (Figure 9a,b). The number of objects was underestimated by the micro-CT, and the volumes, surfaces, and length densities had a tendency toward being overestimated. The size of the error significantly increased with decreasing resolution

when the voxel size exceeded 1/10 of the typical object size (Figure 9c), which simulated the effect of the smallest details that could still be reliably quantified. Similarly, the results became unreliable when the standard deviation of the noise intensity (mean 5.0) exceeded 3.7 arbitrary units, and more filtering and higher threshold values were necessary (see Methods).

3.5 | Examples of practical applications

Verification of micro-CT analysis results of specimen microstructure is hard to achieve or even not possible as was mentioned in 1.3. TelGen software enables evaluation of micro-CT analysis accuracy, image processing effect and bias quantification. Despite the fact, that 3D structures generated by TelGen are simplification of studied specimen, it provides important and unique information, which may improve decision making in image processing and analyzes understanding. The benefit of using the TelGen software will be illustrated in three examples.

3.5.1 | Evaluation of global thresholding effect

A fundamental approach in image thresholding is the use of Global threshold. Separating objects from their background requires a manual selection of grayscale value, which is usually based on operator's subjective assessment. Since there is a gradual transition between object and background, this decision often lacks accuracy and repeatability (typical situations are shown in Figure 10a,b). A solution is as follows: First, TelGen software is employed for generating a dataset with a known structure similar to the specimen under study. Second, a series of different global thresholding values are applied for binarization using the micro-CT analysis. Third, the results of the micro-CT analysis are compared with known structural parameters generated in the first step. Fourth, the most accurate settings are used for further specimen analysis and bias introduced by micro-CT analysis is quantified (e.g., discrepancy between objects volume and surface accuracy). An example of such a simple analysis which required approximately 20 min of work is shown in Table 3.

3.5.2 | Effect of image noise quantification

Image noise is found in all micro-CT scans. However, the effect of image noise on results is usually not considered. TelGen software is used for generating dataset of structures similar to studied specimen with similar level of image noise (Figure 6, see also section 4.1.4). By analyzing the same dataset with and without applying noise reduction algorithms, any bias introduced by noise and micro-CT analysis is quantified, because the impact of noise reduction and filtering is compared with the known structural parameters generated by the TelGen software.

3.5.3 | Image 2D binarization did introduce bias into quantification of object number in isotropic tubular structures

Tissue engineering scaffold based on microfibers is subjected to micro-CT 3D analysis. 2D or 3D threshold is considered. Assessment of thresholding effect based on subjective visual evaluation is usually

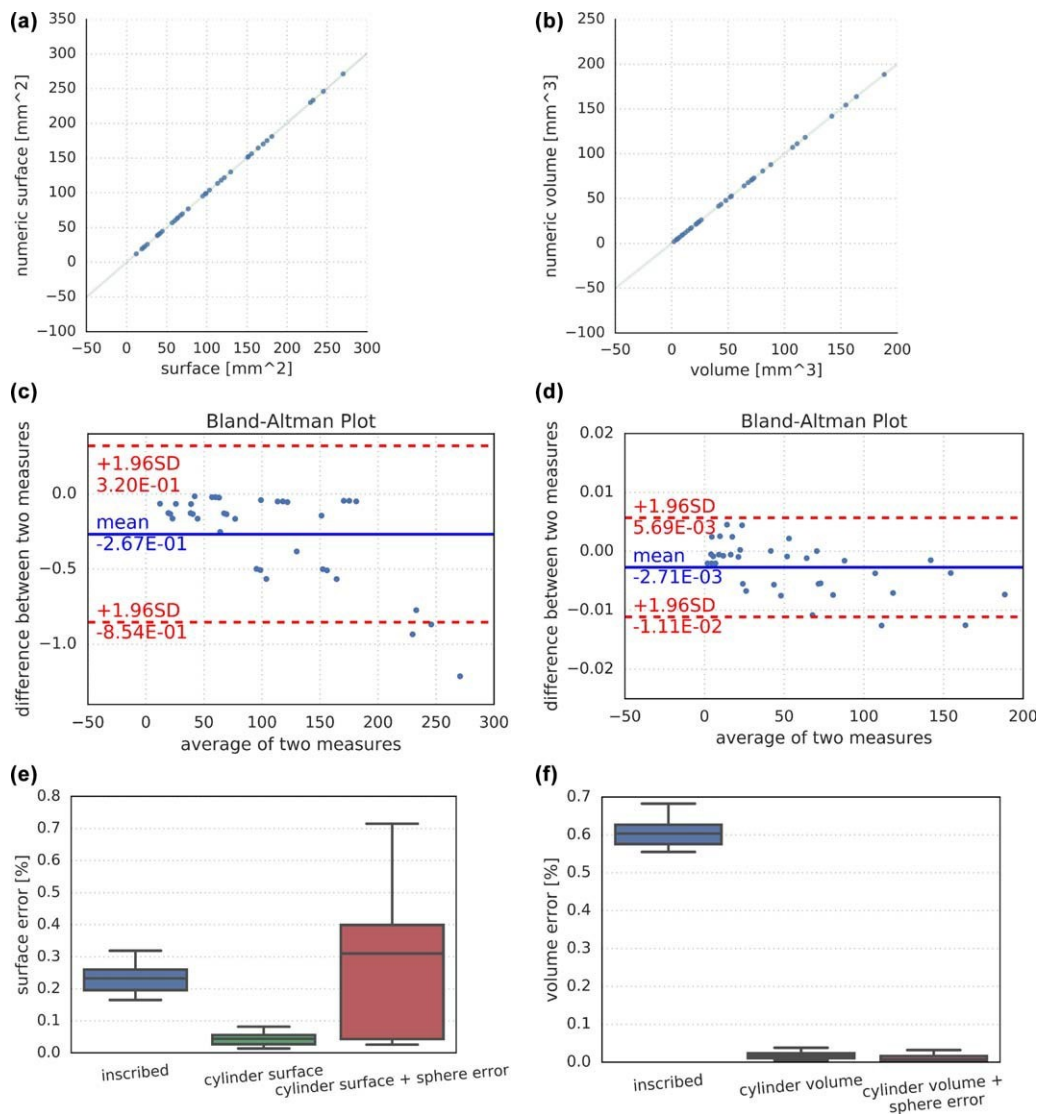


FIGURE 3 Comparing known volumes and surfaces with numerically estimated values. The source data for the graphs are available as Supporting Information S1. (a) Correlation scatter plot displaying the numerically estimated surfaces (Y-axis) against the precisely known surfaces (X-axis) of testing objects. (b) Correlation scatter plot displaying the numerically estimated volumes (Y-axis) against the precisely known volumes (X-axis) of testing objects. (c) Bland-Altman plot displaying the agreement between the numerically estimated surfaces and known surfaces of testing objects. The difference between both values (Y-axis) is plotted against their average (X-axis). The mean difference is shown as a blue line accompanied by a 1.96 standard deviation of the difference. (d) Bland-Altman plot (Altman and Bland, 1983) displaying the agreement between the numerically estimated volumes and known volumes of testing objects. The difference between both values (Y-axis) is plotted against their average (X-axis). The mean difference is shown as a blue line accompanied by a 1.96 standard deviation of the difference. (e) Box plot showing the impact of three methods used for compensation of the surface errors. (f) Box plot showing the impact of three methods used for compensation of the volume errors. In E and F, the relative error was calculated as $1003(\text{value} - \text{numerical estimate}) / \text{value}$. The box spans the lower limits of the 2nd quartile (Q2) and the upper limits of the 3rd quartile (Q3), and the whiskers span the $Q1 - 1.53(Q3 - Q1)$ and $Q3 + 1.53(Q3 - Q1)$ values (Q1 is the 1st quartile) [Color figure can be viewed at wileyonlinelibrary.com]

insufficient and inaccurate. To improve analysis, TelGen software is applied to generate dataset of tubular structures with known parameters. For example, a two-dimensional thresholding resulted in a significant overestimation of number of objects (Figure 7d, see also section 4.1.2) as well as inaccurate surface and volume estimates. In this case, using a three-dimensional thresholding was justified despite its computational time costs, as it provided more accurate results.

4 | DISCUSSION

4.1 | Image processing prior to micro-CT 3D analysis

4.1.1 | Image processing optimization: Aims and basics

Image processing optimization was based on many preliminary analyzes. We aimed to find a simple process (low number of variables

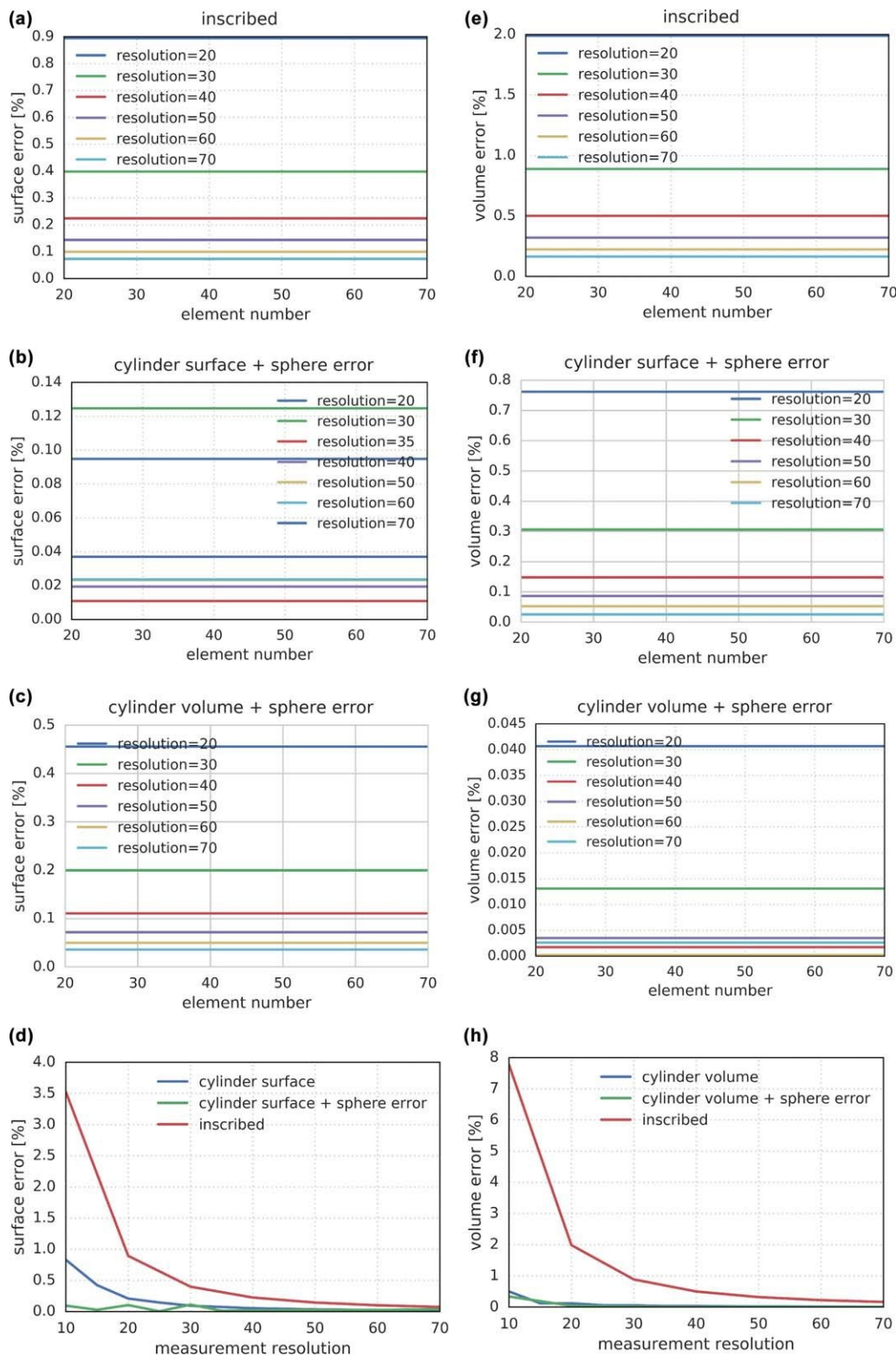


FIGURE 4 Analysis of the sensitivity of surface errors (a–d) and volume errors (e–h) to the number of generated objects (element number, a–c, e–g) and resolution at which the numerical estimates of the surface and volume were performed (d, h). The relative error plotted on the Y-axis was calculated as $1003(\text{true value} - \text{numerical estimate})/\text{value}$. The results are displayed without compensation (a, e) and for several methods of error compensation described in the Methods, namely: a, e—surface and volume error when no compensation is used (the colored lines show various resolutions), b, d—cylinder surface and sphere errors are compensated, c, g—cylinder volume and sphere errors are compensated. d, h—surface and volume measurement errors depending on the measurement resolution [Color figure can be viewed at wileyonlinelibrary.com]

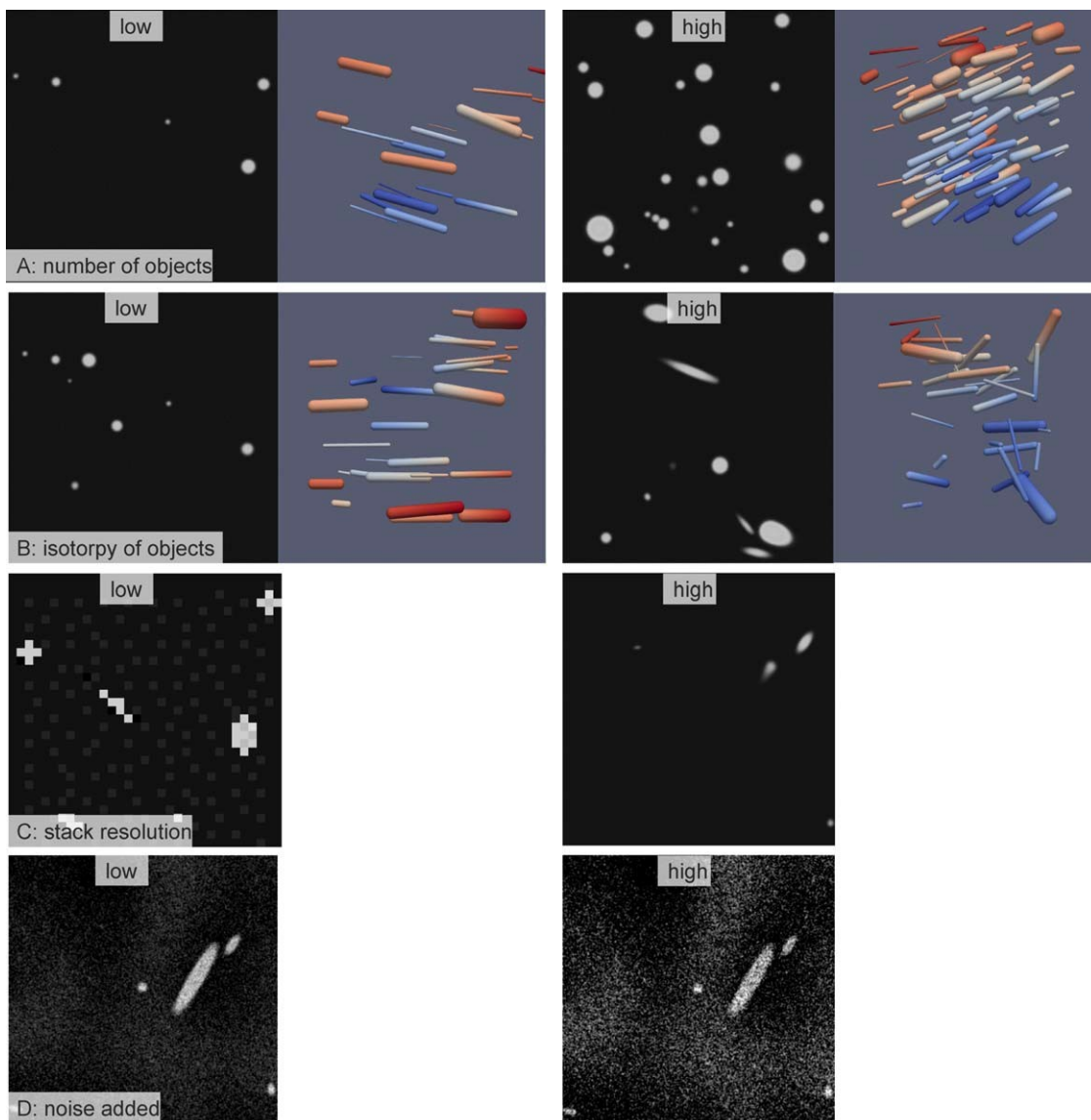


FIGURE 5 Examples of structures generated with various settings of parameters. For every parameter, ten sets of images were generated with values increasing from relatively low to relatively high, namely: (a) number of objects, (b) isotropy of objects, (c) resolution of image stacks, and (d) amount of noise added to the image data. In a-b, both two-dimensional sections and three-dimensional views are presented [Color figure can be viewed at wileyonlinelibrary.com]

influencing outcomes and convenient time efficacy) with satisfactory and reproducible results in all variable parameters of tested datasets. Datasets with the variable *count* were generally uncomplicated compared to *isotropy*, *noise*, and *resolution*, where we encountered more complications that had to be managed.

Image processing modifications by CTAn software were often performed based on subjective assessment by an experienced micro-CT user. This approach is very common in micro-CT analysis (especially in life sciences applications), and therefore it has been chosen for our study. However, this is considered one of the major drawbacks of micro-CT analysis. Reduction of subjectivity was reached by an automated threshold procedure and object count evaluation, which will be described further. This was achievable when assessing various values of object *count*, *isotropy* datasets, whereas *noise* and *resolution* dataset

evaluation was more influenced by subjectivity because individualization of the image processing approach was needed.

Object number count was important in process optimization. A user performing micro-CT analysis would not be aware of dataset parameters generated by TelGen software. Therefore, the object number count is the only parameter where differences between analysis results and dataset 3D visualization (CTVox, Bruker) are noticeable. There is no option for the evaluation of the other parameters (e.g., volume, surface, length) from this point of view.

The following procedures were used in the image processing optimization process. A universally accurate procedure ("standard" procedure) was found for *count* and *isotropy*. For *resolution* and *noise* variables, an individual approach had to be employed. Standard procedure was based of image filtering (Gaussian blur in 3D, radius 52

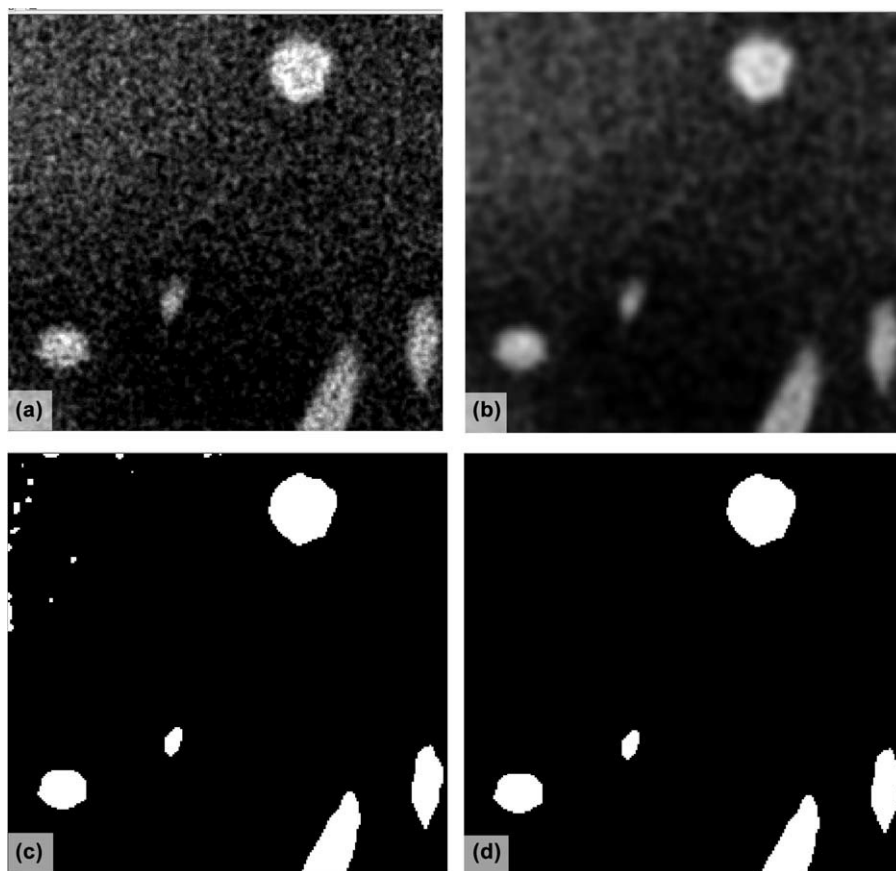


FIGURE 6 Main steps during the image processing of the virtual CT image stacks prior to analysis using the SkyScan 1272 (Bruker) console software. (a) Grayscale cross-section image (NOISE dataset). (b) Application of Gaussian blur in 3D. (c) Image after the binarization procedure (Global threshold). There are white speckles in the upper left corner as a result of image noise. We can observe irregular shapes of all objects as a result of noise and object interaction. (d) Image after performing a despeckle operation in 3D (remove white speckles of less than 50 voxels)

voxels), because some datasets had a gray pixel pattern on the background, and in some cases, they were evaluated as the objects using automatic binarization (Figure 7b). This pattern can imitate image noise in real micro-CT data. An automatic Otsu threshold in 3D was used for image binarization to reduce the influence of subjectivity. A despeckle operation in 3D was performed (remove white speckles less than 12 voxels—more in 4.1.2).

4.1.2 | Number of objects and its variability

Object number count was the only dataset parameter that could be employed in image processing optimization. Reduction of the object count number was observed in many cases, but usually less than 10% of the expected object count. Two causes were identified and explored. First, many datasets presented few relatively small objects, which were presented within a volume of interest only by their edge, so their grayscale values were not sufficient for recognition as an object. We have to consider that the transition from an object to the background is gradual, as we can see in the profile line (Figure 7a,b). In such objects, Gaussian filtering can even reduce their grayscale value, thus increasing the probability of being eliminated by binarization. Second, collision between objects was occasionally observed (Figure 7c), so two former

objects were recognized as one. TelGen should prevent these situations; however, regarding Figure 7a, we can estimate that two objects can be connected just by a gradual transition from object to background, even though their “core” structures are separate. In addition, Gaussian blur can enhance object collisions by creating a connection between the transition areas of two objects.

In contrast, the object count number increase was usually more substantial, i.e., from tens to hundreds of percent of the expected object count. Several causes were identified. In preliminary evaluation of an *isotropy* dataset, we found that objects with relatively small diameter that are almost parallel to the transversal plane were fragmented by the binarization process in 2D (tested for better time efficacy) into many smaller objects (Figure 7d). These objects could be roughly divided into two groups: small objects with volumes of a few voxels and large objects of higher volume but still much smaller than generated objects. These isolated voxels may be connected to the original object by a side or vertex; however, this is not sufficient to be recognized as one object since object voxels are, in CTAn, considered to be connected only when they are in contact via their faces. We decided to employ automatic Otsu thresholding in 3D, which led to significant improvement. However, the object count number was still much higher

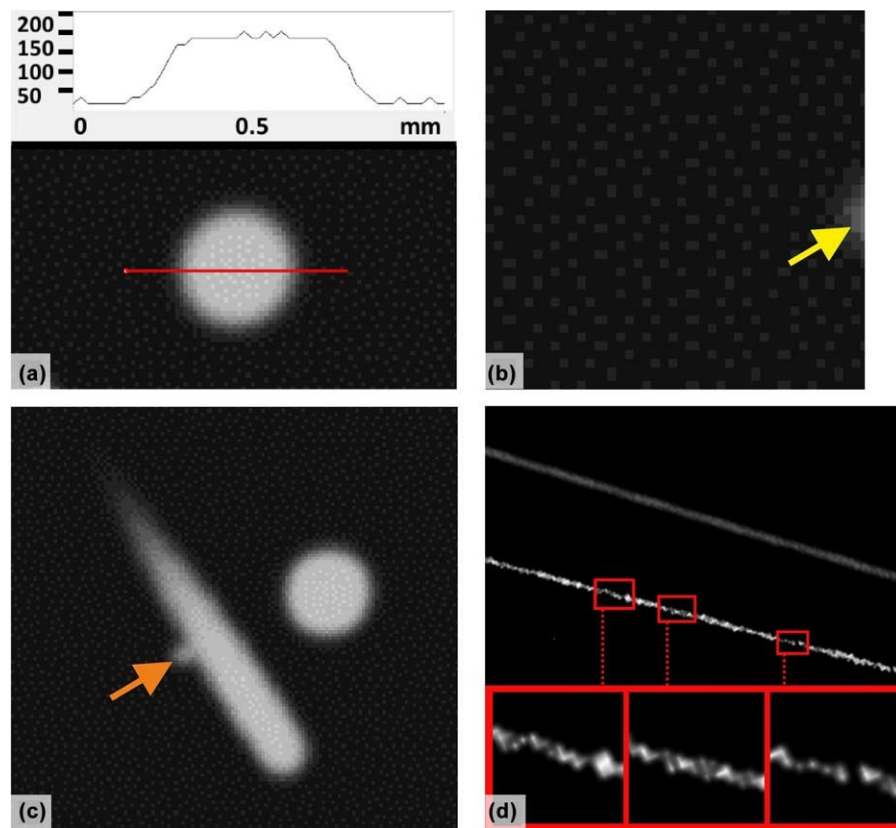


FIGURE 7 Illustration of situations leading to bias in analysis during the image processing. (a) Profile line (red line) presenting the image grayscale value (0–255). A gradual transition is apparent, which is similar to real micro-CT data. This phenomenon is a fundamental problem in image binarization. (b) Object count reduction caused by the peripheral section of an object (yellow arrow), where the grayscale value is not sufficient to be evaluated as an object by the automatic threshold. A pattern of gray pixels is visible in the background; in some data-sets, they were recognized as an object, and thus they have to be eliminated by a filtering procedure. (c) Object count reduction caused by the collision of two objects (orange arrow). These are connected by their transition areas even though their core structures are separate. (d) Object count reduction caused by object fragmentation by the binarization process (especially in 2D). The upper object presents a grayscale 3D model (CTVox), and the lower object is the same object after automatic image binarization in 2D; three areas are enlarged to depict fragmentation. According to Individual Object Analysis, there are 37 objects (!) from the original one [Color figure can be viewed at wileyonlinelibrary.com]

than expected. Individual Object Analysis was performed in 3D, and object volume distribution was achieved and examined. We found that a great number of objects are below 12 voxels in volume, and thus they were considered to be noise and removed by a despeckle operation in 3D (remove white speckles of less than 12 voxels). Modification of these two processes led to accurate dataset analysis regarding object number count.

4.1.3 | Resolution parameter and image processing

In *resolution* variable datasets (pixel size from 10 mm to 500 mm in a $3 \times 10^3 \times 10\text{-mm}^3$ volume), we observed an increase of the object number count with an increase of pixel size. Substantial changes resulted from a shift from 100 mm to 200 mm for pixel size. Objects with defined parameters are generated by TelGen software and subsequently voxelized. In lower resolution, objects can be fragmented as mentioned above (4.1.2). We did not succeed in finding a solution for image processing using CTAn for a pixel size of 200 mm or more for $10 \times 3 \times 10^3 \times 10\text{-mm}^3$ dataset volumes. An optimization process regarding object count evidently led to unacceptable changes in object volume and vice

versa. The pixel size value had to be considered for the parameter of filtering and despeckle operations in means of reduction of its value; for a pixel size of 80 mm or more, these operations were not applied.

4.1.4 | Noise parameter and image processing

Noise datasets (Figure 6a) needed higher individualization (and thus a more subjective approach) since these presented (together with *resolution* datasets) the most variable image data. Because of this, comparison with datasets processed by the “standard” approach is less applicable. The main problem was the gradual decrease of the signal to noise ratio in image data, so the outcome is always a compromise between noise reduction and object number and volume preservation. Filtration was achieved by Gaussian blur in 3D and was used with a gradual increase of the radius from 2 to 5 voxels (Figure 6b). An automatic Otsu threshold in 3D failed to provide reliable binarization because, in some datasets, noise was recognized as an object. A global threshold had to be employed with a progressive increase in the lower threshold value from 87 to 135 as the noise was intensified (Figure 6c). Interaction between noise and generated objects can lead to an

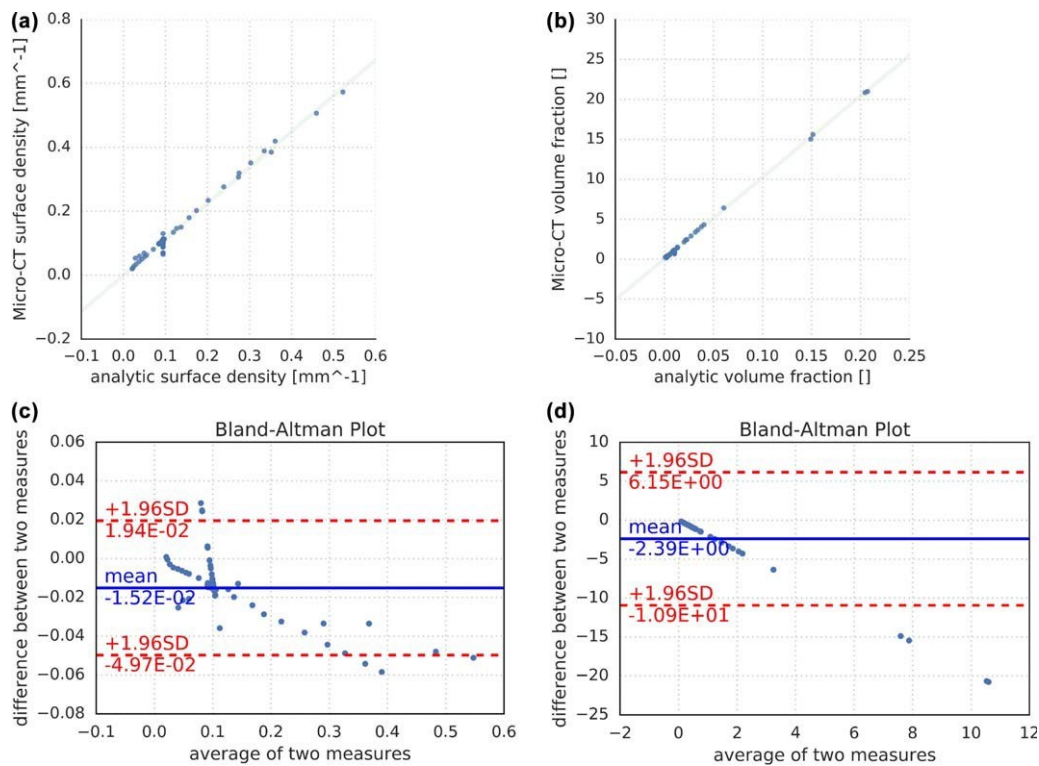


FIGURE 8 Comparing known surface and volume densities of generated objects with the results obtained after thresholding on the micro-CT console. The source data for the graphs are provided as Supporting Information S2. Data sets with known surface and volume densities were processed by the micro-CT software as described above. (a,b) correlation scatter plots displaying the values from micro-CT (Y-axis) against the precisely known surface and volume densities (X-axis) of testing objects. (c,d) Bland-Altman plots displaying the agreement between the surface and volume densities estimated on micro-CT and known values of the same testing objects. The difference between both values (Y-axis) is plotted against their average (X-axis). The mean difference is shown as a blue line accompanied by a 61.96 standard deviation of the difference [Color figure can be viewed at wileyonlinelibrary.com]

alteration of volume, surface and object shape, which is noticeable in Figure 6c. A higher threshold value resulted in a reduction in object number count and object volume. A despeckle operation was performed with an increase of defined volume (removing white speckles less than: from 12 to 250 mm; Figure 6d).

4.2 | Novelty of the present approach

When compared to the ImageJ plugins mentioned in 1.3., the TelGen software allows for generating 3D objects as test images. When compared with the Gensei software (Cimman, 2010), TelGen provides colliding and noncolliding fibrous structures, the geometric characteristics of which can be set by the user. Moreover, TelGen generates also porosities and allows for modeling various types of realistic noise. The application includes both graphical user interface with 3D visualization which facilitates data preparation, as well as batch processing option.

It is recommended that the user performs a real object analysis first, using a micro-CT or scanning electron microscopy, thus estimating the typical range of the quantitative characteristics (i.e., total volumes, surfaces, lengths, and number of objects inside ROI). However, the error between the true and estimated data is unknown. In the second step, the data are used as input data of the TelGen software defining the objects to be generated. In this second step, phantom objects with

geometrical properties statistically similar to the real material are generated, but this time, the geometrical characteristics are precisely known. In the third step, the measurement of these phantom data is repeated and the error between the true known and estimated data is quantified. This can be used for calibration of the whole measurement and for identifying any major sources of bias.

In general, using traceable standard reference materials has always belonged to good laboratory practice. The TelGen software offers a solution by generating virtual standard reference materials. These might either mimic the real materials or be generated according to the best qualified estimates currently available.

4.3 | Further development of the TelGen software and its relevance to manufacturing and characterization of biomaterials

Further development of the TelGen software incorporates improvements in the highest values of filling the space with unconnected objects of increasing volume fraction. This task has theoretical limits that cannot be exceeded (Zidek et al., 2016), but the present algorithm starts to require unacceptable computational time costs when reaching the value of approx. 30% volume fraction. Should more space be filled with the tubes, collisions have to be allowed in the settings.

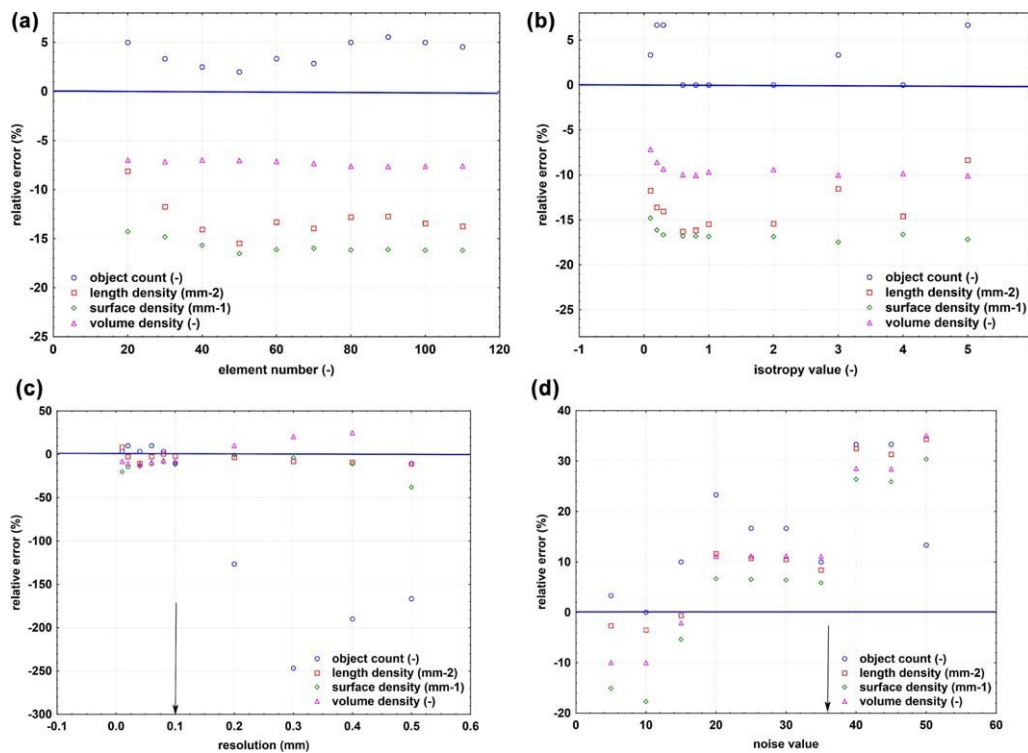


FIGURE 9 Analysis of the sensitivity of the thresholding to various values of parameters in generated image sets. Data sets with known numbers of objects, length densities, surface densities, and volume densities were processed by the micro-CT software as described above. After the morphometry on the micro-CT console was done, the relative errors (Y-axis) were calculated as $100 \times (\text{true value} - \text{numerical estimate}) / \text{value}$ and plotted against gradually changing values of the number of objects (a), isotropy (b), image resolution (c), and noise value (d). (a) Various object counts did not affect the size of the relative error. While the numbers of objects were underestimated by the microCT, the volumes, lengths and surfaces were slightly overestimated. (b) The value of isotropy did not affect the size of the error. (c) The size of the error dramatically increased when the voxel size exceeded 0.1 mm (arrow) in virtual stacks of $103 \times 103 \times 10$ mm containing objects with a mean diameter of 1 mm. (d) The size of the error increased when the noise value exceeded 37 (arrow) [Color figure can be viewed at wileyonlinelibrary.com]

Another challenge for the future would be using the sections of generating objects to simulate the optimum sampling of numbers of image sections and their thicknesses. The TelGen software can become a useful tool for planning of the sampling design of studies in microscopy, including manual and interactive measurements of objects with known size, where the research aim is to find the number and thickness

of sections that are necessary for reliable measurements of numbers, surfaces, and volumes of tubular or spherical objects in studies using stereological counting rules (Mouton et al., 2017).

We greatly acknowledge the wide use of the ImageJ software (Schneider et al., 2012) and its contribution to the scientific community worldwide. Although ImageJ currently supports Python scripting, it

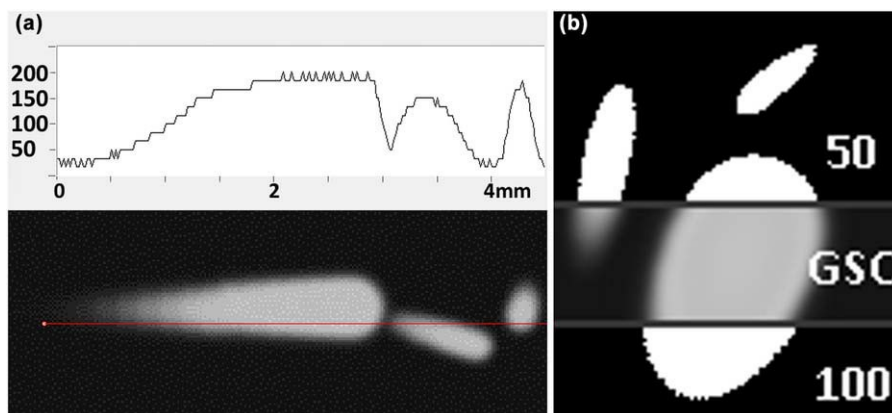


FIGURE 10 Illustration of global thresholding effect. (a) Profile line cutting tubular structures with grayscale value. (b) Different global threshold values (50 and 100; values were chosen to provide apparent differences in this figure) combined with original grayscale image (GSC). Binarized structures appear larger or smaller based on threshold value used [Color figure can be viewed at wileyonlinelibrary.com]

TABLE 3 Example of practical application of the TelGen software

	Object number	Tot.V. (mm ³)	M.Obj.V. (mm ³)	Tot.S. (mm ²)	M.Obj.S. (mm ²)
TeiGen (true value)	30	11.33	0.38	113.39	3.78
Global threshold 5 50	28	16.00	0.57	136.89	4.89
Global threshold 5 75	30	12.42	0.41	116.20	3.87
Global threshold 5 100	29	10.33	0.36	102.17	3.52

Illustration of the effect of Global threshold used during micro-CT processing on analysis results in selected parameters: Tot.V.—total volume of all objects, M.Obj.V.—mean object volume, Tot.S.—total surface of all objects, M.Obj.S.—mean object surface. For details see Figure 10 and section 3.5. This analysis required approximately 20 min of time and revealed the preferred Global threshold settings 575.

currently does not allow for using libraries that are not part of the language kernel (for example, *scipy*, *numpy*, *scikit-image* libraries, and several others). Should the ImageJ support these libraries in the future, the TeiGen software can be incorporated as an ImageJ plugin, thus benefiting from the ImageJ interface and a plethora of other functions. At present TeiGen can cooperate with ImageJ by reading and saving image data from/into the commonly supported file formats.

5 | CONCLUSION

Open-source software for the generation of three-dimensional models of fibrous and porous structures with known volumes, surfaces, lengths and object counts was developed and made freely available to the scientific community. This study provides a software tool for calibrating quantitative micro-CT assessments by producing and saving virtually generated image datasets with known morphometric data on noncolliding tubes, colliding tubes, or material porosities. This tool is useful for identifying combinations of object and image stack properties, which may easily lead to biased results using thresholding procedures of fibrous biomaterials in microCT. Some of these situations were extensively tested in the present article to help users of micro-CT understand where errors can occur, ensuring that micro-CT segmentation procedures can be proved to be valid and correct. We identified combinations of object and image stack properties that may easily lead to biased results using thresholding procedures in microCT. A solution to this problem could be more frequent application of design-based stereological methods during micro-CT analyzes. This method is openly available to researchers involved in morphometry of three-dimensional fibrillar and porous structures in micro-CT scans.

HUMAN AND ANIMAL RIGHTS STATEMENT

This article does not contain any studies with human participants or animals performed by any of the authors. This article does not contain patient data.

ACKNOWLEDGMENTS

The authors thank the following research projects. ZT, PS, and MHK were supported by AZV MZ CR Project No. 15-25813A. MJ, TK, AM, PT, PS, MHK, and MK were also supported by the National

Sustainability Program I (NPU I) Nr. LO1503 provided by the Ministry of Education, Youth and Sports of the Czech Republic, by the Progres Q39 and Progres Q29/LF1 (MB) projects of the Charles University, and by the SVV 260390/2017 and SVV 260392/2017 projects of the Charles University. PK was supported by project LO1506 of the Czech Ministry of Education, Youth and Sports under program NPU I. ZT was also supported by the Ministry of Education, Youth and Sports under the project FIND No. CZ.02.1.01/0.0/0.0/16_019/0000787. The micro-CT part of the study is a result of the project implementation: "Technological development of post doc programs," registration number CZ.1.05/41.00/16.0346, supported by Research and Development for Innovations Operational Programme (RDOP) co-financed by the European regional development fund and the state budget of the Czech Republic. MJ and ZT were also supported by the Charles University Research Centre program UNCE/MED/006 University Center of Clinical and Experimental Liver Surgery.

CONFLICT OF INTEREST

The authors declare that they have no conflicts of interest.

ORCID

Zbynek Tonar  <http://orcid.org/0000-0002-7200-9894>

REFERENCES

- Altman, D. G., & Bland, J. M. (1983). Measurement in medicine: The analysis of method comparison studies. *The Statistician*, 32(3), 307–317.
- Baddeley, A., & Jensen, E. B. (2004). *Stereology for statisticians*. Boca Raton: Chapman & Hall/CRC.
- Bruker Corporation. (2017). *Morphometric parameters measured by Sky-scan™ CT-analyser software*. Billerica: Bruker Corporation.
- Buie, H. R., Campbell, G. M., Klinck, R. J., MacNeil, J. A., & Boyd, S. K. (2007). Automatic segmentation of cortical and trabecular compartments based on a dual threshold technique for in vivo micro-CT bone analysis. *Bone*, 41(4), 505–515.
- Burey, A., Dos Reis, P. J., Santana, Vicentin B. L., Dezan Garbelini, C. C., Grama Hoepfner, M., & Appoloni, C. R. (2018). Polymerization shrinkage and porosity profile of dual cure dental resin cements with different adhesion to dentin mechanisms. *Microscopy Research and Technique*, 71(1), 88–96.

- Burey, A., Dos Reis, P. J., Santana Vicentin, B. L., Dezan Garbelini, C. C., Grama Hoepfner, M., & Appoloni, C. R. (in press). Polymerization shrinkage and porosity profile of dual cure dental resin cements with different adhesion to dentin mechanisms. *Microscopy Research and Technique*. <https://doi.org/10.1002/jemt.22960>.
- Burghardt, A. J., Kazakia, G. J., & Majumdar, S. (2007). A local adaptive threshold strategy for high resolution peripheral quantitative computed tomography of trabecular bone. *Annals of Biomedical Engineering*, 35(10), 1678.
- Cimrman, R. (2010). Gensei – GENErate serial images. Retrieved from <https://github.com/rc/gensei>
- De Souza, E. T., Nunes Tameirao, M. D., Roter, J. M., De Assis, J. T., De Almeida Neves, A., & De-Deus, G. A. (2013). Tridimensional quantitative porosity characterization of three set calcium silicate-based repair cements for endodontic use. *Microscopy Research and Technique*, 76(10), 1093–1098.
- Draenert, M. E., Draenert, A. I., Forriol, F., Cerler, M., Kunzelmann, K. H., Hickel, R., & Draenert, K. (2012). Value and limits of m-CT for non-deminerallized bone tissue processing. *Microscopy Research and Technique*, 75(4), 416–424.
- Gómez, S., Vlad, M. D., López, J., & Fernández, E. (2016). Design and properties of 3D scaffolds for bone tissue engineering. *Acta Biomaterialia*, 42, 341–350.
- Gómez, S., Vlad, M. D., López, J., Navarro, M., & Fernández, E. (2013). Characterization and three-dimensional reconstruction of synthetic bone model foams. *Materials Science & Engineering. C, Materials for Biological Applications*, 33(6), 3329–3335.
- Hara, T., Tanck, E., Homminga, J., & Huiskes, R. (2002). The influence of microcomputed tomography threshold variations on the assessment of structural and mechanical trabecular bone properties. *Bone*, 31(1), 107–109.
- Hildebrand, T., & Ruegsegger, P. (2003). A new method for the model independent assessment of thickness in three dimensional images. *Journal of Microscopy*, 185, 67–75.
- Ho, S. T., & Hutmacher, D. W. (2006). A comparison of micro CT with other techniques used in the characterization of scaffolds. *Biomaterials*, 27(8), 1362–1376.
- Horakova, J., Mikes, P., Saman, A., Svarcova, T., Jencova, V., Suchy, T., ... Prochazkova, R. (2018). Comprehensive assessment of electrospun scaffolds hemocompatibility. *Materials Science & Engineering. C, Materials for Biological Applications*, 82, 330–335.
- Jiménez, P., Thomas, F., & Torras, C. (2001). 3D collision detection: A survey. *Computers & Graphics*, 25, 269–285.
- Jirík, M. (2017). Teigen – TEst Image GENEerator software. Retrieved from <https://mjirik.github.io/teigen/>
- Jirík, M., & Tonar, Z. (2018). User manual for the Teigen – TEst Image GENEerator software. Retrieved from https://github.com/mjirik/teigen/blob/master/user_manual.md
- Jirík, M., Tonar, Z., Králíčková, A., Eberlová, L., Mírka, H., Kochová, P., ... Liska, V. (2016). Stereological quantification of microvessels using semiautomated evaluation of X-ray microtomography of hepatic vascular corrosion casts. *International Journal of Computer Assisted Radiology and Surgery*, 11(10), 1803–1819.
- Jones, A. C., Arns, C. H., Sheppard, A. P., Hutmacher, D. W., Milthorpe, B. K., & Knackstedt, M. A. (2007). Assessment of bone ingrowth into porous biomaterials using Micro-CT. *Biomaterials*, 28(15), 2491–2504.
- Karageorgiou, V., & Kaplan, D. (2005). Porosity of 3D biomaterial scaffolds and osteogenesis. *Biomaterials*, 26(27), 5474–5491.
- Kochová, P., Cimrman, R., Janáček, J., Witter, K., & Tonar, Z. (2011). How to assess, visualize and compare the anisotropy of linear structures reconstructed from optical sections - a study based on histopathological quantification of human brain microvessels. *Journal of Theoretical Biology*, 286(1), 67–78.
- Landis, E. N., & Keane, D. T. (2010). X-ray microtomography. *Materials Characterization*, 61(12), 1305–1316.
- Lorensen, W. E., & Harvey, E. C. (1987). Marching cubes: A high resolution 3d surface construction algorithm. *ACM Siggraph Computer Graphics*, 21(4), 163–169.
- Maia, R. S., Jacob, C., Hara, A. K., Silva, A. C., Pavlicek, W., & Ross, M. J. (2015). An algorithm for noise correction of dual-energy computed tomography material density images. *International Journal of Computer Assisted Radiology and Surgery*, 10(1), 87–100.
- Montufar, E. B., Vojtova, L., Celko, L., & Ginebra, M. P. (2017). Calcium phosphate foams: Potential scaffolds for bone tissue modeling in three dimensions. *Methods in Molecular Biology (Clifton, N.J.)*, 1612, 79–94.
- Moore, M., & Wilhelms, J. (1988). Collision detection and response for computer animation. *Computer Graphics*, 22(4), 289–298.
- Mouton, P. R. (2002). *Principles and practices of unbiased stereology. An introduction for bioscientists*. Baltimore: The Johns Hopkins University Press.
- Mouton, P. R., Phoulady, H. A., Goldgof, D., Hall, L. O., Gordon, M., & Morgan, D. (2017). Unbiased estimation of cell number using the automatic optical fractionator. *Journal of Chemical Neuroanatomy*, 80, A1–A8.
- Neves, A. A., Coutinho, E., Alves, H. D., & de Assis, J. T. (2015). Stress and strain distribution in demineralized enamel: A micro-CT based finite element study. *Microscopy Research and Technique*, 78(10), 865–872.
- Otsu, N. (1979). A threshold selection method from gray-level histograms. *IEEE Transactions on Systems, Man, and Cybernetics*, 9(1), 62–66.
- Parkinson, I. H., Badiei, A., & Fazzalari, N. L. (2008). Variation in segmentation of bone from micro-CT imaging: Implications for quantitative morphometric analysis. *Australasian Physical & Engineering Sciences in Medicine*, 31(2), 160–164.
- Particelli, F., Mecozzi, L., Beraudi, A., Montesi, M., Baruffaldi, F., & Viceconti, M. (2012). A comparison between micro-CT and histology for the evaluation of cortical bone: Effect of polymethylmethacrylate embedding on structural parameters. *Journal of Microscopy*, 245(3), 302–310.
- Plencner, M., East, B., Tonar, Z., Otáhal, M., Prosecká, E., Rampichová, M., ... Amler, E. (2014). Abdominal closure reinforcement by using polypropylene mesh functionalized with poly-ε-caprolactone nanofibers and growth factors for prevention of incisional hernia formation. *International Journal of Nanomedicine*, 9, 3263–3277.
- Prosecká, E., Rampichová, M., Litvinec, A., Tonar, Z., Králíčková, M., Vojtová, L., ... Amler, E. (2015). Collagen/hydroxyapatite scaffold enriched with polycaprolactone nanofibers, thrombocyte-rich solution and mesenchymal stem cells promotes regeneration in large bone defect in vivo. *Journal of Biomedical Materials Research Part A*, 103(2), 671–682.
- Pyka, G., Kerckhofs, G., Schrooten, J., & Wevers, M. (2014). The effect of spatial micro-CT image resolution and surface complexity on the morphological 3D analysis of open porous structures. *Materials Characterization*, 87, 104–115.
- Rau, T. S., Würfel, W., Lenarz, T., & Majdani, O. (2013). Three-dimensional histological specimen preparation for accurate imaging and

- spatial reconstruction of the middle and inner ear. *International Journal of Computer Assisted Radiology and Surgery*, 8(4), 481–509.
- Remy, E., & Thiel, E. (2002). Medial axis for chamfer distances: Computing look-up tables and neighbourhoods in 2D or 3D. *Pattern Recognition Letters*, 23(6), 649–661.
- Schladitz, K. (2011). Quantitative micro-CT. *Journal of Microscopy*, 243(2), 111–117.
- Schneider, C. A., Rasband, W. S., & Eliceiri, K. W. (2012). NIH Image to ImageJ: 25 years of image analysis. *Nature Methods*, 9(7), 671–675.
- Schroeder, W. J., Avila, L. S., & Hoffman, W. (2000). Visualizing with VTK: A tutorial. *IEEE Computer Graphics and Applications*, 20(5), 20–27.
- Schroeder, W., Martin, K. M., & Lorensen, W. E. (1998). *The visualization toolkit (2nd ed.): An object-oriented approach to 3D graphics*. Upper Saddle River: Prentice-Hall.
- Shen, H., Nutt, S., & Hull, D. (2004). Direct observation and measurement of fiber architecture in short fiber-polymer composite foam through micro-CT imaging. *Composites Sci Technol*, 64(13–14), 2113–2120.
- Shepp, L. A., & Logan, B. F. (1974). The Fourier reconstruction of a head section. *IEEE Transactions on Nuclear Science*, 21(3), 21–43.
- Stock, S. R. (2009). *MicroComputed tomography methodology and applications*. Boca Raton: CRC Press.
- Stoyan, D., Kendall, W. S., & Mecke, J. (1995). *Stochastic geometry and its applications*. New York: John Wiley & Sons.
- Suchý, T., Supová, M., Sauerová, P., Verdánová, M., Sucharda, Z., Rýgllová, S., ... Kalbáčková, M. H. (2015). The effects of different cross-linking conditions on collagen-based nanocomposite scaffolds—an in vitro evaluation using mesenchymal stem cells. *Biomedical Materials (Bristol, England)*, 10(6), 065008.
- Szentivanyi, A., Chakradeo, T., Zernetsch, H., & Glasmacher, B. (2011). Electrospun cellular microenvironments: Understanding controlled release and scaffold structure. *Advanced Drug Delivery Reviews*, 63(4–5), 209–220.
- Tonar, Z., Khadang, I., Fiala, P., Nedorost, L., & Kochová, P. (2011). Quantification of compact bone microporosities in the basal and alveolar portions of the human mandible using osteocyte lacunar density and area fraction of vascular canals. *Annals of Anatomy*, 193(3), 211–219.
- Tonar, Z., Kochova, P., Cimrman, R., Witter, K., Janacek, J., & Rohan, V. (2011). Microstructure oriented modelling of hierarchically perfused porous media for cerebral blood flow evaluation. *Key Engineering Materials*, 465, 286–289.
- Yan, Y. B., Qi, W., Qiu, T. X., Teo, E. C., & Lei, W. (2012). The effect of threshold value on the architectural parameters and stiffness of human cancellous bone in micro-CT analysis. *Journal of Mechanics in Medicine and Biology*, 12(05), 1250092.
- Zhang, J., Yan, C. H., Chui, C. K., & Ong, S. H. (2010). Fast segmentation of bone in CT images using 3D adaptive thresholding. *Computers in Biology and Medicine*, 40(2), 231–236.
- Zhong, S., Zhang, Y., & Lim, C. T. (2012). Fabrication of large pores in electrospun nanofibrous scaffolds for cellular infiltration: A review. *Tissue Engineering Part B, Reviews*, 18(2), 77–87.
- Zidek, J., Vojtova, L., Abdel-Mohsen, A. M., Chmelik, J., Zikmund, T., Brtnikova, J., ... Kaiser, J. (2016). Accurate micro-computed tomography imaging of pore spaces in collagen-based scaffold. *Journal of Materials Science: Materials in Medicine*, 27(6), 110.

SUPPORTING INFORMATION

Additional Supporting Information may be found online in the supporting information tab for this article.

How to cite this article: Jirík M, Bartoš M, Tomásek P, et al. Generating standardized image data for testing and calibrating quantification of volumes, surfaces, lengths, and object counts in fibrous and porous materials using X-ray microtomography. *Microsc Res Tech*. 2018;81:551–568. <https://doi.org/10.1002/jemt.23011>

10.6 Příloha VI

MIK, Patrik, TONAR, Zbyněk, MALEČKOVÁ, Anna, EBERLOVÁ, Lada, LIŠKA, Václav, PÁLEK, Richard, ROSENDORF, Jáchym, JIŘÍK, Miroslav, MÍRKA, Hynek, KRÁLÍČKOVÁ, Milena, WITTER, Kirsti, 2018. Distribution of Connective Tissue in the Male and Female Porcine Liver: Histological Mapping and Recommendations for Sampling. *Journal of comparative pathology*. 162, 1–13. ISSN 0021-9975. Dostupné z: <https://doi.org/10.1016/j.jcpa.2018.05.004>
IF_(JCR2017) = 1,364. Q2 (Veterinary sciences)



SPONTANEOUSLY ARISING DISEASE

Distribution of Connective Tissue in the Male and Female Porcine Liver: Histological Mapping and Recommendations for Sampling

P. Mik^{*}, Z. Tonar[†], A. Malešková[‡], L. Eberlová^{*}, V. Liska[‡], R. Pálek[‡],
J. Rosendorf[‡], M. Jirák[‡], H. Mírka[‡], M. Králieková[†] and K. Witter^k

^{*}Department of Anatomy, [†]Department of Histology and Embryology and Biomedical Center, Faculty of Medicine in Pilsen, Charles University, Karlovarska 48, [‡]Department of Surgery and Biomedical Center, Faculty of Medicine in Pilsen, Charles University, Alej Svobody 80, ^xEuropean Centre of Excellence NTIS, Faculty of Applied Sciences, University of West Bohemia, Univerzitni 22, Pilsen, [‡]Department of Imaging Methods and Biomedical Centre, Faculty of Medicine in Pilsen, Charles University, University Hospital in Pilsen, Czech Republic and ^kInstitute of Anatomy, Histology and Embryology, Department for Pathobiology, University of Veterinary Medicine Vienna, Veterinärplatz 1, Vienna, Austria

Summary

The pig is a large animal model that is often used in experimental medicine. The aim of this study was to assess, in normal pig livers, sexual dimorphism in the normal fraction of hepatic interlobular and intralobular connective tissue (CT) in six hepatic lobes and in three macroscopical regions of interest (ROIs) with different positions relative to the liver vasculature. Using stereological point grids, the fractions of CT were quantified in histological sections stained with aniline blue and nuclear fast red. Samples (415 tissue blocks) were collected from healthy piglets, representing paracaval, paraportal and peripheral ROIs. There was considerable variability in the CT fraction at all sampling levels. In males the mean fraction of interlobular CT was 4.7 ± 0.4% (mean ± SD) and ranged from 0% to 11.4%. In females the mean fraction of the interlobular CT was 3.6 ± 0.2% and ranged from 0% to 12.3%. The mean fraction of intralobular (perisinusoidal summed with pericentral) CT was <0.2% in both sexes. The interlobular CT represented >99.8% of the total hepatic CT and the fractions were highly correlated (Spearman $r=0.998$, $P<0.05$). The smallest CT fraction was observed in the left medial lobe and in the paracaval ROI and the largest CT fraction was detected in the quadrate lobe and in the peripheral ROI. For planning experiments involving the histological quantification of liver fibrosis and requiring comparison between the liver lobes, these data facilitate the power analysis for sample size needed to detect the expected relative increase or decrease in the fraction of CT.

© 2018 Elsevier Ltd. All rights reserved.

Keywords: connective tissue; histology; liver; pig

Introduction

Both small and large animals are used to study the mechanisms of the origin and spread of liver fibrosis, often together with the regenerative capacity and healing of the liver. Fibroses of different aetiologies have been studied predominantly in mice (George

et al., 2003; Anstee and Goldin, 2006; Machado *et al.*, 2015) and rats (Yi *et al.*, 2012; Nowatzky *et al.*, 2013; Fakhoury-Sayegh *et al.*, 2015). However, small animal models of liver fibrosis have several limitations due to the small organ size (Lossi *et al.*, 2016). Therefore, it is usually not possible to study phenomena such as portocentral and portoportal bridging fibrosis, modelling of the biomechanics of trauma, lobar resection and regeneration or surgical

Correspondence to: Z. Tonar (e-mail: Zbynek.Tonar@lfp.cuni.cz).

techniques. Large animal models are needed for the improved translation of experimental work into human medicine. Apart from sheep liver (Ghodsizad *et al.*, 2012), the porcine liver is the most widely used large animal model (Avritscher *et al.*, 2011; Kawamura *et al.*, 2014; Bruha *et al.*, 2015; Nygård *et al.*, 2015; Wang *et al.*, 2015) to study improvements in invasive (Croome *et al.*, 2015) and non-invasive methods of liver disease management (Gnutzmann *et al.*, 2015), to interpret animal experiments and to translate the results of animal models to human medicine (Arkadopoulos *et al.*, 2011; Watson *et al.*, 2016; Budai *et al.*, 2017). Chen *et al.* (2013) showed that histological assessment of liver fibrosis in the pig correlates with non-invasive splenic magnetic resonance imaging. Combining the data obtained for connective tissue (CT) with data on the microvascular bed of the porcine liver (Eberlova *et al.*, 2016, 2017) would improve existing models of human liver perfusion. Moreover, fibrosis is an important part of porcine liver diseases, such as in pigs suffering from biliary and peribiliary cysts (Komine *et al.*, 2008) or swine hepatitis E (Lee *et al.*, 2010).

Summarizing the present literature, porcine liver fibrosis and cirrhosis of different aetiologies can be used as a model for human liver fibrosis and cirrhosis (Avritscher *et al.*, 2011). In the porcine liver, fibrosis is usually induced by CCl₄ (Zhang *et al.*, 2009), by alcohol (Lee *et al.*, 2017), by a high-fat diet or by a Western-style diet (Panasevich *et al.*, 2018) or by using pentoxifylline (Peterson and Neumeister, 1996). It has been proposed that porcine liver fibrosis may be staged according to human standards using the Metavir scoring system (Ishak *et al.*, 1995; Zhou *et al.*, 2014; Yin *et al.*, 2017); however, this required several modifications (Huang *et al.*, 2014, 2017).

The major fibrogenic cells in the liver are the hepatic stellate cells, portal fibroblasts, fibrocytes, bone marrow-derived cells that are activated and transdifferentiated into hepatic myofibroblasts and possibly hepatocytes and cholangiocytes that transition to myofibroblasts (Forbes and Parola, 2011; Zhao *et al.*, 2016; Kisseleva, 2017). Histological assessment of the location of fibrosis and identification of the source of fibrogenic cells is necessary when assessing the severity of the liver disease and the patient's prognosis (Takahashi and Fukusato, 2014; Stasi and Milani, 2016). Biopsy samples are usually scored in terms of their grade (Scheuer, 1991) and stage (Saxena, 2011). Six specific foci of liver fibrogenesis have been proposed for scoring, namely portal, pericellular (i.e. perisinusoidal), pericentral (i.e. perivenular), centrilobular, ductal (i.e. periductal) and ductular (Batts and Ludwig, 1995; Gohlke *et al.*,

1996; Brunt *et al.*, 1999; Sakhuja, 2014; Takahashi and Fukusato, 2014).

During chronic hepatitis, fibrosis starts and spreads from portal regions, forming stellate periportal scars or enlarging the portal tracts (Lefkowitz, 2007). Steatofibrosis in alcoholic liver disease begins in the pericentral region and extends in a perisinusoidal pattern, where it is more pronounced than in hepatitis C infection (Zaitoun *et al.*, 2001). This phenomenon leads to centroportal and portoportal bridging and, together with the regenerating nodular parenchyma, results in cirrhosis (Theise, 2013). Similar histological findings have been reported in non-alcoholic fatty liver disease (NAFLD) or non-alcoholic steatohepatitis (NASH), but lack the pericentral origin of fibrosis (Brunt *et al.*, 1999; Kleiner *et al.*, 2005; Takahashi and Fukusato, 2014). Primary biliary cirrhosis involves fibrosis of small intrahepatic bile ducts (Lindor *et al.*, 2009; Working Subgroup for Clinical Practice Guidelines for Primary Biliary Cirrhosis, 2014). Central hepatic veins are often retained in their centrilobular location, even in cirrhosis. Sclerosing cholangitis shows bile duct scarring biliary fibrosis, leading eventually to cirrhosis (Hirschfield *et al.*, 2013; de Vries *et al.*, 2015).

The amount of CT in the human liver is usually estimated during routine analysis of liver biopsy samples, according to widely used scoring systems (Scheuer, 1991; Ishak *et al.*, 1995; Bedossa and Poynard, 1996). However, Standish *et al.* (2006) highlighted several limitations of subjective or semiquantitative scoring as both the interobserver and intraobserver variability might disqualify the data generated from comparative studies or from evaluations of non-invasive methods of liver fibrosis. Therefore, the need for an objective, reproducible measure, preferably generating continuous data, has been articulated (Saxena, 2011).

To the best of our knowledge, no published data are available for continuous quantitative histological parameters that demonstrate the normal intersexual and interindividual variability in the fraction of CT in various macroscopical regions of porcine liver lobes. Therefore, the aim of the present study was to assess the content and distribution of normal hepatic CT in the domestic pig and to provide sampling recommendations for further histopathological studies. The following null hypotheses were tested: (1) the volume fraction of CT in the liver is the same in male and in female pigs, (2) the volume fraction of CT in the liver is the same in all hepatic lobes and (3) the volume fraction of CT in the liver is the same in three macroscopical regions with different positions related to the liver vasculature (regions of interest; ROIs): the peripheral regions of the liver lobes, the regions near

the porta hepatis and the regions adjacent to the caudal vena cava.

Materials and Methods

Animals

As a part of this study we used liver samples collected previously for studies of the size and density of hepatocytes in the porcine liver (Junatas *et al.*, 2017). Five more animals were added. Briefly, liver samples were obtained from 12 healthy Prestice black-pied pigs (Vrtková, 2015) aged 9–15 weeks and weighing 25–45 kg (34.3 ± 5.3 kg, mean ± standard deviation [SD]). Six piglets were male and six piglets were female (see Supplementary Table 1 for sample details). The animals received humane care in compliance with the European Convention on Animal Care and project number 27374/2011-30 was approved by the Faculty Committee for the Prevention of Cruelty to Animals. The animals were premedicated (with atropine, ketamine and azaperone), anaesthetized (with propofol and fentanyl), relaxed (with pancuronium), intubated and mechanically ventilated. Fluid infusion and volume restoration were provided (Plasmalyte solution and Gelofusine solution; B-Braun AG, Melsungen, Germany). Animals were killed under anaesthesia by administration of cardioplegic solution (KCl). Immediately after sacrifice, the whole liver was removed. The fresh liver volumes ranged from 0.640 to 1.200 l and the mean ± SD values were 0.871 ± 0.146 l.

Tissue Sample Collection

Each liver was sectioned into 1.5 cm thick slices and immersed in 10% neutral buffered formalin. From each liver, 36 tissue samples (each approximately 25 × 25 × 15 mm) were collected to represent six hepatic lobes (i.e. left lateral, left medial, right medial, right lateral, caudate and quadrate) and three different positions (ROIs) relative to the liver vasculature (Fig. 1A). In each lobe, two samples represented the peripheral ROIs, two were from the paracaval ROIs and two were from the paraportal ROIs. The peripheral ROIs were defined as located no more than 1 cm from the surface and periphery of each hepatic lobe. The paracaval location was the region of each lobe immediately adjacent to the openings of the hepatic veins into the caudal vena cava. The paraportal (hilar) location was adjacent to the main branches of the portal vein following from the hilum within each anatomical lobe.

In total, 415 tissue samples were collected (in three animals, the size of the quadrate lobe did not allow collection of separate tissue samples; moreover, three other samples were lost during processing). Before

cutting, the orientation of each tissue block was randomized using the orientator scheme (Mattfeldt *et al.*, 1990; Mählfeld *et al.*, 2010).

Volumetric Analysis of Regions of Interest

Volumetric analysis of the ROIs was based on computed tomography. The borders between the ROIs were mapped to guarantee that each region represented approximately one third of the volume of each lobe. Therefore, the sampling described above was not biased by different relative volumes of the ROIs. Prior to sampling, the liver was scanned using a Somatom Definition Flash Dual Source Computed Tomography Scanner (Siemens, Erlangen, Germany) and the Syngo software kernel. The section thickness was 0.65 mm and the voxel size was 0.65 × 0.65 × 0.40 mm³. A typical tomography stack consisted of 700–800 sections. Assignment of the liver parenchyma to the paracaval, paraportal and peripheral ROI was done using the LISA (Liver Surgery Analyzer) software (Jirk *et al.*, 2018), a free and open-source application intended for computer-aided liver surgery and measurement. Liver segmentation was performed using a 3D Graph-Cut algorithm (Boykov and Jolly, 2000). For the measurement of ROI respective volumes, the portal vein vascular bed and the hepatic vein vascular bed were segmented separately. The liver parenchyma was assigned to the respective vascular bed by its position within the half-distance between two vascular beds using the Euclidean Distance Transform. In the second step, we arbitrarily cut-off the peripheral third of the liver parenchyma and assigned it to the peripheral ROI. The mean volumes of each ROI were set to one-third of the total liver parenchyma volume (see an example in Fig. 1B).

Histological Processing

The tissue blocks were processed routinely and embedded in paraffin wax. Three sections (3 mm) were cut from each block and one was selected randomly and used for further analysis. After dewaxing and rehydration, nuclei were stained with nuclear fast red (Waldeck GmbH, Münster, Germany). After washing in distilled water, the sections were differentiated in 5% phosphotungstic acid and washed again in distilled water. Collagen fibres were stained with 0.5% aniline blue (Merck KGaA, Darmstadt, Germany).

Microscopic Sampling and Quantification of Volume Fraction of Connective Tissue

All quantified parameters are listed in Table 1. The first step comprised a systematic uniform random

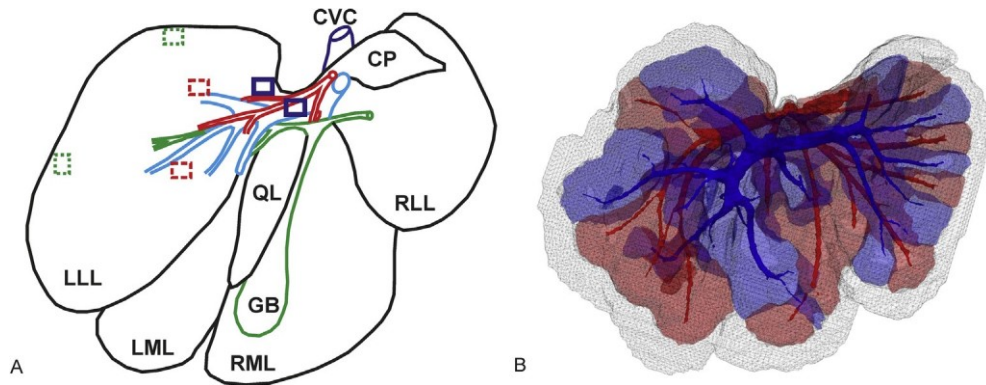


Fig. 1. Collection of tissue samples of the porcine liver for quantitative histology and the relative volumes of the regions of interest (ROIs). (A) As shown on a drawing of the facies visceralis of the porcine liver, the sampling strategy was the same as in [Junatas *et al.* \(2017\)](#). The scheme outlines the left lateral lobe (LLL), left medial lobe (LML), right medial lobe (RML), right lateral lobe (RLL), quadrate lobe (QL) and caudate lobe (mostly hidden behind the vessels, the scheme shows its caudate process, CP, only). The gallbladder (GB) and the caudal vena cava are also shown (CVC). Branching of hepatic arteries is shown in red, branching of the portal vein in blue and branching of the bile ducts in green. The LLL is used as an example of collection of histological samples from three ROIs: paracaval region (dark blue rectangles drawn with a continuous line), parportal region (red rectangles with a dashed line) and the peripheral region (green rectangles with a dotted line). Samples of the other lobes were collected accordingly. (B) Visualization of the ROIs representing approximately the three thirds of the total volume of the porcine liver. The liver was scanned using computed tomography and the reconstruction was rotated so that the visceral surface is shown from a caudal view. In this individual, the paracaval region with associated hepatic veins is shown in red (volume $\frac{1}{4}$ 0.388 l), the peripheral region is shown in black (volume $\frac{1}{4}$ 0.427 l) and the periportal region with the branching of the portal vein is shown in blue (volume $\frac{1}{4}$ 0.400 l). The volumes of the blood vessels were subtracted from the ROIs.

sampling of microscopical image fields within each section according to [Fig. 2A](#). To quantify the interlobular CT V_V (ICT) (i.e. CT surrounding classical lobules), three uniform random fields of view (FOVs) at

10 magnification were captured, while to quantify the perisinusoidal CT V_V (PSCT) (i.e. intralobular CT adjacent to the liver sinusoids) and pericentral CT V_V (PCCT) (i.e. CT surrounding the central veins), four uniform random FOVs at 20 magnification were photographed ([Fig. 2A](#)) at a resolution of 1,280 960 pixels. In the second step, a stereological

point grid was applied over the FOVs in the Ellipse software (ViDiTo, Kosice, Slovak Republic; [Tonar *et al.*, 2015](#); [Kubkova *et al.*, 2017](#)) to quantify the volume fraction of each CT type ([Figs. 2B and C](#)). The areas occupied by the CT were equal to the corresponding volume fractions according to the Delesse principle ([Mouton, 2011](#)). The fibrous capsule of the liver, which was present in the samples from the peripheral region, was omitted from the quantification. Any tissue processing artifacts, such as microcracks or folds, were not evaluated and were subtracted from

Table 1
Stereological parameters assessed for porcine liver connective tissue

Name	Abbreviation and unit	Definition	Stereological technique used for quantification
Volume fraction of interlobular connective tissue	V_V (ICT)	Fraction of connective tissue surrounding classical lobule within the liver	Point grid
Volume fraction of perisinusoidal connective tissue	V_V (PSCT)	Fraction of connective tissue located at or in the lobular sinusoids within the liver lobules	Point grid
Volume fraction of pericentral connective tissue	V_V (PCCT)	Fraction of connective tissue surrounding the central vein within the liver lobules	Point grid
Volume fraction of total connective tissue	V_V (CT)	Sum of the V_V (ICT) + V_V (PSCT) + V_V (PCCT)	None (calculated from previous three parameters)

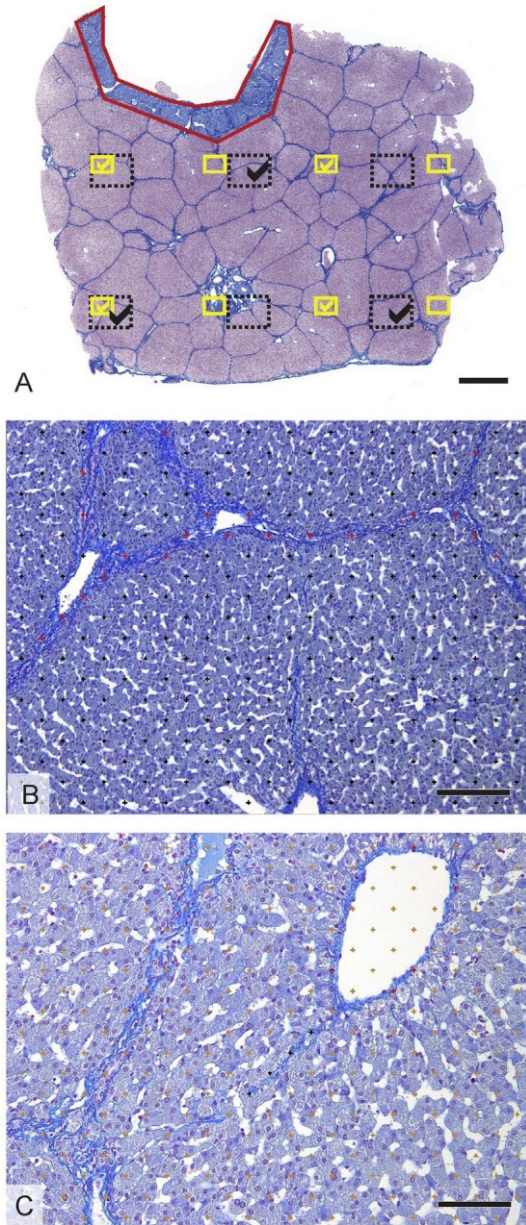


Fig. 2. Histological sampling and quantification of connective tissue. (A) Fields of view (FOVs) sampled, captured and used for quantification of connective tissue. For interlobular connective tissue (ICT), three FOVs observed with 10 objectives were sampled (black dotted rectangles, size of FOV 870×653 mm). For perisinusoidal connective tissue (PSCT) and pericentral connective tissue (PCCT), four FOVs with 20 objectives were used (yellow rectangles, size of FOV 435×326 mm). The first FOV was positioned randomly, starting from the top left corner of the section and further FOVs were placed equidistantly using a microscope stage micrometer. The FOVs photographed from this systematic uniform sampling pattern are marked on the scheme with check marks. The hepatic capsule (outlined red) was omitted from the quantification. (B) Stereological point grid used for quantification of ICT. Points hitting the ICT are highlighted in red. (C) Stereological point grid used for quantification of PSCT (highlighted in black) and PCCT (highlighted in red). Detection of collagen using aniline blue staining; counterstaining with nuclear fast red. Bars, 1 mm (A), 200 μ m (B), 100 μ m (C).

the reference space. We did not observe any differential shrinkage between the CT and the liver parenchyma.

Statistical Analysis

The study was based on the quantification of 2,905 micrographs sampled from 415 histological tissue blocks. The Statistica Base 11 software package (StatSoft, Inc., Tulsa, Oklahoma, USA) was used for the statistical analysis. The Shapiro-Wilk's W -test for normality showed that some of the data were not distributed normally. Therefore, we used non-parametric tests for further analysis. To assess differences between the male and female animals, among the six liver lobes, the differences between the different ROIs, the differences between V_V (PSCT) and V_V (PCCT), the Kruskal-Wallis ANOVA and the Mann-Whitney U -test were used. As an example of the use of our data, the possible sample size calculation for the porcine liver is shown: a power analysis (Chow *et al.*, 2008) was performed to illustrate the sample size needed to detect the expected relative change in the fraction of CT in various hepatic lobes and ROIs.

Coefficient of Error

Estimation of the volume fraction of CT and the size of hepatic lobules was based on two tissue sections per tissue block. However, the values of these parameters might differ between individual histological sections. Therefore, we assessed the volume fraction of CT and the size of hepatic lobules in series of 12 equidistant sections in four randomly selected tissue samples. To provide recommendations for sampling the sections, the variation quantified in the serial sections was estimated using the moving average of the CT fraction and the coefficient of error (CE) (Gundersen and Jensen, 1987).

Results

There was considerable variability in the CT fraction at all sampling levels of the study: between sexes, among individual animals, liver lobes and ROIs. The mean fraction of interlobular CT was greater in males than in females ($P < 0.001$) (Fig. 3A). In males, the mean fraction of interlobular CT was $4.7 \pm 2.4\%$ (mean \pm SD; Fig. 3B) and ranged from 0% to 11.4%. In females, the mean fraction of interlobular CT was $3.6 \pm 2.2\%$ (Fig. 3C) and ranged from 0% to 12.3%. The mean fraction of intralobular (i.e. perisinusoidal summed with pericentral) CT was $< 0.2\%$ both in males and in females; the V_V (PSCT) was $0.003 \pm 0.02\%$ in males and $0.002 \pm 0.02\%$ in

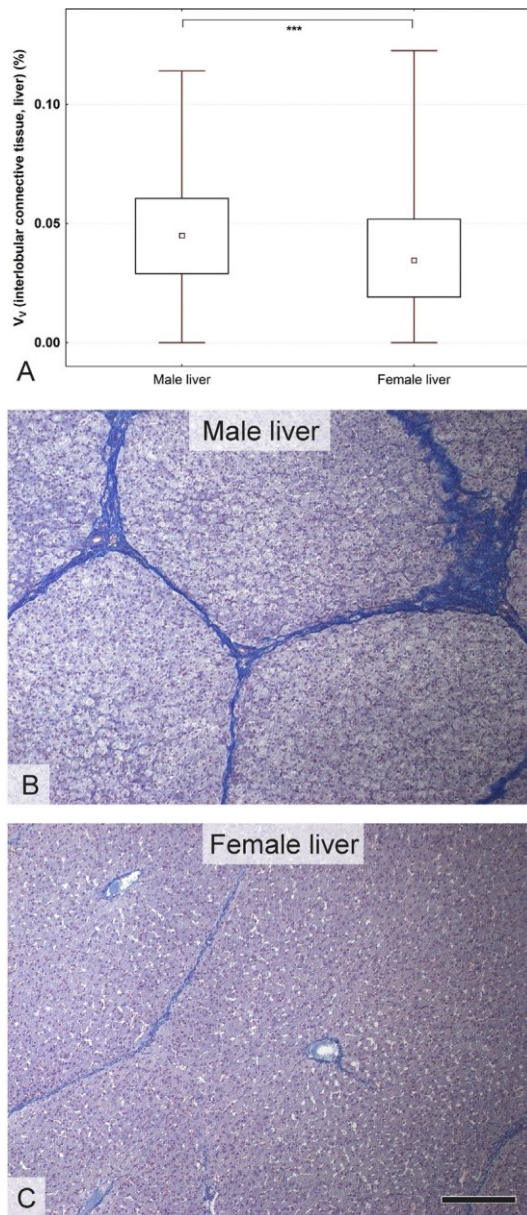


Fig. 3. Fraction of interlobular connective tissue in male versus female animals. (A) In the male porcine liver the volume fraction of connective tissue (mean \pm 4.7%) was significantly higher ($***P < 0.001$, Mann-Whitney U -test) when compared with female liver (mean \pm 3.6%). The statistical findings are illustrated with histological pictures taken randomly from the paracaval region of interest of the lateral lobe in: (B) a male pig and (C) a female pig. Aniline blue and nuclear fast red, Bar, 200 μ m (B).

females and the $V_V(\text{PCCT})$ was $0.03 \pm 0.1\%$ in males and 0.04 ± 0.1 in females. Unlike in females, the fraction of pericentral CT in males was greater than the fraction of the perisinusoidal CT ($P < 0.01$). The interlobular CT represented $>99.9\%$ of the total hepatic CT and their fractions were mutually highly

correlated (Spearman $\rho = 0.998$, $P < 0.05$). The complete stereological results for all samples are provided in [Supplementary Table 1](#).

Volume Fractions of Connective Tissue

In male pigs, the only significant differences in the fraction of interlobular CT among hepatic lobes were observed between the quadrate and left medial lobe ($P < 0.05$) and between the quadrate and right medial lobe ($P < 0.05$) (Fig. 4A). The paracaval ROI was the region with the smallest volume fraction of interlobular CT ($3.9 \pm 2.3\%$, $P < 0.01$). The paraportal ROI (4.9 ± 2.0) and the peripheral ROI (5.2 ± 2.5) had a greater fraction of CT (Fig. 4B). Other differences in interlobular CT among the ROIs were not significant. The same differences were detected when the total CT fraction was analysed. The fractions of both the perisinusoidal and the pericentral CT were negligible ($< 0.2\%$).

In female pigs, the volume fractions of interlobular CT differed between the left medial lobe and the caudate lobe ($P < 0.05$) and the quadrate lobe ($P < 0.05$), and between the right medial lobe and the caudate lobe ($P < 0.05$; Fig. 4A). The volume fraction of interlobular CT was greater in the peripheral ROI (4.1 ± 2.4) than in the paracaval ROI (3.1 ± 2.0) ($P < 0.05$; Fig. 4B). The fractions of both the perisinusoidal and the pericentral CT were negligible ($< 0.2\%$).

Qualitative Findings

Histological images illustrating the typical findings in liver lobes are shown in [Supplementary Fig. 1](#) and [Fig. 5](#). Apart from the typical histological findings of regularly arranged lobules (Fig. 5A), several less common histological characteristics were found. In the paracaval region of the caudate lobe, the hepatocytes within the lobules below the fibrous capsule showed shape elongation (Fig. 5B), which currently cannot be distinguished from an artifact. In the peripheral region of the left medial lobe, more (or branching) central veins were found (Fig. 5C). In the peripheral region of the left medial lobe, incompletely separated lobules (Fig. 5D) were found.

Coefficients of Errors in Serial Sections

Analysis of four series of 12 serial sections revealed the relationship between the CEs and the number of histological sections selected for the analysis (Table 2). The data suggested that using four sections for quantification of both the fraction of CT in liver instead of one section would have reduced the sampling error to an acceptable value of approximately 0.11.

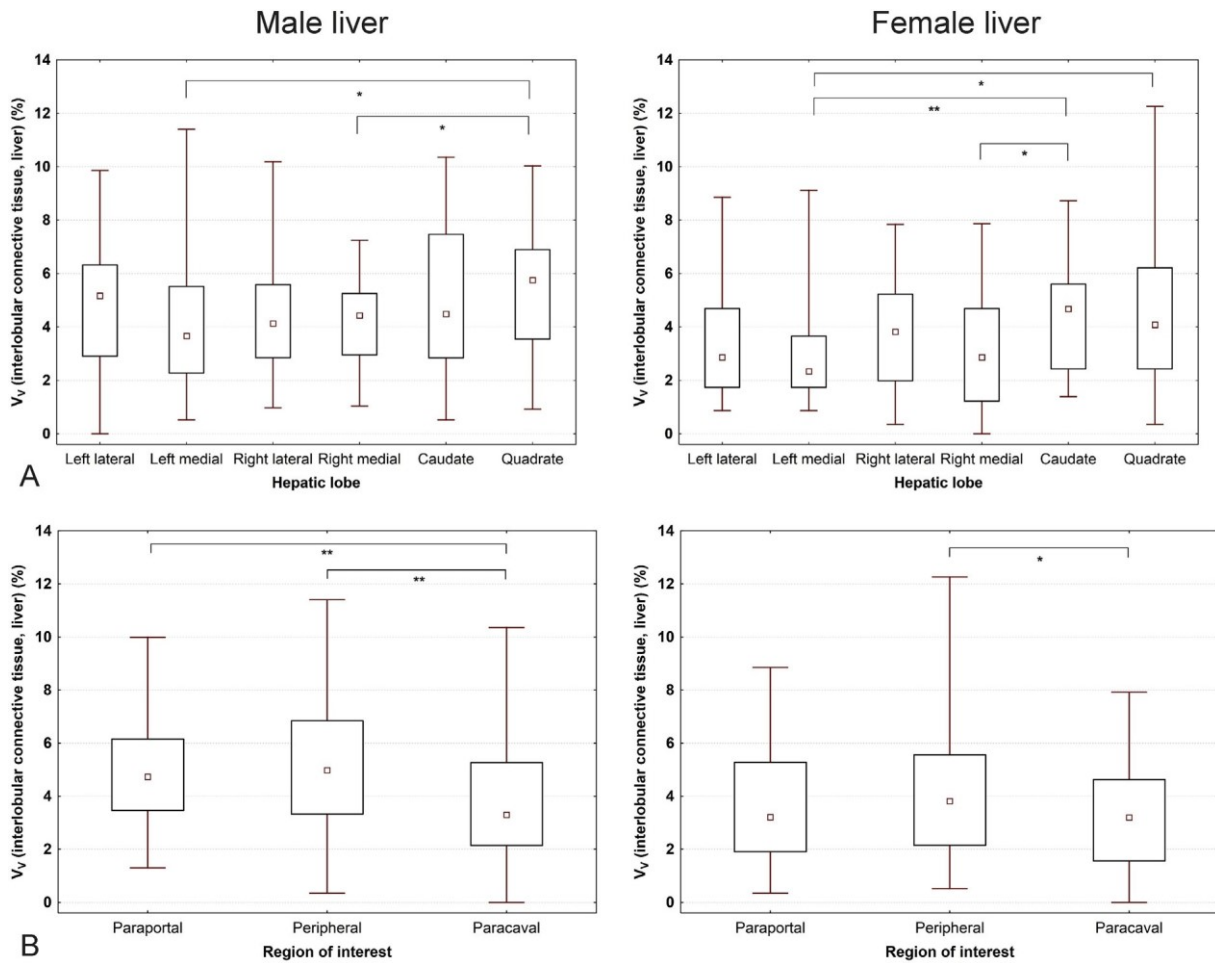


Fig. 4. Fraction of interlobular connective tissue (ICT) in male (on the left) and female (on the right) pig livers. The data are presented in six porcine hepatic lobes (A) and in regions of interest (ROIs) with respect to their proximity to the liver vasculature (B). (A) In males (left), the fraction of ICT was greater in the quadrate lobe than in the left medial and right medial lobes. The left medial lobe contained the smallest fraction of ICT (median 3.67%), the quadrate lobe contained the largest fraction of ICT (median 5.75%). In females (right), the fraction of ICT was greater in the caudate lobe than in the left medial and right medial lobes and was smaller in the left medial lobe than in the quadrate lobe. The left medial lobe contained the smallest fraction of ICT (median 2.34%), the caudate lobe contained the largest fraction of ICT (median 4.67%). (B) In males (left), the fraction of ICT was the smallest in the paracaval ROI (median 3.30%). In females (right), the fraction of ICT was smaller in the paracaval ROI than in the peripheral ROI. Data are displayed as median values with boxes spanning the limits of the first and third quartiles and whiskers spanning the minimum and maximum values for each group. Significant differences (* $P < 0.05$, ** $P < 0.01$, *** $P < 0.001$) identified by the Mann-Whitney U -test are presented. See [Supplementary Table 1](#) for the source data.

Calculating the Sample Size for Histological Evaluation of Hepatic Fibrosis in Pigs

The number of histological samples needed to detect an expected relative increase in the CT fraction in various hepatic lobes and ROIs is shown in [Fig. 6](#). The number of tissue samples needed for comparison rapidly decreased with an increasing expected change. This phenomenon applied especially to lobes with a relatively high (e.g. quadrate lobe, [Fig. 6B](#)) or intermediate (e.g. left lateral lobe, [Fig. 6A](#)) intralobar variation among the ROIs. We also simulated an experiment with pooled lobes (e.g. for cases where

the anatomical origin of the histological samples from the lobes would not be known, but the ROIs would be known) ([Fig. 6C](#)). The case with unknown ROIs, but known lobes, is shown in [Fig. 6D](#). Source data for all lobes and ROIs are provided in [Supplementary Tables 2 and 3](#).

Discussion

The detected variability in the volume fraction of CT between sexes can be attributed to the effect of sex hormones, especially oestrogen that has a protective effect against fibrogenesis ([Yang et al., 2014](#)).

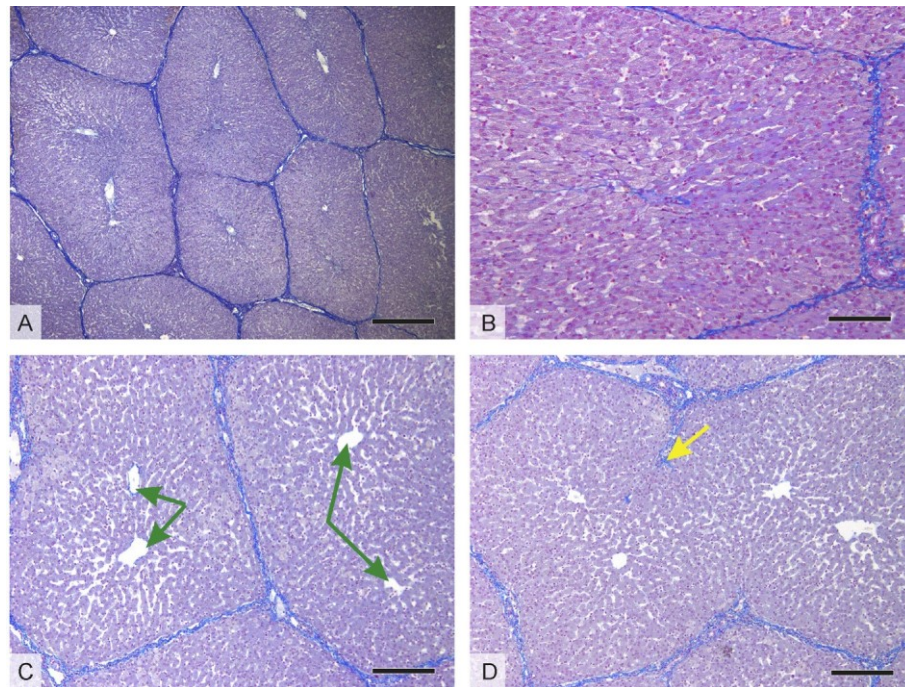


Fig. 5. Illustration of qualitative histological findings in the porcine liver. (A) Typical histological findings of regularly arranged lobules. (B) In the paracaval region of the caudate lobe, the hepatocytes within the lobules adjacent to the fibrous capsule are flattened and elongated. The possibility that this could be an artifact cannot be excluded. (C) In the peripheral region of the left medial lobe, more (or branching) central veins are found (green arrows). (D) In the peripheral region of the left medial lobe, incompletely separated pseudolobules (yellow arrow) are found. Aniline blue and nuclear fast red staining. Bars, 500 μ m (A), 100 μ m (B), 200 μ m (C, D).

Number of serial sections sampled	2	3	4	5	6	7	8	9	10
CE (%)	21.3	14.6	11.3	8.70	8.70	7.49	6.66	5.85	5.47

For each of the four samples the volume fraction of interlobular CT was analysed. The mean CE (Gundersen and Jensen, 1987) decreases with increasing numbers of analysed sections.

Therefore, in pre-menopausal women (Yang *et al.*, 2014), as well as in female Wistar rats (Marcos and Correia-Gomes, 2015), the amounts of CT in the liver tend to reach lower values relative to male counterparts. The sex-related differences in rats included mainly increased perisinusoidal fibrous tissue deposition in males with ageing (Marcos and Correia-Gomes, 2015). Our results adds to the evidence for a greater volume fraction of CT in male porcine livers when compared with their female counterparts.

To our best of our knowledge, no data explaining the differences in variable fractions of CT in various ROIs and lobes have been published. The only known data show preferential distribution of types of collagen, namely: type I and type III collagen co-localize in the same fibre bundles both outside the hepatic lobule (i.e. in the portal tracts) and within the hepatic lobule (Mak *et al.*, 2012), while collagen IV is found only

within the hepatic lobule (Mak *et al.*, 2013). Our present findings on the greater fraction of CT in peripheral ROIs could be answered by further studies: (1) mapping the distribution of fibrogenic cells, and (2) mapping quantitatively the local differences in the hepatic microvascular bed (Zhang *et al.*, 2015). Although fibrogenic cells within the liver have been studied (Zhao *et al.*, 2016; Kisseleva, 2017), their differential distribution within liver compartments has not yet been mapped. The greater content of CT in peripheral ROIs found in our study could be explained by the proximity to mesothelial cells that count as liver fibrogenic cells (Lua *et al.*, 2015).

The fraction of CT in the normal porcine liver in our study was considerably higher than that in most other animals or in man. CT is hardly visible in the dog, goat, horse, cat, rat and man; however, CT is clearly visible in the guinea pig, hamster, sheep and

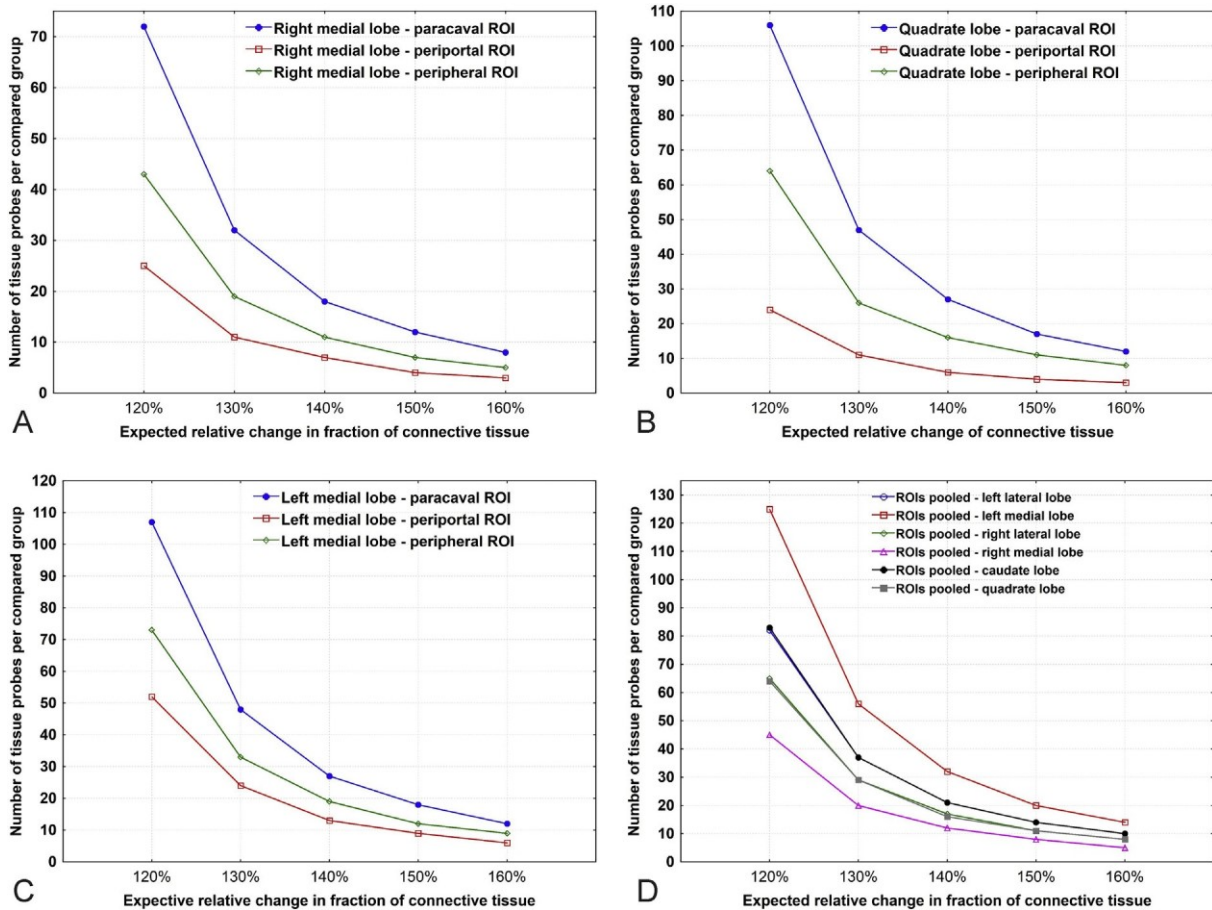


Fig. 6. Examples for calculating the sample size needed to detect a certain expected relative increase in the connective (CT) fraction in various hepatic lobes and ROIs in male pig liver. In each of the graphs, the x-axis shows the expected change in the CT fraction (i.e. an expected 30% increase in the fraction of CT corresponds to 130% on the x-axis). The y-axis shows the number of tissue blocks needed from a group under study to detect the expected change calculated according to [Chow et al. \(2008\)](#). The number of tissue blocks needed for comparison rapidly decreases with an increasing expected change. (A) In male porcine liver, in the right medial lobe, the greatest coefficients of intralobar variability were found ([Supplementary Table 2](#)). Detecting a 30% increase in CT would require, for example, 40 tissue blocks in the paraportal regions and 61 blocks in the paracaval regions. (B) The quadrate lobe had an intermediate intralobar variability of CT (see the coefficients of variation in [Supplementary Table 2](#)), for example, detecting a 30% increase in CT would require 11 tissue blocks in the paraportal regions and 47 tissue samples in the paracaval regions. (C) When all of the lobes are pooled, detection of a 30% increase in the fraction of CT requires at least 24 tissue blocks (paraportal ROI) in each group under study. (D) When comparing the variability inside the lobes by pooling their paracaval, paraportal and peripheral regions, detecting the same increase in the CT fraction inside the right medial lobe (pink line) would require fewer samples than detecting the same changes in the left medial lobe (red line). This observation shows the importance of respecting the anatomical lobes and ROIs when sampling the porcine liver for histological analyses. Source data are provided for male and female animals separately in [Supplementary Tables 2 and 3](#).

pig. Studies using transmission electron microscopy ([Hosoyamada et al., 2000](#)) revealed detailed patterns of length distribution of collagen fibrils. The mean amount of CT in the porcine liver is approximately double that found in the rat liver ([Marcos and Correia-Gomes, 2015](#)). Other numerical data are sparse, both for small and large animals. Moreover, few studies in animals have used an unbiased stereological design ([Zaitoun et al., 1998](#); [Marcos et al., 2012](#) and [Supplementary Table 4](#)). The importance of a quantitative approach proved to be useful: in

our study, quantification revealed several differences, which were scarcely visible using routine qualitative histology ([Supplementary Fig. 1](#)).

For studies of human liver diseases, such as chronic hepatitis C infection ([Besusparis et al., 2014](#)), alcoholic liver disease and non-alcoholic liver disease ([Sakhuja, 2014](#)), primary biliary cirrhosis ([Working Subgroup for Clinical Practice Guidelines for Primary Biliary Cirrhosis, 2014](#)) or sclerosing cholangitis ([de Vries et al., 2015](#)), using porcine liver as an experimental model, it should be noted that the

normal amounts of CT in porcine liver already resemble fibrosis in human livers (Saxena, 2011). Moreover, the distribution of interlobular and intra-lobular CT in pigs and in man has different patterns.

The use of our data as a basis for the design of the following studies is explained in Fig. 6 as follows. In the male porcine liver, the mean fraction of interlobular CT in right medial lobes is $4.27 \pm 1.62\%$; therefore, if we expect, for example, a 30% increase in CT in the porcine liver (to 5.99%), then we should compare at least 11 tissue blocks in each of the compared groups (power $\frac{1}{4}$ 0.8; significance level $\frac{1}{4}$ 0.05); however, this is only true when we know the exact position of the tissue blocks with respect to the liver lobe and to the ROI. If we know only the lobe of origin of the tissue blocks, then we should compare at least 20 tissue blocks in each of the compared groups. If the positions of the tissue blocks for comparison are unknown (i.e. all the lobes would be pooled, e.g. when assessing archival samples), the variability between the lobes, the ROIs and between the individuals would affect the study design in such a way that at least 36 tissue blocks for each of the compared groups should be sampled to detect the same degree of fibrosis. When the sampling scheme of experiments using the porcine liver reflects the differences between the lobes and the ROIs, the same quantitative information may result from a smaller number of samples and therefore provide a more efficient comparison to the situation in which the tissue blocks are harvested in a purely random manner.

The population of animals used in this study was of the minimum size allowed for use of non-parametric statistical tests ($n > 6$). In large animal models, such as the pig, experiments are typically done using relatively small numbers of animals according to the principles of the '3Rs' (replacement, reduction and refinement; Emerson, 2010). This strategy suffers from an increased variability of results caused by interindividual differences, but the researchers are simulated to follow large biological effects that are observable even in small study groups. Since our study was performed on piglets aged 9–15 weeks, an ontogenetic perspective should also be considered in future studies. Age-related differences are to be expected. Although mechanisms of fibrogenesis during liver development have been studied (Lepreux and Desmoulière, 2015), to the best of our knowledge, no study quantifying the amount of CT during liver development has been conducted to date.

In conclusion, for planning experiments involving the histological quantification of liver fibrosis and requiring comparison between the liver lobes, these data facilitate the power analysis for the sample size

needed to detect the expected relative increase or decrease in the fraction of CT.

Acknowledgments

This study was supported by the National Sustainability Programme I (NPU I) number LO1503 and number LO1506 provided by the Ministry of Education, Youth and Sports of the Czech Republic and by the Charles University Research Fund (Progres Q39). The project also received support from Charles University Project numbers SVV 260390/2017, SVV 260392/2017 and GAUK 1206417 and from the project of the Centre of Clinical and Experimental Liver Surgery UNCE/MED/006 and Application of Modern Technologies in Medicine and Industry CZ.02.1.01/0.0/0.0/17_048/0007280. The study also received support from the Ministry of Education, Youth and Sports under the project FIND, number CZ.02.1.01/0.0/0.0/16_019/0000787. Skillful technical support from Ms. A. Flemming, Ms. C. Hächsmann and Ms. B. Machac is gratefully acknowledged.

Supplementary Data

Supplementary data related to this article can be found at <https://doi.org/10.1016/j.jcpc.2018.05.004>.

References

- Anstee QM, Goldin RD (2006) Mouse models in non-alcoholic fatty liver disease and steatohepatitis research. *International Journal of Experimental Pathology*, 87, 1–16.
- Arkadopoulos N, Dektorevas G, Nastos C, Papalois A, Kalimeris K *et al.* (2011) Development of a porcine model of post-hepatectomy liver failure. *Journal of Surgical Research*, 170, e233–e242.
- Avritscher R, Wright KC, Javadi S, Uthamanthil R, Gupta S *et al.* (2011) Development of a large animal model of cirrhosis and portal hypertension using hepatic transarterial embolization: a study in swine. *Journal of Vascular and Interventional Radiology*, 22, 1329–1334.
- Batts KPMD, Ludwig JMD (1995) Chronic hepatitis: an update on terminology and reporting. *Journal of Surgical Pathology*, 19, 1409–1417.
- Bedossa P, Poynard T (1996) An algorithm for the grading of activity in chronic hepatitis C. *Hepatology*, 24, 289–293.
- Besusparris J, Jokubauskiene S, Plancoulaine B, Herlin P, Laurinaviciene A *et al.* (2014) Quantification accuracy of liver fibrosis by in-vivo elastography and digital image analysis of liver biopsy histochemistry. *Analytical Cellular Pathology*, 2014, e317635.
- Boykov Y, Jolly M-P (2000) Interactive organ segmentation using graph cuts. In: *Medical Image Computing and Computer-assisted Intervention – MICCAI 2000*, SL Delp, L Scott, AM DiGoia, B Jaramaz, Eds., Springer, Berlin, pp. 276–286.

- Bruha J, Vycital O, Tonar Z, Mirka H, Haidingerova L *et al.* (2015) Monoclonal antibody against transforming growth factor beta 1 does not influence liver regeneration after resection in large animal experiments. *In Vivo*, 29, 327e340.
- Brunt EM, Janney CG, Di Bisceglie AM, Neuschwander-Tetri BA, Bacon BR (1999) Nonalcoholic steatohepatitis: a proposal for grading and staging the histological lesions. *American Journal of Gastroenterology*, 94, 2467e2474.
- Budai A, Fulop A, Hahn O, Onody P, Kovacs T *et al.* (2017) Animal models for associating liver partition and portal vein ligation for staged hepatectomy (ALPPS): achievements and future perspectives. *European Surgical Research*, 58, 140e157.
- Chen XL, Chen T-W, Zhang X-M, Li Z-L, Li H *et al.* (2013) Spleen magnetic resonance diffusion-weighted imaging for quantitative staging hepatic fibrosis in miniature pigs: an initial study. *Hepatology Research*, 43, 1231e1240.
- Chow S-C, Wang H, Shao J (2008) *Sample Size Calculations in Clinical Research*, 2nd Edit. Chapman and Hall/CRC Biostatistics Series, Boca Raton, pp. 49e82.
- Croome KP, Mao SA, Glorioso JM, Krishna M, Nyberg SL *et al.* (2015) Characterization of a porcine model for associating liver partition and portal vein ligation for a staged hepatectomy. *Journal of the International Hepato Pancreato Biliary Association*, 17, 1130e1136.
- de Vries EMG, Verheij J, Hubscher SG, Leeftang MMG, Boonstra K *et al.* (2015) Applicability and prognostic value of histologic scoring systems in primary sclerosing cholangitis. *Journal of Hepatology*, 63, 1212e1219.
- Eberlova L, Liska V, Mirka H, Gregor T, Tonar Z *et al.* (2016) Porcine liver vascular bed in Biodur E20 corrosion casts. *Folia Morphologica*, 75, 154e161.
- Eberlova L, Liska V, Mirka H, Tonar Z, Haviar S *et al.* (2017) The use of porcine corrosion casts for teaching human anatomy. *Annals of Anatomy*, 213, 69e77.
- Emerson M (2010) Refinement, reduction and replacement approaches to in-vivo cardiovascular research. *British Journal of Pharmacology*, 161, 749e754.
- Fakhoury-Sayegh N, Trak-Smayra V, Khazzaka A, Esseily F, Obeid O *et al.* (2015) Characteristics of non-alcoholic fatty liver disease induced in wistar rats following four different diets. *Nutrition Research and Practice*, 9, 350e357.
- Forbes SJ, Parola M (2011) Liver fibrogenic cells. *Best Practice & Research Clinical Gastroenterology*, 25, 207e217.
- George J, Pera N, Phung N, Leclercq I, Yun Hou J *et al.* (2003) Lipid peroxidation, stellate cell activation and hepatic fibrogenesis in a rat model of chronic steatohepatitis. *Journal of Hepatology*, 39, 756e764.
- Ghodsizad A, Fahy BN, Waclawczyk S, Liedtke S, Berjon JMG *et al.* (2012) Portal application of human unrestricted somatic stem cells to support hepatic regeneration after portal embolization and tumor surgery. *ASAIO Journal*, 58, 255e261.
- Gnutzmann DM, Mechel J, Schmitz A, Kehler K, Krone D *et al.* (2015) Evaluation of the plasmatic and parenchymal elution kinetics of two different irinotecan loaded drug-eluting embolics in a pig model. *Journal of Vascular and Interventional Radiology*, 26, 746e754.
- Gohlke F, Lohse AW, Dienes HP, Lohr H, Märker-Hermann E *et al.* (1996) Evidence for an overlap syndrome of autoimmune hepatitis and primary sclerosing cholangitis. *Journal of Hepatology*, 24, 699e705.
- Gundersen HJG, Jensen EB (1987) The efficiency of systematic sampling in stereology and its prediction. *Journal of Microscopy*, 147, 229e263.
- Hirschfield GM, Karlsen TH, Lindor KD, Adams DH (2013) Primary sclerosing cholangitis. *Lancet*, 382, 1587e1599.
- Hosoyamada Y, Kurihara H, Sakai T (2000) Ultrastructural localisation and size distribution of collagen fibrils in Glisson's sheath of rat liver: implications for mechanical environment and possible producing cells. *Journal of Anatomy*, 196, 327e340.
- Huang SY, Abdelsalam ME, Harmoush S, Ensor JE, Chetta JA (2014) Evaluation of liver fibrosis and hepatic venous pressure gradient with MR elastography in a novel swine model of cirrhosis. *Journal of Magnetic Resonance Imaging*, 39, 590e597.
- Huang Y, Adams LA, Joseph J, Bulsara MK, Jeffrey GP (2017) The ability of Hepascore to predict liver fibrosis in chronic liver disease: a meta-analysis. *Liver International*, 37, 121e131.
- Ishak K, Baptista A, Bianchi L, Callea F, De Groote J *et al.* (1995) Histological grading and staging of chronic hepatitis. *Journal of Hepatology*, 22, 696e699.
- Jirák M, Bartoš M, Tomásek P, Maleeková A, Kural T *et al.* (2018) Generating standardized image data for testing and calibrating quantification of volumes, surfaces, lengths, and object counts in fibrous and porous materials using X-ray microtomography. *Microscopy Research Techniques*, 81, 551e568.
- Junatas KL, Tonar Z, Kubíková T, Liska V, Pálek R *et al.* (2017) Stereological analysis of size and density of hepatocytes in the porcine liver. *Journal of Anatomy*, 230, 575e588.
- Kawamura Y, Ikeda K, Fukushima T, Hara T, Hosaka T *et al.* (2014) Potential of a no-touch pincer ablation procedure for small hepatocellular carcinoma that uses a multipolar radiofrequency ablation system: an experimental animal study. *Hepatology Research*, 44, 1234e1240.
- Kisseleva T (2017) The origin of fibrogenic myofibroblasts in fibrotic liver. *Hepatology*, 65, 1039e1043.
- Kleiner DE, Brunt EM, Van Natta M, Behling C, Contos MJ *et al.* (2005) Design and validation of a histological scoring system for non-alcoholic fatty liver disease. *Hepatology*, 41, 1313e1321.
- Komine M, Kawasako K, Okamoto M, Matsuda K, Hirayama K *et al.* (2008) Histopathological distinction and evaluation of biliary and peribiliary cysts in pig liver. *Journal of Comparative Pathology*, 139, 202e207.
- Kubíková T, Kochová P, Brázdil J, Špatenka J, Burkert J *et al.* (2017) The composition and biomechanical properties of human cryopreserved aortas, pulmonary trunks, and aortic and pulmonary cusps. *Annals of Anatomy*, 212, 17e26.

- Lee YH, Ha Y, Chae C (2010) Expression of interferon-alpha and Mx protein in the livers of pigs experimentally infected with swine hepatitis E virus. *Journal of Comparative Pathology*, 142, 187e192.
- Lee KS, Santagostino SF, Li D, Ramjit A, Serrano K *et al.* (2017) Catheter-directed intraportal delivery of endothelial cell therapy for liver regeneration: a feasibility study in a large animal model of cirrhosis. *Radiology*, 285, 114e123.
- Lefkowitz JH (2007) Liver biopsy assessment in chronic hepatitis. *Archives of Medical Research*, 38, 634e643.
- Lepreux S, Desmoulière A (2015) Human liver myofibroblasts during development and diseases with a focus on portal (myo)fibroblasts. *Frontiers in Physiology*, 6, 1e8.
- Lindor KD, Gershwin ME, Poupon R, Kaplan M, Bergasa NV *et al.* (2009) Primary biliary cirrhosis. *Hepatology*, 50, 291e308.
- Lossi L, D'Angelo L, De Girolamo P, Merighi A (2016) Anatomical features for an adequate choice of experimental animal model in biomedicine: II. Small laboratory rodents, rabbit, and pig. *Annals of Anatomy*, 204, 11e28.
- Lua I, Li Y, Pappoe LS, Asahina K (2015) Myofibroblastic conversion and regeneration of mesothelial cells in peritoneal and liver fibrosis. *American Journal of Pathology*, 185, 3258e3273.
- Machado MV, Michelotti GA, Xie G, de Almeida TP, Boursier J *et al.* (2015) Mouse models of diet-induced non-alcoholic steatohepatitis reproduce the heterogeneity of the human disease. *PLoS One*, 10, e0127991.
- Mak KM, Chen LL, Lee TF (2013) Codistribution of collagen type IV and laminin in liver fibrosis of elderly cadavers: immunohistochemical marker of perisinusoidal basement membrane formation. *Anatomical Record*, 296, 953e964.
- Mak KM, Chu E, Lau KHV, Kwong AJ (2012) Liver fibrosis in elderly cadavers: localization of collagen types I, III, and IV, α -smooth muscle actin, and elastic fibers. *Anatomical Record*, 295, 1159e1167.
- Marcos R, Correia-Gomes C (2015) Liver and gender: are there differences in fibrous tissue before the onset of fibrosis? *Hepatology*, 61, 1093e1094.
- Marcos R, Monteiro RAF, Rocha E (2012) The use of design-based stereology to evaluate volumes and numbers in the liver: a review with practical guidelines. *Journal of Anatomy*, 220, 303e317.
- Mattfeldt T, Mall G, Gharehbaghi H, Müller P (1990) Estimation of surface area and length with the orientator. *Journal of Microscopy*, 159, 301e317.
- Mouton PR (2011) *Unbiased Stereology: A Concise Guide*. Johns Hopkins University Press, Baltimore, pp. 55e57.
- Mühlfeld C, Nyengaard JR, Mayhew TM (2010) A review of state-of-the-art stereology for better quantitative 3D morphology in cardiac research. *Cardiovascular Pathology*, 19, 65e82.
- Nowatzky J, Knorr A, Hirth-Dietrich C, Siegling A, Volk H-D *et al.* (2013) Inactivated Orf virus (Parapoxvirus ovis) elicits antifibrotic activity in models of liver fibrosis. *Hepatology Research*, 43, 535e546.
- Nygaard IE, Mortensen KE, Hedegaard J, Conley LN, Bendixen C *et al.* (2015) Tissue remodelling following resection of porcine liver. *BioMed Research International*, 2015, 1e10.
- Panasevich MR, Meers GM, Linden MA, Booth FW, Perfield JW *et al.* (2018) High-fat, high-fructose, high-cholesterol feeding causes severe NASH and cecal microbiota dysbiosis in juvenile Ossabaw swine. *American Journal of Physiology. Endocrinology and Metabolism*, 314, e78e92.
- Peterson TC, Neumeister M (1996) Effect of pentoxifylline in rat and swine models of hepatic fibrosis: role of fibroproliferation in its mechanism. *Immunopharmacology*, 31, 183e193.
- Sakhuja P (2014) Pathology of alcoholic liver disease, can it be differentiated from nonalcoholic steatohepatitis? *World Journal of Gastroenterology*, 20, 16474e16479.
- Saxena R (2011) *Practical Hepatic Pathology: A Diagnostic Approach*. Saunders, Philadelphia, pp. 203e213.
- Scheuer PJ (1991) Classification of chronic viral hepatitis: a need for reassessment. *Journal of Hepatology*, 13, 372e374.
- Standish RA, Cholongitas E, Dhillon A, Burroughs AK, Dhillon AP (2006) An appraisal of the histopathological assessment of liver fibrosis. *Gut*, 55, 569e578.
- Stasi C, Milani S (2016) Non-invasive assessment of liver fibrosis: between prediction/prevention of outcomes and cost-effectiveness. *World Journal of Gastroenterology*, 22, 1711e1720.
- Takahashi Y, Fukusato T (2014) Histopathology of non-alcoholic fatty liver disease/nonalcoholic steatohepatitis. *World Journal of Gastroenterology*, 20, 15539e15548.
- Theise ND (2013) Histopathology of alcoholic liver disease. *Clinical Liver Disease*, 2, 64e67.
- Tonar Z, Kubkova T, Prior C, Demjen E, Liska V *et al.* (2015) Segmental and age differences in the elastin network, collagen, and smooth muscle phenotype in the tunica media of the porcine aorta. *Annals of Anatomy*, 201, 79e90.
- Vrtkova I (2015) Genetic admixture analysis in Prestice black-pied pigs. *Archives of Animal Breeding*, 58, 115e121.
- Wang L, He F-L, Liu F-Q, Yue Z-D, Zhao H-W (2015) Establishment of a hepatic cirrhosis and portal hypertension model by hepatic arterial perfusion with 80% alcohol. *World Journal of Gastroenterology*, 21, 9544e9553.
- Watson AL, Carlson DF, Largaespada DA, Hackett PB, Fahrenkrug SC (2016) Engineered swine models of cancer. *Frontiers in Genetics*, 7, 78.
- Working Subgroup (English version) for Clinical Practice Guidelines for Primary Biliary Cirrhosis (2014) Guidelines for the management of primary biliary cirrhosis. *Hepatology Research*, 44, 71e90.
- Yang JD, Abdelmalek MF, Pang H, Guy CD, Smith AD *et al.* (2014) Gender and menopause impact severity of fibrosis among patients with non-alcoholic steatohepatitis. *Hepatology*, 59, 1406e1414.
- Yi X, Song M, Yuan Y, Zhang X, Chen W *et al.* (2012) Hepatic stimulator substance alleviates toxin-induced and

- immune-mediated liver injury and fibrosis in rats. *Digestive Diseases and Sciences*, 57, 2079-2087.
- Yin M, Glaser KJ, Manduca A, Mounajjed T, Malhi H (2017) Distinguishing between hepatic inflammation and fibrosis with magnetic resonance elastography. *Radiology*, 284, 694-705.
- Zaitoun AAM, Awad S, Ukabam S, Makadisi S, Record C (2001) Quantitative assessment of fibrosis and steatosis in liver biopsies from patients with chronic hepatitis C. *Journal of Clinical Pathology*, 54, 461-465.
- Zaitoun AAM, Mardini HA, Record CO (1998) Stereology and morphometry of steatosis in human alcoholic (ALD) and non-alcoholic liver disease (NALD). *Acta Stereologica*, 17, 49-58.
- Zhang JJ, Meng XK, Dong C, Qiao JL, Zhang RF *et al.* (2009) Development of a new animal model of liver cirrhosis in swine. *European Surgical Research*, 42, 35-39.
- Zhang Z, Zhang F, Lu Y, Zheng S (2015) Update on implications and mechanisms of angiogenesis in liver fibrosis. *Hepatology Research*, 45, 162-178.
- Zhao YL, Zhu R-T, Sun Y-L (2016) Epithelial-mesenchymal transition in liver fibrosis. *Biomedical Reports*, 4, 269-274.
- Zhou L, Chen T, Zhang X, Yang Z, Tang H *et al.* (2014) Liver dynamic contrast-enhanced MRI for staging liver fibrosis in a piglet model. *Journal of Magnetic Resonance Imaging*, 39, 872-878.

^{1/} Received, March 8th, 2018

^{1/2} Accepted, May 25th, 2018

10.7 Příloha VII

MALEČKOVÁ, Anna, MIK, Patrik, LIŠKA, Václav, PÁLEK, Richard, ROSENDORF, Jáchym, WITTER, Kirsti, TONAR, Zbyněk. Periphery of porcine hepatic lobes has the smallest length density of hepatic sinuoids and bile canaliculi: a stereological histological study.

Periphery of porcine hepatic lobes has the smallest length density of hepatic sinusoids and bile canaliculi: a stereological histological study

Anna Malečková^a, Patrik Mik^b, Václav Liška^c, Richard Pálek^c, Jáchym Rosendorf^c, Kirsti Witter^d, Zbyněk Tonar^a

^aDepartment of Histology and Embryology and Biomedical Center, Faculty of Medicine in Pilsen, Charles University, Karlovarská 48, 301 00, Pilsen, Czech Republic

^bDepartment of Anatomy and Biomedical Center, Faculty of Medicine in Pilsen, Charles University, Karlovarská 48, 301 00, Pilsen, Czech Republic

^cDepartment of Surgery and Biomedical Center, Faculty of Medicine in Pilsen, Charles University, Alej Svobody 76, 323 00, Pilsen, Czech Republic

^dInstitute of Morphology, Department of Pathobiology, University of Veterinary Medicine Vienna, Veterinärplatz 1, Vienna, Austria

Anna Malečková (corresponding author): Anna.Maleckova@lfp.cuni.cz

Patrik Mik: Patrik.Mik@lfp.cuni.cz

Václav Liška: liskav@fnplzen.cz

Richard Pálek: palekr@fnplzen.cz

Jáchym Rosendorf: rosendorfj@fnplzen.cz

Kirsti Witter: kirsti.witter@vetmeduni.ac.at

Zbyněk Tonar: Zbynek.Tonar@lfp.cuni.cz

Abstract:

Background: Porcine liver is widely used in hepatologic research as a large animal model with many anatomical and physiological similarities with humans. However, only limited information on porcine liver spatial microstructure has been published, especially regarding the hepatic sinusoids and bile canaliculi. The aim of our study was to quantify the sinusoidal and bile canalicular network in healthy male and female porcine livers and to compare the distribution of the parameters among six hepatic lobes and among three macroscopic regions related to the liver vasculature.

Methods: Livers from 12 healthy piglets (6 females and 6 neutered males) were sampled into 36 tissue samples per organ, representing six hepatic lobes and three different regions related to the hepatic vasculature (peripheral, paracaval and paraportal region). Histological sections were processed with a random orientation of the cutting plane. The endothelium and the bile canaliculi were stained using Ricinus communis agglutinin I lectin histochemistry. The length densities of hepatic sinusoids $L_V(\text{sinusoids}, \text{liver})$ and bile canaliculi $L_V(\text{bile canaliculi}, \text{liver})$ were estimated using stereological methods. The newly acquired morphometric data were compared with previously published data on density of porcine hepatocytes and fractions of connective tissue.

Results: The length density of hepatic sinusoids $L_V(\text{sinusoids}, \text{liver})$ was $935.1 \pm 148.7 \text{ mm/mm}^3$ and was greater ($p < 0.001$) in females ($990.2 \pm 145.9 \text{ mm/mm}^3$) than in neutered males ($884.3 \pm 132.6 \text{ mm/mm}^3$). The length density of bile canaliculi $L_V(\text{bile canaliculi}, \text{liver})$ was $3697.1 \pm 571.5 \text{ mm/mm}^3$ and was greater ($p < 0.01$) in females ($3785.8 \pm 534 \text{ mm/mm}^3$) than in neutered males ($3615 \pm 593.8 \text{ mm/mm}^3$). The six hepatic lobes had statistically comparable length densities of both sinusoids and bile canaliculi. The $L_V(\text{sinusoids}, \text{liver})$ in the periphery of the hepatic lobes ($870.8 \pm 154.8 \text{ mm/mm}^3$) was smaller ($p < 0.001$) than in the paracaval ($972.1 \pm 139.1 \text{ mm/mm}^3$) and paraportal ($964 \pm 129.7 \text{ mm/mm}^3$) regions. $L_V(\text{bile canaliculi}, \text{liver})$ in the periphery of the hepatic lobes ($3602.9 \pm 603.8 \text{ mm/mm}^3$) was smaller ($p < 0.05$) than in the paraportal region ($3797 \pm 535.4 \text{ mm/mm}^3$). Regions with greater $L_V(\text{sinusoids}, \text{liver})$ had also greater $L_V(\text{bile canaliculi}, \text{liver})$ and were accompanied by greater

density of smaller hepatocytes. Regions with smaller $L_V(\text{sinusoids,liver})$ and $L_V(\text{bile canaliculi,liver})$ contained a greater fraction of interlobular connective tissue.

Conclusions: The length density of hepatic sinusoids is smaller in the peripheral regions of the porcine liver than in other regions related to the hepatic vasculature – paracaval and paraportal regions and smaller in castrated males than in females. Greater length density of liver sinusoids was linked with greater local density of bile canaliculi, with local increase in the density of smaller hepatocytes and, simultaneously, with smaller fractions of hepatic connective tissue. The intrahepatic and inter-sexual variability of the porcine liver morphology needs to be taken into account when designing and interpreting experiments involving the histological quantification of the microvascular network. The complete primary morphometric data describing the distribution of $L_V(\text{sinusoids,liver})$ and $L_V(\text{bile canaliculi,liver})$ within porcine liver were made available to public in a form facilitating the power analysis to justify the minimal number of tissue samples or animals required when designing further histological evaluation studies.

Key words: liver, pig, swine, hepatic sinusoids, bile canaliculi, stereology

1. Introduction

1.1 The porcine liver as a model in translational medicine

From a histological point of view, the porcine liver is an important model organ in translational medicine. It presents marked lobulation with well-defined acinar structures including clear portal triads, similarly to humans (Lossi et al., 2016). Histological evaluation of porcine liver experiments had been used for several research aspects including regeneration after liver resection (Bruha et al., 2015), sinusoidal obstruction syndrome (Palek et al., 2020), microwave ablation (Bressemer et al., 2019), or preparation of decellularized tissue scaffolds (Massaro et al., 2021; Moulisová et al. 2020). Furthermore, the porcine liver hepatic microvascular bed and the system of bile canaliculi can also be the focus of a biological question to be answered during histological examination (Renner et al., 2020).

1.2 Relevance of hepatic sinusoids and bile canaliculi in hepatologic research

The hepatocytes, hepatic sinusoids and the bile canaliculi contribute together to the uniquely organized liver microarchitecture (Eberlová et al., 2020; Saxena, 2018). The microscopic hepatocytes arrangement results from their ability to differentiate into polarized cells. In such multipolar state, each hepatocyte participates in the creation of multiple bile canaliculi via its luminal (apical) domains, whereas the basal domains face the perisinusoidal space of Disse and the endothelium of the hepatic sinusoids (Treyer and Müsch, 2013). The polarization of the hepatocytes is regulated during the development by many signaling pathways that have been extensively studied, both *in vitro* and *in vivo* (Lemaigre, 2009; Ober and Lemaigre, 2018).

The wall of the hepatic sinusoids is composed of a discontinuous endothelium, which contributes to many hepatic functions. The primary functions include removal of potentially dangerous molecules from blood (Sørensen et al., 2015), regulation of molecules and cells trafficking between the liver parenchyma and systemic circulation (Sørensen et al., 2015), immune system regulation (Shetty et al., 2018). The sinusoids also contribute to the development and progression of liver pathologies such as chronic inflammatory liver diseases (Fernández-Iglesias and Gracia-Sancho, 2017; Gracia-

Sancho et al., 2021) and are involved in development of liver fibrosis and regeneration (Lafoz et al., 2020).

The cytoplasmic membranes of adjacent hepatocytes form the bile canaliculi which constitute the initial segments of the biliary tree. The bile canaliculi have been widely studied in the context of the fluid dynamics affected by intrahepatic cholestasis (Burbank et al., 2016; Meyer et al., 2017) and the hepatocellular changes associated with various liver diseases (Gissen and Arias, 2015). Furthermore, formation of bile canaliculi seems to play an important role in the development, survival and functioning of three dimensional liver tissue constructs (Overeem et al., 2019). Moreover, restoration of the biliary tree during liver regeneration is essential for proper organ function (De Assuncao et al., 2017).

1.3 Visualization of hepatic sinusoids and bile canaliculi

Altered tissue microarchitecture is one of the key hallmarks used for determination of the pathological diagnosis of various liver diseases (Saxena, 2018). However, routine pathological analysis is still dependent on analysis of thin sections. Although three-dimensional (3D) imaging and image analysis provides useful insight into spatial distribution of 3D fibrillary structures, such as the hepatic sinusoids and bile canaliculi, 3D reconstruction of the sinusoidal and bile canalicular network is limited by the lack of robust staining methods (Mak and Shin, 2021) and reconstructive algorithms. Nonetheless, visualization of the 3D network is possible e.g. by creating a thick tissue block followed by histological staining, visualization by confocal scanning microscopy and quantification using image analysis protocols (Hammad et al., 2014). An alternative approach utilizes the corrosion casts of the vascular bed visualized by X-ray microtomography with high resolution (micro-CT) (Eberlova et al., 2017). Semi-automated quantitative software (Jiřík et al., 2016) or software provided by micro-CT manufacturers are highly dependent on the segmentation algorithms and requires initial calibration prior to each use (Jiřík et al., 2018).

1.4 Present knowledge gaps in morphometrics of hepatic sinusoids and bile canaliculi

The pig is one of the most important model animals for hepatologic research (more than 5000 search results in Medline (<https://www.ncbi.nlm.nih.gov/pubmed/>) for the search string ((pig) AND liver) AND experim*), March 14, 2022). However, knowledge on morphometrics of the vascular bed within the porcine liver is limited (Jiřík et al., 2016). Indeed, there is lack of information on the distribution of the quantitative parameters of hepatic sinusoids and bile canaliculi in the context of the whole porcine liver. Without the data showing the variability of these microscopic parameters on a complete organ scale, it is not feasible to undertake a formal sample size calculation to justify the number of tissue samples or animals required when designing histological evaluation studies. Fortunately, the design-based stereological method (Marcos et al., 2012; Marcos et al., 2016) allows for unbiased quantification of morphometric features describing the density and spatial heterogeneity of hepatic sinusoids and bile canaliculi using continuous variables (Kubíková et al., 2018). Previous porcine liver studies have shown considerable variability in size and nuclearity of hepatocytes as well as the connective tissue volume fractions among hepatic lobes and regions with various positions related to hepatic blood supply (Junatas et al., 2017; Mik et al., 2018). However, it is unknown whether these differences also affect hepatic microvessels and bile canaliculi.

1.5 Aims of the study

The aim of our study was to provide a quantitative description of the porcine sinusoidal and biliary network in healthy animals. We tested the following null hypotheses:

H₀(A): There are no differences in length density of sinusoids and length density of bile canaliculi in the porcine liver between neutered male and female animals.

H₀(B): There are no differences in length density of sinusoids and length density of bile canaliculi in the porcine liver among the 6 hepatic lobes.

H₀(C): There are no differences in length density of sinusoids and length density of bile canaliculi in the porcine liver among three different regions of interest related to the liver vasculature.

H₀(D): The histological parameters under study do not correlate with hepatocytes size and density parameters nor volume fraction of connective tissue in porcine liver.

Moreover, we aimed to provide the descriptive statistics for a sample size analysis suitable for estimating the minimum number of samples necessary for detecting relative change in the length density of sinusoids and length density of bile canaliculi in the various hepatic lobes and regions of interest related to the liver vasculature.

2. Materials and methods

2.1 Animals

We used archive tissue blocks previously collected from whole porcine livers harvested from animals involved in previous studies on the size and density of hepatocytes (Junatas et al., 2017) and connective tissue distribution (Mik et al., 2018). The liver samples were collected from 12 healthy Prestice black-pied pigs (Eberlová et al., 2020) aged 9–15 weeks and weighing 25–45 kg (34.3 ± 5.3 kg, mean \pm standard deviation [SD]). Six piglets were females and six piglets were neutered males. The animals received humane care in compliance with the European Convention on Animal Care and project number 27374/2011-30 was approved by the Faculty Committee for the Prevention of Cruelty to Animals. According to the project, the animals were used for surgical skills practicing and none of the animals were sacrificed solely for the purpose of harvesting the organs for the proposed study. The animals were pre-medicated (intramuscular administration of atropine, ketamine, azaperone) and all the surgical procedures were performed under general anesthesia (continuous administration of propofol, fentanyl, pancuronium), while the animals were intubated and mechanically ventilated. The piglets received infusion and volume substitution when necessary (Plasmalyte solution and Gelofusine solution; B-Braun AG, Melsungen, Germany). The animals were sacrificed via administration of cardioplegic solution (KCl) whilst under general anesthesia. Immediately after the sacrifice, the whole liver was removed. The volume of each fresh liver was measured by water displacement method and

was calculated as difference of the water volume before and after submersion of the whole liver in water in a scaled cylinder. The liver volume ranged from 0.640 to 1.200 l (0.871 ± 0.146 l – mean \pm SD).

2.2 Tissue sampling

Each liver was sectioned into approximately 1 cm thick slabs and fixed in 10% neutral buffered formalin. The detailed methodology of the whole liver sampling was previously described by Junatas et al. (2017) and Mik et al. (2018). Each liver was extensively sampled, resulting in 36 tissue samples per liver. The tissue samples represented 6 hepatic lobes – left lateral, left medial, right medial, right lateral, caudate and quadrate lobes. Each lobe was represented by 6 tissue blocks with approximate dimensions of $2.5 \times 2.5 \times 1$ cm taken from three different regions of interest (ROIs) related to the liver vasculature – peripheral, paracaval and paraportal region. The peripheral ROIs were located no more than 1 cm from the surface and the periphery of each hepatic lobe. The paracaval ROIs were the regions of each lobe immediately adjacent to the openings of the hepatic veins into the caudal vena cava. The paraportal (hilar) ROIs were adjacent to the main branches of the portal vein within each anatomical lobe. Based on computed tomography volumetric analysis (Mik et al., 2018), each of the described ROIs represents approximately one third of the total volume of the porcine liver. Each of the described regions within a lobe was sampled twice. The orientation of section plane of each tissue block was randomized with respect to the unknown status of isotropy/anisotropy of the hepatic sinusoids and bile canaliculi within the porcine liver. The randomization was ensured by using the orientator scheme (Nyengaard and Gundersen, 2006; Mühlfeld, 2014).

2.3 Histological processing and staining

The tissue samples were dehydrated and embedded in paraffin. Three $3\mu\text{m}$ -thick sections were obtained from each paraffin-embedded tissue block. The sections were deparaffinized and rehydrated. Endogenous peroxidase activity was blocked with 0.9% H_2O_2 in methanol. Unspecific lectin binding was blocked by pre-incubation with 1% bovine serum albumin (Sigma-Aldrich, Vienna, Austria)

in 0.1 M phosphate-buffered saline (PBS, pH 7.4). Sections were then incubated with biotinylated Ricinus communis agglutinin I (RCA-I) (Vector Laboratories, Burlingame, CA, USA ; dilution 20 µg/ml) for 1 hour at room temperature. The binding reaction was detected by an avidin-biotin-peroxidase-complex (ABC, Vector Laboratories, Burlingame, CA, USA) and visualized with diaminobenzidine (Sigma-Aldrich, Vienna, Austria) in a 0.03% H₂O₂ solution in Tris-buffered saline (TBS, pH 7.4). The sections were counterstained with Mayer's haematoxylin, dehydrated and mounted with a medium soluble in xylene.

The microvessels were detected by lectin histochemistry utilizing plant derived lectins, which has been widely used for endothelium detection along with other methods such as immunohistochemistry (IHC) (Nakamura-Ishizu et al., 2008). As the endothelial phenotype differs among vessel types (Shetty et al., 2018), IHC endothelial markers commonly used for detection of endothelium in other porcine organs (von Willebrand factor) or in human vessels (CD31) (Grajciarová et al., 2022) did not offer sufficient and consistent results when used on the porcine liver. RCA-I used in this study binds to the glycocalyx of endothelial cells and of hepatocytes, allowing us to visualize both the discontinuous endothelium of sinusoids and the inner lining of bile canaliculi within the porcine liver.

2.4 Microscopic sampling and quantification

Length density of hepatic sinusoids $L_V(\text{sinusoids}, \text{liver})$ and length density of bile canaliculi $L_V(\text{bile canaliculi}, \text{liver})$, i.e. the total length of the structures of interest per volume unit of tissue, were assessed using well-established stereological methods (Howard and Reed, 2005; Mouton, 2002). Four fields of view (FOVs) per section (12 FOVs per tissue block) were captured in a systematic uniform random manner with the 40× objective (Fig. 1A) according to Kolinko et al. (2022).

The main principle of the length density estimation is based on counting of vessel profiles $Q_A(\text{sinusoids})$ and $Q_A(\text{bile canaliculi})$ within an unbiased counting frame that was applied over the FOVs (Fig. 1). If the orientation of the section plane is randomized, the number of vessel intersections (vessel

profiles) with the section plane directly correlates with the vessel length (Mühlfeld, 2014) and was calculated as follows:

$$L_V = 2Q_A$$

where L_V is the length of vessels per unit volume, and Q_A is the number of intersections of the plane with the vessels per area (Howard and Reed, 2005; Mouton, 2002). The study was based on quantification of 4428 micrographs sampled from 369 tissue blocks. At least 100 intersections of the vascular profiles with the section plane were counted in each sample, as recommended by Tschanz et al. (2014).

2.5 Statistical analysis

The Statistica 10 software (Stat-Soft, Inc., Tulsa, Oklahoma, USA) was used for statistical analysis. The Shapiro–Wilk’s W -test for normality showed that some of the data were not distributed normally. Therefore non-parametric methods were used to test the null hypotheses. The Mann–Whitney U -test was used to assess differences between the neutered male and female animals ($H_0(A)$). The Kruskal–Wallis ANOVA was used to assess differences among six liver lobes ($H_0(B)$) and the differences among the three different ROIs ($H_0(C)$). The correlations between the length density of sinusoids and length density of bile canaliculi and stereological parameters previously quantified (Junatas et al., 2017; Mik et al., 2018) were evaluated using the Spearman correlation coefficient ($H_0(D)$). For the purpose of the correlations, all the values from the ROIs and lobes were pooled. Power analysis according to Chow et al. (2008) was used to calculate the sample size needed to detect the expected change in length densities of liver sinusoids and bile canaliculi.

3. Results

The results are summarized in the Table 1 and Table 2. Complete primary morphometric data are available as supplemental information (S1).

3.1 Hepatic sinusoids

The length density of hepatic sinusoids within the porcine liver was $935.1 \pm 148.7 \text{ mm/mm}^3$ (mean \pm SD). The $L_V(\text{sinusoids}, \text{liver})$ was greater in females than in neutered males (Mann–Whitney U-test, $p < 0.001$) (Fig. 2A, Fig. 3). No significant differences were observed between hepatic lobes (Fig. 2B). The peripheral ROI was the region with smallest $L_V(\text{sinusoids}, \text{liver})$ when compared to the paracaval and to the paraportal ROIs (Kruskal–Wallis ANOVA, $p < 0.001$) (Fig. 2C, Fig. 3).

3.2 Bile canaliculi

The length density of bile canaliculi within the porcine liver was $3697.1 \pm 571.5 \text{ mm/mm}^3$. The $L_V(\text{bile canaliculi}, \text{liver})$ was greater in females than in neutered males (Mann–Whitney U-test, $p < 0.05$) (Fig. 2D; Fig. 3). No significant differences were observed between hepatic lobes (Fig. 2E). We observed a significant difference between the peripheral and paraportal ROIs (Kruskal–Wallis ANOVA, $p < 0.05$) (Fig. 2F; Fig. 3).

3.3 Correlation of the morphometric parameters

Regions with greater $L_V(\text{sinusoids}, \text{liver})$ had also greater $L_V(\text{bile canaliculi}, \text{liver})$ ($R = 0.50$; $p < 0.05$). These data were further correlated with data previously published on the volumes of hepatocytes and fraction of connective tissue in the same animals (Junatas et al., 2017; Mik et al., 2018). There was a negative correlation between the $L_V(\text{sinusoids}, \text{liver})$ and area fraction of connective tissue ($R = -0.28$; $p < 0.05$). Similarly, there was also a negative correlation between the $L_V(\text{sinusoids}, \text{liver})$ and number-weighted mean volume of mononuclear hepatocytes ($R = -0.16$; $p < 0.05$). In contrast, there was positive correlation between $L_V(\text{sinusoids}, \text{liver})$ and numerical density of hepatocytes ($R = 0.20$; $p < 0.05$). While, the $L_V(\text{bile canaliculi}, \text{liver})$ negatively correlated with area fraction of connective tissue ($R = -0.14$; $p < 0.05$).

3.4 Descriptive statistics and power sample analysis

Tables 1 and 2 summarize the descriptive statistics for the parameters under study, namely the mean value, standard deviation, median and interquartile range. The values were calculated for female and male livers, for 6 hepatic lobes and for three regions of interest related to the hepatic vasculature. The mean value and the standard deviation of the length density of hepatic sinusoids and length density of the bile canaliculi were used to calculate the minimum number of samples required when planning experiments on porcine liver. For example, 8 samples would be needed to detect a 20% decrease in length density of the hepatic sinusoids in the periphery of the porcine liver, which displays the highest variability of the three regions of interest related to the hepatic vasculature. This calculation applies for a test strength of 0.8 and type I error of 5%. For a test strength of 0.9, the number of samples required from the periphery should be at least 11. However, only 5 samples (test strength 0.8) or 6 samples (test strength 0.9), would be needed, if we analyzed samples from the parportal region. According to Chow et al. (2008), a similar analysis can be performed for the length density of bile canaliculi.

4. Discussion

4.1 The porcine liver exhibits sexual dimorphism in the length density of sinusoids and bile canaliculi. The assessed differences in morphometric parameters under study between neutered male and female livers (Fig. 2A,D; Fig. 3) were also observed for other morphometric parameters, such as the amount of connective tissue in porcine liver (Mik et al., 2018) and number of hepatocytes or Kupffer cells in the rat liver (Marcos et al., 2016). The present morphological differences are in accordance with the fact that certain liver diseases develop and manifest themselves differently according to the sex of the patients (Buzzetti et al., 2017; Yang et al., 2014). Animals used in our study were 9 – 15 weeks old. Pigs reach sexual maturity accompanied by increased levels of androgen or estrogen at 3 – 7 months depending on the breed (Swindle and Smith, 2016). Therefore, we expect that the differences in the liver morphology between sexually mature intact males and females might be even higher.

4.2 Various porcine hepatic lobes contain sinusoids and bile canaliculi of comparable length density. We found no differences in length densities among the six hepatic lobes (Fig. 2B,E). The number and size of the hepatic lobes varied among animals. The variability in lobe morphology seems to be also breed-specific (Eberlová et al., 2020). Moreover, the size of the smallest quadrate lobe prevented us from differentiating the ROIs related to the liver vasculature in some of the livers. Even though the statistical analysis did not show significant differences in length densities between the lobes, differences in the microscopic structure of the quadrate and caudate lobes were observed in terms of the amount of the connective tissue within porcine liver (Mik et al., 2018). Hence, analyzing liver biopsies solely from the quadrate or the caudate lobe or without knowledge of the sampling location might introduce unnecessary bias to such studies.

4.3 Peripheral regions of the porcine liver contain the smallest length density of sinusoids and bile canaliculi

Peripheral regions of the porcine liver showed significant differences in their microstructure when compared to other regions with regards to the hepatic vasculature (Fig. 2C,F; Fig. 3). Moreover, the smaller values of the length density of sinusoids and bile canaliculi correlated with a smaller number of larger hepatocytes. Such correlations were expected and are now verified by independent measurements. Therefore it seems, that the central (paracaval and paraportal) liver regions might be site of hepatocyte proliferation and growth when compared to the peripheral region. It is suggested that the lower regenerative potential of the periphery of the porcine liver might be caused by its greater volume fraction of the connective tissue (Mik et al., 2018). Furthermore, it has been demonstrated that the increased extracellular matrix stiffness caused by higher condensation of the collagen fibres can influence liver angiogenesis by aggravating sinusoidal cells dysfunction and thus compromise the liver regenerative capacity (Lafoz et al., 2020). Importantly, the differences in the morphological parameters among the different hepatic regions might lead to different distribution of

injury patterns and thus significantly influencing the quality of results of experiments based on random liver biopsies.

4.4 Study implications

The striking differences in the length density of liver sinusoids and bile canaliculi confirm that the sex of the animals is an important confounder and should be taken into account at study design stage. Second, the liver lobes are interchangeable so the sampling of tissue blocks needs to be less extensive than for estimating the volume of hepatocytes (Junatas et al., 2017) or liver fibrosis (Mik et al., 2018). However, the position relative to the hepatic vessels should be kept consistent when comparing tissue samples from various parts of hepatic lobes, otherwise the analysis might be heavily biased by the differences we found (Fig. 2C,F). Alternatively, systematic uniform random sampling of the complete lobe can be performed to obtain information on the whole liver (lobe). Third, a greater length density of liver sinusoids is linked with a greater density of bile canaliculi, with local increase in the density of hepatocytes and, simultaneously, with smaller fractions of hepatic connective tissue. These findings might facilitate interpretation of data acquired by advanced perfusion imaging methods in experimental liver research, as the local signal from the contrast agents depends on the morphometric characteristics of the liver microvascular bed (Bressemer et al., 2019; Nurili et al., 2021).

The density of the sinusoidal network within the liver is only one parameter influencing the biological properties of the sinusoids. The wall of the sinusoids with its single layer of endothelial cells is the key player in many hepatic functions (Gracia-Sancho et al., 2021). The overall surface density of the perfused vessels influences the processes involving the hepatic sinusoidal wall. The surface density of hepatic sinusoids was previously assessed using the corrosion casts of the porcine liver (Jiřík et al., 2016). Nonetheless, the filling of the vessels by the epoxy resin does not reflect the perfusion of the tissue, which is influenced and changes in reaction to different noxae.

Bile canaliculi are often overlooked when evaluating the liver tissue biopsies. However, the morphometrics of bile canaliculi should be more emphasized as the network is involved in many

physiological and pathological processes. Assessing the formation of the bile canalicular network formation is crucial for functional evaluation of complex 3D *in vitro* tissue models (Deharde et al., 2016). Bile canaliculi are also deeply involved in liver regeneration, where they serve as a self-regulatory mechano-sensory system that adapts to the overall metabolic demand of the body. The regulation is enabled by reversible structural and functional changes in apical domains of the hepatocytes (Meyer et al., 2020). Abnormalities in canaliculi formation and thus, changes in network density are often associated with rare inherited disorders as well as common infections such as hepatitis C (Gissen and Arias, 2015).

5. Conclusions

The length density of hepatic sinusoids is smaller in the peripheral regions of the porcine liver than in other regions related to the hepatic vasculature – paracaval and paraportal regions and smaller in castrated males than in females. Greater length density of liver sinusoids was linked with greater local density of bile canaliculi, with local increase in the density of smaller hepatocytes and, simultaneously, with smaller fractions of hepatic connective tissue. Such intrahepatic and inter-sexual variability of the porcine liver morphology needs to be taken into consideration when designing experiments that include histological evaluation of liver tissue samples. Our original data on the distribution of the sinusoidal and the bile canalicular network within the porcine liver are now available for power sample analysis to justify the number of animals, including their sex, and the number of samples required for detecting expected biological effects within the tissue.

Declaration of Competing Interest

The authors declare that they have no known competing financial interests or personal relationships that could have appeared to influence the work reported in this paper.

Acknowledgements

This study was supported by the Charles University Research Fund (Progres Q39); by the Cooperatio Program, research area MED/DIAG of the Charles University; by Charles University Project number SVV 260 536; by the Centre of Clinical and Experimental Liver Surgery UNCE/MED/006; by the Ministry of Education, Youth and Sports under the project FIND No. CZ.02.1.01/0.0/0.0/16_019/0000787. The authors would also like to thank the Chaperon ERA Research Club service for their assistance with the editing of the manuscript.

References

- Bressemer, K. K., Vahldiek, J. L., Erxleben, C., Shnayien, S., Poch, F., Geyer, B., Lehmann, K. S., Hamm, B., & Niehues, S. M., 2019. Improved Visualization of the Necrotic Zone after Microwave Ablation Using Computed Tomography Volume Perfusion in an In Vivo Porcine Model. *Scientific Reports*. 9(1), 1–8. <https://doi.org/10.1038/s41598-019-55026-9>
- Bruha, J., Vycital, O., Tonar, Z., Mirka, H., Haidingerova, L., Benes, J., Palek, R., Skala, M., Treska, V., Liska, V. 2015. Monoclonal Antibody Against Transforming Growth Factor Beta 1 Does Not Influence Liver Regeneration After Resection in Large Animal Experiments. *In vivo (Athens, Greece)*. 29(3), 327–340.
- Burbank, M.G., Burban, A., Sharanek, A., Weaver, R.J., Guguen-Guillouzo, C., Guillouzo, A., 2016. Early alterations of bile canaliculi dynamics and the rho kinase/myosin light chain kinase pathway are characteristics of drug-induced intrahepatic cholestasis. *Drug Metabolism and Disposition*. 44(11), 1780–1793. <https://doi.org/10.1124/dmd.116.071373>
- Buzzetti, E., Parikh, P. M., Gerussi, A., Tsochatzis, E., 2017. Gender differences in liver disease and the drug-dose gender gap. *Pharmacological Research*. 120, 97–108. <https://doi.org/10.1016/j.phrs.2017.03.014>
- Chow, S.C., Wang, H., Shao, J., 2008. *Sample Size Calculations in Clinical Research*, Second ed. Chapman & Hall/CRC Biostatistics Series, Boca Raton.
- De Assuncao, T.M., Jalan-Sakrikar, N., Huebert, R.C., 2017. Regenerative Medicine and the Biliary Tree. *Seminars in Liver Disease*. 37(1), 17–27. <https://doi.org/10.1055/s-0036-1597818>
- Deharde, D., Schneider, C., Hiller, T., Fischer, N., Kegel, V., Lübberstedt, M., Freyer, N., Hengstler, J.G., Andersson, T.B., Seehofer, D., Pratschke, J., Zeilinger, K., & Damm, G., 2016. Bile canaliculi formation and biliary transport in 3D sandwich-cultured hepatocytes in dependence of the extracellular matrix composition. *Archives of Toxicology*. 90(10), 2497–2511. <https://doi.org/10.1007/s00204-016-1758-z>
- Eberlova, L., Liska, V., Mirka, H., Tonar, Z., Haviar, S., Svoboda, M., Benes, J., Palek, R., Emingr, M., Rosendorf, J., Mik, P., Leupen, S., Lametschwandtner, A., 2017. The use of porcine corrosion casts for teaching human anatomy. *Annals of Anatomy*. 213, 69–77. <https://doi.org/10.1016/j.aanat.2017.05.005>
- Eberlova, L., Maleckova, A., Mik, P., Tonar, Z., Jirik, M., Mirka, H., Palek, R., Leupen, S., Liska, V., 2020. Porcine Liver Anatomy Applied to Biomedicine. *Journal of Surgical Research*. 250, 70–79. <https://doi.org/10.1016/j.jss.2019.12.038>

- Fernández-Iglesias, A., Gracia-Sancho, J., 2017. How to face chronic liver disease: The sinusoidal perspective. *Frontiers in Medicine*. 4, 7. <https://doi.org/10.3389/fmed.2017.00007>
- Gissen, P., Arias, I.M., 2015. Structural and functional hepatocyte polarity and liver disease. *Journal of Hepatology*. 63(4), 1023–1037. <https://doi.org/10.1016/j.jhep.2015.06.015>
- Gracia-Sancho, J., Caparrós, E., Fernández-Iglesias, A., Francés, R., 2021. Role of liver sinusoidal endothelial cells in liver diseases. *Nature Reviews. Gastroenterology and Hepatology*. 18(6), 411–431. <https://doi.org/10.1038/s41575-020-00411-3>
- Grajciarová, M., Turek, D., Malečková, A., Pálek, R., Liška, V., Tomášek, P., Králíčková, M., Tonar, Z., 2022. Are ovine and porcine carotid arteries equivalent animal models for experimental cardiac surgery: A quantitative histological comparison. *Annals of Anatomy*. 242, 151910. <https://doi.org/10.1016/j.aanat.2022.151910>
- Hammad, S., Hoehme, S., Friebel, A., von Recklinghausen, I., Othman, A., Begher-Tibbe, B., Reif, R., Godoy, P., Johann, T., Vartak, A., Golka, K., Bucur, P. O., Vibert, E., Marchan, R., Christ, B., Dooley, S., Meyer, C., Ilkavets, I., Dahmen, U., Dirsch, O., Böttger, J., Gebhardt, R., Drasdo, D., Hengstler, J.G., 2014. Protocols for staining of bile canalicular and sinusoidal networks of human, mouse and pig livers, three-dimensional reconstruction and quantification of tissue microarchitecture by image processing and analysis. *Archives of Toxicology*. 88(5), 1161–1183. <https://doi.org/10.1007/s00204-014-1243-5>
- Howard, C.V., & Reed, M.G., 2005. *Unbiased stereology: Three-dimensional measurement in microscopy*, 2nd ed. Garland Science.
- Jiřík, M., Tonar, Z., Králíčková, A., Eberlová, L., Mírka, H., Kochová, P., Gregor, T., Hošek, P., Svobodová, M., Rohan, E., Králíčková, M., Liška, V., 2016. Stereological quantification of microvessels using semiautomated evaluation of X-ray microtomography of hepatic vascular corrosion casts. *International Journal of Computer Assisted Radiology and Surgery*. 11(10), 1803–1819. <https://doi.org/10.1007/s11548-016-1378-3>
- Jiřík, M., Bartoš, M., Tomášek, P., Malečková, A., Kural, T., Horáková, J., Lukáš, D., Suchý, T., Kochová, P., Hubálek Kalbáčová, M., Králíčková, M., & Tonar, Z., 2018. Generating standardized image data for testing and calibrating quantification of volumes, surfaces, lengths, and object counts in fibrous and porous materials using X-ray microtomography. *Microscopy Research and Technique*. 81(6), 551–568. <https://doi.org/10.1002/jemt.23011>
- Junatas, K.L., Tonar, Z., Kubíková, T., Liška, V., Pálek, R., Mik, P., Králíčková, M., Witter, K., 2017. Stereological analysis of size and density of hepatocytes in the porcine liver. *Journal of anatomy*. 230(4), 575–588. <https://doi.org/10.1111/joa.12585>
- Kolinko, Y., Malečková, A., Kochová, P., Grajciarová, M., Blassová, T., Kural, T., Trailin, A., Červenková, L., Havránková, J., Vištejnová, L., Tonarová, P., Moulisová, V., Jiřík, M., Zavadáková, A., Tichánek, F., Liška, V., Králíčková, M., Witter, K., Tonar, Z., 2022. Using virtual microscopy for the development of sampling strategies in quantitative histology and design-based stereology. *Anatomia, histologia, embryologia*. 51(1), 3–22. <https://doi.org/10.1111/ahe.12765>
- Kubíková, T., Kochová, P., Tomášek, P., Witter, K., Tonar, Z., 2018. Numerical and length densities of microvessels in the human brain: Correlation with preferential orientation of microvessels in the cerebral cortex, subcortical grey matter and white matter, pons and cerebellum. *Journal of Chemical Neuroanatomy*. 88, 22–32. <https://doi.org/10.1016/j.jchemneu.2017.11.005>
- Lafoz, E., Ruart, M., Anton, A., Oncins, A., Hernández-Gea, V., 2020. The Endothelium as a Driver of Liver Fibrosis and Regeneration. *Cells*. 9(4), 1–26. <https://doi.org/10.3390/cells9040929>

- Lemaigre, F. P., 2009. Mechanisms of Liver Development: Concepts for Understanding Liver Disorders and Design of Novel Therapies. *Gastroenterology*. 137(1), 62–79. <https://doi.org/10.1053/j.gastro.2009.03.035>
- Lossi, L., D'Angelo, L., De Girolamo, P., & Merighi, A., 2016. Anatomical features for an adequate choice of experimental animal model in biomedicine: II. Small laboratory rodents, rabbit, and pig. *Annals of Anatomy*. 204, 11–28. <https://doi.org/10.1016/j.aanat.2015.10.002>
- Mak, K. M., Shin, D. W., 2021. Hepatic sinusoids versus central veins: Structures, markers, angiocrines, and roles in liver regeneration and homeostasis. *Anatomical record*. 304(8), 1661–1691. <https://doi.org/10.1002/ar.24560>
- Marcos, R., Monteiro, R.A., Rocha, E., 2012. The use of design-based stereology to evaluate volumes and numbers in the liver: a review with practical guidelines. *Journal of anatomy*. 220(4), 303–317. <https://doi.org/10.1111/j.1469-7580.2012.01475.x>
- Marcos, R., Lopes, C., Malhão, F., Correia-Gomes, C., Fonseca, S., Lima, M., Gebhardt, R., & Rocha, E., 2016. Stereological assessment of sexual dimorphism in the rat liver reveals differences in hepatocytes and Kupffer cells but not hepatic stellate cells. *Journal of anatomy*. 228(6), 996–1005. <https://doi.org/10.1111/joa.12448>
- Massaro, M.S., Pálek, R., Rosendorf, J., Červenková, L., Liška, V., Moulisová, V., 2021. Decellularized xenogeneic scaffolds in transplantation and tissue engineering: Immunogenicity versus positive cell stimulation. *aterials science & engineering. C, Materials for biological applications*. 127, 112203. <https://doi.org/10.1016/j.msec.2021.112203>
- Meyer, K., Ostrenko, O., Bourantas, G., Morales-Navarrete, H., Porat-Shliom, N., Segovia-Miranda, F., Nonaka, H., Ghaemi, A., Verbavatz, J. M., Bruschi, L., Sbalzarini, I., Kalaidzidis, Y., Weigert, R., & Zerial, M., 2017. A Predictive 3D Multi-Scale Model of Biliary Fluid Dynamics in the Liver Lobule. *Cell Systems*. 4(3), 277-290.e9. <https://doi.org/10.1016/j.cels.2017.02.008>
- Meyer, K., Morales-Navarrete, H., Seifert, S., Wilsch-Braeuninger, M., Dahmen, U., Tanaka, E.M., Bruschi, L., Kalaidzidis, Y., & Zerial, M., (2020). Bile canaliculi remodeling activates YAP via the actin cytoskeleton during liver regeneration. *Molecular Systems Biology*. 16(2), 1–18. <https://doi.org/10.15252/msb.20198985>
- Mik, P., Tonar, Z., Malečková, A., Eberlová, L., Liška, V., Pálek, R., Rosendorf, J., Jiřík, M., Mírka, H., Králíčková, M., Witter, K., 2018. Distribution of Connective Tissue in the Male and Female Porcine Liver: Histological Mapping and Recommendations for Sampling. *Journal of comparative pathology*, 162, 1–13. <https://doi.org/10.1016/j.jcpa.2018.05.004>
- Moulisová, V., Jiřík, M., Schindler, C., Červenková, L., Pálek, R., Rosendorf, J., Arlt, J., Bolek, L., Šušová, S., Nietzsche, S., Liška, V., Dahmen, U., 2020. Novel morphological multi-scale evaluation system for quality assessment of decellularized liver scaffolds. *Journal of tissue engineering*. 11, 2041731420921121. <https://doi.org/10.1177/2041731420921121>
- Mouton, P.R., 2002. Principles and practices of unbiased stereology. An introduction for bioscientists. The Johns Hopkins University Press, Baltimore, Maryland.
- Mühlfeld, C., 2014. Quantitative morphology of the vascularisation of organs: A stereological approach illustrated using the cardiac circulation. *Annals of Anatomy*. 196(1), 12–19. <https://doi.org/10.1016/j.aanat.2012.10.010>
- Nakamura-Ishizu, A., Morikawa, S., Shimizu, K., Ezaki, T., 2008. Characterization of sinusoidal endothelial cells of the liver and bone marrow using an intravital lectin injection method. *Journal of Molecular Histology*. 39(5), 471–479. <https://doi.org/10.1007/s10735-008-9186-x>

- Nurili, F., Monette, S., Michel, A. O., Bendet, A., Basturk, O., Askan, G., Cheleuitte-Nieves, C., Yarmohammadi, H., Maxwell, A., Ziv, E., Schachtschneider, K.M., Gaba, R.C., Schook, L.B., Solomon, S.B., Boas, F.E., 2021. Transarterial Embolization of Liver Cancer in a Transgenic Pig Model. *Journal of Vascular and Interventional Radiology*. 32(4), 510-517.e3. <https://doi.org/10.1016/j.jvir.2020.09.011>
- Nyengaard, J.R., Gundersen, H.J.G., 2006. Sampling for stereology in lungs. *European Respiratory Review*. 15(101), 107–114. <https://doi.org/10.1183/09059180.00010101>
- Ober, E.A., Lemaigre, F.P., 2018. Development of the liver: Insights into organ and tissue morphogenesis. *Journal of Hepatology*. 68(5), 1049–1062. <https://doi.org/10.1016/j.jhep.2018.01.005>
- Overeem, A.W., Klappe, K., Parisi, S., Drouin, C.A., Weiss, K.H., van Ijzendoorn, S.C.D., 2019. Pluripotent stem cell-derived bile canaliculi-forming hepatocytes to study genetic liver diseases involving hepatocyte polarity. *Journal of hepatology*. 71(2), 344–356. <https://doi.org/10.1016/j.jhep.2019.03.031>
- Palek, R., Rosendorf, J., Maleckova, A., Vistejnova, L., Bajcurova, K., Mirka, H., Tegl, V., Brzon, O., Kumar, A., Bednar, L., Tonar, Z., Hosek, P., Moulisova, V., Eberlova, L., Treska, V., Liska, V., 2020. Influence of Mesenchymal Stem Cell Administration on the Outcome of Partial Liver Resection in a Porcine Model of Sinusoidal Obstruction Syndrome. *Anticancer Research*. 40(12), 6817–6833. <https://doi.org/10.21873/anticancer.14704>
- Renner, S., Blutke, A., Clauss, S., Deeg, C. A., Kemter, E., Merkus, D., Wanke, R., & Wolf, E., 2020. Porcine models for studying complications and organ crosstalk in diabetes mellitus. *Cell and Tissue Research*. 380(2), 341–378. <https://doi.org/10.1007/s00441-019-03158-9>
- Saxena, R., 2018. *Practical Hepatic Pathology: A Diagnostic Approach*. 2nd edition. Elsevier, Philadelphia.
- Shetty, S., Lalor, P.F., Adams, D.H., 2018. Liver sinusoidal endothelial cells — gatekeepers of hepatic immunity. *Nature Reviews. Gastroenterology and Hepatology*. 15(9), 555–567. <https://doi.org/10.1038/s41575-018-0020-y>
- Sørensen, K.K., Simon-Santamaria, J., McCuskey, R.S., Smedsrød, B., 2015. Liver sinusoidal endothelial cells. *Comprehensive Physiology*. 5(4), 1751–1774. <https://doi.org/10.1002/cphy.c140078>
- Swindle, M.M., Smith, A.C., 2016. *Swine in the laboratory: surgery, anesthesia, imaging, and experimental techniques*, third edition. Taylor & Francis Group, Boca Raton.
- Treyer, A., Müsch, A., 2013. Hepatocyte Polarity. *Comprehensive Physiology*. 3(1), 243–287. <https://doi.org/10.1002/cphy.c120009>
- Tschanz, S., Schneider, J.P., Knudsen, L., 2014. Design-based stereology: Planning, volumetry and sampling are crucial steps for a successful study. *Annals of Anatomy*. 196(1), 3–11. <https://doi.org/10.1016/j.aanat.2013.04.011>
- Yang, J.D., Abdelmalek, M.F., Pang, H., Guy, C.D., Smith, A.D., Diehl, A.M., Suzuki, A., 2014. Gender and menopause impact severity of fibrosis among patients with nonalcoholic steatohepatitis. *Hepatology*. 59(4), 1406–1414. <https://doi.org/10.1002/hep.26761>

List of supplements

Supplement 1. Complete primary data of the morphometric analysis of the porcine liver. The results of the stereological analysis of length density of hepatic sinusoids and bile canaliculi in 6 hepatic lobes and three regions of interest related to the hepatic vasculature.

Tables

$L_v(\text{sinusoids, liver})$
(mm/mm³)

Grouping variable	Value	Mean	Standard deviation	Median	Lower quartile	Upper quartile
Sex	Male	884.3	132.6	901.1	785.7	978.1
	Female	990.2	145.9	984.2	895.1	1097.6
Hepatic lobe	Left lateral	946.9	153.8	955.8	866.7	1028.7
	Left medial	922.5	135.8	931.5	830.3	1012.5
	Right medial	932.2	182.4	939.6	789.8	1063.1
	Right lateral	959.1	135.2	947.7	882.9	1036.8
	Caudate	914.9	127.6	915.3	818.1	988.2
	Quadrate	933.6	154.5	937.6	828.2	1044.9
Region related to the liver vasculature	Peripheral	870.8	154.8	858.6	749.3	988.2
	Paracaval	972.1	139.1	959.9	887	1049
	Paraportal	964	129.7	949.7	882.9	1048.9

Table 1: Length density of sinusoids $L_v(\text{sinusoids, liver})$. Descriptive statistics presented for various grouping variables separately as suitable for calculating the minimum number of samples for planning experiments on porcine liver involving the microvascular network.

$L_v(\text{bile canaliculi, liver})$
(mm/mm³)

Grouping variable	Value	Mean	Standard deviation	Median	Lower quartile	Upper quartile
Sex	Male	3615	593.8	3612.6	3159	4066.2
	Female	3785.8	534	3758.4	3385.8	4163.4
Hepatic lobe	Left lateral	3635.4	565.9	3604.5	3175.2	4131
	Left medial	3614.7	536	3596.4	3288.6	3969
	Right medial	3682.3	648.3	3628.8	3296.7	4106.7
	Right lateral	3700.9	525.8	3717.9	3385.8	4050
	Caudate	3705.6	557.2	3677.4	3353.4	4114.8
	Quadrante	3895.6	578.9	3904.2	3434.4	4276.8
	Region related to the liver vasculature	Peripheral	3602.9	603.8	3564	3175.2
	Paracaval	3693.7	560	3693.6	3304.8	4066.2
	Paraportal	3797	535.4	3823.2	3466.8	4179.6

Table 2: Length density of bile canaliculi $L_v(\text{bile canaliculi, liver})$. Descriptive statistics presented for various grouping variables separately as suitable for calculating the minimum number of samples for planning experiments on porcine liver involving the bile canalicular network.

Figure legends

Figure 1: Quantitative analysis of length density of hepatic sinusoids $L_V(\text{sinusoids}, \text{liver})$ and bile canaliculi $L_V(\text{bile canaliculi}, \text{liver})$ in the porcine liver. (A) Each tissue block (36 samples per liver) was represented by three 3 μm thick sections with 4 fields of view (FOVs) in each section (red squares), in total 12 FOVs per tissue block. In each section, the first FOV was positioned randomly, starting from the top left corner of the section. The following FOVs were placed in equidistant positions using the systematic uniform random sampling method. (B) Example of a 222 \times 185 μm unbiased counting frame (left picture) used for counting of hepatic sinusoids profiles $Q_A(\text{sinusoids}, \text{liver})$. The close up of the counting frame (right picture) demonstrates the rules for counting the vascular profiles: only clearly distinguished profiles located within the counting frame or crossing the green inclusion line, but not the red exclusion line, were counted (red asterisks). (C) Four 55 \times 46 μm unbiased counting frames (left picture) used for counting of bile canaliculi profiles $Q_A(\text{bile canaliculi}, \text{liver})$. The close up on the right upper counting frame shows the counting of the bile canaliculi profiles (red circles), that followed the same rules as counting the sinusoids (B). Lectin histochemistry staining (RCA-I), counterstained with Mayer's haematoxylin. Scale bars = 1000 μm (A) and 50 μm (B, C).

Figure 2: Estimation of length density of hepatic sinusoids $L_V(\text{sinusoids}, \text{liver})$ (A, B, C) and length density of bile canaliculi $L_V(\text{bile canaliculi}, \text{liver})$ (D, E, F) in male vs. female porcine liver (A, D), in six hepatic lobes (B, E) and in three regions related to hepatic vasculature (C, F). Data are displayed as single dots representing each measured value; median and limits of the first and third quartiles are shown. Significant differences (*P <0.05, **P <0.01, ***P <0.001) identified by the Mann–Whitney U-test adjusted with respect to the Bonferroni correction are presented.

Figure 3: Microphotographs of porcine liver demonstrating the microscopic architecture of the male (A, B, C) and female (D, E, F) right lateral hepatic lobe and its three regions of interest (ROI) related to hepatic vasculature. Smaller length density of sinusoids and bile canaliculi was found in the neutered

males than in females. Smaller length density was found in the peripheral ROIs (A, D) than in the paracaval (B, E) and paraportal (C, F) ROIs. Lectin histochemistry staining (RCA-I), counterstained with Mayer's haematoxylin. Scale bars = 50 μ m.

Figures

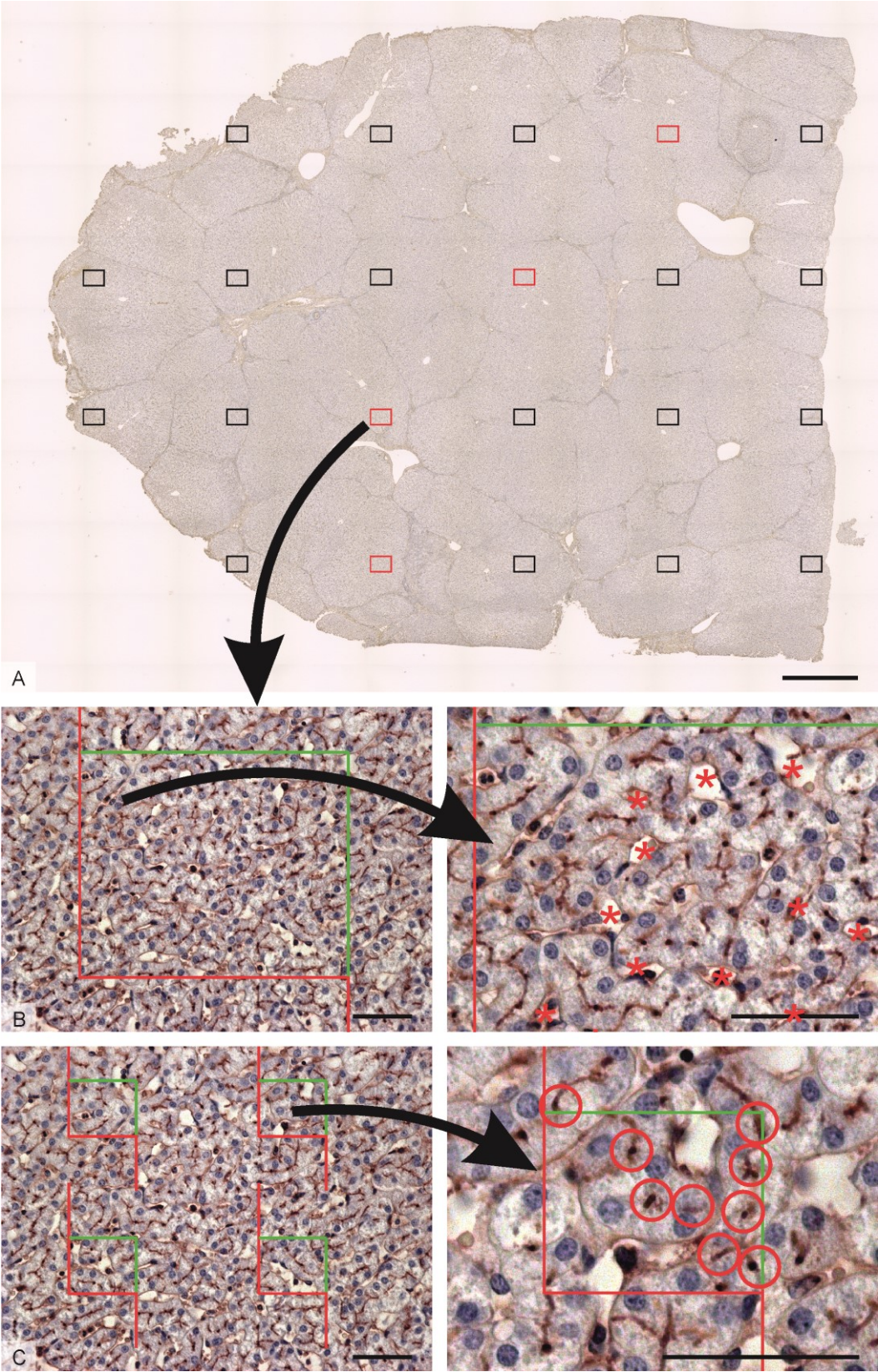


Figure 1

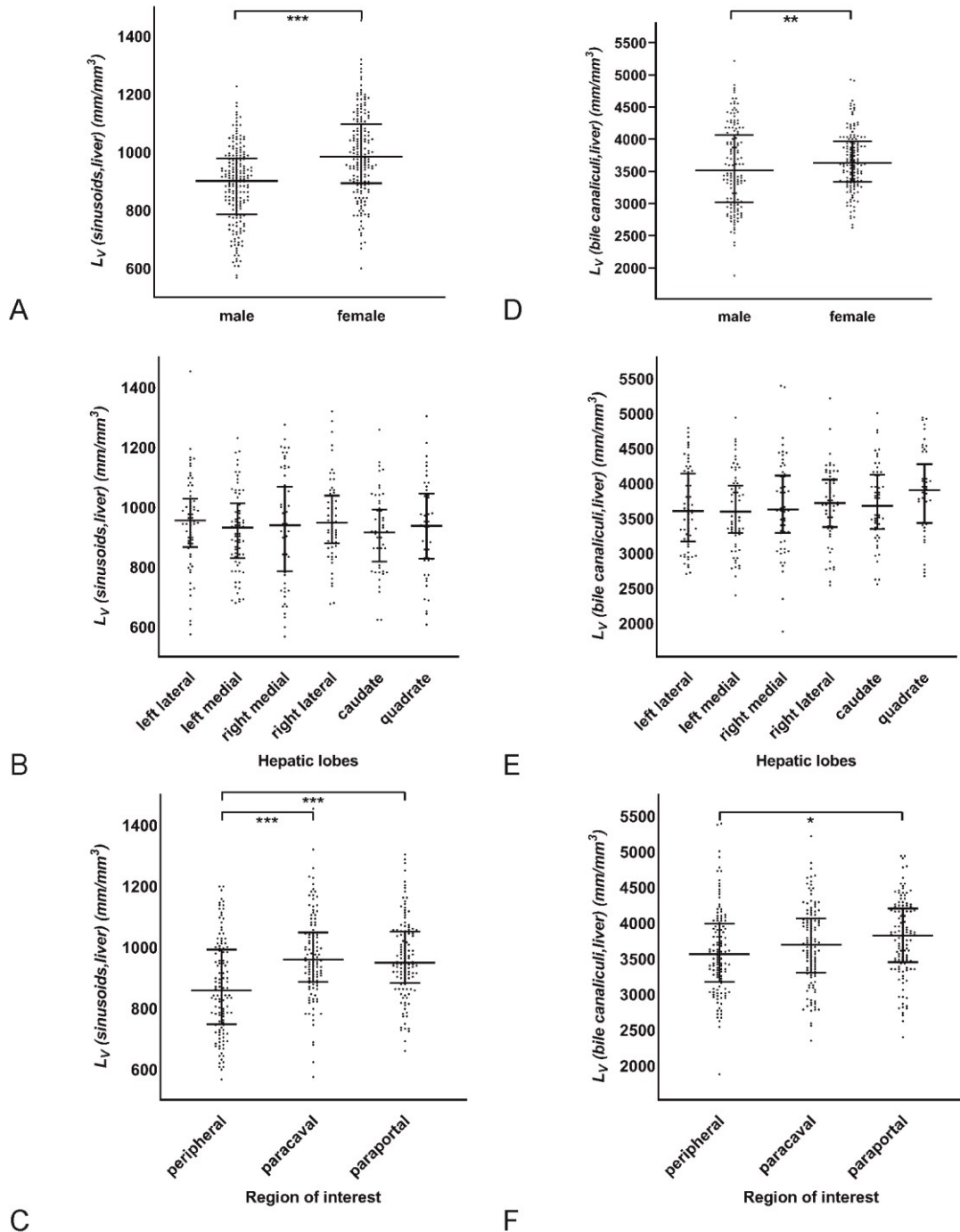


Figure 2

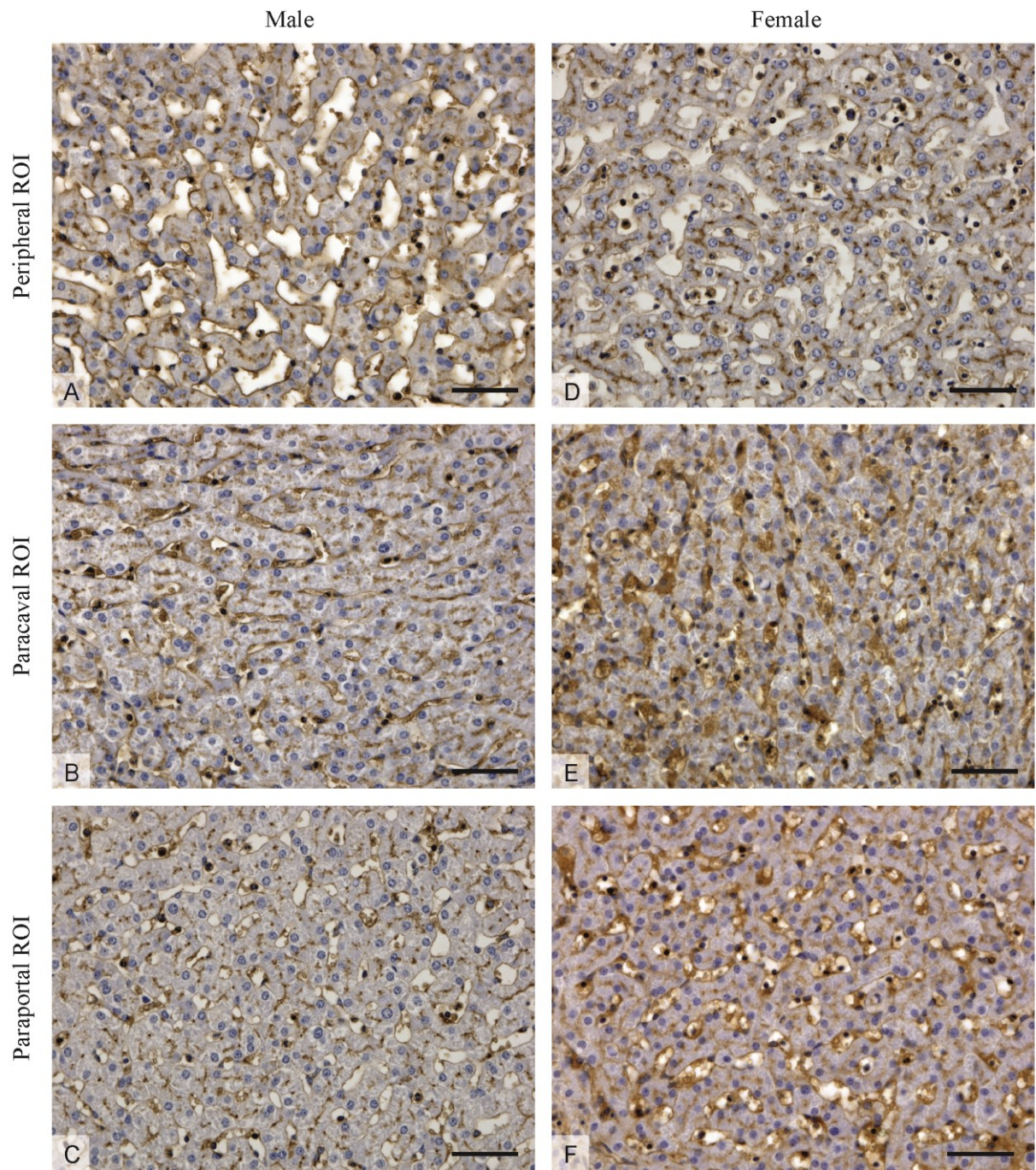


Figure 3

10.8 Příloha VIII

PÁLEK, Richard, LIŠKA, Václav, TŘEŠKA, Vladislav, ROSENDORF, Jáchym, EMINGR, Michal, TÉGL, Václav, **KRÁLÍČKOVÁ, Anna**, BAJCUROVÁ, Kristýna, JIŘÍK, Miroslav, TONAR, Zbyněk, 2018. Sinusoidální obstrukční syndrom indukovaný monokrotalinem v experimentu na velkém zvířeti – pilotní studie. *Rozhledy v chirurgii*. 97(5), 214–221. ISSN 0035-9351. Dostupné z: <https://www.prolekare.cz/en/journals/perspectives-in-surgery/2018-5-2/sinusoidal-obstruction-syndrome-induced-by-monocrotaline-in-a-large-animal-experiment-a-pilot-study-63663>

Původní práce

Sinusoidální obstrukční syndrom indukovaný monokrotalinem v experimentu na velkém zvířeti – pilotní studie

R. Pálek^{1,2}, V. Liška^{1,2}, V. Třeška¹, J. Rosendorf¹, M. Eminger¹, V. Těgl², A. Králíčková³, K. Bajcurová⁴, M. Jiřík², Z. Tonar³

¹Chirurgická klinika, Univerzita Karlova, Lékařská fakulta v Plzni, Fakultní nemocnice Plzeň

²Biomedicínské centrum, Lékařská fakulta Univerzity Karlovy v Plzni

³Ústav histologie a embryologie, Lékařská fakulta Univerzity Karlovy v Plzni

⁴Klinika zobrazovacích metod, Lékařská fakulta Univerzity Karlovy v Plzni

Souhrn

Úvod: Sinusoidální obstrukční syndrom (SOS) je onemocnění vznikající na základě toxického poškození jaterních sinusoid. Tento syndrom bývá nejčastěji navozen myeloablativní radiochemoterapií u pacientů před transplantací hematopoetických kmenových buněk, dále pak oxaliplatinou především u pacientů s jaterními metastázami kolorektálního karcinomu. Cílem naší studie bylo etablovat model SOS na velkém zvířeti, který by umožnil další studium tohoto onemocnění a usnadnil translaci experimentálních výsledků do humánní medicíny.

Metody: Do této pilotní studie bylo zařazeno celkem 27 prasat domácích (plemeno – přeštické černostrakaté prase) (12 samic). Z toho 5 zvířat tvořilo skupinu s vyšším dávkováním monokrotalinu (180 mg/kg) a u zbylých 22 byla podaná dávka monokrotalinu nižší (36 mg/kg). Monocrotalin byl aplikován intraportálně a za týden po jeho aplikaci byla provedena resekce levého laterálního laloku jater. Zvířata byla sledována celkem 3 týdny po aplikaci monokrotalinu. Byla prováděna pravidelná ultrasonografická vyšetření, stanovovány biochemické markery jaterních a ledvinných funkcí a ze získaných biotických vzorků jaterního parenchymu provedeno histologické vyšetření.

Výsledky: Charakter toxického poškození jater, které jsme zaznamenali u všech zvířat, odpovídal jak makroskopicky, tak mikroskopicky obrazu SOS. Zaznamenali jsme elevaci AST, ALT, bilirubinu a amoniaku po aplikaci monokrotalinu. Při ultrasonografickém vyšetření byla patrná vyšší echogenita poškozeného jaterního parenchymu v porovnání s parenchymem zdravým. Ze skupiny prvních pěti zvířat, kterým byla aplikována dávka 180 mg/kg, uhynula všechna zvířata ještě před resekcí levého laterálního laloku jater (1. až 3. den po aplikaci). Ve druhé skupině 22 prasat s nižším dávkováním došlo k úmrtí před provedením jaterní resekce ve 3 případech (6. a 7. den). K předčasnému úmrtí po resekcii jater došlo v 8 případech (7. až 17. den po aplikaci). 11 zvířat přeživalo po celou dobu experimentu. Příčinou úmrtí (v rámci obou skupin) byl u 10 zvířat metabolický rozvrat a u 4 zvířat exsanguinace. V obou případech se jednalo o důsledek těžké hepatopatie. 2 ze zvířat zemřela z důvodu nesouvisajícího přímo s intoxikací monokrotalinem (strangulace tenkého střeva, gastrektázie).

Závěr: Etablovali jsme model SOS na velkém zvířeti navozený aplikací monokrotalinu o dávce 36 mg/kg cestou portální žíly. Jedná se o první nám známý model SOS navozeného monokrotalinem na velkém zvířeti. Tento model může pomoci při výzkumu jak terapeutického ovlivnění, tak pro hodnocení efektu chirurgické léčby v terénu SOS.

Klíčová slova: sinusoidální obstrukční syndrom – monokrotalin – oxaliplatin – hepatotoxicita – experimentální model

Summary

Sinusoidal obstruction syndrome induced by monocrotaline in a large animal experiment – a pilot study

R. Pálek, V. Liška, V. Třeška, J. Rosendorf, M. Eminger, V. Těgl, A. Králíčková, K. Bajcurová, M. Jiřík, Z. Tonar

Introduction: Sinusoidal obstruction syndrome (SOS) is a disease which is caused by toxic injury to hepatic sinusoids. This syndrome is most frequently caused by myeloablative radiochemotherapy in patients before hematopoietic stem cells transplantation and also by oxaliplatin mainly in patients with colorectal liver metastases. The aim of this study was to establish a large animal model of SOS, which would enable further study of this disease and facilitate translation of experimental outcomes into human medicine.

Methods: A total of 27 domestic pigs (Prestice Black-Pied pig) were involved in this study (12 females). A group with a higher dose of monocrotaline (180 mg/kg) included 5 animals, and the remaining 22 pigs formed another group with a lower dose (36 mg/kg). Monocrotaline was administered via the portal vein and one week after the administration, partial hepatectomy of the left lateral liver lobe was performed. The animals were followed up for 3 weeks after monocrotaline administration. Regular ultrasound examinations were performed as well as examination of biochemical markers of liver and kidney functions and histological examination of liver parenchyma samples.

Results: The features of toxic liver injury which we observed in case of all animals were comparable with macroscopic and microscopic appearance of SOS. We recorded AST, ALT, bilirubin and ammonia elevation after monocrotaline administration. Echogenicity on ultrasound images of injured liver parenchyma was higher compared to echogenicity of healthy parenchyma. All the five animals from the first group with a higher monocrotaline dose had died before partial hepatectomy (1st–3rd day after monocrotaline administration). Death before partial hepatectomy occurred in 3 cases (6th and 7th day after monocrotaline administration) in the second group of 22 animals with a lower dose of monocrotaline. Death after partial hepatectomy occurred in 8 cases (7th–17th day after monocrotaline administration) in the same group. 11 animals survived the entire experimental period. The cause of death (in both groups) was metabolic failure in 10 animals and exsanguination in 4 animals, both due to severe hepatopathy. Death of 2 animals was not associated with monocrotaline intoxication (strangulation of small intestine, gastrectasis).

Conclusions: We established a large animal model of SOS induced by monocrotaline administration (36 mg/kg via portal vein). This model can contribute to research of therapeutic modalities for this disease or to evaluation of surgical treatment of patients with SOS.

Key words: sinusoidal obstruction syndrome – monocrotaline – oxaliplatin – hepatotoxicity – experimental model

Rozhl Chir 2018;97:214–221

ÚVOD

Sinusoidální obstrukční syndrom (SOS), známý také jako blue liver syndrome a dříve jako jaterní veno-okluzivní choroba, vzniká na základě toxického poškození jaterních sinusoid. Nejčastěji se lze s tímto onemocněním setkat u pacientů po transplantaci hematopoetických kmenových buněk, kde je navozeno myeloablativní radiochemoterapií [1]. Další z příčin pak bývá léčba oxaliplatinou nejčastěji u pacientů s jaterními metastázami kolorektálního karcinomu [2,3]. Podstatou tohoto syndromu je ztráta integrity stěny jaterních sinusoid vedoucí k jejich obstrukci. Později se může rozvinout i perisinusoidální fibróza či fibrotická obstrukce centrilobulárních žil a nodulární regenerativní hyperplazie [4].

Jsou popsány modely SOS u hlodavců za použití různých pyrolizidinových alkaloidů. Nejčastěji je však uváděn monokrotalin, a to u studií, které se zabývají studiem jeho etiopatogeneze, diagnostických markerů a případného terapeutického ovlivnění [5,6,7]. Některé ze studií dokonce poukazují na možné lepší přihojení transplantovaných hepatocytů v játrech s SOS navozeným monokrotalinem [8,9]. Doposud však nebyl vytvořen model SOS na velkém zvířeti.

Díky zmíněným modelům u hlodavců byla popsána patofyziologie SOS navozeného monokrotalinem. Primárními cílovými buňkami poškozenými monokrotalinem jsou sinusoidální endoteliální buňky jater. Reaktivní metabolit monokrotalinu poškozuje F-aktin v těchto buňkách. Dochází ke ztrátě jejich fenestrace. Vznikají mezi nimi mezery a ztrácí se tak integrita endotelu sinusoid. Erytrocyty protékající sinusoidou tak pronikají do Disseho prostoru, způsobují mikrodisekci endotelu a embolizaci s obstrukcí jaterních sinusoid. Tyto změny jsou patrné již v průběhu prvních 48 hodin po aplikaci monokrotalinu. V důsledku porušené mikrocirkulace na úrovni jaterních sinusoid dochází mezi třetím a pátým dnem po aplikaci k centrilobulárním hemoragickým nekrotázám. V tomto stadiu jsou již přítomny klinické známky v podobě hepatomegalie, ascitu a hyperbilirubinemie. Šestý a sedmý den po aplikaci dochází k subendoteliální a adventiciální fibrotizaci centrilobulárních žil s přetrváváním klinických symptomů. Od osmého až desátého dne dochází u některých zvířat k postupné úpravě jaterního parenchymu, u jiných SOS perzistuje [3,5].

Pokud je u pacientů s jaterními metastázami kolorektálního karcinomu indikována chemoterapie na bázi oxaliplatinu, může dojít ke vzniku SOS, který je pak limitací extenzivní jaterní resekce, může snižovat pooperační regenerační kapacitu jater a zvyšovat pooperační morbiditu a mortalitu [10,6].

Cílem naší studie bylo etablovat model SOS na velkém zvířeti, který by umožnil další studium tohoto onemocnění a usnadnil translaci experimentálních výsledků do domácí medicíny.

METODY

Experiment byl proveden dle platné legislativy a s svolením Ministerstva zemědělství ČR. Byly dodrženy

stávající předpisy a směrnice pro chov a experimentální používání zvířat v souladu se zákonem č. 246/1992 upraveným vyhl. č. 207/2004 s následným výkladem k vyhláše č. 39/2009. Jako experimentální zvíře bylo zvoleno prase domácí (plemeno – přeštické černostrakaté prase), pracovali jsme s jedinci z jatečního chovu o průměrné hmotnosti 28 kg (20,6–40 kg, směrodatná odchylka 6,86 kg).

Do této pilotní studie bylo zařazeno celkem 27 zvířat (12 samic). Z toho 5 zvířat tvořilo skupinu s vyšším dávkováním monocrotalinu (180 mg/kg) a u zbylých 22 byla podaná dávka monocrotalinu nižší (36 mg/kg). Zvířata byla operována v celkové anestezii za použití mechanické ventilace. Na začátku experimentu byl u všech zvířat zaveden port katétr (Smith Medical, Minnesota, USA) cestou v. jugularis. Následně byla provedena střední laparotomie, z levého laterálního laloku jater odebrán bioptický vzorek zdravé jaterní tkáně a poté intraportálně aplikován roztok monokrotalinu (Oakwood Products, Inc., South Carolina, USA). Krystalky monokrotalinu byly rozpuštěny v roztoku 1M HCl (3–4 ml HCl na 1 g monocrotalinu) a následně rozředěny ve fosfátovém pufru (phosphate-buffered saline – PBS) v celkovém množství odpovídajícímu dosažení pH 7,4 [11,12]. U skupiny prvních pěti zvířat jsme aplikovali dávku 180 mg/kg váhy zvířete. Tato dávka byla převzata ze studií zabývajících se přípravou modelu SOS u myši [8,5]. Z důvodu předčasného úmrtí (1x první den po aplikaci, 1x druhý den po aplikaci a 2x třetí den po aplikaci) čtyři zvířata pod obrazem jaterního selhání po aplikaci této vysoké dávky byla dávka snížena. (Jedno zvíře z této skupiny zemřelo první pooperační den z důvodu chirurgických komplikací.) Monokrotalin je využíván také k přípravě modelu plicní arteriální hypertenze (PAH), a to jak u hlodavců, tak u prasat. U hlodavců je dávka potřebná k navození SOS třikrát vyšší než dávka dostatečná k navození PAH [13,14]. U prasat je popsána dávka monokrotalinu pro navození PAH 12 mg/kg [15]. Byl zachován stejný vztah mezi dávkami jako u hlodavců a pro navození SOS u následujících 22 prasat v tomto experimentu byla tedy zvolena dávka 36 mg/kg.

Po aplikaci monocrotalinu byla uzavřena laparotomie, zvířata extubována a v následujícím týdnu sledována. První tři dny po aplikaci měla zvířata úplnou restrikcii stravy z důvodu snížení příjmu dusíkatých látek a byly jim jednou denně podávány infuzní roztoky (Hartmanův roztok – 15 ml/kg, 10% roztok glukózy – 15 ml/kg). V následujících dnech došlo k postupné realimentaci. Přístup k pitné vodě byl zvířatům umožněn v průběhu celého experimentu.

7. den po aplikaci byla zvířata opět operována v celkové anestezii, byla provedena resekce levého laterálního laloku jater. Po tomto výkonu byla zvířata sledována další 2 týdny. 21. den po aplikaci monokrotalinu pak byla zvířata v celkové anestezii usmrcena a byly odebrány bioptické vzorky jater.

V průběhu experimentu byly prováděny pravidelné náběry krve cestou port katétru, a to: 1) před aplikací monocrotalinu, 2) 3. den po aplikaci monokrotalinu, 3) 7. den – před provedením jaterní resekce, 4) 7. den – ihned po resekci a 5) 7. den – 2 hodiny po resekci, dále

6) 8., 7) 10., 8) 14., 9) 17. a 10) 21. poaplikační den. Byly stanoveny tyto biochemické parametry: bilirubin, alkalická fosfatáza (ALP), gamaglutamyltransferáza (GGT), cholinesteráza (CHE), aspartátaminotransferáza (AST), alaninaminotransferáza (ALT), amoniak, urea a kreatinin.

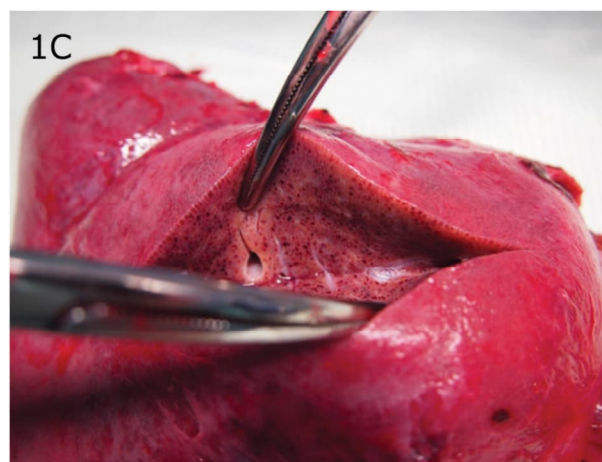
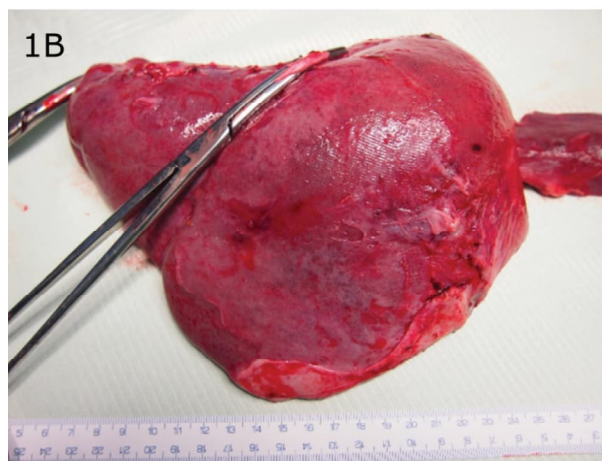
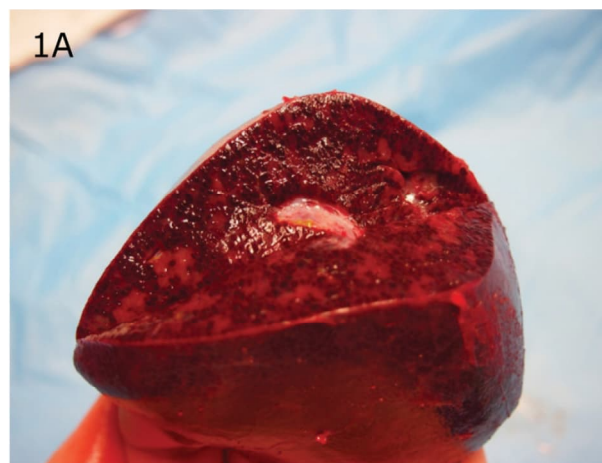
Ultrasonografická vyšetření byla provedena před aplikací monokrotalinu a 7., 10., 14., 17. a 21. den po aplikaci. Při ultrasonografických kontrolách byly sledovány změny charakteru jaterního parenchymu a případný výskyt komplikací uvedeného výkonu.

V rámci histologického vyšetření vzorků jaterní tkáň jsme porovnávali zdravý jaterní parenchym před aplikací monokrotalinu a parenchym poškozený SOS týden a 3 týdny po aplikaci monokrotalinu. U zvířat, která předčasně zahynula, jsme vyšetřili jaterní tkáň získanou při pitvě. Tkáňové bločky byly zpracovány standardní histologickou technikou parafínových řezů o síle 4 μm . Pro histologické hodnocení byly vybrány vždy dva náhodné řezy z jednoho bločku pro každou z metod barvení: hematoxylin a eosin (přehledné barvení) a anilínová modř s jádrovou červení (detekce vaziva).

Výsledky biochemického vyšetření byly převedeny do krabicových grafů. Vyhodnocení časového vývoje jednotlivých biochemických parametrů bylo provedeno porovnáním hodnot těchto parametrů v jednotlivých časových úsecích za pomoci Wilcoxonova testu. Za hladinu významnosti testu byla stanovena hodnota $p=0,05$.

VÝSLEDKY

U všech 27 prasat, kterým byl aplikován monokrotalin, jsme pozorovali známky toxického poškození jaterního parenchymu. Charakter tohoto poškození odpovídal obrazu SOS (Obr. 1). Ze skupiny prvních pěti zvířat, kterým byla aplikována dávka 180 mg/kg, uhynula všechna zvířata ještě před resekci levého laterálního laloku jater, tedy v průběhu prvního týdne po aplikaci alkaloidu (1. až 3. den po aplikaci) (Tab. 1). V jednom z případů se nejednalo o úmrtí způsobené aplikací monokrotalinu a bude vysvětleno dále. Mortalita v důsledku intoxikace v první skupině pěti zvířat s vyšším dávkováním tedy činila 80 %. Ve druhé skupině 22 prasat s nižším dávkováním došlo k úmrtí před provedením jaterní resekce ve 3 případech (6. a 7. den po aplikaci). K předčasnému úmrtí po resekci jater došlo v 8 případech (7. až 17. den po aplikaci). 11 zvířat přeživalo po celou dobu experimentu. V celém souboru zvířat jsme zaznamenali následující příčiny úmrtí. U 10 zvířat byl příčinou metabolický rozvrat v důsledku jaterního selhání vyvolaného intoxikací monokrotalinem. Ve čtyřech případech zvířata uhynula z důvodu exsanguinace do dutiny břišní při koagulopatii způsobené těžkou hepatopatií při SOS. Jedno ze zvířat uhynulo první den po aplikaci monokrotalinu kvůli strangulaci tenkého střeva při rotaci mezenteria, další zvíře pak 17. den po aplikaci pro vysoký ileus a gastrektázi způsobené adhezemi v dutině břišní. V těchto dvou případech se jednalo o komplikace samotného chirurgického výkonu, ne tedy o úmrtí způsobené intoxikací monokrotalinem.



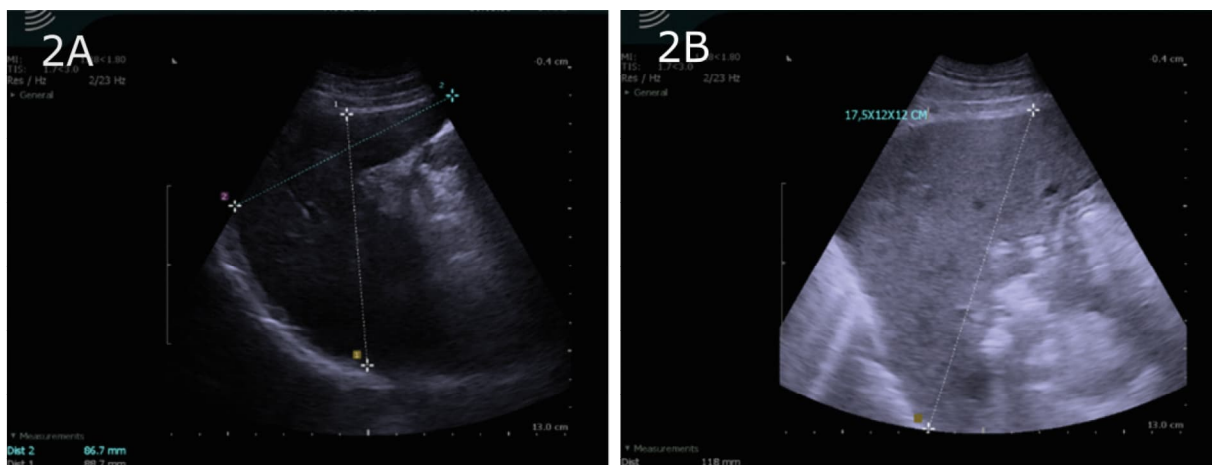
Obr. 1: A – jaterní parenchym u prasete týden po aplikaci monokrotalinu (řez), B – 3 týdny po aplikaci monokrotalinu (povrch), C – 3 týdny po aplikaci monokrotalinu (řez)
Fig. 1: A – liver parenchyma of pig one week after monocrotaline administration (section), B – three weeks after monocrotaline administration (surface), C – three weeks after monocrotaline administration (section)

USG nález

Při ultrasonografických kontrolách jsme zaznamenali vyšší echogenitu jaterního parenchymu poškozeného SOS v porovnání s parenchymem zdravým (Obr. 2).

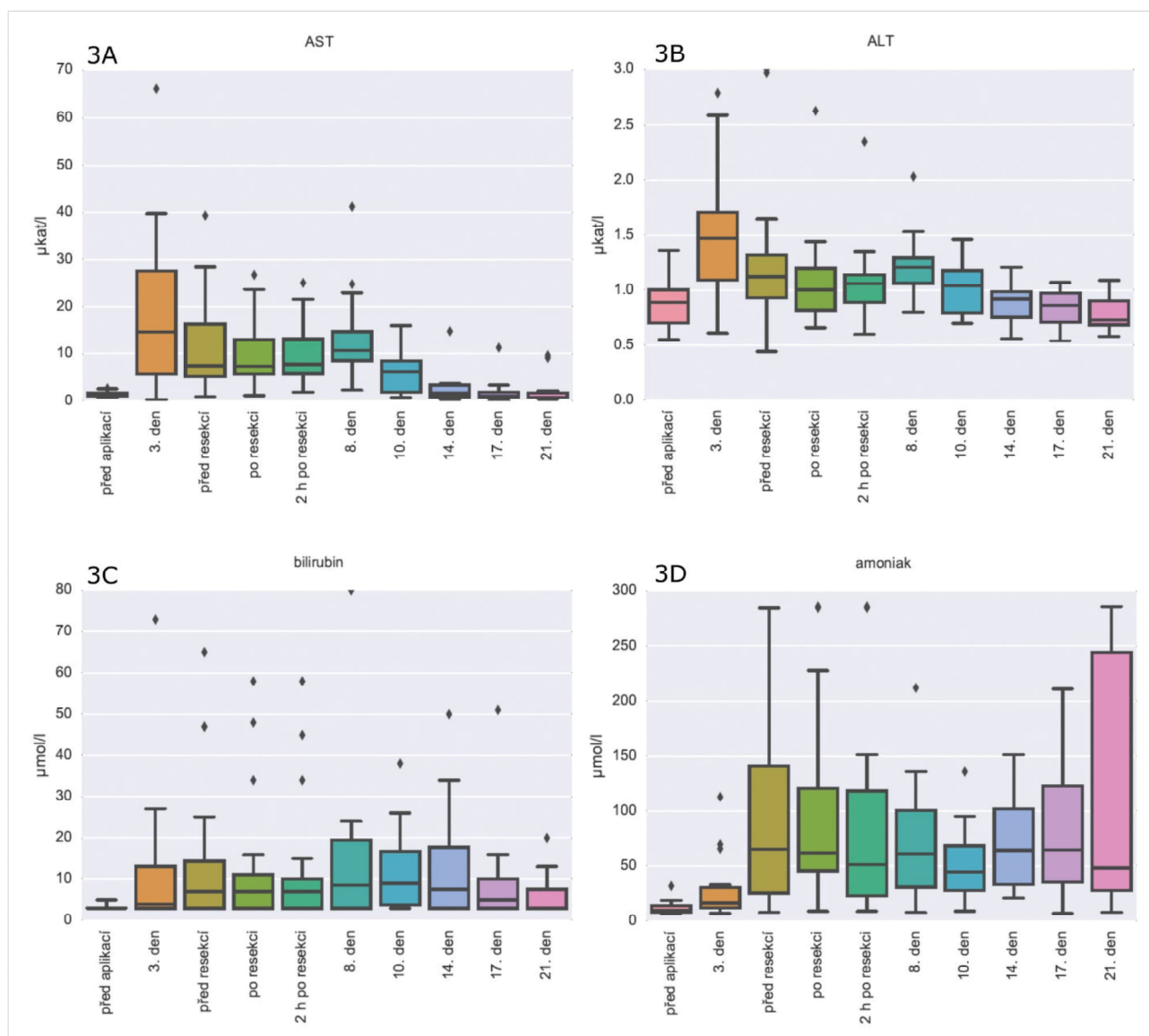
Biochemické vyšetření

Biochemické markery jaterních funkcí korelovaly s rozvojem SOS. Zaznamenali jsme peak sérové hladiny

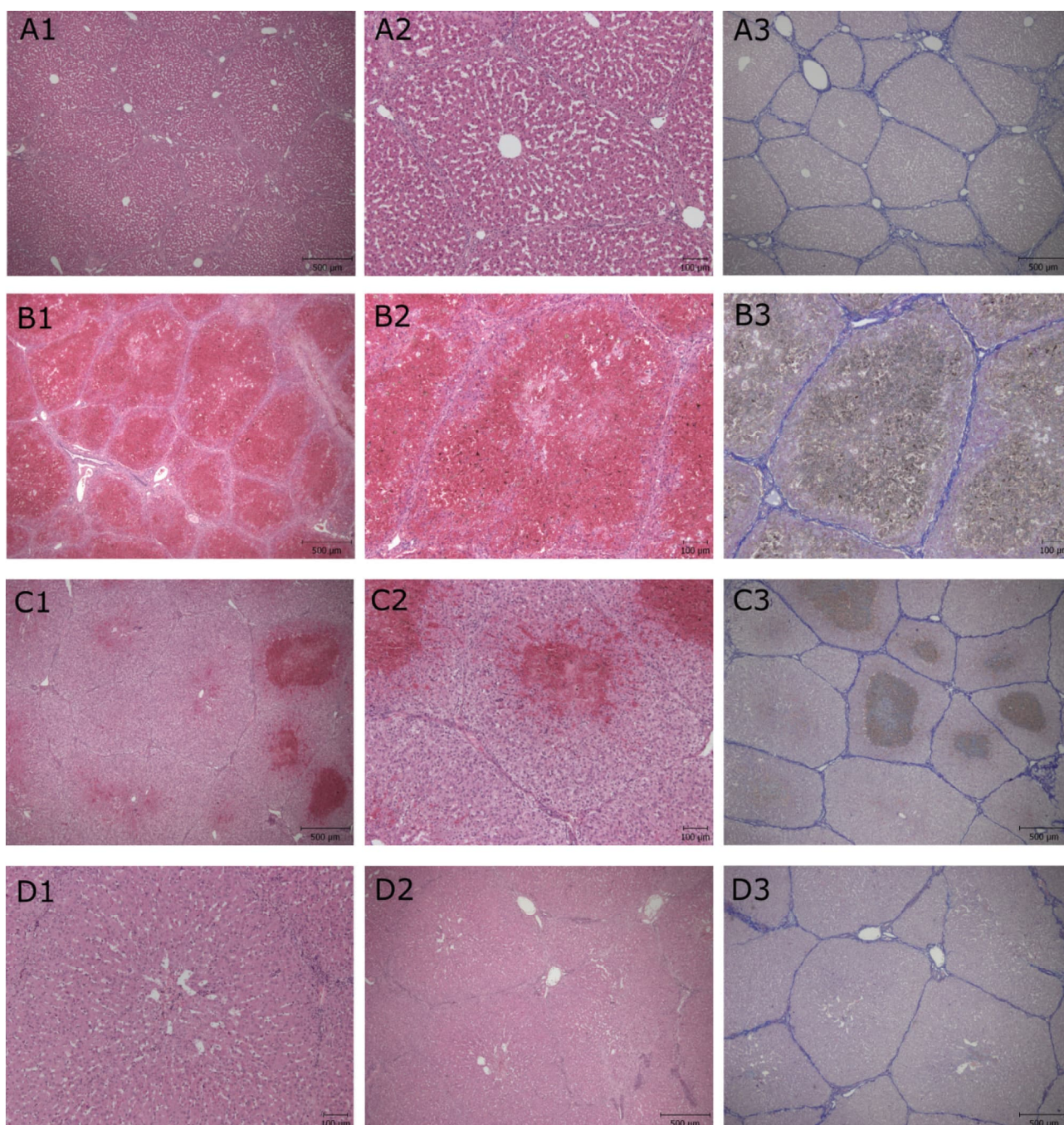


Obr. 2: A – USG nález normální echogenity zdravého jaterního parenchymu (před podáním monocrotalinu), B – zvýšená echogenita jaterního parenchymu 2 týdny po podání monocrotalinu

Fig. 2: A – ultrasound imaging of normal echogenicity of healthy liver parenchyma (before monocrotaline administration), B – higher echogenicity of liver parenchyma 2 weeks after monocrotaline administration



Obr. 3: A – vývoj sérových hladin zkoumaných biochemických parametrů: AST, B – ALT, C – bilirubinu, D – amoniaku
 Fig. 3: A – development of serum levels of the biochemical parameters studied: AST, B – ALT, C – bilirubin, D – ammonia



Obr. 4: Histologický nálezný normálního zdravého jaterního parenchymu prasete (A1,2 – hematoxylin a eosin – různá zvětšení, A3 – anilinová modř s jádrovou červení)

Charakter parenchymu u zvířat uhynulých v rozsahu 3.–7. pooplikačního dne znázorňující rozsáhlou hemoragickou nekrózu většiny objemu všech lobulů, krevní sufuze většinou znemožňují identifikovat centrální žíly (B1,2 – hematoxylin a eosin – různá zvětšení, B3 – anilinová modř s jádrovou červení). Charakter parenchymu v den provedení jaterní resekce (7. pooplikační den) zobrazuje mozaikové poškození jater, v některých lobulech hemoragickou nekrózu center lobulů, jiné lobuly jen s drobnými hemoragiemi či dilatací a překrvěním sinusoid (C1,2 – hematoxylin a eosin – různá zvětšení, C3 – anilinová modř s jádrovou červení). Charakter parenchymu při usmrcení zvířat (21. pooplikační den) s patrnými lobuly bez nekrotizace, jen s drobnými hemoragiemi, mononukleární infiltrací periportálního vaziva (D1,2 – hematoxylin a eosin – různá zvětšení, D3 – anilinová modř s jádrovou červení)

Fig. 4: Histological image of healthy porcine liver parenchyma (A1,2 - hematoxylin and eosin – different magnifications, A3 – aniline blue with nuclear fast red)

Liver parenchyma of animals which died between 3rd and 7th day after monocrotaline administration with apparent extensive hemorrhagic necrosis of almost the entire volume of most liver lobules; suffusions of blood do not enable central veins identification in most of the cases (B1,2 – hematoxylin and eosin – different magnifications, B3 – aniline blue with nuclear fast red). Liver parenchyma on the day of partial hepatectomy (7th day after monocrotaline administration) with apparent mosaic liver parenchyma damage, some of the lobules with hemorrhagic necrosis of their centers, other lobules only with minor hemorrhages or dilated hyperemic sinusoids. (C1,2 – hematoxylin and eosin – different magnifications, C3 – aniline blue with nuclear fast red). Liver parenchyma at the end of experiment (21st day after monocrotaline administration) with non-necrotic lobules, only with minor hemorrhages, mononuclear infiltration of periportal connective tissue (D1,2 – hematoxylin and eosin – different magnifications, D3 – aniline blue with nuclear fast red).

DISKUZE

Rozvoj SOS navozeného aplikací monokrotalinu cestou vena portae u prasete domácího odpovídal rozvoji SOS v případě myšího modelu [5,16]. Struktura našeho experimentu neumožňovala z důvodu použití co možná nejnižšího počtu zvířat získání bioptického vzorku jater dříve než 7. den po aplikaci monokrotalinu při provedení jaterní resekce. Tyto vzorky jsme získali pouze od předčasně uhynulých zvířat. Závažnost postižení jsme proto před samotnou resekci posuzovali pomocí biochemických parametrů. Zaznamenaný peak hladin ALT a AST třetí den po aplikaci alkaloidu odpovídá periodě 3. až 5. dne, ve které DeLeve zastihl u myšího modelu nejtěžší postižení jaterního parenchymu, dokumentované pomocí in vivo mikroskopie i histologického vyšetření [5,16]. Vzestup hladin ALT a AST po aplikaci monokrotalinu uvádí ve své studii i Srinivasan, který však myši usmrcoval již po 24 hodinách [12]. Další peak hladiny AST a ALT spolu s nárůstem hladiny bilirubinu jsme zaznamenali den po provedení jaterní resekce, stejně jako uvádí ve své studii na myších Schiffer [10]. Schiffer ovšem prováděl resekci jater již čtvrtý den po aplikaci monokrotalinu. Námi zaznamenaná elevace hladiny bilirubinu také odpovídá ostatním studiím a je jednou ze známek rozvinutého SOS [10,17]. Insuficience jaterních funkcí při SOS pak vysvětluje zvýšenou hladinu amoniaku.

Histologický obraz jaterní tkáně získané při předčasném úmrtí nebo při jaterní resekci odpovídal popisu jaterního parenchymu u myších modelů SOS [16]. Částečná regrese poškození jater, kterou jsme pozorovali na vzorcích odebraných na konci experimentu, tedy 3 týdny po aplikaci monokrotalinu, odpovídá popisovanému zlepšení stavu v ostatních studiích [3,5].

Makroskopické změny sledované při pitvě, jaterní resekci či ukončení experimentu odpovídají makroskopickému obrazu lidských jater postižených SOS [4].

Zmíněná vysoká úmrtnost u prasat, kterým byla aplikována dávka monokrotalinu 180 mg/kg, byla zaznamenána i ve studii Masabuchiho, který navozoval model SOS u křečků a při perorální dávce 180 mg/kg dosáhl téměř 100% úmrtnosti první den po aplikaci [18]. Joseph naopak ve své studii na myších používal dávku monokrotalinu 200 mg/kg, aplikovanou injekčně do sleziny a nezaznamenal vysokou úmrtnost [8]. Demonstrováné velké rozdíly v toleranci dávky monokrotalinu i mezi jednotlivými druhy hlodavců poukazují na význam etablování modelu monokrotalinem indukovaného SOS u vyššího taxonu, kde předpokládáme ještě větší mezidruhové fyziologické rozdíly.

Robinson publikoval jako první model SOS u myši indukovaný přímo oxaliplatinou slibující podobnější

patofyziologii lidskému SOS, také navozenému oxaliplatinou [19].

Byly zkoumány možnosti farmakologické prevence či terapie SOS, a to jak na zvířecích modelech, tak v humánní medicíně. Například Nakamura ve své studii popisuje použití lidského rekombinantního trombo-modulinu, který v případě myšího modelu zmírnil SOS a zvýšil přežití po resekci jater [20]. Další zkoumanou látkou je regorafenib – nízkomolekulární kinázový inhibitor, který se používá jako monoterapie metastatického kolorektálního karcinomu nebo i v kombinaci s oxaliplatinou. Účinky regorafenibu u myšího modelu SOS zkoumal Okuno a došel k podobným výsledkům jako Nakamura, tedy ke zmírnění SOS a zlepšení pooperační mortality po resekci jater [21]. Klinické studie prokázaly příznivý účinek defibrotidu, antitrombinu III, prostaglandinu E1, nízkomolekulárního heparinu a kyseliny ursodeoxycholové, vzhledem k jejich vedlejším účinkům a horší dostupnosti některých z nich však nejsou příliš využívány [20].

Poznatky z modelu na zvířeti vyššího taxonu, jako je prase domácí, mohou být snáze přeneseny do humánní medicíny. Model SOS na velkém zvířeti umožňuje hodnocení efektu chirurgické léčby, kterou vyžadují pacienti s jaterními metastázami a SOS. Dále lze tento model využít pro testování farmakologického ovlivnění samotného SOS. Význam studia SOS v experimentu umocňuje vysoké procento pacientů v současné době přeléčených chemoterapeutickými režimy obsahujícími oxaliplatinu, a tedy i potenciálních adeptů chirurgické léčby.

ZÁVĚR

Etablovali jsme model SOS na velkém zvířeti navozený aplikací monokrotalinu o dávce 36 mg/kg cestou portální žíly. Tento model může pomoci ve výzkumu terapeutického ovlivnění tohoto syndromu či posloužit jako model pro hodnocení efektu chirurgické léčby v terénu SOS. V rámci další studie na rozšířeném počtu zvířat bude potřeba hlouběji zkoumat histologické a ultrasonografické nálezy.

Tato studie byla podpořena programem UNCE/MED/006 „Centrum klinické a experimentální jaterní chirurgie“ Univerzity Karlovy a Národním programem udržitelnosti I (NPU I) č. LO1503 poskytovaným Ministerstvem školství, mládeže a tělovýchovy.

Konflikt zájmů

Autoři článku prohlašují, že nejsou v souvislosti se vznikem tohoto článku ve střetu zájmů a že tento článek nebyl publikován v žádném jiném časopise.

LITERATURA

1. Helmy A. Review article: updates in the pathogenesis and therapy of hepatic sinusoidal obstruction syndrome. *Aliment Pharmacol Ther* 2006;23:11–25.
2. Rubbia-Brandt L, Lauwers GY, Wang H, et al. Sinusoidal obstruction syndrome and nodular regenerative hyperplasia are frequent oxaliplatin-associated liver lesions and partially prevented by bevacizumab in patients with hepatic colorectal metastasis. *Histopathology* 2010;56:430–9.
3. Ito Y. A novel therapeutic strategy for liver sinusoidal obstruction syndrome. *J Gastroenterol Hepatol* 2009;24:933–4.
4. Rubbia-Brandt L. Sinusoidal obstruction syndrome. *Clin Liver Dis* 2010;14:651–68.
5. DeLeve LD, Ito Y, Bethea NW, et al. Embolization by sinusoidal lining cells obstructs

- the microcirculation in rat sinusoidal obstruction syndrome. *Am J Physiol Gastrointest Liver Physiol* 2003;284:G1045–52.
6. Conote R, Colet JM. A metabonomic evaluation of the monocrotaline-induced sinusoidal obstruction syndrome (SOS) in rats. *Toxicol Appl Pharmacol* 2014;276:147–56.
 7. Nakamura K, Hatano E, Narita M, et al. Sorafenib attenuates monocrotaline-induced sinusoidal obstruction syndrome in rats through suppression of JNK and MMP-9. *J Hepatol* 2012;57:1037–57.
 8. Joseph B, Kumaran V, Berishvili E, et al. Monocrotaline promotes transplanted cell engraftment and advances liver repopulation in rats via liver conditioning. *Hepatology* 2006;44:1411–20.
 9. Wu YM, Joseph B, Berishvili E, et al. Hepatocyte transplantation and drug-induced perturbations in liver cell compartments. *Hepatology* 2008;47:279–87.
 10. Schiffer E, Frossard JL, Rubbia-Brandt L, et al. Hepatic regeneration is decreased in a rat model of sinusoidal obstruction syndrome. *J Surg Oncol* 2009;99:439–46.
 11. Alencar KN, Pereira L, da Silva E, et al. A novel adenosine A2a receptor agonist attenuates the progression of monocrotaline-induced pulmonary hypertension in rats. *J Pulmon Res Med* 2013;54:005.
 12. Srinivasan P, Liu MY. Comparative potential therapeutic effect of sesame oil and peanut oil against acute monocrotaline (Crotalaria) poisoning in a rat model. *J Vet Intern Med* 2012;26:491–9.
 13. Zopf DA, das Neves LA, Nikula KJ, et al. C - 122, a novel antagonist of serotonin receptor 5-HT 2B, prevents monocrotaline-induced pulmonary arterial hypertension in rats. *Eur J Pharmacol* 2011;670:195–203.
 14. Chaumais MC, Ranchoux B, Montani D, et al. N-acetylcysteine improves established monocrotaline-induced pulmonary hypertension in rats. *Respir Res* 2014;15:65.
 15. Zeng GQ, Liu R, Liao HX, et al. Single intraperitoneal injection of monocrotaline as a novel large animal model of chronic pulmonary hypertension in Tibet minipigs. *PLoS One* 2013;8:e78965.
 16. DeLeve LD, McCuskey RS, Wang X, et al. Characterization of a reproducible rat model of hepatic veno-occlusive disease. *Hepatology* 1999;29:1779–29.
 17. Carreras E. How I manage sinusoidal obstruction syndrome after haematopoietic cell transplantation. *Br J Haematol* 2015;168:481–91.
 18. Masubuchi S, Komeda K, Takai S, et al. Chymase inhibition attenuates monocrotaline-induced sinusoidal obstruction syndrome in hamsters. *Curr Med Chem* 2013;20:2723–9.
 19. Robinson SM, Mann J, Vasilaki A, et al. Pathogenesis of FOLFOX induced sinusoidal obstruction syndrome in a murine chemotherapy model. *J Hepatol* 2013;59:318–26.
 20. Nakamura K, Hatano E, Miyagawa-Hayashino A, et al. Soluble thrombomodulin attenuates sinusoidal obstruction syndrome in rat through suppression of high mobility group box 1. *Liver Int* 2014;34:1473–87.
 21. Okuno M, Hatano E, Nakamura K, et al. Regorafenib suppresses sinusoidal obstruction syndrome in rats. *J Surg Res* 2015;193:693–703.

MUDr. Richard Pálek
 Chirurgická klinika, UK, LF v Plzni, FN Plzeň
 alej Svobody 80
 304 60 Plzeň
 e-mail: palekr@fnplzen.cz

10.9 Příloha IX

PÁLEK, Richard, ROSENDORF, Jáchym, MALEČKOVÁ, Anna, VIŠTEJNOVÁ, Lucie, BAJCUROVÁ, Kristýna, MÍRKA, Hynek, TÉGL, Václav, BRZOŇ, Ondřej, KUMAR, Arvind, BEDNÁŘ, Lukáš, TONAR, Zbyněk, HOŠEK, Petr, MOULISOVÁ, Vladimíra, EBERLOVÁ, Lada, TŘEŠKA, Vladislav, LIŠKA, Václav, 2020. Influence of Mesenchymal Stem Cell Administration on The Outcome of Partial Liver Resection in a Porcine Model of Sinusoidal Obstruction Syndrome. *Anticancer research*. 40(12), 6817–6833. ISSN 0250-7005. Dostupné z: <https://doi.org/10.21873/anticanres.14704>
IF_(JCR2019) = 1,994. Q4 (Oncology)

Influence of Mesenchymal Stem Cell Administration on The Outcome of Partial Liver Resection in a Porcine Model of Sinusoidal Obstruction Syndrome

RICHARD PALEK^{1,2}, JACHYM ROSENDORF^{1,2}, ANNA MALECKOVA^{2,3}, LUCIE VISTEJNOVA^{2,3}, KRISTYNA BAJCUROVA^{2,4}, HYNEK MIRKA^{2,4}, VACLAV TEGL^{2,5}, ONDREJ BRZON², ARVIND KUMAR², LUKAS BEDNAR², ZBYNEK TONAR^{2,3}, PETR HOSEK², VLADIMIRA MOULISOVA², LADA EBERLOVA^{2,6}, VLADISLAV TRESKA¹ and VACLAV LISKA^{1,2}

¹Department of Surgery, Faculty of Medicine in Pilsen, Charles University, Pilsen, Czech Republic;

²Biomedical Center, Faculty of Medicine in Pilsen, Charles University, Pilsen, Czech Republic;

³Department of Histology and Embryology,

Faculty of Medicine in Pilsen, Charles University, Pilsen, Czech Republic;

⁴Department of Medical Imaging, Faculty of Medicine in Pilsen, Charles University, Pilsen, Czech Republic;

⁵Department of Anesthesiology and Resuscitation,

Faculty of Medicine in Plzen, Charles University, Pilsen, Czech Republic;

⁶Department of Anatomy, Faculty of Medicine in Pilsen, Charles University, Pilsen, Czech Republic

Abstract. *Background:* In patients with colorectal liver metastases, the possibility for radical liver resection can be limited by oxaliplatin-induced sinusoidal obstruction syndrome (SOS). This study investigates the potential of mesenchymal stem cells (MSC) to improve the outcome of liver resections in pigs with SOS. *Materials and Methods:* SOS was induced in all animals (n=20) on day 0. Animals in the experimental group (n=8) received allogeneic MSC on day 7. Liver resection was performed in all animals on day 14 and the animals were observed until day 28. Ultrasound volumetry, biochemical analysis and histological examination of liver parenchyma was performed during the follow-up period. *Results:* Six animals from the control group died prematurely, while all animals survived in the experimental group. According to histology, biochemical analysis and ultrasound volumetry, there were no significant differences between the groups documenting the effect of MSC. *Conclusion:* Single dose allogeneic MSC administration improved survival of animals with SOS undergoing partial liver

resection. Further experiments with different timing of liver resection and MSC administration should be performed to investigate the effect of MSC in more detail.

More than 50% of patients with colorectal cancer develop liver metastases (1, 2) and the only potentially curative therapy for these patients is radical liver resection (3). However, the extent of resection is limited by the future liver remnant (FLR) volume as well as the FLR functional and regenerative capacity (2, 4, 5). The quality of liver parenchyma may be compromised by pre-existent liver diseases such as liver steatosis, cirrhosis or chemotherapy-associated hepatotoxicity (4, 6). Irinotecan is responsible for an increased risk of steatohepatitis, and oxaliplatin-based chemotherapy can cause sinusoidal obstruction syndrome (SOS) (7-9).

SOS, also known as hepatic veno-occlusive disease, is caused by toxic injury to the endothelium of liver sinusoids by certain exogenous toxins and can be a life-threatening condition (10). Typical clinical symptoms of SOS are painful hepatomegaly, jaundice, fluid retention with ascites and in severe cases even multiorgan dysfunction or failure (11, 12). SOS can present in acute, subacute or chronic forms (13). The first-identified agents of SOS were pyrrolizidine alkaloids synthesized by certain plants and even today, ingestion of herbal teas and herbal medicine preparations containing these alkaloids can be a cause of SOS (10, 14). Most often, however, SOS is reported in patients after hematopoietic stem cell transplantation (HSCT) due to preconditioning by high-dose chemotherapy or hepatic irradiation (10, 11, 15).

Correspondence to: Richard Pálek, Alej Svobody 76, 323 00 Plzen, Czech Republic. Tel: +420 722435599, e-mail: palekrichard@gmail.com and Václav Liška, Alej Svobody 76, 323 00 Plzen, Czech Republic. Tel: +420 732160287, e-mail: vena.liska@skaut.cz

Key Words: Sinusoidal obstruction syndrome, colorectal cancer, liver metastases, liver resection, mesenchymal stem cells, monocrotaline.

Experiments on rats have confirmed that SOS is a risk factor increasing morbidity and mortality after liver resection (16). A similar impact of SOS has been documented in the clinical setting. Patients with SOS had decreased long-term survival and earlier intrahepatic recurrence compared to patients without SOS. Therefore, it is apparent that the presence of SOS can have a major impact on the outcome of patients with colorectal liver metastases, and strategies to prevent or treat this disease are needed (17).

Many animal models of SOS have been established to study the pathophysiology, diagnostic markers and potential prevention or treatment of this syndrome. We have analyzed these studies in more detail in our review (18). Rat models of SOS induced by pyrrolizidine alkaloid monocrotaline helped to characterize the pathophysiology in detail (19-21). A reactive metabolite of monocrotaline binds to F-actin in sinusoidal endothelial cells (SEC) and causes its depolymerization, which results in a change of the shape of SEC and formation of gaps between them. Red blood cells, leucocytes and cellular debris then penetrate through the gaps into the space of Disse, thus causing subsequent dissection of whole sinusoidal lining and embolization of SEC with obstruction of liver sinusoids (19-21). Moreover, the F-actin depolymerization increases the expression and activity of matrix metalloproteinase-9 (MMP-9) in SEC. Increased MMP-9 activity is responsible for breakdown of the extracellular matrix in the space of Disse and facilitates the dissection of SEC (22).

De Leve *et al.* described the development of histological changes of liver parenchyma in their rat model during the first 10 days after monocrotaline administration. Based on this, they defined *early stage* changes (typically days 3-5, characterized by coagulative necrosis) and *late stage* changes (typically days 6-7, characterized by subendothelial and adventitial fibrosis) (22).

Harb *et al.* showed in an experiment with monocrotaline-induced SOS in rats that bone marrow-derived endothelial cell progenitors are able to replace SEC and central venous endothelial cells after injury (23). Furthermore, this study demonstrated the ability of monocrotaline to suppress endothelial cell progenitors in bone marrow as well as in circulation, indicating that the SOS is probably caused by 2 mechanisms, *i.e.* the toxic injury to SEC and toxic injury to bone marrow progenitors. This finding is in accordance with the fact that the most severe acute cases of SOS are caused by HSCT. High-dose chemotherapy preconditioning before HSCT involves the bone marrow as well as SEC (11).

SOS therapy is limited and includes both preventive strategies and treatment of already-present disease. Prevention is focused on consideration of patient-related or transplant-related risk factors before HSCT as well as on pharmacologic prophylaxis (24). Many agents have been tested to verify their prophylactic effect in animal and also clinical studies, but the evidence is limited and none of them has been assigned

indication criteria for clinical use (18, 25). Most of them prevent hemocoagulation and obstruction of sinusoids (*e.g.* heparine, prostaglandin E1, soluble thrombomoduline, cilostazol, *etc.*) (26-29) or inhibit MMP-9 (sesame oil, doxycycline, sorafenib, regorafenib, *etc.*) (20, 21, 30).

Some of the agents tested for their treatment effect act through the same mechanisms as pharmacologic prophylaxis (MMP-9 inhibition and anti-inflammatory effect) (31, 32) or as anticoagulants (33). However, the only treatment of SOS with approved indications in clinical medicine is defibrotide, which protects endothelial cells and causes hydrolysis of fibrin clots (34).

Harb *et al.* used bone marrow-derived endothelial cell progenitors and proposed another mechanism of potential treatment: the replacement of injured SEC by bone marrow-derived cells (23). This method probably corresponds to the mechanism by which the organism itself reverses SEC injury in normal conditions when the bone marrow is not injured. His study demonstrated a therapeutic effect of whole bone marrow administration in rats with monocrotaline-induced SOS (23). In another experiment on mice, infusion of endothelial progenitor cells successfully prevented SOS development after HSCT (35). As it was shown that the disruption of hepatic endothelial barrier during SOS facilitates transplanted cell engraftment, the principle of cell treatment sounds reasonable (36).

In this study we decided to focus on the enhancement of liver regenerative capacity in SOS and the potential treatment of this disease. According to the results of our previous studies, mesenchymal stem cells (MSC) augment liver regeneration in pigs and humans (37, 38). A promising role of MSC in the treatment of liver failure has been shown in animal experiments as well as in clinical settings (39). The aim of this study was to evaluate whether administration of MSC can improve the outcome of animals after partial liver resection in SOS. The effect of MSC administration on the course of monocrotaline-induced SOS was also evaluated.

Materials and Methods

This study was conducted under the oversight of the Ministry of Agriculture of the Czech Republic. All the procedures using animals were approved by the Commission for Work with Experimental Animals at the Charles University, Faculty of Medicine in Pilsen, and the whole study was conducted in accordance with the laws of the Czech Republic, which are compatible with the legislation of the European Union.

Experimental animal and structure of the experiment. The Prestice black-pied pig was chosen as the experimental animal. All pigs were obtained from the agriculture company Mladotice (Mladotice, Czech Republic). Both males and females were included (16 females, 5 males) aged 3-4 months, with an average weight of 34.2 kg (range=23-44 kg, median 34 kg). In all 21 animals, monocrotaline was administered to induce SOS on day 0. The animals were sorted into the experimental (n=8) and control (n=12) groups on day 7.

Animals in the experimental group received MSC intravenously on day 7. No treatment was administered to animals in the control group. All the surviving animals underwent partial liver resection on day 14 and were sacrificed on day 28. One of the animals was not included in the analysis because of its premature death during the first week of the experiment.

Premedication and general anaesthesia. All invasive procedures were performed under general anaesthesia, while blood draws and ultrasound examinations under analgesia. Intramuscular premedication before the first induction of general anaesthesia was done with 10 mg/kg of ketamine (Narkamon – Spofa, Prague, Czech Republic), 5 mg/kg azaperone (Stresnil – Janssen Pharmaceutica NV, Beerse, Belgium) and 1 mg of atropine (Atropin Biotika – Hoechst Biotika, Martin, Slovak Republic). The same mixture in lower doses (1-2 mg/kg ketamine, 0.5-1 mg/kg azaperone, 1 mg atropine) was administered intravenously *via* the ProPort system to provide analgesia during ultrasound examinations and blood draws and as premedication before the second general anaesthesia. General anaesthesia was induced and maintained by intravenous (IV) administration of propofol (1% mixture 5-10 mg/kg/h Propofol, Fresenius Kabi Norges, Halden, Norway). IV administration of fentanyl (1-2 µg/kg/h Fentanyl Torrex, Chiesi cz, Prague, Czech Republic) was used for continuous analgesia. Airways were secured by endotracheal intubation and pigs were mechanically ventilated. Physiological functions were monitored throughout the surgery. During the procedure pigs received infusions and volume substitution when needed: Hartmann's Solution (B.Braun Melsungen AG, Melsungen, Germany) and Plasmalyte (Baxter Healthcare Ltd., Compton, UK). Amoxicillin and Clavulanic acid (Augmentin 1.2 g per pig, GlaxoSmithKline Slovakia., Bratislava, Slovak Republic) were used as antibiotic prophylaxis at the beginning of the procedure; the dose was repeated after 2 hours.

SOS induction. The ProPort Plastic Venous Access System with a PolyFlow polyurethane catheter (Deltec, Smiths Medical, USA) was implanted and introduced through the jugular vein into the superior vena cava in all animals on day 0 of experiment. This venous access simplified the drug and fluid administration in the postoperative period as well as premedication and blood drawing. Subsequently, a midline minilaparotomy was performed and a biopsy from the periphery of left lateral liver lobe was taken; the portal vein was cannulated and a solution with 36 mg of monocrotaline per 1 kg of animal weight was administered over a period of 20 min. The dosage of monocrotaline was established in our previous pilot study (40). To prepare the solution of monocrotaline, the crystals of monocrotaline (Oakwood Products, Inc., SC, USA) were dissolved in 3-4 ml of 1M hydrochloric acid in a warm water bath (40°C). Sterile PBS was added in a sufficient amount to neutralize the pH (approximately 20 ml) and finally distilled water was added to decrease the osmolarity of the solution. The final volume of the solution was approximately 70 ml, depending on the absolute dose of monocrotaline. After monocrotaline administration the minilaparotomy was closed in anatomical layers, animals were extubated, recovered and each pig was placed in a separate pen. They were monitored daily to evaluate their clinical status and detect any surgical complications. During the first postoperative days the doses of granular feed were reduced but the access to water was not limited. Ten ml of Hartmann's Solution per 1 kg of animal weight, the same volume of 5% glucose (B. Braun Melsungen AG, Melsungen, Germany) and 40 mg of pantoprazole (Nolpaza KRKA Slovensko, Bratislava, Slovak Republic) was

administered daily *via* the ProPort system during the first postoperative days. Blood samples were drawn regularly according to the follow-up scheme described below.

MSC cultivation and administration. Bone marrow was harvested by aspiration from the tibia of healthy pigs, matched in age and weight with the animals included in this experiment. Following a puncture with a sterile needle, 15-25 ml of bone marrow was aspirated into a solution of 2 ml saline and 2,500 IU of heparine (Heparine – Zentiva, Prague, Czech Republic). To isolate MSCs, gradient centrifugation (440 × g, 30 min) was performed on Ficoll-Paque Plus (GE Healthcare, North Richland Hills, TX, USA). The layer of mononucleated cells was washed with phosphate buffer saline and plated on a culture flask (75 cm²; TPP, Troy, NY, USA). The culture media consisted of α-MEM cell culture media (Thermo Fisher Scientific, Waltham, MA, USA) with 10 % fetal bovine serum (Thermo Fisher Scientific), 1 mM L-glutamine (Biochrom, Cambridge, UK), 6.0 mg/ml penicillin, 10 mg/ml streptomycin (Biosera, Nuaille, France), and 0.25 mg/ml gentamicin (Biosera). The culture media were changed every other day. After 10 days, MSCs were harvested by EDTA/Trypsin 1x (Biosera) and separated into three culture flasks (75 cm²; TPP). Culture media were again changed every other day and after 10 days, MSCs were harvested by the same method and cryopreserved in liquid nitrogen (1×10⁶ cells/cryotube). MSCs were thawed 4 weeks before transplantation and plated on flasks (150 cm²; TPP) in 20 ml of the same culture media and cultured for 4 weeks to get ~50 million cells with one passage cycle, maintaining their stem cell properties. The stem cell phenotype of transplanted cells was identified by flow cytometric detection of CD90, CD73, and CD44. Differentiation ability of MSC was evaluated by their differentiation into adipo-, chondro- and osteo-genic lineages. On the day of administration, MSC were harvested as described above, counted, and re-suspended in 100 ml of physiological solution (B Braun) (37°C, 10⁶ cells/kg of pig weight) per pig. The solution was administered through the ProPort system by slow infusion (30 min) on day 7 of the experiment in all animals from the experimental group (n=8). Infusion of 5ml/kg of Hartmann's Solution and the same volume of 5% glucose followed the MSC administration. Subsequently, animals were monitored according to the follow-up scheme.

Liver resection. On day 14 of the experiment, a midline laparotomy was performed partly at the location of the previous incision but prolonged cranially and caudally, and the left lateral liver lobe was resected using electrocautery. Blood loss was minimized by the Pringle manoeuvre. The vessels and bile ducts for the left lateral liver lobe were ligated and bipolar forceps were used to eliminate bleeding from the parenchyma at the resection area. Samples of the resected left lateral liver lobe were taken and stored in 10% formaldehyde for subsequent histological examination. The laparotomy was closed, animals were extubated, recovered and monitored during a postoperative period of 2 weeks. The food restriction and intravenous administration of crystalloids followed the same scheme as post-monocrotaline administration.

Follow-up (biochemistry and ultrasound examination). Throughout the experiment, regular blood samples were taken in all animals, on day 0 before monocrotaline administration (1), day 3 (2) and day 7 (for the animals in the experimental group, blood was drawn before MSC administration) (3), day 10 (4), day 14 before (5) and right after (6) liver resection, day 14 (2 hours after liver resection) (7), day 15 (8), 17 (9), 21 (10), 24 (11) and day 28 before sacrifice (12). B-mode and

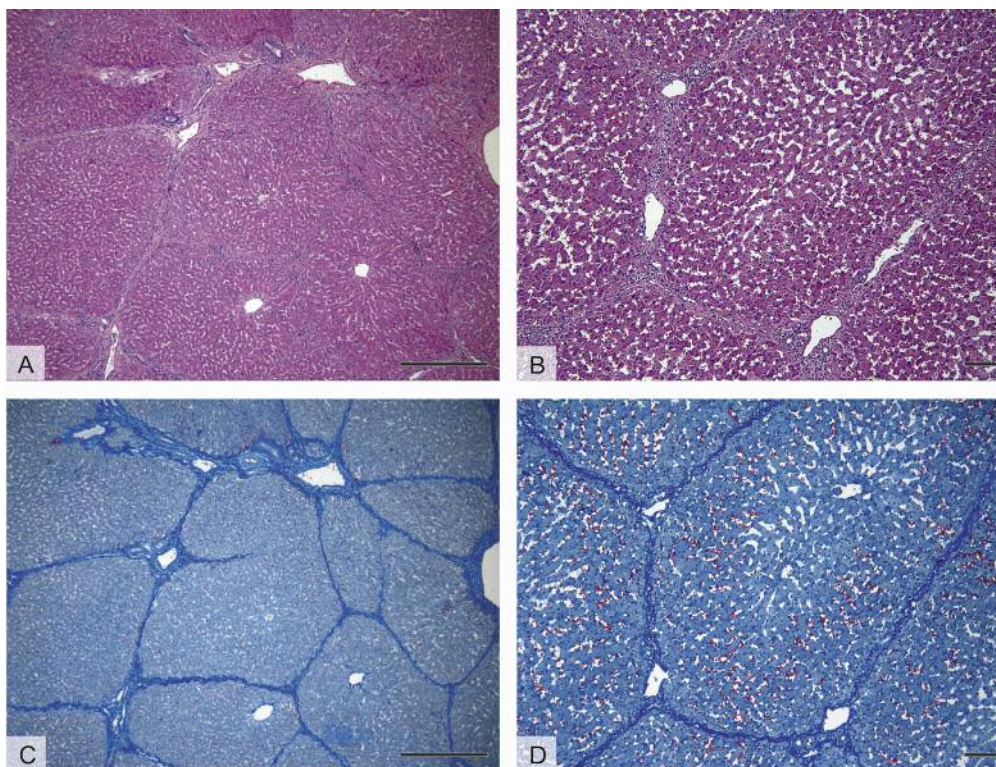


Figure 1. Examples of histological staining, healthy porcine liver. (A, B) Hematoxylin and eosin, (C, D) anilin blue with nuclear fast red used for collagenous connective tissue detection. Scale bars: A and C=500 μm , B and D=100 μm .

Doppler ultrasound examination (Ultrasound Scanner Pro Focus 2202, BK Medical, Herlev, Denmark) was regularly performed in order to assess the toxic liver injury and to follow potential regeneration after the resection. The diameter of the extrahepatic part of the portal vein, maximal blood flow velocity at this area, thickness of the gallbladder wall and liver volume were also measured. For liver volumetry, the liver was measured in B-mode in the axial, sagittal and coronal planes and the volume was calculated using an ultrasonographic formula ($\text{axial} \times \text{sagittal} \times \text{coronal}/2$) according to our previous publication (41). Ultrasound examination followed this scheme in all animals: day 0 before monocrotaline administration (1), day 7 (for animals in the experimental group, ultrasound was performed before MSC administration) (2), day 14 before (3) and after liver resection (4), day 17 (5), 21 (6), 24 (7) and day 28 before sacrifice (8). Samples of liver parenchyma for histology examination were also taken on day 28 at the end of the experiment or during autopsy, in the case of premature death. The animals were then sacrificed by intravenous administration of T 61 solution (MSD Animal Health, Kenilworth, NJ, USA) under general anaesthesia.

Histology. Liver tissue blocks were fixed with 10% formalin, embedded in paraffin wax and cut into 4 μm -thick sections using an automatic microtome (RM2255, Leica Biosystems, Germany). After dewaxing and rehydration, one randomly selected section per tissue block was stained by hematoxylin-eosin and another randomly selected section was stained with 0.5% aniline blue (Merck KGaA, Darmstadt, Germany) and nuclear fast red (Waldeck GmbH, Münster, Germany) (Figure 1).

Evaluation of histopathological changes of liver tissue was based on a semi-quantitative scoring system previously published by DeLeve *et al.* (19) and Schiffer *et al.* (42). The histopathological evaluation included a qualitative description of changes in liver architecture, namely the presence of haemorrhagic necrosis, blood congestion within sinusoids, presence of inflammatory infiltration of lobules and interlobular septa, presence of reactive fibrotic changes and presence of steatosis (Figure 2). In order to quantitatively describe the severity of liver injury, we quantified two further parameters: volume density of centrilobular haemorrhagic necrosis V_V (necrosis, liver) and volume density of viable liver parenchyma V_V (parenchyma, liver).

The V_V (necrosis, liver) and the V_V (parenchyma, liver) were quantified in 6 necrosis and 8 parenchyma microphotographs per section stained with hematoxylin and eosin, captured with 10x (the necrosis quantification), and 40x objectives (the parenchyma quantification) on an Olympus BX41 microscope (Olympus, Hamburg, Germany). Each of the photomicrographs was taken in a systematic uniform random manner. All quantitative estimates were calculated using well established stereological methods, specifically the point-counting method (43). Ellipse software (ViDiTo, Košice, Slovakia) was used for the quantification (Figure 3).

Statistical analysis. Standard frequency tables and descriptive statistics were used to characterize the sample data set. Quantitative histological parameters were evaluated using repeated measures ANOVA (with the 'Group' factor at two measurement levels of 'Time point' and their interaction). In order to isolate the differences

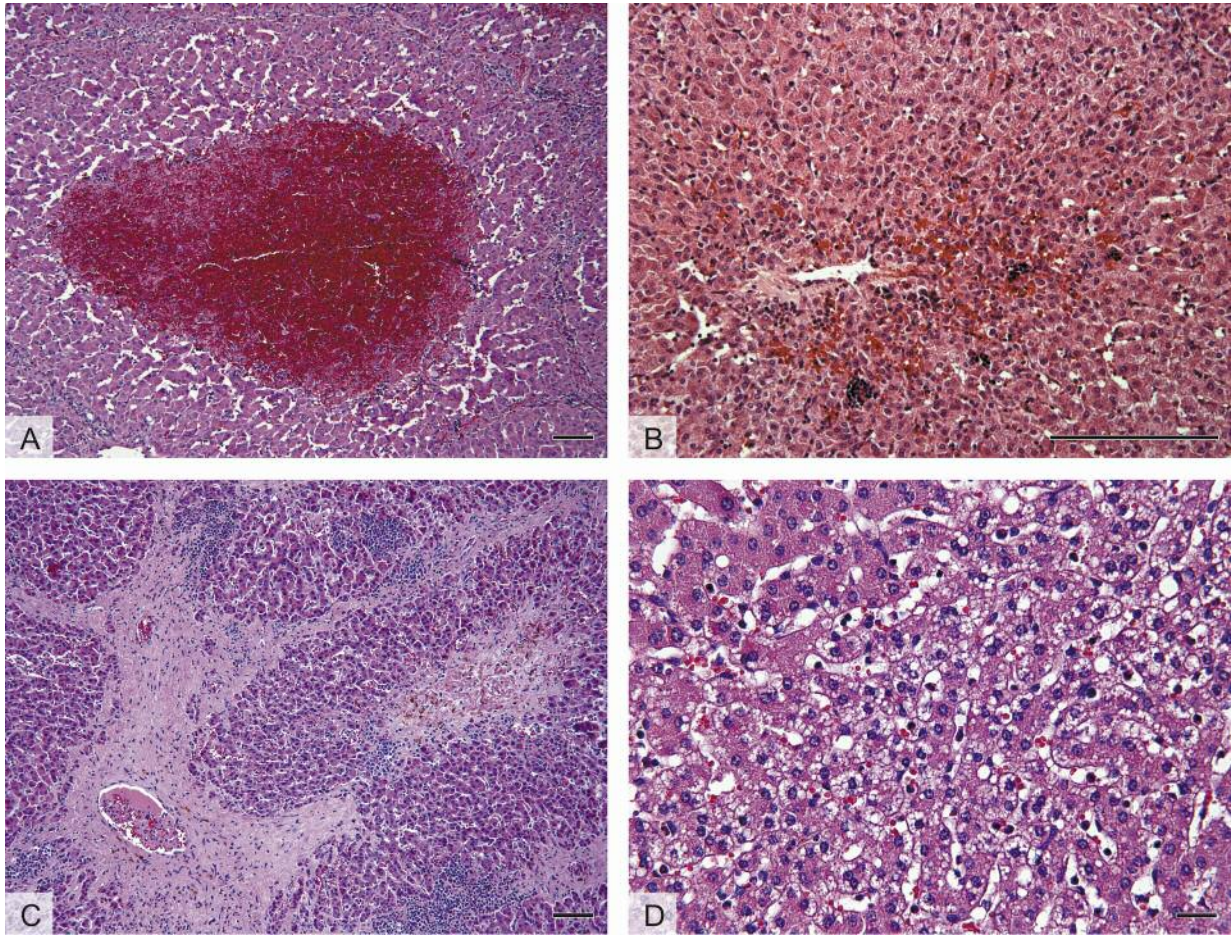


Figure 2. Histopathological changes in liver parenchyma found 14 days (A, B) and 28 days (C, D) after monocrotaline administration. (A) Centrilobular hemorrhagic necrosis in liver sample 14 days after monocrotaline administration. The necrosis represents one of the most important histopathological hallmarks of sinusoidal obstruction syndrome. (B) Congestion of blood causing dilation of hepatic sinusoids. (C) Reactive fibrotic changes that distort normal hepatic architecture. (D) Steatosis in the center of hepatic lobules. Hematoxylin and eosin, scale bars=100 μ m.

in the progression of biochemical variables and ultrasound measurements caused by the application of MSCs from the baseline values that varied randomly among the pigs, the following normalization procedure was carried out. For each variable, the average value before the point of MSC application (or non-application in the case of the control group, *i.e.* the first 3 time points for biochemistry and the first 2 time points for ultrasound measurements) was subtracted from all the subsequent variable values for each pig. These normalized values from the time points after the separation of the groups were subsequently statistically compared using two-way ANOVA (with factors of ‘Group’, ‘Time point’ and their interaction). Raw, non-normalized data from all time points were also analysed (using repeated measures ANOVA) and are also shown. Only the pigs that survived the whole duration of the experiment were included in the statistical analysis. All reported *p*-values are two-tailed and the level of statistical significance was set at $\alpha=0.05$. Statistical processing and testing were performed using the STATISTICA data analysis software (Version 12; StatSoft, Inc., Tulsa, OK, USA).

Results

Survival. Six out of the 12 pigs in the control group died prematurely during the experiment. The deaths occurred before the liver resection in 3 cases (day 10 and in two instances on day 13) and after the liver resection in 3 cases (day 22, 24 and 27). One out of the 6 deaths was not directly caused by liver parenchyma injury but by peritonitis due to fasciitis of the wound after laparotomy. This animal died on day 22. However, in this case the liver injury also undoubtedly had an impact on the overall condition of the animal. The pathological findings in the other 3 animals revealed not only liver injury but also signs of pneumonia. One animal presented with hemopericardium and because the possibility of traumatic or iatrogenic injury was ruled out, the cause was classified as coagulopathy due to the severe liver injury. Only 1 pig showed signs of liver injury without any other pathological findings.

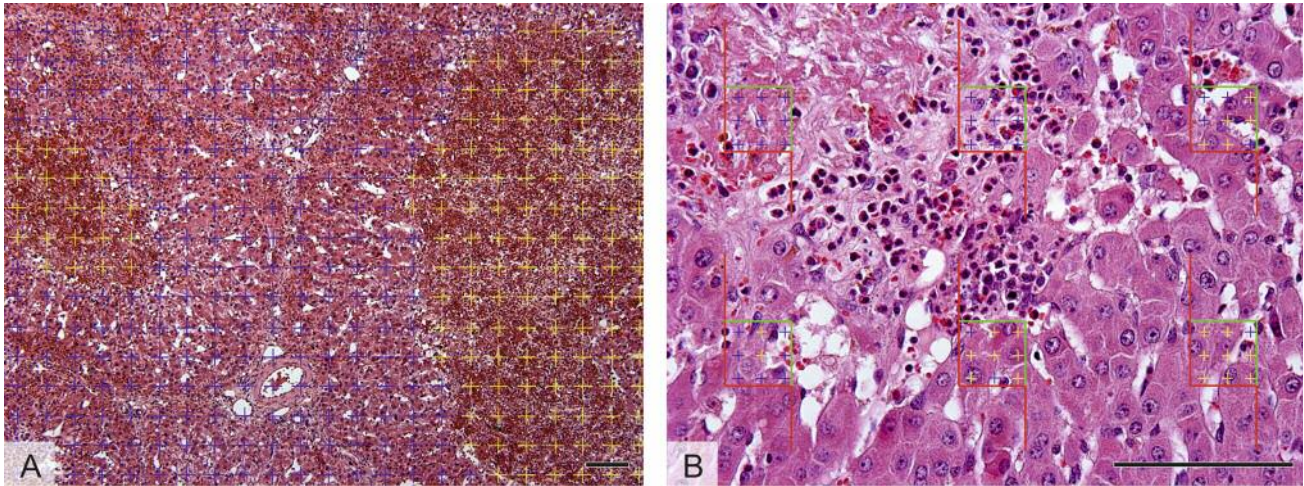


Figure 3. Quantitative analysis of volume density of centrilobular hemorrhagic necrosis V_V (necrosis, liver) and of volume density of viable liver parenchyma V_V (parenchyma, liver). (A) Stereological point grid used for quantification of hemorrhagic necrosis. Points hitting the necrosis are highlighted in yellow. (B) Stereological point grid used for quantification of viable liver parenchyma. The viable parenchyma was defined as hepatocytes organized into one cell thick plate. The hepatocytes had undamaged cytoplasmic membrane and clear, eosinophilic cytoplasm. Points hitting the viable liver parenchyma are highlighted in yellow. Scale bars=100 μm .

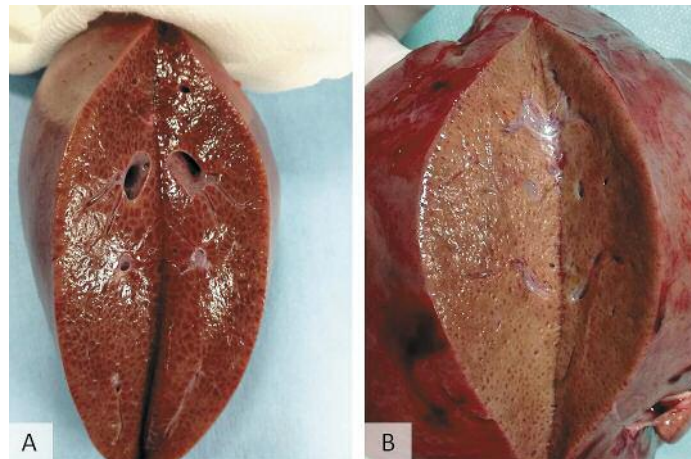


Figure 4. (A) Appearance of resected liver parenchyma on day 14. The dark lesions inside liver lobules correspond to centrilobular necrosis documented by histology. (B) Liver parenchyma at the end of experiment on day 28 when the lesions were smaller but still present.

During autopsy or liver resection, the macroscopic appearance of the liver parenchyma was altered. This is documented in Figure 4. All the animals that died prematurely were discarded from the biochemical analysis, evaluation of the ultrasonography data and from quantitative histological analysis. However, all the liver parenchyma samples underwent qualitative histological analysis.

Evaluation of MSC phenotype and differentiation ability. The stem cell phenotype of transplanted MSC was evaluated by flow cytometry. MSC were transplanted after the third

passage to ensure both minimal loss of stem cell characteristics and minimal differences between MSC groups. Transplanted MSC were positive for CD44^{POS} (99.1%), CD73^{POS} (96.2%), and CD90^{POS} (99.1%), and negative for CD45^{POS} (0.44%) (Figure 5A). The differentiation ability of transplanted MSC was evaluated by differentiation into adipo-, chondro- and osteo-genic lineages. After 21 days of differentiation, MSC were able to accumulate lipid droplets, detected by oil red staining (Figure 5C) as a marker of adipogenic lineage differentiation. They could produce glycosaminoglycans, detected by alcian blue staining (Figure

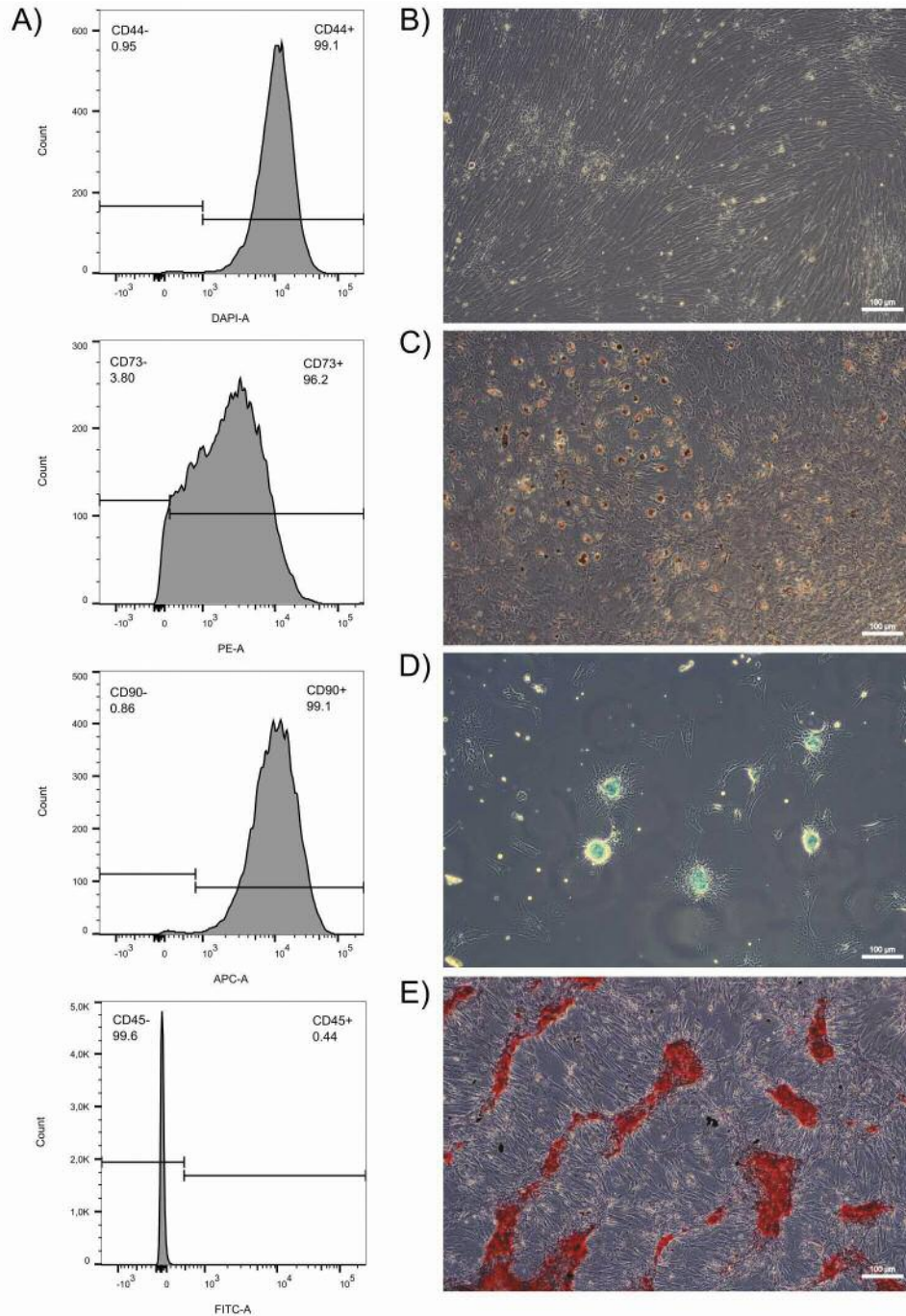


Figure 5. Evaluation of MSC phenotype by flow cytometry and examination of differentiation potential. (A) Representative histograms show that MSCs were negative for CD45 and positive for CD90, CD73 and CD44. Differentiation potential of transplanted MSCs was evaluated by their differentiation in to adipogenic (C), chondrogenic (D) and osteogenic (E) lineages, compared with untreated controls (B). Scale bars=100 μ m.

5D) as a marker of chondrogenic lineage differentiation, and deposits of calcium cations could be identified detected by alizarin red staining (Figure 5E), as a marker of osteogenic lineage differentiation (Figure 5B).

Histology. At the time of liver resection (day 14), we found extensive centrilobular haemorrhagic necrosis in most of the pigs, which is typical of SOS. In two pigs there were no signs of necrosis [one pig from the control group (pig C7) and one

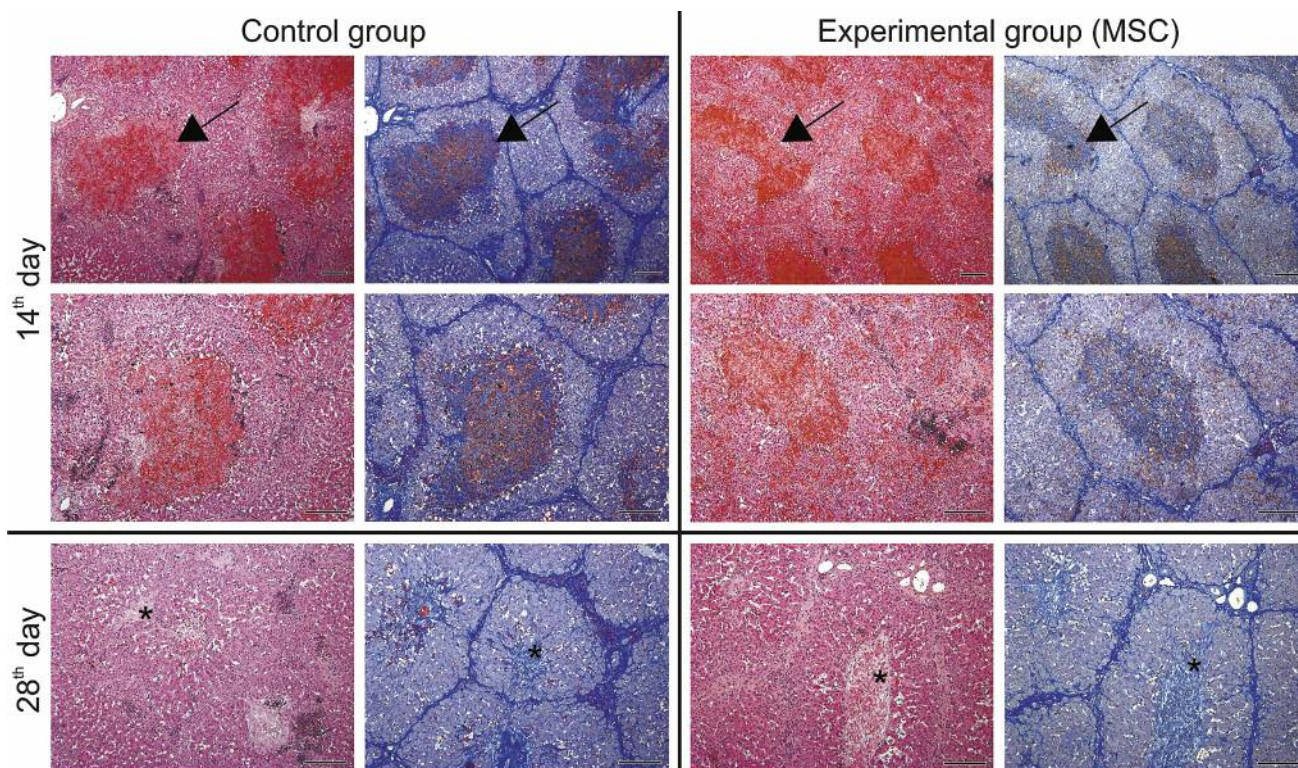


Figure 6. Comparison of liver injury in control and experimental groups 14 and 28 days after monocrotaline administration. 14 days after monocrotaline administration, the liver injury was characterized by denudation of sinusoidal lining, obstruction of the sinusoidal lumina and hemorrhage into the liver parenchyma, leading to extensive centrilobular hemorrhagic necrosis (arrows). After 28 days, the samples showed parenchymal extinction lesions with fibrotic and stenosed hepatic veins (asterisks). Control and experimental groups did not show any significant differences regarding the character and extent of liver injury. Hematoxylin and eosin (1st and 3rd column) and anilin blue with nuclear fast red (2nd and 4th column) were used for staining. Scale bars=200 μ m.

from the experimental group (pig E4)]. The liver parenchyma in these two pigs showed changes which were also observed in the other animals – denudation of SEC and obstruction of the lumen of sinusoids leading to their dilation, as well as inflammatory infiltration. Figure 6 shows the histological changes at the time of liver resection. All the results of qualitative histology for this time point are summarized in Table I.

At the end of the experiment (day 28), haemorrhagic necrosis was no longer present in the majority of animals and was replaced by centrilobular fibrotic lesions. Steatosis was found in the centre of the hepatic lobules. Figure 6 shows the histological findings and Table II the qualitative results.

The most severe change, nodular transformation of the parenchyma, occurred in two animals from the control group that did not survive the experiment. The overview of the liver histology of the animals with premature death is summarized in Table III. The quantitative analyses did not show significant differences in the volume density of haemorrhagic necrosis and viable liver parenchyma between the experimental and control group at the time of liver resection or at the end of the experiment (Figure 7, for more details see Table IV). The

morphology of liver injury was comparable in both groups for both time points. The viable liver parenchyma was chosen as a marker for evaluation of the functional capacity of the liver because the volume of parenchyma was influenced not only by the extent of necrosis but by reactive fibrotic changes, dilation of hepatic sinusoids and by inflammatory infiltration as well.

Biochemistry. The observed levels of biochemical markers of liver and renal functions correspond to severe toxic liver injury (Figure 8). Elevation of aspartate aminotransferase (AST), alanine aminotransferase (ALT), bilirubin and ammonium were observed in both groups. The first peak was observed after monocrotaline administration and the second peak after liver resection. The level of AST returned to the normal range by the end of the experiment. The level of ALT also dropped during the last week of follow-up and was even lower than the initial value, but still within the normal range. The level of ammonium and bilirubin remained elevated until the end of experiment. The level of urea dropped during the first three days after monocrotaline administration and elevation was observed one day after liver resection.

Table I. Overview of qualitative histological findings at the time of liver resection (day 14). E, Animals from the experimental group; C, animals from the control group.

	Control group				Experimental group			
	Animal	Hemorrhagic necrosis	Inflammatory infiltration	Other findings	Animal	Hemorrhagic necrosis	Inflammatory infiltration	Other findings
Liver resection	C1	Yes	Yes	Steatosis in centre of lobules	E1	Yes	Yes	
	C5	Yes	No		E2	Yes	Yes	
	C7	No	Yes	Without hemorrhagic necroses, almost normal appearance of liver parenchyma	E3	Yes	No	
	C10	Yes	Yes		E4	No	Yes	Without hemorrhagic necroses, dilated sinusoids
	C11	Yes	Yes		Small centrilobular hemorrhagic necroses	E5	Yes	Yes
	C12	Yes	Yes	E6		Yes	Yes	Severe inflammation Severe inflammation
				E7	Yes	Yes		
				E8	Yes	Yes		

Table II. Overview of qualitative histological findings at the end of the experiment (day 28). Animals from the experimental group are labeled E, animals from the control group are labeled C.

	Control group					Experimental group				
	Animal	Hemorrhagic necrosis	Inflammatory infiltration	Fibrotic centrilobular reactive lesions	Other findings	Animal	Hemorrhagic necrosis	Inflammatory infiltration	Fibrotic centrilobular reactive lesions	Other findings
End of experiment	C1	No	Yes	Yes	Severe inflammation Almost normal appearance of liver parenchyma	E1	No	Yes	Yes	Steatosis
	C5	No	Yes	Yes		E2	No	Yes	Yes	
	C7	No	No	No		E3	No	Yes	Yes	
	C10	Yes (minimally)	Yes	Yes	Severe inflammation	E4	No	Yes	Yes	Severe inflammation
	C11	Yes	Yes	Yes		Severe inflammation	E5	No	Yes	
	C12	No	Yes	Yes	E6		No	Yes	Yes	Steatosis
					E7	No	Yes	Yes		
					E8	Yes	Yes	No	Centres of lobules with bleeding surrounded by fibrotic tissue	

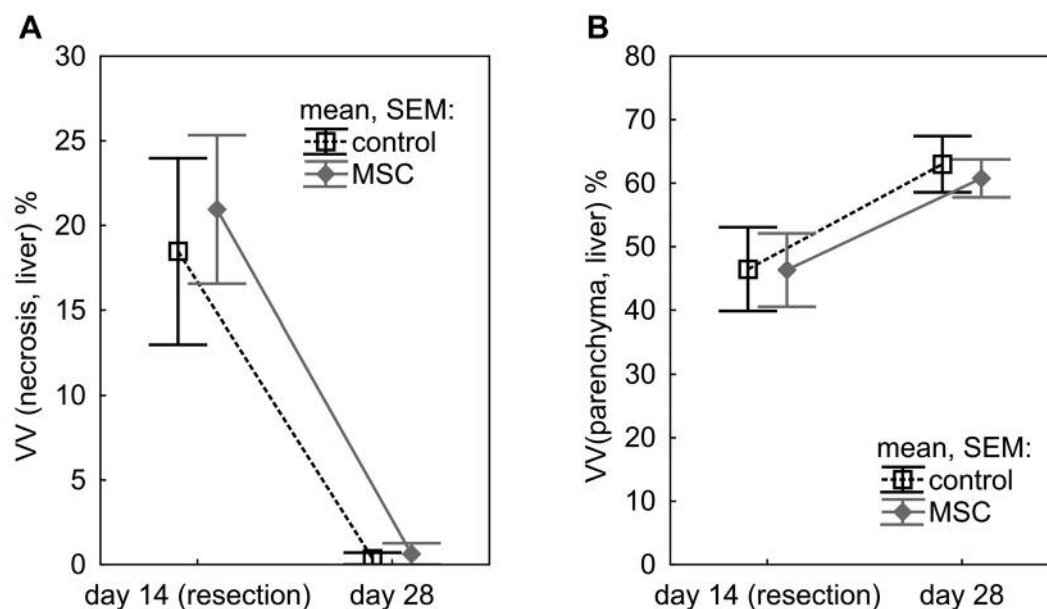


Figure 7. Results of quantitative histological analysis in the experimental (MSC) and control group (control). Neither the volume density of necrosis (A) nor the density of viable parenchyma (B) differed between experimental (MSC) and control groups. The volume density of necrosis was smaller at day 28 than at day 14 (resection). The volume density of viable parenchyma was greater at day 28 than at day 14 (resection). Repeated measures ANOVA was used for quantitative histological analysis.

Table III. Histological findings in samples of liver parenchyma taken during autopsy in animals that died prematurely.

Animal	Sample taken	Death during the experiment		Other findings
		Hemorrhagic necrosis	Inflammatory infiltration	
C2	Death (Day 10)	Yes	Yes	
C3	Resection	Yes	Yes	
C4	Death (Day 24)	No	Yes	Almost normal appearance of liver parenchyma
C6	Death (Day 13)	Yes	No	
C6	Resection	Yes	Yes	
C8	Death (Day 22)	Yes	Yes	Nodular transformation of liver parenchyma, sporadic centrilobular necroses
C8	Resection	Yes	Yes	
C9	Death (Day 27)	Yes	Yes	Nodular transformation of liver parenchyma, sporadic centrilobular necroses
C9	Death (Day 13)	Yes	Yes	

To compare the levels of biochemical markers in the two groups the values were normalized according to the average value before day 7. The comparison of the course of biochemical markers after the day of administration of MSC seemed to be more accurate than comparison of absolute values. However, the analysis of the results for the whole period of follow up without any data normalization was also performed.

The level of ALT and creatinine was significantly higher in the control group during the period after day 7 ($p=0.001$ for both markers). In contrast, the level of bilirubin and ammonium was significantly higher in the experimental group

during the same time period ($p=0.040$ and 0.0001 , respectively). The values of the other markers were comparable between the experimental and the control group.

The analysis for the whole follow-up period did not show any significant differences in biochemical markers between the two groups.

Ultrasound. For the ultrasonography analysis the same data normalization was performed and the groups were compared for the period after day 7. There was no significant difference in the diameter of portal vein or in the blood flow velocity in the

Table IV. Results of quantitative histological analysis of samples taken at the time of liver resection and at the end of the experiment. Volume density of necrosis - V_V (necrosis, liver). Volume density of viable liver parenchyma - V_V (parenchyma, liver).

	Control group			Experimental group		
	Animal	V_V (necrosis, liver) %	V_V (parenchyma, liver) %	Animal	V_V (necrosis, liver) %	V_V (parenchyma, liver) %
Liver resection	C1	30.0	29.2	E1	23.3	49.3
	C5	22.8	46.1	E2	38.2	27.8
	C7	0.3	73.1	E3	23.7	45.6
	C10	20.0	35.4	E4	0.0	77.5
	C11	4.5	56.7	E5	19.4	40.7
	C12	33.4	38.2	E6	17.7	45.6
				E7	10.2	57.4
				E8	35.2	26.6
End of experiment	C1	0.0	47.5	E1	0.0	72.7
	C5	0.0	61.6	E2	0.0	60.6
	C7	0.0	74.5	E3	0.0	50.0
	C10	0.0	76.2	E4	0.0	67.8
	C11	2.1	60.9	E5	0.0	63.4
	C12	0.0	57.4	E6	0.0	47.9
				E7	0.0	64.8
				E8	5.0	58.8

portal vein during the follow-up period between the different groups (Figure 9A, B). The time course of these parameters was not significantly influenced by the SOS induction and by the liver resection. The diameter of the gallbladder wall had a significant tendency to increase throughout the follow-up period ($p=0.004$) and did not differ between the groups (Figure 9C). The volume of liver parenchyma increased during the first week after the monocrotaline administration and dropped after day 7 and after the liver resection (Figure 9D). A smaller increase in liver volume occurred during the first days after the resection and was followed by another period of volume loss. For the period after day 7, the relative liver volume was significantly higher in the control group ($p=0.023$). The ultrasonography detected hyperechogenicity of the liver parenchyma in all animals after day 7 compared to normal echogenicity on day 0. In some animals, reversed flow in the portal vein was observed on day 7 onwards.

Discussion

The study aimed to assess the potential of MSC administration to enhance liver regeneration in SOS and/or its potential to attenuate it. The SOS was induced by intraportal monocrotaline administration in pigs which were then divided into two groups. One of the groups was treated with one intravenous dose of MSC one week after monocrotaline administration, while the second group was a control without any treatment. The survival of animals, levels of biochemical markers,

ultrasonography data and histology of liver parenchyma were compared between the groups to verify the severity of SOS and thus the treatment effect. The capability of liver regeneration after partial liver resection in animals with SOS was also compared to evaluate the effect of MSC.

Induction of SOS. Data from biochemistry, histology and ultrasonography show that SOS was successfully induced in pigs by intraportal monocrotaline administration in a single dose of 36 mg monocrotaline per 1 kg of body weight.

Hepatomegaly and hyperbilirubinemia are mentioned in all diagnostic criteria for SOS used in clinical medicine (44). In this study, the animals showed an increase of liver volume and elevation of bilirubin in the first days after monocrotaline administration. Liver enzymes are also usually elevated in patients with SOS, which corresponds with the finding of elevated AST and ALT during the first days after SOS induction in this study (13, 44). The decrease in the level of urea after monocrotaline administration can correspond with attenuation of liver functions (45, 46). The induction of SOS was also confirmed by histological findings. The denudation of SEC, obstruction of the lumen of sinusoids and hemorrhagic necrosis observed in this study correspond to changes described in rodent models of SOS and in humans (19, 47, 48).

Ultrasonography helped to not only to detect hepatomegaly but also revealed a changed echogenicity of the liver parenchyma, altered flow in the portal vein and increasing

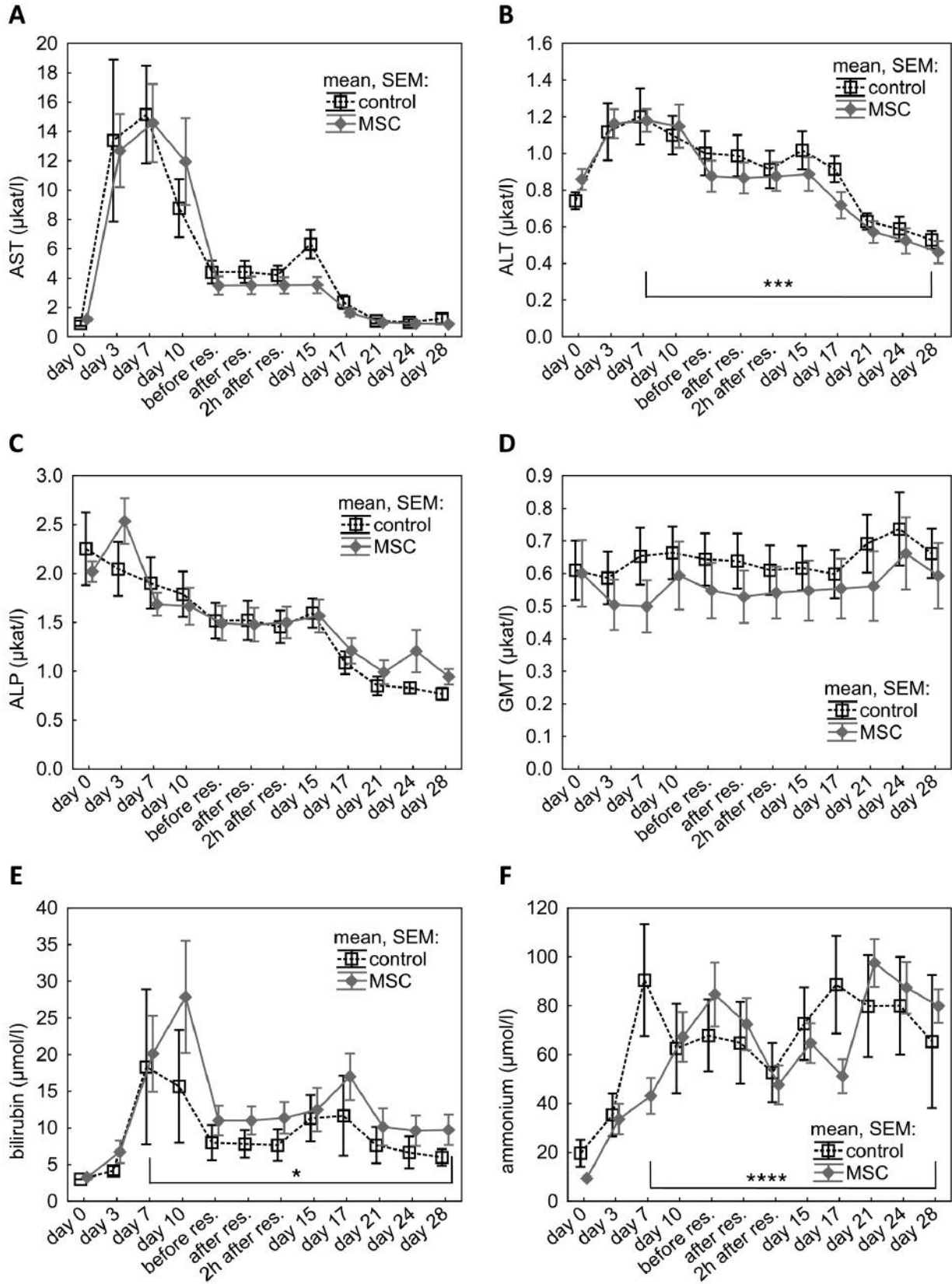


Figure 8. Continued

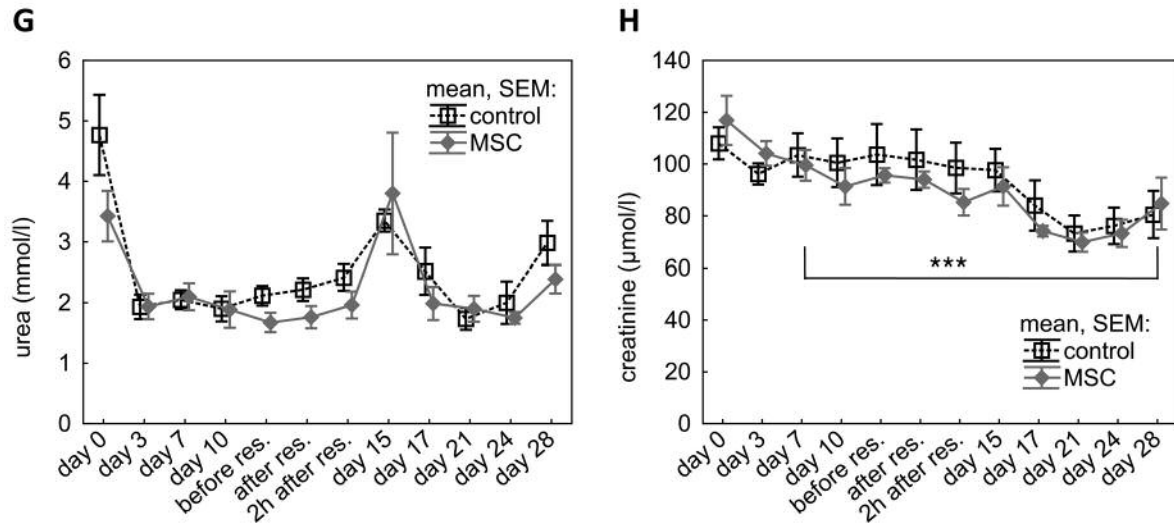


Figure 8. Results of biochemical analysis in the experimental (MSC) and control group (control) throughout the experiment. Significant differences between the groups were observed in the levels of ALT (B) and creatinine (H) (higher in control group after day 7) and in the levels of bilirubin (E) and ammonium (F) (higher in experimental group after day 7). The other markers did not show any significant differences. Two-way ANOVA was used for biochemical analysis after data normalization which is described in methods. The figure shows data before normalization. * $p \leq 0.05$, *** $p \leq 0.001$, **** $p \leq 0.0001$.

thickness of the gallbladder wall. Imaging methods such as ultrasonography, computed tomography and magnetic resonance imaging are now starting to be used for the diagnosis of SOS in clinical medicine (44). The thickening of the gallbladder wall is a typical finding in patients with SOS (14, 49, 50), and retrograde flow in the portal vein is also mentioned (51). According to our results, ultrasonography seems to be a suitable method to help confirm the diagnosis of SOS in large animal models.

Finally, the macroscopic appearance of the liver parenchyma 2 weeks after monocrotaline administration (or earlier in case of premature death) with apparent hemorrhagic necrosis also supports the diagnosis of SOS. It is important to mention that two animals showed only minimal alterations in the levels of biochemical markers and negligible histological changes of liver parenchyma compared to the other pigs. Because one of these animals was from the experimental and one from control group, we decided not to exclude these animals with less severe injury.

Evaluation of the effect of MSC. Data from the control and experimental groups were compared to verify the effect of MSC administration on the course of SOS and on liver regeneration after resection in animals with SOS.

To avoid the confounding effect of potentially different values between the groups before day 7, we decided to focus on the course of biochemical markers after the day of treatment. The same step was taken in evaluation of ultrasonography data to control for differences in body weight.

According to the biochemical analysis, the experimental group had significantly higher levels of bilirubin and ammonium compared to the control group; in contrast, ALT and creatinine were higher. In this experimental setting the level of bilirubin and ammonium reflects liver function (13, 52). ALT indicates injury of hepatocytes and the elevation of creatinine levels is a mark of worse overall status of the animal and can suggest development of hepatorenal syndrome (57, 58). This suggests deteriorating liver functions in animals from the experimental group compared to the surviving animals from the control group. It is important to mention that in the latter, 5 animals with the most severe liver injury died prematurely due to liver failure and were not included in the statistical analysis. In contrast, all animals survived in the experimental group. Therefore, for the statistical evaluation, the animals with most severe liver injury from the experimental group were included. This suggests a positive effect of MSC administration. However, the effect was limited, as the data show significantly better survival in the experimental group but not improved liver function and histological parameters.

MSC have been used in several animal experiments to verify their ability to treat liver failure of different etiologies. They have been shown to have a positive effect on acute liver injuries in rodents. The bone marrow derived MSC acted through reduction of fibrosis and improvement of immunoregulatory mechanisms (55, 56). We assume that these mechanisms probably do not play a dominant role in the early phase of SOS, which may explain the limited effect of MSC administration in our study.

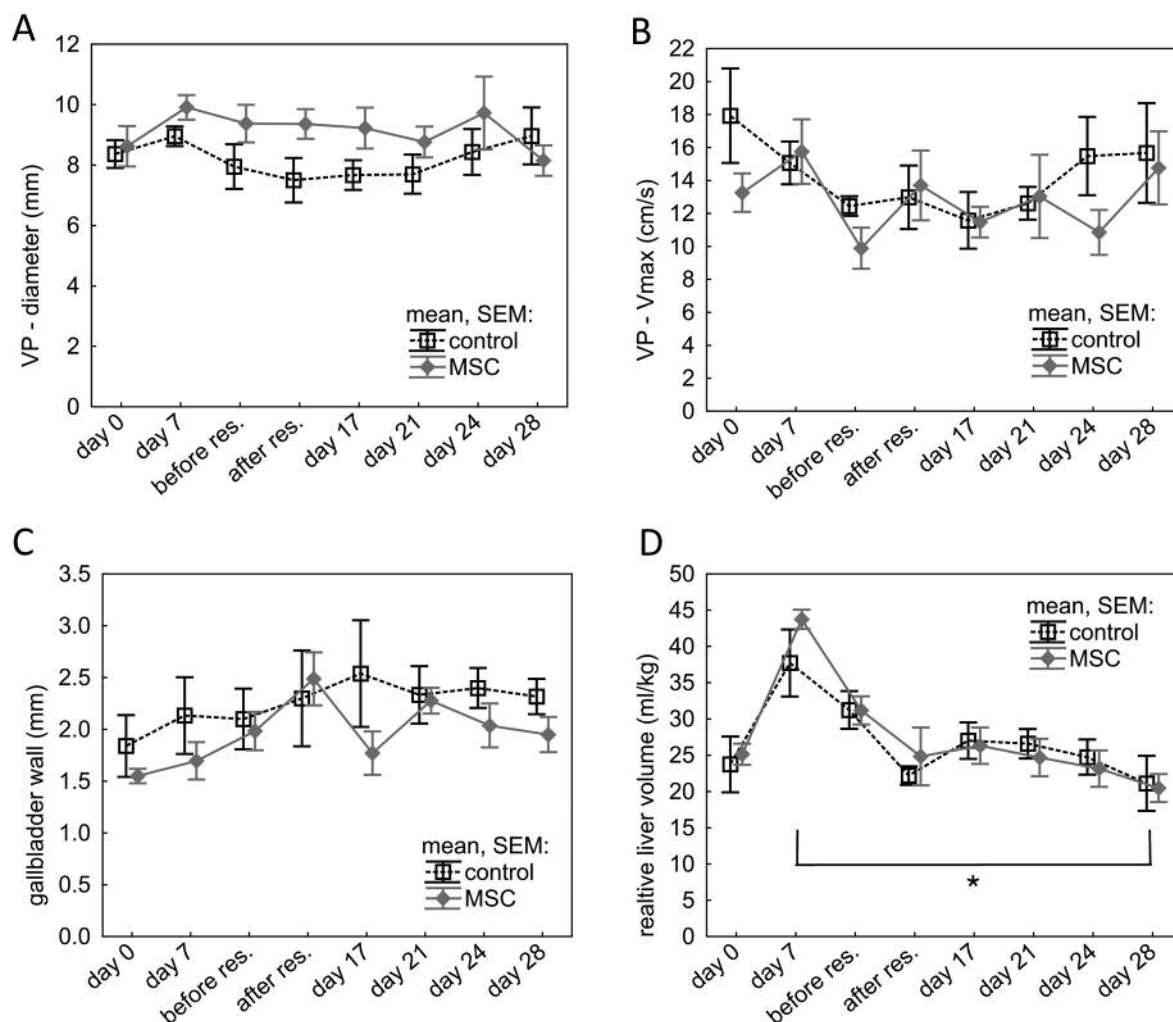


Figure 9. Results of the ultrasound examination in the experimental (MSC) and control group (control). VP stands for portal vein (A), VP – Vmax stands for maximal blood flow velocity in the extrahepatic part of the portal vein (B). The only significant difference was observed in the relative liver volume which was higher in the control group after day 7 (D). Two-way ANOVA was used for evaluation of ultrasound examination after data normalization which is described in methods. The figure shows data before normalization. * $p \leq 0.05$.

Moreover, the antifibrotic effect of MSC is probably caused by induction of MMP-9 expression (57). As increased MMP-9 activity plays a role in the pathogenesis of SOS, it is possible that the MSCs could also have a partially negative effect on the course of SOS, at least in the early phases of the disease.

Because liver fibrosis and inflammatory infiltration was apparent in later phases, it is possible that MSC administration later than day 7 would have a major effect.

However, we also chose this treatment timing according to other functions of MSCs. MSCs are able to reduce hepatocyte apoptosis and promote hepatocyte proliferation. Cytokines and growth factors (e.g. epidermal growth factor) secreted by MSC are responsible for this effect (58). The idea was to attenuate liver failure by promotion of liver regeneration and therefore enable the animals to undergo

liver resection with a better outcome. That is why day 7 was chosen as the most appropriate for MSC administration.

The ability of MSC to alleviate liver failure after resection by promotion of regeneration was confirmed by Ding *et al.* (59). They found improved survival after 90% hepatectomy in rats with a healthy liver after MSC administration via portal vein. They also observed a major increase in liver volume after MSC administration. The impact on survival of animals is in accordance with our results. However, the liver volume results are opposite to those in our experiment. In our study, ultrasonography showed smaller liver volume in MSC-treated animals. This finding cannot be simply explained as attenuated liver regeneration because animals in our study did not have a healthy liver parenchyma. In studies of resection of healthy liver parenchyma, the subsequent regeneration of liver functions

correlates with increasing liver volume (60). This relationship is not present in cases of acute SOS where the liver volume is increasing because of developing hepatomegaly while liver functions are decreasing (11). The liver volume after resection in this experiment was undoubtedly influenced by decreasing hepatomegaly. The liver volume increased only over the first three days after resection and then decreased until the end of the follow-up. The gradual remission of hepatomegaly started after day 7 and was not completed before the liver resection. The smaller liver volume in the experimental group therefore does not have a clear interpretation and can be even a sign of earlier remission of acute SOS in MSC-treated animals.

A model of the chronic or subacute type of SOS would be more accurate for correlation with clinical patients who develop SOS during chemotherapy and require liver resection because of liver metastases. Therefore, further experiments with liver resection postponed to later phases of monocrotaline-induced SOS should be performed to verify the effect of MSCs. In such an experimental setting, repeated administration of MSCs with the second dose at the time of resection would be informative. MSCs are usually administered right after liver resection, which enables them to act more effectively and support liver regeneration (59).

Conclusion

SOS was successfully induced in the pig by intraportal monocrotaline administration. Biochemical analysis, histological findings and ultrasonography confirmed the development of SOS. Intravenous administration of allogeneic MSC one week after induction of SOS improved animal survival. The liver volume after partial resection has to be evaluated with consideration of the hepatomegaly induced by acute SOS. Further experiments with different timing of liver resection and MSC administration should be performed to verify the positive effect of MSC.

Conflicts of Interest

None to be declared.

Authors' Contributions

Study conception and design: RP, VL, AM, LV; Acquisition of data: RP, JR, KB, HM, ZT, OB, AK, LB, VT; Analysis and interpretation of data: RP, VL, AM, PH, LV; Drafting of manuscript: RP, VL, AM, LV; Critical revision of manuscript: VL, PH, VT, VM, LE. All Authors read and approved the final manuscript.

Acknowledgements

The project was supported by the "Centre of clinical and experimental liver surgery" (grant UNCE/MED/006); from the European Regional Development Fund-Project "Application of

Modern Technologies in Medicine and Industry" (No. CZ.02.1.01/0.0/0.0/17_048/0007280); by the Research Fund Progress (grant Q39) and by a grant from Charles University, GA UK (462520). The Authors would like to thank to Dr. Sarah Leupen, Ph.D. for her sensitive and concise language proofreading.

References

- 1 Chakedis J, Squires MH, Beal EW, Hughes T, Lewis H, Paredes A, Al-Mansour M, Sun S, Cloyd JM and Pawlik TM: Update on current problems in colorectal liver metastasis. *Curr Probl Surg* 54: 554-602, 2017. PMID: 29198365. DOI: 10.1067/j.cpsurg.2017.10.002
- 2 Xu F, Tang B, Jin T-Q and Dai C-L: Current status of surgical treatment of colorectal liver metastases. *World J Clin cases* 6: 716-734, 2018. PMID: 30510936. DOI: 10.12998/wjcc.v6.i14.716
- 3 Ito K, Govindarajan A, Ito H and Fong Y: Surgical treatment of hepatic colorectal metastasis: evolving role in the setting of improving systemic therapies and ablative treatments in the 21st century. *Cancer J* 16: 103-110, 2010. PMID: 20404606. DOI: 10.1097/PPO.0b013e3181d7e8e5
- 4 van den Broek MAJ, Olde Damink SWM, Dejong CHC, Lang H, Malago M, Jalan R and Saner FH: Liver failure after partial hepatic resection: definition, pathophysiology, risk factors and treatment. *Liver Int* 28: 767-780, 2008. PMID: 18647141. DOI: 10.1111/j.1478-3231.2008.01777.x
- 5 Cieslak KP, Bennink RJ, de Graaf W, van Lienden KP, Besselink MG, Busch ORC, Gouma DJ and van Gulik TM: Measurement of liver function using hepatobiliary scintigraphy improves risk assessment in patients undergoing major liver resection. *HPB (Oxford)* 18: 773-780, 2016. PMID: 27593595. DOI: 10.1016/j.hpb.2016.06.006
- 6 de Meijer VE, Kalish BT, Puder M and Ijzermans JNM: Systematic review and meta-analysis of steatosis as a risk factor in major hepatic resection. *Br J Surg* 97: 1331-1339, 2010. PMID: 20641066. DOI: 10.1002/bjs.7194
- 7 Rubbia-Brandt L, Mentha G and Terris B: Sinusoidal obstruction syndrome is a major feature of hepatic lesions associated with oxaliplatin neoadjuvant chemotherapy for liver colorectal metastases. *J Am Coll Surg* 202: 199-200, 2006. PMID: 16377516. DOI: 10.1016/j.jamcollsurg.2005.09.010
- 8 Fong Y and Bentrem DJ: CASH (chemotherapy-associated steatohepatitis) costs. *Ann Surg* 243: 8-9, 2006. PMID: 16371729. DOI: 10.1097/01.sla.0000193599.57858.9b
- 9 Limaïem F and Bouraoui S: Chemotherapy-induced liver injury in metastatic colorectal cancer: About 48 cases. *Pan Afr Med J* 30: 1-8, 2018. PMID: 30455827. DOI: 10.11604/pamj.2018.30.198.15548.
- 10 Valla D-C and Cazals-Hatem D: Sinusoidal obstruction syndrome. *Clin Res Hepatol Gastroenterol* 40: 378-385, 2016. PMID: 27038846. DOI: 10.1016/j.clinre.2016.01.006
- 11 Coppell JA, Richardson PG, Soiffer R, Martin PL, Kernan NA, Chen A, Guinan E, Vogelsang G, Krishnan A, Giralt S, Revta C, Carreau NA, Iacobelli M, Carreras E, Ruutu T, Barbui T, Antin JH and Niederwieser D: Hepatic veno-occlusive disease following stem cell transplantation: Incidence, clinical course, and outcome. *Biol Blood Marrow Transplant* 16: 157-168, 2010. PMID: 19766729. DOI: 10.1016/j.bbmt.2009.08.024
- 12 Mohty M, Malard F, Abecassis M, Aerts E, Alaskar AS, Aljurf M, Arat M, Bader P, Baron F, Bazarbachi A, Blaise D, Ciceri F, Corbacioglu S, Dalle JH, Dignan F, Fukuda T, Huynh A, Masszi T, Michallet M, Nagler A, NiChonghaile M, Okamoto S,

- Pagliuca A, Peters C, Petersen FB, Richardson PG, Ruutu T, Savani BN, Wallhult E, Yakoub-Agha I, Duarte RF and Carreras E: Revised diagnosis and severity criteria for sinusoidal obstruction syndrome/veno-occlusive disease in adult patients: A new classification from the European Society for Blood and Marrow Transplantation. *Bone Marrow Transplant* 51: 906-912, 2016. DOI: 10.1038/bmt.2016.130
- 13 Fan CQ and Crawford JM: Sinusoidal obstruction syndrome (hepatic veno-occlusive disease). *J Clin Exp Hepatol* 4: 332-346, 2014. PMID: 25755580. DOI: 10.1016/j.jceh.2014.10.002
- 14 Zhou H, Wang YXJ, Lou HY, Xu XJ and Zhang MM: Hepatic sinusoidal obstruction syndrome caused by herbal medicine: CT and MRI features. *Korean J Radiol* 15: 218-225, 2014. PMID: 24643319. DOI: 10.3348/kjr.2014.15.2.218
- 15 Dalle JH and Giralat SA: Hepatic veno-occlusive disease after hematopoietic stem cell transplantation: risk factors and stratification, prophylaxis, and treatment. *Biol Blood Marrow Transplant* 22: 400-409, 2016. PMID: 26431626. DOI: 10.1016/j.bbmt.2015.09.024
- 16 Jafari A, Wehner S, Kalff JC and Manekeller S: Sinusoidal obstruction syndrome in the animal model: influence on liver surgery. *Langenbeck's Arch Surg* 402: 115-122, 2017. PMID: 27585678. DOI: 10.1007/s00423-016-1506-0
- 17 Tamandl D, Klinger M, Eipeldauer S, Herberger B, Kaczirek K, Gruenberger B and Gruenberger T: Sinusoidal obstruction syndrome impairs long-term outcome of colorectal liver metastases treated with resection after neoadjuvant chemotherapy. *Ann Surg Oncol* 18: 421-430, 2011. PMID: 20844968. DOI: 10.1245/s10434-010-1317-4
- 18 Kumar A, Palek R and Liska V: A critical analysis of experimental animal models of sinusoidal obstruction syndrome. *J Clin Exp Hepatol* 9: 345-353, 2019. PMID: 31360027. DOI: 10.1016/j.jceh.2018.07.002
- 19 DeLeve LD, McCuskey RS, Wang X, Hu L, McCuskey MK, Epstein RB and Kanel GC: Characterization of a reproducible rat model of hepatic veno-occlusive disease. *Hepatology* 29: 1779-1791, 1999. PMID: 10347121. DOI: 10.1002/hep.510290615
- 20 DeLeve LD, Wang X, Kanel GC, Ito Y, Bethea NW, McCuskey MK, Tokes ZA, Tsai J and McCuskey RS: Decreased hepatic nitric oxide production contributes to the development of rat sinusoidal obstruction syndrome. *Hepatology* 38: 900-908, 2003. PMID: 14512877. DOI: 10.1053/jhep.2003.50383
- 21 Nakamura K, Hatano E, Narita M, Miyagawa-Hayashino A, Koyama Y, Nagata H, Iwaisako K, Taura K and Uemoto S: Sorafenib attenuates monocrotaline-induced sinusoidal obstruction syndrome in rats through suppression of JNK and MMP-9. *J Hepatol* 57: 1037-1043, 2012. PMID: 22796153. DOI: 10.1016/j.jhep.2012.07.004
- 22 Deleve LD, Wang X, Tsai J, Kanel G, Strasberg S and Tokes ZA: Sinusoidal obstruction syndrome (veno-occlusive disease) in the rat is prevented by matrix metalloproteinase inhibition. *Gastroenterology* 125: 882-890, 2003. PMID: 12949732. DOI: 10.1016/S0016-5085(03)01056-4
- 23 Harb R, Xie G, Lutzko C, Guo Y, Wang X, Hill CK, Kanel GC and DeLeve LD: Bone marrow progenitor cells repair rat hepatic sinusoidal endothelial cells after liver injury. *Gastroenterology* 137: 704-712, 2009. PMID: 19447108. DOI: 10.1053/j.gastro.2009.05.009
- 24 Corbacioglu S and Richardson PG: Defibrotide for children and adults with hepatic veno-occlusive disease post hematopoietic cell transplantation. *Expert Rev Gastroenterol Hepatol* 11: 885-898, 2017. PMID: 28825848. DOI: 10.1080/17474124.2017.1370372
- 25 Cheuk DKL, Chiang AKS, Ha SY and Chan GCF: Interventions for prophylaxis of hepatic veno-occlusive disease in people undergoing haematopoietic stem cell transplantation. *Cochrane database Syst Rev* CD009311, 2015. PMID: 26017019. DOI: 10.1002/14651858.CD009311.pub2
- 26 Imran H, Tleyjeh IM, Zirakzadeh A, Rodriguez V and Khan SP: Use of prophylactic anticoagulation and the risk of hepatic veno-occlusive disease in patients undergoing hematopoietic stem cell transplantation: a systematic review and meta-analysis. *Bone Marrow Transplant* 37: 677-686, 2006. PMID: 16489362. DOI: 10.1038/sj.bmt.1705297
- 27 Inukai T, Sugita K, Goi K, Akahane K, Hirose K, Nemoto A, Takahashi K, Sato H, Uno K, Furuichi Y, Nakamura M, Miyamoto N, Yamakawa N, Shiraishi K, Kojika S, Tezuka T, Iijima K and Nakazawa S: [Prevention of hepatic veno-occlusive disease by a combination of heparin and prostaglandin E1 in children undergoing hematopoietic stem cell transplantation]. *Rinsho Ketsueki* 45: 297-303, 2004. PMID: 15168445.
- 28 Nakamura K, Hatano E, Miyagawa-Hayashino A, Okuno M, Koyama Y, Narita M, Seo S, Taura K and Uemoto S: Soluble thrombomodulin attenuates sinusoidal obstruction syndrome in rat through suppression of high mobility group box 1. *Liver Int* 34: 1473-1487, 2014. PMID: 24498917. DOI: 10.1111/liv.12420
- 29 Miyata T, Tajima H, Hirata M, Nakanuma S-I, Makino I, Hayashi H, Oyama K, Miyashita T, Takamura H, Ninomiya I, Fushida S, Iseki S, Harada S-I, Wakayama T and Ohta T: Phosphodiesterase III inhibitor attenuates rat sinusoidal obstruction syndrome through inhibition of platelet aggregation in Disse's space. *J Gastroenterol Hepatol* 33: 950-957, 2018. PMID: 28960464. DOI: 10.1111/jgh.14004
- 30 Okuno M, Hatano E, Nakamura K, Miyagawa-Hayashino A, Kasai Y, Nishio T, Seo S, Taura K and Uemoto S: Regorafenib suppresses sinusoidal obstruction syndrome in rats. *J Surg Res* 193: 693-703, 2015. PMID: 25266603. DOI: 10.1016/j.jss.2014.08.052
- 31 Zhang J, Sheng Y, Shi L, Zheng Z, Chen M, Lu B and Ji L: Quercetin and baicalein suppress monocrotaline-induced hepatic sinusoidal obstruction syndrome in rats. *Eur J Pharmacol* 795: 160-168, 2017. PMID: 27979702. DOI: 10.1016/j.ejphar.2016.12.015
- 32 Zheng Z, Shi L, Sheng Y, Zhang J, Lu B and Ji L: Chlorogenic acid suppresses monocrotaline-induced sinusoidal obstruction syndrome: The potential contribution of NFκB, Egr1, Nrf2, MAPKs and PI3K signals. *Environ Toxicol Pharmacol* 46: 80-89, 2016. PMID: 27438897. DOI: 10.1016/j.etap.2016.07.002
- 33 Peres E, Kintzel P, Dansey R, Baynes R, Abidi M, Klein J, Ibrahim RB and Abella E: Early intervention with antithrombin III therapy to prevent progression of hepatic venoocclusive disease. *Blood Coagul Fibrinolysis* 19: 203-207, 2008. PMID: 18388499. DOI: 10.1097/MBC.0b013e3282f2fb5d9
- 34 Richardson P, Aggarwal S, Topaloglu O, Villa KF and Corbacioglu S: Systematic review of defibrotide studies in the treatment of veno-occlusive disease/sinusoidal obstruction syndrome (VOD/SOS). *Bone Marrow Transplant*, 2019. PMID: 30804485. DOI: 10.1038/s41409-019-0474-8
- 35 Qiao J, Qi K, Chu P, Mi H, Yang N, Yao H, Xia Y, Li Z, Xu K and Zeng L: Infusion of endothelial progenitor cells ameliorates liver injury in mice after haematopoietic stem cell transplantation. *Liver Int* 35: 2611-2620, 2015. PMID: 25872801. DOI: 10.1111/liv.12849

- 36 Joseph B, Kumaran V, Berishvili E, Bhargava KK, Palestro CJ and Gupta S: Monocrotaline promotes transplanted cell engraftment and advances liver repopulation in rats *via* liver conditioning. *Hepatology* 44: 1411-1420, 2006. PMID: 17133480. DOI: 10.1002/hep.21416
- 37 Liska V, Slowik P, Eggenhofer E, Treska V, Renner P, Popp FC, Mirka H, Kobl J, Sykora R, Schlitt H-J, Holubec L, Chlumská A, Skalický T, Matejovic M and Dahlke MH: Intraportal injection of porcine multipotent mesenchymal stromal cells augments liver regeneration after portal vein embolization. *In Vivo* 23: 229-235, 2009. PMID: 19414408.
- 38 Treska V, Fichtl J, Ludvik J, Bruha J, Liska V, Treskova I, Kucera R, Topolcan O, Lysak D, Skalický T and Ferda J: Portal vein embolization (PVE) *versus* PVE with haematopoietic stem cell application in patients with primarily non-resectable colorectal liver metastases. *Anticancer Res* 38: 5531-5537, 2018. PMID: 30194213. DOI: 10.21873/anticancer.12888
- 39 De Miguel MP, Prieto I, Moratilla A, Arias J and Aller MA: Mesenchymal stem cells for liver regeneration in liver failure: From experimental models to clinical trials. *Stem Cells Int* 2019, 2019. PMID: 31191671. DOI: 10.1155/2019/3945672
- 40 Palek R, Liska V, Treska V, Rosendorf J, Eminger M, Tegl V, Kralickova A, Bajcurova K, Jirik M and Tonar Z: Sinusoidal obstruction syndrome induced by monocrotaline in a large animal experiment – a pilot study. *Rozhl Chir* 97: 214-221. PMID: 29792719.
- 41 Bruha J, Vycital O, Tonar Z, Mirka H, Haidingerova L, Benes J, Palek R, Skala M, Treska V and Liska V: Monoclonal antibody against transforming growth factor Beta 1 does not influence liver regeneration after resection in large animal experiments. *In Vivo* 29: 327-340, 2015. PMID: 25977378.
- 42 Schiffer E, Frossard J-L, Rubbia-Brandt L, Mentha G and Pastor CM: Hepatic regeneration is decreased in a rat model of sinusoidal obstruction syndrome. *J Surg Oncol* 99: 439-446, 2009. PMID: 19353590. DOI: 10.1002/jso.21276
- 43 Mouton PR: Principles and practices of unbiased stereology: An introduction for bioscientists. Johns Hopkins University Press, 2001.
- 44 Yang XQ, Ye J, Li X, Li Q and Song YH: Pyrrolizidine alkaloids-induced hepatic sinusoidal obstruction syndrome: Pathogenesis, clinical manifestations, diagnosis, treatment, and outcomes. *World J Gastroenterol* 25: 3753-3763, 2019. PMID: 31391770. DOI: 10.3748/wjg.v25.i28.3753
- 45 Glavind E, Aagaard NK, Grønbaek H, Møller HJ, Orntoft NW, Vilstrup H and Thomsen KL: Alcoholic Hepatitis Markedly Decreases the Capacity for Urea Synthesis. *PLoS One* 11: e0158388, 2016. PMID: 27379798. DOI: 10.1371/journal.pone.0158388
- 46 Vilstrup H: Synthesis of urea after stimulation with amino acids: relation to liver function. *Gut* 21: 990-995, 1980. PMID: 7450564. DOI: 10.1136/gut.21.11.990
- 47 Hirata M, Tajima H, Miyashita T, Miyata T, Nakanuma S, Makino I, Hayashi H, Oyama K, Takamura H, Ninomiya I, Fushida S, Nakata H, Iseki S, Harada S, Wakayama T and Ohta T: Extravasated platelet aggregation in the livers of rats with drug-induced hepatic sinusoidal obstruction syndrome. *Mol Med Rep* 15: 3147-3152, 2017. PMID: 28358421. DOI: 10.3892/mmr.2017.6407
- 48 Vreuls CPH, Driessen A, Olde Damink SWM, Koek GH, Duimel H, van den Broek MAJ, Dejong CHC, Braet F and Wisse E: Sinusoidal obstruction syndrome (SOS): A light and electron microscopy study in human liver. *Micron* 84: 17-22, 2016. PMID: 26914502. DOI: 10.1016/j.micron.2016.02.006
- 49 Dietrich CF, Trenker C, Fontanilla T, Gorg C, Hausmann A, Klein S, Lassau N, Miquel R, Schreiber-Dietrich D and Dong Y: New ultrasound techniques challenge the diagnosis of sinusoidal obstruction syndrome. *Ultrasound Med Biol* 44: 2171-2182, 2018. PMID: 30076031. DOI: 10.1016/j.ultrasmedbio.2018.06.002
- 50 Nishida M, Kahata K, Hayase E, Shigematsu A, Sato M, Kudo Y, Omotehara S, Iwai T, Sugita J, Shibuya H, Shimizu C and Teshima T: Novel ultrasonographic scoring system of sinusoidal obstruction syndrome after hematopoietic stem cell transplantation. *Biol Blood Marrow Transplant* 24: 1896-1900, 2018. PMID: 29803752. DOI: 10.1016/j.bbmt.2018.05.025
- 51 Collard M, Coche E, Dragean A and Halut M: Hepatofugal portal venous flow: From normal to pathological, 2019. DOI: 10.31487/j.RDI.2019.03.10
- 52 Sharma P and Sharma BC: Lactulose for minimal hepatic encephalopathy in patients with extrahepatic portal vein obstruction. *Saudi J Gastroenterol* 18: 168-172, 2012. PMID: 22626795. DOI: 10.4103/1319-3767.96448
- 53 Gines P, Sola E, Angeli P, Wong F, Nadim MK and Kamath PS: Hepatorenal syndrome. *Nat Rev Dis Prim* 4: 23, 2018. PMID: 30213943. DOI: 10.1038/s41572-018-0022-7
- 54 Fink JC, Cooper MA, Burkhart KM, McDonald GB and Zager RA: Marked enzyuria after bone marrow transplantation: a correlate of veno-occlusive disease-induced "hepatorenal syndrome". *J Am Soc Nephrol* 6: 1655-1660, 1995. PMID: 8749694.
- 55 Fang B, Shi M, Liao L, Yang S, Liu Y and Zhao RC: Systemic infusion of FLK1(+) mesenchymal stem cells ameliorate carbon tetrachloride-induced liver fibrosis in mice. *Transplantation* 78: 83-88, 2004. PMID: 15257043. DOI: 10.1097/01.tp.00001283.26.95294.14
- 56 Zhu X, He B, Zhou X and Ren J: Effects of transplanted bone-marrow-derived mesenchymal stem cells in animal models of acute hepatitis. *Cell Tissue Res* 351: 477-486, 2013. PMID: 23143676. DOI: 10.1007/s00441-012-1524-3
- 57 Higashiyama R, Inagaki Y, Hong YY, Kushida M, Nakao S, Nioka M, Watanabe T, Okano H, Matsuzaki Y, Shiota G and Okazaki I: Bone marrow-derived cells express matrix metalloproteinases and contribute to regression of liver fibrosis in mice. *Hepatology* 45: 213-222, 2007. PMID: 17187438. DOI: 10.1002/hep.21477
- 58 Natarajan TG and FitzGerald KT: Markers in normal and cancer stem cells. *Cancer Biomark* 3: 211-231, 2007. PMID: 17917151. DOI: 10.3233/cbm-2007-34-506
- 59 Ding HR, Wang JL, Tang ZT, Wang Y, Zhou G, Liu Y, Ren HZ and Shi XL: Mesenchymal stem cells improve glycometabolism and liver regeneration in the treatment of post-hepatectomy liver failure. *Front Physiol* 10: 1-13, 2019. PMID: 31024348. DOI: 10.3389/fphys.2019.00412
- 60 Nadalin S, Testa G, Malago M, Beste M, Frilling A, Schroeder T, Jochum C, Gerken G and Broelsch CE: Volumetric and functional recovery of the liver after right hepatectomy for living donation. *Liver Transplant* 10: 1024-1029, 2004. PMID: 15390329. DOI: 10.1002/lt.20182

Received September 10, 2020

Revised September 30, 2020

Accepted October 12, 2020

10.10 Příloha X

MALEČKOVÁ, Anna, KOCHOVÁ, Petra, PÁLEK, Richard, LIŠKA, Václav, MIK, Patrik, BOŃKOWSKI, Tomasz, HORÁK, Miroslav, TONAR, Zbyněk, 2021. Blunt injury of liver: mechanical response of porcine liver in experimental impact test. *Physiological measurement*. 42(2), 025008. ISSN 0967-3334. Dostupné z: <https://doi.org/10.1088/1361-6579/abdf3c>. Corrigendum: Blunt injury of liver: mechanical response of porcine liver in experimental impact test. *Physiological measurement*. 42(5). Dostupné z: <https://doi.org/10.1088/1361-6579/abf887>
IF_(JCR2020) = 2,833 Q3 (Biophysics; Engineering, biomedical; Physiology)

CORRIGENDUM

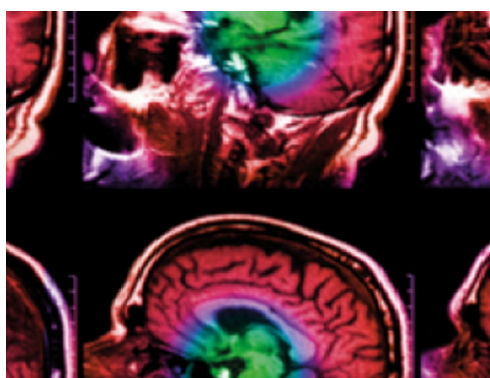
Corrigendum: Blunt injury of liver: mechanical response of porcine liver in experimental impact test (2021 *Physiol. Meas.* [42 025008](#))

To cite this article: Anna Maleková *et al* 2021 *Physiol. Meas.* **42** 059501

View the [article online](#) for updates and enhancements.

You may also like

- [Constrained time-optimal control of double-integrator system and its application in MPC](#)
Marek Fehér, Ondej Straka and Václav Šmíd
- [Evaluation of in-situ deformation experiments of TRIP steel](#)
J Procházka, L Kuerová and M Bystrianský
- [Timepix in LEO Orbit onboard the VZLUSAT-1 Nanosatellite: 1-year of Space Radiation Dosimetry Measurements](#)
T. Baca, M. Jilek, I. Vertat *et al.*



IPEM | IOP

Series in Physics and Engineering in Medicine and Biology

Your publishing choice in medical physics, biomedical engineering and related subjects.

Start exploring the collection—download the first chapter of every title for free.



CORRIGENDUM

Corrigendum: Blunt injury of liver: mechanical response of porcine liver in experimental impact test (2021 *Physiol. Meas.* **42** 025008)

RECEIVED
10 April 2021ACCEPTED FOR PUBLICATION
15 April 2021PUBLISHED
17 June 2021

Anna Malečková^{1,2} , Petra Kochová³, Richard Pálek^{2,4}, Václav Liška^{2,4}, Patrik Mik⁵, Tomasz Bońkowski⁶, Miroslav Horák⁷ and Zbyněk Tonar³

¹ Department of Histology and Embryology, Faculty of Medicine in Pilsen, Charles University, Pilsen, Czech Republic

² Biomedical Center, Faculty of Medicine in Pilsen, Charles University, Pilsen, Czech Republic

³ European Centre of Excellence NTIS, Faculty of Applied Sciences, University of West Bohemia, Pilsen, Czech Republic

⁴ Department of Surgery, Faculty of Medicine and University Hospital in Pilsen, Charles University, Pilsen, Czech Republic

⁵ Department of Anatomy, Faculty of Medicine in Pilsen, Charles University, Pilsen, Czech Republic

⁶ New Technologies—Research Centre, University of West Bohemia, Pilsen, Czech Republic

⁷ Department of Mechanics, Faculty of Applied Sciences, University of West Bohemia, Pilsen, Czech Republic

This corrigendum corrects the wrong description of hepatic lobes in ‘Blunt injury of liver—mechanical response of porcine liver in experimental impact test’ (Malečková *et al* 2021). Right hepatic lobes were wrongly described as left hepatic lobes and vice versa, namely the right lateral lobe was wrongly described as the left lateral lobe; the

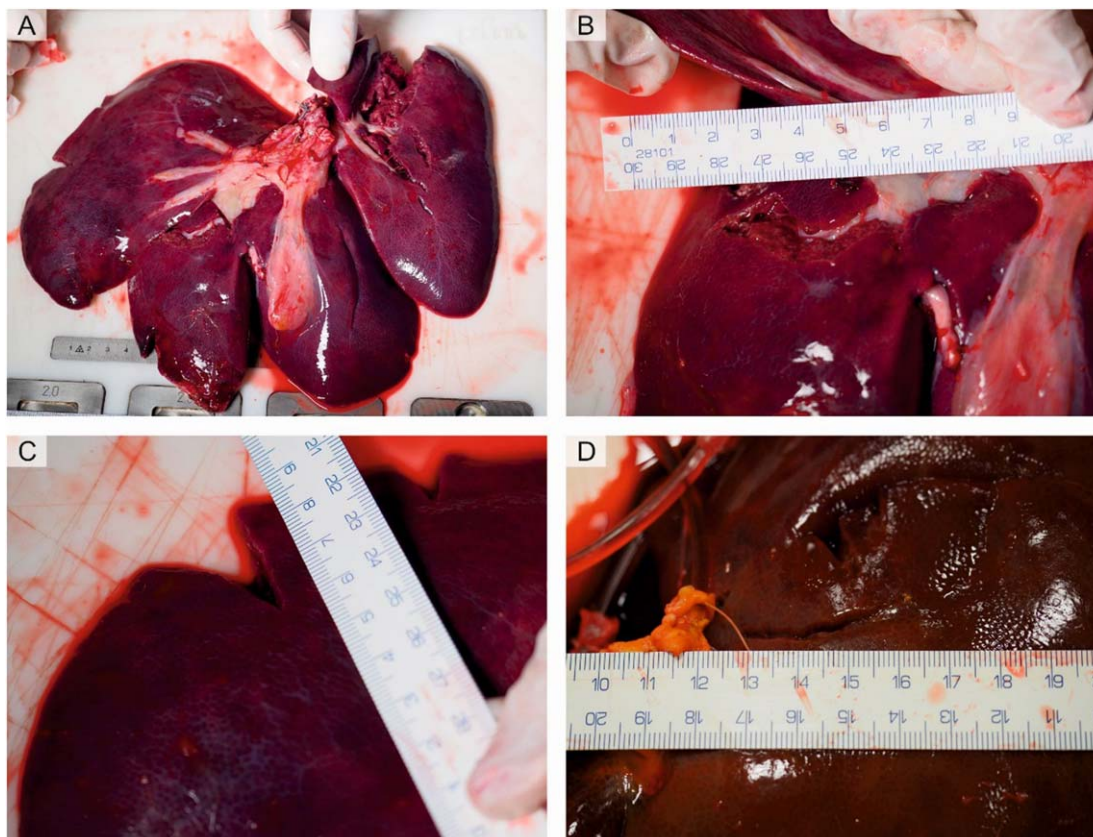


Figure 4. Typical external injury patterns of the porcine liver after the impact test. (A) Laceration of the visceral surface of the liver affecting more than a half of the right lateral lobe, injury grade V. (B) Rupture of the visceral surface of the left medial lobe, that propagates from the hilum along the big vessels and the stromal connective tissue. (C) Peripheral rupture starting at the border of the left lateral lobe. (D) Occasional shallow rupture on the diaphragmatic surface of the liver, most likely caused by the direct impact of the wood plate used in the impact test.

left medial lobe was wrongly described as the right medial lobe. Therefore, the figure caption in figure 4 should be as follows:

Additionally, this error also occurred in Results. The formulation in the section 3.3.1 ‘Ruptures propagated from the hilum along big vessels and were mostly located in the left lateral (figure 4(A)) and right medial lobes (figure 4(B))’ should be changed to ‘Ruptures propagated from the hilum along big vessels and were mostly located in the right lateral (figure 4(A)) and left medial lobes (figure 4(B))’.

ORCID iDs

Anna Malečková  <https://orcid.org/0000-0003-2674-6268>

Reference

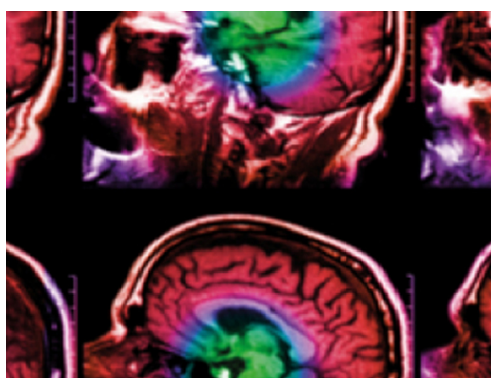
Malečková A, Kochová P, Pálek R, Liška V, Mik P, Bońkowski T, Horák M and Tonar Z 2021 Blunt injury of liver—mechanical response of porcine liver in experimental impact test *Physiol. Meas.* **42** 025008

PAPER

Blunt injury of liver: mechanical response of porcine liver in experimental impact test

To cite this article: Anna Maleková *et al* 2021 *Physiol. Meas.* **42** 025008

View the [article online](#) for updates and enhancements.



IPEM | IOP

Series in Physics and Engineering in Medicine and Biology

Your publishing choice in medical physics,
biomedical engineering and related subjects.

Start exploring the collection—download the
first chapter of every title for free.



PAPER

Blunt injury of liver: mechanical response of porcine liver in experimental impact test

RECEIVED
15 September 2020REVISED
13 January 2021ACCEPTED FOR PUBLICATION
22 January 2021PUBLISHED
9 March 2021

Anna Malečková^{1,2}, Petra Kochová^{3,*}, Richard Pálek^{2,4}, Václav Liška^{2,4}, Patrik Mik⁵, Tomasz Bońkowski⁶, Miroslav Horák⁷ and Zbyněk Tonar³

¹ Department of Histology and Embryology, Faculty of Medicine in Pilsen, Charles University, Pilsen, Czech Republic

² Biomedical Center, Faculty of Medicine in Pilsen, Charles University, Pilsen, Czech Republic

³ European Centre of Excellence NTIS, Faculty of Applied Sciences, University of West Bohemia, Pilsen, Czech Republic

⁴ Department of Surgery, Faculty of Medicine and University Hospital in Pilsen, Charles University, Pilsen, Czech Republic

⁵ Department of Anatomy, Faculty of Medicine in Pilsen, Charles University, Pilsen, Czech Republic

⁶ New Technologies—Research Centre, University of West Bohemia, Pilsen, Czech Republic

⁷ Department of Mechanics, Faculty of Applied Sciences, University of West Bohemia, Pilsen, Czech Republic

* Author to whom any correspondence should be addressed.

E-mail: Anna.Maleckova@lfp.cuni.cz, kochovap@ntc.zcu.cz, palekr@fnplzen.cz, liskav@fnplzen.cz, Patrik.Mik@lfp.cuni.cz, tomasz@ntc.zcu.cz, horak21@kme.zcu.cz and tonar@ntis.zcu.cz

Keywords: porcine liver, mechanical behavior, liver microstructure, reticular fibers,, stereology

Supplementary material for this article is available [online](#)

Abstract

Objective. The liver is frequently injured in blunt abdominal trauma caused by road traffic accidents. The testing of safety performance of vehicles, e.g. belt usage, head support, seat shape, or air bag shape, material, pressure and reaction, could lead to reduction of the injury seriousness. Current trends in safety testing include development of accurate computational human body models (HBMs) based on the anatomical, morphological, and mechanical behavior of tissues under high strain. **Approach.** The aim of this study was to describe the internal pressure changes within porcine liver, the severity of liver injury and the relation between the porcine liver microstructure and rupture propagation in an experimental impact test. Porcine liver specimens ($n = 24$) were uniformly compressed using a drop tower technique and four impact heights (200, 300, 400 and 500 mm; corresponding velocities: 1.72, 2.17, 2.54 and 2.88 m s⁻¹). The changes in intravascular pressure were measured via catheters placed in portal vein and caudate vena cava. The induced injuries were analyzed on the macroscopic level according to AAST grade and AIS severity. Rupture propagation with respect to liver microstructure was analyzed using stereological methods. **Main results.** Macroscopic ruptures affected mostly the interface between connective tissue surrounding big vessels and liver parenchyma. Histological analysis revealed that the ruptures avoided reticular fibers and interlobular septa made of connective tissue on the microscopic level. **Significance.** The present findings can be used for evaluation of HBMs of liver behavior in impact situations.

1. Introduction

Road traffic accidents (RTAs) are one of the main causes of blunt abdominal trauma, which is often accompanied by internal organ injuries, most frequently to the spleen, the liver and the kidney (Elhagediab and Rouhana 1998, Augenstein *et al* 1999, Monchal *et al* 2018). Although soft tissue injuries and bone fractures are the most common types of road traffic injuries, liver trauma is responsible for significant morbidity and mortality (Doklestić *et al* 2015, Vyčítal *et al* 2019). According to the Global Status Report On Road Safety issued by the World Health Organization (2018), vehicle safety is one of the key factors reducing the likelihood of serious injury in RTAs. The importance of both air bag deployment and safety belt restraint in preventing the liver injuries was demonstrated by Holbrook *et al* (2007) in a study that analyzed 311 patients with injuries

suffered in motor vehicle crashes. Therefore, improving safety systems for car occupants became an important tool for the reduction of traffic accident injuries and casualties (Xu *et al* 2018).

Testing the safety performance of newly developed vehicles is usually carried out in two distinct ways: (i) standardized car crash tests using anthropometric testing devices (ATDs) commonly called dummies or (ii) car crash simulations using computational models of ATDs or human body models (HBMs) (Xu *et al* 2018). The current trend in predicting trauma impact on human tissues and organs relies on the development of computational modeling, as only a few large corporations use mechanical dummies for car crash tests (Xu *et al* 2018) and the ATD outputs are only injury criteria based on physically measurable parameters (acceleration, force, compression of chest). The models are based on morphometric data collected from human cadavers (Tropiano *et al* 2004) or imaging modalities such as CT and MRI (Gayzik *et al* 2011), and could be morphed for the wide variety of anthropometries.

The HBMs used for abdominal injury prediction include e.g. the HUman MOdel of Safety, HUMOS (Behr *et al* 2003, Arnoux *et al* 2008), Total Human Model for Safety, THUMS (Golman *et al* 2014), Global Human Body Models Consortium, GHBM (Schoell *et al* 2015, Schwartz *et al* 2015), Wayne State Human Body Models, WSUHAM (Lee and Yang 2001). Arnoux *et al* (2008) used in their experiment a hybrid approach coupling numerical simulation (HUMOS) with experimental data from free fall tests using human cadaver trunks. They provided a complex analysis of the liver behavior within the abdomen in frontal crash situations and proved the importance of experimental data for computational modeling of inner organ behavior. The study has been followed by several experimental studies on human (Cheynel *et al* 2009, Conte *et al* 2012, Untaroiu *et al* 2015) and porcine liver (Chen *et al* 2018, Chen *et al* 2019) biomechanical behavior since then. The studies were mostly focused on the effect of sudden deceleration and impact, two phenomena that were identified as the main causes of liver injury (King and Yang 1995, Cheynel *et al* 2009). The results of those tests were influenced by parameters such as velocity, mass, size, surface area of the impactors, compression and duration of the applied force (Untaroiu *et al* 2015). However, only a few studies were focused on the relationship between liver injury and internal pressure changes (Sparks *et al* 2007, 2008). That is despite the extensive vascular supply of the liver and the previously described dependence of the liver injury severity on rapid increase in internal fluid pressure (Sparks *et al* 2007, 2008, Sparks and Dupaix 2008).

Experiments conducted on human cadavers or organs are valuable sources of biomechanical data (Kemper *et al* 2010, Conte *et al* 2012). Many previous experiments and most of the current liver models, however, include the use of animal tissue to simulate human organs (Melvin *et al* 1973, Wang *et al* 1992, Tamura *et al* 2002, Santago *et al* 2009, Marchesseau *et al* 2017). Using animal cadavers and livers is therefore a plausible and more feasible approach to obtaining biomechanical data. Pig is particularly convenient as it is widely used in different fields of biomedicine for its anatomical and physiological similarities with humans (Eberlova *et al* 2016, Malečková *et al* 2019, Eberlova *et al* 2020). Nevertheless, the anatomical and microscopic differences between human and porcine liver need to be taken into consideration when interpreting data from animal experiments (Huelke *et al* 1986, Kruepunga *et al* 2019). The porcine liver microstructure has already been described in detail using well-established stereological methods (Junatas *et al* 2017, Mik *et al* 2018). The microstructure is organized into well-defined roughly hexagonal hepatic lobules demarcated by fibrous interlobular septa containing portal triads. The interlobular connective tissue originates from the fibrous capsule and enters the liver via the hilum along big branches of hepatic vessels—the portal vein and hepatic artery. The hepatocytes are arranged within lobules into trabeculae surrounded by a delicate network of reticular fibers that separates the hepatocytes from hepatic sinusoids (see supplement S1 (available online at stacks.iop.org/PMEA/42/025008/mmedia)).

The aim of our study was to describe the biomechanical behavior of the whole porcine liver in an experimental impact test, with special emphasis on the internal pressure changes depending on the impact energy. The experiment was designed to enable us to study the effect of impact alone with no influence of deceleration. The severity of liver damage on the macroscopic level was evaluated using the American Association for the Surgery of Trauma (AAST) organ injury scaling and Abbreviated Injury Scale (AIS severity), 2018 update (Kozar *et al* 2018). As the mechanical properties of the soft tissue organs depend on their microscopic structure, we wanted to specifically focus on the relationship between rupture propagation and tissue microstructure, namely on the main fibrillary components of the hepatic interstitial connective tissue matrix. Hence, our biomechanical data were accompanied by histological quantitative analysis. Our aim was also to provide complete primary biomechanical data and make them publicly available for biomechanical modeling of liver crash tests.

2. Methods

2.1. Liver sample preparation

Liver samples were obtained from Prestice Black-Pied pigs (Vrtkova 2015) ($n = 24$). The animals received standard care in compliance with the European Convention on Animal Care, and the project no. MSMT-4428/2018-2 was

approved by the Faculty Committee for the Prevention of Cruelty to Animals. The piglets were pre-medicated by intramuscular administration of 10 mg kg⁻¹ ketamine (Narkamon; Spofa, A.S., Prague, Czech Republic), 5 mg kg⁻¹ azaperon (Stresnil; Janssen Pharmaceutica NV, Beerse, Belgium) and 1 mg atropine (Atropin Biotika; Hoechst Biotika, Martin, Slovak Republic). For general anaesthesia propofol (1% mixture 5–10 mg⁻¹ kg⁻¹ h⁻¹ propofol; Fresenius Kabi Norges AS, Halden, Norway) was administered intravenously. Continuous analgesia was provided by fentanyl (1–2 µg⁻¹ kg⁻¹ h⁻¹ Fentanyl Torre; Chiesi CZ s.r.o, Prague, Czech Republic). Airways were secured by endotracheal intubation and pigs were mechanically ventilated. The piglets received infusion and volume substitution when necessary (Hartmann's Solution; B.Braun Melsungen AG, Melsungen, Germany and Plasmalyte; Baxter Healthcare Ltd, Compton, UK).

Midline laparotomy was performed to enter the abdominal cavity. All the ligaments attaching the liver to the surrounding structures were transected, the common bile duct was ligated and divided, and the portal vein, hepatic artery and the infrahepatic part of the caudate vena cava (equivalent to the inferior vena cava in human anatomy) were dissected. The thoracic cavity was opened to gain access to the thoracic part of the caudate vena cava. The diaphragm was transected in the ventrodorsal direction leaving a small rim around the caudate vena cava. The animal was then heparinized (10 000 IU of heparin; Zentiva, k.s., Prague, Czech Republic) and the portal vein and the thoracic part of the caudate vena cava were cannulated by infusion tubes. These tubes were later used for measuring intravascular pressure in the liver. Finally, all the vessels supplying and draining the liver were ligated and divided and the whole organ, filled with blood, was removed from the body. The animals were sacrificed under general anesthesia via an intravenous administration of a cardioplegic solution (potassium chloride).

2.2. Impact test

Prior to the mechanical experiment, all the specimens were checked for the following conditions that might have been caused by specimen handling: contusions, ruptures and bleeding. Damaged specimens were excluded from further analysis. In total, 24 livers were used for the mechanical experiment. The livers were divided into four groups (six livers per group) based on the impact height (200, 300, 400 and 500 mm and corresponding impact velocity 1.72, 2.17, 2.54 and 2.88 m s⁻¹, respectively). The specimens were kept cool on ice until the mechanical impact test. The maximum time between surgery and impact test was three hours. Firstly, each liver was pressurized through the infusion tubes inserted in the portal vein and caudate vena cava at 7 cm H₂O by 0.9% NaCl solution. Maintaining the turgor of the liver at a level comparable to normal hemodynamic pressures was necessary for simulation of impact injuries (Melvin *et al* 1973). Then the size and weight of the pressurized liver was measured. After that, the livers were put into the measurement device—a drop tower (Sparks *et al* 2008). The livers were uniformly compressed using an impact 6.22 kg plate made of wood with impact area of 29.5 cm × 29.5 cm. The plate was firmly connected to an aluminum beam, which could freely move along the aluminum frame. We neglected the beam friction to simulate the plate free fall by the use of Teflon sliders between the beam and the frame. The plate was covered by a plastic foil and spread with tempera color to visualize the contact area between the plate and the liver.

The pressure was recorded at the portal vein and the caudate vena cava during the impact test using a Silicon Pressure Sensor MPXV5100DP (GND +5V) (NXP Semiconductors N.V., Eindhoven, Netherlands). The sensor was connected to the external opening of the infusion tube, while the intravascular opening was placed in the blood vessels, in a way similar to the setting previously proposed by Sparks *et al* (2008).

Maximal pressure values were used for further quantitative analysis. The position of the impact plate before the impact was measured by two lasers optoNCDT 2300-50 (Micro-Epsilon GmbH, Frankfurt am Main, Germany) on each side of the impacting beam. The velocity of the impact was derived from the position measurement and then averaged from both lasers. Measured signals were acquired by the NI CompactDAQ (National Instruments, Austin, TX, USA) system with SignalExpress software (National Instruments, Austin, TX, USA). The system energy was determined by two formulas:

$$E_K = \frac{1}{2}mv^2$$

where m was the weight of the impact plate and v was the velocity of the impact plate before impact, and

$$E_p = mgh$$

where m was the weight of the impact plate, g was acceleration of gravity, and h was the height of the impact given as impact height minus the liver thickness. The loading area was calculated from the colored part of the liver using Ellipse software (ViDiTo, Košice, Slovak Republic). The impact energy was then calculated as the energy of the plate divided by the loaded area. The loaded area in percentage was calculated as the colored part of liver divided by the total liver area. Both parameters were estimated with Ellipse software using the 'POLYGON' tool in calibrated photographs.

2.3. Macroscopic injury analysis

Immediately after the impact test, ruptures on the surface of the liver were captured by camera and the projection length of the ruptures was measured. The position of the ruptures with respect to the liver lobes was registered to determine the most frequently damaged part of the liver. After that, each liver was cut completely into 1 cm thick slices and the depth of the ruptures and the depth of the contused parenchyma were measured. The depth was defined as the distance between the liver surface and the deepest point of the damaged parenchyma perpendicular to the liver surface. Both the projection length and the depth of the ruptures were measured in calibrated photographs using the Ellipse software 'LINE' tool (ViDiTo, Kosice, Slovak Republic). The injury grade and AIS severity were then determined according to liver injury scaling (Moore *et al* 1989, Kozar *et al* 2018).

2.4. Microscopic injury analysis

For the histological analysis, every fourth tissue slice was selected using systematic uniform random sampling. The first slice was selected randomly using the RANDBETWEEN function in Microsoft Office Excel. The selected slices were trimmed into tissue blocks with dimensions $1 \times 1 \times 1$ cm. Every eighth tissue block was then processed histologically. Each sample was carefully examined for liver abnormalities or signs of liver damage, especially inflammation and liver fibrosis. For the quantitative analysis of the ruptures we selected tissue samples with a macroscopically visible crack, 27 tissue blocks in total. The tissue samples were fixed in 4% buffered formalin, dehydrated and embedded in paraffin blocks. Each selected tissue block was cut into $5 \mu\text{m}$ thick sections. The section plane was perpendicular to the liver capsule. Sections were stained with hematoxylin-eosin (HE) and with Reticulin kit (BioGnost Ltd, Zagreb, Croatia) in order to visualize reticular fibers (type III collagen). Reticular fibers are located within the interlobular septa. They also represent the essential part of a delicate network, that separates the hepatic sinusoids and hepatocytes within the hepatic lobules (supplement S1). The results were based on 189 sections.

To determine the spatial relationship of ruptures and reticular fibers, we used a method previously published by Tonar *et al* (2009) and Kubíková *et al* (2017). Briefly, an isotropic stereological grid with known geometrical parameters was superimposed over the microphotographs. The number of intersections between this grid and reticular fibers was then counted. We compared the estimated value of the intersection intensity of reticular fibers along the rupture $P'_{L(\text{ret.})}$ with the theoretical value $P_{L(\text{ret.})}$ that should be expected in the case of random propagation of the microcracks throughout the liver parenchyma. The values were calculated with the assumption of independence of the ruptures on the reticular fibers.

The theoretical intersection intensity $P_{L(\text{ret.})}$ was calculated as the intersection intensity of a randomly oriented line (i.e. the rupture) with the reticular fibers (Stoyan *et al* 1995). It was defined as follows:

$$P_{L(\text{ret.})} = \frac{2}{\pi} L_{A(\text{ret.})}$$

where $L_{A(\text{ret.})}$ was the 2D length density of reticular fibers within liver. For each analyzed sample the length density L_A was assessed individually as follows:

$$L_A = \frac{L}{A}$$

where L is the length of the reticular fibers and A is the area of the reference space. L was estimated by counting the intersections of circular arcs randomly positioned on the microphotographs with reticular fibers. A was estimated using the point grid.

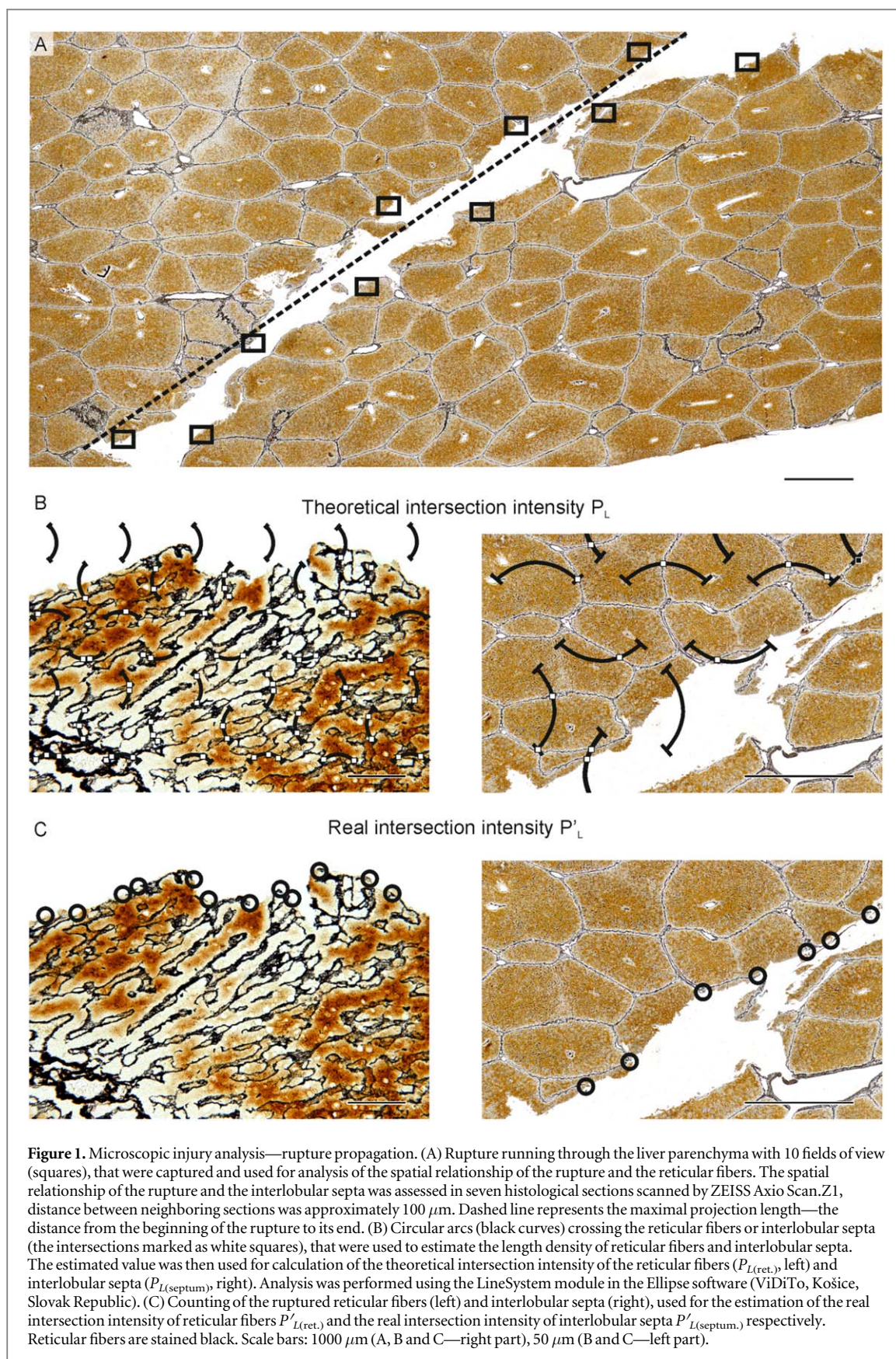
The intersection intensity of reticular fibers $P'_{L(\text{ret.})}$ was defined as follows:

$$P'_{L(\text{ret.})} = \frac{p(\text{ret.})}{l(\text{ret.})}$$

where $p(\text{ret.})$ is the real number of the intersections counted in the histological sections along the rupture of the length l . The length $l(\text{ret.})$ was defined as the shortest distance between the beginning and the end of the crack, the so-called maximal projection length. To estimate all the parameters, we used Ellipse software (ViDiTo, Košice, Slovak Republic) (figure 1).

The same analysis was performed to determine the spatial relationship of ruptures and the interlobular septa. We compared the estimated value of the intersection intensity of interlobular septa along the rupture $P'_{L(\text{septum})}$ with its theoretical value $P_{L(\text{septum})}$.

If the actual propagation of the ruptures throughout the liver parenchyma were at random, there would be no significant difference between the real intersection intensity and the theoretical intersection intensity ($P'_L = P_L$). Therefore, a significant difference between the theoretical value of intersection intensity P_L and the observed intersection intensity P'_L would indicate that the rupture ran predominantly across the reticular fibers or interlobular septa ($P'_L > P_L$) or along the reticular fibers or interlobular septa ($P'_L < P_L$).



2.5. Statistical analysis

The data were processed using Statistica Base 10 (StatSoft, Inc., Tulsa, OK, USA). The normality of the data was tested using the Shapiro–Wilk W -test. All the statistical tests were non-parametric methods, because some data sets did not pass the normality test. To assess the differences among the impact groups, we used the Kruskal–Wallis

Table 1. Morphometric data on pigs and livers.

Impact height (mm)/ impact velocity (m s^{-1})	Sex	Age (weeks)	Pig weight (kg)	Liver weight (kg)	Liver width (mm)	Liver height (mm)	Liver depth (mm)
200/1.74	Female	14	30	1.570	300	216	33
200/1.70	Female	16	25	1.328	278	208	50
200/1.72	Female	16	35	1.636	299	224	47
200/1.74	Male	14	27	1.472	274	241	35
200/1.70	Male	14	24	1.192	267	222	40
200/1.71	Male	14	24.5	1.232	296	216	38
300/2.15	Male	17	28.5	1.336	264	219	47
300/2.16	Male	15	27.2	1.278	298	285	45
300/2.20	Female	15	29.6	1.348	288	240	33
300/2.17	Male	15	36	1.394	280	250	45
300/2.20	Male	16	34.2	1.112	283	208	33
300/2.14	Female	16	37.8	1.400	283	220	37
400/2.52	Female	17	42.8	1.446	273	224	43
400/2.56	Male	15	28.5	1.054	247	226	41
400/2.50	Male	16	33	1.252	257	232	39
400/2.62	Male	16	37	1.650	315	245	40
400/2.51	Male	16	41.5	2.044	287	265	55
400/2.50	Female	16	39.4	1.492	265	275	38
500/2.89	Male	15	36.5	1.030	240	194	37
500/2.92	Male	15	28	1.070	256	184	35
500/2.85	Male	15	25.5	1.108	246	198	40
500/2.84	Male	15	25	1.060	244	191	43
500/2.95	Male	16	37.7	1.572	307	248	40
500/2.86	Male	16	35	1.700	283	235	55

ANOVA test. To compare the paired values of real intersection intensity (P'_L) and theoretical intersection intensity (P_L), we used the Wilcoxon signed-rank test. The level of significance was 0.05.

3. Results

3.1. Liver samples

The livers were collected from 24 Prestice Black-Pied pigs aged 14–17 weeks and weighing 24–42.8 kg (31.9 ± 5.6 kg, mean \pm standard deviation [SD]). Seventeen piglets were neutered male and seven female. The fresh liver weight ranged from 1.030 to 2.044 kg (1.364 ± 0.24 kg, mean \pm standard deviation [SD]) (table 1). None of the specimens had signs of microscopic injury such as inflammatory infiltration or fibrosis.

3.2. Impact test

3.2.1. Greater impact velocity (heights) resulted in increased maximal intravascular pressure accompanied by more severe injury.

The impact plate hit less than a half or about a half of the liver in all cases, figure 2(A). There was an increasing trend of maximal pressure related to the impact velocity, but it did not reach the level of significance, figure 2(B). The impact energies (given by liver height and by plate position measured by laser, figure 2(C)) increased with impact velocity. The higher impact velocity led to more severe injury, figure 2(D, E). The linear regression analysis of the AIS severity and injury grade is shown in figure 2(F). These two parameters are interchangeable. The regression analysis of AIS severity and maximal pressure, and impact energy is shown in figure 3(A), and 3(B), respectively. The results are summarized in table 2 and shown in figure 2. Complete primary biomechanical data are available as supplement S2.

3.3. Macroscopic injury analysis

3.3.1. Ruptures affected mostly the interface between connective tissue surrounding big vessels and liver parenchyma

The major injuries affected the visceral surface of the liver as shown in figure 4. Ruptures propagated from the hilum along big vessels and were mostly located in the left lateral (figure 4(A)) and right medial lobes (figure 4(B)). The depth of the lacerations and contused parenchyma differed among experimental groups as well as among livers within the groups. The injury grade was based both on the length and on the depth of the ruptures. Most severe injuries were found in the group with impact velocity 2.88 m s^{-1} (impact height 500 mm)

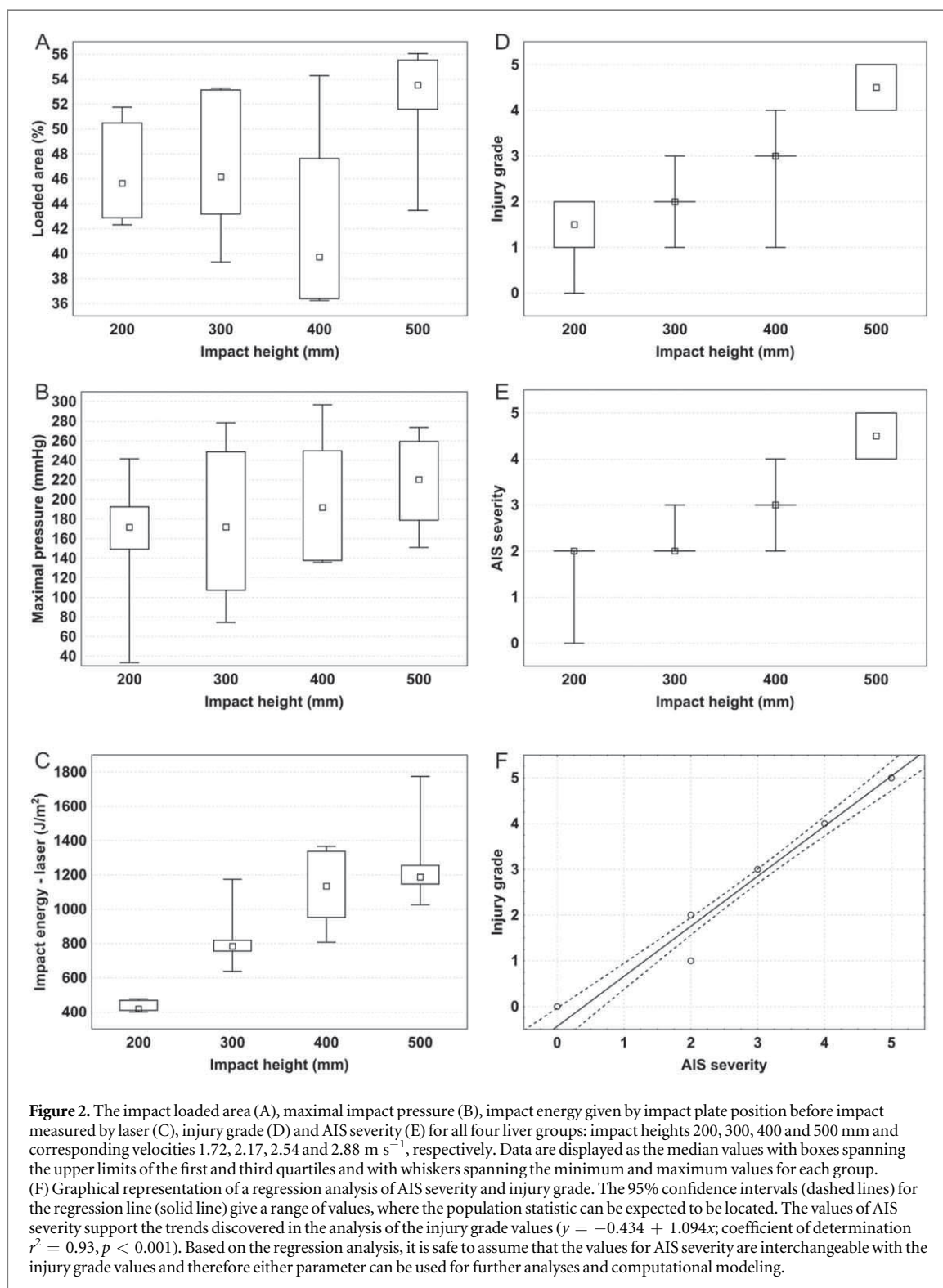


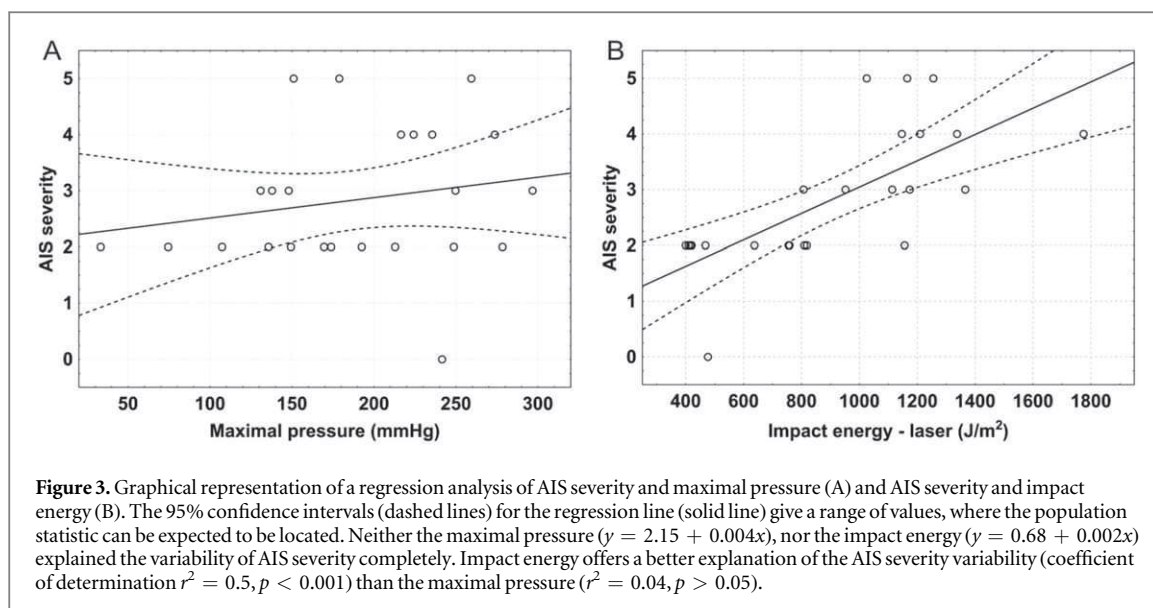
Figure 2. The impact loaded area (A), maximal impact pressure (B), impact energy given by impact plate position before impact measured by laser (C), injury grade (D) and AIS severity (E) for all four liver groups: impact heights 200, 300, 400 and 500 mm and corresponding velocities 1.72, 2.17, 2.54 and 2.88 m s^{-1} , respectively. Data are displayed as the median values with boxes spanning the upper limits of the first and third quartiles and with whiskers spanning the minimum and maximum values for each group. (F) Graphical representation of a regression analysis of AIS severity and injury grade. The 95% confidence intervals (dashed lines) for the regression line (solid line) give a range of values, where the population statistic can be expected to be located. The values of AIS severity support the trends discovered in the analysis of the injury grade values ($y = -0.434 + 1.094x$; coefficient of determination $r^2 = 0.93$, $p < 0.001$). Based on the regression analysis, it is safe to assume that the values for AIS severity are interchangeable with the injury grade values and therefore either parameter can be used for further analyses and computational modeling.

(table 2). In some cases, the ruptures were located on the periphery of the lobe (figure 4(C)) and, occasionally, we found small lacerations on the diaphragmatic surface of the liver (figure 4(D)).

3.4. Microscopic injury analysis

3.4.1. The ruptures avoided reticular fibers and interlobular septa on the microscopic level

The real intersection intensity P'_L was smaller than the theoretical intersection intensity P_L for both the reticular fibers and for the interlobular septa (Wilcoxon signed-rank test, $p < 0.001$) (figure 5). The ruptures thus did not



propagate randomly through the liver parenchyma but predominantly ran along the reticular fibers and interlobular septa avoiding intersections with reticular fibers and interlobular septa.

4. Discussion

This study on porcine liver injury focused on description of the tissue damage and the biomechanical behavior of liver tissue. We combined an impact approach using a drop tower technique, while registering the changes of intravascular pressure in portal vein and caudate vena cava. Our mechanical data focused on the internal fluid pressure changes in impact situations. Even though the liver tissue damage in car crashes is the consequence of both deceleration and impact (Cheynel *et al* 2009), the sole impact approach allowed us to exclude the influence of the deceleration on the biomechanical behavior and to study the effect of impact alone. A similar approach, albeit, by simulating the deceleration injury alone has already been used in studies by Cheynel *et al* (2006, 2009) and by Arnoux *et al* (2008). Such experiments provide data that can be used for validation of the computational models of liver injury.

The finite element method (FEM)-based models of liver are mostly based on the detailed geometry of the real liver. Our study showed that the ruptures were spreading around the vascular branches, thus the vascular tree should be included in the FEM models because of its important contribution to the injury mechanism.

Another factor that should be taken into account in the models is the increased inner liver pressure caused by impact loading. High pressure levels can cause ruptures adjacent to the vascular trees. These ruptures propagate along the reticular fibers and interlobular connective tissue septa as shown in our study.

Our results are further suitable for validation of impact test results in terms of the impact energy and velocity threshold. The impact velocities and the impact energies used in the impact tests in our study should lead to the same injury levels also when used in the simulated impact tests with HBMs. An impact velocity of 1.72 m s^{-1} with impact energy 418 J m^{-2} leads to low injury grade (0–II) and AIS severity (0–2), while the higher impact velocity (energy) caused the injury connected with large blood outflow. An impact velocity higher than 2.88 m s^{-1} , related to an impact energy higher than 1187 J m^{-2} , leads to total disruption of the liver. Also the internal liver pressure in the HBMs should be the same as during our impact test. Note that the high levels of pressure could also lead to the artery or internal structures ruptures.

A recent study by Chen *et al* (2019) provided detailed data on material behavior of porcine liver during high strain rate compression. However, their measurements were performed on tissue samples separated from the whole liver, thus excluding the effect of the fibrous capsule on the biomechanical behavior. It was proven that the content of connective tissue influenced the stiffness of the liver tissue (Mazza *et al* 2007). Neglecting the influence of the capsule could result in significant differences when assessing the biomechanical behavior of the liver parenchyma (Hollenstein *et al* 2006). The test on tissue samples provided us only with information on local material properties. Moreover, the proposed study design using samples of liver tissue cannot be used for studying the relation of internal fluid pressure changes on the impact injury. As previously described, rapid increase in internal fluid pressure is related to the severity of liver injury on the whole organ level (Sparks *et al* 2008). Therefore

Table 2. The impact loaded area, maximal impact pressure, impact velocity, impact energy (given by position of the plate before the impact) measured by laser and given by liver height respectively, AAST injury grade and AIS severity for all four liver groups: impact height 200, 300, 400 and 500 mm. *N* is the number of specimens. The values of impact velocity are presented as mean values. The values of loaded area, maximal vascular pressure and impact energy are presented as medians (lower quartile–upper quartile).

Impact height (mm)	Impact velocity (m s ⁻¹)	Loaded area (%)	Maximal vascular pressure (mmHg)	Impact energy—laser (J m ⁻²)	Impact energy—height (J m ⁻²)	AAST injury grade/AIS severity	<i>N</i>
200	1.72	45.65 (42.88–50.48)	171.69 (149.35–192.52)	418.00 (409.55–467.87)	450.00 (446.57–485.07)	0–II/0–2	6
300	2.17	46.17 (43.17–53.14)	174.85 (107.34–248.69)	783.97 (755.30–818.35)	850.31 (813.06–876.81)	I–III/2–3	6
400	2.54	39.73 (36.40–47.64)	191.77 (137.85–249.69)	1134.79 (952.00–1337.62)	1239.53 (976.22–1435.52)	I–IV/2–4	6
500	2.88	53.53 (51.89–55.54)	220.35 (178.85–259.36)	1187.47 (1146.72–1255.55)	1305.18 (1224.52–1347.71)	IV–V/4–5	6

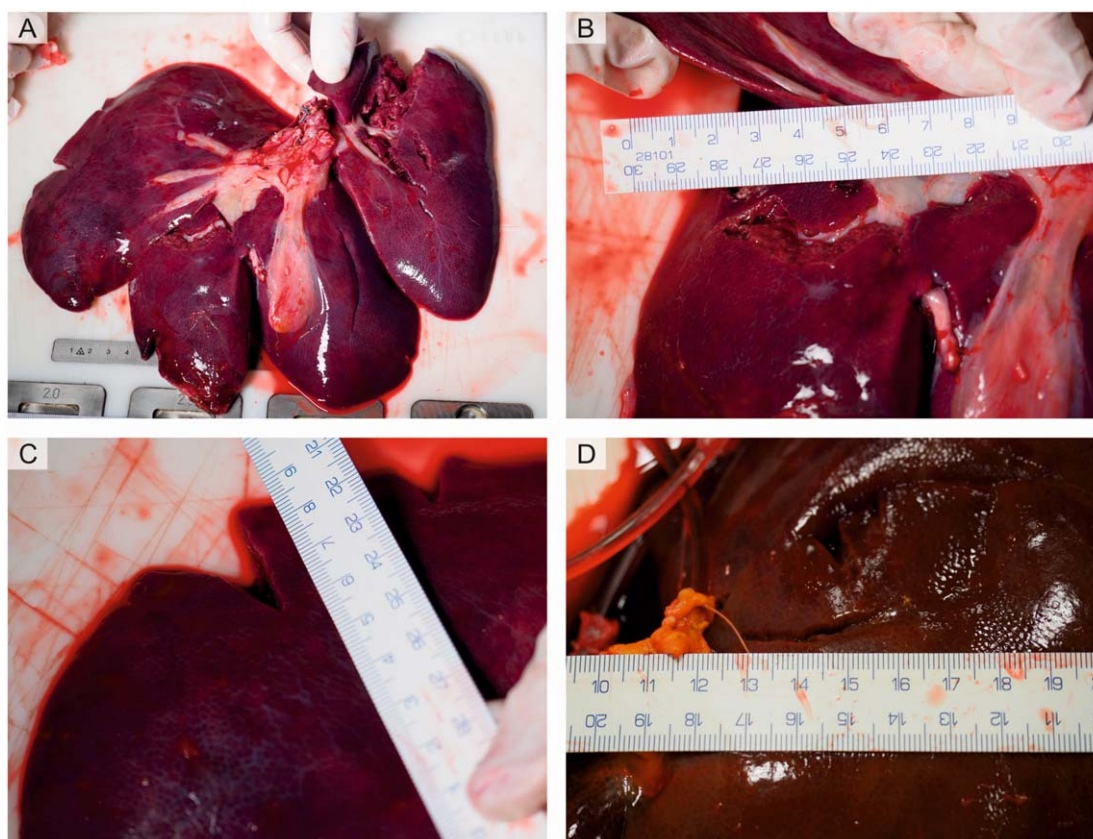


Figure 4. Typical external injury patterns of the porcine liver after the impact test. (A) Laceration of the visceral surface of the liver affecting more than half of the left lateral lobe, injury grade V. (B) Rupture of the visceral surface of the right medial lobe that propagates from the hilum along the big vessels and the stromal connective tissue. (C) Peripheral rupture starting at the border of the right hepatic lobe. (D) Occasional shallow rupture on the diaphragmatic surface of the liver, most likely caused by the direct impact of the wood plate used in the impact test.

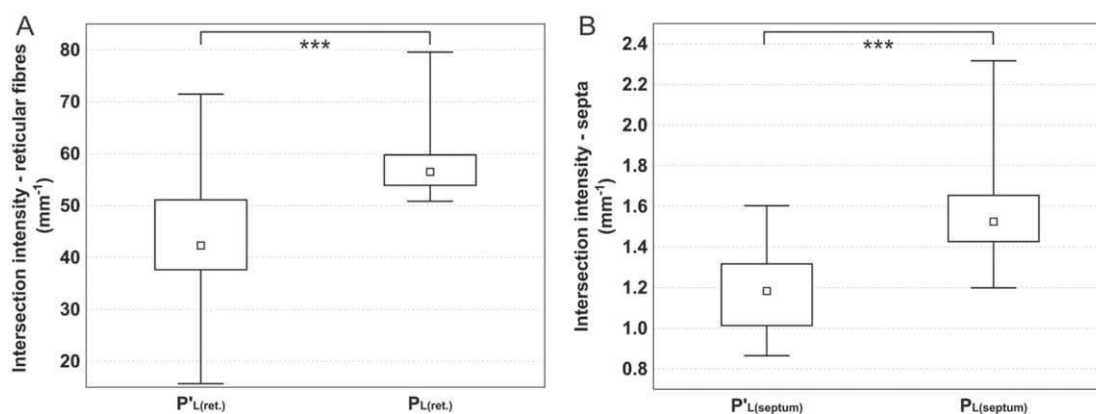


Figure 5. Results of microscopic injury analysis. The Wilcoxon signed-rank test showed statistically significant differences between the real intersection intensity of the reticular fibers $P^L_{(ret.)} = 42$ (38–51) mm^{-1} ; median (lower quartile–upper quartile) and the theoretical intersection intensity of the reticular fibers $P_{L(ret.)} = 57$ (54–60) mm^{-1} ; median (lower quartile–upper quartile), ($p < 0.001$). Significant differences were also found between the real intersection intensity of the interlobular septa ($P^L_{(septum)} = 1.2$ (1–1.3) mm^{-1} ; median (lower quartile–upper quartile) and the theoretical intersection intensity of the interlobular septa $P_{L(septum)} = 1.5$ (1.4–1.7) mm^{-1} , median (lower quartile–upper quartile), ($p < 0.001$). Data are displayed as the median values with boxes spanning the upper limits of the first and third quartiles and with whiskers spanning the minimum and maximum values for each group.

experiments on whole porcine liver are a necessary source of data on liver behavior from the pressure changes point of view.

The whole liver was also used in experiments with human organs. Conte *et al* (2012) investigated macroscopic damage of human liver in a uniaxial compression test. The macroscopic injury consisted mostly of

lacerations of the right lobe. In some cases the lacerations originated in close proximity to the big vessels and propagated along the connective tissue, which was in concordance with the macroscopic injury pattern in our study. Occasional lacerations of the liver diaphragmatic surface found in our study were mostly caused by the setting of the experiment. The diaphragmatic surface was exposed to the direct impact of the wooden plate, which did not correspond to the injury mechanism *in vivo*.

The multiscale analysis by Conte *et al* (2012) also included histological analysis of the damaged tissue. The microscopic injury patterns presented in human liver tissue were described as ‘cracking’ and ‘cavitation’ that appeared to propagate within the hepatic lobules. According to this analysis the cracks’ origin appeared to be located at the interface between the vessel wall and the parenchyma. Their data, however, did not clearly answer how the tissue damage spread in the context of liver microstructure, namely in the context of the fibrous components of the connective tissue matrix.

Our histological quantitative analysis based on stereological methods revealed that the ruptures did not propagate randomly through the liver parenchyma, but rather followed a pattern that was closely related to the tissue microstructure. The weak link of the tissue appeared to be the interface between the reticular fibers and the hepatocytes arranged into trabeculae, as ruptures crossing the reticular fibers were statistically proven to be less likely to occur than ruptures propagating along the above-mentioned interface. Moreover, the interlobular septa that are composed of connective tissue also seemed to represent a strong border that ruptures did not cross.

The components of the extracellular connective tissue matrix, such as collagen III in reticular fibers, influence the response of the organ to mechanical stimuli. Collagen is a rather stiff and hard protein whereas cells on the other hand tend to respond to mechanical stimuli in various ways (Meyers *et al* 2008). The cell rigidity is dependent on its environment, including cell–extracellular matrix interactions. The difference in microscopic structures of porcine and human liver therefore needs to be taken into consideration when extrapolating data from experiments on porcine organs to the human model.

Based on our study and works focused on the macro- and micro-structure of liver, there are three main differences between human and porcine liver that are important for the mathematical modeling. The microstructure of porcine liver is organized into only roughly hexagonal hepatic lobules, while the microstructure of human liver is organized into regular hexagonal hepatic lobules. This difference is important for the mathematical models based on the microstructure. The second main difference is the shape of the whole liver (Ntonas *et al* 2020). The shape of porcine liver is lobular and thick in the centre, becoming thinner at the perimeter of the organ, while human liver has a triangular prism shape, and the size decreases from right to left. Both human and porcine livers consist of sinister, dexter, quadrate, and caudate lobes. Because of the more lobular shape of the porcine liver, the sinister and dexter lobes are each divided into lateral and medial lobes. The arterial vascular system in both humans and pigs have the same structure. The portal veins of the species have minor differences. In human, the division of the portal vein occurs outside the liver parenchyma, while in pigs, it occurs at the hilum. The third difference is the amount of connective tissue, which is significantly higher in pigs compared to humans (Mik *et al* 2018). One of the main aims of our study was to find connection between the impact energy and the range of injury. The results are based on the porcine liver, but the level of injury, the rupture around veins and the rupture spreading should be similar for both species due to similarities in the tissue structure (however, this claim is yet to be verified).

Velocity is recognized to be a critical factor in evaluating the possibility of abdominal organ injuries. According to Brasel and Nirula (2005) the probability of abdominal injury significantly increases at velocity $>20 \text{ km h}^{-1}$. However, in our study, relatively low velocities of the impact plates at the moment of impact still led to severe liver injury. This was probably caused by the absence of the protective effect of the rib cage and of the abdominal wall. Despite this limitation, the analysis showed an increasing trend of maximal pressure related to the impact height and impact velocities, which supported the view that the severity of injury was dependent on the impact energy. The highest loaded velocity (impact height) caused the most severe lacerations.

5. Conclusion

Using an experimental impact approach, this study provides a multiscale analysis of the mechanism of porcine liver injury that gives an accurate description of damage evolution which can also be applied to human liver tissue. Biomechanical behavior of porcine tissue, namely changes in intravascular pressure, was coupled with analysis of rupture propagation on both the macroscopic and microscopic level. The microscopic analysis proved that connective tissue containing reticular fibers influenced the rupture propagation through liver. The pattern of rupture propagation, with regards to differences in the amount of connective tissue in porcine and human liver, should be especially considered when extrapolating data from animal experiments to the human model. The present findings can be used to improve (by incorporating the vascular tree) and validate computational models of liver behavior in impact situations.

Acknowledgments

This study was supported by the LO1506 (PK) provided by the Ministry of Education, Youth and Sports of the Czech Republic, by the Charles University Research Fund (Progres Q39) (AM), by Charles University Project number SVV 260 536 (AM) and GAUK 1098120 (AM), by the Centre of Clinical and Experimental Liver Surgery UNCE/MED/006 (AM, RP, VL, PM), by University of West Bohemia Project number SGS-2019-002 'Computer modelling and monitoring of human body used for medicine' (TB) and by European Regional Development Fund-Project, Application of Modern Technologies in Medicine and Industry' (No. CZ.02.1.01/0.0/0.0/17_048/0007280) (PK, RP, VL, PM, ZT).

Authorship

Study design, literature search, data analysis, data interpretation, and writing—AM, PK, ZT, animal care—RP, VL, histology—AM, PM, ZT, biomechanical measurements—PK, TB, MH, critical revision—ZT, VL, PM.

Disclosure

The authors declare no conflicts of interest.

References

- Arnoux P J, Serre T, Cheynel N, Thollon L, Behr M, Baque P and Brunet C 2008 Liver injuries in frontal crash situations a coupled numerical—experimental approach *Comput. Methods Biomech. Biomed. Engin.* **11** 189–203
- Augenstein J, Bowen J, Perdeck E, Singer M, Stratton J, Horton T, Rao A, Digges K H, Malliaris A C and Steps J 1999 Injury patterns in near-side collisions *Annu. Proc. Assoc. Adv. Automot. Med.* **43** 139–58 (PMCID: [PMC3400216](https://pubmed.ncbi.nlm.nih.gov/3400216/))
- Behr M, Arnoux P J, Serre T, Bidal S, Kang H S, Thollon L, Cavallero C, Kayvantash K and Brunet C 2003 A human model for road safety: from geometrical acquisition to model validation with radioss *Comput. Methods Biomech. Biomed. Engin.* **6** 263–73
- Brasel K J and Nirula R 2005 What mechanism justifies abdominal evaluation in motor vehicle crashes? *J. Trauma* **59** 1057–61
- Chen J, Brazile B, Prabhu R, Patnaik S S, Bertucci R, Rhee H, Horstemeyer M F, Hong Y, Williams L N and Liao J 2018 Quantitative analysis of tissue damage evolution in porcine liver with interrupted mechanical testing under tension, compression, and shear *J. Biomech. Eng.* **140** 0710101–07101010
- Chen J, Patnaik S S, Prabhu R K, Priddy L B, Bouvard J L, Marin E, Horstemeyer M F, Liao J and Williams L N 2019 Mechanical response of porcine liver tissue under high strain rate compression *Bioengineering (Basel)* **6** 49
- Cheynel N, Serre T, Arnoux P J, Baque P, Benoit L, Berdah S V and Brunet C 2006 Biomechanic study of the human liver during a frontal deceleration *J. Trauma* **61** 855–61
- Cheynel N, Serre T, Arnoux P J, Ortega-Deballon P, Benoit L and Brunet C 2009 Comparison of the biomechanical behavior of the liver during frontal and lateral deceleration *J. Trauma* **67** 40–4
- Conte C, Garcia S, Arnoux P J and Masson C 2012 Experimental multiscale analysis of liver damage and failure process under compression *J. Trauma Acute Care Surg.* **72** 727–32
- Doklešić K et al 2015 Surgical management of AAST grades III–V hepatic trauma by damage control surgery with perihepatic packing and definitive hepatic repair—single centre experience *World J. Emerg. Surg.* **10** 34
- Eberlova L et al 2016 Porcine liver vascular bed in Biodur E20 corrosion casts *Folia Morphol. (Warsz)* **75** 154–61
- Eberlova L, Malečková A, Mik P, Tonar Z, Jirik M, Mirka H, Palek R, Leupen S and Liska V 2020 Porcine liver anatomy applied to biomedicine *J. Surg. Res.* **250** 70–9
- Elhagediab A and Rouhana S 1998 Patterns of abdominal injury in frontal automotive crashes *The 16 Int. Technical Conf. on the Enhanced Safety of Vehicles*
- Gayzik F S, Moreno D P, Geer C P, Wuertzer S D, Martin R S and Stitzel J D 2011 Development of a full body CAD dataset for computational modeling: a multi-modality approach *Ann. Biomed. Eng.* **39** 2568–83
- Golman A J, Danelson K A, Miller L E and Stitzel J D 2014 Injury prediction in a side impact crash using human body model simulation *Accid. Anal. Prev.* **3** 1–8
- Holbrook T L, Hoyt D B, Eastman A B, Sise M J, Kennedy F, Velky T, Conroy C, Pacyna S and Erwin S 2007 The impact of safety belt use on liver injuries in motor vehicle crashes: the importance of motor vehicle safety systems *J. Trauma* **63** 300–6
- Hollenstein M, Nava A, Valtorta D, Snedeker J G and Mazza E 2006 Mechanical characterization of the liver capsule and parenchyma *ISBMS 2006: Biomedical Simulation (Lecture Notes in Computer Science vol 4072)* ed M Harders and G Székely (Berlin: Springer) (https://doi.org/10.1007/11790273_17)
- Huelke D F, Nusholtz G S and Kaiker P S 1986 Use of quadruped models in thoraco-abdominal biomechanics research *J. Biomech.* **19** 969–77
- Junatas K L, Tonar Z, Kubíková T, Liška V, Pálek R, Mik P, Králíčková M and Witter K 2017 Stereological analysis of size and density of hepatocytes in the porcine liver *J. Anat.* **230** 575–88
- Kemper A R, Santiago A C, Stitzel J D, Sparks J L and Duma S M 2010 Biomechanical response of human liver in tensile loading *Ann. Adv. Automot. Med.* **54** 15–26 (PMID: [21050588](https://pubmed.ncbi.nlm.nih.gov/21050588/))
- King A I and Yang K H 1995 Research in biomechanics of occupant protection *J. Trauma* **38** 570–6
- Kozar R A, Crandall M, Shanmuganathan K, Zarzaur B L, Coburn M, Cribari C, Kaups K, Schuster K, Tominaga G T and AAST Patient Assessment Committee 2018 Organ injury scaling 2018 update: spleen, liver, and kidney [published correction appears in *J. Trauma Acute Care Surg.* 2019 Aug;87(2):512] *J. Trauma Acute Care Surg.* **85** 1119–22
- Kruepunga N, Hakvoort T B M, Hikspoors J P J M, Köhler S E and Lamers W H 2019 Anatomy of rodent and human livers: what are the differences? *Biochim. Biophys. Acta, Mol. Basis Dis.* **1865** 869–78

- Kubíková T, Kochová P, Brázdil J, Špatenka J, Burkert J, Králíčková M and Tonar Z 2017 The composition and biomechanical properties of human cryopreserved aortas, pulmonary trunks, and aortic and pulmonary cusps *Ann. Anat.* **212** 17–26
- Lee J B and Yang K H 2001 Development of a finite element model of the human abdomen *Stapp Car Crash J.* **11** 79–100
- Malečková A et al 2019 Animal models of liver diseases and their application in experimental surgery *Rozhl Chir.* **98** 100–9
- Marchesseau S, Chatelin S and Delingette H 2017 Non linear biomechanical model of the liver: hyperelastic constitutive laws for finite element modeling *Biomechanics of Living Organs* ed Y Payan and J Ohayon (Cambridge: Academic)
- Mazza E, Nava A, Hahnloser D, Jochum W and Bajka M 2007 The mechanical response of human liver and its relation to histology: an *in vivo* study *Med. Image Anal.* **11** 663–72
- Melvin J, Stalnaker R, Roberts V and Trollope M 1973 Impact injury mechanisms in abdominal organs *Proc. 17th Stapp Car Crash Conf.* (Warrendale, PA: Society of Automotive Engineers) pp 115–26
- Meyers M A, Chen P Y, Lin A Y M and Seki Y 2008 Biological materials: structure and mechanical properties *Prog. Mater. Sci.* **53** 1–206
- Mik P et al 2018 Distribution of connective tissue in the male and female porcine liver: histological mapping and recommendations for sampling *J. Comp. Pathol.* **162** 1–13
- Monchal T, Ndiaye A, Gadegebeku B, Javouhey E and Monneuse O 2018 Abdominopelvic injuries due to road traffic accidents: characteristics in a registry of 162 695 victims *Traffic Inj. Prev.* **19** 529–34
- Moore E E et al 1989 Organ injury scaling: spleen, liver, and kidney *J. Trauma* **29** 1664–6
- Ntonas A, Katsourakis A, Galanis N, Filo E and Noussios G 2020 Comparative anatomical study between the human and swine liver and its importance in xenotransplantation *Cureus* **12** e9411
- Santago A C, Kemper A R, McNally C, Sparks J L and Duma S M 2009 The effect of temperature on the mechanical properties of bovine liver —biomed 2009 *Biomed. Sci. Instrum.* **45** 376–81 (PMID: 19369792)
- Sparks J L, Bolte J H 4th, Dupaix R B, Jones K H, Steinberg S M, Herriott R G, Stammen J A and Donnelly B R 2007 Using pressure to predict liver injury risk from blunt impact *Stapp Car Crash J.* **51** 401–32 (PMID: 18278606)
- Sparks J L and Dupaix R B 2008 Constitutive modeling of rate-dependent stress-strain behavior of human liver in blunt impact loading *Ann. Biomed. Eng.* **36** 1883–92
- Sparks J L, Stammen J, Herriott R and Jones K 2008 Development of a fluid-filled catheter system for dynamic pressure measurement in soft-tissue trauma *Int. J. Crashworthiness* **13** 255–64
- Stoyan D, Kendall W S and Mecke J 1995 *Stochastic Geometry and its Applications* 2nd edn (New York: Wiley)
- Schoell S L, Weaver A A, Urban J E, Jones D A, Stitzel J D, Hwang E, Reed M P, Rupp J D and Hu J 2015 Development and validation of an older occupant finite element model of a mid-sized male for investigation of age-related injury risk *Stapp Car Crash J.* **11** 359–83 (PMID: 26660751)
- Schwartz D, Guleyupoglu B, Koya B, Stitzel J D and Gayzik F S 2015 Development of a computationally efficient full human body finite element model *Traffic Inj. Prev.* **16** S49–56
- Tamura A, Omori K, Miki K, Lee J B, Yang K H and King A I 2002 Mechanical characterization of porcine abdominal organs *Stapp Car Crash J.* **11** 55–69 (PMID: 17096218)
- Tonar Z, Janáček J, Nedorost L, Grill R, Báca V and Zátura F 2009 Analysis of microcracks caused by drop shatter testing of porcine kidneys *Ann. Anat.* **191** 294–308
- Tropiano P, Thollon L, Arnoux P J, Huang R C, Kayvantash K, Poitout D G and Brunet C 2004 Using a finite element model to evaluate human injuries application to the HUMOS model in whiplash situation *Spine (Phila Pa 1976)* **29** 1709–16
- Untaroiu C D, Lu Y C, Siripurapu S K and Kemper A R 2015 Modeling the biomechanical and injury response of human liver parenchyma under tensile loading *J. Mech. Behav. Biomed. Mater.* **41** 280–91
- Vrtkova I 2015 Genetic admixture analysis in Prestice Black-Pied pigs *Arch. Anim. Breed.* **58** 115–21
- Vyčítal O, Horský O, Rosendorf J, Liška V, Skalický T and Třeška V 2019 Treatment of liver injuries at the Trauma Centre of the University Hospital in Pilsen *Rozhl Chir.* **98** 488–91
- Wang B C, Wang G R, Yan D H and Liu Y P 1992 An experimental study on biomechanical properties of hepatic tissue using a new measuring method *Biomed. Mater. Eng.* **2** 133–8
- World Health Organization 2018 Road traffic injuries *World Road Safety Global Status Report on Road Safety* (<https://who.int/news-room/fact-sheets/detail/road-traffic-injuries>) (accessed 8 June 2020)
- Xu T, Sheng X, Zhang T, Liu H, Liang X and Ding A 2018 Development and validation of dummies and human models used in crash test *Appl. Bionics Biomech.* **38** 32850